Hybrid Atom-Optomechanical System in the Quantum Regime

Inauguraldissertation

zur
Erlangung der Würde eines Doktors der Philosophie
vorgelegt der
Philosophisch-Naturwissenschaftlichen Fakultät
der Universität Basel

von

Gian-Luca Schmid

2026

Genehmigt von der Philosophisch-Naturwissenschaftlichen Fakultät
auf Antrag von

Erstbetreuer:	Prof. Dr. Philipp Treutlein
Zweitbetreuer:	Prof. Dr. Patrick Maletinsky
Externer Experte:	Prof. Dr. Witlef Wieczorek

Basel, den 19. November 2024

Prof. Dr. Marcel Mayor
Dekan

Abstract

This thesis reports on light-mediated coupling between the collective spin of a cold atomic ensemble and a mechanical oscillator. In our experiments, we engineer coherent interactions between these distinct systems over a macroscopic distance of 2 metres. Thus, the system presented in this work establishes a versatile platform for implementing *remote*, *coherent*, and *hybrid* quantum mechanical coupling experiments.

Achieving quantum coherent coupling between the systems will enable the execution of quantum protocols on this platform, such as quantum state swaps or entanglement generation. Quantum coherent coupling is possible when both the atomic spin and the mechanical oscillator interact with light with high cooperativity and their noise is limited by quantum backaction noise rather than thermal or technical noise. The first part of this thesis presents a series of improvements and characterisation measurements of both systems, demonstrating that in the current setup both systems operate in the regime of large quantum cooperativity.

Our first system is the collective spin of dipole-trapped cold Rubidium atoms, a well-established platform in quantum optics with a large toolbox for quantum initialisation and manipulation. This thesis presents a theoretical and experimental characterisation of the Faraday spin-light interface, extending beyond the simplified one-dimensional model of two-level atoms. We find that for the relevant experimental parameters, the spin-light interaction is limited by quantum backaction noise and exhibits large cooperativity.

Our second system is a nanomechanical membrane oscillator placed in an optical cavity. Nanomechanical membranes are macroscopic systems that can act as sensitive force sensors. In this work, the optomechanical system is upgraded by exchanging the membrane oscillator; replacing the previously used membrane with a phononic bandgap shield by a state-of-the-art nano-pillar membrane that has a mechanical Q-factor of 5.1×10^7. With this enhancement and operation at cryogenic temperatures we experimentally demonstrate that the membrane-light interface enters the regime of high quantum cooperativity, showing cooling to the quantum backaction noise limit and ponderomotive squeezing of the light.

In a first series of hybrid coupling experiments, strong coupling between the two systems is used to demonstrate coherent cooling of the mechanical oscillator with the atomic spin. The setup can be understood as a coherent feedback platform where the atomic spin acts as the controller. By leveraging the full control provided by the hybrid system, we perform spin-membrane state swaps, combined with stroboscopic spin pumping, to cool the membrane in a room-temperature environment to $T = 216\,\mathrm{mK}$ ($\bar{n}_m = 2.3 \times 10^3$ phonons) in $200\,\mu\mathrm{s}$.

The high cooperativity of the interaction of each system with light theoretically enables quantum coherent coupling of the two systems. Preliminary experiments demonstrate strong coupling between the

systems at cryogenic temperatures, which has not been achieved in previous work. Future experiments can leverage this coupling to demonstrate quantum coherent control, e.g. by inducing entanglement between the two systems through coherent parametric-gain interactions.

Contents

Introduction

As science and technology advance, increasingly specialised tools are developed to tackle specific problems. A single tool may be sufficient for simple tasks, but complex challenges often require the integration of multiple tools. Such a hybrid approach is essential to solve more complicated tasks. The same applies in quantum science: Quantum technologies have seen an impressive progress, leading to the development of numerous individual systems performing very well in one specific task [1]. For instance, photons can be used to transmit quantum information over long distances [2, 3], spins serve as precise magnetometers [4, 5] or atomic clocks [6], and mechanical oscillators are very precise force sensors [7, 8]. However, many real-world problems require quantum devices that can combine different functionalities, making hybrid quantum systems particularly intriguing [9]. By combining quantum systems with complementary functionalities, hybrid systems can leverage the strengths and mitigate the weaknesses of individual components [9, 10, 11].

Different hybrid quantum systems have been proposed and developed [9, 10, 11]. Hybrid systems containing a mechanical oscillator and spins are of particular interest because of the complementary nature of the systems [11]. Mechanical oscillators are linear systems that serve as high-precision force sensors [7, 8], responding to various forces [11, 12], while spins are nonlinear at the quantum level and benefit from a well-established toolbox for quantum state initialisation and manipulation [13]. Furthermore, the coupling of a macroscopic and a microscopic system is of fundamental interest for exploring the limits of quantum mechanics. Hybrid spin-mechanical systems take various forms:

There have been some major efforts to couple mechanical oscillators to solid state spins [10]. Single colour centres in diamond have been coupled to nanowires via external magnetic fields [14] and to cantilevers via mechanical strain [15, 16]. The aim of these experiments is to not only cool the vibrational state of the mechanical oscillator, but also to prepare non-classical states. So far, this level of quantum control has not been achieved due to the limited coupling strength. Nevertheless, the mechanical motion of a cantilever has been used to manipulate the spin state of a diamond nitrogen-vacancy (NV) centre, thereby avoiding the complicated gate structures and stray fields associated with microwave driving fields [17]. In conceptually very similar experiments, quantum dots have been coupled to nanowires, allowing the system to be integrated into GaAs-semiconductors [18, 19].

For most mechanical systems, one of the main limitations in achieving quantum control is thermal decoherence. To achieve low phonon occupation of the thermal bath, the thermal energy must be low compared to the single quantum energy of the system $k_{\mathrm{B}}T < hf$, which is more easily achieved for nanoscale resonators at gigahertz frequencies (cantilevers and nanowires typically have kHz frequencies). Ground-state cooling of such a gigahertz mechanical oscillator in a dilution refrigerator has been demon-

strated by coupling it to a superconducting qubit mediated by a microwave cavity [20, 21] or by direct electrostatic interactions [22].

The high degree of quantum control of atoms [13] makes them a very promising system for coupling to a mechanical system [11, 23]. In early experiments, the spin of an ensemble of atoms in a vapour cell was manipulated using a magnetised cantilever [24]. Furthermore, the centre-of-mass motion of atoms in an optical lattice was coupled to the vibrations of a nanomechanical oscillator [25, 26, 27, 28]. More recently, we coupled the collective spin of a cold atomic cloud strongly to a nanomechanical oscillator [29, 30]. The measurement backaction on the membrane was evaded by interfacing the membrane with the collective spin of an atomic ensemble in a vapour cell [31]. In another experiment, entanglement between the spin and the membrane has been demonstrated by measuring the light after a cascaded interactions with the systems [32].

The degree of control in a hybrid system depends on the coupling strength between the systems. In most of the implementations of hybrid systems cited above [14, 15, 16, 17, 18, 19, 24] the coupling between the individual systems is weak. Strong coupling is achieved when the coupling rate between the spin and the mechanical oscillator exceeds the mean linewidth of the individual systems [33]. In the strong coupling regime, a classical state can be coherently swapped between the systems at a faster rate than it decays. For quantum-mechanical control of the hybrid system, a more stringent requirement must be met: in the quantum coherent regime, the coupling rate exceeds the total decoherence rate of the hybrid system [34, 35]. This total decoherence rate encompasses all interactions with the environment, including thermal excitations driving the individual systems and measurement decoherence when the systems are open to the environment [36, 37]. Quantum coherent coupling has been achieved for hybrid systems consisting of superconducting qubits and nanomechanical oscillators [20, 21, 22], for which low phonon occupation numbers of the environment can be achieved at cryogenic temperatures due to the gigahertz frequencies of the systems.

Different coupling mechanism have been explored to realise hybrid spin-mechanical systems. Coherent interactions between quantum systems are typically generated either by short-range interactions such as mechanical strain [15, 16, 17, 18, 19], magnetic fields [14, 24, 38], or capacitive coupling [22], or they are mediated by a cavity field [20, 21]. All of these coupling mechanisms limit the distance between the systems strongly, due to their unfavourable scaling (e.g. for magnetic coupling) or stability criteria that are difficult to meet for large distances (e.g. for cavities). However, coupling two systems *remotely* is interesting from both a fundamental and technical point of view: Quantum coherent coupling can generate entanglement over a long distance, which can be a resource for quantum information tasks or for experiments on quantum foundations. Technologically, having separate access to each system allows for independent manipulation of each system, so that one system can be steered by manipulating the other [39]. The simplest way to couple two remote systems is to use light, as photons are an excellent carrier of quantum information [40], facilitating communication over long distances. In recent years, various quantum systems have been entangled over long distances using light including cold atomic ensembles [41, 42], single atoms [43, 44], electronic spins in diamond NV-colour centres [45, 46], and single ions [47]. In all of these experiments, entanglement is induced by measurement or by entanglement swapping [41, 42, 43, 44, 45, 46, 47] rather than by a coherent interaction between the systems. However, it is very appealing to combine coherent interaction in a hybrid system with long-range coupling. To achieve this,

it has been theoretically proposed that hybrid Hamiltonian interactions can be engineered by coupling individual systems at different positions to a one-dimensional waveguide [36] or a free-space laser beam [37].

Coupling systems to a propagating light field presents several challenges: The electromagnetic field is subject to quantum shot noise, which drives the coupled systems stochastically. Moreover, information about the systems imprinted on the light leaks out to the environment. This leakage leads to backaction noise on the individual systems. For a coherent light-mediated interaction, the backaction noise of the light on the systems must be suppressed; otherwise, the decoherence induced by the measurement backaction exceeds the coherent interaction [37]. The suppression of backaction noise can be achieved in different ways: For example, a decoherence-free quantum mechanical subspace can be created, which is a particular subspace of the total Hilbert space that is less sensitive to decoherence due to the destructive interference of the dissipative environment [36]. Alternatively, one can consider the theory of cascaded quantum systems with multiple interactions per system. For backaction evasion, the second interaction with each system must be engineered as the time-reversal of the first one, leading to a cancellation of the information about the system on the light field [37]. Both descriptions imply that each system must be coupled multiple times to the propagating field in order to suppress the decoherence associated with the quantum shot noise of that field [36, 37]. Experimental implementations of Hamiltonian interactions mediated by an a propagating light field are scarce: At microwave frequencies Kannan et al. [48] strongly coupled two superconducting qubits by interfacing them with a microwave waveguide. In order to obtain a coherent interaction, each qubit is interfaced two times. The phase of each interaction is engineered to suppress the backaction of the microwave field on both systems. More recently, Wang et al. [49] demonstrated strong coupling between two magnonic spins using a similar coupling geometry. At optical frequencies, our group has pioneered experiments on coherent light-mediated interaction [29, 30]. Using light to mediate remote coupling not only enables for the coupling of similar systems (as demonstrated in [48, 49]), but also allows the engineering of hybrid quantum systems from any set of systems with a light-matter interface [37].

In our experiment, we aim to remotely couple atomic spins and a mechanical membrane in the quantum coherent regime. In our group in Basel, light-mediated interactions between cold atoms and optomechanical membranes have been realised in various forms: The coupling between the centre-of-mass motion of atoms in an optical lattice and a nanomechanical membrane has been demonstrated [25, 26], which was used for sympathetic cooling of the membrane oscillator [27]. In a similar experiment in Hamburg, sympathetic cooling was used to cool the membrane close to the mechanical ground state [28]. However, in both implementations, the atom-membrane coupling did not reach the strong coupling regime. By increasing the number of atoms in the lattice, collective atom-membrane motion with instabilities was observed in the coupled system [50]. The coupling of the membrane to the centre-of-mass motion of the atoms is limited by the sub-megahertz trap frequencies of optical lattices, at which conventional lasers are not shot-noise-limited but the noise is dominated by technical laser noise. Furthermore, the quantum control of the centre-of-mass motion of thermal atomic ensembles is difficult to establish [51].

In this thesis, the next generation experiment is presented, in which the membrane oscillator is coupled to the internal atomic state. In a breakthrough experiment, strong coupling between the atomic spin and the membrane oscillator has been achieved [29]. Following on that, this work explores the path towards

quantum coherent coupling between the membrane oscillator and the spin system and the use of this coupling for coherent feedback control.

Coupling the mechanical oscillator to the collective spin instead of the centre-of-mass motion has several advantages: The collective spin of laser-cooled atomic clouds is a well-established platform in quantum optics, with a large toolbox available to initialise and manipulate the collective spin [13, 52]. Therefore, the collective atomic spin is chosen as the first quantum system for this work. The atomic spin can interact with light in the quantum non-demolition interaction [13]. This interaction is based on the Faraday effect, which causes polarisation rotation of the light even in a dilute atomic ensemble [53]. We use the Faraday interaction to couple the collective spin of the atoms to the light.

The second quantum system in this thesis is a nanofabricated silicon nitride membrane embedded in an optical cavity [54]. Nanofabricated optomechanical devices have evolved significantly in recent years [12]. In the last 15 years, the quality factor of strained mechanical resonators has increased by four orders of magnitude [55]. Advances in nanofabrication have allowed the fabrication of structured devices with high aspect ratios and the creation of so-called *soft-clamped* membranes with excellent quality factors of $Q_\mathrm{m} > 10^8$ [56]. This made it possible to ground state cool a membrane using measurement-based feedback [57], to perform continuous force and displacement measurements below the standard quantum limit [58], and to use the membrane as a memory for light [59] or as a transducer between optical and microwave frequencies [60]. Moreover, membranes are a promising platform for sensitive force measurements [61, 62]. The interaction of the light with quantum cooperativities exceeding unity has been achieved in a cryogenic environment [57] and more recently even at room temperature [63], allowing the integration of membranes in a quantum limited light-mediated interaction. In the course of this work, a new soft-clamped membrane has been implemented in the hybrid system, allowing quantum control of the mechanical system.

Despite the differences between the collective spin of an atomic ensemble and the nanofabricated membrane, their interaction with light shows striking similarities: the mechanical oscillator couples to the the light field via radiation pressure, an interaction that can be understood as Raman transitions between two successive vibrational Fock states. Similarly, the spin-light interaction can be described as Raman transitions between two Zeeman states within the same hyperfine manifold, driven by the off-resonant, two-photon Faraday interaction. When the atoms are well polarised parallel or anti-parallel to the magnetic field, their collective spin can be approximated as a harmonic oscillator [13]. The oscillation frequency of the *spin-oscillator* can be tuned by changing the magnetic field, thus bringing it into resonance with the mechanical oscillator.

Experiments in Copenhagen have demonstrated entanglement between atomic spins in a vapour cell and a membrane, based on a measurement-based, cascaded interaction [32]. In contrast, in our experiment we use light to mediate a Hamiltonian coupling between the collective spin of a cold, dipole-trapped ensemble of Rubidium atoms and a nanofabricated membrane. In this setup, the light interacts first with the spin, then with the membrane and finally with the spin again. This configuration allows for bidirectional coupling and the cancellation of the backaction of the light on the spin in the second interaction [29, 37]. In a series of experiments, we have demonstrated strong coupling between the two oscillators in a room temperature environment [29].

This hybrid strong coupling has been used to implement coherent feedback. Similar to measurement-based feedback which is commonly implemented in many applications, coherent feedback stabilises a system towards a target state [39, 64]. In coherent feedback, however, the feedback is applied by another quantum system, avoiding measurement and the associated decoherence [39]. In our experiment,

we employ optical coherent feedback to remotely cool a nanomechanical membrane oscillator using the collective spin of an atomic ensemble as a controller [30]. We have also extended such schemes to realise an optical coherent feedback loop [65].

For a quantum coherent coupling between the membrane oscillator and the spin system, both oscillators must have a quantum limited coupling to the light (i.e. a cooperativity larger than unity $C_i > 1$). This work describes the optimisation and characterisation of both the membrane and the spin system. It is shown that we can indeed measure a large cooperativity for both systems. Preliminary coupling results between the two improved systems are presented showing strong coupling between the two systems and opening up the prospect of quantum coherent coupling of the systems in the current experimental configuration.

This thesis is structured in the following way:

- In chapter 1, the preparation of a dense, dipole trapped cloud of cold atoms with a high optical depth is described. The collective spin of the atomic cloud is polarised by optical pumping. This collective spin serves as starting point for further experiments.

- Chapter 2 describes the quantum spin-light interface. The Faraday interaction is introduced both, in a simplified one-dimensional picture and then in a more realistic three-dimensional model. The spin can be manipulated by rf-pulses and classical polarisation modulations of the probe light, which is shown both theoretically and experimentally. Finally, the characterisation of the spin ensemble is given, which is crucial to understand the hybrid experiments.

- Chapter 3 shows the quantum optomechanical interface. For the hybrid experiments, two different membranes were used. In this chapter, the characterisation of both of them are shown. One of them is cooled to the cavity cooling limit and could be used to squeeze the light by 1.5 dB.

- Chapter 4 describes how the Hamiltonian coupling between the spin and the membrane is engineered. Starting from the theory of cascaded quantum systems, the coupling Hamiltonian of the hybrid system is derived. In a second part of chapter 4, the experimental implementation of the coupling loop is discussed and some calibration measurements are presented.

- In chapter 5 the coupling is used to implement a coherent feedback loop. Direct time-controlled manipulation of the spins allows to tune the spin-membrane interaction from strong coupling to the overdamped regime. Using a stroboscopic cooling sequence, the cooling rate can be increased by a factor of two, which is used to cool the membrane in a room-temperature environment to 216 mK (2.3×10^3 phonons) in 200 µs. Furthermore, the effect of feedback delay is observed and studied, that is inherent to the macroscopic distance between the system and the controller. The results of this chapter are published in [30].

- In chapter 6 first coupling experiments between the two improved systems are presented. Strong coupling between the membrane and the spin is achieved both at room temperature and at a cryostate temperature of 60 K. With the membrane cryogenically cooled to 10 K, we should see quantum coherent coupling between the two systems.

Chapter 1

Dipole-Trapped Cold Atoms with High Optical Density

In our atom-membrane coupling experiments, we use the collective spin of a cold atomic cloud as one of the quantum systems. Thus, a key aspect of these experiments is preparing a dense atomic cloud in a specific internal atomic state. This chapter details the preparation of a cold, dipole-trapped atomic ensemble with a peak optical density of 1500. The atomic ensemble is mode-matched to the coupling beam used for the hybrid experiments. Further, the collective spin of the cloud is initialised by optical spin pumping. The preparation process involves the following steps: first, the atoms are cooled in a magneto-optical trap (MOT). Then, the cold atoms are transferred to a dipole trap. Finally, the spin of the atoms is polarised by optical pumping. The setup for cooling, trapping, and spin pumping is described in detail here. The resulting atomic cloud is characterised by absorption imaging and rf-spectroscopy.

1.1 Preparation of the Atomic Cloud

In the hybrid experiment, we couple the mechanical membrane to the collective spin of a cold atomic ensemble using light. To achieve strong coupling between the membrane and the spin, the spin-light-interaction must be strong. The collective spin is interfaced with light through a dispersive interaction, more precisely the Faraday interaction. The relevant parameter for the strength of this interaction is the optical density of the spin ensemble. The dispersive spin-light interaction is described in detail in chapter 2. This chapter details the experimental setup and sequence that allows us to achieve a well-polarised spin ensemble with a large optical density.

The starting point for the experiments is the preparation of a cold atomic ensemble in an optical dipole trap. Once in the trap, the atomic system is initialised by polarising the atomic spins, creating a collective spin. Such preparation requires a high vacuum, several lasers and magnetic coils, a schematic of which is shown in figure 1.1.1. The setup has been developed over many years and is largely described in some previous works [66, 67, 68, 69]. In the course of this work, parts of the experimental setup have been rebuilt or modified and will be described in the following sections:

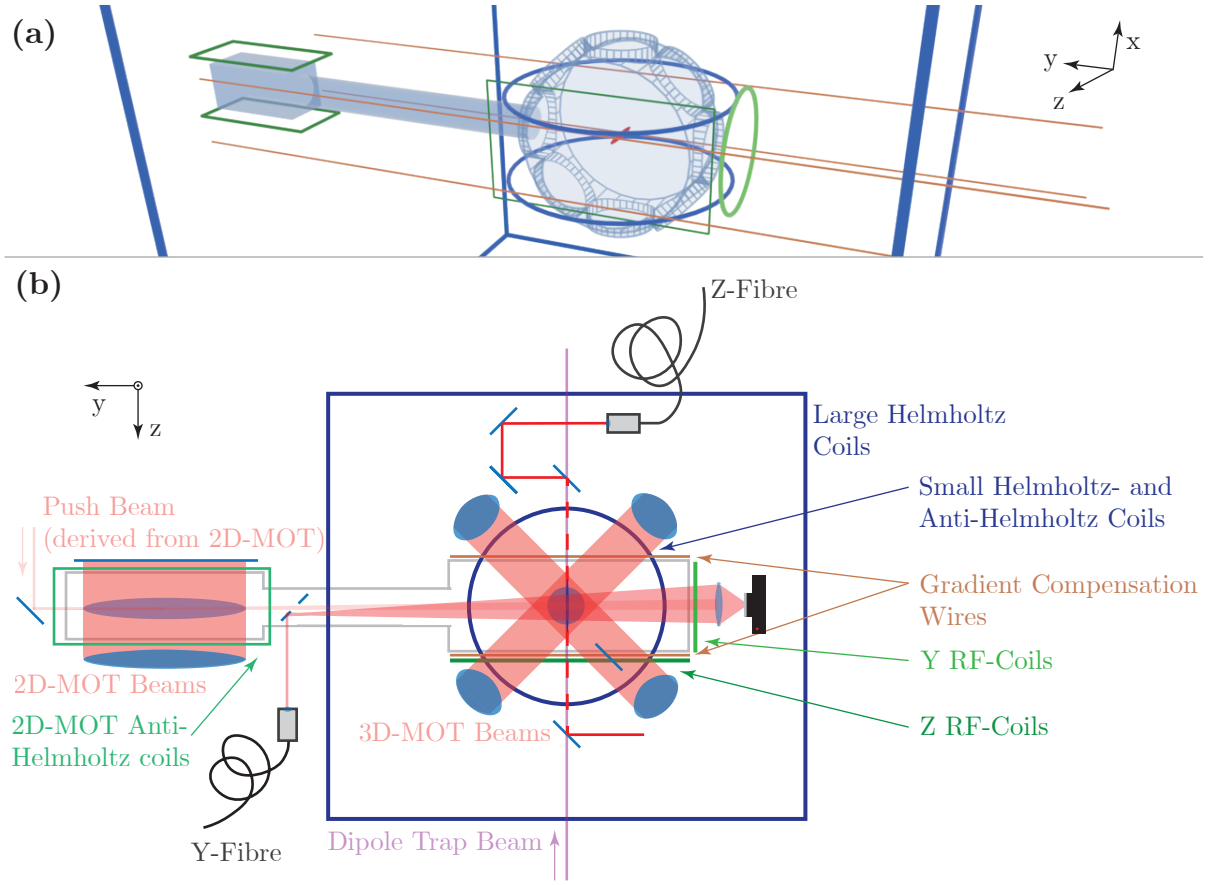

Figure 1.1.1: (a) a 3D-render and (b) a schematic of the atomic chamber: The 2D-MOT chamber is shown on the left. There, the atoms are cooled and confined in two dimension using two beams (which are retro-reflected on mirrors) and a pair of coils in anti-Helmholtz configuration. From the 2D-MOT chamber, the atoms are pushed by a beam to the main atom chamber. In the main chamber, the atoms are manipulated and controlled by different beams. In this figure, the beams propagating along the x-axis are not shown (i.e. two MOT beams and the beam coming from the X-fibre). The magnetic field is controlled by several coils and wires shown here.

The cold atom apparatus consists of two chambers: The science chamber is an octagonal glass cell[1] with two large side windows. The atoms are loaded from a second cuboidal chamber which is connected to the science chamber by a small differential pumping tube [66]. A pressure of $p < 4 \times 10^{-11}$mbar is maintained by a ion pump[2] and a titanium sublimation pump[3] [66]. For the cooling, detection and optical pumping of the atoms, diode lasers are used which are specifically locked to atomic transitions and switched and frequency controlled by acousto-optical modulators (AOM). The laser setup for cooling, detection and optical pumping was completely rebuilt during this work and is described in section 1.2. During the hybrid experiment, the atomic spin precesses in a bias magnetic field, which defines the frequency of the *spin-oscillator*. Thus, the homogeneity and stability of the magnetic field in our experiment strongly affect the precision of the final experiments. Therefore, the magnetic field at the atomic position is actively stabilised as described in [68, 69]. The implementation of the various coils and wires and the basic idea of the feedback circuit, are discussed in section 1.3. The timed computer control system is described in section 1.4. In section 1.5, the different laser-cooling and trapping stages are described. The cooling sequence is very similar and largely inspired by that described in [67]. After laser cooling, the atoms are transferred into an optical dipole trap. The atoms are trapped at the focus of a far red-detuned, high-power commercial laser. The original setup of this laser system is described in [70] and was modified during this work. The modifications and the current atomic cloud geometry are described in the section 1.6. As a final preparation step, the dipole-trapped atoms are spin-polarised, which is described in section 1.7.

1.2 Setup for Cooling, Pumping and Detection Lasers

In our experiment, we work with Rubidium-87 (^{87}Rb) atoms. The ^{87}Rb is an alkali atom with a nuclear spin $i = 3/2$. Thus, the $^2S_{1/2}$ ground state splits into the $F = 1, 2$ hyperfine manifolds. In the experiments, we only use beams at the $D2$-line of ^{87}Rb, which is the $^2S_{1/2} \leftrightarrow {}^2P_{3/2}$ transition at a wavelength of 780 nm. The $D2$-line of ^{87}Rb has a cycling transition which is very convenient for laser cooling and absorption imaging of the atoms.

Cooling, detecting and spin-pumping rubidium atoms require multiple laser beams at different frequencies. In our experiment, atoms are cooled in a MOT, transferred in a far-detuned dipole trap [70] and then spin-polarised to the $|F = 2, m_F = -2\rangle$ state. Loading a MOT requires cooling light near the $F = 2 \leftrightarrow F' = 3$ transition and repumping light at the $F = 1 \leftrightarrow F' = 2$ transition. In addition, a laser at the $F = 2 \leftrightarrow F' = 2$ transition is required to spin polarise the atoms through optical pumping. In this section we present the setup that provides all these beams.

As shown in figure 1.1.1, the atomic cloud is prepared in two different vacuum chambers: The 2D-MOT chamber [71] and the science chamber, where the 3D-MOT and the dipole trap are loaded. Therefore, we need two beams with cooling and repumping light for both the 2D-MOT and the 3D-MOT. To prepare the internal state of the atoms once they are in the trap, we also want to have two beams (along two different axis) containing light for spin polarising the atoms in the $F = 2$ manifold to the $|F = 2, m_F = -2\rangle$ state (called *22-pump*) and light to repump the atoms from $F = 1 \rightarrow F = 2$ (called *repump*). Furthermore, these two beams should contain light at the $F = 2 \leftrightarrow F' = 3$ transition for absorption imaging along two different axes. An overview of all the fibres and the light in these fibres is given in table 1.2 and figure

[1] Presicion Glassblowing: anit-reflection coated mirrors for 0° on both sides
[2] Varian/Agilent VacIon Plus 40 starcell
[3] Agilent Titanium Sublimation Cartridge

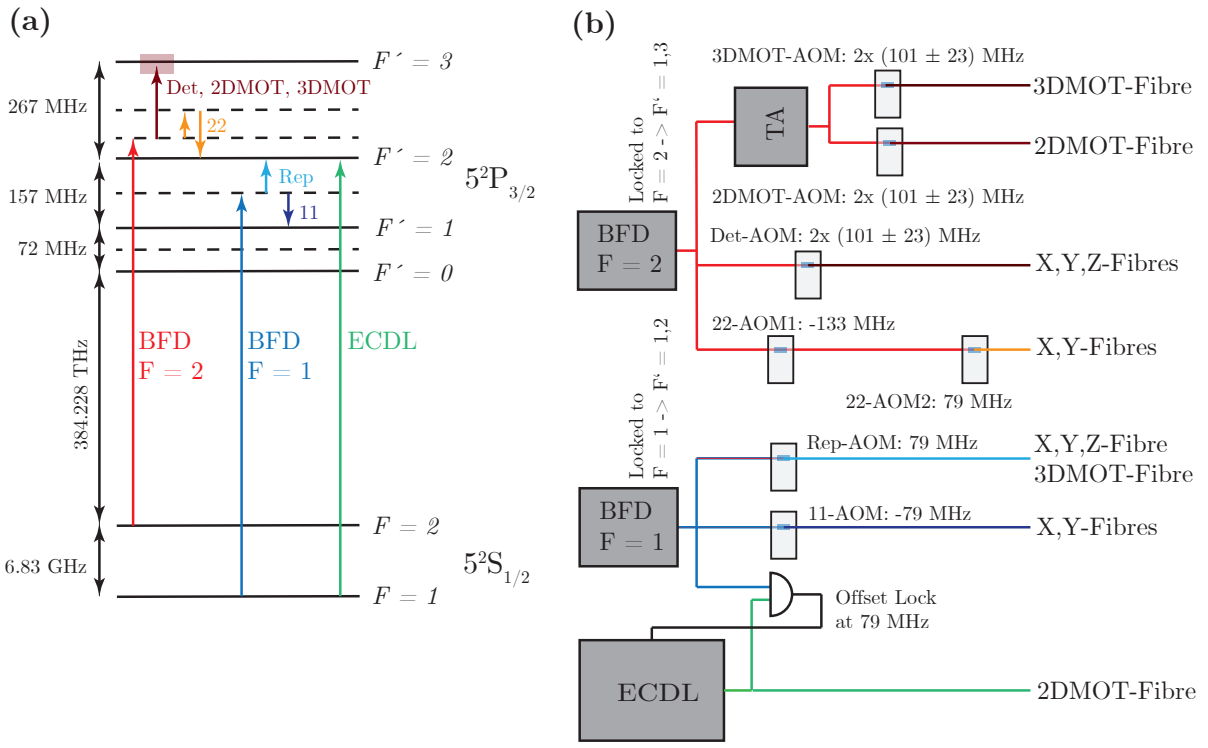

Figure 1.2.1: Overview of the locking and shifting of laser frequencies: (a) shows the levels of the Rubidium-87 D2-line (not to scale) and the laser frequencies of the three lasers (*BFD F=2*, *BFD F=1*, and *ECDL*). The frequency shifts by the AOMs are indicated by arrows. (b) shows again all three lasers and all AOM with the corresponding frequencies. The 3D-MOT-, 2D-MOT- and Det-AOM are in double-pass configuration with a frequency which can be changed during the sequence. On the right, it is labelled in which fibres a certain branch is coupled. A sketch of the full laser setup is shown in figure 1.2.2.

1.2.1. The light for these transitions comes from three lasers. In the following, all three lasers and the setup to control the laser frequencies are introduced.

Butterfly Diode Laser: The splitting between the different hyperfine states in the $^2P_{3/2}$ excited state manifold of the Rubidium-87 D2 line is in the range of hundreds of MHz and can be addressed by a single laser by shifting its frequency with AOMs. The ground state hyperfine splitting on the other hand is 6.8 GHz. So we use two different butterfly diode (BFD) lasers[4] and multiple AOMs to cover the required frequency range. The BFDs have a linewidth of about 1 MHz, well below the linewidth of the Rubidium D2 line of $\gamma_{\mathrm{Rb}} = 2\pi \times 6.1\,\mathrm{MHz}$. Very conveniently, the BFDs have a mode-hop free tuning range that is larger than the ground state hyperfine splitting of Rubidium, so that they can be scanned over the full spectrum (without fine-tuning the laser temperature and current). The BFDs are driven by digital controllers[5] with two analogue modulation inputs for the current (one for AC and one for DC modulation).

Both BFD lasers are frequency locked using Doppler-free saturation spectroscopy. Using AOMs, the

[4]Freespace butterfly laser diodes from *Toptica, Eagleyard*; central wavelength: 780 nm; Specified line width: 0.6 MHz (measured linewidth is slightly worse than the specified value for all tested diodes); Mode-hop free tuning range: 25 pm; Maximum optical power: 80 mW

[5]Digital Laser Controller *CTL200-1-B-200* from *Koheron* with a maximum current of 225 mA

light is frequency-shifted to the required frequency and can be switched. The different frequencies are shown in figure 1.2.1 (a), a general overview of all beams is shown in figure 1.2.1 (b) and a detailed sketch of the laser setup in figure 1.2.2.

Laser for $F = 2$ Manifold: The first BFD (labelled as BFD, $F = 2$) is locked to the Rubidium transition between the $F = 2$ hyperfine ground state and the crossover between the $F' = 1$ and the $F' = 3$ hyperfine excited states (at 384.227 855 THz). The light from this laser is split into two parts: approximately half of the light (35 mW) is used for the absorption imaging and the 22-pump beam, while the remaining half (25 mW) is used to seed a tapered amplifier[6] (TA) providing the required power for the cooling beams. The 3 W output from the TA is then divided into the cooling beams of the 3D-MOT and the 2D-MOT. Each cooling beam passes through a separate double-pass AOM (each pass at 101 ± 23MHz) to chirp their detuning relative to the $F = 2 \leftrightarrow F' = 3$ transition during the sequence, ranging from $-9.2\,\gamma_{\mathrm{Rb}}$ to $5.9\,\gamma_{\mathrm{Rb}}$. These beams are combined with a repump beam and coupled into a fibre, yielding 220 mW of cooling light for the 3D-MOT and 300 mW of cooling light for the 2D-MOT. The frequency of the detection beam is shifted using a double pass AOM (with a tunable range of 101 ± 23MHz) allowing frequency scanning relative to the $F = 2 \leftrightarrow F' = 3$ transition. The 22-pump light passes through two different AOMs: First it is shifted by -133 MHz and then by 79 MHz so that the light has the frequency of the $F = 2 \leftrightarrow F' = 2$ transition (at 384.227 838 THz).

Laser for $F = 1$ Manifold: The second BFD laser (labelled in figure 1.2.1 and 1.2.2 as *BFD, F=1*) is locked to the Rubidium-87 transition between the $F = 1$ hyperfine ground state and the crossover between the $F' = 1$ and the $F' = 2$ hyperfine excited states (at 384.234 658 THz) by Doppler-free spectroscopy. The laser is divided into three parts: most of the light is used as a repump laser. For this, the laser is frequency shifted by 79 MHz to resonance with the $F = 1 \leftrightarrow F' = 2$ transition with an AOM. A small portion of the light can potentially spin-polarise the atoms in the $F = 1$ hyperfine ground state to the $|F = 1, m_F = -1\rangle$ state, although this is not currently utilised in our experimental sequence (this beam is labelled as *11-pump*). For the light to be resonant with the $F = 1 \leftrightarrow F' = 1$ transition, it is shifted by -79 MHz by an AOM. An additional fraction of the light is employed to lock a second repump laser with a frequency offset lock at 79 MHz (see below for more details).

The repump beam is further divided into different laser beams: the majority of it is combined with the cooling light of the 3D-MOT and used during MOT loading. A fraction is combined with the 22-pump, 11-pump, and detection beams, all of which are coupled into two fibres for imaging and spin preparation along the axes X and Y. The repump, 11-pump, 22-pump and detection beams are combined using three 50:50 beam splitters before being coupled into fibres. The remaining light from the unused ports of two of the beam splitters is coupled into a third imaging/pumping fibre to probe the atomic cloud along the Z axis. Currently, the setup allows either the 11-pump and 22-pump beams or the repump and detection beams to be coupled to this fibre.

Third Laser as Additional Repump: To maximise the number of atoms, we recognised the benefit of increasing repump power beyond what one butterfly diode can provide. Consequently, we implemented a home-built external cavity diode laser (ECDL) operating at the frequency of the $F = 1 \leftrightarrow F' = 2$ transition. This second laser is locked to the second BFD ($F = 1$) via a frequency offset lock.

[6] As TA, we use the amplifier stage of a *TA pro - 780* from *Toptica*

fibre	beams	transition	source	AOMs	shutters
3DMOT	Cool	$F = 2 \leftrightarrow F' = 3^*$	BFD F=2, TA	3DMOT-AOM	3DMOT-Shut
	Repump	$F = 1 \leftrightarrow F' = 2$	BFD F=1	Rep-AOM	RepMid-Shut
2DMOT	Cool	$F = 2 \leftrightarrow F' = 3^*$	BFD F=2, TA	2DMOT-AOM	2DMOT-Shut
	Repump	$F = 1 \leftrightarrow F' = 2$	ECDL	no AOM	2DMOT-Shut
X	Detection	$F = 2 \leftrightarrow F' = 3^*$	BFD F=2	Det-AOM	Det-Shut, X-Shut
	22-pump	$F = 2 \leftrightarrow F' = 2$	BFD F=2	22-AOM1, 22-AOM2	22-Shut, X-Shut
	Repump	$F = 1 \leftrightarrow F' = 2$	BFD F=1	Rep-AOM	Rep-Shut, X-Shut
	11-pump	$F = 1 \leftrightarrow F' = 1$	BFD F=1	11-AOM	11-Shut, X-Shut
Y	Detection	$F = 2 \leftrightarrow F' = 3^*$	BFD F=2	Det-AOM	Det-Shut, Y-Shut
	22-pump	$F = 2 \leftrightarrow F' = 2$	BFD F=2	22-AOM1, 22-AOM2	22-Shut, Y-Shut
	Repump	$F = 1 \leftrightarrow F' = 2$	BFD F=1	Rep-AOM	Rep-Shut, Y-Shut
	11-pump	$F = 1 \leftrightarrow F' = 1$	BFD F=1	11-AOM	11-Shut, Y-Shut
Z	Detection	$F = 2 \leftrightarrow F' = 3^*$	BFD F=2	Det-AOM	Det-Shut, Z-Shut
	Repump	$F = 1 \leftrightarrow F' = 2$	BFD F=1	Rep-AOM	Rep-Shut, Z-Shut
	or				
	22-pump	$F = 2 \leftrightarrow F' = 3^*$	BFD F=2	22-AOM1, 22-AOM2	22-Shut, Z-Shut
	11-pump	$F = 1 \leftrightarrow F' = 1$	BFD F=1	11-AOM	11-Shut, Z-Shut

Table 1.2.1: Which beams are in which fibre. The AOMs for the cooling beams (both, 3D-MOT and 2D-MOT) and the detection beam are in a double-pass configuration. Therefore, their frequency is adjustable during the sequence, which is marked with an asterisk (*) in this table.

Phase-Locked Loop: The offset lock is implemented as a phase-locked loop (for detailed technical specification, see appendix A), akin to the lock outlined in [72]. The light from both the *ECDL* and the *BFD F=1* laser is combined using a fibre-coupled beam splitter and detected with a photodiode[7]. The AC component of the photodiode signal serves as the input for an evaluation board[8]. The *ADF4002* chip on the evaluation board features a programmable reference divider which can be used to compare the beat note frequency against a reference frequency. We have modified the evaluation board to output either 0 V or 5 V depending on whether the beat note frequency is higher or lower than the reference frequency. A buffer circuit is used to shift this 0 V to 5 V modulation to -1 V to 1 V, which acts as the error signal for a PI lock implemented on a *Red Pitaya* using the *PyRPL* interface detailed in [73]. The offset lock is set to 79 MHz so that the *ECDL* operates at the $F = 1 \leftrightarrow F' = 2$ transition. The ECDL light is combined with the 2D-MOT cooling light.

1.2.1 Some Considerations for a Next Generation Laser Setup

The laser setup for cooling, pumping and detection currently relies on free-space optics on an optical table. For the next generation of setups, consideration should be given to construct a predominantly fibre-based laser system. In this sub-section, a proposal for a largely fibre-based laser setup is outlined:

One laser needs to be stabilized to atomic spectroscopy or a stable reference laser available in-house [74] to lock all other fibre-coupled BFD lasers via frequency offset locks using phase-locked loops. The offset frequencies of these locks could be adjusted dynamically during experiments, enabling frequency ramps without requiring AOMs. For laser power control and on/off switching, semiconductor optical

[7] *Thorlabs, PDA10A2*: bandwidth of $f_{\mathrm{bw}} = 150$ MHz
[8] *Analog Devices, EVAL-ADF4002*

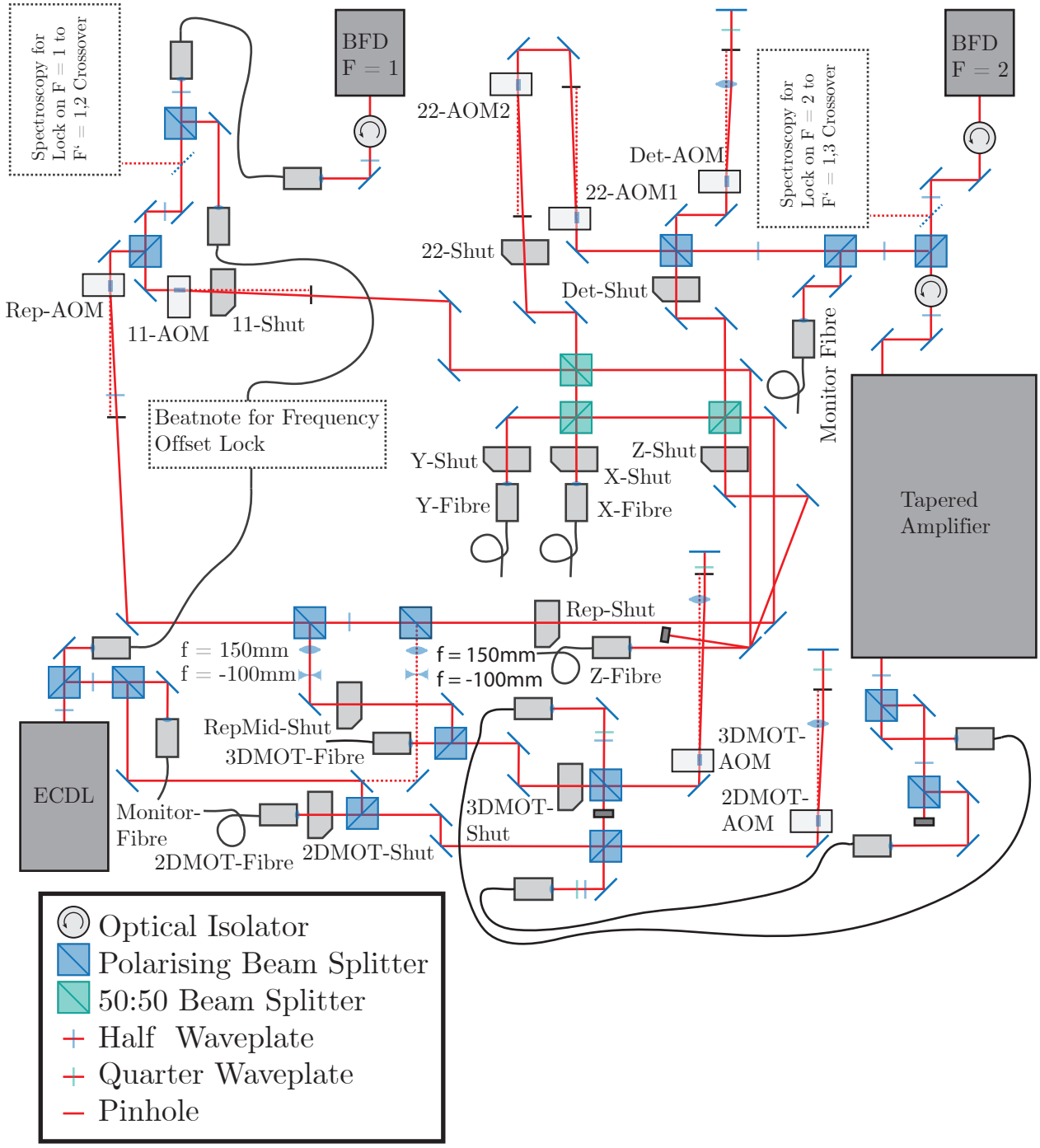

Figure 1.2.2: Scheme of the laser preparation setup. Details are given in the main text.

amplifiers[9] (SOAs) could be employed (as utilised for example in [75]). By cutting off the current supply to the SOA, all light is absorbed in the semiconductor (suppression of $> -75\,\mathrm{dB}$ [76, 77], which is for an input power of $200\,\mu\mathrm{W}$, an output of $< 6.3 \times 10^{-12}\mathrm{W}$). The SOAs serve as switches with high extinction ratios [76], and in conjunction with detuning the laser far from resonance, they potentially eliminate the need for mechanical optical shutters for some beams[10]. SOAs are fully fibre-coupled and can deliver up to 20 mW of optical power. For the cooling beams with higher power requirements, a fibre-coupled TA[11] could be implemented. Similarly to the SOA, current modulation of the TA can be used to regulate or switch the output light power [76]. For the output of the TA, mechanical shutters are required to turn off the light effectively. The output of the fible-coupled TA is free-space and has to be coupled in a fibre again, preferably using fibres terminated with end-caps because of the high optical power[12]. The laser beams could be combined using fibre-based beam splitters (though an alternative solution might be needed for high-power cooling light, given that the damage thresholds of standard fibre couplers is about 300 mW). This approach enables generation of light at various frequencies and power levels for optical cooling, manipulation, and detection, with minimal free-space elements, potentially enhancing the flexibility of the setup for new experiments.

1.3 Magnetic Fields

The magnetic field at the position of the atoms is controlled using various coils and wires, as depicted in figure 1.1.1. Some of the coils are used during the laser cooling stages, while others compensate for stray magnetic fields and establish a bias field for spin manipulation during hybrid experiments. In our experiment, different current sources drive these coils and wires to set the desired magnetic field for the atoms. The stability and noise characteristics of these current sources are crucial for ensuring the reliability and reproducibility of our experiments. The characterisation of several of these current sources is presented here. Additionally, a third subsection introduces the active compensation of magnetic stray fields in our experiment.

1.3.1 Coils and Wires

2D-MOT Anti-Helmholtz Coils: Before transferring the Rubidium atoms to the main experimental chamber, they are loaded and cooled in a 2D-MOT [66, 71]. The 2D-MOT employs a pair of rectangular coils with dimensions $11.45\,\mathrm{cm} \times 4.45\,\mathrm{cm}$ and a relative distance of 7.8 cm. Having $N = 112$ windings [66], this configuration induces in a magnetic field gradient of 8.71 G/Acm. Experimental optimisation of this magnetic field gradient proved to significantly improve the MOT loading rate. At present, we use a magnetic gradient of 15.8 G/cm (by applying 1.83 A).

3D-MOT Anti-Helmoltz Coils: For loading the 3D-MOT, we also need to apply a magnetic field gradient. To generate it, we have again a pair of coils in an anti-Helmholtz configuration. These coils

[9] For example by Superlum, SOA-332-DBUT-PM-FC/APC, output power of up to 20 mW

[10] For an input beam at $200\,\mu\mathrm{W}$ and a suppression of $-75\,\mathrm{dB}$, there are still $2.5 \times 10^6 \mathrm{s}^{-1}$ photons in the beam. For a resonant, circularly polarised beam with a waist of $w_0 = 5\,\mathrm{mm}$ this yields a single atom scattering rate of $R_{\mathrm{sc}} = 0.043\,\mathrm{s}^{-1}$. By detuning lasers far from resonance during current switching of the SOA, the likelihood of atoms interacting with light is reduced further. Detuning the beam by $2\pi \times 1\,\mathrm{GHz}$, the scattering rate is reduced to $R_{\mathrm{sc}} = 3.9 \times 10^{-7}\mathrm{s}^{-1}$, which is approximately one photon per second for the entire atomic cloud.

[11] For example by Eagleyard, EYP-TRA-0780-0300-4006-BTU02-0000, maximal power of 3 W

[12] At the moment, we use fibres from Schäfter&Kirchhoff, PMC-E-780-5.1-NA012-2-APC.EC-200P.

have a diameter of 15 cm, a relative spacing of 7 cm, and $N = 65$ windings. By applying a current of $I = 15$ A, magnetic field gradients of up to 15 G/cm can be achieved [66]. The heat dissipation of the relatively large amount of power leads to heating of the coils and the surrounding area. This is why these coils are water cooled[13] to 20 °C (in continuous operation, the temperature of the coils stabilises at higher temperatures, see [66]).

Small Helmholtz Coils: A pair of coils in Helmholtz configuration (with very similar dimensions to the 3D-MOT anti-Helmholtz coils, see [66]) is mounted on the same frame as the 3D-MOT anti-Helmholtz coils. These are used to set static magnetic fields along the x-axis. These coils with $N = 20$ windings, induce magnetic fields of 2.33 G/A [66]. Using a homebuilt current source controller and an analogue power amplifier (details in the next section and table 1.3.1), currents of up to 1.7 A can be applied, sufficient for our experiments. However, the small diameter of these coils introduces magnetic field inhomogeneities across the elongated atomic cloud in the dipole trap. Because the Larmor precession frequency of the atomic spin is proportional to the magnetic field, any inhomogeneity of the magnetic field leads to inhomogeneous broadening of the collective spin of the atomic spin. This leads to a faster de-phasing of the *spin-oscillator*. Therefore, we want to avoid any inhomogeneity of the magnetic field across the atomic cloud. The inhomogeneity of the small Helmholtz coils could not be fully compensated by the gradient compensation wires (see below). Nevertheless, we still need to use these coils to apply sufficiently large magnetic fields at the position of the atoms, because the magnetic field induced by the large Helmholtz coils is limited (see next paragraph).

Large Helmholtz Coils: In addition to the small Helmholtz coils, larger square Helmholtz coils are used for inducing magnetic fields along the x, y, and z-axis. These coils feature side lengths and spacings of between 64 cm and 83 cm (details are given in [66]). Due to this large size, the coils generate a very homogeneous magnetic field. However, it is technically difficult to generate large fields with these coils because much larger currents are needed than for the small Helmholtz coils (here, we have only 0.4 G/A). At the moment, we are using current sources, which provide up to 3 A or 5 A (Munich source, see below). This allows us to apply fields of up to 1 G or 1.5 G, which is too low for our experiments, meaning we have to apply the magnetic field partly with the small Helmholtz coils. In addition, it is hard to switch the large Helmholtz coils quickly because they have a large inductance of > 6 mH due to their large size (compared to 0.29 mH for the small Helmholtz coils). The large Helmholtz coils are primarily used for active compensation of the surrounding magnetic field (see section 1.3.3) and to apply static bias fields.

Fast (Large) Helmholtz Coils: A second set of Helmholtz coils is placed on top of the large Helmholtz coils. These coils have fewer windings ($N = 7$ compared to $N \approx 40$) and can be used for faster compensation of the magnetic stray field or for short switching times. Initial tests with low-bandwidth current sources (Munich current source, see table 1.3) showed no improvement in field stability. Reevaluation with faster current sources could be considered if magnetic field stability becomes a constraint in future experiments.

Gradient Compensation Wires: The Larmor precession frequency of the atomic spin is proportional to the magnetic field. Consequently, any magnetic field gradient across the atomic cloud leads to dephasing

[13] Chiller: Orion, ETU702 302 201-VW: cooling capacity: 700 W; accuracy: ±0.03 °C; pump capacity: 10 L min^{-1}; tank capacity: 2 L

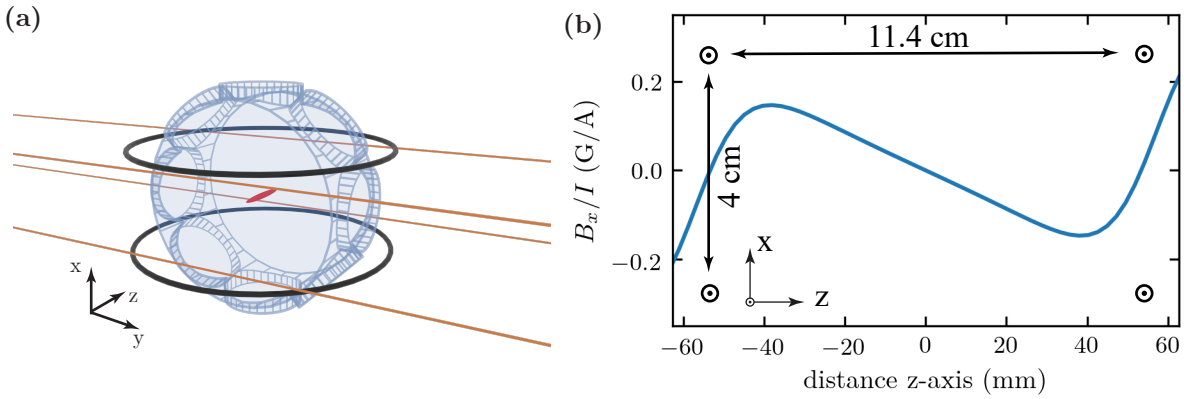

Figure 1.3.1: Magnetic field compensation wires: (a) A 3D-representation of the setup. In red, the cigar-shaped dipole trapped atoms are shown (not in scale). The cloud is elongated along the z-axis and has a very small waist along the x- and y-axis. The gradient compensation wires are shown in orange. The current flows in all wires along $+y$. The anti-Helmholtz coils are shown in black for orientation. (b) The plot shows the calculated magnetic field at the height of the atoms $x = 0$ induced by a current in the four compensation wires. It can be seen that in the region of interest around $z \approx \pm 10\,\mathrm{mm}$, the magnetic field gradient is constant. The wire configuration is indicated in the graph.

of the collective atomic spin, as individual atoms are exposed to different magnetic fields. The final dipole-trapped cloud is elongated along the z-axis, while being very thin along the x- and y-axes (aspect ratio of ~ 400). It was therefore decided that compensation should be made for the magnetic field gradient of B_x along the z-axis. To this end, four wires have been installed in a rectangular configuration (see figure 1.3.1 (a), design inspired by [78]). In the four wires, the current flows in the same direction along the y-axis. The wires are separated by a distance of $d = 4\,\mathrm{cm}$ in the x-direction and $D = 11.4\,\mathrm{cm}$ in the z-direction. They are placed so that the atomic cloud is situated in the middle between the wires. Along the axis of the atomic cloud, the magnetic field gradient is constant over a distance of approximately 4 cm with a gradient of $\Delta B/I = 0.427\,\mathrm{mG/(A \cdot mm)}$ (shown in figure 1.3.1 (b), deviation from linear of $0.04\,\mathrm{mG/A}$ for $\pm 10\,\mathrm{mm}$ from the centre). The coherence time of the collective atomic spin was increased by an order of magnitude by correcting the magnetic field gradient (for further details, see [79]).

1.3.2 Current Sources

The frequency of the atomic oscillator in the hybrid experiment is given by the spin Larmor precession frequency. This frequency is directly dependent on the magnetic field. Therefore, it is necessary to apply a stable and reproducible magnetic field in order to perform reproducible measurements in which the spin is not linewidth broadened by drifts of magnetic fields. In order to achieve this, it is essential to use very stable current sources. In addition to earth's magnetic field, the different devices of our experiment induce magnetic stray fields. To obtain reliable magnetic fields at the atomic position, we have to actively compensate for the stray fields. For this purpose, current sources are required, which drive the coils with a bandwidth of (ideally) up to 400 Hz.

In the course of this work, we have tested some of the current sources using the large Helmholtz coils. For each of the current sources, we have measured the bandwidth, the low frequency noise, the high frequency noise and the long-term drifts. The results are summarised in table 1.3.1. The following current sources were characterised:

Current source	Range	Bandwidth	rms ($\leq 1.2\,$kHz)	rms (0.2 to 1 MHz)	rms (0.2 to 4 MHz)	relative DC-Drift
Munich 3A	$\pm 3\,$A	160 Hz	3.3×10^{-2}mA	3.17×10^{-8}G	2.93×10^{-8}G	1.88×10^{-6}
Workshop analog	$\pm 1.7\,$A	1.4 kHz	2.8×10^{-2}mA	1.41×10^{-8}G	2.93×10^{-8}G	1.54×10^{-6}
Workshop digital	$\pm 5\,$A	1.1 kHz	4.4×10^{-2}mA	1.45×10^{-8}G	3.03×10^{-8}G	6.73×10^{-7}
HighFinesse 3A	$\pm 3\,$A	330 Hz	4.6×10^{-2}mA	1.60×10^{-8}G	3.03×10^{-8}G	5.86×10^{-6}

Table 1.3.1: The characterisation of different current sources: The bandwidth of the current sources connected to the large Helmholtz coils is measured by analysing the response of the current source on a oscillating signal. The low frequency RMS noise is measured with a measurement resistor in series with the large Helmholtz coils. It is integrated from dc to 1.2 kHz. The high frequency RMS noise is the integrated noise for frequencies between 200 kHz and 1 MHz or 4 MHz, respectively. This measurement is performed with a pick-up coil in close proximity to the atomic position. In order to characterise the dc drift, the relative rms value is given for a current of 1.6 A over 11 h. Further details of the current sources and the measurements are provided in the main text.

- *Munich 3A* is a current source that was homebuilt in Munich [80] and has been used for a considerable period in our experiment.
- *Workshop analogue* was constructed by the electric workshop of our institute. The system comprises a controller unit (PCCS Controller (SP 1064a)), which measures the current and compares it with a control input signal, setting the control voltage for a linear power amplifier unit, which is homebuilt. The separation of the control and power amplification into two boxes is beneficial for long-term current stability. Otherwise, the thermal load of the power amplifier affects the measurement of the current by heating the measurement resistor, limiting long-term stability.
- *Workshop digital* is a homebuilt current source. Like the *Workshop analogue* it consists of two parts, a controller unit (PCCS Controller (SP 1064a)) and a power amplifier. The power amplifier is a homebuilt switching power amplifier (PCCS Controller (SP 1064b)).
- *HighFinesse 3A* is a commercial current source. The model employed here is the *BCS 3/12*.

The bandwidth of the current sources is estimated by sending an oscillating signal to the control input of the current source. The current is measured by using a $0.1\,\Omega$ measuring resistor[14] (shown in figure 1.3.3 (a)). The RMS amplitude of the oscillating signal (see figure 1.3.3 (b)) and the phase lag between the control input and the response (see figure 1.3.3 (c)) is estimated. In table 1.3.1, the bandwidth is estimated by modelling the system as a low-pass filter, whereby the frequency at which the phase between control voltage and current lags by $\pi/2$ is identified.

The low frequency noise of the current sources is measured by using a $0.3\,\Omega$ measuring resistor[15] in series with the large Helmholtz coils (shown in figure 1.3.2). For this measurement a dc current of 1.7 A is applied. The voltage across the resistor is amplified by a battery-powered low noise preamplifier[16] and measured with a battery-powered oscilloscope[17]. The rms is calculated by integrating over the power spectral density (PSD) of the measured time trace. The background rms noise (which is dominated by the noise floor of the preamplifier) is given by 3.4×10^{-2}mA. We observe that the *HighFinesse 3A* has a group of high and large noise peaks at frequencies between 100 Hz and 400 Hz.

[14] Vishay foil resistor VCS301
[15] Vishay foil resistor VCS332
[16] Standford Research Systems, low-noise preamplifier, model SR560
[17] Tektronix TPS 2024B; four channel digital oscilloscope

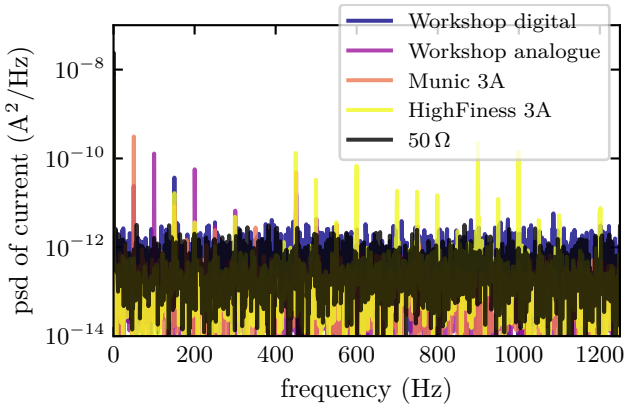

Figure 1.3.2: Power spectral density (PSD) of the low frequency noise of the various current sources: The current is measured across a 0.3 A measuring resistor. The resulting voltage is amplified by a battery-powered low noise amplifier and measured with a battery-powered oscilloscope to avoid ground loops. The data labelled with "50 Ω" is a background measurement for which the input of the amplifier is shortened with a 50 Ω resistor.

The AC noise is measured by using a pickup coil[18] positioned in close proximity to the position of the atoms. A current of 1 A is applied to the large Helmholtz coils in the x-direction, resulting in a field of 0.3 G. Fluctuations of the magnetic field induce a current in the circuit of the pick-up coil, which is then amplified by a low-noise amplifier[16] and measured with a spectrum analyser[19]. One measurement is shown in figure 1.3.3 (d)). The rms noise is calculated by integrating the current spectrum density over a bandwidth of either 0.8 MHz or 3.8 MHz (starting from 200 kHz, see an example in figure 1.3.3 (e) and the results in table 1.3.1). Due to the low noise of the current sources at higher frequencies and the intrinsic noise of the amplifier, the main contribution to the noise is given by the detection chain. In particular, for the Munich source, the noise induced by the current source is only a few percent higher than the background noise. This measurement allows us to compare different current sources, but for all measurements, the detection is the dominating noise source. Nevertheless, one observations should be made here: For the current source *Workshop digital*, we observe the switching frequency of the digital amplifier at 380 kHz in the measurement of the magnetic field, despite efforts to filter out this particular frequency. Our objective is to ascertain whether this noise peak could influence the atomic state: To this end, we tune the Larmor frequency to resonance with the 380 kHz noise peak by changing the magnetic field. There is no evidence to suggest that this noise peak is driving the spin. If this proves to be a problem for a particular experiment in the future, the switching frequency can be changed.

The dc drift of the current sources is measured by utilising a stable data logger[20] and a stable voltage source[21] to provide the setpoint for the current source. For a period of 11 h every 4 s, the current is measured using a 0.3 Ω measuring resistor[22]. The control voltage and the temperature of the resistor are recorded in order to exclude them as sources of drifts. In table 1.3.1, the rms value relative to the applied current of 1.6 A is shown.

[18] Homemade pickup coil with $N = 110$ windings and an area of $A = 9.35\,\mathrm{cm}^2$
[19] Rohde&Schwarz, FSV, 7 GHz
[20] Keysight, DAQ970A
[21] Homebuild high resolution DAC (SP 927), specification see `https://physik.unibas.ch/en/department/technical-services/electronics-lab`
[22] Vishay foil resistor VCS331

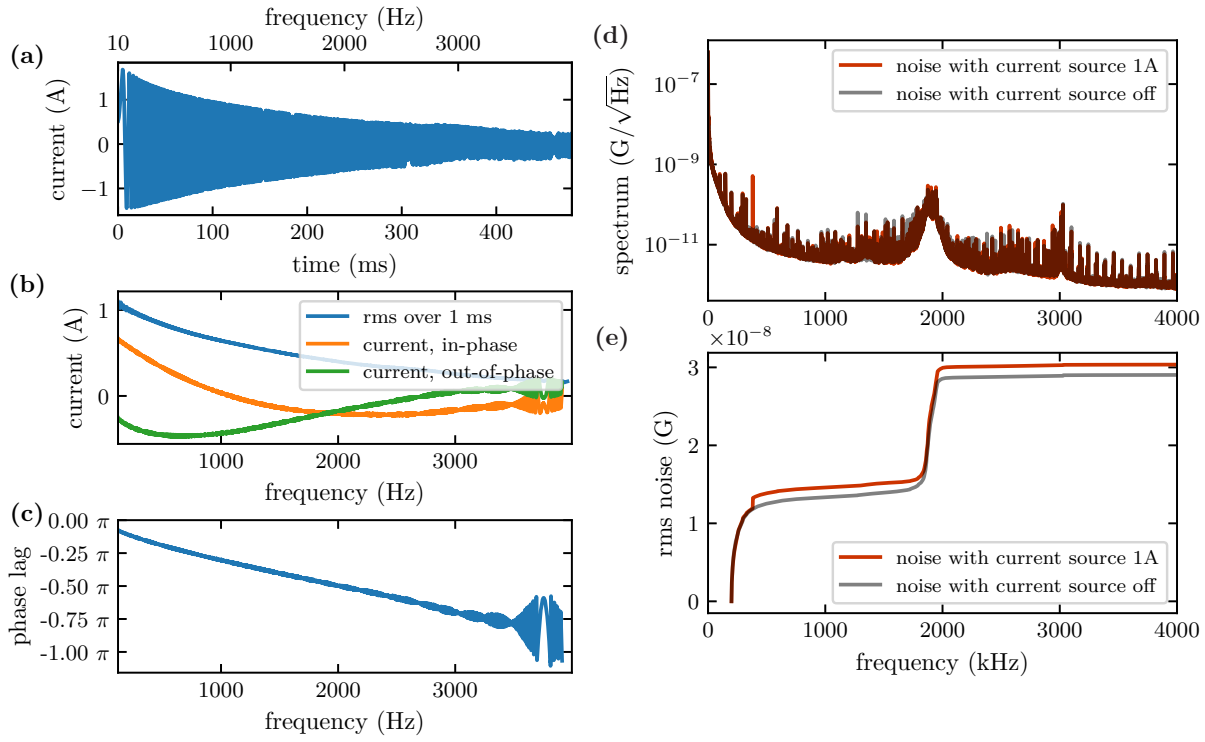

Figure 1.3.3: The characterisation measurements of the workshop current source with the digital amplifier: (a) to (c) show the response of the current source to a signal: An oscillating signal is applied as a control input ramping the frequency from 10 Hz to 4 kHz. The output signal is shown in (a). The rms of the output signal is calculated by integrating the squared signal over 1 ms represented by the blue curve in (b). By comparing the oscillating output signal with the input control, it is possible to estimate the in-phase ((b), orange) and out-of-phase ((b), green) components of the oscillation. This allows to calculate the phase between the control and the output current, shown in (c). (d) and (e) show the result of the ac noise measurement with a pick-up coil: The noise peak at 380 kHz is the dominant feature, exceeding the measurement noise. This is the switching frequency of the digital power amplifier. (e) shows the integral of the spectrum starting at 200 kHz. Here, the noise peaks at about 1.9 MHz comes from the pre-amplifier. At low frequencies, the detection is constrained by the response function of the pick-up coil.

Current Sources in the Experiment: The various wires and coils are driven by different current sources and in different configurations: For the experiments described in this work, the gradient compensation wires and the small Helmholtz coils are powered by a *Workshop analogue* current source. The large Helmholtz wires are powered by *Munich 3A* current sources (the z-axis by a *Munich 5A* [80], which is not characterised here). The anti-Helmholtz coils are powered by commercial current sources[23]. In future experiments, it would be beneficial to replace the existing *Munich 3A* current sources with the new *Workshop digital* current sources. This would enhance the bandwidth of the active compensation of magnetic stray fields from 160 Hz to 1.1 kHz allowing for a much faster feedback, particularly of the dominant noise frequency in our laboratory at 150 Hz.

1.3.3 Active Stabilisation of the Magnetic Field

The devices, cables and power lines in the laboratory induce stray magnetic fields. The most prominent frequency contributions are observed at 150 Hz, at 50 Hz (frequency of the main power lines) and higher harmonics.

To characterise the noise at the position of the atoms, we measure the Larmor frequency (which depends linearly on the magnetic field) of the atomic spin to determine the local magnetic field. For this purpose, the atoms are loaded into the dipole trap and spin-polarised in the direction of a bias magnetic field along the x-axis. The spin is tilted slightly ($\pi/10$) away from the bias magnetic field, such that it precesses around the magnetic field axis. This is achieved by applying a short rf pulse which is described in detail in section 2.5. The z-component of the spin is read out by the Faraday interaction (further details can be found in the following chapter). The z-component of the spin and therefore the resulting Faraday signal oscillates at the Larmor frequency due to the precession of the spin around the x-axis. This oscillation signal can be used to calculate the magnetic field at the position of the spin. If the sequence is not triggered on the 50 Hz of the main line, each repetition of the experiment starts at a different phase in the 50 Hz and 150 Hz noise environment. Consequently, by taking many successive repetitions, it is possible to characterise the magnetic field noise.

Without active stabilisation of the magnetic field, an rms noise of 1.12 mG is observed (measured at a bias field of 2.28 G). To actively stabilise the magnetic field at the position of the atoms, a 3D fluxgate sensor[24] is placed 9 cm above (x-axis) the atoms, on top of the small Helmholtz coils (i.e. these coils cannot be used in closed loop). Therefore the large Helmholtz coils are employed for feedback. A calibrated value is added to the setpoint to account for the magnetic field produced by the small Helmholtz coils. The feedback loop comprises the fluxgate sensor, which measures the magnetic field in all three dimensions, three homebuilt PID boxes[25] with calibrated setpoints, and the large Helmholtz coils inducing fields along the x, y and z axes. Active stabilisation is employed to reduce the rms noise to 60 µG at the position of the atoms (at a bias field of 2.28 G. This is a shot-by-shot measurement using the atoms as magnetic field sensor. Because of integration of the signal, the bandwidth is limited to 300 Hz). Furthermore, the experimental sequence is locked to the phase of the main power line, thereby improving the shot-to-shot reproducibility further.

[23] 3D-MOT: Delta Elektronika SM 15-100; 2D-MOT: EA-PS 2016-050

[24] Bartington Mag-03MCTP: range: ±2.5 G; bandwidth: 3 kHz

[25] Magnetic Field Stabilisation (SP 962), specification see `https://physik.unibas.ch/en/department/technical-services/electronics-lab`

Considering a Magnetoresistive Sensor: Fluxgate sensors have a low noise floor and high sensitivity, however this comes at the cost of a relatively narrow bandwidth, the emission of high frequency magnetic field noise and a relatively large size. While we do not observe any effect of the high frequency magnetic field noise emitted by the fluxgate sensor, a smaller sensor would allow us to place the sensor closer to the atoms, which could further improve the stability. A magnetoresistive sensor[26] was therefore tested, but we encountered some difficulties. Magnetoresistive sensors have the advantage of not inducing magnetic fields and being much smaller (and cheaper) than fluxgate sensors. They also have a very high bandwidth (in our case 5 MHz).

The magnetic field sensor (both fluxgate and magnetoresistive) is saturated during the MOT loading. Once saturated, the magnetoresistive sensor must be reset by a short current pulse. This was implemented by loading a pair of capacitors and discharging them after the anti-Helmholtz coils are ramped down. However, the magnetoresistive sensor has a non-negligible temperature dependence which introduces a non-deterministic hysteresis after heating its environment. We suspect that this is the reason why the dc reading of the magnetoresistive sensor was not consistent in successive measurements. When using it to stabilise the magnetic field, the atomic spin shot-by-shot variations is measured to be of the order of 0.85 mG. In order to utilise the magnetoresistive sensor in our experiment (e.g. to take advantage of the large bandwidth), the DC setpoint of the magnetoresistive sensor would have to be recalibrated for each experimental shot using the fluxgate sensor. We decided not to implement this due to the considerably higher complexity and the sufficiently long spin coherence achieved with the fluxgate sensor alone.

1.4 Experiment Control System

The loading, trapping and spin-pumping of the atoms necessitates the implementation of a time-controlled sequence. The various stages of the sequence have different timescales, spanning from microseconds to seconds. Consequently, it is necessary to control a sequence of a few seconds in duration with microsecond time resolution. In order to achieve this, the software package *labscript suite* [81] is employed. Labscript is a software package written in Python (currently we are utilising the version in Python 2, however, there is a Python 3 version of Labscript available). The software enables the user to control the experimental hardware from a Windows computer. This can be done either manually via a graphical interface or in a pre-programmed, timed sequence.

In a typical sequence, the majority of devices, including function generators, lock-in amplifiers, spectrum analysers and oscilloscopes, are initialised by Labscript prior to the start of the sequence and read out after it has finished. Precise timing during the sequence is provided by the National Instrument IO cards[27], which are timed by a pseudo clock[28]. The National Instrument IO cards provide digital trigger signals (5 V) for various devices and timed analogue voltages (± 10 V) for direct control of current sources, AOM drivers and a range of other devices. The sampling rate of the sequence is constrained by the National Instrument IO card to 100 kHz. The response time is very different for the analogue and digital outputs. While the digital outputs have a rise time of 0.5 µs, the analogue outputs have a rise time of 5.3 µs for the same programmed pulse (reaching 90 % of the target value). The pseudo clock has the functionality of awaiting the next instruction in response to a trigger input. This option is employed to trigger the sequence at the 50 Hz mains frequency thereby ensuring greater reproducibility of experiments.

[26] Honeywell HMC1001
[27] NI 6535, 2x NI 6733, NI6723
[28] Implemented with a 32-bit microcontroller: *Digilent chipKIT Max32*

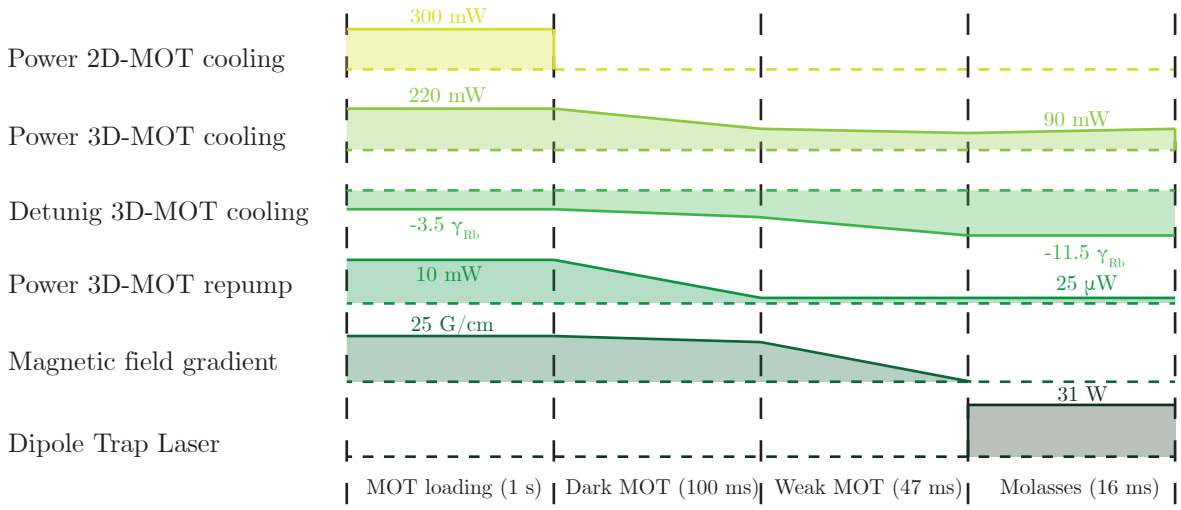

Figure 1.5.1: Summary of the MOT loading sequence with the most important parameters which are scanned during the loading sequence.

In the current state of the experiment, all National Instrument IO cards are plugged directly into the computer. This has two major disadvantages. Firstly, the number of National Instrument IO cards is limited by the number of slots in the computer and cannot be easily expanded. As the complexity of the experimental setup increases, with two quantum systems and various locks to control and couple them, this becomes limiting. Secondly, and more importantly, the National Instrument IO cards are not galvanically isolated from the computer and from each other. In the future, it may be beneficial to upgrade the experimental control system to the Python 3 version of Labscript and utilise a PXI chassis for the National Instrument IO cards connected to the computer through an optical thunderbolt cable, rather than of plugging them directly into the computer.

1.5 From MOT Loading to Dipole Trap Loading

Having introduced the relevant lasers, coils and power sources, this section provides an overview of the loading sequence. The loading of the atomic cloud comprises five stages, which are presented below. An overview of the sequence is shown in figure 1.5.1.

MOT Loading: The first stage is to load as many atoms as possible into the 3D-MOT. This is achieved by pre-cooling the atoms in a 2D-MOT and then pushing them towards the main atomic chamber using radiation pressure, as described in [66, 71]. For the 2D-MOT, we use a total cooling beam power of 300 mW and a total repump power of 15 mW. This corresponds to a maximum cooling beam intensity of $I_{\text{peak}} = 18 I_{\text{sat}}$. The detuning of the 2D-MOT cooling beams has been experimentally optimised to $\Delta_{\text{2D}} = -2.5\,\gamma_{\text{Rb}}$. For the 3D-MOT, a total cooling light power of 220 mW (peak intensity of $I_{\text{peak}} = 40.5 I_{\text{sat}}$) and a total repump power of 10 mW is employed. For the MOT loading, the cooling beam detuning is set to $\Delta_{\text{3D}} = -3.5\,\gamma_{\text{Rb}}$ and the magnetic field gradient is set to $B_{\text{grad}} = 25\,\text{G/cm}$. The number of atoms in the cloud can be estimated by absorption imaging, as detailed in section 1.6.4. The loading curve of the 3D-MOT is shown in figure 1.5.2 (a): A simple model, assuming a constant loading rate and

one-body losses, is fitted to the number of atoms versus the loading time. This yielded a loading rate of $R = 5.04 \times 10^9 \mathrm{s}^{-1}$ and a saturation atomic number of 3.3×10^9. In the experiment, the duration of the MOT loading is used to control the number of atoms. At the end of the MOT loading stage, the atomic motion temperature is 3 mK, which is too high to efficiently transfer them into a dipole trap with a trap depth of approximately 200 µK.

Dark MOT: During the first loading stage, the density of the MOT is limited by the reabsorption process of already scattered photons [67, 82, 83]. In a subsequent stage, the density of the atomic cloud is increased and the temperature is lowered. This is accomplished by reducing the repump power to 60 µW. By reducing the repump laser power, the atoms spend more time in the $F = 1$ manifold, resulting in a reduction in light scattering. At the same time, the detuning of the cooling laser is increased to $\Delta_{3D} = -4\,\gamma_{Rb}$ and the gradient field is ramped down to $B_{grad} = 19\,\mathrm{G/cm}$. The parameters at the end of the dark MOT are optimised so that the repump power is just below the critical power at which the depumping by the cooling light is faster than the repump rate by the repump laser. Upon reaching this critical point, the temperature decreases and the density increases abruptly (see figure 1.5.2 (b) and (c)). During this 100 ms stage, the loss of atoms is minimal, yet the cloud diameter is reduced from about 4 mm to about 2.5 mm and the temperature is lowered to 1 mK.

Weak MOT: The third loading stage represents a transition from the dark MOT stage to the subsequent stage, designated as molasses. During the 47 ms of the weak MOT stage, the magnetic field gradient is gradually decreased and the detuning of the cooling light is increased to $\Delta_{3D} = -8\,\gamma_{Rb}$. Both processes result in a reduction in cloud density as the atoms are laser cooled. This further reduces the temperature to 150 µK (see figure 1.5.2 (e)). At the end of this stage, there are still 2.3×10^9 atoms trapped (see figure 1.5.2 (f)).

Molasses: In the final stage the magnetic field gradient is turned off. Here, the atoms are cooled by polarisation gradient cooling, using the circularly polarised MOT-cooling beams [84] with a detuning of $\Delta_{2D} = -8\,\gamma_{Rb}$ (and a repump beam at 65 µW). The atoms are cooled further to a temperature of 40 µK (see figure 1.5.2 (e)). During this process, a significant loss of atoms is observed (see figure 1.5.2 (f)). Therefore, it is necessary to make a trade-off between temperature and the number of atoms. In order to maximise the number of atoms loaded into the dipole trap, the duration of the molasses is set to 16 ms, after which the temperature of the cloud is 40 µK. Figure 1.5.2 (d) shows a second loading curve for the number of atoms at the end of the molasses stage as a function of the first stage MOT loading time.

Transfer to the Dipole Trap: During the molasses stage, the dipole trap laser is switched on. After 16 ms of molasses stage, the cooling and the repump beams are turned off. The atoms which are not trapped in the dipole trap beam fall under gravity. After 200 ms of hold time, the spin state of the atoms is initialised (see section 1.7).

1.6 Dipole Trap

In our experiment, we want to interface the atomic spin with a mechanical oscillator using light. In order to achieve quantum coherent interactions between the two systems, we must engineer a quantum limited

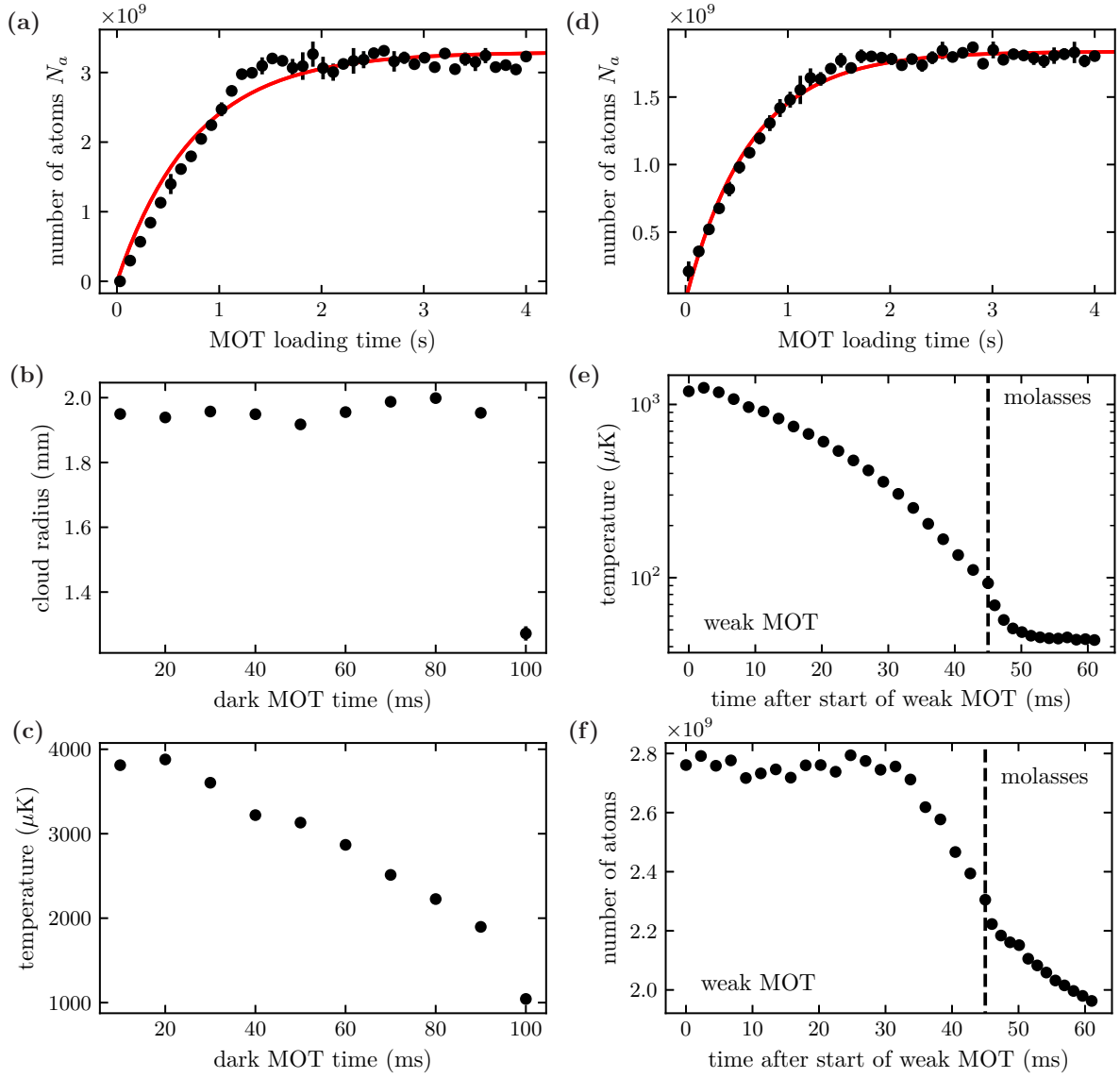

Figure 1.5.2: (a) and (d) show the loading curve of atoms (i.e. the number of atoms as a function of the MOT loading duration) with the number of atoms N_a measured (a) after the first MOT and (d) after the molasses, respectively. The red line represents a fit with the saturation function $N_\mathrm{a}(t) = N_\mathrm{sat}(1 - \exp(t/\tau))$. The loading rate is defined as $R = N_\mathrm{sat}/\tau$. We yield a loading rate of (a) $R = 4.32 \times 10^9 \mathrm{s}^{-1}$ after the first stage and a saturation atom number of (a) 3.3×10^9 after the first stage and of (d) 2.38×10^9 after the molasses stage. (b) and (c) show the width and the temperature of the atomic cloud during the dark MOT. The time in (b) and (c) is defined as commencing at the start of the dark MOT stage. (e) and (f) show the number of the atoms and the temperature during the weak MOT and the molasses stage. The time is defined as commencing at the start of the weak MOT stage. For this experiment, the MOT loading duration was set to 1 s.

spin-light interface. Employing a dipole trap to hold the atoms, offers several advantages to achieve this goal. Firstly, the trap's lack of magnetic properties allows to apply a homogeneous magnetic field across the atomic cloud. Secondly, the decoherence due to photon scattering can be kept to a minimum, thus extending the lifetime of the atoms in the trap far beyond the coherence time of the atomic spin. In the following section, we provide a brief overview of the principles underlying optical dipole traps, after which we present the characterisation of our dipole trap.

1.6.1 Shape of Atomic Cloud

As part of this work, the dipole trap laser was replaced. Apart from some minor technical changes, this presented an opportunity to reconsider the shape of the trapping potential. The dipole trap potential must fulfil several requirements: In the final experiment, the atomic cloud is trapped by the trapping laser at a wavelength of $\lambda_{\mathrm{trap}} = 1064\,\mathrm{nm}$ and then interfaced with a probe/coupling laser at a wavelength of $\lambda_{\mathrm{pr}} = 780\,\mathrm{nm}$. As will be demonstrated in greater detail in chapter 2, the coupling strength between the atomic spin and the coupling laser is dependent on the number of atoms that scatter light into the mode of the coupling laser [85]. To optimise this coupling strength, it is necessary to consider two factors: Firstly, it is desirable to have as many atoms as possible interfaced with the coupling beam. To achieve this, an atomic cloud with a high optical density must be generated by loading as many atoms as possible into the trap. To do this, we need to use the available optical power to achieve a deep trapping potential. Secondly, the collectively enhanced scattering from the atomic cloud should be overlapped with the coupling beam [85, 86]. In the final experiment, only the light which is scattered into the mode of the incoming coupling beam interacts with the membrane or can be detected in a homodyne detection. Therefore, it is crucial to ensure good mode matching between the incident and scattered light. This can be achieved by shaping the atomic cloud correctly. The necessary equations that guided our choice are summarised below.

The radially-symmetric potential created by the far-off resonant, Gaussian trapping laser can be approximated by a harmonic potential of frequencies $\omega_{a,r}$ and $\omega_{a,z}$ in the radial and axial direction, respectively [87]

$$U(\mathbf{r}) \approx U_0 + \frac{1}{2} m_{\mathrm{Rb}} \omega_{a,r}^2 r^2 + \frac{1}{2} m_{\mathrm{Rb}} \omega_{a,z}^2 z^2 \tag{1.6.1}$$

where m_{Rb} is the mass of a Rubidium atom and the trap depth $U_0 < 0$ is negative for our parameters. The trap depth is given by

$$U_0 = \frac{\pi c^2 \gamma_{\mathrm{Rb}}}{2\omega_0^3} \left(\frac{2 + \mathcal{P} g_{\mathrm{F}} m_{\mathrm{F}}}{\Delta_{2,\mathrm{F}}} + \frac{1 - \mathcal{P} g_{\mathrm{F}} m_{\mathrm{F}}}{\Delta_{1,\mathrm{F}}} \right) \frac{2P_{\mathrm{trap}}}{\pi w_{0,\mathrm{trap}}^2} \tag{1.6.2}$$

where c is the speed of light, ω_0 is the frequency of the trap laser, $g_{\mathrm{F}} \approx 1/2$ is the Landé factor, $\mathcal{P}$ characterises the laser polarisation, P_{trap} is the power of the trapping beam, and $w_{0,\mathrm{trap}}$ is the $1/\mathrm{e}^2$ waist (radius) of the trap beam at the focus, $\Delta_{2,\mathrm{F}} = \omega_0 - \omega_{2,\mathrm{F}}$ is the detuning on the D2 line and $\Delta_{1,\mathrm{F}} = \omega_0 - \omega_{1,\mathrm{F}}$ is the detuning on the D1 line, i.e. these are the detunings with respect to the transition between a particular hyperfine ground state F and the centre of the excited hyperfine manifold ${}^2P_{3/2}$ and ${}^2P_{1/2}$, respectively. In our case, the laser is linearly polarised, i.e. $\mathcal{P} = 0$. For $\sigma^{\pm}$ cicularly

polarised light, we get $\mathcal{P} = \pm 1$. The trap frequencies are given by

$$\omega_{a,r} = \sqrt{\frac{-4U_0}{m_{\mathrm{Rb}} w_{0,\mathrm{trap}}^2}} \qquad \text{and} \qquad \omega_{a,z} = \sqrt{\frac{-2U_0}{m_{\mathrm{Rb}} z_{\mathrm{R,trap}}^2}}. \tag{1.6.3}$$

where $z_{\mathrm{R,trap}} = \pi w_{0,\mathrm{trap}}^2/\lambda_{\mathrm{trap}}$ is the Rayleigh length of the trap beam. A thermal ensemble of atoms will have a steady state temperature that is lower than U_0/k_B due to the evaporation of the most energetic atoms from the trap and the subsequent equilibration of the remaining atoms at a lower steady state temperature. The shape of the atomic cloud can be calculated from the temperature and the trap laser parameter. In a harmonic potential, a thermal atomic ensemble will form a three dimensional Gaussian cloud of density profile [87]

$$n(r,z) = N_{\mathrm{a}} \sqrt{\frac{1}{\pi^3 w_{a,r}^4 w_{a,z}^2}} \exp\left(-\frac{r^2}{w_{a,r}^2}\right) \exp\left(-\frac{z^2}{w_{a,z}^2}\right), \tag{1.6.4}$$

where N_{a} is the total number of atoms in the cloud and the waists of the atomic cloud are given by

$$w_{a,i} = \frac{1}{\omega_{a,i}} \sqrt{\frac{2k_{\mathrm{B}}T}{m_{\mathrm{Rb}}}}. \tag{1.6.5}$$

Here, we define the 1/e waist of the atomic cloud, which differs from its standard deviation by the factor $w_{a,i} = \sqrt{2}\sigma_i$.

The atomic cloud must be designed in such a way that the interaction between the atomic spin and the probe light is maximised while decoherence is minimised. In our simplified model, all light which is scattered into the same mode as the probe laser participates in the coherent light-spin interaction while we trace over the light which is scattered into different modes, thus this leads to decoherence. The spin-light interface will be introduced in detail in a later chapter 2. For this chapter, it is sufficient to make some very basic geometrical considerations: In order to optimise the spin-light interface, it is necessary to maximise the scattering into the spatial mode of the probe laser, while minimising the scattering into any other mode. To minimise scattering into all unwanted modes, a very short and radially large cloud is optimal [85]. However, the optical density of such a cloud is very low, resulting in small spin-light coupling. To optimise both the axial optical density and the decoherence due to coupling into unwanted modes, cigar-shaped clouds have been demonstrated to be an effective choice [85, 86]. The size of the atomic cloud must then be chosen to ensure that the scattering cone of the atoms matches the probe beam [86].

In a simplified picture, this can be achieved by matching the divergence angle of the probe beam (which is focused onto the atoms) θ_{pr} to the divergence angle of the scattering cone θ_{sc}, as shown in figure 1.6.1. Thereby, the divergence (full) angle of the probe beam is given by $\theta_{\mathrm{pr}} = 2\lambda_{\mathrm{pr}}/(\pi w_{\mathrm{pr},0}) = 2w_{\mathrm{pr},0}/z_{\mathrm{pr,R}}$, where $w_{\mathrm{pr},0}$ is the waist of the probe beam and $z_{\mathrm{pr,R}} = \pi w_{\mathrm{pr},0}^2/\lambda_{\mathrm{pr}}$ its Rayleigh length, and the divergence (full) angle of the scattering cone is given by [86, 88]

$$\theta_{\mathrm{sc}} = 2\sqrt{\frac{\lambda_{\mathrm{pr}}}{\pi w_{a,z}}}. \tag{1.6.6}$$

Rewriting this condition, we get that the length of the cloud should match the Rayleigh length of the probe beam $w_{a,z} = z_{\mathrm{pr,R}}$. Müller *et al.* [86] present in their work a correction to this simplified model

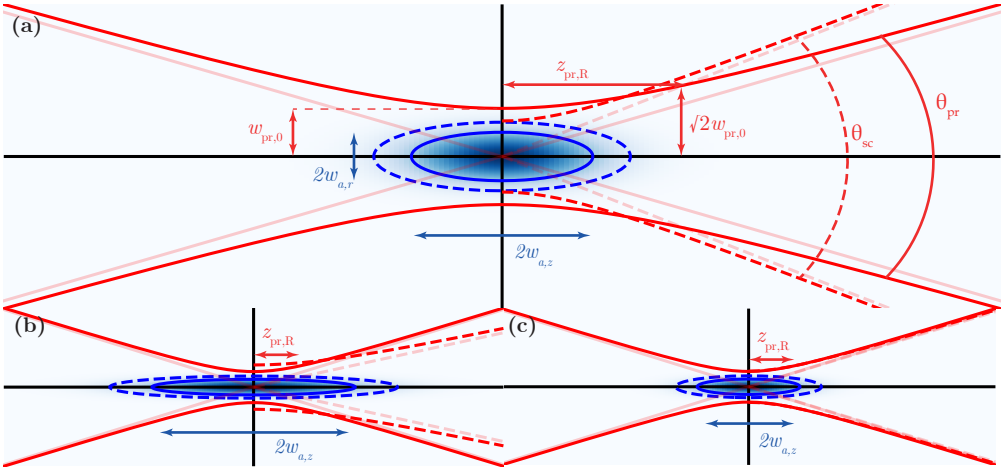

Figure 1.6.1: Mode matching of the probe beam (red solid line) and the scattering cone (red dashed line). The relations for the scattering cone given in this thesis are only valid in the far field, so the scattering cone shown here is not the correct intensity close to the atomic cloud but only gives an intuition for the far field. The Gaussian atomic cloud is shown in blue, with the solid line representing the $1/e$ radius and the dashed line representing the $1/e^2$ radius of the cloud. (a) shows the scattering of a short cloud (i.e. $w_{a,z} = z_{\mathrm{pr,R}}/2$). The definitions of the cloud and beam parameters are labelled here. (b) shows the scattering of a long cloud (i.e. $w_{a,z} = 2z_{\mathrm{pr,R}}$). The divergence angle of the scattering cone is smaller than the divergence angle of the probe laser. (c) shows a well mode matched atomic cloud (i.e. $w_{a,z} = z_{\mathrm{pr,R}}$).

which takes into account that for long atomic clouds there is a phase missmatch along the propagation direction of the light. They obtain a corrected criterion for the mode match of the scattering of a long cloud to a probe beam

$$\frac{w_{a,z}}{z_{a,\mathrm{R}}} = \left(\frac{w_{\mathrm{pr},0}}{w_{a,r}}\right)^2 \cdot \frac{\sqrt{\left(1+\left(\frac{w_{\mathrm{pr},0}}{w_{a,r}}\right)^2\right)^2 - 1}}{1+\left(\frac{w_{\mathrm{pr},0}}{w_{a,r}}\right)^2}, \tag{1.6.7}$$

where $z_{a,\mathrm{R}} = \pi w_{a,r}^2/\lambda_{\mathrm{pr}}$ is the characteristic length of the atomic ensemble [86]. The correction, given by the second term on the right-hand side of the equation, is of order unity for $w_{\mathrm{pr},0} \approx 2w_{a,r}$, which is the case in our experiment.

1.6.2 Dipole Trap Laser Setup

The atoms are trapped by a single laser beam with a wavelength of $\lambda_{\mathrm{trap}} = 1064\,\mathrm{nm}$ (*Mephisto MOPA Pro,* 55 W from *Coherent*) (see figure 1.6.2). The laser can be switched on and off by a Pockels cell[29]. The Pockels cell is mounted on a 5-axis translation stage to optimise alignment with the laser. In order to ensure the reproducibility of the operation, the Pockels cell must be temperature stabilised. This is achieved by placing a Peltier element (controller: *Meerstetter, TEC-1091*) between the Pockels cell housing and the 5-axis translation stage. The heat sink of the Peltier element is thus provided by the moving part of the 5-axis translation stage and is therefore very poorly connected to the optical table

[29] Pockels cell with anti-reflection coating from *Qubig*: Bandwidth up to 100 MHz, $V_\pi \approx 1200\,\mathrm{V}$ at 1064 nm, crystal size of $3 \times 3\,\mathrm{mm}^2$. The Pockels cell is operated by a high voltage switch from *Qubig*: pulse length down to 20 ns, rise/fall time: 5 ns

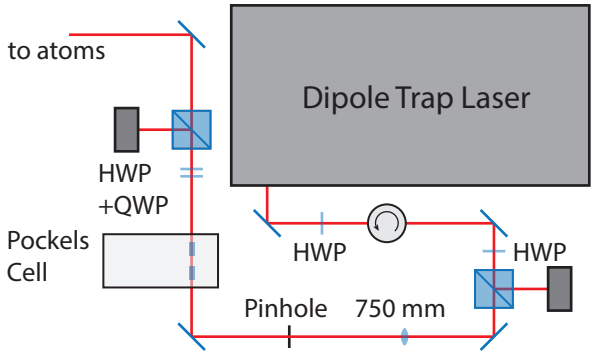

Figure 1.6.2: Optical path of the dipole trap laser. The laser can be switched on and off using a Pockels cell and a PBS.

or any other large heat sink. Consequently, the Peltier element is unsuitable for removing heat from the Pockels cell, but only for stabilising its temperature around a steady state temperature.

Despite the laser being weakly focused on the Pockels cell (waist $w = 700\,\mu\text{m}$), there was stray light from the laser that hit the metal capacitors glued to the crystals of the Pockels cell, causing the cell to heat up considerably. To avoid this heating, an iris with an aperture of 3 mm is placed in front of the Pockels cell. This approach is not sufficient to stabilise the temperature, therefore a metal radiator and a fan is mounted on the box of the Pockels cell to dampen the heat generated by the residual absorption of approximately 5 % of the laser light. After the PBS, the laser is directed towards the atomic chamber (not shown in figure 1.6.2).

In order to match the scattering cone of the atomic cloud with the divergence of the probe beam, it is necessary to shape the atomic cloud by suitably adjusting the potential created by the dipole trap beam. For shaping the atomic cloud a number of lenses were tested which focused the trap beam. For each lens, the length and waist of the cloud was characterised. From these two parameters the deviation of the expected scattering cone from the probe laser was calculated (see equation (1.6.7)). Finally, a lens with a focal length of $f = 200\,\text{mm}$ was chosen to focus the dipole trap beam.

From geometrical calculations, the beam waist is found to be between $w_{0,\text{trap}} = 90.3\,\mu\text{m}$ and $w_{0,\text{trap}} = 117.3\,\mu\text{m}$, depending on whether the optimal value for $M^2 = 1$ or the upper limit in the laser specification of $M^2 = 1.3$ is used. With a laser power of $P_{\text{trap}} = 31\,\text{W}$ (measured in front of the chamber), we evaluated a trap depth between $U_0/k_\text{B} = -369\,\mu\text{K}$ ($M^2 = 1$) and $U_0/k_\text{B} = -219\,\mu\text{K}$ ($M^2 = 1.3$).

1.6.3 Loading of the Diople Trap

The parameters of the molasses stage have been optimised so that the final temperature of the atoms matches the expected temperature of the atoms in the dipole trap. This temperature is about a factor of seven or eight lower than U_0/k_B. The dipole trap laser is switched on during the molasses phase. The position of the dipole trap beam is optimised in order to maximise the number of atoms in the dipole trap. Subsequently, the atoms are held in the trap for a period of 200 ms. During this time, the atoms that have not been transferred to the dipole trap fall under the influence of gravity out of the detection region, while the atoms within the dipole trap undergo a process of thermalisation (see figure 1.6.3).

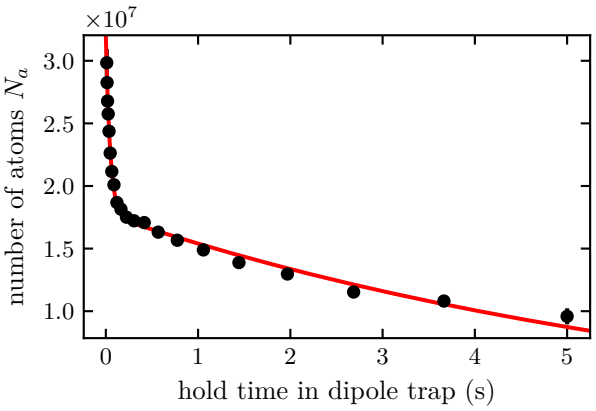

Figure 1.6.3: Number of atoms in the dipole trap versus the hold time in the dipole trap. The data was fitted with a double exponential decay. In the first 200 ms there is natural evaporation of the most energetic atoms from the trap during which a lot of atoms are lost. The decay time of this process is $\tau_{\text{therm}} = 46.9\,\text{ms}$. The remaining atoms have a much longer lifetime of $\tau = 7.0\,\text{s}$. They are lost by collisions with the residual background gas and by scattering photons from the dipole trap laser. For the slow decay, the fitted pre-factor yields a initial number of atoms of $N_0 = 17 \times 10^6$.

During this process, a significant number of atoms are lost. Following the initial rapid loss of atoms, the number of remaining atoms is approximately $N_{\text{at}} = 17 \times 10^6$.

1.6.4 Characterisation of the Atomic Cloud

The atomic cloud was primarily characterised by absorption imaging. For absorption imaging, the atoms are prepared in the $|F = 2, m_F = 2\rangle$-state. For the majority of measurements, the dipole trap laser is switched off after preparing the atoms. After a time of flight (TOF) ranging from 0 ms to 10 ms, the atomic cloud is probed with a detection pulse of duration between 50 µs and 300 µs. The beam is resonant with the $|F = 2, m_F = 2\rangle \longleftrightarrow |F = 3, m_F = 3\rangle$ cycling transition (in this case the quantisation axis is chosen to be the propagation axis of the imaging beam). The beam is directed to a CCD camera[30]. In each sequence, a reference image without atoms is captured in order to calculate the optical density (OD) of the atoms. Given the resonant absorption cross-section of the atoms σ_0, the 2D-density of the cloud can be calculated directly from the Lamber-Beer law [89] for probe intensities well below the saturation intensity

$$n_{\text{2D}} = \frac{\text{OD}}{\sigma_0} = -\frac{1}{\sigma_0} \ln\left(\frac{I_{\text{img}}}{I_{\text{ref}}}\right) \tag{1.6.8}$$

where I_{img} is the image with the atoms and I_{ref} is the reference image without the atoms. Integration over this 2D density yields the number of atoms in the detected region. Some OD images for different TOF are shown in figure 1.6.4 (a).

Radial Dipole Trap Images: The main technique for characterising the dipole trap is to image the atomic cloud from the side. It would be very convenient to measure the size of the atomic cloud from the radial dipole trap image. However, we are currently limited by the size of the imaging beam and the resolution of the camera. The atomic cloud is longer than the imaging field of view of the camera, which means that it is impossible to directly measure the exact number of atoms or the length of the

[30]For radial images: Allied Vision; Manta G-145B NIR: 15.0 frames per second, pixel size of 6.45 µm × 6.45 µm

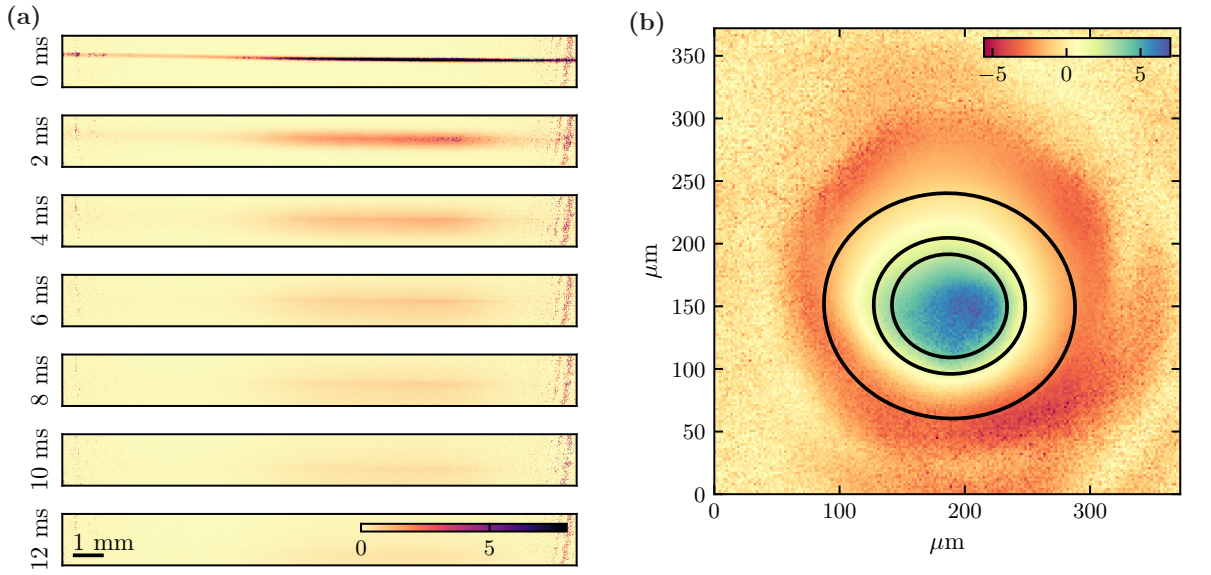

Figure 1.6.4: (a) Radial dipole trap images with a resonant imaging beam for different TOF (labelled on the left). Here the directly measured OD is shown. (b) Axial dipole trap image at a large detuning. Here the directly measured OD is shown, i.e. $\mathrm{OD}_{\mathrm{opt}} = -\ln(I_{\mathrm{img}}/I_{\mathrm{ref}})$ where I_{img} is the image of the atomic cloud and I_{ref} is the reference image without the atoms. The image is taken at a detuning of approximately $\Delta_{\mathrm{img}} \approx -10\,\gamma_{\mathrm{Rb}}$.

atomic cloud. Nevertheless, we employ radial imaging to measure the number of atoms, assuming that we are capturing the majority of the atomic cloud. With a comparable degree of confidence, we can fit the atomic density in the axial direction and get a cloud length of $w_{a,z} = 6.5\,\mathrm{mm}$. In the radial direction, the resolution of the image is on the order of the waist of the trapped atomic cloud. It is therefore impossible to measure the waist of the cloud directly. A linear extrapolation from a number of different TOFs gives an atomic waist of $w_{a,r} = 20 \pm 3\,\mu\mathrm{m}$. This result is not accurate, as it is obtained from a linear extrapolation. However, the expansion of an atomic cloud is given by

$$w(t)^2 = \frac{2k_{\mathrm{B}}T}{m\omega_{a,r}^2}\left[1 + (\omega_{a,r}t)^2\right] \tag{1.6.9}$$

which is linear for large enough times. But for short times the expansion is no longer linear and the image resolution is too low to resolve $\omega_{a,r}$, so this extrapolation only gives a lower limit on the atomic waist. Nevertheless, the radial dipole trap image is a crucial measurement for checking and optimising the atomic loading process.

Axial Dipole Trap Images: In contrast to radial imaging, the on-axis imaging employs an imaging system that is capable of resolving the atomic radial waist (using an enlarging lens and a CCD camera[31]). The z-fibre is employed to send the detection and repump beam to the atoms. This beam is then focused onto the atomic cloud by a 200 mm lens and collimated after the atomic cloud by another 200 mm lens (not shown in the figure 1.1.1). For detection, the collimated beam is again focused onto a camera using a 500 mm lens. This magnifies the image by a factor of 2.5. The numerical aperture of the imaging

[31] For axial images: Allied Vision; Guppy F-146: 17.0 frames per second, 1.4 MP resolution, pixel size of 4.65 µm × 4.65 µm

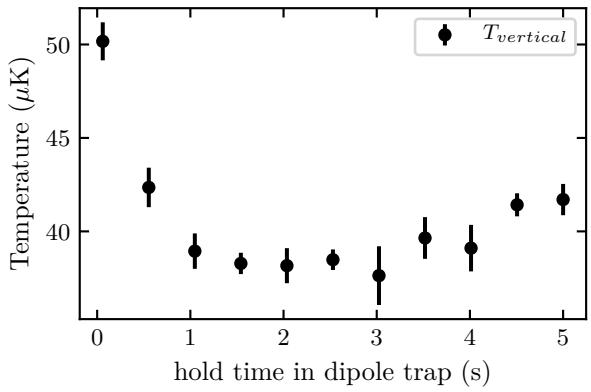

Figure 1.6.5: Temperature of the atomic cloud measured with a time of flight sequence. Here, the hold time in the dipole trap was scanned. Initially, many (hot) atoms are trapped (compare with figure 1.6.3). The hottest atoms evaporate from the trap in the first tens of milli-seconds. After that, the temperature is stable.

system is NA = 0.063, limiting the image resolution to 3.8 µm, which is about the pixel size of the camera (considering the magnification). Because the OD of the cloud in the axial direction is very large, the imaging is performed with a large detuning of about $\Delta_{\text{img}} \approx -10\,\gamma_{\text{Rb}}$. Although we have the spatial resolution to measure the diameter of the cloud, we were not able to make a successful measurement of the atomic waist. From the axial image of the cloud shown in figure 1.6.4 (b), we do not get a conclusive result: In some regions of the image, the OD is consistently negative. This results from the limited depth of field of the imaging of DOF = 194 µm which is much smaller than the cloud length. Most of the cloud is not in the focus of the imaging and thus diffracts the beam. Lensing by dense, cold rubidium cloud has been previously reported [90, 91], even for perfectly mode-matched clouds [88]. Further investigation are required in order to gain a deeper understanding of the current images and to interpret the data, for example, for calculating a cloud waist from this image.

Temperature: The temperature of the atoms is measured by imaging the atomic cloud radially after a varying TOF (raw data shown in figure 1.6.4 (a)). The TOF is set to be significantly larger than an oscillation period in the trap $t_{\text{TOF}} \gg 1/\omega_{a,r}$. This ensures that the expansion is independent of the trap frequency (see equation (1.6.9)). A linear fit to the atomic waist as a function of the TOF allows the temperature to be directly inferred (see figure 1.6.5). The steady-state temperature is reached after a hold time of about 700 ms. Prior to this, the cloud is at a higher temperature, consistent with the evaporation observed in figure 1.6.3. At the end, the atoms equilibrate at a temperature of 38 µK.

Radial Trap Frequency: The trap frequency can be measured by exciting the motion of the atoms in the trap and then measuring the collective oscillation of the atoms. In the radial direction, the motion can be excited by turning off the dipole trap for a duration of 1 ms and then turning it back on again. The centre of mass motion of the atomic cloud cannot be resolved by our (radial) imaging system. However, the first vibrational breathing mode can be detected after a short TOF of 10 µs. Figure 1.6.6 (a) shows the waist of the atomic cloud as a function of the waiting time after excitation. The breathing mode oscillates at twice the frequency of the trapping mode. A trap frequency of $\omega_{a,r} = 2\pi \times 539\,\text{Hz}$ is measured for this trap. Using the trap frequency and the optical power a dipole trap laser waist of $w_{0,\text{trap}} = 99.5\,\mu\text{m}$

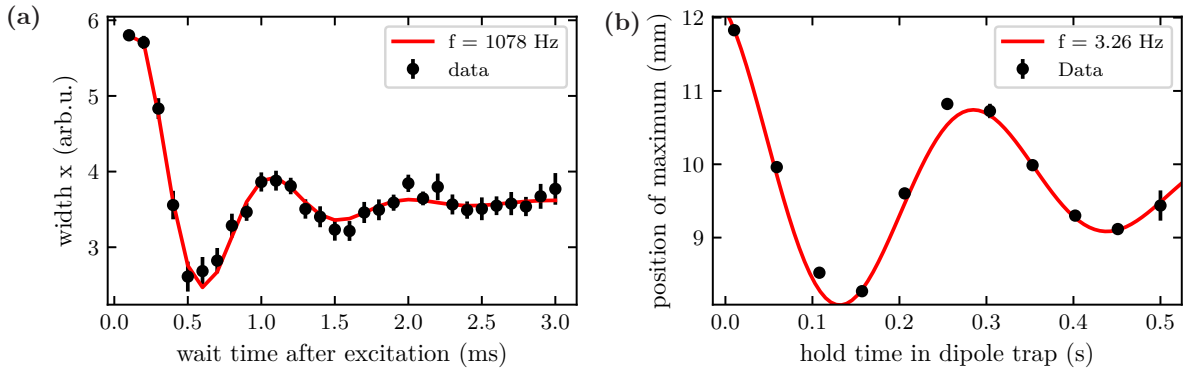

Figure 1.6.6: Measurement of the (a) radial and (b) axial trap frequencies of the dipole trap. (a) For measuring the radial trap frequency, the breathing mode of the atoms is excited. After that, the atoms are held for a variable time (given here as x-axis). The cloud is imaged after a short TOF. To the width, a decaying cosine is fitted, which gives a breathing mode frequency of $f = 1078\,\mathrm{Hz}$. (b) For measuring the axial trap frequency, the position of the fitted maximum of the atomic cloud in z-direction is shown after loading the atoms not to the potential minimum. The atoms start to oscillate in the trap. The data is fitted with a sine function. This experiment was performed with a different trap configuration than all the other experiments (see main text for details).

is calculated using equations (1.6.2) and (1.6.3). This gives a trap potential of $U_0/k_\mathrm{B} = -297\,\mu\mathrm{K}$, which is consistent with the geometrical considerations for the dipole trap beam and with the temperature measurement. From the temperature of the cloud and the trap frequency, the waist of the atomic cloud can be calculated. We obtain an atomic waist of $w_{a,r} = 25.2\,\mu\mathrm{m}$, which is consistent with the lower bound set by the radial dipole trap images.

We used an alternative method to measure the trap frequency and confirm the above results: For this, the amplitude of the dipole trap laser is modulated. If the modulation frequency is precisely twice the trap frequency, the atoms are heated, which reduces the number of atoms in the trap [92]. By scanning the modulation frequency and imaging the atomic cloud, the trap frequency can be evaluated. This method yields the same trap frequency but with less sensitivity than the method used above.

Axial Trap Frequency: The axial trap frequency is determined by misaligning the lens that focuses the dipole trap so that the focus of the dipole trap laser does not overlap perfectly with the MOT. Consequently, the atoms are not loaded at the lowest potential position. This results in the atomic cloud oscillating in the axial direction around the centre of the trap. By scanning the hold time in the dipole trap, we are able to image the cloud at different positions and fit a sine to the fitted centre of the cloud (shown in figure 1.6.6 (b)). This experiment was carried out for a dipole trap that was more tightly focused than in the final configuration. Here, a 150 mm lens was used to focus the dipole trap laser (in the final configuration we used a 200 mm lens). The sinusoidal fit yields a trap frequency of $\omega_{a,z} = 2\pi \times 3.26\,\mathrm{Hz}$. Assuming that the axial temperature of the atoms is the same as the radial one, we obtain an atomic cloud length of $w_{a,z} = 6.48\,\mathrm{mm}$ (taking into account the higher atomic temperature of 92 µK and the smaller beam waist of 73.9 µm of this configuration). This shorter cloud configuration is in agreement with calculations that can be made using the Rayleigh length of the beam (estimated from the radial trap frequency) and the temperature of the atoms. The estimation of the scattering cone for the atomic cloud in this configuration reveals that a longer trap is advantageous for matching the scattering

Trap laser beam waist	w_0	99.5 µm
Trap laser Rayleigh length	z_R	29.2 mm
Trap laser power	P	31 W
Trapping potential depth	$-U_0/k_\mathrm{B}$	297 µK
Radial trap frequency	$\omega_{a,r}$	$2\pi \times 539$ Hz
Axial trap frequency	$\omega_{a,z}$	$2\pi \times 1.30$ Hz
Atomic temperature	T	38 µK
Number of atoms	N_at	1.7×10^7
Lifetime in the trap	τ_trap	7.0 s
Radial atomic cloud waist	$w_{a,r}$	25.2 µm
Axial atomic cloud waist	$w_{a,z}$	10.5 mm
Peak axial optical density	$\mathrm{OD}_{\mathrm{peak},z}$	2500
Waist of probe beam	$w_{\mathrm{pr},0}$	50 µm
Characteristic length of atomic ensemble	$z_{a,\mathrm{R}}$	2.55 mm
Ratio between axial atomic waist and characteristic length	$w_{a,z}/z_{a,\mathrm{R}}$	4.10
Squared ratio between probe waist and radial atomic waist	$(w_{\mathrm{pr},0}/w_{a,r})^2$	3.95

Table 1.6.1: Parameters of the dipole trap and the atomic cloud in the dipole trap. The values are calculated from measurement of the trap frequency, atomic temperature and laser power. The characteristic length $z_{a,\mathrm{R}}$ is calculated for a probe laser at $\lambda_\mathrm{pr} = 780$ nm with a waist of $w_{\mathrm{pr},0} = 50$ µm.

cone with the probe laser. Consequently, we now use the 200 mm lens to focus the dipole trap laser, resulting in a longer atomic cloud. However, for this longer trap we could not repeat the measurement of the axial trap frequency. Fitting the atomic distributions did not work properly, most likely because the length of the atomic cloud is similar to the imaging field of view. Extrapolating the result from the 150 mm lens to the 200 mm lens configuration yields a significantly longer atomic cloud with a length of $w_{a,z} = 10.4$ mm.

Conclusion for the Characterisation: The temperature of the atoms and the radial frequency of the dipole trap can be used to calculate the parameters that characterise the atomic cloud. The final results of the atomic cloud characterisation are summarised in table 1.6.1. Given that the cloud contains $N_\mathrm{at} = 1.7 \times 10^7$ atoms in the cloud and has a waist of $w_{a,r} = 25.2$ µm (calculated from the trap frequency $\omega_{a,r}$ and the temperature T), the peak optical density is calculated to be $\mathrm{OD}_{\mathrm{peak},z} = 2500$. From the cloud parameters, it can be seen that the condition in equation (1.6.7) is very nearly satisfied (see the last two rows of table 1.6.1). A more detailed analysis of the corresponding spin-light coupling and decoherence rates is given in chapter 2.

Influence of the Probe Beam on the Trap Potential

In the atom-membrane coupling experiment, the atomic cloud is coupled to a probe beam at a wavelength of 780 nm. This probe beam is much weaker than the trap beam, but is much closer to resonance. Therefore, the probe beam also exerts a spatially dependent potential $U_\mathrm{probe}(\mathbf{r})$ on the atoms. Due to the large frequency difference between the trap beam and the probe beam, the interference between the two beams can be neglected and the total trap potential can be written as $U_\mathrm{tot}(\mathbf{r}) = U(\mathbf{r}) + U_\mathrm{probe}(\mathbf{r})$. Assuming that both potentials can be approximated as harmonic potentials, the resulting potential is

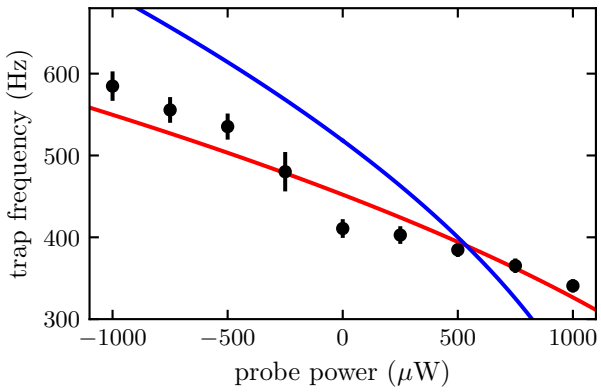

Figure 1.6.7: Trap frequency in presence of the dipole trap beam and the coupling beam. Here, the detuning is ±40 GHz. Negative powers correspond to measurements at negative detuning. The theory for the measured powers and detunings is plotted as a blue line; a fit to the data is plotted in red.

again harmonic and the expected trap frequency is given by

$$\omega_{a,r,\mathrm{tot}} = \sqrt{\omega_{a,r}^2 + \omega_{a,r,\mathrm{probe}}^2}. \tag{1.6.10}$$

The radial trap frequency is measured in the presence of the dipole trap beam and the probe beam at a detuning of ±40 GHz and different powers (see figure 1.6.7). The effect of the probe beam on the trap frequency is on the order of what would be expected from a simple theoretical model. Comparing the fit and the theory, we observe smaller trap frequencies for both the dipole trap beam and the probe beam than expected. This is not yet understood and is not fully consistent with other experiments presented here.

In the following chapter we consider the dynamics of the collective spin of the atomic cloud. It is assumed that the atoms do not move in space during the probe time of up to 20 ms. However, switching on the coupling beam abruptly changes the trap potential, which could excite a breathing mode of the atomic cloud. The time scale of this oscillation is similar to that of the longest probe duration. It would be beneficial to investigate the influence of this motion on the light-spin interface in future experiments.

1.7 Optical Spin Pumping

Once the atoms have been loaded into the dipole trap, the internal state of the atomic cloud is prepared in a single Zeeman state, specifically $|F = 2, m_F = -2\rangle$ (quantisation along the x-axis). This is achieved through a process known as optical spin pumping. In our experiment, we apply two circularly polarised laser beams propagating parallel to a static magnetic field along the x-axis. One of the beams is tuned to resonance with the $F = 2 \leftrightarrow F' = 2$ transition (22-pump), while the other is tuned to resonance with the $F = 1 \leftrightarrow F' = 2$ transition (repump). Each scattered photon of either beam changes the m_F of an atom on average by -1. The stretched state $|F = 2, m_F = -2\rangle$ is the sole dark state of both laser beams, resulting in the accumulation of atoms in this state.

The 22-pump light and the repump light are coupled into the X-fibre (see figure 1.2.2). After the X-fibre, the polarisation of the light is cleaned by a PBS. A cylindrical lens is employed to shape the

beam profile to match with the extreme aspect ratio of the dipole trap. Subsequently, a QWP is used to set the circular polarisation (Stokes vector $\langle S_z\rangle/\bar{S}_0 > 0.99$, see definition in section 2.2.1).

The degeneracy of the Zeeman states is lifted by the presence of a magnetic field. The magnetic Hamiltonian can be expanded in a linear and a quadratic term (provided that the magnetic interaction is small compared to the hyperfine splitting). While the linear Zeeman effect leads to equidistant splitting between the Zeeman levels, the quadratic Zeeman splitting leads to different transition energies of successive Zeeman states (a detailed discussion is given in section 2.3.2). A bias field of 2.8 G along the x-axis is used to induce a quadratic splitting of approximately $\delta\Omega_\mathrm{s}/2 = 2\pi \times 1.3\,\mathrm{kHz}$. The precession frequency of the spin around the bias magnetic field is determined by the energy difference between two successive Zeeman levels, which is different for each transition because of the quadratic splitting. Spin spectroscopy is performed to resolve the different transitions between Zeeman levels.

In the experiment, the spin is prepared by optical pumping along the x-axis and then driven with a weak rf field. The rf field is applied to drive a single transition between two Zeeman states (the other transitions are not resonant due to the quadratic splitting). The frequency of the rf field is scanned over the different transition energies. The driven spin is continuously probed by measuring the Faraday rotation of a probe beam along the z-axis (power of 100 µW at a detuning of −20 GHz). Due to the Faraday effect, the z-component of the spin is mapped on the polarisation state of light, which can be read out by polarisation homodyne measurement. Thus, by measuring the polarisation state of the probe light we have direct access to the spin precession. For further details on the experimental procedure, the reader is referred to the chapter 2.

The results of two such spectroscopy experiments are presented in figure 1.7.1 (a) for a not yet pumped atomic ensemble and in figure 1.7.1 (b) for an atomic ensemble after 500 µs of pumping. By comparing the areas of the fitted peaks, the occupancy in each Zeeman level can be calculated. For the purpose of this calculation, it is assumed that the $|F = 2, m_F = 2\rangle$ state is not occupied at all. This is not a good assumption for the unpumped ensemble. However, once we add some pumping, the peak of the $|F = 2, m_F = 2\rangle \leftrightarrow |F = 2, m_F = 1\rangle$ transition cannot be resolved spectroscopically, indicating that neglecting the population of the $|F = 2, m_F = 2\rangle$ state is a good approximation.

After spin pumping, the atoms are found to be in the $|F = 2, m_F = -2\rangle$ state with a probability of 87 % (see figure 1.7.1 (c) for different pump durations). The occupation of the different Zeeman levels allows us to calculate the polarisation of the atoms [93], which is given by

$$p = \frac{1}{F}\sum p_{m_F} m_F. \tag{1.7.1}$$

In our spin ensemble, the polarisation is $p = -0.92$ (see figure 1.7.1 (d)). It is unclear what limits the polarisation of the atoms. One possibility is that it is the spin-pumping. However, it is also possible that this measurement is limited by the probe itself, which adds decoherence to the spin: We observe that the probe beam depolarises the spin for a probe of 100 µW at −20 GHz and a probe duration of $t_\mathrm{probe} > 3\,\mathrm{ms}$. In order to resolve the different transition energies for successive Zeeman levels, we need to probe for more than $t_\mathrm{probe} > 4\pi/\delta\Omega_\mathrm{s} = 0.8\,\mathrm{ms}$. The integration time for the analysis is set to 5 ms which allows the analysis to be not Fourier limited and enables the fitting of individual peaks. Instead of shortening the integration time, one could decrease the probe power to reduce the spin decoherence. However, a reduction in the probe power results in a decrease in signal to noise. As such, this measurement serves as a lower bound on the spin polarisation of the atomic ensemble.

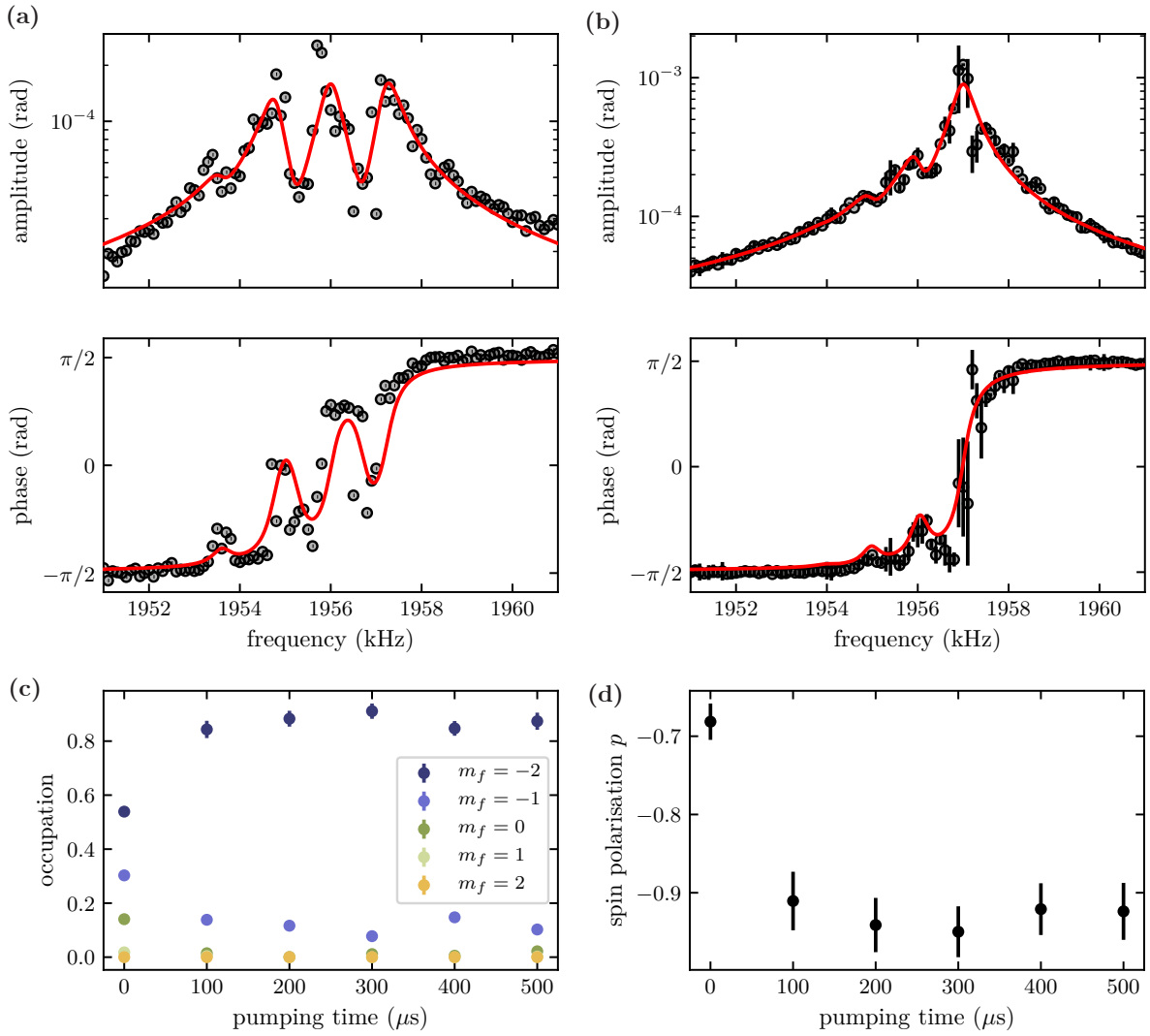

Figure 1.7.1: Characterisation of the spin pumping sequence: Spectroscopy of the atomic spin (a) without spin pumping and (b) after 500 µs of spin pumping. For the amplitude, the Faraday signal was demodulated at the applied rf-frequency, integrated over 5 ms and then normalised to Faraday angle units. The phase corresponds to the phase difference between the rf-drive and the detected signal. The solid red line is a fit to the data using the fit function given in equation 2.5.21. From the fit, the occupation of different Zeeman levels is obtained, which is shown in (c) for different durations of optical pumping. (d) shows the resulting spin polarisation as function of the pump time. The errorbar shows only the statistic error and neglects the systematic error of the measurement due to depumping during the probe.

Chapter 2

Spin-Light Quantum Interface

In this chapter, the quantum interface between the light and the spin is introduced. The polarisation state of the light and the collective spin of a dipole-trapped atomic ensemble are coupled via the Faraday interaction. Here, the theory and the experimental implementation of the Faraday interface is presented. The interaction of the spin with the probe light is simulated and characterised experimentally. In a first part, we use a single atom description to understand the spin dynamics in presence of the optical field. In a second part, the three-dimensional coupling of the atomic cloud to multiple optical modes is introduced. This leads to an inhomogeneity of the coupling across the cloud which can be modelled by using effective spin operators. These effective spin operators are used to model the experimental results of the spin-light interface. Measurements show that the spin-light interface can indeed be operated in the quantum regime.

2.1 Introduction

In our hybrid experiment, we couple two different systems over a macroscopic distance of 2 m using light as a carrier of the quantum signals [29]. In order to perform remote hybrid coupling experiments, we require that all individual systems are interfaced with the light with high quantum cooperativities [37]. The spin of cold atoms is a suitable quantum system, because the collective spin of cold atomic ensembles is a well-established platform in quantum optics. Not only because there is a large toolbox available to initialise and manipulate the collective spin [13, 52], but also because it can interact strongly with the optical field.

Reaching large cooperativities with atoms presents two major challenges: First, the coherent coupling of a single atom to the light scales with the atom-light interaction cross-section $\sigma_0 \sim \lambda^2$ divided by the cross-section of the optical mode A where λ is the wavelength of a resonant laser [94]. Usually, σ_0/A is a small number. Second, the overlap between the scattered light of a single atom and the desired Gaussian optical mode is small. Placing atoms in high-finesse optical cavities addresses both challenges but goes along with an increase of experimental complexity [13]. In our experiment a different approach is pursued. It has been shown that the forward scattering of a large, dilute and disordered atomic ensemble interferes

constructively while the decay into other modes interferes destructively [95]. For large atom numbers, the atoms can be interfaced with a far detuned laser beam and a large signal is still obtained [96, 97, 98]. We use a quantum non-demolition interaction to interface the atomic ensemble with the light [13]. This interaction is based on the Faraday effect, which causes a rotation of the polarisation of the light even in a dilute atomic ensemble [53].

The cooperativity C_s of the Faraday interface is defined as the ratio between the coherent scattering rate $S_\mathrm{qba} = \Gamma_\mathrm{s}$ into the Gaussian mode of the probe beam and the rate $S_\mathrm{dec} = \gamma_\mathrm{s}/2$ of the incoherent coupling to other optical modes (environment), $C_\mathrm{s} = S_\mathrm{qba}/S_\mathrm{dec} = 2\Gamma_\mathrm{s}/\gamma_\mathrm{s}$ (the definition contains a factor 1/2 because $n_s \approx 0$ and only the quantum noise is relevant. The definition of C_s is consistent with the definition given in chapter 3 for a mechanical oscillator). In order to get a large cooperativity for our Faraday-interface, we have to understand the coherent and the dissipative interactions of the atoms with the light: The coherent, collective forward scattering of the atomic cloud is usually described in a 1D-picture [99]. It is assumed that all atoms are independent scatterers, which is valid for an atomic density $n < \lambda^{-3}$ [100]. In this limit, the total forward scattering depends on the interaction of a single atom with the light times the total number of atoms. The decoherence of the atomic spin arises from photon scattering into any mode but the one of the incoming laser beam. Because the atoms are randomly distributed in the cloud, the scattering into 4π is not fully cancelled, not even for a perfectly mode-matched cloud. The resulting scattering rate into modes except for the one of the probe laser corresponds exactly to the spontaneous emission rate of a single atom [101]. So the spin decoherence rate only depends on the interaction strength of a single atom with the light. Thus, for an atomic ensemble, the cooperativity scales with the number of atoms in the atomic cloud $C_\mathrm{s} \propto N_\mathrm{a}$.

A large quantum cooperativity of the Faraday interface means that the shot noise of the light is the primary noise source driving the atomic spin, and that the spin signal is mostly mapped onto the mode of the incoming beam (rather than scattered into other optical modes). These two conditions can be tested experimentally by measuring the quantum noise of the light after the interaction with the atoms. In the quantum-noise limited scenario, the noise of the outgoing light has three contributions [97]: the shot noise of the incoming light, the spin noise resulting from the intrinsic quantum uncertainty of the atomic spin (projection noise), and the fluctuations of the spin caused by driving the spin with the shot noise of the light (backaction noise). Each of these contributions exhibits a unique scaling with probe power and number of atoms. In order to claim a large quantum cooperativity, it is necessary to demonstrate that the noise of the spin-light interface is predominantly governed by the backaction noise of the Faraday interaction, as opposed to technical noise, higher-order coupling effects or collective atomic interactions.

In this chapter, the coherent and dissipative dynamics of the atom-light interface is introduced theoretically and experimentally: In a first section, the interaction between the atoms and the light is described theoretically. First, the simpler models of a spin-1/2 atom and a spin-1 atom are considered before showing the interaction for the Rubidium-87 D2-line. In section 2.3, the experimental implementation of the spin-light interface is shown. The dynamics of a spin in a bias magnetic field is introduced and some measurements are presented to give a first intuition on the spin-light interaction. Section 2.4 discusses the effect of inhomogeneous coupling between the Gaussian optical beam and the Gaussian atomic cloud. The limitation of the 1D-picture and the quantum noise for a 3D-cloud are discussed. In chapter 2.5 the dynamics of a classically driven spin is discussed, which is used in many experiments for spin initiation or spin characterisation. Finally in chapter 2.6, the characterisation of the spin-light interface is shown.

2.2 Far Detuned Atom-Light Interaction

In this section, the interaction of an atom with a far-detuned electromagnetic field is derived. For this, we follow the lecture notes of Steck [102] and use the sign conventions which are introduced there. We consider an atom with one valence electron. In our model, an optical field couples the ground state manifold with a total electron angular momentum j to a single excited state fine structure manifold with total electron angular momentum j'. Both the ground state manifold and the excited state manifold are split into different hyperfine states f. The atomic Hamiltonian is given by

$$\hat{H}_0 = \hbar \sum_{f,m_f} \Delta_f |f, m_f\rangle\langle f, m_f| + \hbar \sum_{f',m'_f} (\omega_0 + \Delta_{f'}) |f', m'_f\rangle\langle f', m'_f|, \tag{2.2.1}$$

where Δ_f and $\Delta_{f'}$ are the frequency shifts of the hyperfine levels due to the coupling of the total electron angular momentum j and j' to the total nuclear angular momentum i (the hyperfine structure), $\hbar\omega_0$ is the transition energy from the ground state manifold to the excited state manifold (when neglecting the hyperfine structure) and m_f and m'_f are the total atomic angular momentum projections. The atom is interfaced with a paraxial mode of the electromagnetic field which is described by the unitless mode function $u(\mathbf{r})$ (normalised to $\max(u(\mathbf{r})) = 1$, see appendix B.1.1 for details). Applying the slowly varying envelope approximation, the electric field is given by

$$\hat{\mathbf{E}}(\mathbf{r}, t) = \mathcal{E}_0(\hat{a}_H(z,t)\mathbf{e}_H + \hat{a}_V(z,t)\mathbf{e}_V)u(\mathbf{r})\mathrm{e}^{\mathrm{i}(k_0 z - \omega_\mathrm{L} t)} + \mathrm{h.c.}, \tag{2.2.2}$$

where $\mathcal{E}_0 = \sqrt{\hbar\omega_\mathrm{L}/(2\epsilon_0 c A)}$ is the vacuum electric field density (per $s^{-1/2}$ bandwidth), $A = \pi w_0^2/2$ is the cross-section area of the (Gaussian) optical mode, $\hat{a}_H$ ($\hat{a}_V$) the annihilation operators of the horizontally (vertically) polarised field (units of $s^{-1/2}$), $\mathbf{e}_H$ ($\mathbf{e}_V$) the unit-vector for horizontal (vertical) polarisation, $k_0 = 2\pi/\lambda$ the wave vector of the field, ω_L the angular frequency of the field, c the speed of light and ϵ_0 the vacuum permittivity. In this description, the intensity of the field (averaged over one optical period) is given by [103]

$$I(\mathbf{r}) = c\epsilon_0 \langle |\hat{\mathbf{E}}(\mathbf{r}, t)|^2 \rangle_t = 2c\epsilon_0 \langle \hat{\mathbf{E}}^{(-)}(\mathbf{r}, t) \cdot \hat{\mathbf{E}}^{(+)}(\mathbf{r}, t) \rangle \tag{2.2.3}$$

$$= \frac{\hbar\omega_\mathrm{L}}{A} |u(\mathbf{r})|^2 \Phi_\mathrm{L} = \frac{P}{A} |u(\mathbf{r})|^2 \tag{2.2.4}$$

where the positive and negative frequency components of the electric field are given by $\hat{\mathbf{E}}^{(\pm)}(\mathbf{r}, t)$, the mean photon flux by $\Phi_\mathrm{L} = \langle \hat{a}_H^\dagger \hat{a}_H + \hat{a}_V^\dagger \hat{a}_V \rangle$ and the optical power in the mode $u(\mathbf{r})$ by P (in W). Here, the time dependency on the slowly varying envelope function is omitted (i.e. for $I(\mathbf{r})$, Φ_L, P).

The interaction between the atom and the field is given by the well-known electric dipole Hamiltonian, $\hat{H}_\mathrm{int} = -\hat{\mathbf{d}} \cdot \hat{\mathbf{E}}(\mathbf{r}, t)$, where $\hat{\mathbf{d}}$ is the atomic dipole operator and $\mathbf{r}$ is the position of the nucleus [104]. The dipole operator can be expressed in terms of the electron position operator $\hat{\mathbf{r}}_e$, which results in

$$\hat{H}_\mathrm{int} = -e\hat{\mathbf{r}}_e \cdot \hat{\mathbf{E}}(\mathbf{r}, t), \tag{2.2.5}$$

where e is the elementary charge and $\mathbf{r}$ is the classical position of the nucleus of the atom [104]. The position operator $\hat{\mathbf{r}}_e$ couples the atomic ground state manifold to the excited state manifold (but not states within the ground state or the excited state manifolds) and can therefore be decomposed into $\hat{\mathbf{r}}_e^{(+)} = \hat{P}_g \hat{\mathbf{r}}_e \hat{P}_e$ which de-excites the atom and oscillates at a positive frequency ω_0 and $\hat{\mathbf{r}}_e^{(-)} = \hat{P}_e \hat{\mathbf{r}}_e \hat{P}_g$

which excites the atom and oscillates at a negative frequency $-\omega_0$. Here, P_g (P_e) is the projector into the atomic ground (excited) state manifold. For simplifying the interaction Hamiltonian, we assume that the optical frequency ω_L is on the order of the atomic transition frequency ω_0, so the fast rotating terms in the dipole Hamiltonian are neglected using the rotating wave approximation (for details, see appendix B.2).

It is also useful to express the Hamiltonian in one particular basis. Due to the symmetry of the problem given by the optical beam, the spherical basis is a natural choice, as defined in [102]. The resulting Hamiltonian in the spherical basis is explicitly shown in appendix B. By choosing the quantisation axis along the propagation of the electromagnetic field, we obtain

$$\hat{H}_\mathrm{int} = \hbar\tilde{\Omega}_{jj'}\left(\hat{a}_-\hat{\sigma}_1^\dagger + \hat{a}_+\hat{\sigma}_{-1}^\dagger\right) u(\mathbf{r})\exp[\mathrm{i}(k_0 z - \Delta t)] + \mathrm{h.c.}, \tag{2.2.6}$$

where $\tilde{\Omega}_{jj'} = -\mathcal{E}_0\langle j||e\hat{\mathbf{r}}_e||j'\rangle/\hbar$ is the transition strength between two fine-structure manifolds j and j' (units of $\mathrm{s}^{-1/2}$), $\hat{a}_\pm = \mp(\hat{a}_H \pm \mathrm{i}\hat{a}_V)/\sqrt{2}$ are the annihilation operators for circularly polarised photons (units of $\mathrm{s}^{-1/2}$), $\hat{\sigma}_q^\dagger$ are the atomic raising operators (definition see below) and the doubled bars $\langle\cdot||\cdot||\cdot\rangle$ indicate that the matrix element is reduced. In this expression, the different detunings of the hyperfine levels are neglected and the detuning between the probe field and the atomic resonance is given by $\Delta = \omega_\mathrm{L} - \omega_0$. The spherical basis is defined in such a way that $\sigma_1^\dagger$ couples the states of the so-called σ^--transition, where $m_f' = m_f - 1$, while $\sigma_{-1}^\dagger$ couples the states of the σ^+-transition with $m_f' = m_f + 1$. In the hyperfine basis, the atomic lowering operators are defined as

$$\hat{\sigma}_q = \sum_{f,m_f,f',m_f'} \frac{\langle f||\hat{\mathbf{r}}_e||f'\rangle}{\langle j||\hat{\mathbf{r}}_e||j'\rangle}\langle f', m_f'; 1, q|f, m_f\rangle|f, m_f\rangle\langle f', m_f'| \tag{2.2.7}$$

where we sum over all ground state hyperfine levels $|f, m_f\rangle$ and all relevant excited state hyperfine levels $|f', m_f'\rangle$ (in our case only the D2 line is considered). Here, q is the spherical coordinate and $\langle f', m_f'; 1, q|f, m_f\rangle$ is a Clebsch-Gordan coefficient. From the Clebsch-Gordan coefficient we see that $q = 0$ couples states with the same Zeeman number $m_f' = m_f$ (π-transition). The $\hat{\sigma}_0^\dagger$ raising operator does not appear in the Hamiltonian given in equation (2.2.6), because these states are only coupled by light which is linearly polarised along the z-axis, which is not described here. The lowering operator $\hat{\sigma}_{\pm1}$ couples states with a quantum number m_f differing by one, namely $m_f' = m_f \mp 1$. This corresponds to a change in angular momentum by one quantum. The uncommon sign convention results from the particular spherical basis used in this derivation [102]. Note that in the interaction Hamiltonian given by equation (2.2.6), the angular momentum is conserved, e.g. by absorbing a σ^+ circularly polarised photon (i.e. by $\hat{a}_+$), the angular momentum of the photon is transferred to the atom by $\hat{\sigma}_{-1}^\dagger$ which excites the atom along the σ^+-transition. The derivation and a more useful (but more evolved) analytic expression for lowering operators $\hat{\sigma}_q$ are given in appendix B.2. For future calculations, it is useful to write the transition strength between two fine-structure manifolds in terms of the natural population decay rate γ_Rb of the excited state which is known from literature. It is given by [105]

$$|\tilde{\Omega}_{jj'}|^2 = \frac{2j'+1}{2j+1}\frac{\sigma_0}{4A}\gamma_\mathrm{Rb}. \tag{2.2.8}$$

The light-atom interaction strength depends on the ratio of the atomic cross-section $\sigma_0 = 3\lambda^2/(2\pi)$ (here, of the cycling transition of Rubidium $|f = 2, m_f = -2\rangle \to |f' = 3, m_f' = -3\rangle$ [105]) and the area of the

light beam $A = \pi w_0^2/2$ (here for a Gaussian beam, see appendix B.1.1 for details). This ratio determines how many photons are scattered by a single atom.

For a good understanding of the atomic dynamic, we have to consider the decoherence mechanism of the atoms in presence of the optical field. In this work, we consider a cold, dipole trapped atomic ensemble. For cold atoms, we can assume that the ground state is stable and that the decoherence arises mainly from the radiative decay of the excited state manifold. The excited states decay to the ground state at the natural decay rate γ_{Rb}. To calculate the full dynamics of the atom, this decay can be modelled with the following jump operators [102]

$$\hat{J}_{\sigma^+} = \sqrt{\gamma_{\mathrm{Rb}} \frac{2j'+1}{2j+1}}\hat{\sigma}_{-1}, \qquad \hat{J}_{\pi} = \sqrt{\gamma_{\mathrm{Rb}} \frac{2j'+1}{2j+1}}\hat{\sigma}_{0}, \qquad \hat{J}_{\sigma^-} = \sqrt{\gamma_{\mathrm{Rb}} \frac{2j'+1}{2j+1}}\hat{\sigma}_{1}. \tag{2.2.9}$$

where the indices of the jump operator denote the polarisation of the emitted photon (and do not give the coordinate q). The decay of the atom creates a photon with a k-vector in a random direction and a polarisation which conserves the angular momentum in the process (e.g. $\hat{J}_{\sigma^+} \to \hat{a}_+^\dagger$). Now we have the Hamiltonian and the decoherence processes governing the light-matter interaction of a general alkali atom. Before moving on directly to the Rubidium atoms, two much simpler systems will be considered. These simpler level-structures can be used to introduce most of the important concepts.

2.2.1 Model of an Atom with a spin-1/2 ground state

We begin by examining the simplest atom which exhibits some dynamics within the ground state manifold. In this section, we consider a model atom with no nuclear spin, $i = 0$, a ground state of $j = 1/2$ which is optically coupled to an excited-state with $j' = 3/2$. This elementary atom allows us to introduce the majority of the dynamics that characterise our system [106, 107]. In the case of the spin-1/2 atom, the matrix representation of the atomic lowering operator $\hat{\sigma}_q$ are given by

$$\hat{\sigma}_1 = \nu^* |g_{+1/2}\rangle\langle e_{-1/2}| + \mu^* |g_{-1/2}\rangle\langle e_{-3/2}|, \tag{2.2.10}$$

$$\hat{\sigma}_0 = \eta^* \left(|g_{+1/2}\rangle\langle e_{+1/2}| + |g_{-1/2}\rangle\langle e_{-1/2}| \right), \tag{2.2.11}$$

$$\hat{\sigma}_{-1} = \mu^* |g_{+1/2}\rangle\langle e_{+3/2}| + \nu^* |g_{-1/2}\rangle\langle e_{+1/2}|, \tag{2.2.12}$$

with $\mu = 1/\sqrt{2}$, $\nu = 1/\sqrt{6}$, and $\eta = 1/\sqrt{3}$. Here, we see again that the operator $\hat{\sigma}_1$ couples the σ^--transition, the operator $\hat{\sigma}_0$ the π-transition, and the operator $\hat{\sigma}_{-1}$ the σ^+-transition. For an atom at the focus of the optical field (assuming that $u(\mathbf{r}) = 1$, $z = 0$), the interaction Hamiltonian reads as

$$\begin{aligned} \hat{H}_{\mathrm{int}} = \hbar\tilde{\Omega}[&\hat{a}_-(\nu|e_{-1/2}\rangle\langle g_{+1/2}| + \mu|e_{-3/2}\rangle\langle g_{-1/2}|) \\ &+ \hat{a}_+(\mu|e_{+3/2}\rangle\langle g_{+1/2}| + \nu|e_{+1/2}\rangle\langle g_{-1/2}|)] \exp(-\mathrm{i}\Delta t) + \mathrm{h.c.} \end{aligned} \tag{2.2.13}$$

where the transition strength is given by $\tilde{\Omega} = \tilde{\Omega}_{1/2,3/2} = \sqrt{\gamma_{\mathrm{Rb}}\sigma_0/(2A)}$. The level diagram of the spin-1/2 atom and the driven transitions are shown in figure 2.2.1. In the following, we treat the atom in a rotating frame with respect to the optical field. We assume that the Zeeman levels of the ground state are degenerate. The detuning of the optical field with respect to the atomic transition is $\Delta_m = \omega_{\mathrm{L}} - \omega_{0,m}$, where $\omega_{0,m}$ is the resonance frequency with respect to the excited state level $|e_m\rangle$. Thus, the Hamiltonian

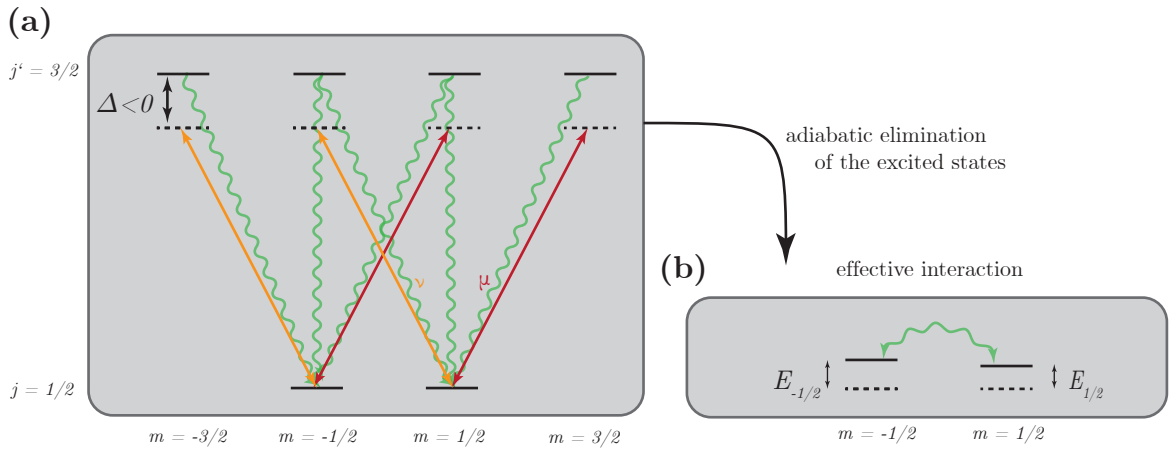

Figure 2.2.1: Level diagram of the considered spin-1/2 atom (a) without and (b) with the adiabatic elimination of the excited state. The orange and red arrows indicate the coherent interaction, while the green arrows show the decoherent process due to the spontaneous decay of the excited-state. Applying the adiabatic elimination, light effectively shifts the ground state levels by $E_{\pm 1/2}$ which depends on the polarisation of the light. Furthermore, it results in an effective decoherence channel between the two ground states (green arrow).

of the atom in the absence of the interaction is given by

$$\hat{H}_0 = -\hbar \sum_m \Delta_m |e_m\rangle\langle e_m|. \tag{2.2.14}$$

Energy Shift of the Ground State: From the total Hamiltonian $\hat{H}_{\text{tot}} = \hat{H}_0 + \hat{H}_{\text{int}}$, it is possible to calculate the eigenenergy of the atomic states. Assuming that the excited states are degenerate (i.e. $\Delta_m = \Delta$) and that the detuning of the field is much larger than the energy shift due to the light, the interaction shifts the atomic ground-state levels by

$$E_{-1/2} = \frac{\hbar|\tilde{\Omega}|^2}{\Delta}\left(|\mu|^2\langle \hat{a}_-^\dagger \hat{a}_-\rangle + |\nu|^2\langle \hat{a}_+^\dagger \hat{a}_+\rangle\right), \tag{2.2.15}$$

$$E_{1/2} = \frac{\hbar|\tilde{\Omega}|^2}{\Delta}\left(|\mu|^2\langle \hat{a}_+^\dagger \hat{a}_+\rangle + |\nu|^2\langle \hat{a}_-^\dagger \hat{a}_-\rangle\right). \tag{2.2.16}$$

For linearly polarised light (i.e. $\langle \hat{a}_+^\dagger \hat{a}_+\rangle = \langle \hat{a}_-^\dagger \hat{a}_-\rangle$), this light-shift is a common energy shift for both levels. However, if the input light is circularly polarised, the two Zeeman levels are shifted differently. Consequently, the circular polarisation of the light acts on the spin like a fictitious magnetic field [108] (compare with section 2.3.2). In order to gain a deeper understanding of the dynamics of the spin in the presence of a far detuned electromagnetic field, it is beneficial to adiabatically eliminate the excited states.

Adiabatic Elimination of the Excited States: If the optical field is far detuned, it is reasonable to assume that the excited-state manifold is not occupied. Thus, the dynamics of the atom can be reduced to the ground state manifold. This dynamics is obtained by adiabatically eliminating the excited states (explained in detail in [13] and explicitly shown in appendix B.2.2). In order to eliminate the excited-

state manifold, it is necessary to re-express all transition matrix elements $|e_m\rangle\langle g_{m'}|$ of the interaction Hamiltonian in terms of ground state matrix elements $|g_m\rangle\langle g_{m'}|$. For this to be the case, we assume that the coherences are in a steady state, i.e. $\frac{d}{dt}|g_m\rangle\langle e_{m'}| = 0$, and that the excited states are not occupied, $|e_m\rangle\langle e_{m'}| = 0$. From this, we get steady state values for the coherences $|g_m\rangle\langle e_{m'}|$. These steady state values of the coherences can be introduced into the expression of the interaction Hamiltonian given by equation (2.2.13). For simplicity, we assume that all detunings $\Delta_m = \Delta$ are equal and obtain

$$\hat{H}_{\text{int}} = \frac{2\hbar|\tilde{\Omega}|^2}{\Delta}\left[(\hat{a}_-^\dagger\hat{a}_-|\nu|^2 + \hat{a}_+^\dagger\hat{a}_+|\mu|^2)|g_{1/2}\rangle\langle g_{1/2}| + (\hat{a}_-^\dagger\hat{a}_-|\mu|^2 + \hat{a}_+^\dagger\hat{a}_+|\nu|^2)|g_{-1/2}\rangle\langle g_{-1/2}|\right]. \quad (2.2.17)$$

The atomic Hamiltonian can be rewritten in terms of the ground state by writing the excited-state populations as $|e_i\rangle\langle e_i| = |e_i\rangle\langle g_j|g_j\rangle\langle e_i|$ [13]. We get $\hat{H}_0 = -\hat{H}_{\text{int}}/2$ and thus yield an effective ground state Hamiltonian

$$\hat{H}_{\text{eff}} = \hat{H}_{\text{int}}/2. \quad (2.2.18)$$

To further simplify this expression, it is useful to define spin operators for the atomic state and the light field, which is done in the next paragraphs.

Stokes Vector

The state of the light can be expressed as a four-dimensional vector, known as the *Stokes vector*. The first entry of the Stokes vector $\hat{S}_0$ is proportional to the total photon flux Φ_{L}. Its mean value is given by the laser power $\langle\hat{S}_0\rangle = P/(2\hbar\omega) = \Phi_{\text{L}}/2$. The polarisation state of the light is represented by a point on the *Poincaré sphere* in a space spanned by $\bar{S}_{x,y,z}$. The radius of the *Poincaré sphere* is given by $p\langle\hat{S}_0\rangle$ where p is the degree of polarisation. Each coordinate axis gives the flux difference between two orthogonal polarisation states of the light. $\hat{S}_x$ denotes the flux difference between horizontal and vertical polarised light, $\hat{S}_y$ between $+45°$ polarised and $-45°$ polarised light and $\hat{S}_z$ between σ^+ and σ^- polarised light. The quantum mechanical *Stokes vector* can be defined in terms of the creation and annihilation operators [109] as

$$\hat{S}_0(\xi) = \frac{1}{2}(\hat{a}_+^\dagger(\xi)\hat{a}_+(\xi) + \hat{a}_-^\dagger(\xi)\hat{a}_-(\xi)), \quad (2.2.19)$$

$$\hat{S}_x(\xi) = \frac{1}{2}(\hat{a}_+^\dagger(\xi)\hat{a}_-(\xi) + \hat{a}_-^\dagger(\xi)\hat{a}_+(\xi)), \quad (2.2.20)$$

$$\hat{S}_y(\xi) = \frac{1}{2\mathrm{i}}(\hat{a}_+^\dagger(\xi)\hat{a}_-(\xi) - \hat{a}_-^\dagger(\xi)\hat{a}_+(\xi)), \quad (2.2.21)$$

$$\hat{S}_z(\xi) = \frac{1}{2}(\hat{a}_+^\dagger(\xi)\hat{a}_+(\xi) - \hat{a}_-^\dagger(\xi)\hat{a}_-(\xi)). \quad (2.2.22)$$

where ξ is a generalised position coordinate along the propagation direction of the light. The position coordinate is given by the position on the optical path and the time $\xi \to z_{\text{opt}} - ct$. Knowing the commutation relations of the photon creation and annihilation operators (given explicitly in equations (B.1.7) to (B.1.8)), it can be seen that the Stokes vector components satisfy spin commutation relations [110]

$$[\hat{S}_j(\xi), \hat{S}_k(\xi')] = \mathrm{i}\epsilon_{jkl}c\delta(\xi - \xi')\hat{S}_l(\xi), \quad [\hat{S}_j(\xi), \hat{\mathbf{S}}(\xi')^2] = 0 \quad \text{and} \quad [\hat{S}_j(\xi), \hat{S}_0(\xi')] = 0 \quad (2.2.23)$$
$$\text{for} \quad \{j,k,l\} = \{x,y,z\},$$

where ϵ_{jkl} is the *Levi-Civita symbol*. Thus, the light can be modelled as a spin with the spin length given by the photon flux. Note, that the Stokes vectors are given in units of s^{-1}. In this chapter, we mostly consider one position in the optical path and therefore write only the time-dependency of the operators.

Atomic Spin

The atomic spin for a single hyperfine manifold f can be written as

$$\hat{f}_x = \frac{1}{2}\left(\hat{f}_+ + \hat{f}_-\right), \qquad \hat{f}_y = \frac{1}{2\mathrm{i}}\left(\hat{f}_+ - \hat{f}_-\right), \qquad \hat{f}_z = \sum_{m_f} m_f |f, m_f\rangle\langle f, m_f|, \tag{2.2.24}$$

where the ladder operators are given by

$$\hat{f}_+ = \sum_{m=-f}^{f-1} C(f,m)|f, m+1\rangle\langle f, m|, \qquad \hat{f}_- = \hat{f}_+^\dagger, \tag{2.2.25}$$

where $C(f,m) = \sqrt{f(f+1) - m(m+1)}$. The raising operator $\hat{f}_+$ increases the angular momentum by one quantum, $m_f \to m_f + 1$, while the lowering operator $\hat{f}_-$ lowers the angular momentum by one quantum, $m_f \to m_f - 1$. But both ladder operators act within a given ground state manifold. For a spin-1/2 system, this is a complete description of the internal state (as long as the electron remains in this specific manifold). However, for atoms with larger spins, tensor components need to be considered (which are introduced in section 2.2.3).

Faraday Interaction Hamiltonian of the Spin-1/2 Atom

Having defined the spin operators and the Stokes vector, the effective ground state Hamiltonian of a spin-1/2 atom in a far detuned field given in equation (2.2.18) can be written as

$$\hat{H}_{\mathrm{eff}} = \hbar\alpha_0 \hat{\mathbb{1}}_g \hat{S}_0 + \hbar\alpha_1 \hat{f}_z \hat{S}_z, \tag{2.2.26}$$

where the atomic scalar and vector polarisability constants α_0 and α_1 are defined as

$$\alpha_0 = \frac{|\tilde{\Omega}|^2}{\Delta}(|\nu|^2 + |\mu|^2) = \frac{\sigma_\pi}{2A}\frac{\gamma_{\mathrm{Rb}}}{\Delta} = \frac{\sigma_0}{3A}\frac{\gamma_{\mathrm{Rb}}}{\Delta}, \tag{2.2.27}$$

$$\alpha_1 = \frac{2|\tilde{\Omega}|^2}{\Delta}(|\mu|^2 - |\nu|^2) = \frac{\sigma_\pi}{2A}\frac{\gamma_{\mathrm{Rb}}}{\Delta}, \tag{2.2.28}$$

where $\sigma_\pi = \lambda^2/\pi$ is the atomic cross-section for linearly polarised light and $A = \pi w_0^2/2$ is the cross-section of the optical mode. The first term of the Hamiltonian $\hat{H}_0 = \hbar\alpha_0 \hat{\mathbb{1}}_g \hat{S}_0$ is a *scalar* component that generates a global energy shift. It leads to a general attraction or repulsion force, depending on the detuning Δ of the light. Much more relevant to this work is the *vector* component $\hat{H}_1 = \hbar\alpha_1 \hat{f}_z \hat{S}_z$. It couples the polarisation state of the light to the atomic spin. Using the spin-1/2 system as an example, we will discuss the dynamics of this so-called Faraday interaction. After that, larger spin systems will be discussed. But even for larger spins the general dynamics of the Faraday interaction remains the same, only the polarisability constants have to be adjusted and a higher-order coupling term has to be added to the interaction Hamiltonian.

Collective Spin

In our experiment, rather than a single atom, a large cloud of atoms is coupled to the light. In order to model a realistic experiment, the coupling constant for each individual atom scales with the local electromagnetic field amplitude $u(\mathbf{r}_i)$ and thus, the collective scattering of the atomic cloud has to be summed over all the atoms. This rigorous description of the spin-light interface is given in section 2.4. Here, we assume that the spin-light interaction can be well approximated by a 1D model, which is a good approximation for large Fresnel numbers $F = w_0^2/(\lambda L)$ where w_0 is the laser waist, L the length of the atomic cloud and λ the laser wavelength [13]. In this 1D desciption, the collective atomic spin can be written as the sum over all the individual spins,

$$\hat{\mathbf{F}} = \sum_{i=1}^{N_\mathrm{a}} \hat{\mathbf{f}}^{(i)}, \tag{2.2.29}$$

where N_a is the total number of the atoms. The collective Faraday Hamiltonian can be written simply by replacing the single spin operator with the collective spin operator,

$$\hat{H} = \hbar\tilde{\alpha}_1 \hat{F}_z \hat{S}_z. \tag{2.2.30}$$

Here, an adjusted polarisability constant $\tilde{\alpha}_1$ is used in the Hamiltonian (see below). So far we have assumed that there is a single atom in the focus of the laser beam, so the peak intensity of the laser is considered for the interaction. If all atoms are at the focus of the laser beam, we get $\tilde{\alpha}_1 = \alpha_1$. In a more realistic model, not all atoms are in the laser focus. Commonly, for a well mode-matched atomic ensemble, it is assumed that the atoms interact with the mean intensity of the laser $\bar{I} = I_0/2$ (detailed in section 2.4). In previous works in our project, this was taken into account by adapting the definition of the laser mode area $A = \pi w_0^2/2 \to \pi w_0^2$ [68, 69] which then leads to an adapted polarisability constant $\alpha_1 \to \tilde{\alpha}_1 = \alpha_1/2$. This redefinition works if the mean spin is considered; however, a more advanced analysis is necessary for spin noise, which is discussed in section 2.4. For the remainder of this theory subchapter, we will neglect the inhomogeneous coupling and leave the careful discussion to section 2.4.

Input-Output Relations of the Light

As light passes through the atomic ensemble, its polarisation state is changed. To evaluate the effect of the atomic spin on the light, we integrate the spin-light interaction over the full interaction region. Assuming that we have a strong, coherent input field and the interaction is weak, we can neglect propagation effects within the cloud (i.e. all atoms are exposed to the same input polarisation). The effect of the spin to the light can be expressed to first order in the interaction by the following input-output relation of the light [106]

$$\hat{S}_x^{(\mathrm{out})} = \hat{S}_x^{(\mathrm{in})} - \alpha_1 \hat{S}_y^{(\mathrm{in})} \hat{F}_z, \tag{2.2.31}$$

$$\hat{S}_y^{(\mathrm{out})} = \hat{S}_y^{(\mathrm{in})} + \alpha_1 \hat{S}_x^{(\mathrm{in})} \hat{F}_z, \tag{2.2.32}$$

$$\hat{S}_z^{(\mathrm{out})} = \hat{S}_z^{(\mathrm{in})}. \tag{2.2.33}$$

The interaction between the atomic spin and the light results in a rotation of the linear polarisation, while the circular component remains unaffected. This interaction can be employed to map the spin state

onto the light, either for interacting with the membrane in the hybrid experiment or for measuring the spin state. Assuming that the input light is sufficiently strong and polarised along the horizontal axis, i.e. $\langle \hat{S}_x \rangle = \bar{S}_0$ and $\bar{S}_0 \gg \langle \hat{S}_y \rangle, \langle \hat{S}_z \rangle$, the z-projection of the spin state can be read out by measuring $\hat{S}_y \approx \alpha_1 \bar{S}_0 \hat{f}_z$. The $\hat{S}_y$ component of the Stokes vector of the light can be measured by a polarisation homodyne measurement (see section 2.3.3 for details).

It is often useful to normalise the measured homodyne signal with respect to the total flux. For this purpose, the so-called Faraday angle can be defined as the angle by which the interaction with the atoms rotates the linear polarisation of the light [96]. Here, we assume that the incoming light is strong and polarised along $\hat{S}_x$ so that $\hat{S}_x^{(\mathrm{out})} \approx \hat{S}_x^{(\mathrm{in})} \approx \bar{S}_0$ and define the Faraday angle as

$$\tan(2\hat{\theta}) = \frac{\hat{S}_y^{(\mathrm{out})}}{\hat{S}_x^{(\mathrm{out})}} \approx \frac{\hat{S}_y^{(\mathrm{out})}}{\bar{S}_0}. \tag{2.2.34}$$

For small angles, the Faraday angle can be approximated by $\hat{\theta} = \hat{S}_y^{(\mathrm{out})}/(2\bar{S}_x^{(\mathrm{out})})$. For a horizontally polarised input field, the Faraday angle is given by $\hat{\theta} = \alpha_1 \hat{F}_z/2$ (shot noise is neglected here) and therefore depends only on the atomic state and the vector polarisability constant.

Light Induced Spin Rotations

The spin state is not only mapped onto the light; the light also acts on the spin state. First, we consider the coherent dynamics of the spin induced by the interaction Hamiltonian. Using the effective Hamiltonian given in equation (2.2.26), we can calculate the equations of motion of the spin,

$$\frac{\mathrm{d}}{\mathrm{d}t}\hat{f}_x = -\alpha_1 \hat{f}_y \hat{S}_z, \tag{2.2.35}$$

$$\frac{\mathrm{d}}{\mathrm{d}t}\hat{f}_y = \alpha_1 \hat{f}_x \hat{S}_z, \tag{2.2.36}$$

$$\frac{\mathrm{d}}{\mathrm{d}t}\hat{f}_z = 0. \tag{2.2.37}$$

When the light is circularly polarised, it induces a spin rotation around the z-axis. This is consistent with the above result that circularly polarised light acts like a fictitious magnetic field along the propagation axis of the light. It should also be noted that the light in this state does not modify the $\hat{f}_z$ component of the spin. However, this component is mapped onto the polarisation state of the light (shown in equation (2.2.32)). Therefore, the Faraday interaction can be considered as a quantum non-demolition measurement of the spin-1/2 [95].

Decay of the Spin-1/2 System

In order to obtain a complete understanding of the light-induced spin dynamics, the spin decoherence must be taken into account. The effective decoherence of the spin can be calculated from the jump operators defined in equation (2.2.9). For here, we assume that the input light is in a coherent state linearly polarised at an angle φ with respect to the horizontal axis (i.e. light along $\mathbf{e}_{\mathrm{lin}} = \cos(\varphi)\mathbf{e}_H + \sin(\varphi)\mathbf{e}_V$) and neglect the (quantum) fluctuations of the light. We solve the Master equation in the Heisenberg picture, considering the interaction Hamiltonian (equation (2.2.26)) and the jump operators (equation

(2.2.9)) and obtain

$$\frac{\mathrm{d}}{\mathrm{d}t}\hat{f}_x = -\frac{\gamma_{\mathrm{Rb}}}{2\Delta}\alpha_0\bar{S}_0\left[\left(1-\frac{\cos(2\varphi)}{3}\right)\hat{f}_x - \frac{\sin(2\varphi)}{3}\hat{f}_y\right], \tag{2.2.38}$$

$$\frac{\mathrm{d}}{\mathrm{d}t}\hat{f}_y = -\frac{\gamma_{\mathrm{Rb}}}{2\Delta}\alpha_0\bar{S}_0\left[\left(1+\frac{\cos(2\varphi)}{3}\right)\hat{f}_y - \frac{\sin(2\varphi)}{3}\hat{f}_x\right], \tag{2.2.39}$$

$$\frac{\mathrm{d}}{\mathrm{d}t}\hat{f}_z = -\frac{\gamma_{\mathrm{Rb}}}{2\Delta}\alpha_0\bar{S}_0\frac{2}{3}\hat{f}_z. \tag{2.2.40}$$

The spin dynamics shown here is purely incoherent because we assumed that $\hat{S}_z^{(\mathrm{in})} = 0$. As a consequence of spontaneous emission, the degree of spin polarisation decays. The decoherence rate of spin components that are orthogonal to the propagation axis of the light depends on the polarisation angle of the light (assuming linearly polarised light). This can be understood from a geometrical perspective: In the case of $\varphi = 0$, the electric field component of the light is aligned with the $\hat{f}_x$ spin while it is orthogonal to the $\hat{f}_y$ spin. For a more quantitative consideration of the decoherence rates, recall that the photon scattering rate of a two-level atom in the limit of large detuning is given by (see [105] or the derivation in appendix B.2.1)

$$\gamma_{\mathrm{sc}} = \frac{\sigma_0}{A}\left(\frac{\gamma_{\mathrm{Rb}}}{2\Delta}\right)^2\Phi_{\mathrm{L}} = \frac{3\gamma_{\mathrm{Rb}}}{2\Delta}\alpha_0\bar{S}_0. \tag{2.2.41}$$

The decoherence of the $\hat{f}_z$ spin component (which is independent of the polarisation angle) is not directly given by the spontaneous scattering rate: Starting from the state $|g_{1/2}\rangle\langle g_{1/2}| = \hat{\mathbb{1}}$, the evolution of the expectation value of $\hat{f}_z$ is given by $\langle\hat{f}_z(t)\rangle = \langle\hat{f}_z(0)\rangle\exp(-\gamma_{\mathrm{decoh}}t)$ with a decoherence rate of $\gamma_{\mathrm{decoh}} = 2\gamma_{\mathrm{sc}}/9$. In previous works of our group, it was assumed that the spin decoherence rate is simply given by the spontaneous scattering rate [68, 69]. While the spin decoherence is caused by spontaneous emission, the spin decoherence rate is not directly given by scattering rate of a two-level atom, because some scattering events do not change the ground state of the atom.

Quantum Limited Spin-Light Interface

In the hybrid coupling experiment, we aim to couple two quantum systems. The spin-light interface must therefore be operated in a quantum-limited regime. For the atomic spin, the common uncertainty relations of a quantum mechanical spin are valid, which can be derived from the commutation relations of a spin given by $[\hat{f}_j, \hat{f}_k] = \mathrm{i}\epsilon_{jkl}\hat{f}_l$. Here, we assume that the spin is well polarised along the x-axis, so that the collective spin along the x-axis can be classically approximated by $\bar{F}_x = fN_{\mathrm{a}}$ where f is the hyperfine quantum number. The uncertainty relation for the transverse axes is then given by $[\hat{F}_y, \hat{F}_z] = \mathrm{i}fN_{\mathrm{a}}$.

During the interaction with the light, the quantum noise of the spin is mapped onto the light. This signal then can either be measured or be used for the interaction with the membrane in the hybrid setup. During the interaction, the quantum noise of the light (shot noise) also drives the spin. This adds additional noise to the spin dynamics, which increases the effective variance of the collective spin. In order to quantify the variance of the spin and of the outgoing light, we assume that the incoming light is linearly polarised along the horizontal axis. We can then approximate $\hat{S}_x$ by its classical mean value $\bar{S}_x = \Phi_{\mathrm{L}}/2$. By doing this approximation we can write the uncertainty relation of the transverse components as $[\hat{S}_y(t), \hat{S}_z(t')] = \mathrm{i}\bar{S}_x\delta(t-t')$. Here, we assumed a fixed position z of the interaction but a varying time t (compare with equations 2.2.23). These approximations (for the spin and the light) lead to the description of the atomic spin and the polarisation of the light as harmonic oscillators (called

Holstein-Primakov approximation), which is discussed in detail in section 2.7. The evolution of the shot-noise-driven spin in a bias magnetic field along the B_x axis is given by

$$\frac{\mathrm{d}}{\mathrm{d}t}\hat{F}_y(t) = -\Omega_\mathrm{s}\hat{F}_z(t) - \frac{\gamma_\mathrm{s}}{2}\hat{F}_y(t) + \hat{h}_y(t) + \alpha_1\hat{F}_x\hat{S}_z(t), \tag{2.2.42}$$

$$\frac{\mathrm{d}}{\mathrm{d}t}\hat{F}_z(t) = \Omega_\mathrm{s}\hat{F}_y(t) - \frac{\gamma_\mathrm{s}}{2}\hat{F}_z(t) + \hat{h}_z(t), \tag{2.2.43}$$

where the first term is the Larmor precession in the magnetic field with the Larmor precession frequency $\Omega_\mathrm{s} = \mu_B g_f B_x/\hbar$ (see section 2.3.2 for details), the second term describes the spin decay, where the decay constant γ_s results from the interaction with the light and from incoherent processes such as magnetic field inhomogeneities. The spin decay gives rise to Langevin force terms $\hat{h}_i(t)$ which are necessary to preserve the commutation relations according to the fluctuation dissipation theorem [111]. The last term of the equation (2.2.42) comes from the circular polarisation component of the light driving the atomic spin via the Faraday interaction. The different noise contributions encoded in the spin signal are easiest to assess in the frequency domain, so it is worth Fourier transforming the equations of motion (see definition given in equation (C.1.1)) and then use the input-output relations for the light variables (see equation (2.2.32)), which yields

$$\hat{S}_y^{(\mathrm{out})}(\omega) = \hat{S}_y^{(\mathrm{in})}(\omega) + \alpha_1\bar{S}_x \cdot \frac{(\gamma_\mathrm{s}/2 - \mathrm{i}\omega)\hat{h}_z(\omega) + \Omega_\mathrm{s}[\hat{h}_y(\omega) + \alpha_1\bar{F}_x\hat{S}_z^{(\mathrm{in})}(\omega)]}{(\Omega_\mathrm{s} - \omega)(\Omega_\mathrm{s} + \omega) + (\gamma_\mathrm{s}/2)^2 - \mathrm{i}\gamma_\mathrm{s}\omega}. \tag{2.2.44}$$

The power spectral density (PSD) of $\hat{S}_y^{(\mathrm{out})}$ is given by

$$S_{S_yS_y}(\omega) = \int_{-\infty}^{\infty}\langle\hat{S}_y^{(\mathrm{out})\dagger}(-\omega)\hat{S}_y^{(\mathrm{out})}(\omega')\rangle\mathrm{d}\omega' = \int_{-\infty}^{\infty}\langle\hat{S}_y^{(\mathrm{out})}(\omega)\hat{S}_y^{(\mathrm{out})}(\omega')\rangle\mathrm{d}\omega'. \tag{2.2.45}$$

The definition of the PSD is given in appendix C. In order to evaluate the PSD, the noise statistics of the operators have to be considered. For the incoming light, we assume a coherent state, such that the uncertainties are equally distributed, i.e.

$$\langle\hat{S}_y^{(\mathrm{in})}(\omega)\hat{S}_y^{(\mathrm{in})}(\omega')\rangle = \langle\hat{S}_z^{(\mathrm{in})}(\omega)\hat{S}_z^{(\mathrm{in})}(\omega')\rangle = \delta(\omega+\omega')\frac{\bar{S}_x}{2}. \tag{2.2.46}$$

For the Langevin force operators, we obtain [111]

$$\langle\hat{h}_y(\omega)\hat{h}_y(\omega')\rangle = \langle\hat{h}_z(\omega)\hat{h}_z(\omega')\rangle = \delta(\omega+\omega')\frac{\gamma_\mathrm{s}}{2}|\bar{F}_x|, \tag{2.2.47}$$

$$\langle\hat{h}_y(\omega)\hat{h}_z(\omega')\rangle = -\langle\hat{h}_z(\omega)\hat{h}_y(\omega')\rangle = \delta(\omega+\omega')\mathrm{i}\frac{\gamma_\mathrm{s}}{2}\bar{F}_x. \tag{2.2.48}$$

Performing the narrow band approximation $\gamma_\mathrm{s}, |\Omega_\mathrm{s} - \omega| \ll \Omega_\mathrm{s}$, the resulting PSD can be written as

$$\bar{S}_{S_yS_y}(\omega) = \frac{\bar{S}_x}{2} + \frac{(\alpha_1\bar{S}_x/2)^2}{(\Omega_\mathrm{s}-\omega)^2 + (\gamma_\mathrm{s}/2)^2} \cdot \left(\gamma_\mathrm{s}|\bar{F}_x| + \frac{(\alpha_1\bar{F}_x)^2\bar{S}_x}{2}\right). \tag{2.2.49}$$

The spectrum of the outgoing light is given by a Lorentzian spin signal on top of a white noise background due to the shot noise of the light. It is illustrative, to normalise this expression by the input flux of light. For this we go from the Stokes vector component to the so-called Faraday angle $\theta = \langle\hat{\theta}\rangle$. The PSD of the Faraday angle is given by $\bar{S}_{\theta\theta}(\omega) = \bar{S}_{S_yS_y}(\omega)/(2\bar{S}_x)^2$. The variance of the signal can be calculated

from the PSD by integrating over the Lorentzian peak (Parseval's theorem) [112], see equation (C.3.7). In practice, the PSD of the Faraday angle is integrated over the bandwidth $\Delta_{\mathrm{BW}} \gg \gamma_{\mathrm{s}}$, we get

$$\mathrm{var}(\theta) = 2\int_{\Omega_{\mathrm{s}}-\Delta_{\mathrm{BW}}/2}^{\Omega_{\mathrm{s}}+\Delta_{\mathrm{BW}}/2} \bar{S}_{\theta\theta}(\omega)\frac{\mathrm{d}\omega}{2\pi} = \frac{\Delta_{\mathrm{BW}}}{2\pi}\frac{1}{4\bar{S}_x} + \frac{\alpha_1^2}{16}\cdot\left(2|\bar{F}_x| + \frac{(\alpha_1\bar{F}_x)^2\bar{S}_x}{\gamma_{\mathrm{s}}}\right). \tag{2.2.50}$$

The first term in this expression is due to the quantum shot-noise of the light. Increasing the power of the light reduces the relative imprecision of the measurement, that is why this term scales with the inverse of the flux. The second term scales with the number of atoms (or the spin length of the collective spin), but not with the photon flux. It is the projection noise of the spin mapped onto the light, which comes from the quantum uncertainty of the atomic spin. The third term is due to the backaction noise of the light driving the spin, which is then read out by the light. This interaction therefore is proportional to the square of the spin length. The backaction term is inversely proportional to the linewidth of the spin, which depends on the interaction with the light $\gamma_{\mathrm{s}} \propto \bar{S}_x$. Thus, in the limit where scattering is the dominant decoherence channel, the dependence of the backaction term on the photon flux $2\bar{S}_x$ cancels out.

Summary

Considering a spin-1/2 system, we have seen that circularly polarised light acts like an effective magnetic field along the propagation axis of the light. Assuming a large detuning, an effective interaction Hamiltonian was derived that couples the $\hat{f}_z$ spin component to the $\hat{S}_z$ Stokes-vector component. Furthermore, the different noise contributions driving a well-polarised spin were analysed and the power spectral density of the outgoing light was derived. In the following, this interface is used to engineer the spin-light interface for the hybrid experiment.

Moreover, we have seen that the spin decoherence in this simple model depends on the linear polarisation of the light. The spin dynamics become even more developed when considering an atom with two hyperfine ground state manifolds, as will be shown in the next section.

2.2.2 Model of an Atom with a Spin-1 Ground State

The next step is to make the atomic model slightly more complicated to get an even better intuition for the interaction of a Rubidium atom with far detuned light. The simplest model that has two hyperfine ground state manifolds is an atom with nuclear spin $i = 1/2$. For this atom, we consider a ground state manifold with $j = 1/2$ and an excited-state manifold with $j' = 1/2$. In the ground state manifold we have a total of four levels, one with $f = 0$ and three with $f = 1$. We assume that the hyperfine splitting of the ground state is Δ_{hf} while we neglect the hyperfine splitting of the excited state.

The interaction Hamiltonian is rather developed and is represented schematically in figure 2.2.2 and given explicitly in appendix B.2.5. As before, the coupling of the atoms to far-detuned light is considered and therefore the excited states can be adiabatically eliminated. The adiabatic elimination of the excited states can be done as described for the spin-1/2 model, but there are simpler ways to obtain the effective ground-state dynamics. Reiter *et al.* [113] provided a general approach to calculate the effective Hamiltonian and effective jump operators by adiabatic elimination of the excited state. For this, we assume that the dynamics of the full system is described by a master equation with coupling to a Markovian

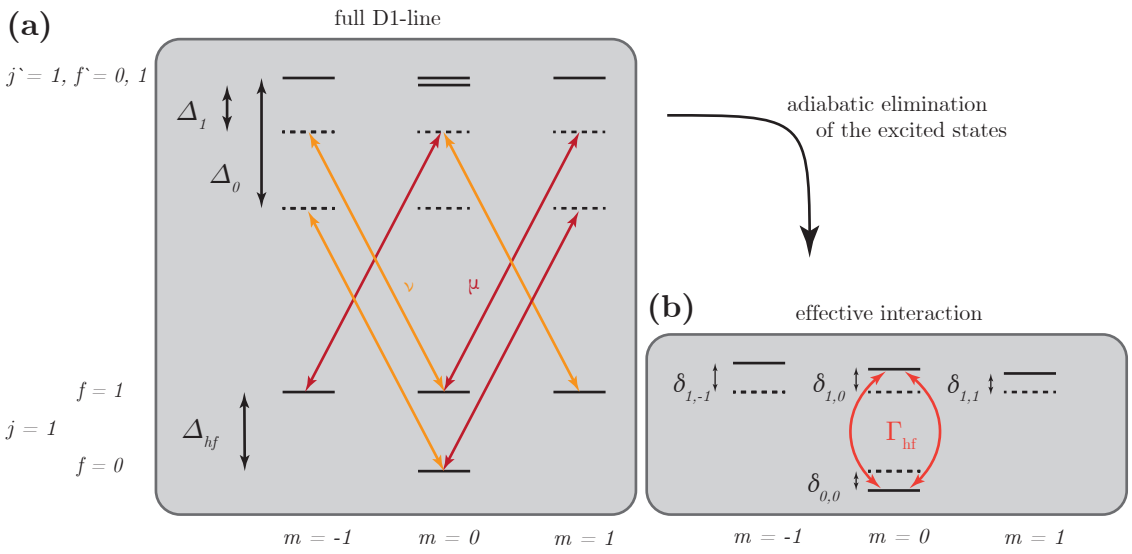

Figure 2.2.2: Level diagram of the considered spin-1 atom (a) without and (b) with the adiabatic elimination of the excited state. By the light, the levels of the ground state get effectively shifted by $\delta_{0,0} = -2|\Omega_{j,j'}|\bar{S}_0/(3\Delta_{f=0})$, $\delta_{1,-1} = 2|\Omega_{j,j'}|(\bar{S}_0 + \bar{S}_z)/(3\Delta_{f=1})$, $\delta_{1,0} = 2|\Omega_{j,j'}|\bar{S}_0/(3\Delta_{f=1})$, and $\delta_{1,1} = 2|\Omega_{j,j'}|(\bar{S}_0 - \bar{S}_z)/(3\Delta_{f=1})$. Additionally, there is an exchange term between the levels $\Gamma_{\mathrm{hf}} = |\Omega_{j,j'}|\bar{S}_z(\Delta_{f=0} + \Delta_{f=1})/(3\Delta_{f=0}\Delta_{f=1})$.

bath. This approach, summarised in appendix B.2.4, is used to calculate the effective dynamic of the atom both analytically and numerically.

Effective Dynamics of the Spin-1 System

Applying the adiabatic elimination of the excited states for the spin-1 system, we end up with a Hamiltonian that couples the two hyperfine ground-state manifolds (explicitly shown in appendix B.2.5 and schematically shown in figure 2.2.2). The coherences between the two ground-state manifolds oscillate at the hyperfine splitting Δ_{hf} and can be neglected. Besides the coherent coupling between the two hyperfine ground-state manifolds, there are incoherent decay channels between the two hyperfine ground-state manifolds in the effective dynamics of the system. Although we are mainly interested in the dynamics within one particular hyperfine state manifold, it is necessary to consider the other hyperfine state manifold in order to understand the decoherence mechanism of the system. In many simple calculations we assume that the decoherence of a state depends only on the detuning of the light for this particular state, but it turns out that the incoherent coupling between the two hyperfine state manifolds depends on the detuning of the light with respect to the transition from both ground state hyperfine state manifolds to the excited state manifold.

Simulation of the Spin Dynamics: Explicit analytical expressions for the spin-1 systems can be obtained but they are too complicated to gain any intuitive understanding. Therefore, the dynamics of the spin-1 atom is simulated numerically. In a first set of simulations, the dynamics for the full $D1$-line of the spin-1 atom is simulated. However, for a light-field detuned by several gigahertz, time steps of nanoseconds are required to follow the dynamics. Therefore, a numerical version of the adiabatic elimination of the excited state was implemented, using the formalism presented in [113]. In addition,

the simulations are performed in a frame rotating at the hyperfine splitting between the two hyperfine ground-state manifolds Δ_{hf}. We are interested in the dynamics at megahertz frequencies, such that the terms oscillating at $\Delta_{\mathrm{hf}} \sim$ GHz can be neglected. Applying the adiabatic elimination and neglecting the terms oscillating at Δ_{hf}, the simulation time can be reduced by more than an order of magnitude.

The result of one simulation is shown in figure 2.2.3 (a). For this simulation, we assume that the initial spin is aligned with a magnetic field in the z-direction (i.e. initial state $|f = 1, m_f = 1\rangle$). Due to the incoherent scattering of the light, the population in the $|f = 1, m_f = 1\rangle$ decays to the other levels. The decay rate depends on the detuning and the intensity of the applied optical field. It turns out that the steady state population is significantly changed by reversing the sign of the detuning (but it does not depend on the laser intensity), as shown in figure 2.2.3 (c). Nevertheless, the dynamics of the expectation value of $\hat{f}_z$ does not depend on the sign of the detuning (see figure 2.2.3 (b)). The simulation was repeated for different powers and detunings and the decoherence rate of the expectation value of $\hat{f}_z$ is consistently found to be $\gamma_{\mathrm{decoh}} = \gamma_{\mathrm{sc}}/9$. This is half the rate of the spin-1/2 atom, which is consistent with the difference in the scalar polarisability constant.

2.2.3 Model of the D2-line of Rubidium-87

In our experiment, we operate on the D2-line of the Rubidium-87 atom. For Rb-87, the nuclear spin is $i = 3/2$, so the ground state $^2S_{1/2}$ is split into two hyperfine state manifolds $f = 1, 2$ and the $^2P_{3/2}$ excited-state manifold is split into four hyperfine state manifolds $f' = 0, 1, 2, 3$. As for the simpler atom models, the excited state can be eliminated if the probe light has a large detuning and the excited state is not effectively populated. The coherent coupling terms between the two hyperfine manifolds oscillate at gigahertz frequencies and do not contribute to the dynamics at megahertz frequencies, as we have seen in the spin-1 model. Therefore these terms are neglected in the following. Here, only the effective Hamiltonian of one hyperfine state is shown. The jump operators are included in the numerical simulations of the system but are not explicitly written here.

The effective Hamiltonian can be decomposed into three different parts, a scalar, a vector and a tensor component [106, 110, 114]

$$\hat{H}_f = \hat{H}_{0,f} + \hat{H}_{1,f} + \hat{H}_{2,f}, \tag{2.2.51}$$

where the scalar and the vector Hamiltonians are the same as for the spin-1/2 model (with just a modified polarisability constant, see below) but the tensor component is new and comes from the finite detuning between the different excited-state hyperfine levels. We have

$$\hat{H}_{0,f} = \hbar\alpha_{f,0}\hat{\mathbb{1}}_g\hat{S}_0, \tag{2.2.52}$$

$$\hat{H}_{1,f} = \hbar\alpha_{f,1}\hat{f}_z\hat{S}_z, \tag{2.2.53}$$

$$\hat{H}_{2,f} = \hbar\alpha_{f,2}(\hat{S}_x\hat{t}_{x^2-y^2} + \hat{S}_y\hat{t}_{xy} + \frac{1}{3}\hat{S}_0[3\hat{t}_{z^2} - f(f+1)\hat{\mathbb{1}}_f]), \tag{2.2.54}$$

where the spin alignment tensors are given by

$$\hat{t}_{x^2-y^2} = \hat{f}_x^2 - \hat{f}_y^2, \tag{2.2.55}$$

$$\hat{t}_{xy} = \hat{f}_x\hat{f}_y + \hat{f}_y\hat{f}_x, \tag{2.2.56}$$

$$\hat{t}_{z^2} = \hat{f}_z^2. \tag{2.2.57}$$

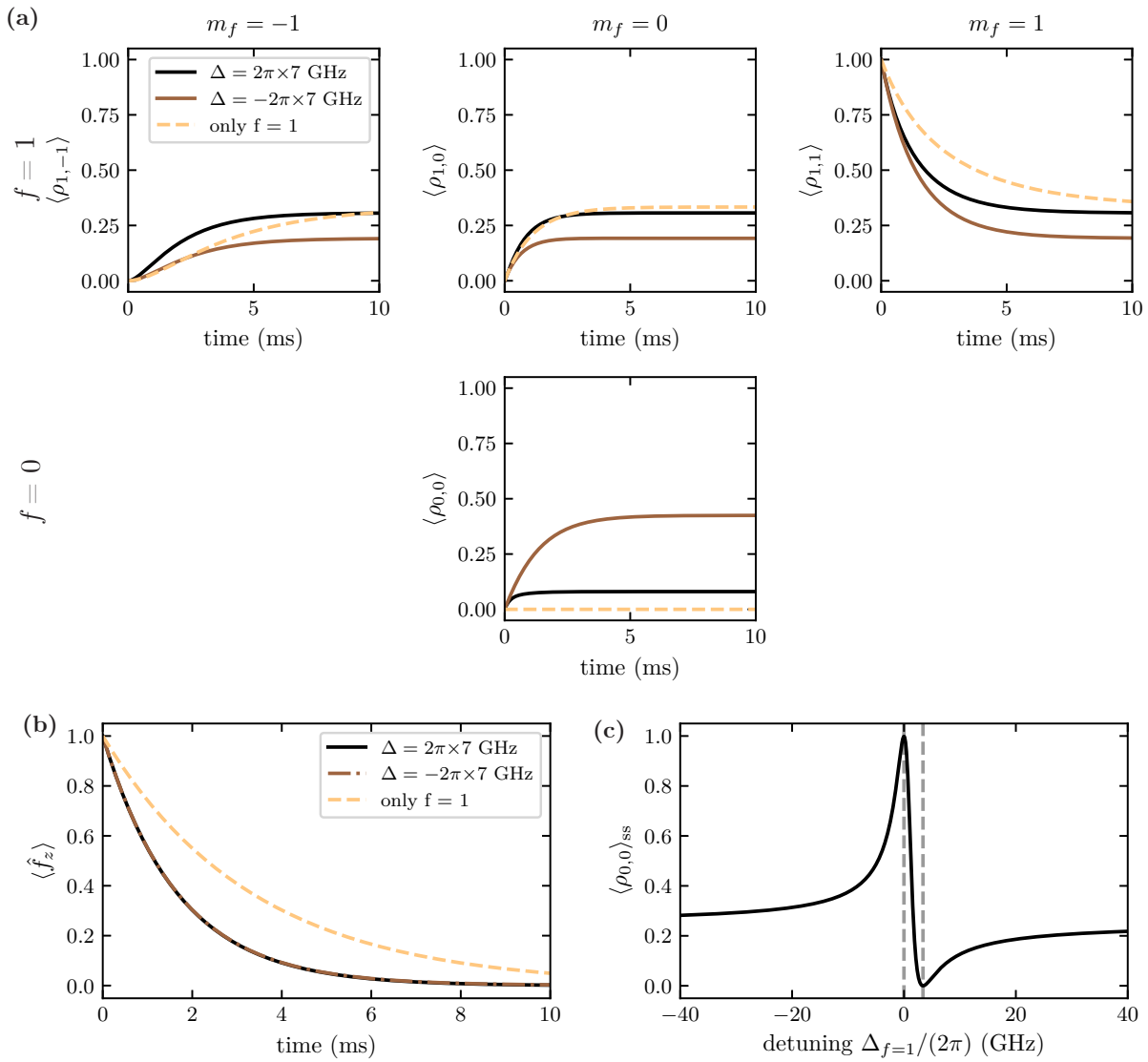

Figure 2.2.3: Simulation of the dynamics of a spin-1 atom at the focus of the laser for a probe power of 200 µW and a beam waist of 50 µm. (a) The population in the different Zeeman states for a probe with a detuning of $\Delta_{f=1} = \pm 2\pi \times 7\,\mathrm{GHz}$. The top row shows the $f = 1$ manifold, the bottom row the $f = 0$ hyperfine state. In addition, the unphysical situation is shown in dashed orange, where the depumping to $f = 0$ is manually switched off. Changing the sign of the detuning alters the light-induced dynamics and the final steady state of the atom. However, the dynamics of the expectation value of $\hat{f}_z$ is the same for both detuning signs, as shown in (b). (c) shows the steady state occupation of the $|f = 0, m_f = 0\rangle$ state. The dashed lines show the resonance conditions for the $f = 1$ manifold and the $f = 0$ manifold, for which in the steady state the atom is fully pumped into only one of the hyperfine manifolds.

For the alignment tensors, the commutation relations are given by $[\hat{t}_{x^2-y^2}, \hat{f}_z] = -\mathrm{i}2\hat{t}_x y$, $[\hat{t}_{xy}, \hat{f}_z] = \mathrm{i}2\hat{t}_{x^2-y^2}$. The exact expressions for the polarisability constants $\alpha_{f,0}$, $\alpha_{f,1}$ and $\alpha_{f,2}$ are given in appendix B.2.6. For this work, mostly the limit for detunings much larger than the hyperfine splitting of the excited-state manifold is sufficient, which is given by

$$\alpha_{f,0} = \frac{\sigma_\pi}{2A}\frac{\gamma_{\mathrm{Rb}}}{\Delta}, \tag{2.2.58}$$

$$\alpha_{f,1} = \frac{\sigma_\pi}{8A}\frac{\gamma_{\mathrm{Rb}}}{\Delta}(-1)^f, \tag{2.2.59}$$

for the scalar and the vector polarisability constants. Two observations can be made here: (1) the vector polarisability constant is smaller for the real Rubidium atom than for the spin-1/2 model. This is due to the fact that the Rubidium total spin contains contributions from the nuclear spin, which does not couple to the light. (2) The vector polarisability constant has a different sign for the two ground-state hyperfine manifolds.

The tensor polarisability constants have a slightly different form for the two ground-state hyperfine manifolds

$$\alpha_{f=1,2} = \frac{\sigma_\pi}{8A}\frac{\gamma_{\mathrm{Rb}}}{\Delta}\frac{-4\delta_{f'=0} + 5\delta_{f'=1} - \Delta_{f'=2}}{4\delta}, \tag{2.2.60}$$

$$\alpha_{f=2,2} = \frac{\sigma_\pi}{8A}\frac{\gamma_{\mathrm{Rb}}}{\Delta}\frac{-\delta_{f'=1} + 5\delta_{f'=2} - 4\delta_{f'=3}}{20\Delta}, \tag{2.2.61}$$

where $\delta_{f'}$ is the frequency offset of a given excited hyperfine manifold with respect to the centre of the ${}^2P_{3/2}$ manifold (for more details, see appendix B.2.6). While the scalar and vector polarisability constants scale with $1/\Delta$, the tensor polarisability constant scales with $1/\Delta^2$ for large detunings. Thus, large detunings $\Delta \gg \delta_{f'}$ allow us to neglect the effect of the tensor interaction for most of the experiments [115]. An experimental study of the effect of the tensor Hamiltonian is given in section 2.3.7.

The dynamics of the Rubidium atom has been simulated using the same approximations and procedure as for the spin-1 atom. The simulation results are presented in combination with measurement results in the next section (e.g. in figure 2.3.3 and 2.3.4).

2.3 Experimental Implementation of the Spin-Light Interface

In the last section, the theory for spin-light interaction has been presented. This section introduces the experimental implementation of such a Faraday interface. The experimental setup, the spin in a bias magnetic field and the polarisation homodyne measurement are discussed. After that, some standard experiments are shown, which are useful in gaining a better understanding of the spin-light interaction.

2.3.1 Experimental Setup

In our experiment, the Faraday interface is implemented using a cold, dipole-trapped atomic ensemble. The loading and characterisation of the atomic cloud are presented in chapter 1. The atomic cloud is interfaced with a detuned laser beam derived from a commercial titanium-sapphire laser[1] (Ti:Saph). An AOM is used to switch the laser and control its intensity. The light is then coupled into a single-mode optical fibre. After the fibre, the polarisation of the coupling beam is cleaned by a Glan-Thompson

[1] MSqured SolsTiS 5000 PSX XF laser system

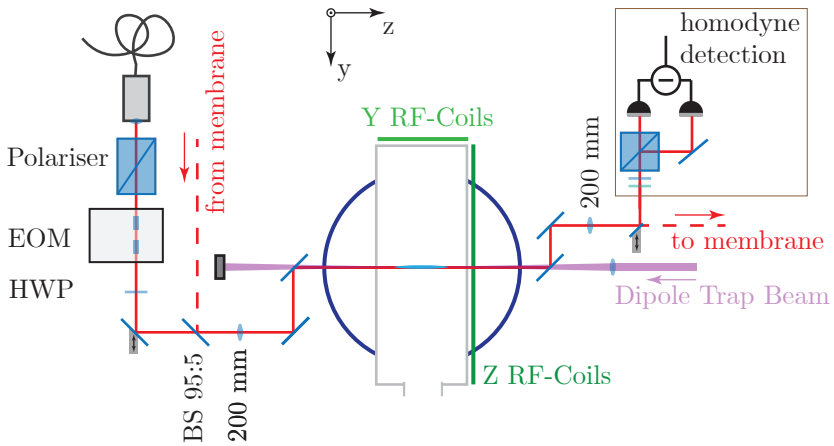

Figure 2.3.1: Scheme of the experimental setup of the Faraday interface. Details are given in the text.

polariser[2] (setup shown in figure 2.3.1). A free space EOM[3] is used to modulate the polarisation of the light. This can be used to drive the atomic spin, which is detailed in section 2.5. The half waveplate (HWP) after the EOM is used to adjust the angle of the linear polarisation. After the HWP, there is a mirror on a translation stage, which is used to displace the beam, followed by a 95 : 5 beam splitter. Both, the mirror on the translation stage and the beam splitter, are used to allow the light to interact twice with the atomic cloud in the hybrid experiment and are discussed in chapter 4. A 200 mm lens focuses the coupling beam onto the atomic cloud. The coupling beam is overlapped with the counter-propagating dipole trap beam on a dichroic mirror. After the atomic chamber, the beam is recollimated by a second 200 mm lens. For the hybrid experiment, the laser is then sent to the membrane setup. For the experiments described in this chapter, the beam is directly detected in a polarisation homodyne detection, which is detailed in section 2.3.3. However, before giving details of the detection, the spin interaction with the bias magnetic field will be introduced.

2.3.2 Spin in a Magnetic Field

The Faraday experiments are performed in the presence of a bias magnetic field. The magnetic fields are applied and actively stabilised by the small and the large Helmholtz coils, described in section 1.3. The external magnetic field $\mathbf{B}$ couples individually to the electron and nuclear spins of the atoms. Our experiments are carried out in the limit of small magnetic fields, where the energy shifts due to the magnetic field are small compared to the hyperfine coupling $\mu_\mathrm{B} g_j \mathbf{B} \ll \hbar\Delta_\mathrm{hf}$, where μ_B is the Bohr magneton and g_j is the Landé g-factor of the electron. In this limit, the coupling between the hyperfine spin and the magnetic field can be treated as a perturbation and f, m_f are still good quantum numbers. Thus, a hyperfine Landé g-factor can be defined, which for the $f = 2$ manifold of the Rubidium ground state is given by $g_f = g_s/4 + 3g_i/4$, where $g_s \approx 2$ is the electron spin Landé g-factor and $g_i \approx -10^{-3}$ is the nuclear Landé g-factor [105]. In most experiments, the magnetic field is applied along the x-axis,

[2]Custom made Glan-Thompson polariser from *B-Halle* with an extinction ratio of $< 10^{-8}$, an anti-reflection coating and a wavefront distortion of $< \lambda/10$

[3]PCA4R-NIR from *Qubig*: bandwidth up to 150 MHz, anti-reflective coating

resulting in the magnetic Hamiltonian

$$\hat{H}_{\mathrm{B}} = \hbar\Omega_{\mathrm{s}}\hat{f}_x + \hbar\delta\Omega_{\mathrm{s}}\hat{f}_x^2, \tag{2.3.1}$$

where the Larmor precession frequency is given by $\Omega_{\mathrm{s}} = \mu_{\mathrm{B}}B_x(g_s + 3g_i)/(4\hbar) = \mu_{\mathrm{B}}g_f B_x/\hbar$ with the hyperfine state Landé g-factor g_f and the prefactor of the quadratic Zeeman term given by $\delta\Omega_{\mathrm{s}} = -(\mu_{\mathrm{B}}B_x(g_s - g_i)/(4/\hbar))^2/\Delta_{\mathrm{hf}}$ [105, 116]. The first term in this Hamiltonian is the *linear Zeeman* effect and leads to a spin precession around the magnetic field. The second term is called the *quadratic Zeeman* effect and is the second order perturbation contribution of the full interaction Hamiltonian with the magnetic field. It leads to different transition energies for adjacent Zeeman states, i.e. $\Omega_{m,m+1} = \Omega_{\mathrm{s}} + \delta\Omega_{\mathrm{s}}(2m+1)$, and thus leads to a splitting of the spin spectrum into four (two) peaks for $f = 2$ ($f = 1$). The relative strength between the two terms can be simplified by assuming that $g_s \gg g_i$ and yields $\Omega_{\mathrm{s}}/\delta\Omega_{\mathrm{s}} \approx -\Delta_{\mathrm{hf}}/\Omega_{\mathrm{s}}$. In our experiments, this is a large number $> 10^3$. Assuming again that the magnetic field is applied along B_x, it is useful to write the time evolution of the spin operators as

$$\hat{f}_y(t) = \tilde{f}_y(t)\cos(\Omega_{\mathrm{s}}t) - \tilde{f}_z(t)\sin(\Omega_{\mathrm{s}}t), \tag{2.3.2}$$

$$\hat{f}_z(t) = \tilde{f}_z(t)\cos(\Omega_{\mathrm{s}}t) + \tilde{f}_y(t)\sin(\Omega_{\mathrm{s}}t), \tag{2.3.3}$$

where $\tilde{f}_{y,z}(t)$ are the operators in the rotating frame at Ω_{s}. The dynamics of their expectation value depends on the quadratic Zeeman effect and on other interactions of the spin as for example the spin-light interaction.

2.3.3 Polarisation Homodyne Measurement

The spin is read out by measuring the polarisation state of the light after the Faraday interaction. The Faraday interaction maps the $\hat{F}_z$ component of the collective spin onto the $\hat{S}_y$ polarisation of the light (assuming the input light is polarised along $\bar{S}_x$, see equation (2.2.32)). The $\hat{S}_y$ polarisation component of the Stokes vector can be measured in a polarisation homodyne measurement. The implementation of the polarisation homodyne measurement in our setup first includes a quarter waveplate (QWP). This QWP is used to rotate the local oscillator from $\bar{S}_x$ to the circular polarisation quadrature of the light, i.e. it performs a rotation $\hat{S}_x \to \hat{S}'_z$, $\hat{S}_y \to \hat{S}'_y$, $\hat{S}_z \to -\hat{S}'_x$. Then a half waveplate (HWP) at an angle of θ_{homo} and a polarising beam splitter (PSB) are placed (see figure 2.3.1). The intensity difference between the two output ports of the PBS is given by

$$\hat{d}_1^\dagger\hat{d}_1 - \hat{d}_2^\dagger\hat{d}_2 = 2\cos(4\theta_{\mathrm{homo}})\hat{S}_y + 2\sin(4\theta_{\mathrm{homo}})\hat{S}_z, \tag{2.3.4}$$

where $\hat{d}_i$ denotes the field in the two output ports of the PBS. The intensity in both ports is measured and electronically subtracted from each other by a homebuilt balanced photodetector[4]. Depending on the angle of the half waveplate, any superposition of $\hat{S}_y$ and $\hat{S}_z$ can be measured. The ability to measure superpositions between $\hat{S}_y$ and $\hat{S}_z$ turns out to be a useful feature for characterising the spin-light interaction strength and will be used in sections 2.6.3 and 2.6.4. For most measurements, the angle of the half waveplate is set to $\theta_{\mathrm{homo}} = 0$ such that the $\hat{S}_y$ component of the light is measured.

[4]Balanced photodetector SP 1'023 with an amplification of 10^4.

Magnetic Field along the Propagation Axis of the Light

The collective spin length of the atomic cloud can be measured by applying a magnetic field along the propagation axis of the light and polarising the atoms along the same axis. The $\hat{F}_z$ component of the spin is then static and can be approximated by $\bar{F}_z = fN_\mathrm{a}$. The measurement yields $\bar{S}_y = \alpha_1 \bar{S}_x \bar{F}_z$. By calibrating the photon flux $\bar{S}_x$, this gives direct access to the spin length $\bar{F}_z$.

During the spin initialisation, the spin is always polarised along the x-axis. In order to obtain a spin along the z-axis, the magnetic field is slowly rotated from B_x to B_z after spin-pumping (represented in figure 2.3.2 (a) and (b)). The mean spin follows the magnetic field adiabatically. The signal from the balanced detector is measured with an oscilloscope[5] with a high impedance input. Some measurement traces are shown in figure 2.3.3.

Oscillating Spin Signal

In order to implement a spin-oscillator as required for the hybrid experiment, a bias magnetic field is applied along the x-axis orthogonal to the k-vector of the light along the z-axis. The spin is polarised along the magnetic field. An rf pulse can be employed to tilt the spin with respect to the x-axis, as detailed in section 2.5. The $\hat{F}_z$ component of the precessing spin is mapped onto the $\hat{S}_y$ polarisation. Thus, the measured Faraday signal oscillates at the Larmor frequency. The detected signal is then demodulated by a lock-in amplifier[6] or a spectrum analyser[7]. In the demodulation process, the homodyne signal $D(t) = \langle \hat{d}_1^\dagger \hat{d}_1 - \hat{d}_2^\dagger \hat{d}_2 \rangle / 2$ is mixed with a reference signal $V_r(t) = \sqrt{2}\exp(-\mathrm{i}\Omega_0 t)$ at the demodulation frequency Ω_0. The signal is then low-pass filtered in order to obtain the in-phase $I(t)$ and the quadrature $Q(t)$ components

$$\langle D(t) V_r(t) \rangle_t = Z(t) = I(t) + \mathrm{i}Q(t). \tag{2.3.5}$$

In order to get an intuition for the demodulation process, it is useful to consider a spin initially polarised along the z-axis in a magnetic field aligned with the x-axis. The equation of motion of the spin can be expressed in terms of the rotating frame variables (see equation (2.3.3)), whereby the detection is given by

$$D(t) = \langle \hat{S}_y \rangle = \alpha_1 \bar{S}_x \langle \hat{f}_z \rangle = \alpha_1 \bar{S}_x \left(\langle \tilde{f}_z \rangle \cos(\Omega_\mathrm{s} t) + \langle \tilde{f}_y \rangle \sin(\Omega_\mathrm{s} t) \right), \tag{2.3.6}$$

where the quantum fluctuations were neglected and the homodyne angle is set to $\theta_\mathrm{homo} = 0$. The demodulation of the signal results in the following traces

$$I(t) = \frac{1}{\sqrt{2}} \alpha_1 \bar{S}_x \left(\langle \tilde{f}_z \rangle \cos(\delta t) + \langle \tilde{f}_y \rangle \sin(\delta t) \right), \tag{2.3.7}$$

$$Q(t) = \frac{1}{\sqrt{2}} \alpha_1 \bar{S}_x \left(-\langle \tilde{f}_y \rangle \cos(\delta t) + \langle \tilde{f}_z \rangle \sin(\delta t) \right), \tag{2.3.8}$$

where $\delta = \Omega_\mathrm{s} - \Omega_0$ is the detuning between the Larmor frequency and the demodulation frequency. Reconstruction of the slowly rotating spin components can be achieved from the detected quadrature signals. Care has to be taken, because the detection efficiency is not included in these equations. Moreover, the lock-in amplifier and the spectrum analyser have an input impedance of 50 Ω, which makes it necessary to consider an additional factor of two. The rms-signal is defined as the geometrical mean of the in-phase

[5] Keysight, InfiniiVision DSOX2004A: bandwidth: 70 MHz; sampling rate: 2 GSa/s
[6] Zurich instrument HF2LI
[7] Rohde & Schwarz, FSV, 7 GHz

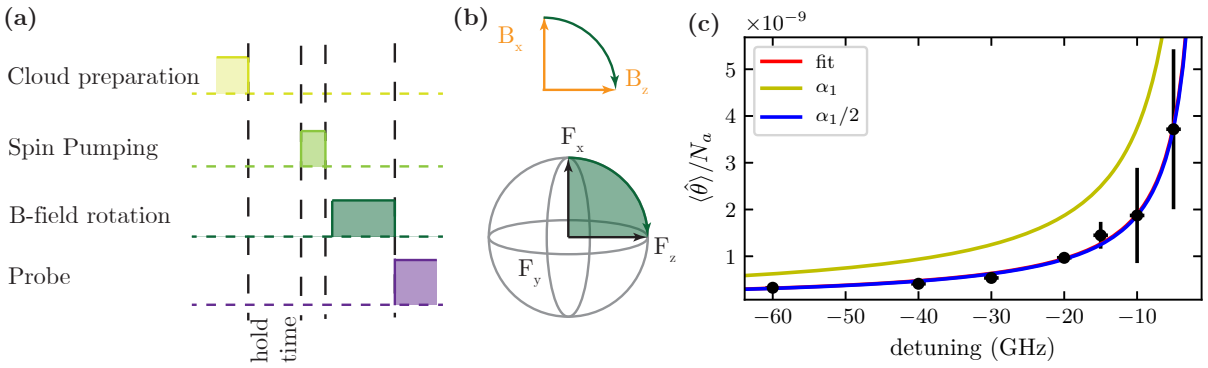

Figure 2.3.2: (a) Experimental sequence for the on-axis Faraday experiments. (b) Schematic representation of the spin preparation in the $\bar{F}_z$ state by slowly rotating the magnetic field. (c) Faraday angle for different detunings. The Faraday angle is normalised by the number of atoms in the cloud which is obtained from absorption imaging. The Faraday angle is smaller than what is expected for N_a atoms in the focus of the laser (yellow line). The fit (red line) overlaps nearly perfectly with the model of an atom interfaced by the average intensity of the Gaussian laser (blue line).

and the quadrature components. In case of the example given, this can be expressed as

$$R(t) = \sqrt{I(t)^2 + Q(t)^2} = \frac{1}{\sqrt{2}}\alpha_1 \bar{S}_x \sqrt{\langle \tilde{f}_y \rangle^2 + \langle \tilde{f}_z \rangle^2}. \tag{2.3.9}$$

From the in-phase and quadrature components, the PSD is calculated using a python-code. This is presented in appendix C.4.

2.3.4 Faraday Interaction with an On-Axis Spin

The Faraday effect predicts that the linear polarisation of the light is rotated proportionally to the collective spin component along the propagation axis of the light. A first experiment demonstrates this effect in its simplest form: The collective atomic spin is polarised along the z-axis and then probed with a far-detuned laser beam. This experiment is used to calibrate the strength of the spin-light interaction. Assuming that the laser is polarised along $\bar{S}_x = \bar{S}_0$, for small rotation angles the outgoing polarisation is given by $\hat{S}_y^{(\mathrm{out})} = \hat{S}_y^{(\mathrm{in})} + \alpha_1 \bar{S}_x \hat{F}_z$. In the experiment, the input power is calibrated so that the measured Faraday signal can be normalised to obtain the Faraday angle

$$\langle \hat{\theta} \rangle = \frac{\langle \hat{S}_y^{(\mathrm{out})} \rangle}{2\bar{S}_x} = \frac{1}{2}\alpha_1 \langle F_z \rangle. \tag{2.3.10}$$

If the atoms are well polarised, the total spin length is given by $\langle F_z \rangle = 2N_\mathrm{a}$, where the number of atoms in the cloud N_a can be measured by absorption imaging, as described in the previous chapter.

In the experiment, the atoms are first polarised along the x-axis parallel to a bias magnetic field (sequence schematically shown in figure 2.3.2 (a) and (b)). The magnetic field is then slowly rotated by 90° from the x-axis to the z-axis so that the mean spin follows adiabatically. After the spin rotation, the atoms are interfaced with far-detuned light. Atom counting by absorption imaging is performed in a separate measurement.

The Faraday angle is measured for different optical powers and numbers of atoms (varied by changing

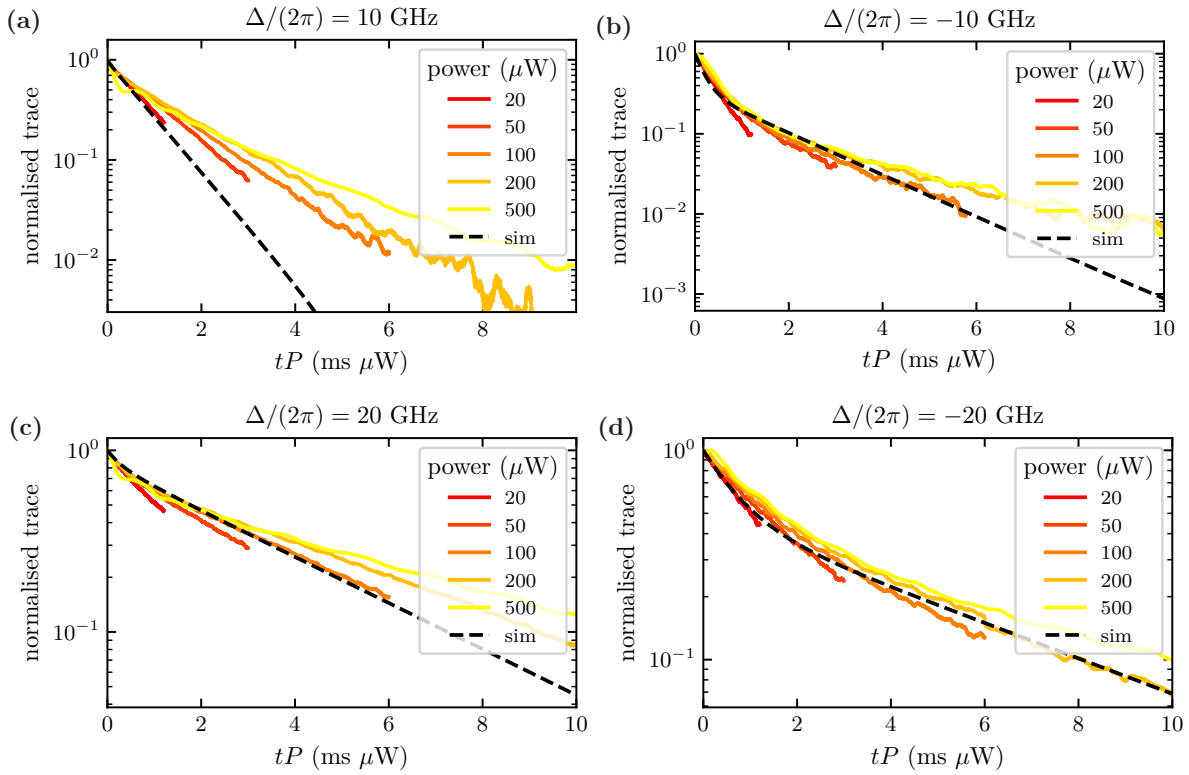

Figure 2.3.3: Data (in colours) and simulation (dashed black line) of the atoms prepared in the $f = 2, m_f = -2$ state and then probed with light for different detunings and different powers. In all plots, the x-axis is rescaled by the probe power to point out the scaling of the decay with power. Changing the power for the simulation only changes the time scale of the dynamics. So if the x-axis is rescaled by the power, the simulated dynamics is independent of the probe power.

the duration of the MOT loading time). The measured signal is divided by the number of atoms in the cloud and is shown in figure 2.3.2 (c). If all the atoms were in the laser focus, the Faraday angle would be $\langle\hat{\theta}\rangle = \alpha_1 N_\mathrm{a}$, shown as the yellow line in figure 2.3.2 (c). However, because the atomic cloud waist is about the same size as the waist of the laser beam, the average spin-light coupling is at a lower intensity and the Faraday signal is reduced. The fitted reduction factor for this experiment is $\langle\eta\rangle = 0.52$ (red line) and depends on the geometry of the laser and the atomic cloud. Here, we see that this effective coupling factor is relevant for characterising the spin-light interface. Therefore a more formal introduction is given in section 2.4. However, before considering the effective collective scattering of a realistic atomic cloud, this measurement will be analysed in more detail.

2.3.5 Spin Decay for an On-Axis Spin

As in the last section, we consider an atomic ensemble polarised parallel to a magnetic field along the axis of propagation of the light (z-axis). In this section, we consider the spin dynamics during the probe. As mentioned before, the resulting Faraday signal is then given by $\bar{S}_y^{(\mathrm{out})} = \alpha_1 \bar{S}_x \bar{F}_z$. Probing the spin with light leads to the spontaneous scattering of photons, depolarising the spin. If the atoms are modelled as a spin-1/2 system, we expect an exponential decay of the $\langle\hat{F}_z\rangle$ component of the collective spin (shown in equation (2.2.40)). Furthermore, for the spin-1/2 atom, the decay rate scales with P/Δ^2, where P

is the optical power. Even for the more complicated spin-1 model, the $\langle \hat{F}_z \rangle$ decays exponentially with a rate $\gamma_s \propto P/\Delta^2$. However, the measurement results from the cold Rubidium-87 ensemble are more complex: The decay of the expectation value of $\hat{F}_z$ looks more like a double-exponential decay than a single exponential decay, as shown in figure 2.3.3. The measurement traces scale with the optical power, but show a qualitatively different dynamics for different detunings.

In order to understand the spin dynamics for this measurement, a simulation of a single Rubidium atom in the presence of a bias magnetic field and a linearly polarised laser was performed, similar to the simulation described in section 2.2.2 and shown in figure 2.2.3 for the spin-1 model. The simulation overlaps well with the measured data for sufficiently large detunings, shown in figure 2.3.3. There is a discrepancy in the decay rate between experiment and theory for a detuning of $\Delta = 2\pi \times 10\,\mathrm{GHz}$ which is not understood so far. But for the other detunings, the theory reproduces the data quite well.

Since the simulation reproduces the measurement data quite well, we can use the simulation to gain understanding of the dynamics of the atoms (e.g. the occupation in each Zeeman state), which cannot be directly accessed by a Faraday measurement. In figure 2.3.4 (a) the occupation in the different Zeeman states is shown for the detunings $\Delta = \pm 2\pi \times 10\,\mathrm{GHz}$. It seems that for a detuning of $\Delta = 2\pi \times 10\,\mathrm{GHz}$, the incoherent spin-light interaction mainly redistributes the occupation within the $f = 2$ hyperfine manifold, whereas for a detuning of $\Delta = -2\pi \times 10\,\mathrm{GHz}$ the atom decays with a higher probability into the $f = 1$ hyperfine manifold. For a better understanding of this dynamics, the steady state occupation of the $f = 2$ hyperfine state manifold is shown in figure 2.3.4 (b) as a function of the detuning. If the light is resonant with $f = 2$, the population accumulates in the $f = 1$ manifold and vice versa. For a detuning of $\Delta = 2\pi \times 10\,\mathrm{GHz}$ the final expectation value of the projector on the $f = 2$ hyperfine state manifold $\hat{P}_2$ is indeed much larger than for a detuning of $\Delta = -2\pi \times 10\,\mathrm{GHz}$.

In order to understand the double-exponential decay of $\langle \hat{F}_z \rangle$, the expectation values of $\langle \hat{F}_z \rangle$ and $\langle \hat{P}_2 \rangle$ are plotted in figure 2.3.4 (c) as a function of time. The initial decay of the expectation value of both operators is approximately the same for both simulated detunings $\Delta = \pm 2\pi \times 10\,\mathrm{GHz}$ (as can be seen in the inset). This indicates that the initial decay is caused by a decay to the $f = 1$ manifold and not by a redistribution within the $f = 2$ hyperfine manifold. This initial decay continues for much longer for a detuning of $\Delta = -2\pi \times 10\,\mathrm{GHz}$ than for a detuning of $\Delta = 2\pi \times 10\,\mathrm{GHz}$. For a detuning of $\Delta = 2\pi \times 10\,\mathrm{GHz}$, the $f = 1$ manifold is coupled by the light with a smaller detuning, therefore its hyperfine relax-rate is much faster and the steady state is reached faster. This may be the reason why the traces for a detuning of $\Delta = -2\pi \times 10\,\mathrm{GHz}$ have a very clear double-exponential shape while the traces for a detuning of $\Delta = 2\pi \times 10\,\mathrm{GHz}$ seem to decay much more exponentially (while it is still a double-exponential with a very fast first decay rate). The slower decay is then caused by a redistribution within the $f = 2$ manifold. Interestingly this rate seems to be larger for a positive detuning than for a negative detuning.

In summary, the decoherence dynamics of Rubidium is more complex than the spin-1/2 model. Similar to the spin-1 model, both hyperfine manifolds are relevant in the decay process. But, unlike the simplified spin-1 model, in Rubidium even the decay of $\langle \hat{F}_z \rangle$ changes when the sign of the detuning is reversed (compare to section 2.2.2).

2.3.6 Faraday Interaction of a Precessing Spin

In the last two sections, experiments with the magnetic field and the spin aligned with the propagation axis of the light were discussed. In these experiments, the spin is static (except for the decay). For the

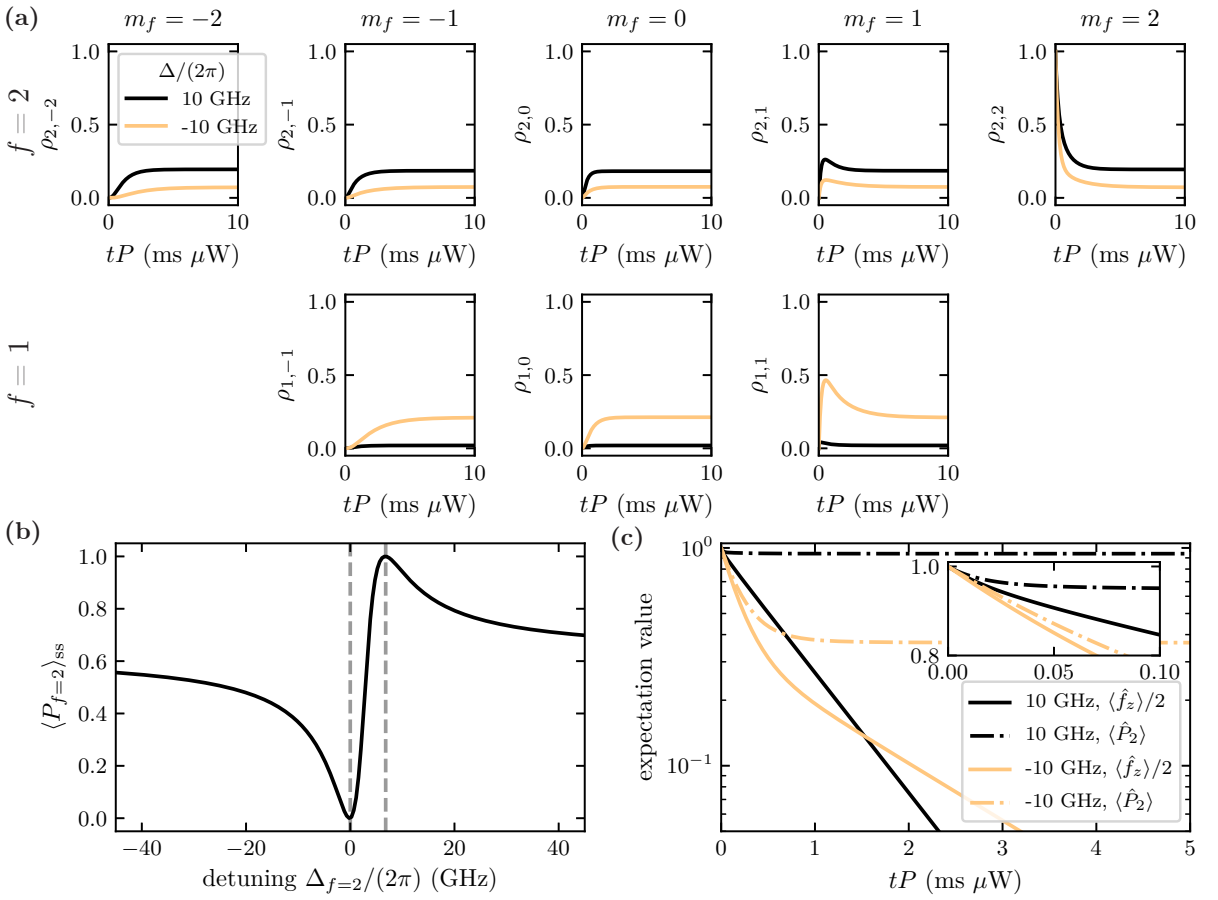

Figure 2.3.4: Simulation of the atoms prepared in the $f = 2, m_f = 2$ state and then probed with light for different detunings of $\Delta = \pm 2\pi \times 10\,\mathrm{GHz}$. The x-axis is rescaled by the probe power to point out the scaling of the decay with power. (a) shows the occupation in different Zeeman levels. In (b) the steady state occupation of the $f = 2$ hyperfine manifold is shown for different detunings. The dashed lines mark the resonance conditions for the $f = 2$ and $f = 1$ hyperfine states. (c) depicts the dynamics of the expectation values of $\hat{f}_z$ (in the $f = 2$ hyperfine manifold) and of the projector into the $f = 2$ manifold $\hat{P}_2$.

hybrid coupling experiment, a precessing *spin-oscillator* is needed. This *spin-oscillator* is realised by placing the atoms in a magnetic field which is orthogonal to the direction of propagation of the light. In our experiment, this bias magnetic field is applied along the x-coordinate, as described in section 2.3.2. In this section, the spin precession around the magnetic field is discussed.

For the spin precession experiments, the spin is polarised along the x-axis (sequence is shown schematically in figure 2.3.5 (a) and (b)). In order to tilt the spin macroscopically, a rf drive is applied after the optical spin pumping. With two rf coils (shown in figure 2.3.1), the spin can be tilted by any angle. The duration of the rf drive is set to $t_{\mathrm{rf}} = 30\,\mu\mathrm{s} \ll 1/\delta\Omega_{\mathrm{s}}$, so that its bandwidth is higher than the quadratic splitting of the Zeeman levels and addresses all transitions between the Zeeman states. The rotation angle is controlled by adjusting the amplitude of the rf drive. When the coupling laser is switched on, the F_z component of the spin is mapped onto the polarisation of the light. Due to the precession of the spin around the magnetic field, the projection of the spin along the z-axis (and thus the Faraday signal) oscillates. The Faraday signal is measured and demodulated at the precession frequency of the spin. Two typical measurement traces are shown in figure 2.3.5 (c) and (d). The in-phase component is shown in red, the quadrature component in blue and the rms-amplitude in black. For a weak rf-drive (as shown in figure 2.3.5 (c)), only the first two Zeeman states are occupied. Therefore, there is only one Lorentzian peak. If a strong rf-drive is applied, (e.g. for $\vartheta_{\mathrm{rf}} = \pi/2$ as shown in figure 2.3.5 (d)), all Zeeman levels are occupied. Due to the quadratic Zeeman component, this leads to a dephasing and rephasing of the individual Zeeman states. In the time-trace this is shown as a decay and revival of the spin signal (see figure 2.3.5 (d)). In the spectrum, there are four Lorentzian peaks which correspond to the four different transition energies between the Zeeman levels.

2.3.7 Tensor Interaction

In our experiment, the Faraday interaction is used to couple the collective spin to the light. But in addition to the Faraday interaction, which can be modelled with the spin-1/2 atom, the light-atom interaction has a higher-order term for the more complex Rubidium atom. The so-called tensor interaction arises from the hyperfine splitting of the excited state manifold [110]. It is given by the Hamiltonian in equation (2.2.54), which is rewritten here for clarity

$$\hat{H}_2 = \hbar\alpha_2(\hat{S}_x\hat{t}_{x^2-y^2} + \hat{S}_y\hat{t}_{xy} + \frac{1}{3}\hat{S}_0[3\hat{t}_{z^2} - f(f+1)\mathbb{1}_f]). \tag{2.3.11}$$

The terms in the tensor Hamiltonian depend on higher order spin operators as $\hat{t}_{x^2-y^2} = \hat{f}_x^2 - \hat{f}_y^2$, $\hat{t}_{xy} = \hat{f}_x\hat{f}_y + \hat{f}_y\hat{f}_x$ and $\hat{t}_{z^2} = \hat{f}_z^2$. In general, this leads to non-trivial dynamics of the atomic spin. However, assuming that there is a bias magnetic field along the x-axis, the tensor components can be re-expressed in terms of the operators in the rotating frame

$$\hat{t}_{x^2-y^2} = \tilde{f}_x^2 - \frac{\tilde{f}_y^2 + \tilde{f}_z^2}{2} - \frac{\tilde{f}_y^2 - \tilde{f}_z^2}{2}\cos(2\Omega_{\mathrm{s}}t) - \frac{\tilde{f}_y\tilde{f}_z + \tilde{f}_z\tilde{f}_y}{2}\sin(2\Omega_{\mathrm{s}}t), \tag{2.3.12}$$

$$\hat{t}_{xy} = (\tilde{f}_x\tilde{f}_y + \tilde{f}_y\tilde{f}_x)\cos(\Omega_{\mathrm{s}}t) + (\tilde{f}_x\tilde{f}_z + \tilde{f}_z\tilde{f}_x)\sin(\Omega_{\mathrm{s}}t), \tag{2.3.13}$$

$$\hat{t}_{z^2} = \frac{\tilde{f}_y^2 + \tilde{f}_z^2}{2} - \frac{\tilde{f}_y^2 - \tilde{f}_z^2}{2}\cos(2\Omega_{\mathrm{s}}t) - \frac{\tilde{f}_y\tilde{f}_z + \tilde{f}_z\tilde{f}_y}{2}\sin(2\Omega_{\mathrm{s}}t). \tag{2.3.14}$$

We are interested in the dynamics of the quantities co-rotating in the rotating frame. Therefore, the terms rotating at $2\Omega_{\mathrm{s}}$ are neglected for the further calculations. Furthermore, the terms can be simplified

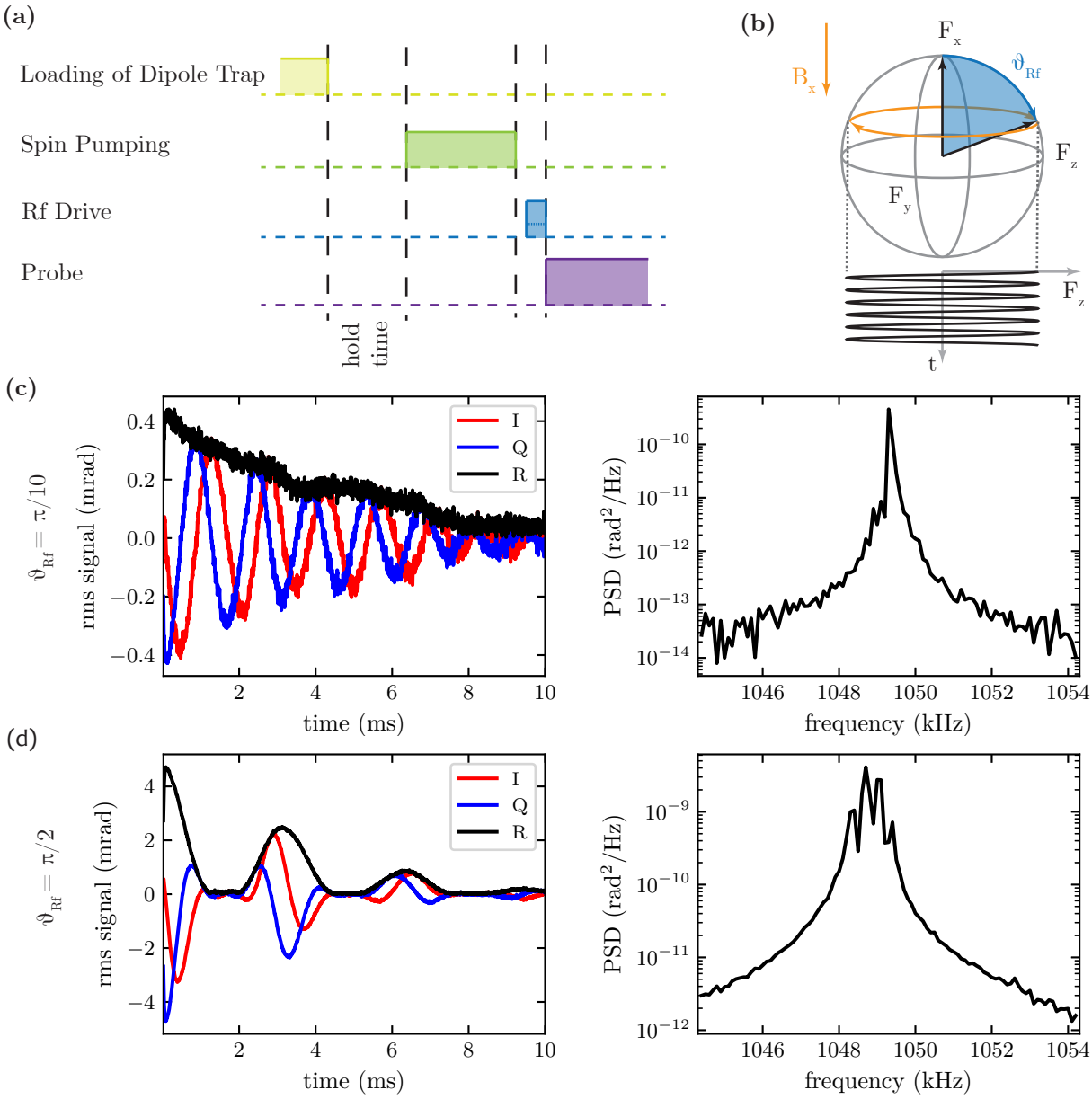

Figure 2.3.5: A typical spin precession measurement: (a) shows the sequence, which is illustrated on a spin-sphere in (b). The rf-angle ϑ_{rf} is controlled by setting the power of the rf drive. (c) and (d) show the measurement for a weak (c) and a strong (d) rf pulse. The time trace shows the demodulated signal with the in-phase (red), the quadrature (blue) and the rms (black) of the Faraday signal. The power spectral density of the signal is calculated.

by using that $\tilde{f}_x^2+\tilde{f}_y^2+\tilde{f}_z^2 = f(f+1)$ and assuming that the spin is well polarised parallel or anti-parallel to the magnetic field. We yield

$$\hat{t}_{x^2-y^2} = \frac{1}{2}(3\hat{f}_x^2 - f(f+1)\hat{\mathbb{1}}_f), \tag{2.3.15}$$

$$\hat{t}_{xy} = \mathrm{sgn}(\langle\hat{f}_x\rangle)(2f-1)\hat{f}_y, \tag{2.3.16}$$

$$\hat{t}_{z^2} = -\frac{1}{2}(\hat{f}_x^2 - f(f+1)\hat{\mathbb{1}}_f). \tag{2.3.17}$$

These simplifications will help to understand the dynamics of the tensor interaction. But before the tensor Hamiltonian is rewritten in the approximate form, the polarisation state of the light is also re-written: In the experiments, the atoms are interfaced with linearly polarised light. For the Faraday interaction, the angle of the linear polarisation with respect to the spin and the magnetic field is irrelevant, as long as the correct quadrature is detected. In the case of the tensor interaction, the dynamics strongly depend on the angle of polarisation. Therefore, a HWP is placed after the polariser (see figure 2.3.1), which rotates the polarisation angle by φ. Here, we define the polarisation angle so that $\varphi = 0$ corresponds to horizontally polarised light and $\varphi = \pi$ corresponds to vertically polarised light. The Stokes vector after the HWP is given by

$$\hat{S}'_x = \hat{S}_x\cos(2\varphi) - \hat{S}_y\sin(2\varphi), \tag{2.3.18}$$

$$\hat{S}'_y = \hat{S}_y\cos(2\varphi) + \hat{S}_x\sin(2\varphi), \tag{2.3.19}$$

$$\hat{S}'_z = -\hat{S}_z. \tag{2.3.20}$$

Inserting this into the tensor Hamiltonian and using the simplified expressions for the tensor spin operators, the tensor Hamiltonian can be re-expressed as

$$\begin{aligned}\hat{H}_{2,f} = \hbar\alpha_{f,2}\Bigg[&f(f+1)\hat{\mathbb{1}}_f\left(\frac{1}{6}\hat{S}_0 - \frac{1}{2}\hat{S}'_x\cos(2\varphi) - \frac{1}{2}\hat{S}'_y\sin(2\varphi)\right)\\ &+ \hat{f}_y\mathrm{sgn}(\langle\hat{f}_x\rangle)(2f-1)\left(\frac{1}{2}\hat{S}'_y\cos(2\varphi) - \frac{1}{2}\hat{S}'_x\sin(2\varphi)\right)\\ &+ \hat{f}_x^2\left(\frac{3}{2}\hat{S}'_x\cos(2\varphi) + \frac{3}{2}\hat{S}'_y\cos(2\varphi) - \frac{1}{2}\hat{S}_0\right)\Bigg].\end{aligned} \tag{2.3.21}$$

In this Hamiltonian, the first term is just a global energy shift that depends on the local intensity of the laser. This adds to the scalar Hamiltonian of the light-atom interaction and can be modified by changing the polarisation of the input light. The second term is already much more sophisticated: It couples the y-component of the atomic spin to the linear polarisation of the light. Thus, the tensor interaction couples different components of the atomic spin and the polarisation of the light than the Faraday interaction. This interaction can become important if the outgoing light is coupled to the spin a second time. In this scenario, the spin can interact with itself (for more details, consider [68]). So far, we have not observed this self-interaction, so we focus on the third term. The third term is a quadratic interaction with the x-component of the spin. As such, it is similar to the quadratic Zeeman splitting. Assuming that the mean polarisation before the half waveplate is given by $\bar{S}_x = \bar{S}_0$, the quadratic term can be written as

$$\hat{H}_{2,f}^{(\mathrm{quad})} = \hbar\alpha_{f,2}\bar{S}_0\frac{3\cos(2\varphi)-1}{2}\hat{f}_x^2 = \hbar\delta\Omega_{\mathrm{ten}}\hat{f}_x^2, \tag{2.3.22}$$

where the shot noise of the light is neglected. The quadratic splitting $\delta\Omega_{\mathrm{ten}}$ depends on the polarisation angle of the light, on the tensor polarisability constant (which depends on the detuning) and the probe power.

In the experiment, this quadratic splitting is most easily observed by scanning the optical power at a given polarisation angle. For this experiment, the atomic spin is again pumped along the magnetic field B_x. Before probing with the light, the spin is rotated by $\pi/2$ using a rf-drive so that it begins precessing around the magnetic field. The oscillating $\hat{F}_z$ component of the spin is observed via the Faraday interaction. In figure 2.3.6 (a) to (c) the time traces and the spectra of the Faraday signal are shown for different powers and polarisation angles. At low optical power, the quadratic splitting by the tensor interaction is negligible and the atomic levels are split mainly due to the quadratic Zeeman effect. This leads to decay and revival in the time traces and to a splitting into four distinct Lorentzian peaks in the spectrum. With increasing optical power, the quadratic level splitting is increased (for $\theta_{\mathrm{pol,in}} = \pi/2$) or decreased (for $\varphi = 0$) by the contributions of the tensor Hamiltonian. At the magic angle $\theta_{\mathrm{pol,in}} \approx 35°$, the light does not change the quadratic splitting of the different Zeeman levels.

In figure 2.3.6 (d) a more systematic analysis of the quadratic splitting is shown for three different probe powers. A cosine is fitted to the quadratic splitting of the Zeeman levels. From the offset of the cosine, the splitting due to the quadratic Zeeman effect can be calculated (dashed line), which corresponds to the expected value for the applied bias field. From the amplitude of the fitted cosine, the prefactor $\alpha_2 \bar{S}_0$ can be evaluated, as shown in figure 2.3.6 (e). A theoretical line for the prefactor is plotted in yellow, assuming that all the atoms are in the focus of the laser beam. If the atoms are exposed to the average intensity, the coupling is reduced by a factor of two which is shown in blue. In this experiment, the fitted coupling strength (red) is somewhere in between. From this experiment, an effective coupling strength can be calculated that does not depend on the length of the atomic spin. This experiment has been performed with the old dipole trap geometry and is therefore not comparable with the calibrations shown in section 2.6. For more details on the effective coupling strength, the reader is referred to section 2.4.

The frequency splitting due to the tensor interaction could in principle be used to compensate for the quadratic Zeeman splitting [116] (as can be seen in figure 2.3.6 (a)) so that the atomic levels have equal precession frequencies. In the experiment, this is not done for two reasons: (1) by setting the input polarisation, the experiment is restricted to a specific combination of detuning and power for which the tensor splitting exactly counteracts the quadratic Zeeman effect. Thus, we could not scan the parameters as easily as before. (2) In the real cloud, the atoms are at different positions in the Gaussian beam, so that the levels of each atom are split differently, depending on the local intensity at the position of the atom. Using the light to shift the atomic lines therefore leads to dephasing of the atoms relative to each other. For the experiments, the polarisation angle is set so that $\delta\Omega_{\mathrm{ten}} = 0$ to minimise the effect of the tensor Hamiltonian. The decay of the spin signal has been analysed for different polarisation angles, as shown in figure 2.3.6 (f). For an input polarisation that shifts the light only minimally, the decay is minimised. Therefore, the polarisation angle was set to $\varphi \approx 35°$, so that the tensor Hamiltonian does not produce a quadratic energy splitting of the Zeeman states.

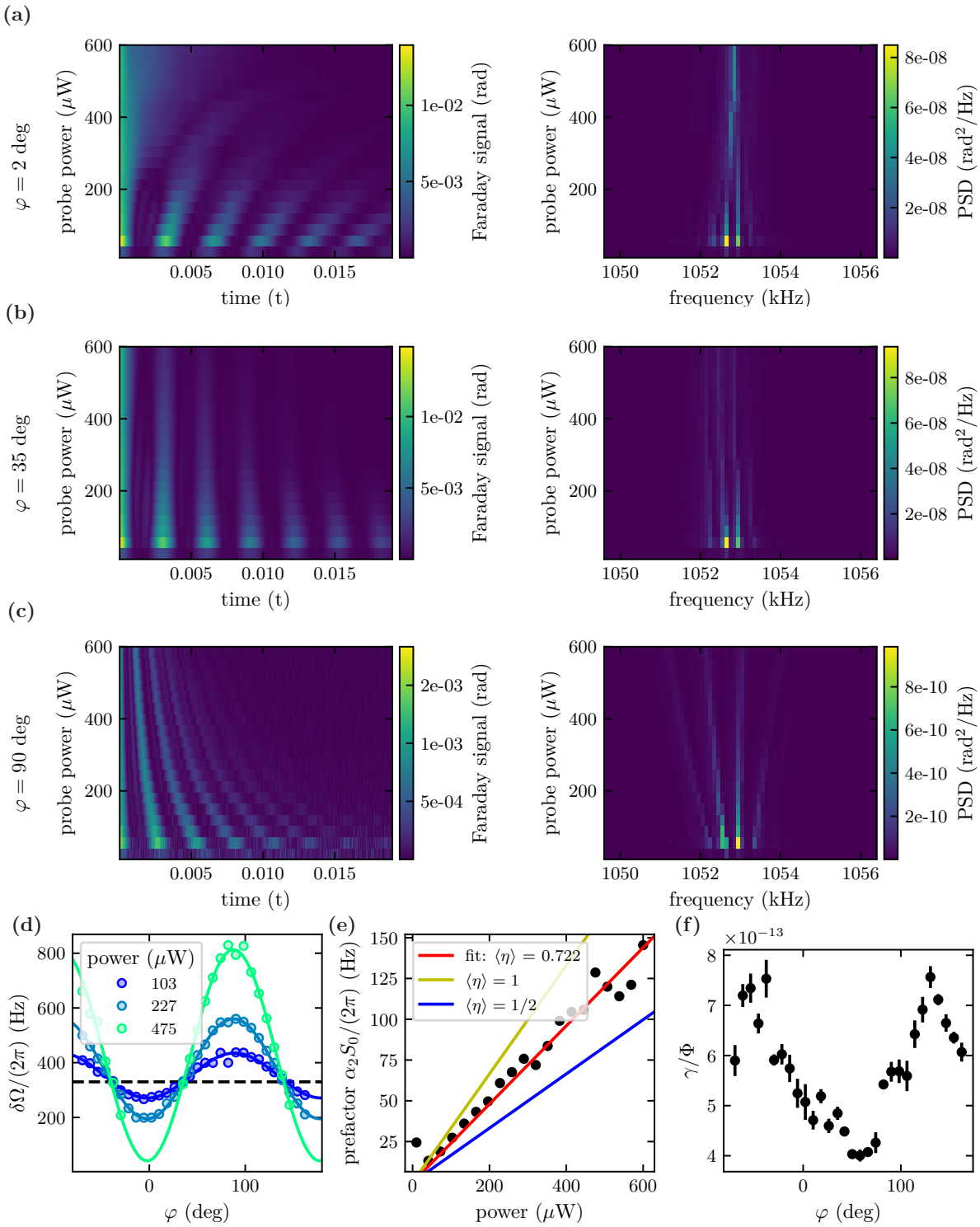

Figure 2.3.6: Measurement of the effect of the tensor Hamiltonian on the atoms at a detuning of −40 GHz: (a) to (c) show data of three different polarisation angles φ for different probe powers. (d) shows the quadratic splitting of the atoms as function of the polarisation angle for three probe powers. The dashed line denotes the quadratic Zeeman splitting. In (e), the fitted pre-factor is plotted and in (f) the fitted decay rate of the signal.

2.4 Collective Scattering of an Atomic Cloud

So far, we have only considered the dynamics of a single atom in the presence of light which scatters all light into the same mode as the input mode (see for example equation (2.2.32)). In order to obtain a collective spin operator, the spin operator of a single atom was multiplied by the total number of atoms. But both assumptions are not straightforward to make and it turns out that they are not fully valid in our case. In this section we will discuss the more realistic scattering of an ensemble of atoms. Having a realistic model for the light-spin interaction enables us to calculate the projection noise and the backaction noise of the full atomic cloud [98].

But before we move on to an ensemble of atoms, let us look at the scattering of a single atom: For a single atom only a small fraction of the scattered light overlaps with the mode of the incoming probe light [94] (shown in appendix D.2). In our implementation, only the light that is scattered into the same mode as the probe light is detected or used in later experiments for the coupling to the membrane. All the rest of the scattered light is not detected or used and therefore contributes to the decoherence of the system. To get a more quantitative understanding of the system, one can perform a calculation, simplifying the atom as a classical oscillator and the light as a classical drive [94]. In the following, we assume that the mode of the incoming light is the Gaussian u_{00} mode (explicitly defined in equation (D.1.12)). The fraction of light which is scattered into the incoming Gaussian mode is given by the overlap integral between the radiation mode $u_{\mathrm{rad}}^{(\mathrm{single})}$ and the Gaussian mode u_{00}

$$\frac{\mathcal{E}_{00}}{\mathcal{E}_{\mathrm{rad}}} = \frac{1}{A}\int_0^\infty \int_0^{2\pi} u_{00}^* u_{\mathrm{rad}}^{(\mathrm{single})} \mathrm{d}\phi r \mathrm{d}r, \tag{2.4.1}$$

where $\mathcal{E}_{00}$ is the amplitude of the radiated field into the incoming Gaussian mode and $\mathcal{E}_{\mathrm{rad}}$ is the amplitude of the total scattering. The ratio between the total scattering of the atom and the scattering into the u_{00} mode can be defined as the single atom cooperativity. The (forward scattering) cooperativity of a single atom is then found to be given by the ratio of the atomic cross-section and the area of the Gaussian beam $C_{\mathrm{single}} = P_{00}/P_{\mathrm{rad}} = \sigma_0/(2A)$ [94] (see appendix D.2). In order to obtain a large single-atom cooperativity, one would have to focus the laser to a waist smaller than the wavelength of the light $C_{\mathrm{single}} > 1 \Rightarrow w_0 < \lambda$, which is not feasible, or use a cavity. In our experiment we take a different approach and work with an ensemble of atoms.

2.4.1 Collective Hamiltonian

As soon as there is more than one atom, the scattered photons from individual atoms interfere. This interference changes the mode of the scattered light u_{rad}. In the optimal case, the atoms are placed so that the scattering interferes destructively in all modes except the Gaussian u_{00} mode. The geometry of the atomic cloud can be engineered so that its scattering cone is perfectly mode-matched to the incoming light. In a thermal gas, however, the position of the atoms is random. Sørensen and Sørensen have shown that the mean position of the atoms gives the refractive index of the atomic gas while the random position of the atoms gives rise to quantum fluctuations equivalent to decoherence by local spontaneous emission [101]. Expressed in other words this means that a perfectly homogeneous cloud could be shaped in such a way that there is only scattering into the Gaussian u_{00} mode and the scattering into all other modes interferes destructively. But in a thermal atomic ensemble, the discrete position of the atoms is random, which leads to an imperfect destructive interference of scattering into transverse modes and thus

to a remaining scattering into 4π. It turns out that this incoherent scattering corresponds exactly to the spontaneous emission of a single atom times the number of atoms in the cloud.

For the calculations, the atomic scattering can be partitioned into scattering into paraxial modes with a small opening angle and scattering into non-paraxial, diffusive modes [117]. First, we focus on the scattering into the paraxial modes. Here, we decompose the paraxial modes into Laguerre-Gaussian modes u_{pl} (given in equation (D.1.3)). The collective Faraday Hamiltonian is then given by the sum over all atoms j and over all paraxial modes p, l

$$\hat{H}_{1,\text{parax}} = -\mathrm{i}\hbar\frac{\alpha_1\sqrt{\Phi_\text{L}}}{2}\sum_{j,p,l}(\beta^*_{pl}(\mathbf{r}_j)\hat{a}_{pl}(z_j,t) - \beta_{pl}(\mathbf{r}_j)\hat{a}^\dagger_{pl}(z_j,t))\hat{f}^{(j)}_z, \tag{2.4.2}$$

where the local amplitude for scattering from the fundamental mode u_{00} into the mode u_{pl} is given by $\beta_{pl}(\mathbf{r}_j) = u^*_{pl}(\mathbf{r}_j)u_{00}(\mathbf{r}_j)$ [85]. There is collective scattering of the atomic cloud into all modes u_{pl}. For this work, the scattering of the atomic cloud into paraxial modes is partitioned in two parts: the scattering into the incoming Gaussian mode u_{00} and the scattering into all other paraxial modes $u_{pl\neq 00}$. In order to get the dynamics of the system, all modes except for the fundamental Gaussian mode are traced out (i.e. only the atoms and the fundamental Gaussian mode are considered as *system*, all other modes are part of the *environment*). So not only the scattering into the non-paraxial modes, but also the scattering into the modes $u_{pl\neq 00}$ leads to decoherence. But before we look at decoherence, the coherent part of the interaction will be considered in the next sections.

2.4.2 Collective Faraday Interaction

The coherent interaction in our system is given by the scattering of photons into the fundamental Gaussian mode u_{00}. Thus, scattering in all other modes cause decoherence and is not considered in this section. We consider only the u_{00} mode of the interaction Hamiltonian given in equation (2.4.2). For this mode $\beta_{00}(\mathbf{r}_j) = |u_{00}(\mathbf{r}_j)|^2$ is real. Therefore, we can simplify $-\mathrm{i}\sqrt{\Phi_\text{L}}(\hat{a}_{00} - \hat{a}^\dagger_{00})/2 \approx \hat{S}_z$ (detailed in section 2.7) and get

$$\hat{H}^{(00)}_1 = \hbar\alpha_1\hat{S}_z\sum_{j=1}^{N_\text{a}}\eta^{(j)}_\text{s}\hat{f}^{(j)}_z. \tag{2.4.3}$$

where the effective coupling of the jth atom to the light is given by the local intensity of the laser $\eta^{(j)}_s = \beta_{00}(\mathbf{r}_j)$. In the definition for α_1 used in this work (using the mode area $A = \pi w_0^2/2$), the effective coupling is $\eta^{(j)}_s = 1$ for an atom at the focus of the laser $\mathbf{r}_j = (0,0,0)$. Effective spin operators can be defined in order to write the Hamiltonian in a simpler form. In order to obtain effective spin operators which still satisfy spin commutation relations, the first order collective spin is defined as [118]

$$\hat{\mathbf{F}}^{(1)} = \sum_{j=1}^{N_\text{a}}\frac{\eta^{(j)}_s}{\eta_{s,\text{eff}}}\hat{\mathbf{f}}^{(j)}, \tag{2.4.4}$$

where the effective coupling strength is given by $\eta_{s,\text{eff}} = \langle\eta_s^2\rangle/\langle\eta_s\rangle$ with $\langle\eta_s^2\rangle = \sum_{j=1}^{N_\text{a}}\eta_s^{(j)2}/N_\text{a}$ and $\langle\eta_s\rangle = \sum_{j=1}^{N_\text{a}}\eta_s^{(j)}/N_\text{a}$ [118]. By defining an effective polarisability constant $\tilde{\alpha}_1 = \eta_{s,\text{eff}}\alpha_1$, the coupling Hamiltonian can be written as

$$\hat{H}_1 = \hbar\tilde{\alpha}_1\hat{S}_z\hat{F}^{(1)}_z. \tag{2.4.5}$$

$\hat{F} = \sum_j^{N_\mathrm{a}} \hat{f}^{(j)}$	$\hat{F}^{(n)} = \sum_j^{N_\mathrm{a}} \left(\frac{\eta_\mathrm{s}^{(j)}}{\eta_{\mathrm{s,eff}}}\right)^n \hat{f}^{(j)}$ $= \frac{\langle \eta_\mathrm{s}^n \rangle}{\eta_{\mathrm{s,eff}}^n} \hat{F}$
$\alpha_1 = \frac{\lambda^2}{8\pi A} \frac{\gamma_\mathrm{Rb}}{\Delta}$	$\tilde{\alpha}_1 = \eta_{\mathrm{s,eff}} \alpha_1$ with $\eta_{\mathrm{s,eff}} = \frac{\sum \eta_\mathrm{s}^{(i)2}}{\sum \eta_\mathrm{s}^{(i)}} = \frac{\langle \eta_\mathrm{s}^2 \rangle}{\langle \eta_\mathrm{s} \rangle}$
$\hat{H}_1 = \hbar \alpha_1 \hat{S}_z \hat{F}_z$	$\hat{H}_1 = \hbar \alpha_1 \hat{S}_z \sum_i^{N_\mathrm{a}} \eta_\mathrm{s}^{(i)} \hat{f}_z^{(i)}$ $= \hbar \tilde{\alpha}_1 \hat{S}_z \hat{F}_z^{(1)}$

Holstein-Primakov approximation, assume identical spins $\hat{f}_i = \hat{f}$

$\hat{X}_\mathrm{s} = \frac{\hat{F}_z}{\sqrt{fN}}$	$\hat{\tilde{X}}_\mathrm{s} = \frac{\langle \eta_\mathrm{s} \rangle}{\sqrt{\langle \eta_\mathrm{s}^2 \rangle}} \hat{X}_\mathrm{s}$
$\hat{P}_\mathrm{s} = -\mathrm{sng}(\bar{F}_x) \frac{\hat{F}_y}{\sqrt{fN}}$	$\hat{\tilde{P}}_\mathrm{s} = \frac{\langle \eta_\mathrm{s} \rangle}{\sqrt{\langle \eta_\mathrm{s}^2 \rangle}} \hat{P}_\mathrm{s}$
$\Gamma_\mathrm{s} = \frac{\alpha_1^2 \bar{F}_x \bar{S}_x}{4}$	$\tilde{\Gamma}_\mathrm{s} = \langle \eta_\mathrm{s}^2 \rangle \Gamma$

Table 2.4.1: Collective spin variables for homogeneous and inhomogeneous coupling to the light considering a ^{87}Rb atom.

Due to the effective coupling of the atoms to the light, two quantities are re-normalised, the spin length and the polarisability constant (see table 2.4.1 for all definitions). This is done to preserve the commutation relations of the collective spin. However, it comes at the cost that a single measurement is not sufficient to characterise both renormalised quantities.

Input-Output Relations: Assuming that the light is polarised along the $\bar{S}_x = \bar{S}_0$ axis, the output field after the interaction with the atomic cloud can be written as

$$\hat{S}_y^{(\mathrm{out})} = \hat{S}_y^{(\mathrm{in})} + \tilde{\alpha}_1 \hat{F}_z^{(1)} \tag{2.4.6}$$

$$= \hat{S}_y^{(\mathrm{in})} + \langle \eta_\mathrm{s} \rangle \alpha_1 \hat{F}_z. \tag{2.4.7}$$

So the interaction with the light is rescaled by the average light intensity at the atomic positions $\langle \eta_s \rangle$.

Quantum Limited Spin-Light Interface: The mean spin-light interaction scales with $\langle \eta_s \rangle$. But it cannot be assumed that this scaling is the same for the projection noise and the backaction noise. In order to obtain the scaling of the quantum noise contributions, the equations of motion of each individual spin (similar to equations (2.2.42) and (2.2.43), except that the Faraday term has to be scaled by $\eta_s^{(i)}$) have to be included in the input-output relation of the polarisation quadratures of the light (the derivation is explicitly shown in appendix D.3). The resulting spectrum is given by

$$\bar{S}_{S_y S_y}(\omega) = \frac{\bar{S}_x}{2} + \frac{(\alpha_1 \bar{S}_x/2)^2}{(\Omega_\mathrm{s} - \omega)^2 + (\gamma_\mathrm{s}/2)^2} \cdot \left(\sum_{i=1}^{N_\mathrm{a}} \gamma_\mathrm{s} \eta_s^{(i)2} |\bar{f}_x^{(i)}| + \sum_{i=1}^{N_\mathrm{a}} \sum_{j=1}^{N_\mathrm{a}} \alpha_1^2 \eta_s^{(i)2} \eta_s^{(j)2} \bar{f}_x^{(i)} \bar{f}_x^{(j)} \bar{S}_x/2 \right), \tag{2.4.8}$$

where the decay rate of the spins γ_s is assumed to be the same for all spins. While the contribution from shot noise of the light has not changed, the second and third terms depend on the sum over the individual spins times the intensity squared $\sum_{i=1}^{N_\mathrm{a}} \eta_s^{(i)2} \bar{f}_x^{(i)}$. To simplify this expression, it is useful to generalise the

definition of the effective spin operator to higher orders [118]

$$\hat{\mathbf{F}}^{(n)} = \sum_{j=1}^{N_\mathrm{a}} \left(\frac{\eta_s^{(j)}}{\eta_{s,\mathrm{eff}}} \right)^n \hat{\mathbf{f}}^{(j)}. \tag{2.4.9}$$

With this definition, the PSD of the $\hat{S}_y$ Stokes-vector component can be written as

$$\bar{S}_{S_y S_y}(\omega) \approx \frac{\bar{S}_x}{2} + \frac{(\tilde{\alpha}_1 \bar{S}_x/2)^2}{(\Omega_\mathrm{s} - \omega)^2 + \gamma_\mathrm{s}^2/4} \cdot \left(\gamma_\mathrm{s} |\bar{F}_x^{(2)}| + \frac{\tilde{\alpha}_1^2 \bar{F}_x^{(2)2} \bar{S}_x}{2} \right). \tag{2.4.10}$$

which is the same as equation (2.2.49) but with a scaled polarisability constant and a second order effective spin operator $\hat{\mathbf{F}}^{(2)}$. Note that the spin noise scales differently with the coupling efficiency than the mean spin. However, if all spins are assumed to be initialised in the same state, the first and the second order spin operators are the same $\hat{\mathbf{F}}^{(1)} = \hat{\mathbf{F}}^{(2)}$, which simplifies the problem.

In order to calibrate the spin signal, often an on-axis measurement of the spin is performed. The measured Faraday signal is compared with the number of atoms calculated from an absorption image, as shown in section 2.3.4. This measurement gives only the first order $\langle \eta_s \rangle$ effective coupling. It cannot be used to calibrate the quantum noise without making any assumptions about the geometry. For a full characterisation of the collective spin, a measurement of $\eta_{s,\mathrm{eff}}$ has to be performed. This can be done by measuring the spin noise rather than the mean spin.

Overlap Integral

In order to calculate $\langle \eta_s \rangle$, $\langle \eta_s^2 \rangle$ and $\eta_{s,\mathrm{eff}}$ for a specific geometry, the atomic cloud is approximated by a homogeneous cloud with atomic density $n(\mathbf{r})$ (i.e. given in equation (1.6.4) for a Gaussian cloud). The effective coupling of individual atoms to the light can be written for a homogeneous cloud as continuous variable $\eta_\mathrm{s}^{(j)} \to \eta_\mathrm{s}(\mathbf{r}) = \beta_{00}(\mathbf{r})$. Furthermore, it is assumed that all atoms are in an identical internal state so that we can write $\hat{\mathbf{f}}^{(j)} \to \hat{\mathbf{f}}$. The sum over all atoms can then be approximated by an integral over the atomic density, i.e.

$$\sum_{j=1}^{N_\mathrm{a}} \to \int \mathrm{d}V n(\mathbf{r}) \tag{2.4.11}$$

where the density of the atomic cloud is normalised so that the integral over the total volume gives the total number of atoms $\int n(\mathbf{r}) \mathrm{d}V = N_\mathrm{a}$. In the following, values for $\langle \eta_s \rangle$, $\langle \eta_s^2 \rangle$ and $\eta_{s,\mathrm{eff}}$ are estimated for given geometries. For this, the atomic cloud is approximated by a 3D-Gaussian distribution

$$n(r,z) = N_\mathrm{a} \sqrt{\frac{1}{\pi^3 w_{a,r}^4 w_{a,z}^2}} \exp\left(-\frac{r^2}{w_{a,r}^2} \right) \exp\left(-\frac{z^2}{w_{a,z}^2} \right), \tag{2.4.12}$$

as derived in section 1.6.1 for a dipole-trapped cloud. The full analytical expressions for the overlap integrals are given in appendix D.4.

Analytical Integration: Only for a few special cases do the integrals have analytical and readable solutions: The integrals can be simplified by setting the atomic waist to $w_{a,r} = w_0/\sqrt{2}$ where w_0 is the beam waist of the optical mode. Going to the limit of large Rayleigh lengths much longer than the atomic

		Our Experiment	Large Fresnel Number, mode-matched waist	Vapour Cell with atomic density n
Cloud waist	$w_{a,r}$	25.2 µm	$w_{a,r} = w_0/\sqrt{2}$	homogeneous distribution
Cloud length	$w_{a,z}$	10.5 mm	$w_{a,z} \ll z_\mathrm{R}$	cell length l
Mean coupling	$\langle \eta_s \rangle$	0.53	1/2	$\frac{nAl}{N_\mathrm{a}} = 1$
Mean coupling squared	$\langle \eta_s^2 \rangle$	0.33	1/3	$\frac{nAz_\mathrm{R}}{N_\mathrm{a}} \arctan\left(\frac{l}{2z_\mathrm{R}}\right)$ $= \pi/8 \approx 0.39$

Table 2.4.2: Calculation of the overlap integrals for the atomic cloud in our experiment and some limit cases. For the vapour cell the case for an atomic density of $n = N_\mathrm{a}/V$ and a cell length of $l = 2z_\mathrm{R}$ is calculated explicitly.

cloud length (i.e. the limit of large Fresnel number $F = w_0^2/(\lambda w_{a,z})$), we get $\hat{\mathbf{F}}^{(1)} = \hat{\mathbf{F}}^{(2)} = 3\hat{\mathbf{F}}/4$ and $\tilde{\alpha}_1 = 2\alpha_1/3$. In theory, this limit is described as the limit where the 1D- approximation is still valid [13]. Here, the mean spin coupling rate is reduced by a factor of $\langle \eta_s \rangle = 1/2$. In a previous work [68], this factor of two was taken into account by rescaling the mode area of the light to $A = \pi w_0^2$ which results in rescaling α_1 but not the collective spin operators. This approach does work for mean values but not for the variances, which must be rescaled by a factor of $\langle \eta_s^2 \rangle = 1/3$.

Another special case, where the analytical integration provides intuitively understandable results, is a hot atomic ensemble in a vapour cell. Assuming that the cell is in radial direction much larger than the probe beam, the effective coupling amplitude is given by $\langle \eta_s \rangle = nAl/N_\mathrm{a}$ where n is the uniform atomic density in the cell and l is the cell length. In this example N_a does not have a physical meaning and only results from the definition of $\langle \eta_s \rangle$ which is motivated by a cold atomic cloud. Calculating the equations of motions for the spin or the input-output relations for the light, the factor N_a cancels. For here, we define the number of atoms $N_\mathrm{a} = nV$ by taking the "volume" of the optical beam in the cell $V = lA$ and get $\langle \eta_s \rangle = 1$. Then, the variance has to be rescaled by a factor of $\langle \eta_s^2 \rangle = \arctan(l/(2z_\mathrm{R}))(z_\mathrm{R}/l)$. This approaches $\langle \eta_s^2 \rangle = 1/2$ for small $l \ll z_\mathrm{R}$ and gets smaller for longer cells.

Numerical Integration: For most geometries, no analytical expression for the integral is obtained. Therefore, the integration is performed numerically. The mean (square) intensities are shown for different parameters in figure 2.4.1. The overlap of the Gaussian mode and the atomic cloud is best for a short cloud with a minimal width. This makes sense because for this cloud all atoms are in the focus of the laser. But in the next section we will see that this configuration leads to a faster decoherence of the spin due to the coupling to higher order modes of the light.

The cloud parameters of the atomic cloud in our experiments are given in table 1.6.1. The radial waist is given by $w_{a,r} = 25.2\,\mu\mathrm{m}$ while the length of the cloud is estimated to be $w_{a,z} = 10.5\,\mathrm{mm}$. The probe beam is at a wavelength of $\lambda = 780\,\mathrm{nm}$, has a waist of $w_0 = 50\,\mu\mathrm{m}$ and thus a Rayleigh length of $z_\mathrm{R} = 10.1\,\mathrm{mm}$. All calculated values are listed in table 2.4.2.

2.4.3 Decay due to Collective Scattering into Higher Order Modes

The next step is to consider the scattering into paraxial modes with $p, l \neq 0, 0$. As explained above, only the fundamental mode is measured in our experiment. Thus, we define that the spin and the scattered u_{00} mode are part of the *system* while all other scattered modes are part of the *environment* and trace

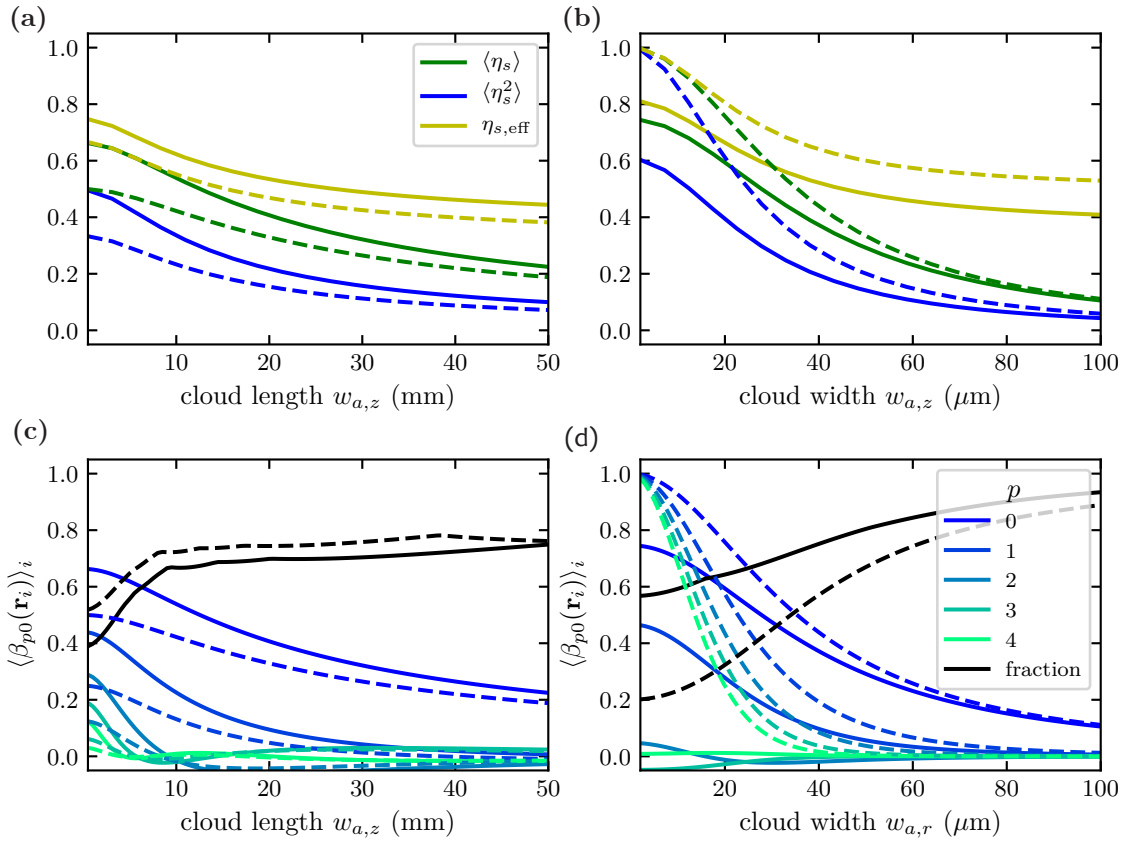

Figure 2.4.1: Calculations of the overlap integrals for different geometries and different optical modes: In (a) and (b) the first order and the second order overlap integrals are plotted. In (c) and (d) the cloud overlap with different scattering amplitudes $\langle\beta_{p,l=0}(\mathbf{r}_i)\rangle_i = \sum_i \beta_{p,l=0}(\mathbf{r}_i)/N_\mathrm{a}$ are plotted against the cloud length (c) and the cloud width (d) (consider that $\langle\beta_{00}(\mathbf{r}_i)\rangle_i = \langle\eta_\mathrm{s}\rangle$). In all plots, a probe laser with a wavelength of $\lambda = 780\,\mathrm{nm}$ and a waist of $w_0 = 50\,\mu\mathrm{m}$ is considered. In (a) and (c), the waist of the atomic cloud is chosen to be $w_{a,r} = 25.2\,\mu\mathrm{m}$ (solid line) and $w_{a,r} = w_0/\sqrt{2}$ (dashed line). In (b) and (d), the length of the atomic cloud is set to $w_{a,z} = 10.5\,\mathrm{mm}$ (solid line) and $w_{a,z} = 0.1\,\mathrm{mm}$ (dashed line). The black lines (dashed and solid) in (c) and (d) show the fraction of the scattering into the fundamental mode, i.e. $\sum_i \beta_{00}(\mathbf{r}_i)/\left(\sum_{p=0}^{4}\sum_i \beta_{p0}(\mathbf{r}_i)\right)$.

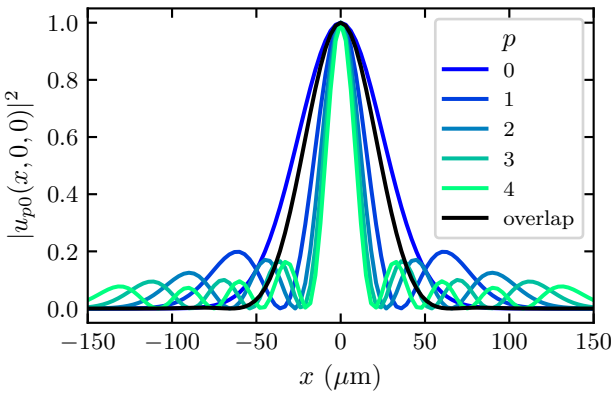

Figure 2.4.2: The cross-section of the first few Laguerre-Gauss modes at the focus of the laser. The mode for $p = 0$ corresponds to the input beam. The black line shows the mode of the scattered photons, which is calculated by summing the plotted Laguerre-Gauss modes weighted with the coupling efficiency $\langle \beta_{p,l}(\mathbf{r}_i)\rangle_i = \sum_i \beta_{pl}(\mathbf{r}_i)/N_\mathrm{a}$

over the environment. Assuming a memoryless environment, this yields the following Master equation

$$\frac{\mathrm{d}}{\mathrm{d}t}\mathrm{Tr}_\mathrm{R}(\hat{\rho}) = \frac{1}{\mathrm{i}\hbar}[\hat{H}_1^{(00)}, \hat{\rho}] + \frac{\alpha_1^2\Phi_\mathrm{L}}{2} \cdot \sum_{p,l\neq 0,0} \mathcal{D}\left(\sum_j^{N_\mathrm{a}} \beta_{pl}(\mathbf{r}_j)\hat{f}_z^{(j)}\right)\hat{\rho}. \tag{2.4.13}$$

This is a complicated Master equation and it is beyond the scope of this thesis to solve it. However, some intuition can be gained: The pre-factor of the jump operators is given (in the continuum approximation, see above) by the overlap integral between β_{pl} and the atomic cloud. In order to estimate the relevance of this decoherence process, this overlap integral can be calculated and compared with the overlap integral with the fundamental mode β_{00}. For a symmetric coupling between a Gaussian cloud and a Gaussian input beam, all overlap integrals with $l > 0$ are zero. In figure 2.4.1 (c) and (d) some of the overlap integrals are plotted for different cloud geometries.

From the numerical calculation shown in figure 2.4.1, some trends can be seen: The shorter the cloud and the smaller its waist, the stronger is the coupling not only to the fundamental mode but also to higher order modes. As the cloud becomes longer and wider, the overlap becomes smaller. Thus, a trade-off must be made between effectively coupling the cloud to the fundamental Gaussian mode and not coupling it too strongly to higher order modes. It is also worth noting that for higher optical order p, the coupling becomes smaller. For an intuitive understanding, the fraction between the coupling to the fundamental mode and the coupling to all modes $p < 5$ is shown in figure 2.4.1 (c) and (d). This fraction may provide some intuition but it has a major shortcoming: The different optical modes couple to different spin waves, given by the overlap of the atomic cloud with a particular optical mode $\mathbf{F}^{(1,pl)} = \sum_j \beta_{pl}(\mathbf{r}_j)\mathbf{f}^{(j)}$. The spin wave for the fundamental Gaussian mode is given in equation 2.4.4, the spin waves for higher order optical modes have $\beta_{pl}(\mathbf{r}_j)$ as weighting factor (instead of $\eta_s^{(j)} = \beta_{00}(\mathbf{r}_j)$). In general, the spin waves for different optical modes are not orthogonal, so the decoherence of one spin wave affects the dynamics of the others.

As a final geometrical estimation, the shape of the scattered mode is evaluated. For this, the scattering into different modes has to be summed. If all atoms are initialised in the same state, the scattering of photons into a given Laguerre-Gauss mode is determined by the overlap factor $\sum_i \beta_{pl}(\mathbf{r}_i)$. In this case,

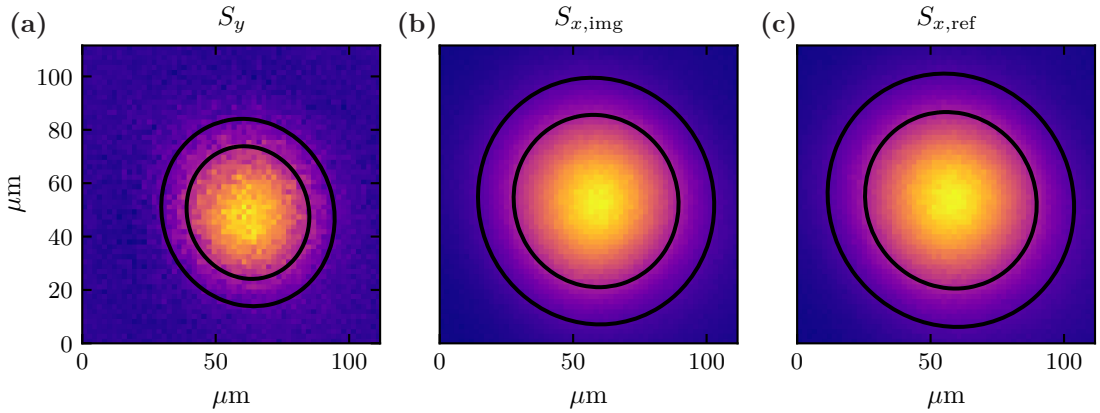

Figure 2.4.3: Spatially resolved Faraday rotation by the spin-polarised atomic ensemble. Using a camera, the beams from the two ports of the PBS in the polarisation homodyne setup are imaged. By subtracting the two images, $\bar{S}_y$ is obtained (a), by adding the images, $\bar{S}_x$ is obtained, shown in (b) for the actual experiment and in (c) for a reference image without atoms. The black contour lines show the 1/e and $1/e^2$ lines of a 2D-Gaussian fit.

the beam shape of the scattered photons (into a paraxial mode) can be estimated by summing the modes u_{pl} weighted by the coupling efficiency $\langle \beta_{pl}(\mathbf{r}_i)\rangle_i = \sum_i \beta_{pl}(\mathbf{r}_i)/N_\mathrm{a}$. For the geometry of our experiment, the resulting mode is again Gaussian (see figure 2.4.2) with a waist of $w_0^\mathrm{sc} = 39\,\mu\mathrm{m}$, somewhat smaller than the waist $w_0 = 50\,\mu\mathrm{m}$ of the probe beam.

2.4.4 Measurement of the Scattering Cone

The scattering cone of the atoms can be imaged and compared with the theoretical estimates above. For this, the atoms are polarised along the propagation axis of the probe light. The probe light is detuned by $-10\,\mathrm{GHz}$. The Faraday effect rotates the linear polarisation of the input light. Normally, this polarisation rotation is detected by a homodyne detection (as for example in the experiment described in section 2.3.4). Here, instead of measuring the polarisation with a photodiode, a camera is used. The two beams from the PBS output ports are focused onto the camera so that the focal plane of the beam is imaged. In the data processing, the two images from both beams can be added or subtracted from each other. Adding the two images from the PBS ports gives the spatially resolved $S_x^{(\mathrm{out})}$. By subtracting the two images, $S_y^{(\mathrm{out})}$ is measured. As such, a spatially resolved polarisation homodyne measurement is performed.

The result of one experiment is shown in figure 2.4.3: The input beam is polarised along $\hat{S}_x$. The mode of the $\hat{S}_x$ polarisation is shown in (b) for the experiment with atoms and in (c) for a reference measurement without atoms. The two images are very similar, so the atoms do not significantly change the mean polarisation. However, the atoms scatter some photons into the orthogonal $\hat{S}_y$ polarisation. The mode of the scattering cone is shown in figure 2.4.3 (a). The beam images are fitted with a 2D-Gaussian to obtain the beam waist. The waist of the scattered beam is $w_0^\mathrm{sc} = 38 \pm 2\,\mu\mathrm{m}$. This agrees well with the theoretical expectations.

2.4.5 Summary and Conclusion

The interaction between a dipole-trapped ensemble of atoms and light is frequently represented by a 1D-model [98, 106, 110, 114, 115]. This provides a good first-order description of our experiment. In order to provide an accurate 3D-description, it is necessary to consider that the atomic cloud and the light exhibit an inhomogeneous distribution in space. Still, the Faraday interaction can be treated in a 1D-description by defining an effective polarisability constant and effective spin operators. The measurement outcomes of different measurements scale differently with the intensity distribution over the cloud: If the mean spin is observed, the effective coupling scales with the mean local intensity at the position of the atoms. However, the spin variance scales with the intensity squared. For the geometry in our experiment, we get $\langle \eta_s \rangle = 0.53$ and $\langle \eta_s^2 \rangle = 0.33$, respectively.

In addition to the coherent interaction with the Gaussian u_{00} mode, the atomic cloud also scatters photons into other modes. These other modes are considered as an *environment*, the coupling to which leads to decoherence. Such coupling to the environment has two different contributions: The random position of the atoms in the thermal cloud leads to scattering of light into non-paraxial modes [101]. This incoherent scattering occurs at the spontaneous emission rate of a single atom and is therefore covered by the single atom description. In addition, there is coherent, collective scattering of the atoms into paraxial modes $p, l \neq 0, 0$ which are not measured due to imperfect mode-matching between the scattering cone of the atoms and the incoming u_{00} laser beam. The decoherence rate of this process has not been calculated in this work but some estimates can be made: Assuming that all spins are in an identical state, only about 65 % of the forward scattered photons are scattered into the mode of the incoming beam. The expected total decoherence is therefore significantly larger than the decoherence of a single atom. We speculate that the additional decoherence rate will be about 35%/65% of the desired coherent coupling, i.e. $\gamma_{\mathrm{add}} = (0.35/0.65)\Gamma_{\mathrm{s}}$. But to confirm this, one has to solve equation (2.4.13) rigorously.

2.5 Classically Driven Spin System

For manipulating the atomic spin there is a large toolbox available. In previous sections (see e.g. section 1.7), the initialisation of the spin system in a given state via optical pumping is presented. In our sequence, this initial polarisation is along the bias magnetic field B_x. Once all the spins have been initialised to the same state, the collective spin can be driven using radiofrequency (rf) fields. This is an important technique for both initialisation and characterisation of the spin. In the spin initialisation, the rf drive can be used to rotate the mean spin with respect to the magnetic field before a probe field is applied. For characterising the spin system, the rf field is applied during the probe. The spin response to the rf field is then measured by the Faraday interaction. This section provides an overview of the ways in which rf fields can be applied and of the resulting state or dynamics of the driven spin.

Experimentally, the rf fields can be applied by using coils. An analogous effect can be achieved by modulating the polarisation of the light at radio frequencies:

Radiofrequency Coils: The atomic spin is typically manipulated by the direct application of rf magnetic fields using coils. In the experiment, two coils are installed, one along the y-axis and one along the z-axis (shown in figure 2.3.1). Driving one of the coils with an rf modulation creates an oscillating magnetic field along B_z or B_y, depending on the rf coil. In the following, we consider the rf coil along

the z-axis. The interaction Hamiltonian for the total magnetic field with a single spin is extended to

$$\hat{H}_B = \hbar\Omega_\mathrm{s}\hat{f}_x + \hbar\delta\Omega_\mathrm{s}\hat{f}_x^2 + \hbar 2\Omega_\mathrm{R}\cos(\Omega_\mathrm{rf}t)\hat{f}_z \tag{2.5.1}$$

where Ω_rf is the rf frequency and Ω_R is the Rabi frequency proportional to the rf amplitude. The Rabi frequency Ω_R depends on the driving voltage, the coil parameters and the distance between the coil and the atoms.

Radiofrequency Modulation of the Polarisation: An alternative approach is to utilise the Faraday effect to drive the atomic spin. An EOM[8] can be employed to modulate the polarisation of the light (shown in figure 2.3.1). The polarisation is set such that the circularly polarised component of the light is modulated. As a result of the Faraday interaction, a fictitious magnetic field is induced along the propagation axis of the light. The resulting Hamiltonian for a circular polarisation modulation at a frequency Ω_rf can be written as

$$\hat{H} = \hbar\Omega_\mathrm{s}\hat{f}_x + \hbar\delta\Omega_\mathrm{s}\hat{f}_x^2 + \hbar\alpha_1\bar{S}_z^{(\mathrm{mod})}\cos(\Omega_\mathrm{rf}t)\hat{f}_z \tag{2.5.2}$$

where $\bar{S}_z^{(\mathrm{mod})}$ is the modulation amplitude of the circularly polarised light. In this section, the shot-noise contribution of the light is neglected, as it is only a discussion of the mean spin dynamics. By setting $2\Omega_\mathrm{R} = \alpha_1\bar{S}_z^{(\mathrm{mod})}$, the same result as for the driving with the rf-coils is obtained. Therefore, in the following, a general atomic drive is considered, which describes both possible driving mechanisms.

2.5.1 Two Level System

It is convenient to look at the spin dynamics in the model of a spin-1/2 atom first, before moving on to the more evolved case of the Rubidium $f = 2$ ground state with five levels. Writing the Hamiltonian in the x-basis instead of the z-basis (denoted by an index) allows us to obtain the Hamiltonian of a classically driven two-level system in the form commonly used in quantum optics

$$\hat{H} = \frac{\hbar}{2}\begin{pmatrix} -\Omega_\mathrm{s} & -\mathrm{i}2\Omega_\mathrm{R}\cos(\Omega_\mathrm{rf}t) \\ \mathrm{i}2\Omega_\mathrm{R}\cos(\Omega_\mathrm{rf}t) & \Omega_\mathrm{s} \end{pmatrix}_x . \tag{2.5.3}$$

Using the rotating wave approximation and defining the detuning between the Larmor frequency and the rf-drive as $\delta = \Omega_\mathrm{rf} - \Omega_\mathrm{s}$, the Hamiltonian can be approximated in the rotating frame to

$$\hat{\tilde{H}} = \frac{\hbar}{2}\begin{pmatrix} \delta & -\mathrm{i}\Omega_\mathrm{R} \\ \mathrm{i}\Omega_\mathrm{R} & -\delta \end{pmatrix}_x . \tag{2.5.4}$$

The dynamics of the driven spin is described by the well-known optical Bloch equations. But before writing the dynamics of the system explicitly, the decay is modelled. In this section, the decay is given

[8] PCA4R-NIR from *Qubig*: bandwidth up to 150 MHz, anti-reflective coating

by the following three jump operators

$$\hat{L}_- = \sqrt{\gamma_-}\hat{f}_{-'} = \sqrt{\gamma_-}(\hat{f}_y - i\hat{f}_z), \tag{2.5.5}$$

$$\hat{L}_+ = \sqrt{\gamma_+}\hat{f}_{+'} = \sqrt{\gamma_+}(\hat{f}_y + i\hat{f}_z), \tag{2.5.6}$$

$$\hat{L}_\phi = \sqrt{\gamma_\phi}\hat{f}_x. \tag{2.5.7}$$

where $\hat{L}_-$ corresponds to lowering the $m_{F,x}$ state by one, $\hat{L}_+$ increases the $m_{F,x}$ by one and $\hat{L}_\phi$ is a pure dephasing of the precession around the x-axis. Given the Hamiltonian and the decoherence processes, the equations of motion for the mean spin operators can be derived. They are given by

$$\frac{\mathrm{d}}{\mathrm{d}t}\langle\hat{\bar{f}}_x\rangle = \Omega_\mathrm{R}\langle\hat{\bar{f}}_y\rangle - \gamma_-\left(\langle\hat{\bar{f}}_x\rangle + \frac{1}{2}\right) - \gamma_+\left(\langle\hat{\bar{f}}_x\rangle - \frac{1}{2}\right), \tag{2.5.8}$$

$$\frac{\mathrm{d}}{\mathrm{d}t}\langle\hat{\bar{f}}_y\rangle = -\Omega_\mathrm{R}\langle\hat{\bar{f}}_x\rangle + \delta\langle\hat{\bar{f}}_z\rangle - \frac{\gamma_+ + \gamma_- + \gamma_\phi}{2}\langle\hat{\bar{f}}_y\rangle, \tag{2.5.9}$$

$$\frac{\mathrm{d}}{\mathrm{d}t}\langle\hat{\bar{f}}_z\rangle = -\delta\langle\hat{\bar{f}}_y\rangle - \frac{\gamma_+ + \gamma_- + \gamma_\phi}{2}\langle\hat{\bar{f}}_z\rangle. \tag{2.5.10}$$

Here, the equations of motion are written in a frame rotating at Ω_rf (which is different from the definition in equations (2.3.2) and (2.3.3)). These equations of motion are the starting point for further discussion. Note that in the experiment the spin can be optically pumped along the x-axis, which corresponds to optically increasing the decoherence rate γ_- or γ_+, depending on the helicity of the circular polarisation of the pump laser. The optical pumping into the maximally polarised states with $\langle\hat{f}_x\rangle = \pm 1/2$ can be directly seen in these equations of motion by setting an imbalance between γ_- and γ_+.

Rf Pulse for Spin Initialisation

For many experiments (e.g. those described in sections 2.3.6 and 2.3.7), a short rf pulse is applied to the spin before it interacts with the probe light. For this, the rf coils are preferred over the EOM to avoid the decoherence associated with the probe light. Assuming that the spin decay during the short pulse can be neglected and the rf-pulse is resonant, the equations of motion for the spin are given by $\frac{\mathrm{d}}{\mathrm{d}t}\langle\hat{\bar{f}}_x\rangle = \Omega_\mathrm{R}\langle\hat{\bar{f}}_y\rangle$ and $\frac{\mathrm{d}}{\mathrm{d}t}\langle\hat{\bar{f}}_y\rangle = -\Omega_\mathrm{R}\langle\hat{\bar{f}}_x\rangle$. This corresponds to a rotation of the spin in the xy-plane. By setting the duration of the pulse and the amplitude Ω_R, the angle of rotation can be set. In this way a spin with a mean polarisation along the y-axis can be initialised while the magnetic field still points along the x-axis.

Continuous Rf Drive during Probe

Alternatively, the rf drive can be applied during the probe. In order to simplify the equations of motion, it is assumed that the decay of the system is symmetric (which is not generally true as shown in the equations (2.2.38) to (2.2.40)), i.e. the spin decoherence is defined as $\gamma/4 = \gamma_+ = \gamma_- = \gamma_\phi/2$. The equations of motion of the spin can be solved most easily in the frequency domain. A Laplace transformation is performed, assuming that the spin is initially polarised along the x-axis $\langle\hat{\bar{f}}_x(t=0)\rangle = \bar{f}_x$. In the frequency domain, the system of equations is solved and transformed back. In the measurement, the detected light is demodulated at the rf frequency Ω_rf. To analyse these spectroscopy experiments, the in-phase and quadrature signals are integrated separately over the measurement duration. This corresponds

to an integration of the slowly rotating spin components, namely

$$I_{\text{int}} = \frac{\alpha_1 \bar{S}_x}{\sqrt{2}} \int_0^\infty \langle \hat{\tilde{f}}_z(t) \rangle \mathrm{d}t = -\frac{\alpha_1 \bar{S}_x}{\sqrt{2}} \frac{\bar{f}_x \Omega_R \delta}{\gamma/2[(\gamma/2)^2 + \delta^2 + \Omega_R^2]}, \tag{2.5.11}$$

$$Q_{\text{int}} = \frac{\alpha_1 \bar{S}_x}{\sqrt{2}} \int_0^\infty \langle \hat{\tilde{f}}_y(t) \rangle \mathrm{d}t = \frac{\alpha_1 \bar{S}_x}{\sqrt{2}} \frac{\bar{f}_x \Omega_R}{(\gamma/2)^2 + \delta^2 + \Omega_R^2}. \tag{2.5.12}$$

From this result we can ascertain certain characteristics of the measurement outcome directly. Upon scanning the rf frequency over the spin resonance (i.e., changing δ), I_{int} exhibits a dispersive shape whereas Q_{int} displays a Lorentzian shape. In case of strong driving $\Omega_R \gg \gamma$, the dispersive shape dominates. Conversely, in the weak driving regime, the Lorentzian peak is larger by a factor 2 than the dispersive signal. More quantitative, the fraction between the peaks of the Lorentzian and the dispersive signal is given by $I_{\max}/Q_{\max} = \sqrt{1 + (2\Omega_R/\gamma)^2}/2$. For the dispersive signal, the frequency difference between the maximal and minimal in-phase signal is given by $\delta_{I_{\max/\min}} = \pm\sqrt{(\gamma/2)^2 + \Omega_R^2}$ and thus directly depends on the drive amplitude. In the case of a two level atom this could be employed as a means of calibrating the drive amplitude without the necessity for any further calibration. Often, the rms of the signal is of interest, which is given by

$$R_{\text{int}} = \sqrt{I_{\text{int}}^2 + Q_{\text{int}}^2} = \frac{\alpha_1 \bar{S}_x}{\sqrt{2}} \frac{\bar{f}_x \Omega_R \sqrt{(\gamma/2)^2 + \delta^2}}{\gamma/2[(\gamma/2)^2 + \delta^2 + \Omega_R^2]}. \tag{2.5.13}$$

The shape of the integrated rms of the system depends strongly on the drive amplitude. At large drive amplitudes the eigenvalues of the spin are dressed and there are two resonance peaks (Autler-Townes splitting). This dressing signature is related to the dominant dispersive signal in the I_{int} quadrature. For a weak drive $\Omega_R \ll \gamma$, the integrated rms is reduced to a single Lorentzian

$$R_{\text{int}} \approx \frac{\alpha_1 \bar{S}_x}{\sqrt{2}} \frac{\bar{f}_x \Omega_R}{\gamma/2\sqrt{(\gamma/2)^2 + \delta^2}}. \tag{2.5.14}$$

Signal Interference with the Classical Drive: Measuring the response to a drive can be used to calibrate the spin system. However, this requires the drive amplitude Ω_R to be known. In order to make a calibration independent of the drive amplitude, the interference between the drive and the spin signal can be measured [119]. This is done by driving the spin with a polarisation modulation of $\hat{S}_z^{(\text{in})}$. The atomic signal is imprinted onto the $\hat{S}_y$ polarisation, while the $\hat{S}_z$ component remains unchanged by the Faraday interaction. In the detection, the spin signal and the drive can be interfered by choosing a homodyne angle $\theta_{\text{homo}} \neq n\pi$.

In the last paragraph, we assumed that the spin decay is symmetric, i.e. that $\langle \hat{\tilde{f}}_{x,y,z} \rangle$ all have the same decay rate γ. But in the experiments we observed that the dephasing rate γ_ϕ is often much larger than the decay of the mean spin $\langle \hat{\tilde{f}}_x \rangle$. For simplicity, we assume here that $\gamma_+ = \gamma_- = 0$ and set $\gamma_\phi = 2\gamma$. Furthermore, we assume that the Rabi drive is weak and therefore the mean spin is not changed, i.e. $\langle \hat{\tilde{f}}_x(t) \rangle = \bar{f}_x$ (these are the implicit assumptions by doing the Holstein-Primakov approximation in [119]). We integrate the signal over a time $t_{\text{int}} \gg 1/\gamma$ ($t_{\text{int}} \ll 1/\Omega_R$, else our assumptions are not valid any

more). For an arbitrary homodyne angle θ_{homo}, the measurement record is given by

$$I_{\text{int}} = \frac{1}{\sqrt{2}} \int_0^{t_{\text{int}}} \left[\alpha_1 \bar{S}_x \langle \hat{\bar{f}}_z(t) \rangle \cos(\theta_{\text{homo}}) + \bar{S}_z^{(\text{mod})} \sin(\theta_{\text{homo}}) \right] \mathrm{d}t \tag{2.5.15}$$

$$= -\frac{\alpha_1 \bar{S}_x}{\sqrt{2}} \frac{\bar{f}_x \Omega_R \delta t_{\text{int}}}{(\gamma/2)^2 + \delta^2} \cos(\theta_{\text{homo}}) + \frac{\bar{S}_z^{(\text{mod})} t_{\text{int}}}{\sqrt{2}} \sin(\theta_{\text{homo}}), \tag{2.5.16}$$

$$Q_{\text{int}} = \frac{\alpha_1 \bar{S}_x}{\sqrt{2}} \int_0^{t_{\text{int}}} \langle \hat{\bar{f}}_y(t) \rangle \cos(\theta_{\text{homo}}) \mathrm{d}t = \frac{\alpha_1 \bar{S}_x}{\sqrt{2}} \frac{\bar{f}_x \Omega_R t_{\text{int}} \gamma/2}{(\gamma/2)^2 + \delta^2} \cos(\theta_{\text{homo}}). \tag{2.5.17}$$

Again, only the classical mean values are considered and the quantum noise is neglected. The in-phase component of the measurement includes the drive and the dispersive part of the atomic response, while the quadrature component is given by the Lorentzian response. If the drive is weak, the resulting rms signal reads

$$R_{\text{int}}^2 = \frac{(\bar{S}_z^{(\text{mod})} t_{\text{int}})^2}{2} \left(\sin^2(\theta_{\text{homo}}) + \frac{4\Gamma_{\text{s}}}{(\gamma/2)^2 + \delta^2} \left(\delta \sin(\theta_{\text{homo}}) \cos(\theta_{\text{homo}}) + \Gamma_{\text{s}} \cos^2(\theta_{\text{homo}}) \right) \right), \tag{2.5.18}$$

where $\Gamma_{\text{s}} = \alpha_1^2 \bar{f}_x \bar{S}_x / 4$ is the spin measurement rate. The modulation amplitude appears only as a prefactor. Scanning the homodyne angle θ_{homo} allows the spin measurement rate to be measured independently of the drive amplitude. The experimental implementation of this calibration is presented in section 2.6.2.

2.5.2 Five Level System

Analytically solving the equations of motion for a five level system, requires a lot of computation. Due to the quadratic Zeeman effect, all levels have different spacings. This complicates the general solution of a driven spin-2 atom so that no useful intuition can be gained from it. Therefore, the equations of motion for the spin-2 hyperfine manifold are not solved in general, but only in the limits where either the drive is weak or the problem can be approximated by a spin-1/2 model. The solutions are compared with a numerical simulation to check their validity.

Pulsed Regime: To prepare the spin, a short, resonant rf pulse is applied. The duration of the pulse τ is chosen so that its bandwidth is much larger than the spin damping rate and the quadratic Zeeman splitting, i.e. $1/\tau \gg \gamma_{\text{s}}, \delta\Omega_{\text{s}}$. For such a pulse, the Rabi drive is the same for all transitions between Zeeman levels, so the atom behaves like a spin-1/2 system and a perfect spin rotation can be performed. As such, the spin can be tilted by any angle using short pulses.

Continuous Regime for Weak Driving: For continuous weak driving of the spin, the different transitions between the Zeeman levels can be resolved. In order to derive the result for the weak driving regime, it is convenient to choose the quantisation axis along the bias magnetic field B_x. For weak Rabi drive, the populations in the Zeeman levels do not change and one can approximate $\dot{\rho}_{m,m,x} \approx 0$. Following the derivation presented in [93], in this limit the coherences are given by

$$\rho_{m,m+1,x} = \frac{\mathrm{i}\Omega_{\text{R}}}{2} \frac{C(f,m)(\Pi_{m+1,x} - \Pi_{m,x})}{\gamma_{\text{s}}/2 - \mathrm{i}(\Omega_{\text{rf}} - \Omega_{m,m+1})} \mathrm{e}^{-\mathrm{i}\Omega_{\text{rf}} t - \gamma_{\text{s}} t/2}, \tag{2.5.19}$$

where $C(f,m) = \sqrt{f(f+1) - m(m+1)}$, $\Pi_{m,x} = \rho_{m,m,x}$ are the populations and $\Omega_{m,m+1}$ are the transition frequency between two levels including the quadratic Zeeman effect. The expectation value of the spin projection along the propagation axis of the light is given by

$$\langle \hat{f}_z(t) \rangle = \frac{1}{2\mathrm{i}} \sum_{m=2}^{f-1} C(f,m)(\rho_{m,m+1,x} - \rho_{m+1,m,x}) \tag{2.5.20}$$

$$= \frac{\Omega_\mathrm{R}}{2} \sum_{m=2}^{f-1} C(f,m)^2 (\Pi_{m+1,x} - \Pi_{m,x}) \mathrm{Re}\left(\frac{\mathrm{e}^{-\mathrm{i}\Omega_\mathrm{rf} t - \gamma_\mathrm{s} t/2}}{\gamma_\mathrm{s}/2 - \mathrm{i}(\Omega_\mathrm{rf} - \Omega_{m,m+1})} \right). \tag{2.5.21}$$

Again we use the Faraday interaction to monitor the system. The expectation value $\langle \hat{f}_z(t) \rangle$ is mapped onto the polarisation state of the light, which is measured with a homodyne measurement. Demodulating the signal yields the quadratures

$$I(t) = \frac{\alpha_1 \bar{S}_x}{\sqrt{2}} \sum_{m=2}^{f-1} \frac{C(f,m)^2 (\Pi_{m+1,x} - \Pi_{m,x})}{2} \frac{\Omega_\mathrm{R}(\Omega_{m,m+1} - \Omega_\mathrm{rf})}{(\gamma_\mathrm{s}/2)^2 + (\Omega_\mathrm{rf} - \Omega_{m,m+1})^2} \mathrm{e}^{-\gamma_\mathrm{s} t/2}, \tag{2.5.22}$$

$$Q(t) = \frac{\alpha_1 \bar{S}_x}{\sqrt{2}} \sum_{m=2}^{f-1} \frac{C(f,m)^2 (\Pi_{m+1,x} - \Pi_{m,x})}{2} \frac{\Omega_\mathrm{R}\gamma_\mathrm{s}/2}{(\gamma_\mathrm{s}/2)^2 + (\Omega_\mathrm{rf} - \Omega_{m,m+1})^2} \mathrm{e}^{-\gamma_\mathrm{s} t/2}. \tag{2.5.23}$$

The results again show a dispersive signal for $I(t)$ and a Lorentzian shape for $Q(t)$. Unlike the spin-1/2 model, here the signal is the sum of four resonances, one at each transition frequency $\Omega_{m,m+1}$. The amplitude of these peaks depends on the population difference in the levels. This can be used to evaluate the population in the different levels, as described in section 1.7. Thus, rf-spectroscopy is a good tool for spin characterisation. In the limit of small quadratic splitting (e.g. for $\delta\Omega_\mathrm{s} \ll \gamma_\mathrm{s}$), all transition frequencies can be assumed to be equal and a global detuning can be written $\delta \approx \Omega_{m,m+1} - \Omega_\mathrm{rf}$. In this regime the Lorentzian function does not depend on m and the sum can be simplified to $\sum_{m=2}^{f-1} C(f,m)^2(\Pi_{m+1,x} - \Pi_{m,x})/2 = \langle \hat{f}_x \rangle$. Integrating this approximate expression over time gives the result of the spin-1/2 atom (see equations (2.5.11) and (2.5.12)).

Continuous Regime for Strong Driving: In the presence of a strong, continuous drive, the approximations in the last section no longer hold. However, if the Rabi drive Ω_R is large, the Lorentzian peak is broadened, as can be seen in the equations (2.5.11) and (2.5.12). In the literature this effect is called *power broadening* [102]. In the limit of strong driving, the broadening due to the driving exceeds the quadratic splitting of the levels $\Omega_\mathrm{R} \gg \delta\Omega_\mathrm{s}$. Again, the spin-1/2 model describes well the dynamics of the system.

Continuous Driving of the Spin with Different Rabi Frequencies

To illustrate the theory above, a series of experiments with continuous drive are discussed here. For the different experiments, the drive amplitude and the detuning of the drive are scanned: for weak drives, the four transitions between Zeeman levels can be resolved. If the system is strongly driven, the transitions are power-broadened and the states are dressed, as discussed theoretically above. This series of experiments can be used to calibrate the drive amplitude.

In the experimental sequence, the spin is polarised along the x-axis parallel to a bias magnetic field. After preparing the atomic spin, the atoms are probed with $-10\,\mathrm{GHz}$ detuned light with a power of

100 µW. The linearly polarised light is modulated by the EOM to produce a circularly polarised component of the light oscillating at rf that drives the atomic spin. The spin state of the atoms is mapped onto the light by the Faraday interaction. The Faraday signal is measured with a balanced detector and demodulated at the drive frequency. The demodulated signal is integrated over an interaction time t_{int}. Results for two different integration times are shown in figure 2.5.1.

For a short integration time, the spin remains well polarised over the entire integration time. Thus, by applying a weak drive, the transition between $m_{f,x} = -2$ and $m_{f,x} = -1$ is mainly observed, resulting in a single Lorentzian peak. However, if the spin is probed for longer, there is light-induced depumping to other levels. Therefore, by integrating over longer times, the spectrum shows all four transitions in the $f = 2$ manifold. The spin also decays into the $f = 1$ hyperfine manifold. The splitting between the Zeeman levels in the $f = 1$ manifold is larger by a factor ~ 1.004 than the level splitting in the $f = 2$ manifold due to a different g-factor[9] so the two transition energies of the $f = 1$ manifold can be observed at slightly higher frequencies (at about 1.993 MHz instead of 1.985 MHz).

As the drive becomes stronger, the levels are power-broadened and dressed. The transition between weak and strong driving is nicely seen in the integral of $I(t)$. For long integration times, there are multiple dispersive signals in the weak-driving regime, one for each transition. As the Rabi drive exceeds the quadratic splitting, only two peaks are distinguishable, corresponding to the dressed states. Integrating over longer durations, we can see that there are two sets of dressed states, one for each hyperfine manifold.

To calibrate the EOM drive, two different quantities can be calculated from the data. The ratio of the maxima of the in-phase and quadrature signals, $I_{\max}/Q_{\max} = \sqrt{(\gamma/2)^2 + \Omega_R^2}/\gamma$, is plotted in figure 2.5.2 (a). To the data a linear regression is fitted. It follows the expected trend. We obtain $A = 5.66\,\mathrm{V}^{-1}$ (defined as $\Omega_{\mathrm{R}}/\gamma_{\mathrm{s}} = AU_{\mathrm{EOM}}$ where U_{EOM} is the control voltage for the EOM). With a spin linewidth of $\gamma_{\mathrm{s}} = 2\pi \times 500\,\mathrm{Hz}$, this gives a Rabi frequency of $\Omega_{\mathrm{R}} = 2\pi \times 5.6\,\mathrm{kHz\,V}^{-1} \times U_{\mathrm{EOM}}$. For the dispersive signal, the frequency splitting between the maximum and minimum in-phase signal is given by $\Delta\delta_{I_{\max/\min}} = 2\sqrt{(\gamma/2)^2 + \Omega_R^2}$, which is plotted in 2.5.2 (b). For large Rabi drives, the splitting does not follow the expected relation. The Rabi coupling of the light to the spins is inhomogeneous. At large drive amplitudes, this could lead to a broadening or a de-phasing of the spins which is not considered in the theory. Maybe this could be an explanation for the observations.

2.6 Characterisation of the Spin-Light Interface

In the current stage of the experiment, we are interested in a precise, quantitative understanding of the spin-light interaction in two different scenarios: (1) for a classical, mean spin along the propagation axis of the light and (2) for the measurement of the variance of the spin when polarising it perpendicular to the propagation axis of the light. If all spins are exposed to the same intensity of light, it is sufficient to know the number of atoms contributing to the coupling and the intensity of the light. In section 2.4 we have seen that for a 3D-Gaussian cloud interfaced with a Gaussian beam, the signal of the collective mean spin and the collective spin noise scale differently with the distribution of the light intensity. The scaling factors were calculated from the geometry of the experiment. However, this assumes that the

[9] We have [105]

$$g_f = g_j \frac{f(f+1) - i(i+1) + j(j+1)}{2f(f+1)} + g_i \frac{f(f+1) + i(i+1) - j(j+1)}{2f(f+1)}. \tag{2.5.24}$$

So we have for the $f = 2$ manifold $g_f = (g_j + 3g_i)/4 \approx 0.4998$ and for the $f = 1$ manifold $g_f = (-g_j + 5g_i)/4 \approx -0.5018$.

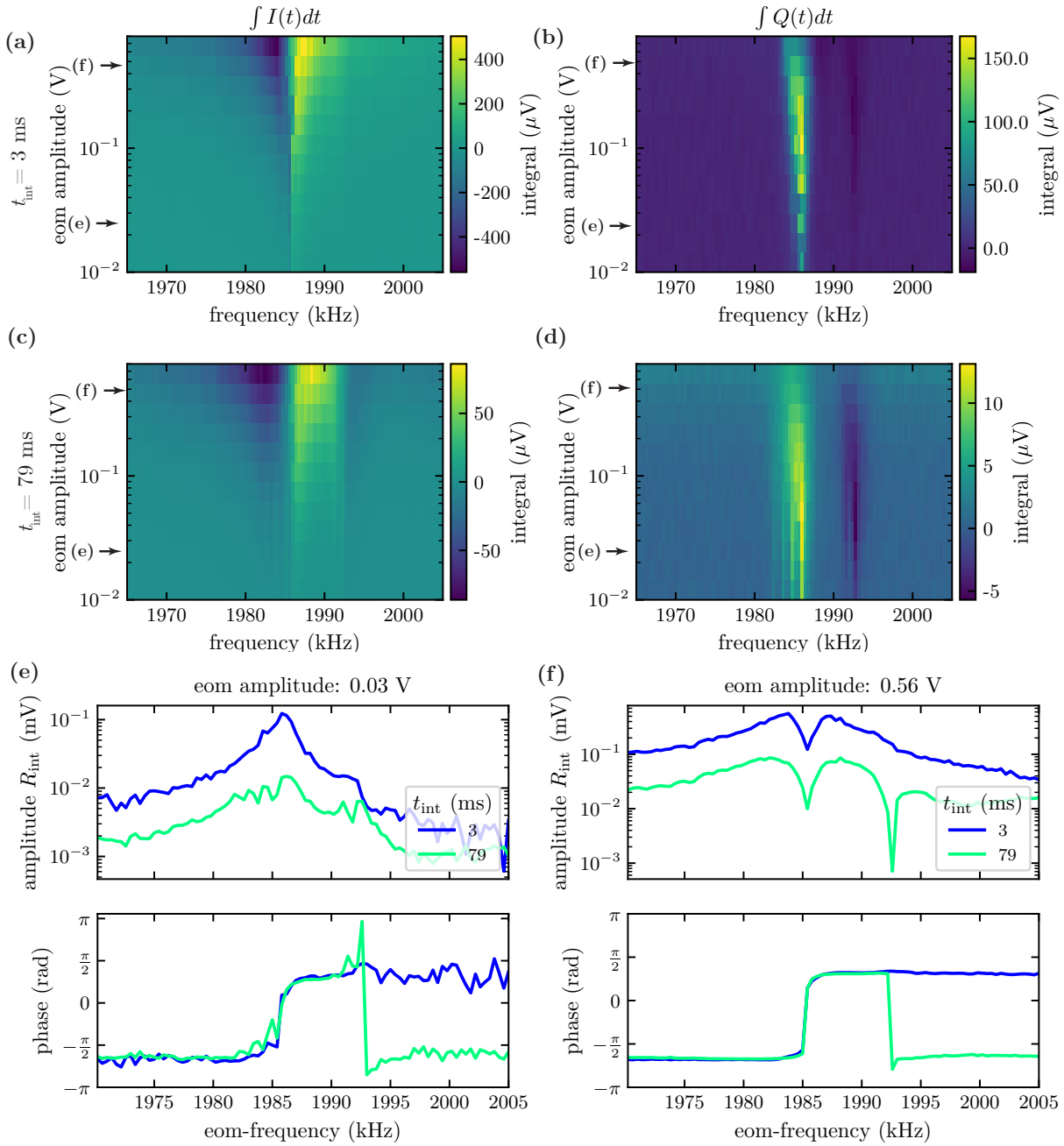

Figure 2.5.1: Response of the spin to a continuous drive. The Faraday signal on the light is detected and demodulated. In the analysis, the demodulated quadratures are integrated over $t_{\mathrm{int}} = 3\,\mathrm{ms}$ for (a) and (b) and over $t_{\mathrm{int}} = 79\,\mathrm{ms}$ for (c) and (d). The measurement is repeated for different EOM amplitudes, corresponding to different drive amplitude Ω_{R}. The data for two different drive strengths is shown in (e) and (f). Here, the rms amplitude $R_{\mathrm{int}} = \sqrt{I_{\mathrm{int}}^2 + Q_{\mathrm{int}}^2}$ and the phase $\phi = \arctan(I_{\mathrm{int}}/Q_{\mathrm{int}})$ of the signal are shown.

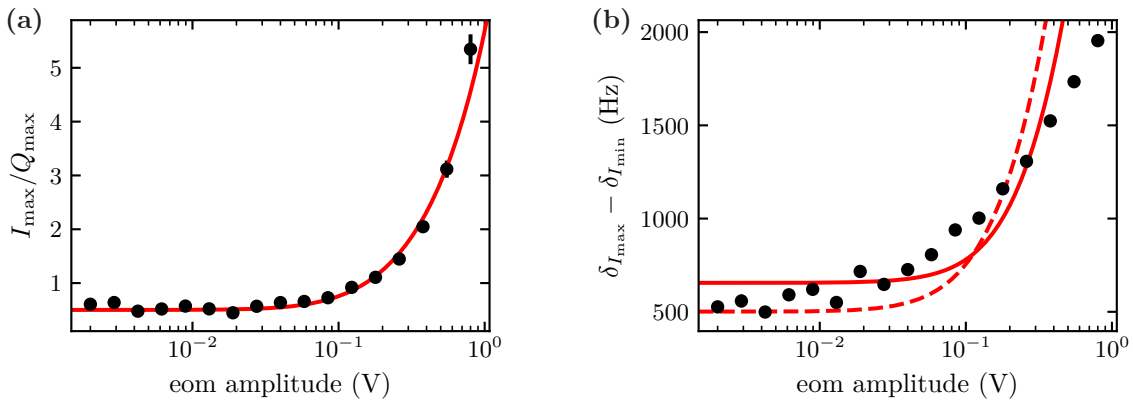

Figure 2.5.2: From the rf-spectroscopy two quantities are calculated which depend only on the spin linewidth and the Rabi frequency: (a) shows the fraction between the maximum of the dispersive and the Lorentzian signal. It is fitted with the function $I_{\max}/Q_{\max} = \sqrt{1/4 + (AU_{\mathrm{EOM}})^2}$. (b) shows the frequency difference between the maximum and the minimum of the dispersive signal. It is fitted with the theoretical model $\Delta\delta_{I_{\max/\min}} = 2\sqrt{(\gamma/2)^2 + (BU_{\mathrm{EOM}})}$ (solid red line). As dashed red line, the fit result of plot (a) is shown in (b), assuming a spin linewidth of $\gamma_{\mathrm{s}} = 2\pi \times 500\,\mathrm{Hz}$. The fit is failing for large Rabi frequencies.

geometry is well known. Alternatively, Faraday measurements can be performed to directly measure the collective coupling of the atoms to the light for the different scenarios.

In this section, calibration measurements are presented that allow us to calculate all the relevant quantities for the effective coupling. In the first measurement shown in section 2.6.1, a quantum noise measurement is compared with a measurement of the mean spin. It is observed that for some parameters the measured noise is limited by the quantum uncertainty noise of the spin and the probe light. Moreover, correction factors are obtained that are similar to those calculated from the cloud geometry. In a second experiment described in section 2.6.2, the cooperativity of the spin-light interface is directly calibrated by modulating the circular polarisation of the light. Finding a large cooperativity, the spin can be used to squeeze the light, which is shown in section 2.6.4. Furthermore, the decay rate of the spin is a very important quantity for our experiment, which is calibrated in section 2.6.3.

2.6.1 Characterisation of the Spin-Light Coupling Rate

A first experiment to characterise the effective spin length is shown in section 2.3.4. From this measurement, the effective first order correction $\langle \eta_{\mathrm{s}} \rangle = 0.52$ is inferred. For the probe geometry in our experiment, we have calculated a theoretical value of $\langle \eta_{\mathrm{s}} \rangle_{\mathrm{th}} = 0.53$ (given in table 2.4.2). In a second experiment, the noise of the light is evaluated after the interaction with the spin. Integrating over the PSD of the outgoing S_y polarisation component described in equation (2.4.10), we get the variance of the spin signal (see equation (C.3.7)). By normalising the measurement with the photon flux of the local oscillator, the variance of the Faraday angle is obtained,

$$\mathrm{var}(\theta_{\mathrm{AC}}) = \frac{\Delta_{\mathrm{BW}}}{2\pi} \frac{1}{4\bar{S}_x} + \frac{\tilde{\alpha}_1^2}{16} \left(2\bar{F}_x^{(2)} + \frac{\tilde{\alpha}_1^2 \bar{F}_x^{(2)2} \bar{S}_x}{\gamma_{\mathrm{s}}} \right), \tag{2.6.1}$$

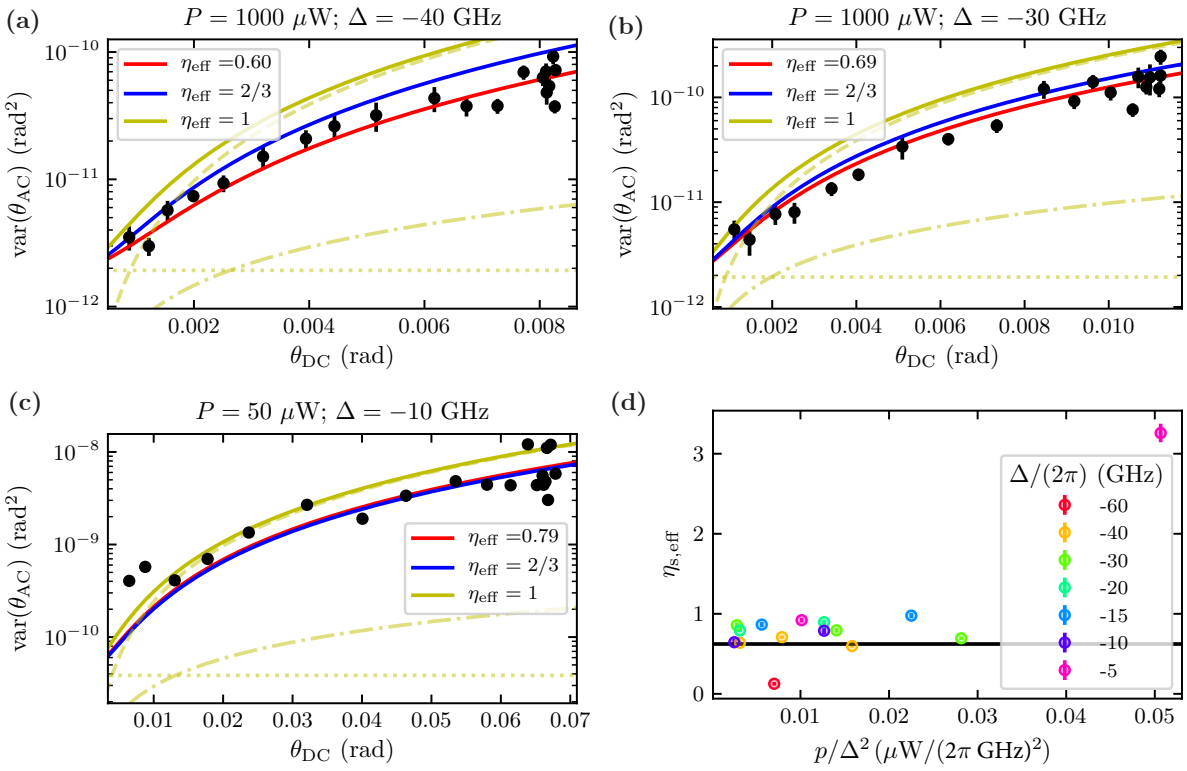

Figure 2.6.1: Spin calibration data: In (a) to (c), the variance of the ac Faraday angle after the interaction with the spin is plotted for different atom numbers, here as a function of the on-axis dc Faraday angle (calibrated in a second experiment). The data are fitted with a single fit parameter $\eta_{\rm s,eff}$ (red line). The theory for perfect overlap is shown in yellow and the theory for $\langle\eta_{\rm s}\rangle = 1/2$ and $\langle\eta_{\rm s}^2\rangle = 1/3$ is shown in blue. For the yellow curve the different noise contributions are plotted separately, as dotted line the shot noise, as dash-dotted line the projection noise and as dashed line the backaction noise. (d) shows the resulting effective coupling for different experimental parameters. The black line shows the theoretically calculated coupling for our experimental geometry.

where $\Delta_{\rm BW}$ is the integration bandwidth. This variance can be compared to the DC-measurement of the spin length $\theta_{\rm DC} = \langle\eta_{\rm s}\rangle\alpha_1\bar{F}_z^{(\rm DC)}/2$ (where $\bar{F}_z^{(\rm DC)} = \bar{F}_x^{(\rm AC)}$, e.g. in section 2.3.4), which directly yields $\eta_{\rm s,eff}$

$$\mathrm{var}(\theta_{\rm AC}) = \frac{\Delta_{\rm BW}}{2\pi}\frac{1}{4\bar{S}_x} + \frac{\alpha_1}{4}\left(\eta_{\rm s,eff}\theta_{\rm DC} + \eta_{\rm s,eff}^2\frac{\theta_{\rm DC}^2\alpha_1\bar{S}_x}{\gamma_{\rm s}}\right). \tag{2.6.2}$$

Here, it is assumed that all spins are well polarised. The photon flux $2\bar{S}_x$ is easy to calibrate, α_1 is known from theory, but we do not have a good estimate for the spin decay $\gamma_{\rm s}$. In order to compare the measured noise with the theoretical model one can either calibrate the spin decay, take the theoretical spin scattering constant or alternatively choose a short integration time $t_{\rm int} \ll 1/\gamma_{\rm s}$ such that the variance depends on the integration time instead of the spin linewidth, i.e. $\gamma_{\rm s} \to 2\pi/t_{\rm int}$. The second approach is used here in order to be as calibration-free as possible.

In two consecutive measurements, the spin length (i.e. $\theta_{\rm DC}$) and the spin noise (i.e. $\theta_{\rm AC}$) are measured for the same set of experimental parameters. In the experiment, the number of atoms is varied by changing the MOT-loading time. The result of some measurements is shown in figure 2.6.1 (a) - (c). The equation (2.6.2) is fitted to the data with only $\eta_{\rm s,eff}$ as fit parameter. For different powers and detunings, values

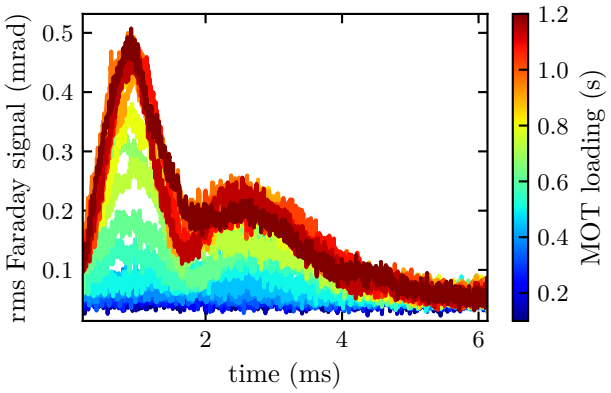

Figure 2.6.2: Spin measurement for a probe of $\Delta/(2\pi) = -5\,\mathrm{GHz}$, $P = 50\,\mu\mathrm{W}$ for different numbers of atoms. Even if the collective spin is only driven by the quantum noise of the light, there is a macroscopic, coherent spin signal that cannot be described by single spin physics.

between $\eta_{\mathrm{s,eff}}^{(\mathrm{fit})} = 0.6$ and $\eta_{\mathrm{s,eff}}^{(\mathrm{fit})} = 0.9$ are obtained (when neglecting two outlayers for small and large detuning, see figure 2.6.1 (d)). From geometrical considerations we expect $\eta_{\mathrm{s,eff}}^{(\mathrm{th})} = 0.62$ which is within the range of the fitted values.

Integrating over short enough times and operating the experiment at not too high measurement rates (i.e. small P/Δ^2), the measured noise corresponds to what we expect for a quantum noise-limited spin ensemble. However, at high measurement rates, the variance is much higher than expected from theory. There is even a coherent, macroscopic signal that is not expected from a purely noise-driven spin signal (see figure 2.6.2). This could be due to collective, self-driving dynamics of the spins, but we do not yet have a conclusive model for this.

2.6.2 Spin Measurement Rate

In the last section, the spin was driven only by the quantum shot noise of the light. This result is compared in this section with the measurements where the atoms are driven with a classical drive. In this second calibration experiment, the atomic spin is driven by a weak, classical modulation of the circularly polarised light as described in section 2.5. A detailed description of the method used here can be found in [119]. The z-projection of the spin state is mapped onto the $\hat{S}_y$ quadrature of the light, which is orthogonal to the drive along $\hat{S}_z$. Using polarisation homodyne detection, different quadratures of the light can be detected: either the spin signal imprinted on $\hat{S}_y$ or the drive on $\hat{S}_z$ or the interference of spin and drive. The detected signal is integrated over a measurement duration of $t_{\mathrm{int}} = 3\,\mathrm{ms}$. The results are shown in figure 2.6.3 (a) - (c) for three different homodyne angles and various probe powers. The experimental data are fitted with equation (2.5.18) using a global fit function that includes the data from all homodyne angles. The fit directly gives the measurement rate and the spin linewidth without any calibration of the drive strength. The fitted measurement rate and spin linewidth are shown in figure 2.6.3 (d). The measurement rate increases with power, as expected. The fitted linewidth is Fourier limited at short integration times. For longer integration times, light-induced decoherence leads to significant occupancy in all Zeeman levels (not shown here). The multilevel structure of the atom is not taken into account in the fit function, so occupancy in multiple Zeeman levels leads to broadening when using this model. Nevertheless, the obtained linewidth can serve as an upper bound for the spin linewidth.

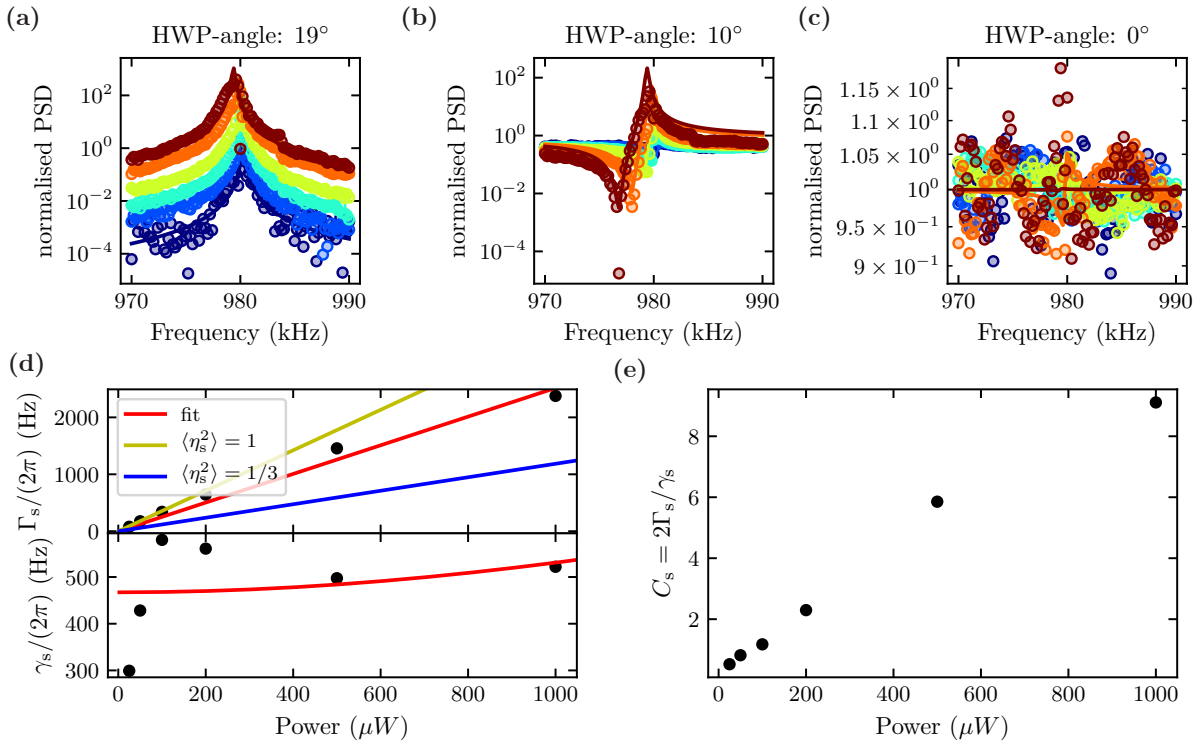

Figure 2.6.3: Spin spectroscopy: The spin is driven by a modulation of the circularly polarised light. The light is measured at three different homodyne (HWP) angles for different probe powers (different colors). In (a) - (c) the integral of the demodulated signal is shown. Fitting the integral gives the measurement rate and the spin linewidth, shown in (d). The yellow and blue theory lines are obtained by assuming $N_a = 26 \times 10^6$ atoms in the dipole trap, measured by absorption imaging. The red lines are fits to the data. The spin cooperativity can be calculated from the measurement rate and the spin linewidth, shown in (e).

In section 2.5, only one single spin is considered for the derivation. It can be shown (see section 2.7) that considering the realistic three-dimensional coupling, the measurement rate is given by

$$\tilde{\Gamma}_\mathrm{s} = \frac{\tilde{\alpha}_1^2 |\bar{F}_x^{(2)}||\bar{S}_x|}{4} \approx \langle \eta_\mathrm{s}^2 \rangle \frac{\alpha_1^2 |\bar{F}_x||\bar{S}_x|}{4}. \tag{2.6.3}$$

So, the measurement rate has to be corrected by the mean square intensity. In order to compare the data with theory, the number of atoms is measured by absorption imaging. Comparing the measured spin response with the theoretical expectation gives a correction factor of $\langle \eta_\mathrm{s}^2 \rangle = 0.71$. This is a factor of two larger than what would be expected from geometrical considerations or from the measurement presented in the last section. This discrepancy is not yet understood. From the measurement rate and the linewidth, the spin cooperativity can be calculated, as shown in figure 2.6.3 (e). The spin cooperativity exceeds unity by an order of magnitude.

2.6.3 Characterisation of the Spin Decoherence Rate

In the last two sections, the coherent interaction of the spin with light was considered. Here a characterisation of the spin decoherence rate is given. To measure the spin decoherence rate, the spin is polarised along the x-axis and then tilted by 90° by a short $\pi/2$ rf-pulse. After initialisation, the spin precesses around the bias magnetic field B_x. A far detuned laser is used as probe. The light is measured with polarisation homodyne detection and demodulated at the spin precession frequency. Some example data are shown in figure 2.6.4 (a). The oscillations of the envelope function shown in figure 2.6.4 (a) are caused by the dephasing and rephasing of the different Zeeman transitions due to the quadratic Zeeman effect. An exponential decay is fitted to the oscillation maxima to extract the decoherence rate. These decay rates are shown in figure 2.6.4 (b) for various detunings and powers. The spontaneous scattering rate of the two-level atom scales with P/Δ^2. Here we see that the decoherence of the spin does not strictly follow this relation, otherwise all the curves in figure 2.6.4 (b) would overlap perfectly.

The decay rate is normalised to the probe power and plotted as function of the detuning in figure 2.6.4 (c). In addition, the spontaneous scattering rate is plotted for two different cloud geometries (blue and yellow curve). From the overlap geometry and using the oversimplified decoherence model of the scattering of a two-level atom, we expect the decay to follow approximately the theory line for $\langle \eta_\mathrm{s} \rangle = 1/2$. But the data are not even symmetric with respect to a sign change in the detuning. Therefore, the decoherence constants for negative and positive detunings were fitted separately with a fit function $f(\Delta) = A/(\Delta - \Delta_0)^2$. Interestingly, not only the amplitude A but also the offset detuning Δ_0 is different for the two fits: For positive detuning, a value of $\Delta_0 = -2\pi \times 10.5\,\mathrm{GHz}$ is obtained, for negative detunings a value of $\Delta_0 = 2\pi \times 6.8\,\mathrm{GHz}$. In order to understand the spin decoherence, simulations are performed with the same parameters as the experiment. While the simulation does not follow the scattering model of a two-level atom, the different Δ_0 for different signs of detuning could not be reproduced with the single-atom model.

In the previous sections it has been shown that spin decoherence is not given by the spontaneous scattering rate, but a more advanced analysis is needed to understand spin decoherence. In order to get the full picture of the spin decoherence, the following effects have to be estimated: (1) The spin decoherence of real Rubidium is not just given by the spontaneous scattering rate. However, the simulation of a single Rubidium atom does not reproduce all the features observed in the experiment. So, there must be other explanations for the spin decoherence. (2) The different atoms in the cloud spontaneously scatter

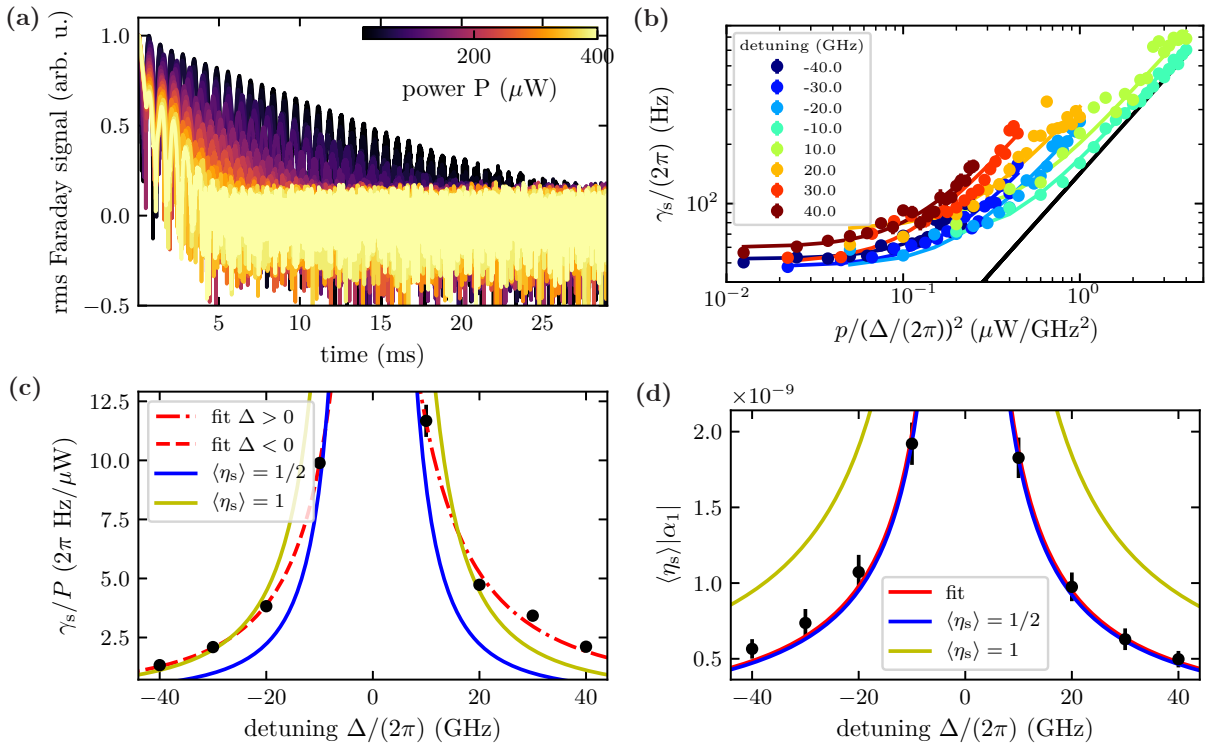

Figure 2.6.4: (a) Demodulated traces for a probe with a detuning of $\Delta = 2\pi \times -10\,\mathrm{GHz}$ for different probe powers. The higher the probe power, the faster the spin signal decays. (b) Fitted spin decay rates for different detunings and powers. The data for each detuning is fitted separately with a slope and a constant offset (e.g. due to magnetic inhomogeneities). The fitted slopes are plotted as a function of the detuning in (c). For (d), the effective coupling is calculated from the amplitude of the Faraday signal. The coherent coupling to the light is symmetric with respect to the detuning.

at different rates (due to different local intensities) and contribute with different weights to the scattering into the fundamental mode. Additionally, the atoms overlap with different amplitudes with higher order optical modes, which in turn leads to different dynamics of different atoms in the cloud. Ultimately, the dynamics induced by a multimode Hamiltonian has to be solved to fully understand the decay. (3) In addition, the coupling laser changes the trapping potential of the laser (as shown in section 1.6.4). A red-detuned laser increases the trapping potential, while a blue-detuned laser pushes atoms out of the trapping region. This potentially contributes to the decay of the atoms. (4) The atomic loss from the trap is slow compared to the experimental timescale but could also be included.

The experiment presented here can also be used to calibrate the effective spin length. The amplitude of the Faraday signal can be used to calibrate $\langle \eta_\mathrm{s} \rangle$. Mostly this is done using the spin polarised along the magnetic field B_z (as discussed in section 2.3.4). But it can be done with a precessing spin, as shown in figure 2.6.4 (d). The fit yields an effective coupling of $\langle \eta_\mathrm{s} \rangle = 0.52$ which is in good agreement with the other experiments.

2.6.4 Squeezing of the Light Using the Spin

The cooperativity of the spin-light interface exceeds unity, as shown in section 2.6.2. In this limit, the atomic spin can be used to squeeze the light, which benchmarks that the spin-light interface can be operated in the quantum regime. In order to observe this squeezing, an experiment inspired by the ponderomotive squeezing experiments in optomechanics is performed [63, 120]. Thereby, the Faraday interaction is used to correlate two orthogonal (non-commuting) polarisation components of the light (in ponderomotive squeezing, two orthogonal axes in the phase-space of the light are correlated). By exploiting these correlations, noise below the standard quantum limit can be observed for some frequencies and polarisation angles.

In detail, this is achieved as follows: Input shot noise in the circularly polarised component of the light $\hat{S}_z^{(\mathrm{in})}$ drives the collective spin of the atoms through the Faraday interaction. At the same time, the z-projection of the atomic spin is mapped onto the $\hat{S}_y^{(\mathrm{out})}$ of the light. In the limit of large cooperativity, the spin is mainly driven by the shot noise of the $\hat{S}_z^{(\mathrm{in})}$. After the interaction with the spin, this spin noise is mapped onto $\hat{S}_y^{(\mathrm{out})}$, while the $\hat{S}_z^{(\mathrm{in})}$ remains unchanged to first order. Thus, the noise in $\hat{S}_y^{(\mathrm{out})}$ and $\hat{S}_z^{(\mathrm{out})}$ are correlated. By detecting a superposition of the $\hat{S}_y^{(\mathrm{out})}$ and the $\hat{S}_z^{(\mathrm{out})}$ quadrature, this correlation can be measured. The PSD for this squeezing experiment is formally derived in appendix B.2.3. The resulting PSD at a homodyne angle θ_homo is given by

$$\bar{S}^{\mathrm{sn}}_{S_\theta S_\theta} = 1 + \frac{4\Gamma_\mathrm{s}}{(\Omega_\mathrm{s}-\omega)^2 + (\gamma_\mathrm{s}/2)^2} \left(\cos^2(4\theta_\mathrm{homo}) \left(\gamma_\mathrm{s}/2 + \Gamma_\mathrm{s}\right) + \sin(4\theta_\mathrm{homo}) \cos(4\theta_\mathrm{homo}) (\Omega_\mathrm{s} - \omega) \right), \quad (2.6.4)$$

where the spectrum is normalised to the shot noise (see equation (B.2.59)). For some homodyne angles, the second term of this equation is negative for some frequencies, corresponding to noise below the standard quantum shot noise limit at those frequencies. Note that this equation is very similar to equation (2.5.18), where the spin is driven by a classical drive. The difference is that if the spin is driven by the shot noise of the light, the first term (which accounts for the shot noise) is not multiplied by $\sin^2(\theta_\mathrm{homo})$ because the shot noise is present on both light components $\hat{S}_y^{(\mathrm{in})}$ and $\hat{S}_z^{(\mathrm{in})}$. The classical drive is only applied to one polarisation component, so there is a pre-factor $\sin^2(\theta_\mathrm{homo})$ in equation (2.5.18).

In the experiment, the spin is polarised along the x-axis and then interfaced with a far detuned probe

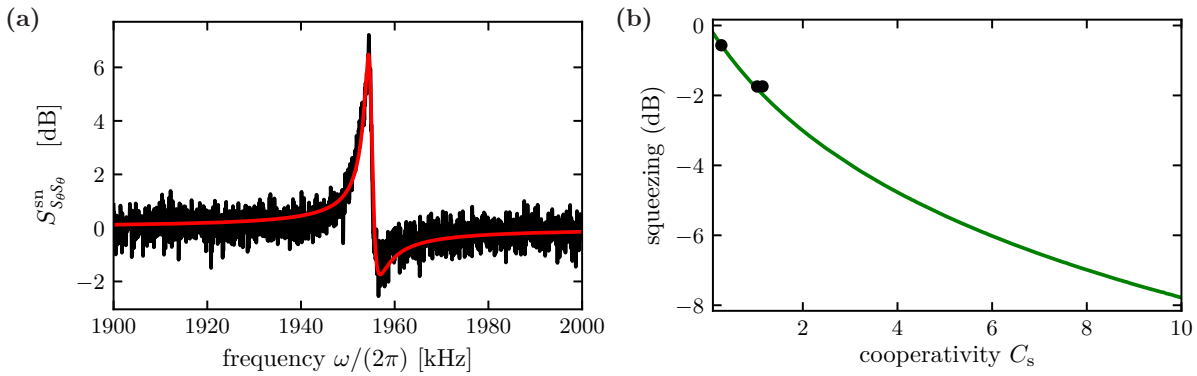

Figure 2.6.5: (a) Squeezing of the polarisation of the light by −1.7 dB using the spin as non-linear element. The data are taken at a detuning of −40 GHz and a probe power of 990 µW. The power spectral density shown here is fitted using equation (2.6.4) as the fit function (red line). (b) Calculation of the squeezing for a given cooperativity. The angle and the detuning are optimised to maximise the squeezing. Some selected data are shown in black.

light. The light is detected by a homodyne detection at a homodyne angle θ_{homo}. The results are shown in figure 2.6.5 (a). The maximum squeezing of the light is measured to be −1.7 dB. Note that this measurement was made early in the project with the old dipole trap design at a cooperativity of 1.1. With the larger cooperativity achieved in the current setup, the squeezing could be significantly larger, see figure 2.6.5 (b).

2.7 Spin-Oscillator

For a large spin ensemble well polarised along a magnetic field, the collective spin can be approximated by a harmonic oscillator by applying the so-called Holstein-Primakov approximation [121]. This is a projection of the Bloch sphere onto the two-dimensional phase space. Intuitively, it can be understood that this mapping is a good approximation at the poles of the Bloch sphere where the curvature is small while it fails towards the equator of the Bloch sphere. To describe the hybrid experiment, we approximate both the spin ensemble and the polarisation state of the light by a harmonic oscillator.

Holstein-Primakov Approximation for the Stokes Vector: Assuming that the light is well polarised along the $\hat{S}_x$ polarisation, i.e. $\sqrt{\langle \hat{S}_y^2 \rangle}$, $\sqrt{\langle \hat{S}_z^2 \rangle} \ll \langle \hat{S}_x \rangle$, the commutation relation of the transverse polarisation components is given by $[\hat{S}_y(\xi), \hat{S}_z(\xi')] \approx \mathrm{i}\bar{S}_0(\xi) c\delta(\xi - \xi')$. This is the commutation relation of a harmonic oscillator since $\bar{S}_0(\xi)$ is not an operator but a number. The quadratures of the harmonic oscillator can be written by normalising the transverse Stokes vector components,

$$\hat{X}_{\mathrm{L}} = \frac{\hat{S}_y}{\sqrt{\bar{S}_0}}, \tag{2.7.1}$$

$$\hat{P}_{\mathrm{L}} = \frac{\hat{S}_z}{\sqrt{\bar{S}_0}}, \tag{2.7.2}$$

where $\hat{X}_{\mathrm{L}} = (\hat{a}_{\mathrm{L}}^\dagger + \hat{a}_{\mathrm{L}})/\sqrt{2}$ and $\hat{P}_{\mathrm{L}} = \mathrm{i}(\hat{a}_{\mathrm{L}}^\dagger - \hat{a}_{\mathrm{L}})/\sqrt{2}$ are given in units of the square-root of flux. The new light quadratures satisfy the canonical commutation relations $[\hat{X}_{\mathrm{L}}(\xi), \hat{P}_{\mathrm{L}}(\xi')] = \mathrm{i}\delta(z_{\mathrm{opt}}/c - t - z'_{\mathrm{opt}}/c + t')$

where c is the speed of light (compare with equations (2.2.23)).

Holstein-Primakov Approximation for the Homogeneous Spin Ensemble: Assuming that the atomic spins are well polarised along the x-axis, we can write the x-component of the spin as classical mean value $\hat{F}_x \to \bar{F}_x = \langle \hat{F}_x \rangle$. Then the commutation relation of the spin takes the form of the commutation relation of a harmonic oscillator $[\hat{F}_y, \hat{F}_z] = \mathrm{i}\bar{F}_x$. We can define spin quadratures by normalising the orthogonal spin components[10]

$$\hat{X}_\mathrm{s} = \frac{\hat{F}_z}{\sqrt{|\bar{F}_x|}}, \tag{2.7.6}$$

$$\hat{P}_\mathrm{s} = -\mathrm{sgn}(\bar{F}_x)\frac{\hat{F}_y}{\sqrt{|\bar{F}_x|}}. \tag{2.7.7}$$

Again, the creation and annihilation operators can be defined conventionally as $\hat{X}_\mathrm{s} = (\hat{a}_\mathrm{s}^\dagger + \hat{a}_\mathrm{s})/\sqrt{2}$ and $\hat{P}_\mathrm{s} = \mathrm{i}(\hat{a}_\mathrm{s}^\dagger - \hat{a}_\mathrm{s})/\sqrt{2}$. The spin quadratures satisfy the canonical commutation relation $[\hat{X}_\mathrm{s}, \hat{P}_\mathrm{s}] = \mathrm{i}$. The sense of rotation of a spin state in phase space depends on the sign of $\bar{F}_x$ with respect to the magnetic field, which can be seen from the prefactor of the spin momentum operator. If the mean spin $\bar{F}_x$ is anti-parallel to the magnetic field B_x, the spin state oscillates clockwise in phase space, similar to a mechanical oscillator. But if the mean spin is oriented parallel to the magnetic field, the spin state oscillates counter-clockwise in the phase space. In order to write the (linear) magnetic Hamiltonian in the Holstein-Primakov approximation, the mean spin is approximated by $\hat{F}_x \approx \bar{F}_x - \mathrm{sgn}(\bar{F}_x)(\hat{X}_\mathrm{s}^2 + \hat{P}_\mathrm{s}^2)/2$. Neglecting a constant energy offset, this yields

$$\hat{H}_0 = -\mathrm{sgn}(\bar{F}_x)\hbar\Omega_\mathrm{s}\frac{\hat{X}_\mathrm{s}^2 + \hat{P}_\mathrm{s}^2}{2}. \tag{2.7.8}$$

Here it becomes even more apparent, that the sign of the oscillation frequency of the *spin-oscillator* $\Omega = -\mathrm{sgn}(\bar{F}_x)\Omega_\mathrm{s}$ depends on the orientation of the mean spin. For a positive oscillation frequency, the spin is prepared in the lowest energy state $\bar{F}_x = -Nf$. Any excitation (e.g. by interaction with light or the membrane) increases the energy of the spin. If instead the magnetic field is inverted, the optical pumping prepares the spin in the highest energy state $\bar{F}_x = Nf$. Any excitation reduces the energy of this negative frequency oscillator. The possibility of implementing a negative frequency oscillator has allowed the observation of parametric instabilities [122] and inducing entanglement between remote atomic ensembles [123] and between an atomic ensemble and a membrane [32]. In our experiment, it allows us to generate parametric-gain dynamics between the collective spin and the membrane oscillator [29], as

[10] To follow the Holstein-Primakov approximation more formally, it makes sense to first write the in the *Schwinger boson representation*. The spin can be perfectly mapped on two bosonic modes $\hat{a}_\mathrm{s}$ and $\hat{b}_\mathrm{s}$ by writing

$$\hat{F}_z = \frac{1}{2}\left(\hat{a}_\mathrm{s}^\dagger\hat{b}_\mathrm{s} + \hat{b}_\mathrm{s}^\dagger\hat{a}_\mathrm{s}\right), \quad \hat{F}_y = -\frac{1}{2\mathrm{i}}\left(\hat{a}_\mathrm{s}^\dagger\hat{b}_\mathrm{s} - \hat{b}_\mathrm{s}^\dagger\hat{a}_\mathrm{s}\right), \quad \hat{F}_x = \frac{1}{2}\left(\hat{a}_\mathrm{s}^\dagger\hat{a}_\mathrm{s} - \hat{b}_\mathrm{s}^\dagger\hat{b}_\mathrm{s}\right) \tag{2.7.3}$$

on can show that the commutation relations of the spin operators are fulfilled by this mapping. The bosonic Hilbert space is finite by enforcing

$$\hat{a}_\mathrm{s}^\dagger\hat{a}_\mathrm{s} + \hat{b}_\mathrm{s}^\dagger\hat{b}_\mathrm{s} = 2\bar{F}_x \tag{2.7.4}$$

where $\bar{F}$ is the total spin length. In our experiment, we polarise the spin either along $\bar{F}_x = |\bar{F}_x|$ or $\bar{F}_x = -|\bar{F}_x|$, i.e. most excitations are in the mode $\hat{b}_\mathrm{s}$ or $\hat{a}_\mathrm{s}$. For $\langle \hat{F}_x \rangle \approx -|\bar{F}_x|$, $\hat{a}_\mathrm{s}^\dagger\hat{a}_\mathrm{s} \ll \hat{b}_\mathrm{s}^\dagger\hat{b}_\mathrm{s}$ and we can approximate

$$\hat{b} \approx \sqrt{2\bar{F}_x - \hat{a}_\mathrm{s}^\dagger\hat{a}_\mathrm{s}} \tag{2.7.5}$$

This we can plug in the definition of the spin definition given in equations (2.7.3). Performing a Taylor expansion and only take the first order terms, leads to the Holstein-Primakov approximation.

will be shown in chapter 4.

The Faraday Hamiltonian can be written in terms of the harmonic oscillator quadratures

$$\hat{H} = \hbar\sqrt{4\Gamma_\mathrm{s}}\hat{X}_\mathrm{s}\hat{P}_\mathrm{L}, \tag{2.7.9}$$

where $\Gamma_\mathrm{s} = \alpha_1|\bar{S}_x||\bar{F}_x|/4$ is the measurement rate of the system. The measurement rate of the system is the rate at which a spin quantum is read out by the light. Having defined a measurement rate, a spin cooperativity can be written as $C = 2\Gamma_\mathrm{s}/\gamma_\mathrm{s}$. The higher order coupling terms due to the tensor interaction are neglected here. The interested reader is referred to the PhD thesis of Thomas Karg [68].

Holstein-Primakov Approximation for the Inhomogeneous Coupling: For the inhomogeneous coupling of the spins to the light, the definitions of the harmonic oscillator quadratures have to be adapted in such a way that the canonical commutation relations are still fulfilled [118]. Assuming that each individual spin commutes with all other spins (i.e. uncorrelated spins), the modified quadratures can be written as

$$\hat{\tilde{X}}_\mathrm{s} = \frac{\langle\eta\rangle}{\sqrt{\langle\eta^2\rangle}}\hat{X}_\mathrm{s} = \frac{\hat{F}_z^{(1)}}{\sqrt{|\bar{F}_x^{(1)}|}}, \tag{2.7.10}$$

$$\hat{\tilde{P}}_\mathrm{s} = \frac{\langle\eta\rangle}{\sqrt{\langle\eta^2\rangle}}\hat{P}_\mathrm{s} = \frac{\hat{F}_y^{(1)}}{\sqrt{|\bar{F}_x^{(1)}|}}, \tag{2.7.11}$$

and the measurement rate as

$$\tilde{\Gamma}_\mathrm{s} = \frac{\tilde{\alpha}_1^2|\bar{F}_x^{(2)}||\bar{S}_x|}{4} \approx \langle\eta_\mathrm{s}^2\rangle\frac{\alpha_1^2|\bar{F}_x||\bar{S}_x|}{4}. \tag{2.7.12}$$

With this definition, the Hamiltonian can be written as

$$\hat{H} = \hbar\sqrt{4\tilde{\Gamma}_\mathrm{s}}\hat{\tilde{X}}_\mathrm{s}\hat{\tilde{P}}_\mathrm{L}, \tag{2.7.13}$$

for the effective Faraday interaction.

Experimental Calibration of the Spin Quadrature: In the experiment, we measure the homodyne signal of the spin detection using a lock-in amplifier. The obtained voltage $V_\mathrm{rms}^{50\Omega}$ depends on the efficiency and the amplification of the balanced photodiodes of the homodyne detection. To calculate the Faraday angle, we have to compare this voltage to the maximal peak-to-peak contrast of the homodyne detection $V_\mathrm{pp} = 2V_0$. This voltage can be measured by continuously rotating the half waveplate of the homodyne detection and measure the amplitude of the sine-signal. Considering that the V_0 is measured using an oscilloscope with high impedance input, the Faraday angle is given by

$$\theta = \frac{2\sqrt{2}V_\mathrm{rms}^{50\Omega}}{2V_0} \tag{2.7.14}$$

where $V_\mathrm{rms}^{50\Omega}$ is multiplied by a factor 2 to account for the impedance mismatch between the oscilloscope and the lock-in amplifier and by a factor $\sqrt{2}$ to convert the signal from rms to the (peak) amplitude.

The factor two in the denominator comes from the definition of the Faraday angle. The effective $\hat{\tilde{X}}_{\mathrm{s}}$ quadrature of the spin is then given by

$$\langle \hat{\tilde{X}}_{\mathrm{s}} \rangle = \frac{\langle \hat{F}_z^{(1)} \rangle}{\sqrt{|\bar{F}_x^{(1)}|}} = \frac{2\langle \hat{\theta} \rangle}{\tilde{\alpha}_1 \sqrt{|\bar{F}_x^{(1)}|}} \tag{2.7.15}$$

$$= \frac{2\langle \hat{\theta} \rangle}{\sqrt{\langle \eta_{\mathrm{s}}^2 \rangle} \alpha_1 \sqrt{|\bar{F}_x|}} = \frac{1}{\sqrt{\langle \eta_{\mathrm{s}}^2 \rangle}} \frac{V_{\mathrm{rms}}^{50\Omega} 2\sqrt{2}}{V_{\mathrm{pp}} \alpha_1 \sqrt{|\bar{F}_x|}}. \tag{2.7.16}$$

Here, the spin length $|F_x| = 2N_{\mathrm{a}}$ can be directly calculated from the number of atoms N_{a} measured by absorption imaging and the atomic polarisability constant α_1 is calculated from the theory. In order to calculate the spin quadrature of the effective spin from the measurement record, we have to normalise the signal by the squared coupling efficiency $\langle \eta_{\mathrm{s}}^2 \rangle$. An effective occupation of the *spin-oscillator* can be calculated using the equipartition theorem

$$\tilde{n}_{\mathrm{s}}(t) + \frac{1}{2} = \frac{\langle \hat{\tilde{X}}_{\mathrm{s}}(t)^2 + \hat{\tilde{P}}_{\mathrm{s}}(t)^2 \rangle}{2} = \langle \hat{\tilde{X}}_{\mathrm{s}}(t)^2 \rangle_t. \tag{2.7.17}$$

2.8 Conclusion and Outlook

In this chapter, the interface used to couple the spin of the atomic cloud to the polarisation state of the light has been presented both theoretically and experimentally. We have shown that the Faraday effect can be used to engineer a linear coupling between the atomic spin and the light. For a multilevel Rubidium atom there are higher order tensor coupling terms of the light-spin coupling. By choosing an appropriate polarisation angle of the light and performing measurements at large detunings the contribution of these higher order terms can be minimised. Furthermore, it was observed that the spin decoherence is more complicated than a decay at the spontaneous scattering rate. For some experimental configurations (spin parallel to the k-vector of the light), the simulation of the atoms in the presence of the light could reproduce the spin decoherence dynamics.

The coupling between the atomic cloud and the laser is strongly inhomogeneous due to the similar dimensions of the atomic cloud and the waist of the laser. It was shown that we can account for this inhomogeneity by defining effective spin operators and scaling the polarisability constant. The correction factors for the effective coupling were calculated for the experimental geometry and compared with calibration measurements. It was found that there is a good agreement between experiment and theory for the coherent coupling.

It was shown that the spin-light interface can be operated in the quantum limited regime: A cooperativity of $C_{\mathrm{s}} = 9$ was measured by driving the spin with a polarisation modulation. For the same set of parameters, the measured spin noise was in agreement with theory ($\Delta = -2\pi \times 40\,\mathrm{GHz}$, $P = 1\,\mathrm{mW}$). The spin is mainly driven by the shot noise of the light which could be verified by squeezing the light using the spin. We can conclude that for this set of parameters quantum control of the spin-light interface is established.

But, there are some unresolved questions: The decoherence of the spins has not yet been modelled in a way that matches our experimental observations. Moreover, at higher spin-light coupling rates (e.g. for smaller detunings), the laser induces strong coherent spin dynamics. In the past, this phenomenon was attributed to collective spin dynamics due to the highly non-linear dependence on the number of atoms

[68]. In the centre of the atomic cloud, the atomic density is relatively high, with a value of $n\lambda^3 = 0.26$. Consequently, the experiment is operated close to the limit of the approximation which treats the atoms as independent scatterers. Nevertheless, we do not yet have a physical model to understand this dynamics.

Still, the spin can be used as a quantum system with high cooperativity if the parameters are chosen in the regime where the spin dynamics is understood. In the following chapters the spin is modelled as a harmonic oscillator, which is a good approximation for small tilts of the spin. With the relevant set of parameters for the coupling experiment ($\Delta = -2\pi \times 40\,\mathrm{GHz}$, $P = 1\,\mathrm{mW}$), the characterised measurement rate of this oscillator is $\Gamma_\mathrm{s} = 2\pi \times 2.5\,\mathrm{kHz}$ with a linewidth of $\gamma_\mathrm{s} = 2\pi \times 520\,\mathrm{Hz}$.

Chapter 3

Membrane-Light Quantum Interface

In this chapter, the optomechanical system is introduced. It is demonstrated that this macroscopic system can be coupled to the light in the quantum backaction-dominated regime. This is a fundamental prerequisite for conducting hybrid experiments in the quantum coherent regime.

For this, it is necessary to ensure that the coupling of the membrane to the light field is both strong and coherent. Therefore, a cavity is employed to enhance the optomechanical interaction. However, for cascaded quantum systems the time delay in the loop should be small compared to the oscillation period of the individual oscillators. This is achieved by operating in the so-called unresolved sideband regime. The following chapter will introduce our implementation of a membrane in such a cavity. Two different membranes are characterised: a membrane with a phononic bandgap shield around it and a nano-pillar membrane. The nano-pillar membrane, which is currently installed in the experiment, was optically cooled to the cavity dynamical backaction cooling limit of $n_{\mathrm{opt,min}} = 11$. Furthermore, an optomechanical cooperativity $C_{\mathrm{m}} > 1$ was measured. This high cooperativity enables the observation of ponderomotive squeezing of the light by 1.5 dB. The ability to perform ponderomotive squeezing experiments with the membrane oscillator shows that we are in a regime where quantum coherent coupling of the membrane and the spin are in reach.

3.1 Brief Introduction to Optomechanics

3.1.1 Mechanical Oscillator

In our experiment, we consider the vibrational modes of a membrane. The different out-of-plane vibrational modes of our membranes are well decoupled from each other, allowing each mode to be treated as an independent harmonic oscillator. The Hamiltonian of one vibrational mode can be described as a quantum mechanical harmonic oscillator with frequency Ω_{m} and with an effective mass m_{eff}

$$\hat{H}_{\mathrm{m}} = \frac{\hat{p}_{\mathrm{m}}^2}{2m_{\mathrm{eff}}} + \frac{m_{\mathrm{eff}}\Omega_{\mathrm{m}}^2\hat{x}_{\mathrm{m}}^2}{2}, \tag{3.1.1}$$

where $\hat{p}_\mathrm{m}$ and $\hat{x}_\mathrm{m}$ are the momentum and the position operators of the membrane [54]. For the purpose of subsequent calculations, we define dimensionless mechanical operators $\hat{X}_\mathrm{m} = \hat{x}_\mathrm{m}/(\sqrt{2}x_0)$ and $\hat{P}_\mathrm{m} = \sqrt{2}x_0\hat{p}_\mathrm{m}/\hbar$ for the membrane oscillator such that they satisfy the commutation relation $[\hat{X}_\mathrm{m}, \hat{P}_\mathrm{m}] = \mathrm{i}$. Here, the zero-point fluctuation amplitude of the membrane position is given by $x_0 = \sqrt{\hbar/(2m_\mathrm{eff}\Omega_\mathrm{m})}$. The resulting Hamiltonian of the mechanical oscillator is then

$$\hat{H}_\mathrm{m} = \hbar\Omega_\mathrm{m}\frac{\hat{X}_\mathrm{m}^2 + \hat{P}_\mathrm{m}^2}{2}. \tag{3.1.2}$$

The membrane is coupled to the environment with an intrinsic coupling rate γ_m, which depends on the material and geometry of the membrane oscillator. An important property of mechanical oscillators is the number of coherent oscillations before the amplitude decays to 1/e, which is given by the Q-factor $Q_\mathrm{m} = \Omega_\mathrm{m}/\gamma_\mathrm{m}$. Including the coupling to the environment, the Langevin equations for the membrane are given by

$$\begin{aligned}\partial_t\hat{X}_\mathrm{m} &= \Omega_\mathrm{m}\hat{P}_\mathrm{m},\\ \partial_t\hat{P}_\mathrm{m} &= -\Omega_\mathrm{m}\hat{X}_\mathrm{m} - \gamma_\mathrm{m}\hat{P}_\mathrm{m} + \sqrt{2\gamma_m}\hat{P}_\mathrm{th},\end{aligned} \tag{3.1.3}$$

where the thermal bath of the environment with an average thermal occupation $n_\mathrm{th} = k_\mathrm{B}T/(\hbar\Omega_\mathrm{m})$ for $n_\mathrm{th} \gg 1$ acts as a stochastic driving force $\hat{P}_\mathrm{th} = \mathrm{i}(\hat{b}^\dagger_{m,\mathrm{in}} - \hat{b}_{m,\mathrm{in}})/\sqrt{2}$ with white noise correlator $\langle\hat{P}_\mathrm{th}(t)\hat{P}_\mathrm{th}(t')\rangle = (n_\mathrm{th} + 1/2)\delta(t - t')$. From this, the rate at which phonons from the environment excite the membrane oscillator can be deducted, which is defined as the thermal decoherence rate $\gamma_\mathrm{m,th} = (n_\mathrm{th} + 1/2)\gamma_\mathrm{m}$.

3.1.2 Membrane in a Cavity

The coupling of the membrane to the propagating light field can be increased by placing the membrane into an optical cavity. In the following, a short overview of the most important equations of a membrane in a cavity is given. For a more detailed discussion of the following section, the reader is directed to [54] for a general introduction to cavity optomechanics and to [68, 124] for the implementation in our experiment.

Each cavity mode can be described by a harmonic oscillator. By placing the membrane in a cavity, the resonant frequency of the cavity is altered. Here, we only consider a single cavity mode driven and interrogated with a laser, given by

$$\hat{H}_\mathrm{cav} = \hbar\Omega_\mathrm{c}(\hat{x}_\mathrm{m})\left(\hat{c}^\dagger\hat{c} + \frac{1}{2}\right), \tag{3.1.4}$$

where $\hat{c}^\dagger$ ($\hat{c}$) is the (unitless) creation (annihilation) operator of a photon in the cavity. The cavity resonance frequency $\Omega_\mathrm{c}(\hat{x}_\mathrm{m})$ depends on the position of the membrane. For small mechanical displacements, the cavity frequency can be expanded to $\Omega_\mathrm{c}(\hat{x}_\mathrm{m}) = \Omega_\mathrm{c} - G\hat{x}_\mathrm{m}$ where $G = -\mathrm{d}\Omega_\mathrm{c}/\mathrm{d}x_m$ is the cavity frequency shift per membrane displacement. We define the vacuum optomechanical coupling strength $g_0 = Gx_0$, quantifying the interaction strength between a single photon and a single phonon. For a membrane in the middle geometry, the value of g_0 depends on the position of the membrane in the cavity

[125]. Omitting the constant terms, the optomechanical Hamiltonian reads as

$$\hat{H}_{\mathrm{om}} = -\hbar\sqrt{2}g_0\hat{X}_m\hat{c}^\dagger\hat{c}. \tag{3.1.5}$$

We assume that the cavity field is driven to a large coherent amplitude by a coupling laser. After linearising the cavity Hamiltonian [54] and neglecting the offset which does not depend on the cavity fluctuations, we get

$$\hat{H}_{\mathrm{om}} = -\hbar g_0\sqrt{n_{\mathrm{c}}}\sqrt{2}\hat{X}_{\mathrm{m}}\left(\hat{c}+\hat{c}^\dagger\right) \tag{3.1.6}$$

where $n_{\mathrm{c}} = \langle\hat{c}^\dagger\hat{c}\rangle$ is the average number of photons in the cavity. The coupling rate between the dimensionless quadratures of the cavity field and the membrane is defined as the optomechanical coupling rate $g_{\mathrm{om}} = g_0\sqrt{n_{\mathrm{c}}}$. It should be noted that the optomechanical coupling rate is dependent on the number of photons in the cavity and so the membrane-light interaction is enhanced by the optical field. In our experiment, we use a highly asymmetric cavity. Consequently, it can be assumed that the cavity is only coupled through one port, i.e. the cavity linewidth is approximately given by the coupling rate through the first mirror $\kappa_1 \approx \kappa$. In the following, we assume operation in the fast cavity regime, also called unresolved sideband regime, where the cavity linewidth is much larger than the mechanical resonance frequency $\kappa \gg \Omega_{\mathrm{m}}$.

Dynamical Backaction

Form the linearised optomechanical Hamiltonian given in equation (3.1.6), the equations of motions for the cavity operators and the membrane quadratures can be derived. The cavity operators are transformed into a rotating frame at the light frequency. Furthermore, we assume that the cavity is driven by a free-space light field with amplitude $\hat{a}_{\mathrm{in}}$ (units of $\mathrm{s}^{-1/2}$). The resulting Langevin equations of the systems are given by

$$\partial_t\hat{c} = -\left(\frac{\kappa}{2} - \mathrm{i}\Delta_{\mathrm{c}}\right)\hat{c} - \mathrm{i}g_{\mathrm{om}}\sqrt{2}\hat{X}_{\mathrm{m}} - \sqrt{\kappa}\hat{a}_{\mathrm{in}} \tag{3.1.7}$$

$$\partial_t\hat{X}_{\mathrm{m}} = \Omega_{\mathrm{m}}\hat{P}_{\mathrm{m}},$$

$$\partial_t\hat{P}_{\mathrm{m}} = -\Omega_{\mathrm{m}}\hat{X}_{\mathrm{m}} - \gamma_{\mathrm{m}}\hat{P}_{\mathrm{m}} - \sqrt{2}\left(g^*_{\mathrm{om}}\hat{c} + g_{\mathrm{om}}\hat{c}^\dagger\right) + \sqrt{2\gamma_m}\hat{P}_{\mathrm{th}}, \tag{3.1.8}$$

where the detuning between the light and the cavity is given by $\Delta_{\mathrm{c}} = \omega_{\mathrm{L}} - \Omega_{\mathrm{c}}$. By solving the linearised coupled equations of motion for the cavity operator and the membrane quadratures, one can derive the dynamical effects of the radiation pressure on the mechanical oscillator [54]. If the cavity mode of interest is driven by an optical beam detuned by Δ_{c}, the membrane resonance frequency is shifted by

$$\delta\Omega_{\mathrm{m}} = \frac{2g_0^2 n_{\mathrm{c}}\Delta_{\mathrm{c}}}{\kappa^2/4 + \Delta_{\mathrm{c}}^2}. \tag{3.1.9}$$

In addition, the light can act as a damping force for a negative cavity detuning $\Delta_{\mathrm{c}} < 0$ or a driving force for a positive detuning $\Delta_{\mathrm{c}} > 0$. Damping or driving the membrane alters its linewidth of the membrane to $\gamma_{\mathrm{m}} + \gamma_{\mathrm{m,opt}}$ with

$$\gamma_{\mathrm{m,opt}} = -\frac{4g_0^2 n_{\mathrm{c}}\Delta_{\mathrm{c}}\kappa\Omega_{\mathrm{m}}}{(\kappa^2/4 + \Delta_{\mathrm{c}}^2)^2}. \tag{3.1.10}$$

In case of the damping force, the light can be used to cool the membrane. The maximum cooling rate is obtained for $\Delta_{\mathrm{c}} = \kappa/\sqrt{12}$. In the unresolved sideband regime, the optomechanical interaction

is insufficient to cool the membrane to its ground state. The cooling limit of the optical cooling by dynamical backaction in this regime is given by [54]

$$n_{\mathrm{fin,min}} = \frac{\kappa^2/4 + \Delta_\mathrm{c}^2}{4\Omega_\mathrm{m}\Delta_\mathrm{c}} \xrightarrow[\Delta_\mathrm{c}=-\kappa/2]{} \frac{\kappa}{4\Omega_\mathrm{m}}, \quad \xrightarrow[\Delta_\mathrm{c}=-\kappa/\sqrt{12}]{} \frac{\kappa}{\sqrt{12}\Omega_\mathrm{m}}. \tag{3.1.11}$$

Here, the limits for the lowest temperature and for the largest cooling rate are given. The final temperature of the membrane in presence of an optomechanical cooling beam is given by

$$n_\mathrm{fin} = \frac{n_\mathrm{fin,min}\gamma_\mathrm{m,opt} + n_\mathrm{th}\gamma_\mathrm{m}}{\gamma_\mathrm{m,opt} + \gamma_\mathrm{m}}. \tag{3.1.12}$$

For high temperatures ($n_\mathrm{th} \gg n_\mathrm{opt,min}$), this equation can be approximated by $n_\mathrm{fin} \approx \gamma_\mathrm{m,th}/(\gamma_\mathrm{m,opt} + \gamma_\mathrm{m})$ where the numerator is given by the thermal decoherence rate. The additional term $n_\mathrm{opt,min}\gamma_\mathrm{m,opt}$ takes into account the heating of the membrane by the backaction of the cooling beam and thus results in the cooling limit discussed above.

Interaction with the Propagating Field Outside the Cavity

In the hybrid coupling experiment, the cavity is tuned on resonance with the coupling beam. This allows for turning on and off the coupling to the atomic spin without changing the membrane frequency and linewidth. For a resonantly driven cavity in the unresolved sideband regime, the optomechanical Hamiltonian given in equation (3.1.6) can be written in terms of the propagating light field outside the cavity as

$$\hat{H}_\mathrm{om,eff} = -\hbar 2\sqrt{\Gamma_\mathrm{m}}\hat{X}_\mathrm{m}\hat{X}_\mathrm{L}, \tag{3.1.13}$$

where it is assumed, that the optomechanical coupling is weak $g_\mathrm{om} \ll \kappa$ [68]. Here, $\hat{X}_\mathrm{L} = (\hat{a}_\mathrm{in}^\dagger + \hat{a}_\mathrm{in})/\sqrt{2}$ is the amplitude quadrature of the travelling light field (units of $\mathrm{s}^{-1/2}$) and the membrane measurement rate is given by

$$\Gamma_\mathrm{m} = \frac{4g_\mathrm{om}^2}{\kappa} = \left(\frac{4g_0}{\kappa}\right)^2 \Phi_\mathrm{L}, \tag{3.1.14}$$

where $\Phi_\mathrm{L} = \langle \hat{a}_\mathrm{in}^\dagger \hat{a}_\mathrm{in} \rangle$ is the photon flux in front of the cavity. The cooperativity is the ratio between the quantum backaction noise S_qba imparted by the light on the system and the thermal noise S_th driving the system due to the coupling to the environment, $C_\mathrm{m} = S_\mathrm{qba}/S_\mathrm{th}$. For a resonant beam $\Delta_\mathrm{c} = 0$, the membrane cooperativity is given by $C_\mathrm{m} = \Gamma_\mathrm{m}/\gamma_\mathrm{m,th}$. If the cooperativity is greater than one $C_\mathrm{m} > 1$, the backaction noise of the laser dominates over the thermal noise on the membrane.

Starting from the Hamiltonian in equation (3.1.13), we can write the input-output relation of the light and the equation of motion for the membrane oscillator [68, 124]

$$\begin{aligned} \hat{X}_\mathrm{L}^\mathrm{(out)}(t) &= \hat{X}_\mathrm{L}^\mathrm{(in)}(t), \\ \hat{P}_\mathrm{L}^\mathrm{(out)}(t) &= \hat{P}_\mathrm{L}^\mathrm{(in)}(t) + 2\sqrt{\Gamma_\mathrm{m}}\hat{X}_\mathrm{m}(t), \end{aligned} \tag{3.1.15}$$

$$\begin{aligned} \partial_t \hat{X}_\mathrm{m} &= \Omega_\mathrm{m}\hat{P}_\mathrm{m}, \\ \partial_t \hat{P}_\mathrm{m} &= -\Omega_\mathrm{m}\hat{X}_\mathrm{m} - \gamma_\mathrm{m}\hat{P}_\mathrm{m} + \sqrt{4\Gamma_m}\hat{X}_\mathrm{L}^\mathrm{(in)} + \sqrt{2\gamma_m}\hat{P}_\mathrm{th}. \end{aligned} \tag{3.1.16}$$

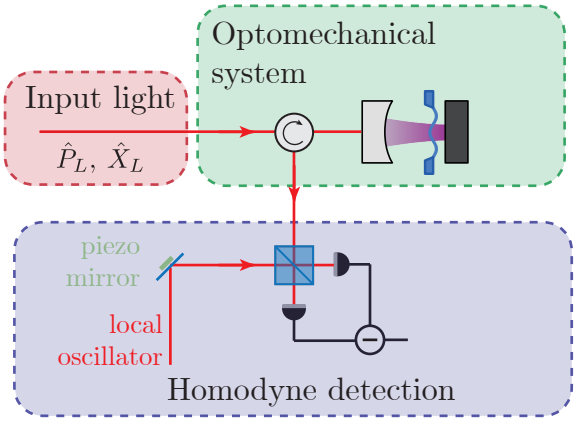

Figure 3.1.1: Coherent input light drives an optical cavity with a membrane inside, interacting with the membrane vibrations through radiation pressure. The light leaving the cavity is measured by homodyne detection. For this, it is combined with a local oscillator which is derived from the driving laser. The phase between the driving beam and the local oscillator can be controlled with a mirror glued on a piezo crystal. By changing this phase, any superposition between the amplitude quadrature $\hat{X}_L$ and the phase quadrature $\hat{P}_L$ of the output light can be detected.

where $\hat{X}_{\mathrm{L}}^{(\mathrm{in})} = (\hat{a}_{\mathrm{in}} + \hat{a}_{\mathrm{in}}^{\dagger})/\sqrt{2}$ and $\hat{P}_{\mathrm{L}}^{(\mathrm{in})} = (\hat{a}_{\mathrm{in}} - \hat{a}_{\mathrm{in}}^{\dagger})/(\mathrm{i}\sqrt{2})$ are the quadratures of the input field (with units of $\mathrm{s}^{-1/2}$). For a resonantly coupled cavity, the vibrations of the membrane are mapped onto the phase quadrature of the light while the membrane is driven by the amplitude quadrature of the light. If there is a detuning $\Delta_{\mathrm{c}} \neq 0$, the equation of motion are more complicated [54, 124]. But for the purpose of this work, the resonant equation of motions are sufficient.

3.1.3 Measurement of the Membrane Phonon Occupation

The membrane vibrations are measured by detecting the light which is reflected from the cavity. This section, which is published as an appendix to [30], describes the calibration of the detected signal. The vibrations of the membrane are detected via their effect on the phase of the beam reflected from the cavity [54] (see figure 3.1.1). As described above, the membrane vibrations modulate the cavity resonance frequency Ω_{c}. For a single-sided cavity, the phase ϕ_{c} of the beam reflected from the cavity with respect to the incoming beam is related to the cavity detuning by [54]

$$\phi_{\mathrm{c}} = \arctan\left[\frac{\kappa\Delta_{\mathrm{c}}}{(\kappa/2)^2 + \Delta_{\mathrm{c}}^2}\right], \tag{3.1.17}$$

where κ is the cavity linewidth. A change in the cavity frequency $\delta\Omega_{\mathrm{c}} = Gx_m$ thus leads to a change in the phase of the reflected beam by an amount $\delta\phi_{\mathrm{c}} = -(\mathrm{d}\phi_{\mathrm{c}}/\mathrm{d}\Delta_{\mathrm{c}})\delta\Omega_{\mathrm{c}} \approx -4Gx_{\mathrm{m}}/\kappa$, where the approximation holds for small detunings $|\Delta_{\mathrm{c}}| \ll \kappa$. We can write the previous expression in terms of the vacuum optomechanical coupling rate g_0 as

$$\delta\phi_{\mathrm{c}} = -\frac{4g_0}{\kappa}\frac{x_{\mathrm{m}}}{x_0}, \tag{3.1.18}$$

where we have used the zero-point fluctuation amplitude of the membrane x_0. These phase variations $\delta\phi_{\mathrm{c}}$ can now be measured interferometrically by means of balanced homodyne detection (laser path is shown in figure 3.3.2 (a)). For this, the beam reflected from the cavity is combined with a strong local

oscillator on a polarising beam splitter. A half waveplate in front of the beam splitter is set so that both beams have a splitting ratio of 50:50. The output beams are subsequently photodetected and the output signals subtracted. The recorded balanced voltage can be written as

$$V = V_0 \cos(\Delta\phi), \tag{3.1.19}$$

with V_0 the modulation amplitude, proportional to the square-root of the power of the beam reflected from the cavity and of the local oscillator beam and with $\Delta\phi = \phi_\mathrm{c} - \phi_\mathrm{LO}$ where ϕ_LO is the phase of the local oscillator.

The modulation amplitude V_0 is inferred by modulating ϕ_LO, thanks to a movable mirror in the local oscillator path which allows to generate path differences of a few wavelengths (*piezo mirror*, see figure 3.3.2 (a)). V_0 can be extracted from the contrast of the observed interference fringes. In order to detect the phase fluctuations $\delta\phi_\mathrm{c}$ of ϕ_c induced by the membrane motion, the relative phase $\Delta\phi$ is locked to $\pi/2$, i.e., the point where the slope of the fringes is maximal. For small shifts $\delta\phi_\mathrm{c} \ll \pi/2$, the recorded voltage variation $\delta V(t)$ is directly proportional to $\delta\phi_\mathrm{c}(t)$, and thus to $x_m(t)$. In practice, $\delta V(t)/V_0$ is effectively modified by a factor $1/\eta_\mathrm{c}$ due to imperfect cavity coupling, where $\eta_\mathrm{c} = \kappa_1/\kappa$ is the fraction between the cavity loss through the incoupling mirror κ_1 and the total cavity loss κ. We get

$$x_\mathrm{m}(t) = \frac{\delta V(t)}{\eta_\mathrm{c} V_0} \frac{x_0 \kappa}{4 g_0}. \tag{3.1.20}$$

In order to determine the membrane phonon occupation n_m, we convert this to the dimensionless quadrature operator $\hat{X}_\mathrm{m}$. By means of the equipartition theorem, we can also obtain $\langle \hat{X}_\mathrm{m}(t)^2 \rangle_t = \langle \hat{P}_\mathrm{m}(t)^2 \rangle_t$ and thus relate the measured voltage variations to the membrane phonon occupation number.

In the experiment, the homodyne detection signal is demodulated by a lock-in amplifier[1], which is described in detail for the spin signal in section 2.3.3. This means that we do not measure the voltage $\delta V(t)$ but its rms value $\delta V(t)^{50\,\Omega}_\mathrm{rms}$, which we further need to multiply by a factor of 2 due to the impedance mismatch between the high-impedance output of the photodetector[2] and the $50\,\Omega$ input impedance of the lock-in amplifier. To convert the measured rms value to amplitude variations, we therefore need a total factor of $2\sqrt{2}$. This finally yields

$$\begin{aligned} \bar{n}_\mathrm{m}(t) + \frac{1}{2} &= \frac{\langle X_\mathrm{m}(t)^2 \rangle + \langle P_\mathrm{m}(t)^2 \rangle}{2} = \langle X_\mathrm{m}(t)^2 \rangle_t \\ &= \frac{\langle \hat{x}_m^2 \rangle_t}{2 x_0^2} = \frac{1}{2} \left(\frac{\kappa \langle \delta\phi_\mathrm{c} \rangle_t}{4 g_0} \right)^2 = \frac{1}{8} \left(\frac{\kappa}{2 g_0} \right)^2 \left(\frac{\langle \delta V(t) \rangle_t}{\eta_\mathrm{c} V_0} \right)^2 \\ &= \left(\frac{\delta V(t)^{50\,\Omega}_\mathrm{rms}}{\eta_\mathrm{c} V_0} \right)^2 \left(\frac{\kappa}{2 g_0} \right)^2. \end{aligned} \tag{3.1.21}$$

The values of κ and g_0, can be independently calibrated from the width of the Pound-Drever-Hall signal and by measuring the optomechanical cooling using a detuned coupling beam (see for example section 3.3.3), respectively.

[1] Zurich Instrument HF2LI
[2] Balanced photodetector Sp 1'023 with a signal gain of 10^4.

Power Spectral Density

In practice, it is often more common and easier to analyse the contributions to the mechanical signal (thermal noise, backaction noise, zero-point fluctuations) in the spectral domain than in the time domain. In the spectral domain, different noise sources can be more easily distinguished due to their different frequency dependence. The mechanical spectrum can be obtained by solving the equations of motion in the frequency domain. We get

$$\hat{X}_{\mathrm{m}}(\omega) = \chi_{\mathrm{m}}(\omega)\left(2g_{\mathrm{om}}\hat{X}_{\mathrm{c}}(\omega) - \sqrt{2\gamma_{\mathrm{m}}}\hat{P}_{\mathrm{th}}(\omega)\right), \tag{3.1.22}$$

where $\chi_{\mathrm{m}}^{-1} = (\Omega_{\mathrm{m}}^2 - \omega^2 - \mathrm{i}\gamma_{\mathrm{m}}\omega)/\Omega_{\mathrm{m}}$ is the mechanical susceptibility and $\hat{X}_{\mathrm{c}}(\omega) = (\hat{c} + \hat{c}^\dagger)/\sqrt{2}$ is the amplitude quadrature of the cavity field. The membrane is driven by the shot noise of the light (first term) and the thermal noise (second term). From this expression, the symmetrised power spectral density can be obtained[3] [112]

$$\bar{S}_{X_{\mathrm{m}}X_{\mathrm{m}}}(\omega) = 2|\chi_{\mathrm{m}}(\omega)|^2\left(\bar{S}_{\mathrm{qba}}(\omega) + \bar{S}_{\mathrm{th}}(\omega)\right), \tag{3.1.25}$$

where the backaction power spectral density is defined as [124]

$$\bar{S}_{\mathrm{qba}}(\omega) = \frac{g_{\mathrm{om}}^2}{2}\left(\frac{\kappa}{(\kappa/2)^2 + (\Delta_{\mathrm{c}} + \omega)^2} + \frac{\kappa}{(\kappa/2)^2 + (\Delta_{\mathrm{c}} - \omega)^2}\right) \tag{3.1.26}$$

and the thermal power spectral density is defined as

$$\bar{S}_{\mathrm{th}}(\omega) = \gamma_{\mathrm{m}}\frac{\omega}{\Omega_{\mathrm{m}}}\left(n_{\mathrm{th}} + \frac{1}{2}\right). \tag{3.1.27}$$

Integrating the power spectral density over the resonance peak gives the occupation of the vibrational mode of the membrane

$$2\int_0^\infty \bar{S}_{X_{\mathrm{m}}X_{\mathrm{m}}}(\omega)\frac{\mathrm{d}\omega}{2\pi} = \left(n_{\mathrm{th}} + \frac{1}{2}\right) + \frac{\bar{S}_{\mathrm{qba}}(\Omega_{\mathrm{m}})}{\gamma_{\mathrm{m}}} = n_{\mathrm{eff}} + \frac{1}{2}. \tag{3.1.28}$$

There are two driving terms after the first equality. The first term corresponds to the occupation due to the thermal environment, while the second term results from an increased occupation due to the shot noise drive of the probe laser. The thermal environment and the shot noise drive result in an overall occupation of the membrane vibrational mode given by n_{eff}. If the membrane is optically cooled, the mechanical susceptibility is modified as shown in equations (3.1.9) and (3.1.10). This optical cooling can be taken into account in equation (3.1.28) by substituting $\gamma_{\mathrm{m}} \to \gamma_{\mathrm{m}} + \gamma_{\mathrm{m,opt}}$ and $n_{\mathrm{th}} \to n_{\mathrm{fin}}$.

In a real experiment, we cannot measure the power spectral density of the membrane directly, but we rather measure the power spectral density of the light reflected from the cavity where this signal is encoded. If the power spectral density of the homodyne signal is measured (see equation (3.1.21) for the

[3] For an operator with stationary statistics, the Wiener - Chinchin theorem can be applied to obtain the PSD [112]

$$S_{OO}(\omega) = \int_{-\infty}^{\infty} \mathrm{e}^{\mathrm{i}\omega t}\langle\hat{O}^\dagger(t)\hat{O}(0)\rangle\mathrm{d}t = \int_{-\infty}^{\infty}\langle\hat{O}^\dagger(-\omega)\hat{O}(\omega')\rangle\mathrm{d}\omega'. \tag{3.1.23}$$

From this, the symmetrised PSD can be calculated by summing over the positive and negative frequency components

$$\bar{S}_{OO}(\omega) = \frac{S_{OO}(\omega) + S_{OO}(-\omega)}{2}. \tag{3.1.24}$$

See appendix C for more details.

time trace), we obtain

$$\bar{S}_{VV}(\omega) = 2\left(\frac{4\eta_c V_0 g_0}{\kappa}\right)^2 \bar{S}_{X_m X_m}(\omega) + \frac{(\eta_c V_0)^2}{2\Phi_L}\bar{S}_{P_L^{(in)} P_L^{(in)}}, \tag{3.1.29}$$

where the first term is the mechanical signal and the second term is a white noise term from the phase noise of a coherent light source $\bar{S}_{P_L^{(in)} P_L^{(in)}} = 1/2$. The shot noise is a constant background and can be subtracted in the analysis. By integrating the resulting power spectral density, the effective membrane occupation is obtained directly

$$n_{\text{eff}} + \frac{1}{2} = \left(\frac{\kappa}{4\eta_c V_0 g_0}\right)^2 \int_0^\infty \left(\bar{S}_{VV}(\omega) - \frac{(\eta_c V_0)^2}{4\Phi_L}\right)\frac{\mathrm{d}\omega}{2\pi}. \tag{3.1.30}$$

In this derivation it is assumed that the cavity is probed with a resonant beam. In order to obtain membrane occupation with a detuned probe beam, a correction factor is included to account for the finite detuning of the cavity, for further details see [124].

3.2 Phononic Bandgap Shielded Membrane

Two different membranes have been used in this thesis: a membrane with a phononic bandgap shield around it [126] in a first set of experiments (shown in chapter 5) and a nano-pillar membrane [127] in a second set (shown in chapter 6). Both membranes used in this work are made out of silicon nitride. Stoichiometric Si_3N_4 membranes can be fabricated with thicknesses of tens of nanometres and tensile stresses on the order of GPa [128]. This results in vibrational modes at MHz frequencies with high Q-factors and low effective masses of $\sim 10\,\text{ng}$, rendering them appealing for optomechanical applications [55].

The phononic bandgap shielded membrane presented below has been extensively described in previous works by members of our group [68, 124]. Therefore, for this membrane only a very brief overview will be given here. The phononic bandgap shielded membrane[4] has a thickness of 100 nm and a square shape with a side length of 270 µm. The silicon frame of the membrane is 200 µm thick and patterned with a phononic crystal [126] (photograph shown in figure 3.2.1 (a)). This creates a bandgap for acoustic modes ranging from 1.5 MHz to 2.6 MHz. For the experiment, we used the 2, 2-mode (see figure 3.2.1 (b) and (d)) of the membrane vibrating at a frequency of $\Omega_m = 2\pi \times 1.957\,\text{MHz}$ with a room temperature Q-factor of $Q_{\text{RT}} = 1.46 \times 10^6$ (a ringdown experiment is shown in figure 3.2.2 (a)).

The membrane chip has a footprint of 5 mm × 5 mm (shown in figure 3.2.1 (a)). It is clamped to a titanium mount using a brass and a kapton sheet (figure 3.3.2 (b) illustrates the novel cavity design, which does not incorporate the brass sheet. The original cavity design which is used for the phononic bandgap shielded membrane is presented in [68]). The membrane is embedded in an optical cavity consisting of a concave mirror with a reflectivity of $r_1^2 = 0.995$ and a curvature of $R = 30\,\text{mm}$ and a planar mirror with a reflectivity of $r_2^2 = 0.9999$. The cavity length is $L_c = 1.2\,\text{mm}$, resulting in a finesse of $\mathcal{F}_0 = 1230$ (empty). The membrane is installed at a distance of $\bar{x}_m = 0.2\,\text{mm}$ from the planar mirror. The position of both mirrors can be finely adjusted by using piezoelectric crystals[5]. The piezoelectric crystal of the planar mirror is used to alter the effective position of the membrane within the cavity and position it

[4] custom made by NORCADA Inc. (Canada)
[5] Piezomechanik, HPCh 150/15-8/3: maximal stroke: > 3 µm; capacitance: 790 nF

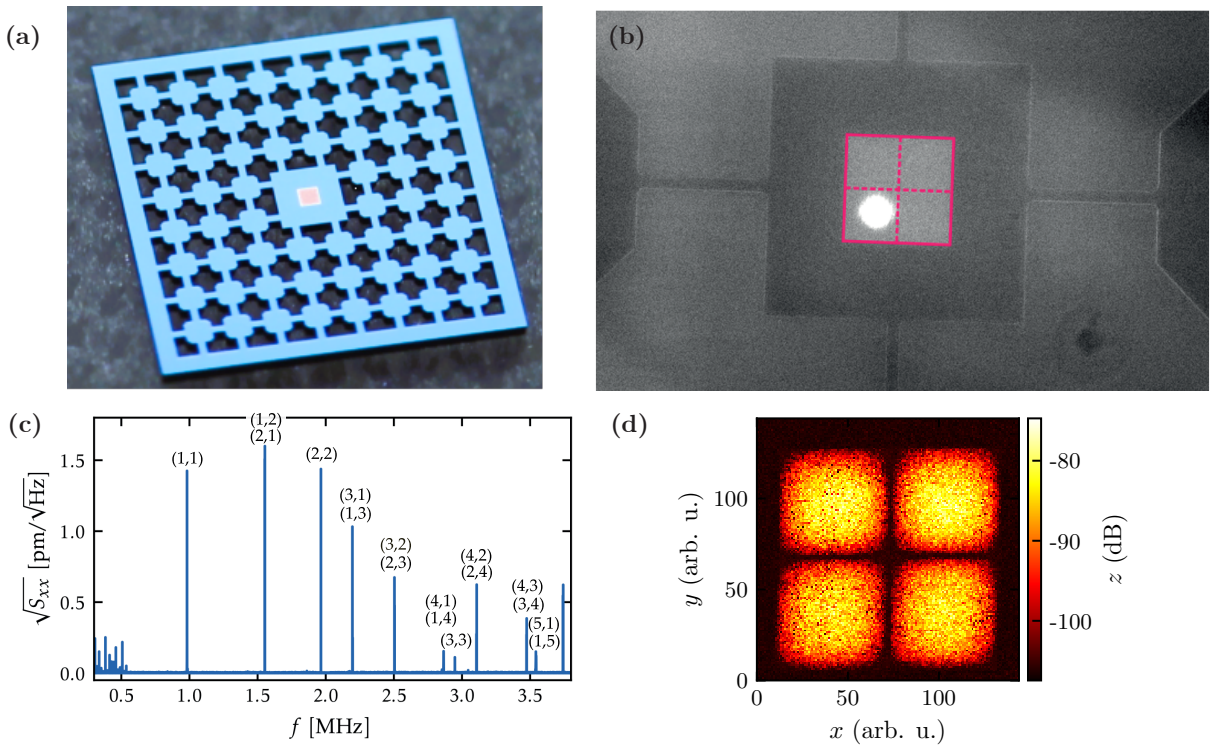

Figure 3.2.1: Phononic bandgap shielded membrane used in our experiment: In (a) a photograph of the membrane (white) embedded in the phononic bandgap structure (light blue) is shown. (b) shows a zoom to the membrane. In the experiment, we want to couple to the $2,2$-mode of the membrane. In (d), a raster scan of this mode is shown, in (b) we see that the beam overlaps well with one of the antinodes of this mode. (c) shows a spectrum of the membrane displacement measured at the position of the beam in (b).

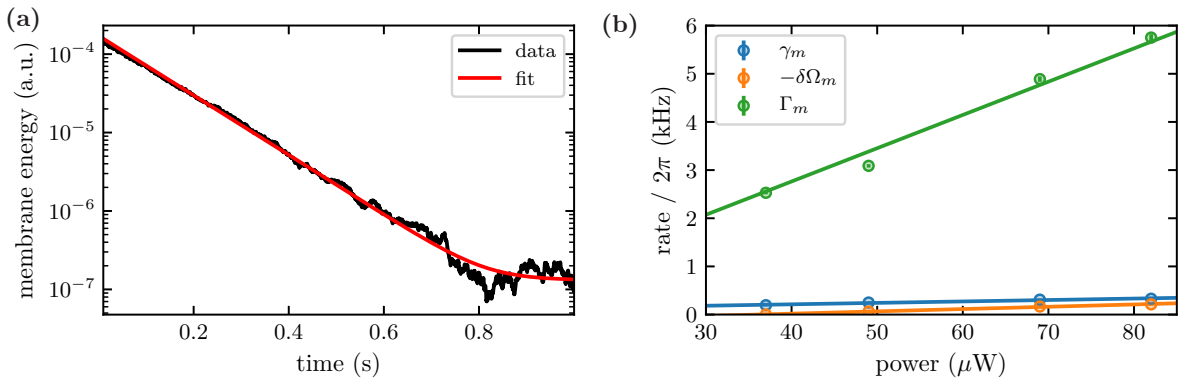

Figure 3.2.2: (a) Plot of a ringdown measurement of the 2, 2-mode of the phononic bandgap shielded membrane. For this measurement, the cavity is locked on resonance. The membrane is positioned inside the cavity by moving the planar mirror to minimise coupling to the light, thereby avoiding any cooling effect. (b) Result of the optomechanical response measurement versus the power in front of the cavity (for further details, see section 3.3.3).

to achieve the greatest possible coupling to the light. The length of the cavity is actively stabilised by applying a feedback on the position of the concave mirror. For this, an error signal is generated by using the Pound-Drever-Hall (PDH) technique [129, 130]. By placing the membrane in the position that provide the greatest coupling to the light, the cavity linewidth is also minimised. Fitting the slope of the PDH signal, the linewidth of the cavity containing the membrane is found to be $\kappa = 2\pi \times 77\,\mathrm{MHz}$. We characterise the membrane measurement rate (in the cavity) at different powers (see figure 3.2.2 (b)) and calculate from this the vacuum optomechanical coupling strength $g_0 = 2\pi \times 224\,\mathrm{Hz}$.

3.3 Nano-Pillar Membrane

3.3.1 Nano-Pillar Membrane

The phononic structure effectively shields the relevant membrane mode from external dissipation. However, it has been demonstrated that the primary limitation for the coherence of the vibrational modes of phononic bandgap shielded membranes is the bending losses at the boundaries between the thin silicon nitride membrane and the thick silicon substrate [131]. To overcome this limitation, the so-called soft-clamped membranes have been developed [56]. In contrast to the approach in which the support is patterned with a phononic bandgap structure, the membrane itself is patterned with a phononic bandgap structure. A defect is engineered in the centre of the patterned membrane, which localises a vibrational mode at the centre of the membrane. The membrane is designed so that the vibrational frequency of the defect is within the bandgap, resulting in an exponential decay of the vibration amplitude in the phononic bandgap structure. Consequently, at the edge of the membrane, the amplitude of the defect mode is close to zero, thereby mitigating clamping losses. A multitude of different designs of soft-clamped membranes have been implemented so far [55, 56, 127, 132, 133]. The majority of these designs rely on the periodic removal of mass from the membrane by etching holes in the silicon nitride to form the phononic bandgap structure [56, 132, 133]. In this work, we use a membrane on which arrays of nano-pillars have been grown to periodically vary the material density of the membrane [127].

Similar to a membrane where mass is removed, a periodic density change by adding mass creates a

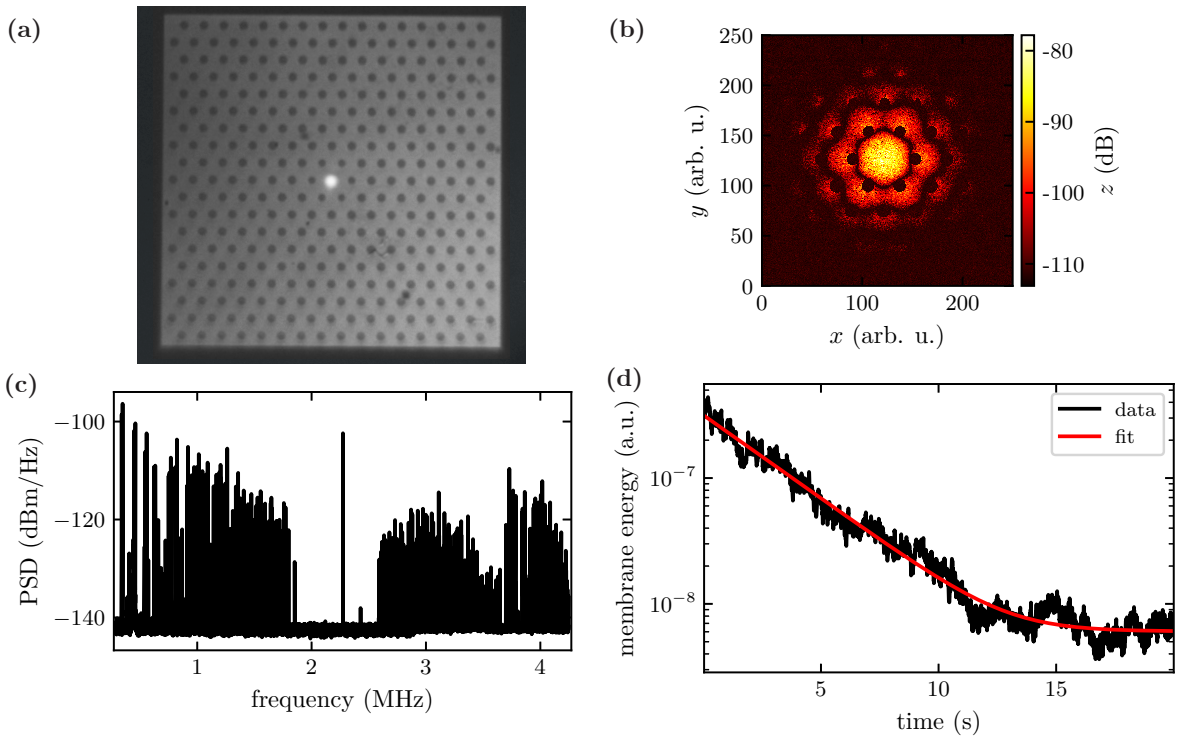

Figure 3.3.1: The nano-pillar membrane used in our experiment. (a) shows a image of the membrane. In dark, one can see the arrays of nano-pillars. The bright spot in the middle is the light of the cavity mode. The dust particles on this image come from the imaging system and are not on the membrane itself. In (b) a raster scan of the (thermally driven) vibration amplitude of the defect mode of the membrane central region is shown. The dark spots in the raster scan are the regions with the nano-pillar arrays, where there is no reflection from the membrane. (c) shows the thermal spectrum of the membrane. It has a clearly visible bandgap from 1.79 MHz to 2.59 MHz. The defect mode has a frequency of $\Omega_m = 2\pi \times 2.274\,\mathrm{MHz}$. In (d) a ringdown is presented for the membrane in a 10 K environment which yields $Q_{10\mathrm{K}} = 5.1 \times 10^7$.

bandgap. However, by simply adding mass by modulating the thickness of the membrane, the stiffness is increased and again the bending losses will affect the coherence of the oscillator. By patterning the membrane with an array of nano-pillars in the regions of higher mass, the dissipation effect can be reduced. In order for this approach to be effective, the diameter of the nano-pillars must be small compared to the wavelength of the phononic mode [127].

The nano-pillar membrane in our experiment has been fabricated by the group of Ulrik Lund Andersen at DTU in Lyngby, Denmark and is described in [127, 134]. In the fabrication process, a 20 nm thin layer of stoichiometric silicon nitride is grown on a silicon wafer via low-pressure chemical vapour deposition [134]. A 1 µm thick layer of silicon nitride is deposited using plasma-enhanced chemical vapour deposition (PECVD). The pillar pattern is transferred to the membrane by uv-lithography of a photo resist followed by reactive ion etching of the PECVD layer. A window is etched from the backside to remove the silicon bulk in the membrane region [127].

In our experiments, we use a square membrane with side length of 3.7 mm. The membranes have been patterned with a hexagonal unit cell containing regions without nano-pillars and circular regions with arrays of nano-pillars (see figure 3.3.1 (a)). One array of nano-pillars has a diameter of 73 µm. The array of nano-pillars is again formed by hexagonal unit cells of nano-pillars with a diameter of 1 µm, a height of 1 µm and a centre-to-centre distance of 2.5 µm. In the centre of the membrane, one array of nano-pillars is missing. This defect in the phononic crystal localises vibration modes in the centre of the membrane. For our membrane, the central defect has a diameter of 370 µm.

A vibration spectrum of the nano-pillar membrane is shown in figure 3.3.1 (c). It is evident that the periodic structure of the nano-pillar arrays creates a bandgap, within which there is an isolated mode at $\Omega_{\mathrm{m}} = 2\pi \times 2.274\,\mathrm{MHz}$. This mode can be driven by light, while the smaller modes in the bandgap do not respond to an amplitude modulation of the light. The Q-factor of the mode at $\Omega_{\mathrm{m}} = 2\pi \times 2.274\,\mathrm{MHz}$ is measured by red-detuning the cavity by multiple cavity linewidths (for which the cavity is locked to the cavity transmission instead of the PDH as error signal) and a probe power of only 20 µW. It should be noted that the membrane resonance may still be broadened by the red-detuned light, which means that the Q-factor given here is only a lower bound. At room-temperature, we measure a Q-factor of $Q_{\mathrm{RT}} = 1.5 \times 10^7$. Going to a temperature of 10 K, the Q-factor increases to $Q_{10\mathrm{K}} = 5.1 \times 10^7$ (shown in figure 3.3.1 (d)).

Mode Imaging by Raster Scan: We can image the spatial shape of the vibrational mode of the membrane in a separate setup (similar to [135]). For this, the membrane is placed in a vacuum chamber (without cavity). A beam of light is focused with an objective lens onto the membrane, which results in a beam waist of 4 µm. An automated 2D-piezo stage is used to move the laser focus across the membrane. At each point, a spectrum of the mechanical displacement in the thermal environment is acquired by homodyne detection of the reflected light (more details are given in [124]). In order to obtain an image of a specific mode, the spectrum is integrated over a bandwidth of 50 kHz around the vibrational frequency of the mode of interest. The image of the defect mode of a nano-pillar membrane is shown in figure 3.3.1 (b).

3.3.2 Cavity Design, Operation in the Cryostat

To enhance the coupling of the membrane vibrations to the light, the membrane is placed in an optical cavity. For this, the membrane is clamped to a titanium mount using only a kapton sheet. It has been

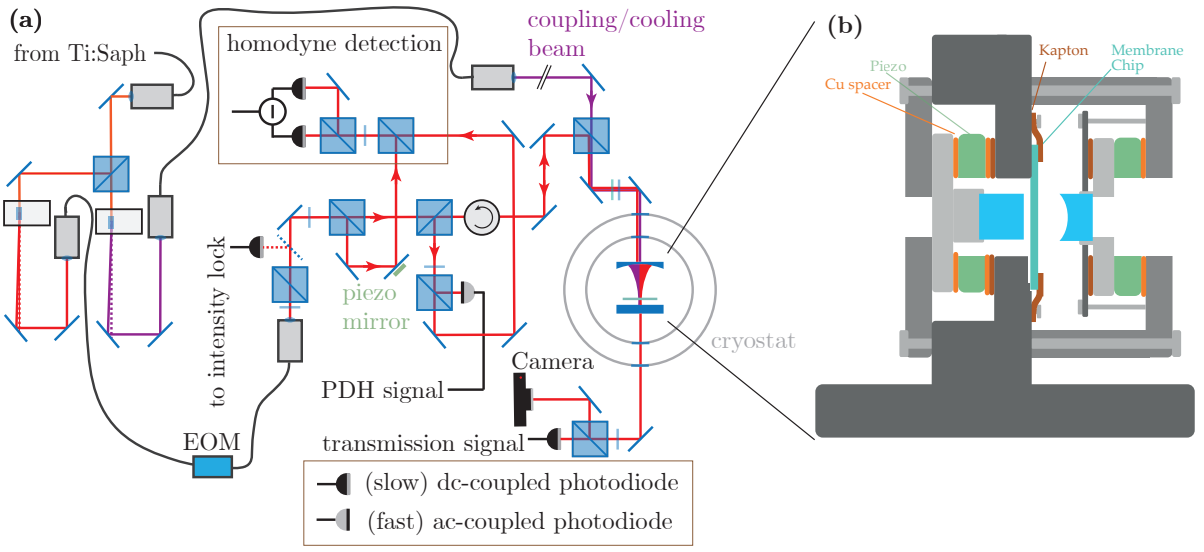

Figure 3.3.2: (a) Laser path of the optomechanical setup. The Ti:Saph laser is split into two parts. One is used as locking beam (right), the other one is used as coupling or cooling beam. The coupling/cooling beam is frequency shifted by 95 MHz for coupling and by 128 MHz for cooling operation with an AOM. It passes the atomic chamber (not shown here, see figure 4.3.1 for more details) and is combined with the locking beam on the last PBS before the cavity. The locking beam is shifted by 100 MHz with an AOM. A fibre coupled electrical optical modulator (EOM) is used to put sidebands at 513 MHz for the PDH lock. The locking beam is intensity stabilised by a PID control on the AOM. After the fibre, the locking beam is split into a local oscillator part (570 µW), which is used for homodyne detection and a cavity arm (10 µW), which is sent to the membrane. The transmission of the cavity is very small and can be used to lock the cavity in transmission. Most of the light is reflected. A small part of the reflected is measured by an ac-photodiode for the PDH lock. The rest is detected in a homodyne detection by mixing it with the local oscillator. (b) Schematic representation of the cavity design. All metallic pieces (in gray) are made out of titanium.

observed that the frame of these nano-pillar membranes is more fragile than those of other membrane types (e.g. described in [124]). Multiple frames have broken when using the brass sheet for clamping. The updated cavity design is shown in figure 3.3.2 (b). As was the case with the phononic bandgap shielded membrane, we use a concave mirror with a reflectivity of $r_1^2 = 0.995$ and a curvature of $R = 30\,\mathrm{mm}$ and a planar mirror with a reflectivity of $r_2^2 = 0.9999$. A further copper spacer is incorporated into the design of the cavity resulting in a length of $L_c = 1.31\,\mathrm{mm}$. For the empty cavity, the finesse is expected to be $\mathcal{F}_0 = 1232$. Upon inserting the membrane, we observe a cavity linewidth of $\kappa = 2\pi \times 94\,\mathrm{MHz}$ (optimised by positioning the membrane) which corresponds to a slightly reduced finesse of $\mathcal{F} = 1177$. The cavity mirrors are glued on a titanium holder on three distinct points using epoxy[6]. The relative position of the membrane in the cavity can be finetuned by positing the mirrors using piezoelectric crystals[7].

The cavity with the membrane is placed in a liquid helium flow cryostat[8]. The chamber is held at low pressure ($< 10^{-7}$mbar) using an ion-getter pump[9]. The titanium cavity is mounted on a cryogenic sample platform, which is cooled by a heat exchanger. The heat exchanger is continuously cooled by a

[6]Temperature stable and vacuum compatible epoxy: Stycast 2850 FT, catalyst 9
[7]Piezomechanik, HPCh 150/15-8/3: maximal stroke: $> 3\,\mu\mathrm{m}$; capacitance: 790 nF
[8]KONTI-Micro from CryoVac GmbH
[9]NEXTorr D100-5 by SAES Getters

liquid helium flow, with the temperature being controlled by a PID feedback on the flow of liquid helium coming from a dewar. Further details of the cryogenic setup are specified in [68].

3.3.3 Characterisation Measurements

In the hybrid experiments and characterisation measurements, the cavity is interfaced with two laser beams with orthogonal linear polarisations. One (weak) beam is used to lock the cavity length, thereby stabilising the detuning of the cavity. The laser path of this locking beam is shown in figure 3.3.2 (a). The membrane signal on this lock beam is used to estimate the vibrational state of the membrane. The other beam (which is used in the main experiment as spin-membrane coupling beam, see section 4.3.1 for further details) is employed here as a cooling or coupling beam. It is combined with the locking beam on the final PBS before the cavity. The beams are in orthogonal polarisations and their cavity reflection is separated with great care. In this configuration, the homodyne detection depicted in figure 3.3.2 (a) only detects the cavity reflection of the locking beam.

The optomechanical setup is characterised by two measurements which are described in the following. In the first measurement, a cooling beam is used to cool the membrane by cavity dynamical backaction cooling. Red sideband cooling to the cavity cooling limit is observed. From the frequency shift and the broadening of the membrane signal, the vacuum optomechanical coupling rate g_0 is calculated. In the second measurement, the optomechanical response of the membrane to a modulation of the input light was measured. From this response, the optomechanical measurement rate and cooperativity are calculated.

Dynamical Backaction Cooling

The membrane-light interface can be characterised by measuring the effect of the dynamical backaction of the light on the membrane. For these dynamical backaction cooling experiments, two beams are used, both derived from the same commercial titanium sapphire laser[10]: The cavity is locked using the PDH lock technique with a weak 12 µW beam close to resonance. The cooling beam is detuned by $-\kappa/\sqrt{12} \approx -2\pi \times 28\,\mathrm{MHz}$ with respect to the locking beam. The two beams are coupled into the cavity with orthogonal linear polarisations. By changing the power of the cooling beam, the mechanical linewidth, mechanical resonance frequency and the occupation of the mechanical mode is altered. The membrane signal is measured by performing a homodyne detection on the locking beam, which is reflected from the cavity (for further details on the calibration of this measurement, please refer to section 3.1.3).

The power spectral density of the measured membrane signal (see figure 3.3.3 (a) for some examples) is fit with a Lorentzian function. Both, the frequency shift and the broadening due to the cooling beam scale linearly with the cooling beam power (shown in figure 3.3.3 (c) and (d)). The vacuum optomechanical coupling rate g_0 can be calculated from both the frequency shift and the optical broadening using formula (3.1.9) and (3.1.10). Having the power of the locking beam and the intrinsic damping rate of the membrane γ_m (from a ringdown measurement), the precise detuning of the locking beam can be evaluated from the broadening of the peak with only the locking beam present, using equation (3.1.10). For this estimation, the vacuum optomechanical coupling rate has to be guessed. It can be adapted iteratively until the calibration is consistent. The measured vacuum optomechanical coupling rates are consistently found to

[10] MSquared SolsTiS 5000 PSX XF laser system

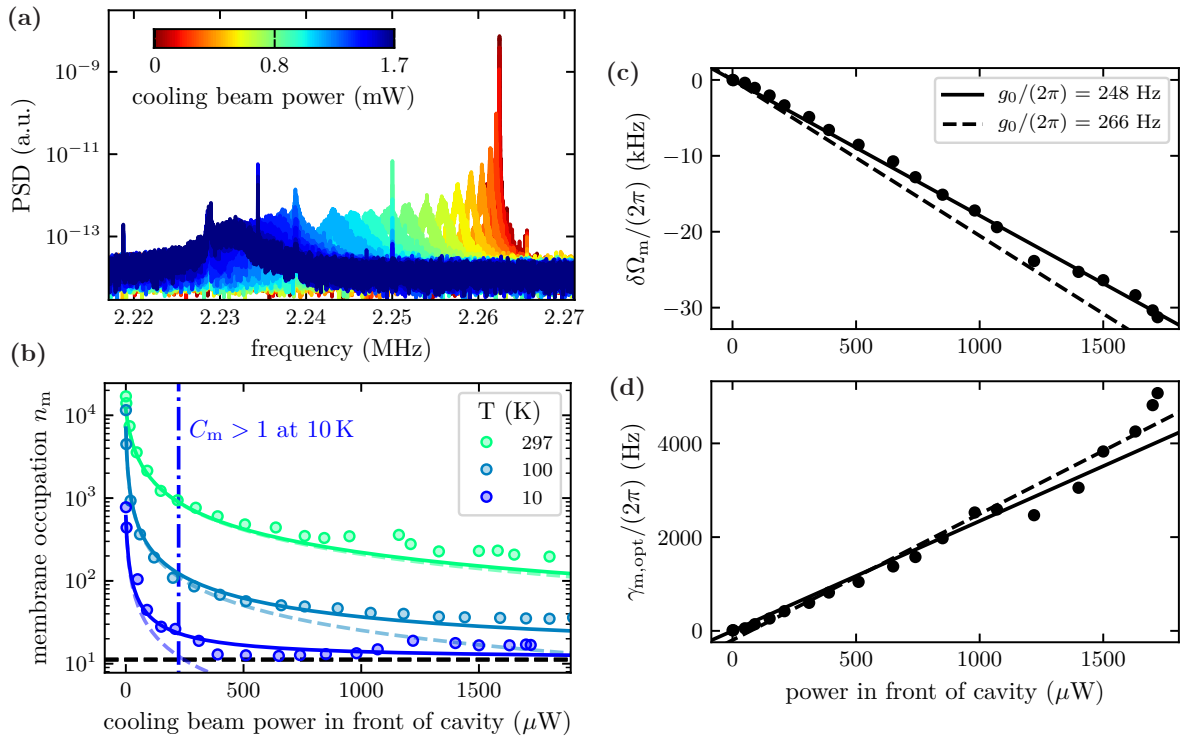

Figure 3.3.3: Dynamical backaction cooling experiment of the membrane: The cavity is locked with a weak beam at a detuning of $\sim -2\pi \times 4\,\mathrm{MHz}$ from the cavity resonance. The cooling beam has a detuning of $-2\pi \times 32\,\mathrm{MHz}$. In (a), some example data is shown (at 10 K cryostat temperature). As the power increases, the membrane occupation is no longer limited by the thermal occupation of the environment, but rather by the backaction of the cooling light. In this regime, the peak areas are not observed to diminish any more with increasing power. In (b), the temperature of the membrane mode is shown for three distinct cryostat temperatures. The theoretical model (given in equation (3.1.12)) without free parameters is plotted as solid line to the data. The dashed lines show the theoretical classical occupation (by neglecting the backaction of the cooling light) in colours while the backaction limit is shown in black. The dash-dotted line indicates at which optical power the cooperativity exceeds one for a cryostat temperature of $T = 10\,\mathrm{K}$. (c) and (d) show the effect of the dynamical backaction on the membrane: (c) shows the frequency shift while (d) depicts the broadening of the membrane in the cavity at 10 K. The data is fit with a linear function to evaluate the vacuum optomechanical coupling strength g_0. The fit to the frequency shift is shown as solid line while the fit to the broadening is shown as a dashed line.

be around $g_0 \approx 2\pi \times 250\,\mathrm{Hz}$ for measurements at different temperatures between room temperature and 10 K.

The membrane temperature can be calculated from the area under the Lorentzian peak with the membrane displacement power spectral density calibrated as described in section 3.1.3. The membrane occupations for three different cryostat temperatures and diverse cooling beam powers are shown in figure 3.3.3 (b). The cavity cooling limit of $n_{\mathrm{opt,min}} = 11$ phonons is approached closely for a cryostat temperature of 10 K. In this regime, the membrane is mainly driven by the backaction of the cooling light and not by thermal noise. A measure of this is the membrane cooperativity, which is greater than one $C_{\mathrm{m}} > 1$ for a mean cooling power in front of the cavity of $P > 224\,\mu\mathrm{W}$ (at a detuning of $\Delta_{\mathrm{c}} \approx -2\pi \times 28\,\mathrm{MHz}$) at 10 K cryostat temperature, assuming thermalisation of the membrane phonon bath at this temperature.

Optomechanical Response Measurement

For the measurement of the optomechanical response of the system, again a weak locking beam (10 µW) is used to lock the cavity with the PDH lock. But now, the second beam is detuned by +5 MHz from the locking beam so that it is closer to the cavity resonance. This coupling beam is amplitude modulated. If the amplitude modulation frequency is resonant with the membrane frequency, it drives the vibrations of the membrane. The displacement of the membrane is imprinted on the phase of the outgoing light. Thus, on the outgoing coupling beam, there is the applied modulation signal on the amplitude quadrature of the light and the membrane response on the phase quadrature of the light. Using homodyne detection, any interference between amplitude and phase can be detected by locking the homodyne detection at different angles (shown in figure 3.3.4 (a) and (b)).

Fitting the signal from different homodyne angles with a global fit directly yields the measurement rate Γ_{m} of the optomechanical system. A derivation of the fit function is shown in [68, 124]. The fitting results are shown in figure 3.3.4 (c).

The measurement rate characterised using this method is the relevant quantity for coupling later the membrane to the atomic spin, because this experiment is very similar to the way how the optomechanical system is included in the spin-membrane coupling (see section 4.2.2 to compare): Here, the light is amplitude modulated by an AOM. In the hybrid experiment, the amplitude of the light is modulated by the spin in concoction with a polarising beam splitter (PBS). The outgoing light is combined with a local oscillator on a PBS to transform the the phase modulation into a polarisation modulation which then again acts on the spin. The detuning and power of the locking and coupling beams are similar in the spin-membrane coupling experiment as for this characterisation measurement. Thus, this measurement actually characterises directly the membrane measurement rate which enters the spin-membrane coupling strength.

From the measurement rate, the linewidth and the cryostat temperature, the membrane cooperativity can be calculated, assuming that the membrane is thermalised to the cryostat temperature. In this particular series of measurements, the quantum cooperativity of the membrane does not exceed one, as shown in figure 3.3.4 (d). However, we can interface the cavity with more optical power so that the cooperativity exceeds one, similar to the cooling experiments shown in figure 3.3.3.

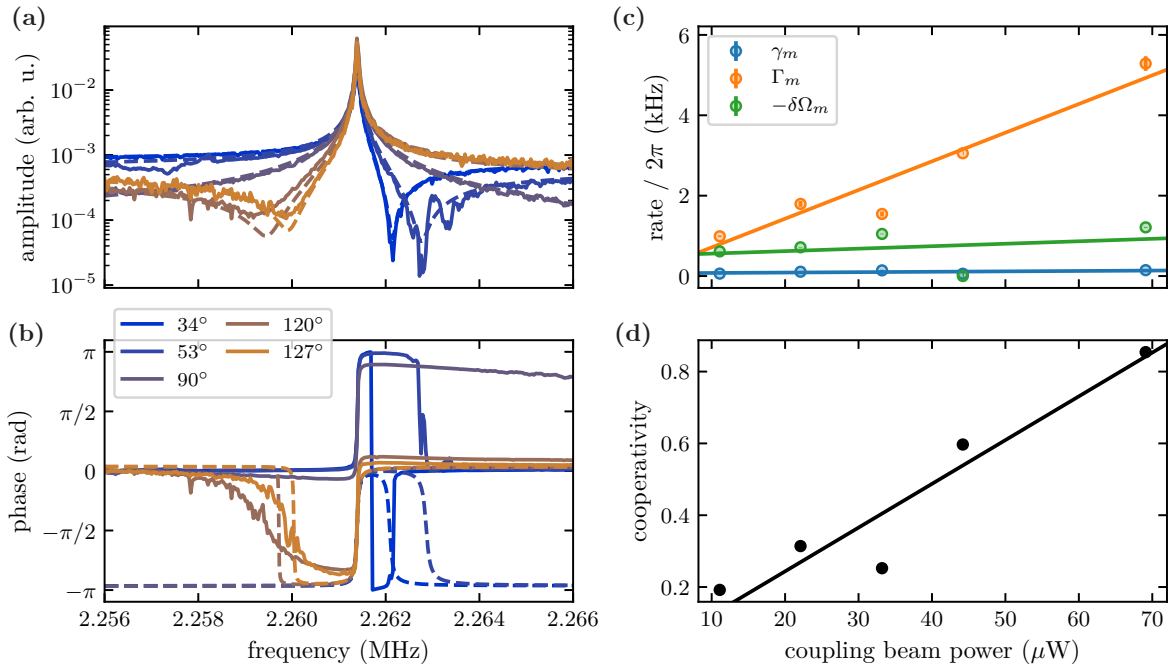

Figure 3.3.4: Optomechanical response measurement of the membrane at a cryostat temperature of 10 K: (a) and (b) show the result for the optomechanical response measurement with 11 µW of probe power for different homodyne angles. Here, an angle of 90° corresponds to the detection of only the phase quadrature of the light with the membrane signal. The solid lines are the measured data and the dashed lines a global fit to the data, using the fit function derived in [68, 124]. (c) shows the fitted measurement rates for different optical powers in the coupling beam. Knowing the Q-factor from a ringdown measurement, we can calculate the thermal decoherence rate at a certain temperature and thus the mechanical cooperativity shown in (d).

3.3.4 Ponderomotive Squeezing

In the previous section, we have seen that the optomechanical system can be operated at high cooperativity. In this regime, the membrane is driven more strongly by the noise of the light than by its thermal environment. Having this control, the membrane can be used to squeeze the state of the light [136, 137]. The mechanism of this so-called ponderomotive squeezing is described in the following:

For a resonantly driven cavity, the amplitude noise of the laser drives the vibrations of the membrane. In our experiment, the laser is shot-noise limited at the membrane frequency. Thus, the membrane is driven by the quantum fluctuations of the amplitude quadrature $\hat{X}_{\mathrm{L}}^{(\mathrm{in})}$ of the light. The membrane vibrations are then mapped onto the phase quadrature of the outgoing light $\hat{P}_{\mathrm{L}}^{(\mathrm{out})}$. The amplitude quadrature of the light remains unchanged. Because the membrane vibrations are driven by the amplitude noise of the laser, the outgoing phase of the light depends on the incoming amplitude noise of the light via the membrane response. Thus, after the interaction with the membrane, there is a correlation between the amplitude and phase quadratures of the light. This correlation can be measured, by performing a homodyne measurement of a mixed quadrature at an angle ϕ. For a cavity in the unresolved sideband regime which is resonantly driven, the symmetrised power spectral density of a homodyne signal $D(\omega)$ is given by [138]

$$\frac{\bar{S}_{DD}(\omega)}{2|\alpha_{\mathrm{LO}}|^2\eta_{\mathrm{det}}} = \frac{1}{2} + 8\Gamma_{\mathrm{m}}|\chi_{\mathrm{m}}(\omega)|^2\Big[(\omega-\Omega_{\mathrm{m}})\sin(\phi)\cos(\phi) + (\Gamma_{\mathrm{m}}+\gamma_{\mathrm{m,th}})\sin^2(\phi)\Big], \tag{3.3.1}$$

where $\chi_{\mathrm{m}}(\omega)$ is the susceptibility of the membrane oscillator, $|\alpha_{\mathrm{LO}}|^2$ the flux of the local oscillator in the homodyne detection and η_{det} the detection efficiency. The derivation of this expression and the formula for the more general case is shown in appendix E. In this equation, the first term accounts for the shot noise of the light. The second term can be negative for $(\omega-\Omega_{\mathrm{m}})\sin(\phi)\cos(\phi) < 0$ for some frequencies, thus part of the spectrum can be below shot noise.

Ponderomotive squeezing of light has previously been demonstrated using silicon nitride membranes [120, 138], including a recent demonstration at room temperature [63]. In our optomechanical setup, the light can be squeezed by 1.5 dB using the membrane in a very broad cavity ($\Omega_{\mathrm{m}}/\kappa = 2.3\times10^{-2}$, significantly broader than the ones reported in [63, 120, 138]). In order to obtain ponderomotive squeezing in our experiment, we use the nano-pillar membrane in a 10 K environment (parameters given in table 3.4.1). The broad cavity is locked by using a weak auxiliary beam. The cavity is coupled with a much stronger, red-detuned beam ($\Delta_{\mathrm{c}} \approx -2\pi\times 40\,\mathrm{MHz}$, $P = 2\,\mathrm{mW}$), which provides some cooling of the membrane. The light reflected from the cavity is measured by homodyne measurement. By setting the phase between the cavity beam and the local oscillator, the measured light quadrature can be defined. The measurement shown in figure 3.3.5 is taken at a very small homodyne angle ($\phi \approx 4.8\times10^{-3}$) so that mostly the amplitude quadrature of the light is measured. The measured quadrature of the light shows squeezing of the light for $\omega > \Omega_{\mathrm{m}}$ and anti-squeezing for $\omega < \Omega_{\mathrm{m}}$. The power spectral density is fitted with the model described in appendix E. From the parameters obtained by the fit, the measurement rate $\Gamma_{\mathrm{m}} = 4n_{\mathrm{c}}g_0^2/\kappa$ and the thermal decoherence rate $\gamma_{\mathrm{m,th}}$ are obtained from which an optomechanical cooperativity of $C_{\mathrm{m}} = 9.00$ is calculated.

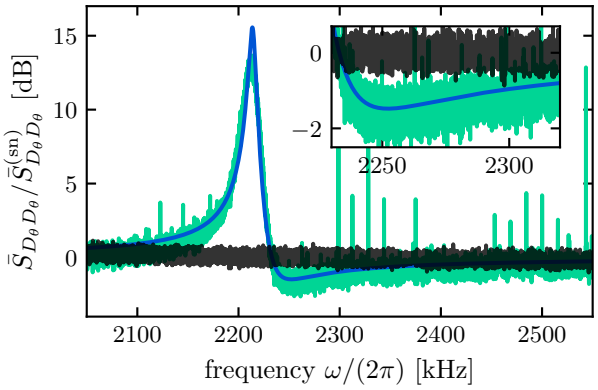

Figure 3.3.5: Result of the ponderomotive squeezing of the light. The ponderomotive squeezing data is shown in green and the shot noise level in black. The data is fitted (blue) with a function similar to equation (3.3.1) but accounts for optical losses and a finite detuning, given in appendix E.

3.4 Summary and Outlook

In this chapter, the optomechanical systems are presented. The characterised parameters for both membranes are summarised in table 3.4.1. The first membrane used in this work was the membrane with phononic bandgap shield. The $(2,2)$-mode of this membrane has a Q-factor of 1.46×10^6 at a frequency of $\Omega_\mathrm{m} = 2\pi \times 1.957\,\mathrm{MHz}$. This membrane was only operated at room temperature because the cavity missaligned when cooling the cryostat. This optomechanical setup was used to show strong coupling to the collective atomic spin [68]. Furthermore, we used this strong coupling to sympathetically cool the membrane oscillator by the *cold* atomic spin, which is presented in chapter 5 and published in [30].

In the course of this thesis, we switched from the phononic bandgap shielded membrane to a nano-pillar membrane. The nano-pillar membrane used in the current set-up provides a ten times higher Q-factor than the phononic bandgap shielded membrane, which lowers the decoherence rate of optomechanical system by a factor of ten. This is an important step towards quantum coherent coupling of the membrane to the atomic spin. The nano-pillar membrane is placed in a new cavity (described in detail in [124]), such that it can be cooled down to 10 K in the cryostat. By operating the membrane at a temperature of 10 K, we demonstrate sideband cooling to the cavity dynamical backaction cooling limit. This quantum coherent control is used to squeeze the light by 1.5 dB using the mechanism of ponderomotive squeezing. In the hybrid experiment, the membrane is interfaced with an effective optical power of 90 µW, for which we obtain a cooperativity of $C_\mathrm{m} = 1.2$, if the membrane environment is cooled to a temperature of 10 K. This level of quantum control over the membrane oscillator in our setup is a good basis to perform hybrid experiments in the quantum coherent regime. In chapter 6 hybrid experiments with the nano-pillar membrane are shown.

There are some ideas to develop the optomechanical system further: It was observed that thermal fluctuations of the cavity mirrors can be a limiting factor for optomechanical experiments in a membrane in the middle configuration [139, 140, 141]. Two approaches have been suggested to address this issue: (1) Use highly reflective, thin SiN-membranes (exoskeleton mirrors) as cavity mirrors. For this, Enzian et al. [142] have patterned the central defect of a soft-clamped membrane with a photonic crystal structure such that the reflectivity of the membrane reached $\sim 99.9\,\%$. Approaching the issue differently, Huang et al. [63] engineered the vibration spectrum of the mirror with phononic crystal structures to suppress

		Phononic Bandgap Shielded	Nano-Pillar
Q-factor at RT	Q_{RT}	1.46×10^6	1.5×10^7
Q-factor at 20 K	$Q_{20\mathrm{K}}$	-	4.2×10^7
Q-factor at 10 K	$Q_{10\mathrm{K}}$	-	5.1×10^7
Membrane frequency	Ω_{m}	$2\pi \times 1.957\,\mathrm{MHz}$	$2\pi \times 2.274\,\mathrm{MHz}$
Cavity linewidth	κ	$2\pi \times 77\,\mathrm{MHz}$	$2\pi \times 94\,\mathrm{MHz}$
Vacuum optomechanical coupling strength	g_0	$2\pi \times 224\,\mathrm{Hz}$	$2\pi \times 248\,\mathrm{Hz}$
Measurement rate (at resp. coupl. beam power)	Γ_{m}	$2\pi \times 7.5\,\mathrm{kHz}$	$2\pi \times 4.1\,\mathrm{kHz}$

Table 3.4.1: Final parameters of optomechanical systems. The measurement rate is given for both systems at the optical power at which the coupling experiments were performed: 110 µW for the phononic bandgap shielded membrane and 90 µW for the nano-pillar membrane.

mirror vibrations at the mechanical frequency. For this, they use a precision circular saw to pattern the macroscopic glass mirror. We have taken first steps to reproduce the phononic bandgap mirrors shown in [63]. For this, we use an automatic dicing saw[11] available in the clean room of the D-BSSE department of the ETH Zürich. Preliminary results show that the mirror coating is not damaged by the sawing procedure with continuous water cooling of the mirror and the cavity built with sawed mirrors has the expected finesse.

One of the major current experimental challenges is the stability of the cavity lock. We believe that low frequency membrane modes are driven by the light and interfere with the cavity lock. This creates instabilities in the lock. It may be interesting to evaluate alternatives to the usual PDH-lock. One option is to detune the locking beam much further from resonance and use the cavity transmission signal for locking. The locking beam would then cool all membrane modes by dynamical backaction cooling, which proved to stabilise the membrane-cavity system. Alternatively, there are experiments in which the membrane vibration spectrum itself is used to generate the error signal [143].

[11] Disco automatic dicing saw, DAD3240. Dicing blade: Miniton, diamond dicing blade 2.25-8-30S21

Chapter 4

Coherent Coupling between an Atomic Spin and an Optomechanical System

---

After introducing the spin and the membrane-light interfaces, in this chapter, the coupling mechanism between the atomic spin and the optomechanical system is introduced. In a first part, the theoretical framework of remote, light-mediated coherent coupling is presented and applied to our systems. In the second part, the experimental implementation of the coupling is shown, including the active stabilisation of the path length of the loop and the double-pass interface of the atomic spin. In the third part of this chapter, the characterisation of the spin oscillator in the coupling configuration is presented.

Some subsections of this chapter have already been published as an appendix of [30].

4.1 Principle of the Coupling Between the Atomic Spin Ensemble and the Nanomechanical Membrane

In this chapter, the coherent coupling between the atomic spin ensemble and the optomechanical system is shown. First, we discuss the theoretical concepts of such a platform, and then we present its experimental implementation and some results. But before going into details, a short summary of the main key aspects is given in this section.

We remotely couple the atomic spin to the vibrations of the membrane. The Hamiltonian interaction between the two systems is mediated by light. In order to mediate a Hamiltonian interaction between two systems, some fundamental conditions have to be fulfilled, which follow directly from the definition of a Hamiltonian interaction. Two of these conditions strongly govern the design of our coupling scheme: (1) A Hamiltonian interaction between two systems must be *bidirectional* and (2) a Hamiltonian interaction describes the evolution of a *closed* system. Both conditions are not automatically fulfilled if the coupling is mediated by a propagating field. Therefore, a special coupling geometry must be implemented to achieve bidirectional and closed interactions mediated by light [37]:

For a bidirectional, light-mediated interaction between the spin and the membrane, light must travel

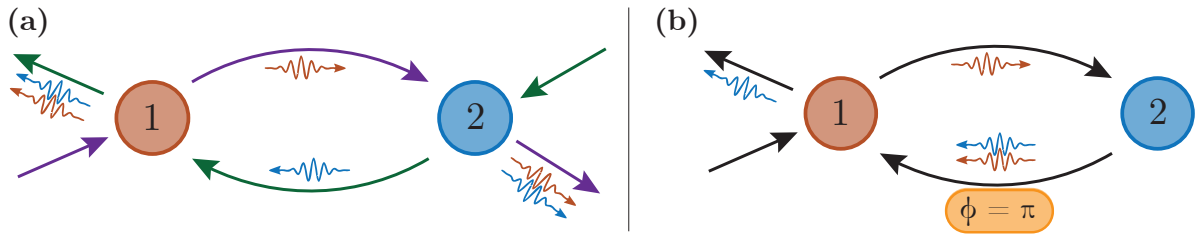

Figure 4.1.1: Two possible coupling schemes for bidirectional coupling: In (a), there are two lasers (purple and green), one going from system 1 to system 2, the other the other way round. The signal from both systems is leaking out of the system (sketched as blue and red wave packets). In the other scheme (b), there is only one laser, which forms a loop geometry. By adequately adjusting the phase ϕ between the first and second interaction of system 1 with the light (see main test), the second interaction is the time reversal of the first interaction, and thus there is no quantum signal of system 1 leaking out to the environment. This scheme is implemented in our experiment.

from the spin to the membrane and from the membrane to the spin. In general, this can be implemented in very different geometries. For example, one can imagine two lasers, one going from the spin to the membrane and the other from the membrane to the spin, as sketched in figure 4.1.1 (a). Alternatively, a single carrier can be considered that interacts first with the spin, then with the membrane, and finally with the spin again, as shown in figure 4.1.1 (b). To choose one of these geometries, the condition of having a closed system imposes some constraints. Signal leaking out of the coupled system leads to decoherence [144] and thus limits the Hamiltonian nature of the interaction between the systems. A way to avoid this signal leakage to the environment is by working in a loop geometry: the light interacts first with the spin, then with the membrane, and finally with the spin again. After the interaction with the membrane, the quantum signal encoded in the light is phase-shifted by $\phi = \pi$. This renders the second interaction with the spin the time reversal of the first one [37]. The signal of the spin on the light is removed by the second interaction. Thus (neglecting optical losses and the propagation delay), there is no spin signal going to the environment, and so the hybrid system is closed for the spin (but open for the membrane). A scheme of such a loop is shown in figure 4.1.2.

Tracing out the optical field, the effective atom-membrane interaction can be written as a Hamiltonian interaction between the systems and a dissipative dynamics of the membrane oscillator. For the moment, we focus on the Hamiltonian interaction. Approximating the spin as a harmonic oscillator (see section 2.7), we can write the effective spin-membrane interaction as

$$\hat{H}_{\text{eff}} = \hbar 2g \hat{X}_{\text{m}} \hat{X}_{\text{s}}. \tag{4.1.1}$$

The loop couples the spin and mechanical quadratures operators $\hat{X}_i$ (defined in sections 2.7 and 3.1.1) with coupling strength $g = \sqrt{4\Gamma_{\text{s}}\Gamma_{\text{m}}}$. Here Γ_i are the rates at which the individual systems interact with the light. When the spin oscillator is tuned in resonance with the membrane, we can apply the rotating wave approximation and neglect some terms of the Hamiltonian. Implementing the spin as a positive frequency oscillator results in a beam-splitter Hamiltonian

$$\hat{H}_{\text{eff,bs}} = \hbar g \left(\hat{b}_{\text{m}}^{\dagger} \hat{b}_{\text{s}} + \hat{b}_{\text{s}}^{\dagger} \hat{b}_{\text{m}} \right). \tag{4.1.2}$$

In the limit of strong coupling $2g > \gamma_{\text{s}} + \gamma_{\text{m}}$ the membrane and spin modes hybridise. Here γ_i is the

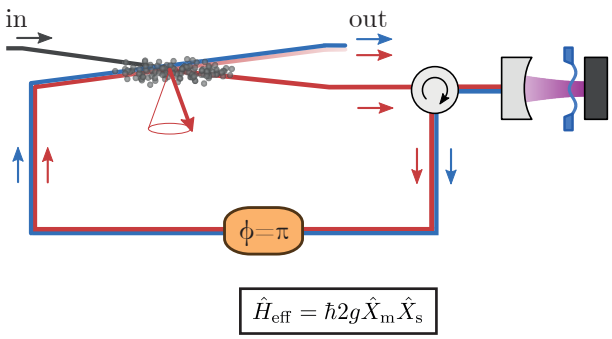

Figure 4.1.2: Coupling geometry in our experimental setup: The light interacts first with the spin, then with the membrane, and finally with the spin again. Between the membrane and the second spin interaction, the quantum signal is phase-shifted by $\phi = \pi$.

linewidth of system i in the presence of the coupling beam. The beam-splitter Hamiltonian can be used for state flips between the spin and the membrane. Since the atomic spin is initialised in a low-entropy state, these state flips can be used to effectively cool the membrane oscillator. This is shown experimentally in chapter 5.

By inverting the magnetic field, the spin actually forms a negative frequency oscillator [29, 123]. With the spin as a negative frequency oscillator, the Hamiltonian, given in equation (4.1.1), can be approximated as a parametric-gain interaction

$$\hat{H}_{\mathrm{eff,pg}} = \hbar g \left(\hat{b}_{\mathrm{m}}\hat{b}_{\mathrm{s}} + \hat{b}_{\mathrm{s}}^{\dagger}\hat{b}_{\mathrm{m}}^{\dagger}\right). \tag{4.1.3}$$

This interaction creates correlations between the two systems. In the limit of quantum coherent coupling $2g > \gamma_{\mathrm{s,dec}} + \gamma_{\mathrm{m,dec}}$, this interaction Hamiltonian can be used to induce entanglement between the spin and the membrane over a distance. Here, $\gamma_{i,\mathrm{dec}}$ is the total decoherence rate of system i, including thermal decoherence and the decoherence induced by backaction noise.

In the following, these interaction Hamiltonians are derived from the theory of cascaded quantum systems [37] (section 4.2). The physical implementation is then described in detail in section 4.3. Finally, some spin calibrations are shown in section 4.4.

4.2 Remote Hamiltonian Interaction Between Two Systems Mediated by Light

4.2.1 Coupling Theory

For the theoretical description of the coupling between the collective spin and the membrane, the theory of cascaded quantum systems is used [145]. In this subsection, the theory for multiple quantum systems coupled in a loop geometry, presented in [37], is reviewed for an arbitrary cascaded scheme before discussing our specific experiment in the next subsections.

We consider that we have several quantum systems that interact with a single bosonic meter (for here, we assume a laser beam) in a cascaded way. The meter travels in one dimension, parametrised by the position coordinate ξ along the propagation of the light, and can be measured at the end after all

interactions. Each system can have multiple interactions with the meter and internal dynamics. For n interactions, the interaction Hamiltonian can be written as

$$H_{\text{int}} = \hbar \sum_{j=1}^{n} \sqrt{2\Gamma_j} \left(\hat{B}_j^\dagger \hat{a}_{\text{L}}(\xi_j) + \hat{a}_{\text{L}}^\dagger(\xi_j) \hat{B}_j \right) \tag{4.2.1}$$

where $\hat{a}_{\text{L}}$ is the continuum annihilation operator of the light field (units of $\text{s}^{-1/2}$), ξ_j is the position coordinate of the interaction, B_j is the corresponding interaction operator of the system at position ξ_j, and Γ_j is the measurement rate of the system by the light field. First, we only consider the dynamics of the systems. For this, we trace out the light field. In the interaction frame, the dynamics of the coupled systems can be written in terms of a propagation operator $\tilde{A}$ and a jump processes $\mathcal{J}$ [37]. The evolution of the spin-mechanical density matrix $\tilde{\rho}$ can then be written as [37, 145]

$$\dot{\tilde{\rho}} = \mathcal{L}[\rho] = -\tilde{A}\tilde{\rho} - \tilde{\rho}\tilde{A}^\dagger + \mathcal{J}\tilde{\rho}, \tag{4.2.2}$$

with

$$\tilde{A} = \sum_j \sum_{k<j} \eta_{jk} \sqrt{4\Gamma_j \Gamma_k} \tilde{B}_j^\dagger(t) \tilde{B}_k(t - \tau_{jk}) + \sum_j \Gamma_j \tilde{B}_j^\dagger(t) \tilde{B}_j(t), \tag{4.2.3}$$

and

$$\begin{aligned} \mathcal{J}\tilde{\rho} = &\sum_j \sum_{k<j} \eta_{jk} \sqrt{4\Gamma_j \Gamma_k} \tilde{B}_k(t - \tau_{jk}) \tilde{\rho} \tilde{B}_j^\dagger(t) + \text{h.c.} \\ &+ \sum_j 2\Gamma_j \tilde{B}_j(t) \tilde{\rho} \tilde{B}_j^\dagger(t). \end{aligned} \tag{4.2.4}$$

Here, the tilde denotes operators in the interaction frame. The time τ_{jk} is the propagation delay of the light from interaction j to k and η_{jk} is the (amplitude) transmission of the light between the interation j and k. To calculate the Gaussian dynamics of a system, we sort the operators in a different way and write the propagation as

$$\dot{\tilde{\rho}} = -\sum_j \sum_{k<j} \eta_{jk} \sqrt{4\Gamma_j \Gamma_k} \left([\tilde{B}_j^\dagger(t), \tilde{B}_k(t - \tau_{jk}) \tilde{\rho}] + \text{h.c.} \right) - \sum_j \Gamma_j \left([\tilde{B}_j^\dagger(t), \tilde{B}_j(t) \tilde{\rho}] + \text{h.c.} \right). \tag{4.2.5}$$

Hamiltonian and Dissipator: The dynamics of the coupled system can be described in the form of the more conventional Master equation in the lab frame [37]

$$\dot{\hat{\rho}} = \frac{1}{\text{i}\hbar} [\hat{H}_{\text{eff}} + \hat{H}_0, \hat{\rho}] + \sum_k \mathcal{D}[\hat{J}_k]\hat{\rho} + \sum_k \mathcal{D}[\hat{J}_{0,k}]\hat{\rho}, \tag{4.2.6}$$

where the effective coupling Hamiltonian is proportional to the imaginary part of the propagator $\hat{A}$,

$$\hat{H}_{\text{eff}} = \frac{\hbar}{2\text{i}} (\hat{A} - \hat{A}^\dagger). \tag{4.2.7}$$

The Hamiltonian $\hat{H}_0$ describes the hermitian dynamics of the individual systems. The Lindblad term reads as $\mathcal{D}[\hat{J}_k]\hat{\rho} = \hat{J}_k \hat{\rho} \hat{J}_k^\dagger - \{\hat{J}_k^\dagger \hat{J}_k, \hat{\rho}\}/2$, where $\{\cdot, \cdot\}$ is the anti-commutator. The Lindblad terms of the

coupled dynamics can be written in form of a dissipator

$$\Lambda_{\text{eff}} := \sum_k \hat{J}_k^\dagger \hat{J}_k = \hat{A} + \hat{A}^\dagger \tag{4.2.8}$$

and a jump process $\mathcal{J}\hat{\rho} = \sum_k \hat{J}_k \hat{\rho} \hat{J}_k^\dagger$. In equation (4.2.6), we added the local decoherence of the systems described by the jump operators $\hat{J}_{0,k}$.

4.2.2 Coupling of the Spin of an Atomic Ensemble to the Vibrations a Membrane

In the previous chapters we have seen that both the vibrations of the membrane and the collective atomic spin couple to the light. But the two systems couple to different quantities of light: The spin couples to the polarisation state of the light while the the membrane vibrations couple to the amplitude and phase quadratures of the light. Therefore, the theory of cascaded systems cannot be applied without a transformation. First, the signal imprinted on the light by the spin has to be converted from the polarisation basis to the amplitude and phase space of the light, and after the interaction with the membrane back to the polarisation basis, so that both systems interact with the adequate quantity of the light. This conversion is done using a polarisation interferometer, as will be shown below. A polarisation interferometer can convert a polarisation modulation into an amplitude modulation and a phase modulation back to a polarisation modulation.

A second challenge for the design of the coupling loop is to interface the spin system twice: The light interacts with the spin system once before and once after the interaction with the optomechanical system. The outgoing light from the two spin-light interactions must be separated using two different modes of the light. The quantum signal is encoded in the polarisation of the light, so we separate the two spin-light interactions by using two different spatial modes of the light.

In this section we will first describe how the optomechanical system is integrated into a polarisation interferometer. This gives us an expression for how the vibrations of the membrane are coupled to the polarisation state of the light outside the polarisation interferometer. In a second step, the spin-light interaction with two different spatial modes is presented. Finally, the theory for cascaded systems is applied to the spin and optomechanical system inside a polarisation interferometer.

Optomechanical System in a Polarisation Interferometer

In our coupling loop, the quantum signal is encoded in the polarisation state of the light. The mechanical oscillator is included in the coupling loop by means of a polarisation interferometer (shown in figure 4.2.1). A polarisation interferometer consists of a first polarising beam splitter (PBS1 in figure 4.2.1) which splits the incoming light into two paths. The polarisation of the incoming light determines the amplitude of the light in each arm of the interferometer. By implementing the optomechanical system in one of the arms, it is coupled to the polarisation basis of the incoming light. On a second PBS (PBS4 in figure 4.2.1), the two arms of the interferometer are recombined. The polarisation of the outgoing light depends on the phase difference of the light in the two arms at this second PBS. The signal from the optomechanical system is imprinted on the phase quadrature of one interferometer arm. This signal on the phase quadrature of one of the interferometer arms is mapped onto the polarisation basis by recombining the two interferometer

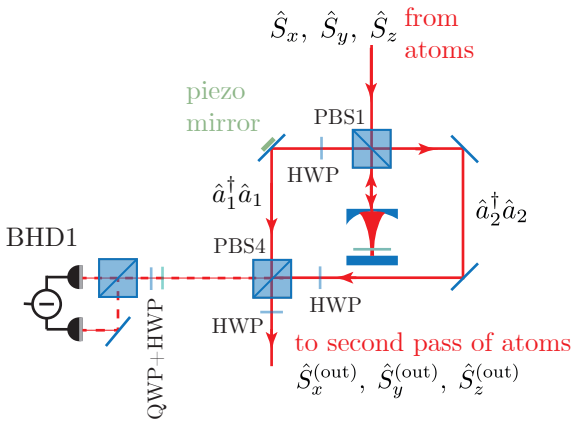

Figure 4.2.1: Polarisation interferometer: The spin signal is imprinted on the light as a polarisation modulation. PBS1 converts the polarisation modulation to an amplitude modulation, which can drive the membrane. The membrane vibrations, on the other hand, are imprinted on the phase quadrature of one interferometer arm, which is then converted into a polarisation modulation by combining the to arms on PBS4. Details are given in section 4.2.2.

arms at the second PBS. In summary, the polarisation interferometer converts the light signal from the polarisation basis to amplitude quadrature and from a phase quadrature back to the polarisation basis.

To understand the polarisation interferometer more quantitatively, we follow the state of the light step by step through the polarisation interferometer (see in figure 4.2.1). The light after the atomic cloud contains the spin signal encoded in the polarisation quadrature $\hat{X}_{\mathrm{L}}^{\mathrm{pol,in}}$ (in the Holstein-Primakov approximation). If we consider that the beam is horizontally polarised (in the experiment it has some angle, which is not considered here for simplicity), the Stokes vectors can be approximated as follows

$$\begin{aligned}
\hat{S}_x &\simeq \hat{S}_0 = \bar{S}_0 + \sqrt{\bar{S}_0}\hat{X}_{\mathrm{H}}^{\mathrm{pol,in}} = \bar{S}_0 + \sqrt{\frac{\bar{S}_0}{2}}\left(\hat{a}_{\mathrm{H}}^{\mathrm{in}\dagger} + \hat{a}_{\mathrm{H}}^{\mathrm{in}}\right), \\
\hat{S}_y &= \sqrt{\bar{S}_0}\hat{X}_{\mathrm{L}}^{\mathrm{pol,in}} = \sqrt{\frac{\bar{S}_0}{2}}\left(\hat{a}_{\mathrm{V}}^{\mathrm{in}\dagger} + \hat{a}_{\mathrm{V}}^{\mathrm{in}}\right), \\
\hat{S}_z &= \sqrt{\bar{S}_0}\hat{P}_{\mathrm{L}}^{\mathrm{pol,in}} = \mathrm{i}\sqrt{\frac{\bar{S}_0}{2}}\left(\hat{a}_{\mathrm{V}}^{\mathrm{in}\dagger} - \hat{a}_{\mathrm{V}}^{\mathrm{in}}\right).
\end{aligned} \tag{4.2.9}$$

where $\hat{X}_H^{\mathrm{pol}}$ is the quantum fluctuation around the mean value of the horizontally polarised input light and $\hat{a}_{\mathrm{H}}^{\mathrm{in}}$ ($\hat{a}_{\mathrm{V}}^{\mathrm{in}}$) is the annihilation operator for horizontally (vertically) polarised photons. Here we use the superscript *pol* to denote the polarisation basis and the subscript L to denote the polarisation quadratures as defined in section 2.7. We want to maximise the coupling between the membrane and the spin. To do this, the polarisation quadrature $\hat{X}_{\mathrm{L}}^{\mathrm{pol,in}}$ must be optimally converted into an amplitude quadrature in the interferometer arms. Similar to polarisation homodyne detection, this can be achieved by balancing the local oscillator at both outputs of the PBS (PBS1 in figure 4.2.1). For this, a half waveplate is placed in front of the polarisation interferometer at an angle θ_{H}. The Stokes vector after the half waveplate is

given by

$$\begin{aligned}\hat{S}'_x &= \hat{S}_x \cos(4\theta_{\mathrm{H}}) + \hat{S}_y \sin(4\theta_{\mathrm{H}}),\\ \hat{S}'_y &= -\hat{S}_y \cos(4\theta_{\mathrm{H}}) + \hat{S}_x \sin(4\theta_{\mathrm{H}}),\\ \hat{S}'_z &= -\hat{S}_z.\end{aligned} \tag{4.2.10}$$

After the first PBS of the interferometer, the light is split into two parts. For the horizontally polarised transmission (going to the optomechanical cavity), we have $\hat{a}_1^\dagger \hat{a}_1 = \hat{a}_{\mathrm{H}}'^\dagger \hat{a}'_{\mathrm{H}} = \hat{S}'_0 + \hat{S}'_x$ and for the vertically polarised reflection we have $\hat{a}_2^\dagger \hat{a}_2 = \hat{S}'_0 - \hat{S}'_x$. We use the fact that we started with a fully horizontally polarised laser beam to write $\hat{a}_{\mathrm{H}} \to \bar{a}_{\mathrm{H}} + \hat{a}_{\mathrm{H}}$ and neglect all terms that do not depend on $\bar{a}_{\mathrm{H}}$. We get

$$\hat{a}_1^\dagger \hat{a}_1 = \hat{S}_0 + \hat{S}_x \cos(4\theta_{\mathrm{H}}) + \hat{S}_y \sin(4\theta_{\mathrm{H}}) \tag{4.2.11}$$

$$\approx \frac{1}{2}\left((1-\cos(4\theta_{\mathrm{H}}))\left(\frac{\phi_{\mathrm{L}}}{2} + \sqrt{\frac{\phi_{\mathrm{L}}}{2}}\hat{X}_H^{\mathrm{pol,in}}\right) + \sin(4\theta_{\mathrm{H}})\sqrt{\frac{\phi_{\mathrm{L}}}{2}}\hat{X}_{\mathrm{L}}^{\mathrm{pol,in}}\right). \tag{4.2.12}$$

where $\Phi_{\mathrm{L}} = |\bar{a}_{\mathrm{H}}|^2 = 2\bar{S}_0$ is the total flux in front of the interferometer. The light in front of the cavity can be described by the classical field $(1-\cos(4\theta_{\mathrm{H}}))\Phi_{\mathrm{L}}/4$ and two quantum fluctuation terms: $\hat{X}_H^{\mathrm{pol,in}}$ describes the amplitude fluctuation of the laser while on $\hat{X}_{\mathrm{L}}^{\mathrm{pol,in}}$ the spin signal is imprinted. For a resonant cavity in the fast cavity limit, we can write the optomechanical interaction Hamiltonian as $\hat{H}_{\mathrm{om}} = \hbar\sqrt{2\Gamma_{\mathrm{m}}/\Phi_{\mathrm{L}}}\hat{a}_1^\dagger \hat{a}_1 \hat{X}_{\mathrm{m}}$. Plugging the expression for $\hat{a}_1^\dagger \hat{a}_1$ in equation (4.2.12) in the optomechanical Hamiltonian, we neglect the constant offset and get

$$\hat{H}_{\mathrm{om}} = \hbar\sqrt{\Gamma_{\mathrm{m}}}\hat{X}_{\mathrm{m}}\left((1-\cos(4\theta_{\mathrm{H}}))\hat{X}_H^{\mathrm{pol,in}} + \sin(4\theta_{\mathrm{H}})\hat{X}_{\mathrm{L}}^{\mathrm{pol,in}}\right). \tag{4.2.13}$$

The membrane is driven by noise in the horizontal input polarisation $\hat{X}_H^{\mathrm{pol,in}}$ and by modulations in the vertical input polarisation $\hat{X}_{\mathrm{L}}^{\mathrm{pol,in}}$. The $\hat{X}_H^{\mathrm{pol,in}}$ quadrature of the input light carries no signal and consists only of laser amplitude noise. Therefore, coupling the membrane to this quadrature only increases the backaction noise acting on the mechanical oscillator. The spin signal is imprinted on the vertical input polarisation $\hat{X}_{\mathrm{L}}^{\mathrm{pol,in}}$. We want to maximise the coupling of the membrane to this light quadrature in order to maximise the effective spin-membrane coupling. To reduce the backaction noise on the membrane, the HWP in front of the interferometer is set so that $(1-\cos(4\theta_{\mathrm{H}}))$ is small. The coupling of the membrane to the light can be described by defining an effective flux of $\Phi_{\mathrm{m}} = \Phi_{\mathrm{L}}\sin(4\theta_{\mathrm{H}})^2/4$ and an effective measurement rate $\Gamma_{\mathrm{m,eff}} = (4g_0/\kappa)^2\,\Phi_{\mathrm{m}}$. Neglecting the noise from the horizontal input polarisation for clarity, we can write

$$\hat{H}_{\mathrm{om}} = \hbar 2\sqrt{\Gamma_{\mathrm{m,eff}}}\hat{X}_{\mathrm{m}}\hat{X}_{\mathrm{L}}^{\mathrm{pol}}. \tag{4.2.14}$$

To summarise the derivation so far: The $\hat{X}_{\mathrm{L}}^{\mathrm{pol}}$ quadrature of the polarisation state (where the spin signal is imprinted) in front of the interferometer couples to the membrane with a modified coupling rate $\Gamma_{\mathrm{m,eff}}$. So far we have only considered how the light drives membrane vibrations, not how the membrane vibrations affects the light. To do this, consider a general polarisation interferometer. If the polarisation in front of the interferometer is given by $\hat{\mathbf{S}}'$, then a polarisation interferometer with a path-length difference of

phase $\Delta\phi$ will change the polarisation of the light according to

$$\begin{aligned}\hat{S}''_x &= \hat{S}'_x,\\ \hat{S}''_y &= \hat{S}'_y\cos(\Delta\phi) + \hat{S}'_z\sin(\Delta\phi),\\ \hat{S}''_z &= -\hat{S}'_z\cos(\Delta\phi) - \hat{S}'_y\sin(\Delta\phi),\end{aligned} \tag{4.2.15}$$

where $\hat{\mathbf{S}}''$ is the output polarisation of the interferometer. In the Stokes vector representation, this corresponds to a rotation around the x-axis. In our experiment, the phase difference $\Delta\phi$ can be actively changed by moving a mirror mounted on a piezo crystal. In addition to the active control, the membrane modulates the phase of the cavity arm by $\delta\hat{\phi}_\mathrm{c} = \hat{P}_\mathrm{L}^\mathrm{pha}/\sqrt{2\Phi_\mathrm{m}}$. Note that the modulation of the cavity is applied to $\hat{P}_\mathrm{L}^\mathrm{pha}$ in the phase space of the light and not to the polarisation state of the light. After the polarisation interferometer, a HWP at an angle θ_H is placed so that the mean polarisation is again along $\hat{S}_x$. The path length difference of the interferometer is actively stabilised to an interferometer phase of $\Delta\phi = 0$ (technical details are given in section 4.3.2). For this interferometer phase we can expand $\sin(\Delta\phi) = \delta\hat{\phi}$ and $\cos(\Delta\phi) = 1$ and get

$$\begin{aligned}\hat{S}_x^{(\mathrm{out})} &= \hat{S}_x - \hat{S}_z\delta\hat{\phi},\\ \hat{S}_y^{(\mathrm{out})} &= \hat{S}_y + \cos(4\theta_\mathrm{H})\hat{S}_z\delta\hat{\phi},\\ \hat{S}_z^{(\mathrm{out})} &= \hat{S}_z - \hat{S}_x\delta\hat{\phi} - \sin(4\theta_\mathrm{H})\hat{S}_y\delta\hat{\phi}.\end{aligned} \tag{4.2.16}$$

The interaction with the membrane mixes the $\hat{S}_y$ and $\hat{S}_z$ Stokes vector components. But this is a small effect because both $\langle\hat{S}_y\rangle = \langle\hat{S}_z\rangle = 0$. Neglecting these terms, we see that the circularly polarised Stokes vector component can be written as

$$\hat{S}_z^{(\mathrm{out})} \approx \hat{S}_z - \hat{S}_x\delta\hat{\phi} \approx \sqrt{\bar{S}_0}\hat{P}_\mathrm{L}^\mathrm{pol,in} + \sqrt{\bar{S}_0}\hat{P}_\mathrm{L}^\mathrm{pha}. \tag{4.2.17}$$

Thus the output phase space quadrature of the cavity $\hat{P}_\mathrm{L}^\mathrm{pha}$ is mapped onto the circular polarisation quadrature $\hat{P}_\mathrm{L}^\mathrm{pol,out}$ (and mixed with the input noise $\hat{P}_\mathrm{L}^\mathrm{pol,in}$). Remember that the vibrations of the membranes are imprinted on the phase of the light $\hat{P}_\mathrm{L}^\mathrm{pha}$ by the optomechanical interaction. This phase is mapped onto the circular polarisation quadrature $\hat{P}_\mathrm{L}^\mathrm{pol,in}$ by the polarisation interferometer, which can act then on the spin via the Faraday interaction.

A Proposal for an Alternative Implementation of the Polarisation Interferometer: In our experiment, the polarisation interferometer is implemented as a free-space interferometer as shown in figure 4.2.1. There are also some proposals to implement it in a more monolithic design: Abbas et al. showed in [146] that using a polarising beam displacer/combiner (implemented by a birefingent crystal) instead of a free-space interferometer, a polarisation interferometer can be built with a much smaller spatial footprint. In their design, the polarising beam displacer creates a small angle between the signal beam and the reference beam (corresponding to the two arms of the interferometer). Both beams are focused by a lens onto the first cavity mirror. One of them is coupled in the cavity while the other is reflected by the first cavity mirror due to its different angle. The beams are recombined at the beam displacer. According to Abbas et al. [146], this design has the advantage of being more robust, lock-free, and providing good mode matching between the recombined beams. In the future, this idea could be considered for our experiment.

Engineering Two Light-Spin Interactions of One Atomic Cloud

In this paragraph, the atom-light interaction Hamiltonian for two spatially modes of the light is introduced. Having two interactions with two different spatial laser modes, requires a re-evaluation of the 3D-Hamiltonian of the spin-light interaction derived in section 2.4. Starting from the spin Hamiltonian for a 3D-spin-light coupling given in equation (2.4.2), we can write a Hamiltonian for an electric field resulting from the superposition of the two input light modes u_{fst} and u_{snd}. For here, we write two Hamiltonians, one for each output mode, namely

$$\hat{H}_{\mathrm{int,fst}} = -\mathrm{i}\hbar\frac{\alpha_1\sqrt{\bar{\Phi}_{\mathrm{L}}}}{2}\sum_j \Big(u_{\mathrm{fst}}(\mathbf{r}_j)(u^*_{\mathrm{fst}}(\mathbf{r}_j)+\eta^2 u^*_{\mathrm{snd}}(\mathbf{r}_j))\hat{a}_{\mathrm{fst}} - u^*_{\mathrm{fst}}(\mathbf{r}_j)(u_{\mathrm{fst}}(\mathbf{r}_j)+\eta^2 u_{\mathrm{snd}}(\mathbf{r}_j))\hat{a}^\dagger_{\mathrm{fst}}\Big)\hat{f}^{(j)}_z, \tag{4.2.18}$$

$$\hat{H}_{\mathrm{int,snd}} = -\mathrm{i}\hbar\frac{\alpha_1\sqrt{\bar{\Phi}_{\mathrm{L}}}}{2}\sum_j \Big(u_{\mathrm{snd}}(\mathbf{r}_j)(u^*_{\mathrm{fst}}(\mathbf{r}_j)+\eta^2 u^*_{\mathrm{snd}}(\mathbf{r}_j))\hat{a}_{\mathrm{snd}} - u^*_{\mathrm{snd}}(\mathbf{r}_j)(u_{\mathrm{fst}}(\mathbf{r}_j)+\eta^2 u_{\mathrm{snd}}(\mathbf{r}_j))\hat{a}^\dagger_{\mathrm{snd}}\Big)\hat{f}^{(j)}_z. \tag{4.2.19}$$

Here, $\hat{a}_{\mathrm{fst}}$ ($\hat{a}_{\mathrm{snd}}$) is the annihilation operator of the light in the first (second) interaction. Furthermore, the amplitude loop transmission for the full loop is given by η^2 (transmission of η on each the spin-membrane and the membrane-spin path). If the loop losses are neglected $\eta = 1$, the two Hamiltonians are symmetric. In general, the coupling Hamiltonians can be simplified by defining $\beta_{\mathrm{fst}} = u^*_{\mathrm{fst}}(u_{\mathrm{fst}} + \eta^2 u_{\mathrm{snd}})$ and $\beta_{\mathrm{snd}} = \eta^2 u^*_{\mathrm{snd}}(u_{\mathrm{fst}} + \eta^2 u_{\mathrm{snd}})$. In the experiment, both spatial modes are Gaussian laser beams which have a small angle relative to the long axis of the atomic cloud (and relative to each other, see figure 4.3.2). The light of the two interactions interferes. With only one laser, $u^*_{\mathrm{fst}}u_{\mathrm{fst}}$ is a real quantity. However, by having a second laser, the resulting mode function β_{fst} is complex. Because of this, a coupling to both quadratures of the light is obtained

$$H_{\mathrm{int},i} = \hbar\alpha_1\sqrt{\bar{S}_0}\sum_j\Big(\hat{P}_{\mathrm{L}}\mathrm{Re}(\beta_i(\mathbf{r}_j)) + \hat{X}_{\mathrm{L}}\mathrm{Im}(\beta_i(\mathbf{r}_j))\Big)\hat{f}^{(j)}_z \tag{4.2.20}$$

where the coupling amplitude are given by the real and imaginary parts of β_i. Thus, in contrast to the single-pass Faraday Hamiltonian, this double-pass Faraday Hamiltonian couples the spin mode to the $\hat{P}_{\mathrm{L}}$ and the $\hat{X}_{\mathrm{L}}$ polarisation quadratures of the light. The coupling to the $\hat{P}_{\mathrm{L}}$ quadrature is the desired coupling because it couples to the membrane in the final experiment and the backaction which is associated with this coupling is well cancelled. The coupling to the $\hat{X}_{\mathrm{L}}$ quadrature is not intended because it does not couple to the membrane. It leads to additional decoherence because the backaction cancellation would require a different loop phase and it also induces to a spin-spin coupling in the loop [68]. For both couplings, we can write an effective measurement rate, similar to equation (2.7.12). It is given by $\tilde{\Gamma}_{\mathrm{s},i,P} = \langle\mathrm{Re}(\beta_i)^2\rangle_{N_{\mathrm{a}}}\Gamma_{\mathrm{s,1D}}$ for the coupling to $\hat{P}_{\mathrm{L}}$ and by $\tilde{\Gamma}_{\mathrm{s},i,X} = \langle\mathrm{Im}(\beta_i)^2\rangle_{N_{\mathrm{a}}}\Gamma_{\mathrm{s,1D}}$ for the coupling to $\hat{X}_{\mathrm{L}}$ where $\Gamma_{\mathrm{s,1D}}$ is the measurement rate for perfect coupling with all atoms in the focus of the laser and $\langle\cdot\rangle_{N_{\mathrm{a}}}$ is the average over all atoms. In the experimental implementation, we observe that $\tilde{\Gamma}_{\mathrm{s},i,X} \ll \tilde{\Gamma}_{\mathrm{s},i,P}$, see section 4.3.4. Therefore, we neglect the coupling of the atomic cloud to the $\hat{X}_{\mathrm{L}}$ polarisation quadrature in the following.

The two passes do not couple to the same spin wave. However, it is crucial for the coupling experiment that the same atoms are addressed twice. Therefore, we have to make sure that the overlap between the

two spin waves is large. The overlap can be defined by

$$\eta_{\mathrm{ol}} = 1 - \frac{|\sum_j \left(\mathrm{Re}(\beta_{\mathrm{fst}}(\mathbf{r}_j)) - \mathrm{Re}(\beta_{\mathrm{snd}}(\mathbf{r}_j))\right)|}{N_{\mathrm{a}}(\langle \mathrm{Re}(\beta_{\mathrm{fst}})\rangle_{N_{\mathrm{a}}} + \langle \mathrm{Re}(\beta_{\mathrm{snd}})\rangle_{N_{\mathrm{a}}})}. \tag{4.2.21}$$

Cascaded Theory for Our Spin-Membrane System

Having coupled the vibrations of the membrane to the polarisation state of the light by using a polarisation interferometer, we can describe the spin-membrane interaction in the formalism of cascaded systems given in [37] and reviewed in section 4.2.1. Our cascaded system consists of three interactions: First the light interacts with the spin, then with the membrane and finally again with the spin. We have seen that the coupling of the spin to the light in the Holstein-Primakov approximation is given by (compare to equation (2.7.9))

$$\hat{H}_{\mathrm{spin,eff}} = \hbar\sqrt{2\Gamma_{\mathrm{s}}}\hat{X}_{\mathrm{s}}\mathrm{i}(\hat{a}_{\mathrm{L}}^{\dagger} - \hat{a}_{\mathrm{L}}), \tag{4.2.22}$$

where the spin measurement rate Γ_{s} is given by $\tilde{\Gamma}_{\mathrm{s,fst},P}$ for the first spin-light interaction and by $\tilde{\Gamma}_{\mathrm{s,snd},P}$ for the second spin-light interaction, as described above. For simpplicity, we assume in the following that the coupling rates are identical and omit the extra-indices. The membrane-light interface is described by the Hamiltonian (given in equation (4.2.14))

$$\hat{H}_{\mathrm{om,eff}} = \hbar\sqrt{2\Gamma_{\mathrm{m,eff}}}\hat{X}_{\mathrm{m}}(\hat{a}_{\mathrm{L}}^{\dagger} + \hat{a}_{\mathrm{L}}). \tag{4.2.23}$$

In the following, the extra index *eff* is omitted for simplicity. Here the two interaction Hamiltonians are rearranged into the form of the terms in the interaction Hamiltonian given by equation (4.2.2). In our experiment, the light interacts first with the spin and then with the membrane. After the interaction with the membrane, the quantum signal is phase-shifted by π. This phase shift can be accounted for by changing the sign of the third interaction. Writing the interaction in terms of the $\tilde{B}_j$ defined in equation (4.2.1), we have $\tilde{B}_1 = \mathrm{i}\tilde{X}_{\mathrm{s}}$, $\tilde{B}_2 = \tilde{X}_{\mathrm{m}}$ and $\tilde{B}_3 = -\mathrm{i}\tilde{X}_{\mathrm{s}}$. For the following derivations, we assume that the delay and the losses are the same on both paths, i.e. $\tau_{12} = \tau_{23} = \tau$ and $\eta_{12} = \eta_{23} = \eta$. This yields a propagator for the dynamics

$$\begin{aligned}\hat{A} = {} & \mathrm{i}\eta\sqrt{4\Gamma_{\mathrm{s}}\Gamma_{\mathrm{m}}}\left[\tilde{X}_{\mathrm{s}}(t)\tilde{X}_{\mathrm{m}}(t-\tau) + \tilde{X}_{\mathrm{m}}(t)\tilde{X}_{\mathrm{s}}(t-\tau)\right] \\ & + 2\Gamma_{\mathrm{s}}\left[\tilde{X}_{\mathrm{s}}(t)\tilde{X}_{\mathrm{s}}(t) - \eta^2\tilde{X}_{\mathrm{s}}(t)\tilde{X}_{\mathrm{s}}(t-2\tau)\right] + \Gamma_{\mathrm{m}}\tilde{X}_{\mathrm{m}}(t)\tilde{X}_{\mathrm{m}}(t).\end{aligned} \tag{4.2.24}$$

Assuming that the propagation delay of the light is shorter than any dynamics of the oscillator other than the oscillator frequency (i.e. $\tau \ll \gamma_j^{-1}, g^{-1}, |\delta^{-1}|$ where $\delta = \Omega_{\mathrm{s}} - \Omega_{\mathrm{m}}$), we can approximate

$$\tilde{X}_i(t-\tau) \approx \tilde{X}_i\cos(\Omega_i\tau) - \tilde{P}_i\sin(\Omega_i\tau). \tag{4.2.25}$$

In the interaction frame, the quadratures of the oscillators are given by $\tilde{X}_j = (\hat{b}_j^{\dagger}e^{\mathrm{i}\Omega_i t} + \hat{b}_j e^{-\mathrm{i}\Omega_i t})/\sqrt{2}$. The membrane is always a positive frequency oscillator, while the sense of oscillation of the spin can be changed by changing the relative orientation of the magnetic field. Applying the rotating wave approximation this results in two different interaction Hamiltonians. These two Hamiltonians are discussed in the following two sections. Moreover, dissipative coupled dynamics can be implemented by setting the loop phase to $\phi \neq \pi$ [29] which is not discussed here. Some examples for dynamics with a loop phase of $\phi \neq \pi$ are given in appendix G.

4.2.3 Beam-Splitter Hamiltonian

Assuming that the spin forms a positive frequency oscillator, the effective Hamiltonian can be simplified to

$$\begin{aligned}\hat{H}_{\mathrm{eff,bs}} = &\hbar g(\hat{b}_{\mathrm{s}}^{\dagger}\hat{b}_{\mathrm{m}} + \hat{b}_{\mathrm{m}}^{\dagger}\hat{b}_{\mathrm{s}})\cos(\bar{\Omega}\tau)\cos(\delta\,\tau/2)\\ &- \mathrm{i}\hbar g(\hat{b}_{\mathrm{s}}^{\dagger}\hat{b}_{\mathrm{m}} - \hat{b}_{\mathrm{m}}^{\dagger}\hat{b}_{\mathrm{s}})\cos(\bar{\Omega}\tau)\sin(\delta\,\tau/2),\end{aligned} \tag{4.2.26}$$

where the detuning between the systems is given by $\delta = \Omega_{\mathrm{s}} - \Omega_{\mathrm{m}}$, the mean oscillator frequency by $\bar{\Omega} = (\Omega_{\mathrm{s}} + \Omega_{\mathrm{m}})/2$, and the coupling rate by $g = \eta\sqrt{4\Gamma_{\mathrm{s}}\Gamma_{\mathrm{m}}}$. The coupling rate g of the beam-splitter Hamiltonian depends on the measurement rate of both systems and the optical losses. The Hamiltonian interaction is reduced by any delay in the loop. It is also interesting to note that there is an asymmetry in δ. Depending on the sign of the detuning δ, this leads to a damping or a driving force. If the delay and the losses of the loop are neglected, the simplified expression given in section 4.1 is obtained. The dissipator of the system reads as

$$\begin{aligned}\hat{\Lambda}_{\mathrm{eff,bs}} = &4\Gamma_{\mathrm{s}}\left(\hat{b}_{\mathrm{s}}^{\dagger}\hat{b}_{\mathrm{s}} + \frac{1}{2}\right)\left(1 - \eta^2\cos(2\Omega_{\mathrm{s}}\tau)\right)\\ &+ 2\Gamma_{\mathrm{m}}\left(\hat{b}_{\mathrm{m}}^{\dagger}\hat{b}_{\mathrm{m}} + \frac{1}{2}\right),\end{aligned} \tag{4.2.27}$$

where the first term describes the imperfect cancellation of the backaction acting on the spin due to delay and optical losses and the second line is the backaction acting on the membrane. Since there is no cancellation of the membrane signal in the loop, there is a dissipative term for the membrane that remains independent of the detuning and the delay.

Time Evolution of the Coupled System

After discussing the Hamiltonian and the dissipator of the coupled system, the equations of motion for the spin and the membrane oscillator are written to give further insight into the dynamics of the coupled system (derived from [37]). We include the oscillator dynamics of each individual system and obtain

$$\dot{\hat{X}}_{\mathrm{s}} = \Omega_{\mathrm{s}}\hat{P}_{\mathrm{s}} - \frac{\gamma_{\mathrm{s}}}{2}\hat{X}_{\mathrm{s}} + \sqrt{\gamma_{\mathrm{s}}}\hat{X}_{\mathrm{s}}^{(\mathrm{th})}, \tag{4.2.28}$$

$$\begin{aligned}\dot{\hat{P}}_{\mathrm{s}} = &-\Omega_{\mathrm{s}}\hat{X}_{\mathrm{s}} - \frac{\gamma_{\mathrm{s}}}{2}\hat{P}_{\mathrm{s}} + \sqrt{\gamma_{\mathrm{s}}}\hat{P}_{\mathrm{s}}^{(\mathrm{th})} - 2g\hat{X}_{\mathrm{m}}(t-\tau)\\ &+ \sqrt{4\Gamma_{\mathrm{s}}}\left(-\hat{P}_{\mathrm{in}}(\xi_1) + \eta^2\hat{P}_{\mathrm{in}}(\xi_3)\right) - \sqrt{4\Gamma_{\mathrm{s}}}\sqrt{1-\eta^4}\hat{P}^{(\nu)},\end{aligned} \tag{4.2.29}$$

$$\dot{\hat{X}}_{\mathrm{m}} = \Omega_{\mathrm{m}}\hat{P}_{\mathrm{m}}, \tag{4.2.30}$$

$$\dot{\hat{P}}_{\mathrm{m}} = -\Omega_{\mathrm{m}}\hat{X}_{\mathrm{m}} - \gamma_{\mathrm{m}}\hat{P}_{\mathrm{m}} + \sqrt{2\gamma_{\mathrm{m}}}\hat{P}_{\mathrm{m}}^{(\mathrm{th})} - 2g\hat{X}_{\mathrm{s}}(t-\tau) - \sqrt{4\Gamma_{\mathrm{m}}}\eta\hat{X}_{\mathrm{in}}(\xi_2) - \sqrt{4\Gamma_{\mathrm{m}}}\sqrt{1-\eta^2}\hat{X}^{(\nu)}. \tag{4.2.31}$$

For simplicity, the time is given as an explicit argument only for the terms for which the time is shifted by some propagation delay. The first terms in each line are the dynamics of the individual oscillators (oscillation, decay and noise associated with the decay). The thermal noise enters the spin system symmetrically on both quadratures. For the membrane, only the P-quadrature is driven by thermal noise. In this section, the linewidth of the systems γ_i is the effective linewidth in presence of the coupling beam (and for the membrane the locking beam). If the membrane is pre-cooled and broadened by

the beams, γ_m has to be substituted by $\gamma_\mathrm{m,opt}$. The light-mediated coupling between the two systems enters into the dynamics of the P-quadratures of both systems as $2g\hat{X}_\mathrm{s/m}(t-\tau)$. Here, the coupling is delayed and can therefore lead for $\tau \neq 0$ to more complicated dynamics such as instabilities (see below). In addition to the coupling term, each oscillator is driven stochastically by the quantum noise of the coupling light, which is taken into account by the terms containing $\hat{P}_\mathrm{in}$ and $\hat{X}_\mathrm{in}$. For these terms, ξ_i notes the position coordinate in the loop at the interaction i. The light interacts once with the membrane at the position coordinate ξ_2 and twice with the spin, at the position coordinates ξ_1 and ξ_3. If the delay is small enough (i.e. $\tau \ll \gamma_j^{-1}, g^{-1}, |\delta^{-1}|$), the optical noise drives effectively two different quadratures of the spin and we can write

$$\dot{\hat{X}}_\mathrm{s} = ... + \sqrt{4\Gamma_\mathrm{s}}\eta^2 \sin(2\Omega_\mathrm{s}\tau)\hat{P}_\mathrm{in}(\xi_1), \tag{4.2.32}$$

$$\dot{\hat{P}}_\mathrm{s} = ... - \sqrt{4\Gamma_\mathrm{s}}\left(1-\eta^2\cos(2\Omega_\mathrm{s}\tau)\right)\hat{P}_\mathrm{in}(\xi_1). \tag{4.2.33}$$

For short propagation delays $\tau\Omega_\mathrm{s} \ll \pi$, the input noise is partially cancelled for the spin. How well it is cancelled depends on the losses in the loop and the loop delay. The last terms in equations (4.2.28) to (4.2.31) consider the vacuum noise due to the optical losses in the loop, which are modelled as an optical beam splitters. The noise generated by the losses in the loop drives the oscillators stochastically.

Strong coupling between the oscillators is achieved when the coupling rate between the oscillators g is greater than the mean of the linewidths of the oscillators, i.e. $2g > \gamma_\mathrm{s}+\gamma_\mathrm{m}$. In the strong coupling regime, a state swap can be performed at a faster rate than the mean decay rate of the oscillators. However, the rate at which the oscillators are driven by noise may still be greater. To perform a state swap of a quantum state, the coupling rate between the oscillators must be larger than the rate at which noise drives the system. In order to quantify this, we take a closer look at the noise processes that drive the systems: The correlators of the noise operators are defined as

$$\langle\hat{P}_i^{(\mu)}(t)\hat{P}_i^{(\mu)}(t')\rangle = \langle\hat{X}_i^{(\mu)}(t)\hat{X}_i^{(\mu)}(t')\rangle = \left(\bar{n}_i+\frac{1}{2}\right)\delta(t-t'), \tag{4.2.34}$$

$$\langle\hat{P}_i^{(\mu)}(t)\hat{X}_i^{(\mu)}(t')\rangle = -\langle\hat{X}_i^{(\mu)}(t)\hat{P}_i^{(\mu)}(t')\rangle = \frac{\mathrm{i}}{2}\delta(t-t'), \tag{4.2.35}$$

where $\mu \in \{\nu, \mathrm{th}\}$ and $i \in \{\mathrm{s}, \mathrm{m}, \mathrm{in}\}$. For the thermal noise operators $\bar{n}_i$ is the occupation of the local thermal environment. If the membrane is cooled by a second beam, the thermal occupation of the environment $\bar{n}_\mathrm{th}$ must be substituted by the effective membrane occupation n_fin (see section 3.1.2 for details). For the optical input noise we assume a vacuum state in the X and P quadratures, i.e. $\bar{n}_\mathrm{in} = 0$.

For clarity, we rewrite the equation of motion again in a different form and combine all the noise terms into a single driving force term. We get the very common form of two, driven and coupled oscillators

$$\ddot{\hat{X}}_\mathrm{s} + \gamma_\mathrm{s}\dot{\hat{X}}_\mathrm{s} + \Omega_\mathrm{s}^2\hat{X}_\mathrm{s} = -2g\Omega_\mathrm{s}\hat{X}_\mathrm{m}(t-\tau) + \Omega_\mathrm{s}\hat{\mathcal{F}}_\mathrm{s}, \tag{4.2.36}$$

$$\ddot{\hat{X}}_\mathrm{m} + \gamma_\mathrm{m}\dot{\hat{X}}_\mathrm{m} + \Omega_\mathrm{m}^2\hat{X}_\mathrm{m} = -2g\Omega_\mathrm{m}\hat{X}_\mathrm{s}(t-\tau) + \Omega_\mathrm{m}\hat{\mathcal{F}}_\mathrm{m}. \tag{4.2.37}$$

The stochastic driving forces are given by

$$\hat{\mathcal{F}}_\mathrm{s} = \sqrt{2\gamma_\mathrm{s}}\hat{P}_\mathrm{s}^{(\mathrm{th})} - \sqrt{4\Gamma_\mathrm{s}}\left(\hat{P}_\mathrm{in}(1-\eta^2\cos(2\Omega_\mathrm{s}\tau)) + \mathrm{i}\hat{P}_\mathrm{in}\eta^2\sin(2\Omega_\mathrm{s}\tau)\right) - \sqrt{4\Gamma_\mathrm{s}}\sqrt{1-\eta^4}\hat{P}^{(\nu)}, \tag{4.2.38}$$

$$\hat{\mathcal{F}}_\mathrm{m} = \sqrt{2\gamma_\mathrm{m}}\hat{P}_\mathrm{m}^{(\mathrm{th})} - \sqrt{4\Gamma_\mathrm{m}}\eta\hat{X}_\mathrm{in} - \sqrt{4\Gamma_\mathrm{m}}\sqrt{1-\eta^2}\hat{X}^{(\nu)}. \tag{4.2.39}$$

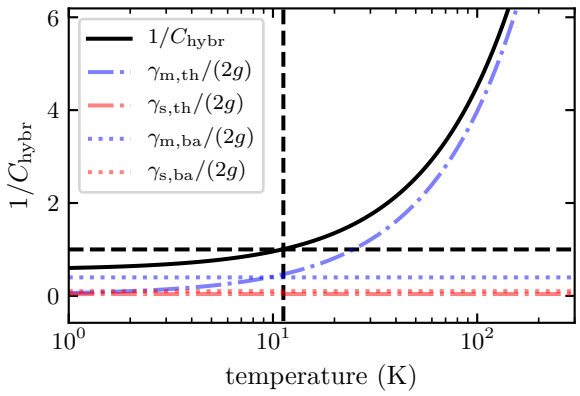

Figure 4.2.2: Calculation of the inverse hybrid cooperativity for different environment temperatures of the membrane. For high temperatures, the thermal noise on the membrane limits the cooperativity (dashed-dotted blue line). For lower temperatures, the backaction noise on the membrane starts to limit the cooperativity (dotted blue line). The backaction noise on the spin (dotted red line) is small because it is cancelled. At a temperature of 10 K, the cooperativity is given by $C_{\mathrm{hybr}} = 1.27$. The detuning of the light from the spin resonance is $\Delta = -30\,\mathrm{GHz}$. The calculation parameters are given in table 4.2.1.

The stochastic driving terms of the spin and the membrane are uncorrelated. Thus, for the simulation, we can assume that both oscillators are driven by uncorrelated, stochastic forces. We can simulate the noise by just one random, normalised variable per oscillator[1] multiplied by a weight, which is a sum over all prefactors of the different noise driving sources. The simulation of the coupled system is described in appendix F. The total decoherence rate of the systems can be written as the sum of all the noise terms, i.e. $\gamma_{i,\mathrm{dec}} = \langle \hat{\mathcal{F}}_i^\dagger(t)\hat{\mathcal{F}}_i(t)\rangle/2$. This is the rate at which noise enters the systems. For quantum coherent coupling of the spin and the membrane, the coupling constant g has to be larger than the mean decoherence rates of both systems $\gamma_{\mathrm{s,dec}}$ and $\gamma_{\mathrm{m,dec}}$. For our hybrid interface, we can define a (quantum) cooperativity $C_{\mathrm{hybr}} = 2g/(\gamma_{\mathrm{s,dec}} + \gamma_{\mathrm{m,dec}})$ [34, 68]. Figure 4.2.2 shows the hybrid cooperativity for a realistic set of parameters given in table 4.2.1. The main constraint on the cooperativity is the thermal noise driving the membrane oscillator at high temperatures and the backaction noise acting on the membrane at lower temperatures.

Power Spectral Density of the Coupled Oscillators

It is illustrative to calculate the spectrum of the coupled oscillators. For strong spin-membrane coupling, the modes hybridise to common modes, which can be observed in the spectrum. Experimental data for these hybrid modes are shown in figure 5.3.1 (b). To derive the effective susceptibilities for both oscillators, the Fourier transform of the equations of motion (4.2.36) and (4.2.37) are calculated,

$$\chi_{\mathrm{m},0}(\omega)^{-1}\hat{X}_{\mathrm{m}}(\omega) + 2g\,\mathrm{e}^{\mathrm{i}\omega\tau}\hat{X}_{\mathrm{s}}(\omega) = -\hat{\mathcal{F}}_{\mathrm{m}}(\omega), \tag{4.2.40}$$

$$\chi_{\mathrm{s},0}(\omega)^{-1}\hat{X}_{\mathrm{s}}(\omega) + 2g\,\mathrm{e}^{\mathrm{i}\omega\tau}\hat{X}_{\mathrm{m}}(\omega) = -\hat{\mathcal{F}}_{\mathrm{m}}(\omega), \tag{4.2.41}$$

[1] We assume a normalised, white noise variable $\eta(t)$ (units of $\mathrm{s}^{-1/2}$) with $\langle\eta(t)\rangle = 0$ and $\langle\eta(t)\eta(t')\rangle = \delta(t-t')$.

Parameter		Value
Membrane Oscillator Frequency	Ω_m	$2\pi \times 2.274\,\mathrm{MHz}$
Membrane Oscillator Measurement Rate	Γ_m	$2\pi \times 3.5\,\mathrm{kHz}$
Membrane Oscillator Linewidth	γ_m	$2\pi \times 44\,\mathrm{mHz}$
Membrane Locking Beam Detuning	$\Delta_\mathrm{c,lock}$	$-2\pi \times 7\,\mathrm{MHz}$
Membrane Locking Beam Power	P_lock	$10\,\mu\mathrm{W}$
Membrane Coupling Beam Detuning	$\Delta_\mathrm{c,coup}$	$-2\pi \times 2\,\mathrm{MHz}$
Membrane Coupling Beam Power	P_cav	$200\,\mu\mathrm{W}$
Membrane Optical Broadening	$\gamma_\mathrm{m,opt}$	$2\pi \times 22\,\mathrm{Hz}$
Membrane Effective Thermal Occupation at 10 K	n_fin	104
Membrane Thermal Decoherence Rate	$\gamma_\mathrm{m,th}$	$2\pi \times 4.1\,\mathrm{kHz}$
Spin Oscillator Frequency	Ω_s	$2\pi \times 2.274\,\mathrm{MHz}$
Spin Oscillator Measurement Rate	Γ_s	$2\pi \times 1.5\,\mathrm{kHz}$
Spin Oscillator Linewidth	γ_s	$2\pi \times 800\,\mathrm{Hz}$
Loop Losses	η	0.9
Loop Delay	τ	15 ns
Loop Phase	ϕ	π
Coupling Rate	g	$2\pi \times 3.4\,\mathrm{kHz}$

Table 4.2.1: Typical set of parameters for the hybrid experiment. The optical broadening $\gamma_\mathrm{m,opt}$ of the membrane is caused by the weak, red-detuned cavity lock beam. The interaction with this second laser beam leads to some pre-cooling of the membrane oscillator, which can be considered by defining an effective membrane occupation n_fin. For the calculations in this chapter, the optical broadened membrane with $\gamma_\mathrm{m,opt}$ and n_fin is considered.

where the bare susceptibility of each oscillator is defined as

$$\chi_{i,0}(\omega) = \frac{\Omega_i}{\Omega_i^2 - \omega^2 - \mathrm{i}\omega\gamma_i}. \tag{4.2.42}$$

Solving for $\hat{X}_\mathrm{m}$ and $\hat{X}_\mathrm{s}$ yields

$$\hat{X}_\mathrm{m}(\omega) = \chi_{m,\mathrm{eff}}(\omega)\big[-\hat{\mathcal{F}}_\mathrm{m}(\omega) + 2g\,\mathrm{e}^{\mathrm{i}\omega\tau}\chi_{\mathrm{s},0}(\omega)\hat{\mathcal{F}}_\mathrm{s}(\omega)\big], \tag{4.2.43}$$

$$\hat{X}_\mathrm{s}(\omega) = \chi_{\mathrm{s},\mathrm{eff}}(\omega)\big[-\hat{\mathcal{F}}_\mathrm{s}(\omega) + 2g\,\mathrm{e}^{\mathrm{i}\omega\tau}\chi_{\mathrm{m},0}(\omega)\hat{\mathcal{F}}_\mathrm{m}(\omega)\big], \tag{4.2.44}$$

where the effective susceptibilities of the membrane and spin oscillators are introduced as

$$\chi_{\mathrm{m},\mathrm{eff}}(\omega)^{-1} = \chi_{\mathrm{m},0}(\omega)^{-1} - 4g^2\mathrm{e}^{\mathrm{i}2\omega\tau}\chi_{\mathrm{s},0}(\omega), \tag{4.2.45}$$

$$\chi_{\mathrm{s},\mathrm{eff}}(\omega)^{-1} = \chi_{s,0}(\omega)^{-1} - 4g^2\mathrm{e}^{\mathrm{i}2\omega\tau}\chi_{\mathrm{m},0}(\omega). \tag{4.2.46}$$

We used this model to fit the power spectral densities of the mechanical displacement spectra (see figure 5.3.1 (b)) using as the fit function $a^2|\chi_{m,\mathrm{eff}}(\omega)|^2$ where a is a global scaling factor accounting for the noise terms driving the system.

Sympathetic Cooling of the Membrane: The thermal environment of the two oscillators differs stongly from one another. While the membrane is clamped to a mount that is in thermal contact with the environment, the thermal bath of the spin is given by the light and is therefore assumed to be in the ground state $\bar{n}_\mathrm{s} = 0$. The coupling between the spin and the membrane can be used to sympathetically cool the membrane. In this paragraph, the derivation of the sympathetic cooling rate for the mechanical oscillator in the limit of a broad spin oscillator $\gamma_\mathrm{s} > g$ is shown. To do this, we first write the equation (4.2.45) explicitly

$$\chi_{\mathrm{m},\mathrm{eff}}(\omega)^{-1} = \frac{1}{\Omega_\mathrm{m}}\left(\Omega_\mathrm{m}^2 - \omega^2 - \mathrm{i}\omega\gamma_\mathrm{m} - 4g^2\mathrm{e}^{\mathrm{i}2\omega\tau}\frac{\Omega_\mathrm{m}\Omega_\mathrm{s}\left(\Omega_\mathrm{s}^2 - \omega^2 + \mathrm{i}\omega\gamma_\mathrm{s}\right)}{\left(\Omega_\mathrm{s}^2 - \omega^2\right)^2 + \left(\omega\gamma_\mathrm{s}\right)^2}\right). \tag{4.2.47}$$

To evaluate the cooling rate, the broadening of the membrane oscillator due to the interaction with the collective spin is calculated. Extracting the cooling rate from the broadening of a single oscillator is a simple model that is only valid if the spin-membrane modes are not hybridised, i.e. in the weak coupling limit $\gamma_\mathrm{s} + \gamma_\mathrm{m} > 2g$. In the strong coupling limit, a more sophisticated calculation of the membrane steady state is required. However, in the weak coupling limit, the effective susceptibility can be written in the form of a harmonic oscillator with modified frequency and broadening

$$\chi_{\mathrm{m},\mathrm{eff}}(\omega)^{-1} = \frac{1}{\Omega_\mathrm{m}}\left[\Omega_\mathrm{m}^2 - \delta\Omega_\mathrm{shift}^2 - \omega^2 - \mathrm{i}\omega\left(\gamma_\mathrm{m} + \gamma_\mathrm{sym}\right)\right]. \tag{4.2.48}$$

Here, we have defined an effective frequency shift $\delta\Omega_\mathrm{shift}$ and the sympathetic cooling rate γ_sym. In general $\delta\Omega_\mathrm{shift}$ and γ_sym depend on the frequency ω, but in the limit of a broad spin oscillator, i.e. $\gamma_s > g$, the effective frequency shift and the sympathetic cooling rate can be evaluated at the membrane resonance

frequency $\omega = \Omega_\mathrm{m}$ and obtain

$$\delta\Omega^2_\mathrm{shift} = \frac{4g^2\Omega_\mathrm{m}\Omega_\mathrm{s}}{\left(\Omega_\mathrm{s}^2 - \Omega_\mathrm{m}^2\right)^2 + \left(\Omega_\mathrm{m}\gamma_\mathrm{s}\right)^2}\left[\left(\Omega_\mathrm{s}^2 - \Omega_\mathrm{m}^2\right)\cos\left(2\Omega_\mathrm{m}\tau\right) - \Omega_\mathrm{m}\gamma_\mathrm{s}\sin\left(2\Omega_\mathrm{m}\tau\right)\right], \tag{4.2.49}$$

and

$$\gamma_\mathrm{sym} = \frac{4g^2\Omega_m\Omega_s}{\left(\Omega_s^2 - \Omega_m^2\right)^2 + \left(\Omega_m\gamma_s\right)^2}\left[\gamma_s\cos\left(2\Omega_m\tau\right) + \frac{\Omega_s^2 - \Omega_m^2}{\Omega_m}\sin\left(2\Omega_m\tau\right)\right]. \tag{4.2.50}$$

For $\Omega_\mathrm{s} \approx \Omega_\mathrm{m}$, the expressions for the frequency shift and sympathetic cooling rate is further simplified to

$$\delta\Omega^2_\mathrm{shift} \approx \frac{4g^2\Omega_\mathrm{m}}{4\delta^2 + \gamma_\mathrm{s}^2}\left[2\delta\cos\left(2\Omega_\mathrm{m}\tau\right) - \gamma_\mathrm{s}\sin\left(2\Omega_\mathrm{m}\tau\right)\right], \tag{4.2.51}$$

$$\gamma_\mathrm{sym} \approx \frac{4g^2}{4\delta^2 + \gamma_\mathrm{s}^2}\left[\gamma_\mathrm{s}\cos\left(2\Omega_\mathrm{m}\tau\right) + 2\delta\sin\left(2\Omega_\mathrm{m}\tau\right)\right]. \tag{4.2.52}$$

In this simplified expression, the maximum cooling rate is reached for $\gamma_\mathrm{s} \to 0$. But in this limit, the spin-membrane modes are hybridised and the approximation to evaluate the cooling rate at $\omega = \Omega_\mathrm{m}$ fails. Further calculations show that the best cooling rate for a system without propagation delay $\tau = 0$ is obtained for $\gamma_\mathrm{s} = 2g$ (see figure 5.4.2 (a) for data and simulation results).

Normal Modes

The eigenmodes of the coupled systems can be found by solving the equations of motion for the normal mode frequencies and damping rates. This is more easily done in the rotating wave approximation at the centre frequency $\bar{\Omega} = (\Omega_\mathrm{m} + \Omega_\mathrm{s})/2$. From the eigenvalue analysis, we get

$$\Omega_\pm + \mathrm{i}\frac{\gamma_\pm}{2} = \bar{\Omega} + \mathrm{i}\frac{\gamma_\mathrm{m} + \gamma_\mathrm{s}}{4} \pm \sqrt{\left(\frac{\delta}{2} + \mathrm{i}\frac{\gamma_\mathrm{m} - \gamma_\mathrm{s}}{4}\right)^2 + g^2\mathrm{e}^{\mathrm{i}2\bar{\Omega}\tau}}. \tag{4.2.53}$$

In the very simple case of no propagation delay $\tau = 0$ and resonance $\delta = 0$, the frequency splitting between the modes is exactly $\Delta\Omega = 2\sqrt{g^2 + (\gamma_\mathrm{m} - \gamma_\mathrm{s})^2/16} \approx 2g$ and the damping of the two modes are symmetrical $\gamma_\pm = (\gamma_\mathrm{m} + \gamma_\mathrm{s})/2$. For large detunings $|\delta| > g$, one of the modes will have the characteristics of the spin oscillator and the other the characteristics of the membrane oscillator. Thus, in this limit, the two systems are decoupled. If there is a propagation delay, the two modes start to be asymmetric even at resonance. For small delays $\Omega_\mathrm{m}\tau > \pi/2$, the anti-symmetric mode Ω_+,γ_+ is driven and the symmetric mode Ω_-,γ_- is damped by the propagation delay. For some parameters, one of the decay rates becomes negative. At this point, the spin-membrane system becomes unstable and is driven to large amplitudes. The stability of a system can be evaluated with the Routh-Hurwitz criterion from control theory. This is done in the next subsection.

Routh-Hurwitz Stability Criterion of the Coupled System

In classical physics, coupling two oscillators with a delay can lead to unstable dynamics [147]. This is similar for the spin-membrane system [67]. As in classical physics, the delay in our hybrid experiment can cause instabilities in the coupled system. The stability of our spin-membrane system can be analysed by applying the Routh-Hurwitz criterion from control theory to our linearly coupled spin-membrane

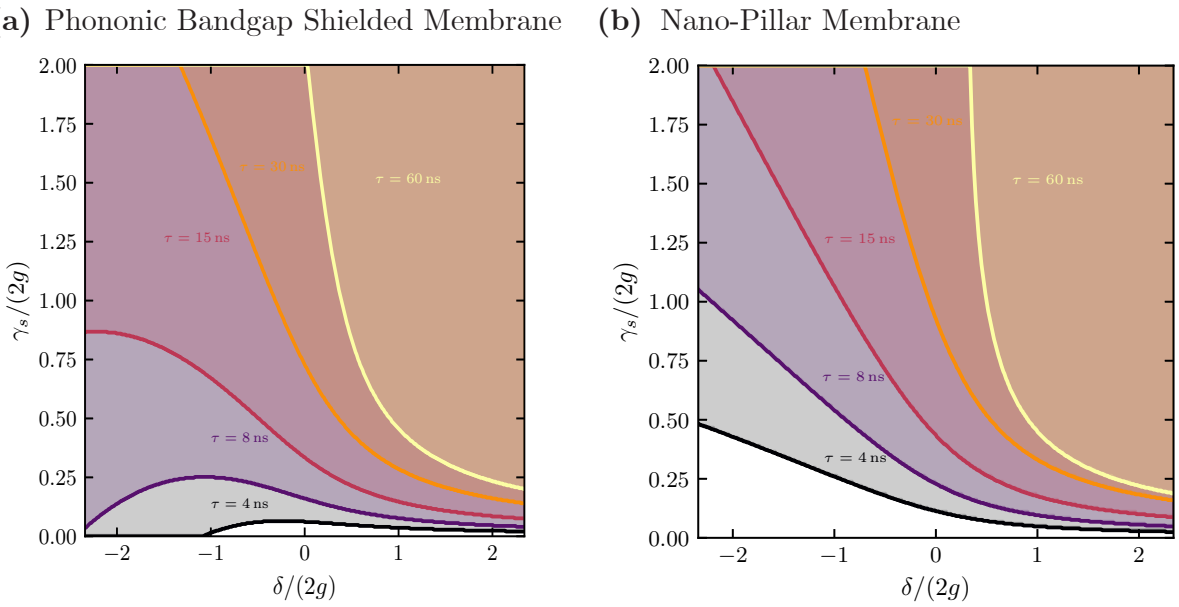

Figure 4.2.3: Evaluation of the stability of the coupled system using the Routh-Hurwitz criterion: The coloured regions (i.e. the region above each solid line) show the sets of parameters for which the coupled dynamics is stable for a given value of the propagation delay τ. Without propagation delay, any set of detuning $\delta = \Omega_\mathrm{s} - \Omega_\mathrm{m}$ and spin damping rate γ_s leads to stable dynamics. (a) shows the stability of the loop with the phononic bandgap shielded membrane for the experimental parameters described in chapter 5. For $\tau = 60\,\mathrm{ns}$ we have $\Omega_\mathrm{m}\tau \approx 0.75$, so the validity of the Taylor expansion of the exponential function in the presence of small delays reaches its limit. For the stability estimations shown here, we used $2g = 2\pi \times 6.8\,\mathrm{kHz}$, $\gamma_\mathrm{m} = 2\pi \times 262\,\mathrm{Hz}$, and $\Omega_\mathrm{m} = 2\pi \times 1.957\,\mathrm{MHz}$. (b) shows the stability for the parameters for the nano-pillar membrane given in table 4.2.1. Because of the larger frequency and reduced membrane linewidth, the system is less stable than the one with the photonic bandgap membrane.

oscillators. The criterion provides a convenient means of assessing the stability of a linear system without solving the equations of motion [147]. In this treatment, the Langevin noise is excluded, as we are interested in whether the dynamics of the delayed coupled oscillator dynamics is stable by itself. We then explore the experimental parameter space to see under what conditions the coupled system becomes unstable.

We take the equations of motion for the delayed coupled system equations (4.2.36) and (4.2.37), neglecting the noise terms and substituting the ansatz $\hat{X}_j(t) = \hat{X}_j(s)\,\mathrm{e}^{st}$ where $s \in \mathbb{C}$ yields

$$\left(s^2 + s\gamma_\mathrm{m} + \Omega_\mathrm{m}^2\right)\hat{X}_\mathrm{m}(s) = -2g\Omega_\mathrm{m}\,\mathrm{e}^{-s\tau}\hat{X}_\mathrm{s}(s), \tag{4.2.54}$$

$$\left(s^2 + s\gamma_\mathrm{s} + \Omega_\mathrm{s}^2\right)\hat{X}_\mathrm{s}(s) = -2g\Omega_\mathrm{s}\,\mathrm{e}^{-s\tau}\hat{X}_\mathrm{m}(s). \tag{4.2.55}$$

Solving the simultaneous equations (4.2.54) and (4.2.55), we obtain the characteristic equation for non-trivial solutions $\hat{X}_\mathrm{m} \neq 0$,

$$\left(s^2 + s\gamma_\mathrm{m} + \Omega_\mathrm{m}^2\right)\left(s^2 + s\gamma_\mathrm{s} + \Omega_\mathrm{s}^2\right) - 4g^2\Omega_\mathrm{m}\Omega_\mathrm{s}\,\mathrm{e}^{-2s\tau} = 0. \tag{4.2.56}$$

We consider here small propagation delays $\tau \ll 1/\Omega_j$ and apply a first-order Taylor expansion $\exp(-2s\tau) \approx (1 - 2s\tau)$ (in the actual simulation shown in figures 4.2.3 and 5.4.2 we keep the terms

up to 4th order). We then obtain

$$\begin{aligned} 0 = {} & s^4 + (\gamma_\mathrm{s} + \gamma_\mathrm{m})s^3 + (\Omega_\mathrm{m}^2 + \Omega_\mathrm{s}^2 + \gamma_\mathrm{m}\gamma_\mathrm{s})s^2 \\ & + (\Omega_\mathrm{s}^2\gamma_\mathrm{m} + \Omega_\mathrm{m}^2\gamma_\mathrm{s} + 8g^2\Omega_\mathrm{m}\Omega_\mathrm{s}\tau)s \\ & + \Omega_\mathrm{m}\Omega_\mathrm{s}(\Omega_\mathrm{m}\Omega_\mathrm{s} - 4g^2). \end{aligned} \tag{4.2.57}$$

Having the spin-membrane dynamics in this polynomial form, we can define the polynomial coefficients of a fourth order polynomial by

$$p(s) = a_4 s^4 + a_3 s^3 + a_2 s^2 + a_1 s + a_0 = 0,\ a_4 > 0. \tag{4.2.58}$$

In order to apply the Routh-Hurwitz criterion, the so-called Hurwitz matrix, which contains the polynomial coefficients, has to be defined [147]. For a fourth order polynomial, this matrix reads

$$H_4 = \begin{pmatrix} a_3 & a_1 & 0 & 0 \\ a_4 & a_2 & a_0 & 0 \\ 0 & a_3 & a_1 & 0 \\ 0 & a_4 & a_2 & a_0 \end{pmatrix}. \tag{4.2.59}$$

According to the Routh-Hurwitz criterion, the system dynamics are asymptotically stable if all the principal minors of the Hurwitz matrix are non-zero and positive. Applying the Hurwitz criterion gives to the following stability criteria for a fourth-order polynomial system

$$\Delta_1 = a_3 > 0, \tag{4.2.60}$$

$$\Delta_2 = \begin{vmatrix} a_3 & a_1 \\ a_4 & a_2 \end{vmatrix} = a_2 a_3 - a_4 a_1 > 0, \tag{4.2.61}$$

$$\Delta_3 = \begin{vmatrix} a_3 & a_1 & 0 \\ a_4 & a_2 & a_0 \\ 0 & a_3 & a_1 \end{vmatrix} = a_1\Delta_2 - a_3^2 a_0 > 0, \tag{4.2.62}$$

$$\Delta_4 = \det(H_4) = a_0 \cdot \Delta_3 > 0. \tag{4.2.63}$$

For the spin-membrane system, the coefficients are given explicitly by

$$a_4 = 1, \tag{4.2.64}$$

$$a_3 = \gamma_\mathrm{s} + \gamma_\mathrm{m}, \tag{4.2.65}$$

$$a_2 = \Omega_\mathrm{s}^2 + \Omega_\mathrm{m}^2 + \gamma_\mathrm{s}\gamma_\mathrm{m}, \tag{4.2.66}$$

$$a_1 = \gamma_\mathrm{m}\Omega_\mathrm{s}^2 + \gamma_\mathrm{s}\Omega_\mathrm{m}^2 + 8g^2\Omega_\mathrm{m}\Omega_\mathrm{s}\tau, \tag{4.2.67}$$

$$a_0 = \Omega_\mathrm{s}\Omega_\mathrm{m}\left(\Omega_\mathrm{s}\Omega_\mathrm{m} - 4g^2\right). \tag{4.2.68}$$

Since $\Omega_\mathrm{s}\Omega_\mathrm{m} \gg 4g^2$, all coefficients a_i are positive. So the criterion Δ_1 is fulfilled and the criterion Δ_4 depends directly on the criterion Δ_3. Therefore, only Δ_2 and Δ_3 remain to be checked.

In order to check Δ_2 and Δ_3, we can explicitly calculate them and then expand the expression in terms of Ω_s, Ω_m. Because the oscillation frequencies Ω_s, Ω_m are orders of magnitudes larger than any

other dynamics, we only look at the terms of highest order of Ω_s, Ω_m. But thereby, we have to consider that τ is a very small number and that $\tau\Omega_{\mathrm{s,m}} \approx 0.1$. Therefore, each τ *reduces* the order of a term by one again. Doing this, we obtain the following expansion for Δ_2

$$\Delta_2 = \Omega_\mathrm{m}^2(\gamma_\mathrm{m}+\gamma_\mathrm{s}) + \Omega_\mathrm{m}(2\gamma_\mathrm{s}\delta - 8g^2\tau\Omega_\mathrm{m}) + \left(\gamma_\mathrm{m}\gamma_\mathrm{s}(\gamma_\mathrm{m}+\gamma_\mathrm{s}) + \gamma_\mathrm{s}\delta^2 - 8g^2\delta\tau\Omega_\mathrm{m}\right). \tag{4.2.69}$$

Here, the first term is clearly much larger than the second and the third. Therefore, we only have to consider the first term for our estimation. Because the first term is always positive (for our system), $\Delta_2 > 0$ and thus, only Δ_3 remains to be checked. Here, we only write the leading term $\propto \Omega_\mathrm{m}^2$, because the full expression is lengthy and can be evaluated easily if needed (and all other terms are much smaller)

$$\Delta_3 \approx \Omega_\mathrm{m}^2\left(16g^2(\bar{\gamma}^2 + \delta\Delta\gamma\tau\Omega_\mathrm{m}) + (\bar{\gamma}^2+\delta^2)(4\bar{\gamma}^2 - \Delta\gamma^2) - 64g^2\tau^2\Omega_\mathrm{m}^2\right). \tag{4.2.70}$$

Here we define $\bar{\gamma} = (\gamma_\mathrm{m}+\gamma_\mathrm{s})/2$ and $\Delta\gamma = \gamma_\mathrm{s} - \gamma_\mathrm{m}$. The last term of this expression is always negative. Thus, the first two terms must compensate it for the system to be stable. The second term is always positive and maximum if the decay rate of both systems is balanced. The first term is the most interesting one: Assumed that $\gamma_\mathrm{s} > \gamma_\mathrm{m}$ (which is our experimental situation), $\delta\Delta\gamma\tau\Omega_\mathrm{m} > 0$ for $\delta > 0$ and therefore the stability is increased and $\delta\Delta\gamma\tau\Omega_\mathrm{m} < 0$ for $\delta < 0$ which makes the system more unstable. This gives the observed asymmetry with respect to the detuning δ which relies on the asymmetry of the decay rates. If there is no optical delay, the system is stable for all experimentally feasible parameter sets.

In order to get an intuition about the stability for different parameters, figure 4.2.3 shows the stable regions as a function of spin damping rate γ_s, detuning δ and delay τ. In figure 4.2.3, one can clearly see that the stability is not symmetric with respect to the detuning δ. The system becomes more unstable as the delay τ and the coupling strength g are increased.

4.2.4 Parametric-Gain Hamiltonian

In the last section, the coupling of the membrane to a positive frequency spin oscillator was discussed. Alternatively, the spin can be implemented as a negative frequency oscillator, which gives rise to very different coupled dynamics. By inverting the magnetic field, the direction of rotation of the Larmor precession changes. Applying the Holstein-Primakov approximation, the effective spin oscillator rotates counter-clockwise in the phase space instead of clockwise (see section 2.7). If the spin frequency is tuned into resonance with the membrane oscillator $\Omega_\mathrm{s} \approx -\Omega_\mathrm{m}$, the rotating wave approximation can be applied to the propagator given in equation (4.2.24) and we yield an interaction Hamiltonian

$$\begin{aligned}\hat{H}_{\mathrm{eff,pg}} = {}& \hbar g(\hat{b}_\mathrm{s}\hat{b}_\mathrm{m} + \hat{b}_\mathrm{m}^\dagger\hat{b}_\mathrm{s}^\dagger)\cos(\bar{\Omega}\tau)\cos(\delta\,\tau/2) \\ & - \mathrm{i}\hbar g(\hat{b}_\mathrm{s}\hat{b}_\mathrm{m} - \hat{b}_\mathrm{m}^\dagger\hat{b}_\mathrm{s}^\dagger)\cos(\bar{\Omega}\tau)\sin(\delta/2\,\tau),\end{aligned} \tag{4.2.71}$$

where the detuning between the systems is given by $\delta = |\Omega_\mathrm{s}| - \Omega_\mathrm{m}$, the mean frequency by $\bar{\Omega} = (|\Omega_\mathrm{s}| + \Omega_\mathrm{m})/2$, and the coupling rate $g = \eta\sqrt{4\Gamma_\mathrm{s}\Gamma_\mathrm{m}}$. This is the Hamiltonian of a two-mode squeezing interaction between the two systems. The hybrid interaction creates correlations between the spin oscillator and the membrane oscillator. The rate g at which these correlations are created is the same as the coupling rate of the beam-splitter interaction described in the last section. Again, the prefactor of the Hamiltonian dynamics is reduced by the delay and losses in the loop. If the delay and the losses of the loop are neglected, we obtain the simplified expression given in section 4.1. The dissipator of the system is the

same as for the beam-splitter interaction

$$\hat{\Lambda}_{\mathrm{eff,bs}} = 4\Gamma_{\mathrm{s}}\left(\hat{b}_{\mathrm{s}}^{\dagger}\hat{b}_{\mathrm{s}} + \frac{1}{2}\right)\left(1 - \eta^2\cos(2\Omega_{\mathrm{s}}\tau)\right) + 2\Gamma_{\mathrm{m}}\left(\hat{b}_{\mathrm{m}}^{\dagger}\hat{b}_{\mathrm{m}} + \frac{1}{2}\right), \tag{4.2.72}$$

where the first term describes the imperfect cancellation of the backaction acting on the spin due to the delay and the second line arises due to the quantum backaction acting on the membrane. Since there is no cancellation of the membrane signal, there is a dissipative term for the membrane that remains independent of the detuning and the propagation delay.

Solving the Covariance Dynamics

The hybrid system can be effectively approximated as a coupling between two harmonic oscillators, which are assumed to be in a Gaussian state. If the atomic spin and the membrane are modelled as Gaussian states, the systems can be fully described in terms of the first and second momentum of $\hat{X}_i$ and $\hat{P}_i$ [148]. The equations of motion for the second momentum can be used to quantify correlations between the two systems [37] and thus to witness entanglement between the spin and the membrane oscillator.

Short Summary on Gaussian Dynamics: Before calculating the Gaussian dynamics of our system, the relevant equations of motion for a general Gaussian state are given below. If the Hamiltonian of a system contains only linear and quadratic terms and the jump operators of the system are linear in canonical operators, then the master equation of a system can be written in the form [149]

$$\dot{\hat{\rho}} = -\sum_{k,j} K_{jk}[\hat{Q}_j(t), \hat{Q}_k(t)\rho] + \mathrm{h.c.} \tag{4.2.73}$$

where K is a matrix containing the coupling rates, and $\hat{Q}_i$ are hermitian operators with the commutation relations $[\hat{Q}_i, \hat{Q}_j] = \mathrm{i}J_{ij}$, where J is a square matrix. The first moments of the system can be written as a vector $\bar{\mathbf{Q}}$. The symmetric covariance matrix is defined as follows

$$\bar{C}_{kl} = \frac{1}{2}\langle \hat{Q}_k\hat{Q}_l + \hat{Q}_l\hat{Q}_k\rangle - \langle\hat{Q}_k\rangle\langle\hat{Q}_l\rangle. \tag{4.2.74}$$

With the mean values $\bar{\mathbf{Q}}$ and the covariance matrix $\bar{C}$, the Gaussian state is completely described. The equation of motion of the mean values can be written as

$$\frac{\mathrm{d}}{\mathrm{d}t}\bar{\mathbf{Q}} = F\bar{\mathbf{Q}} \tag{4.2.75}$$

and the propagation of the covariance matrix is given by the Lyapunov equation [37]

$$\frac{\mathrm{d}}{\mathrm{d}t}\bar{C} = F\bar{C} + \bar{C}F + N, \tag{4.2.76}$$

where the drift matrix is defined by $F = 2J\mathrm{Im}(K)$ and the diffusion matrix by $N = J\mathrm{Re}(K + K^T)J^T$ [149].

Gaussian Dynamics of the Hybrid System: In equation (4.2.5), the master equation for the cascaded system is already expressed in the form of equation (4.2.73). Thus the entries of K can be read off directly. In the following, the system operator is defined as $\hat{\mathbf{Q}} = (\hat{X}_\mathrm{m}, \hat{P}_\mathrm{m}, \hat{X}_\mathrm{s}, \hat{P}_\mathrm{s})$. The the parameter matrix is given by

$$K = K_\mathrm{int} + K_\mathrm{osc} \tag{4.2.77}$$

with

$$K_\mathrm{int} = \begin{pmatrix} \Gamma_\mathrm{m} & 0 & \mathrm{i}g\cos(\Omega_\mathrm{s}\tau) & \mathrm{i}g\sin(\Omega_\mathrm{s}\tau) \\ 0 & 0 & 0 & 0 \\ \mathrm{i}g\cos(\Omega_\mathrm{m}\tau) & \mathrm{i}g\sin(\Omega_\mathrm{m}\tau) & 2\Gamma_\mathrm{s}(1-\eta^2\cos(2\Omega_\mathrm{s}\tau)) & \eta^2\Gamma_\mathrm{s}\sin(2\Omega_\mathrm{s}\tau) \\ 0 & 0 & 0 & 0 \end{pmatrix}, \tag{4.2.78}$$

$$K_\mathrm{osc} = \begin{pmatrix} \mathrm{i}\Omega_\mathrm{m}/2 + \gamma_\mathrm{m,th}/2 & \mathrm{i}\gamma_\mathrm{m}/4 & 0 & 0 \\ -\mathrm{i}\gamma_\mathrm{m}/4 & \mathrm{i}\Omega_\mathrm{m}/2 + \gamma_\mathrm{m,th}/2 & 0 & 0 \\ 0 & 0 & \mathrm{i}\Omega_\mathrm{s}/2 + \gamma_\mathrm{s,th}/2 & \mathrm{i}\gamma_\mathrm{s}/4 \\ 0 & 0 & -\mathrm{i}\gamma_\mathrm{s}/4 & \mathrm{i}\Omega_\mathrm{s}/2 + \gamma_\mathrm{s,th}/2 \end{pmatrix} \tag{4.2.79}$$

where the matrix for the cascaded interaction K_int and the matrix for the individual oscillators K_osc are written separately. With this matrix, the dynamics of both, the mean value of the system and the covariance matrix can be simulated.

Logarithmic Negativity as a Witness of Entanglement: The logarithmic negativity quantifies the amount by which the Peres-Horodecki PPT criterion for separability is violated, which is a necessary and (for the 2×2 dimensional case) sufficient condition that two quantum mechanical states are separable [150]. To calculate the logarithmic negativity, the covariance matrix of the Gaussian state is written in terms of three 2×2-matrices α, β, γ in the form

$$\tilde{C} = \begin{pmatrix} \alpha & \gamma \\ \gamma^T & \beta \end{pmatrix}, \tag{4.2.80}$$

which can be done for any two-mode Gaussian state [151]. From this new covariance matrix, the symplectic eigenvalues are calculated. For a two-mode Gaussian state they are given by $c_\pm = \sqrt{(p \pm \sqrt{p^2-4q})/2}$, where $p = \det(\alpha) + \det(\beta) - 2\det(\gamma)$ and $q = \det(\tilde{C})$ [152]. The Peres-Horodecki PPT criterion for separability reduces to an inequality for the smallest symplectic eigenvalue, namely $c_- \geq 1$ [153]. If this inequality is violated, the two-mode Gaussian state is entangled. The amount of entanglement is quantified by the so-called logarithmic negativity of a state, defined as

$$E_\mathcal{N}(\rho) = \max(0, -\ln(c_-)). \tag{4.2.81}$$

This expression directly quantifies the amount by which the PPT condition for separability is violated [154]. We have entanglement for $E_\mathcal{N}(\rho) > 0$.

Duan Criterion as a Witness of Entanglement: Instead of logarithmic negativity, the so-called Einstein-Podolsky-Rosen (EPR) quadratures can be considered to quantify the violation of the non-

separability criterion [155]. For this, the EPR quadratures [156] are defined as

$$\hat{X}_{\pm} = \frac{1}{\sqrt{2}}\left(\hat{X}_{\mathrm{s}} \pm \hat{X}_{\mathrm{m}}\right), \tag{4.2.82}$$

$$\hat{P}_{\pm} = \frac{1}{\sqrt{2}}\left(\hat{P}_{\mathrm{s}} \pm \hat{P}_{\mathrm{m}}\right). \tag{4.2.83}$$

The separability criterion is violated for $\langle \hat{X}_{-}^2 \rangle + \langle \hat{P}_{+}^2 \rangle < 1$ [155]. This criterion is a sufficient but not a necessary condition to prove entanglement of two quadratures. In order to obtain a necessary condition for entanglement of a two-mode Gaussian state, the EPR quadratures are generalised by adding a weight a to the quadratures

$$\hat{X}_{\pm,a} = \frac{1}{\sqrt{2(a^2 + 1/a^2)}}\left(a\hat{X}_{\mathrm{s}} \pm \frac{1}{a}\hat{X}_{\mathrm{m}}\right), \tag{4.2.84}$$

$$\hat{P}_{\pm,a} = \frac{1}{\sqrt{2(a^2 + 1/a^2)}}\left(a\hat{P}_{\mathrm{s}} \pm \frac{1}{a}\hat{P}_{\mathrm{m}}\right). \tag{4.2.85}$$

Duan et al. [155] have proven that if the system is separable, it satisfies the inequality $\xi_{\mathrm{Duan,a}} = \langle \hat{X}_{-,a}^2 \rangle + \langle \hat{P}_{+,a}^2 \rangle \geq 1$ for any real number a. So if there is a real number a for which this inequality is violated, the generalised EPR quadratures are entangled.

Simulation Results: The covariance matrix is simulated for a realistic set of parameters given in table 4.2.1. For each simulated time, the logarithmic negativity $E_{\mathcal{N}}(\rho)$ is calculated [153], as shown in figure 4.2.4 (a) for different environment temperatures of the membrane. Entanglement between the two systems can be generated at sufficiently low temperatures. The time dynamics of the entanglement is interesting: there is a maximum of entanglement after 10 µs to 50 µs. After that, the entanglement decreases probably due to the dephasing of the states. But for sufficiently low temperatures, there is still some entanglement after more than 400 µs. In figure 4.2.4 (b) the maximum logarithmic negativity is plotted as a function of the membrane environmental temperature. Not surprisingly, the entanglement increases with decreasing temperature.

Instead of the logarithmic negativity, the Duan criterion can be considered [155]. For this, the Duan entanglement parameter $\xi_{\mathrm{Duan,a}}$ is minimised by optimising the weight a for each simulated time. In figure 4.2.4 (c) the minimum entanglement parameter is shown for a given membrane environment temperature. The evaluation of the Duan criterion gives the same general picture as the logarithmic negativity. Comparing the simulation data with the calculation of cooperativity shown in figure 4.2.2, we see that the occurrence of entanglement coincides with the regime of large hybrid cooperativity. This is expected [68].

In order to make the simulation more relevant to the experiment, detection noise is introduced for the detection of the spin system. For this, we normalise the detection noise floor (given by the shot noise) to the spin occupation, such that it can be written as effective spin occupation $n_{\mathrm{s}}^{(det)}$. As we can see in figure 4.2.4 (d), the detectable entanglement disappears if there is only a small amount of noise in the spin detection. This will be a major challenge for the detection of entanglement.

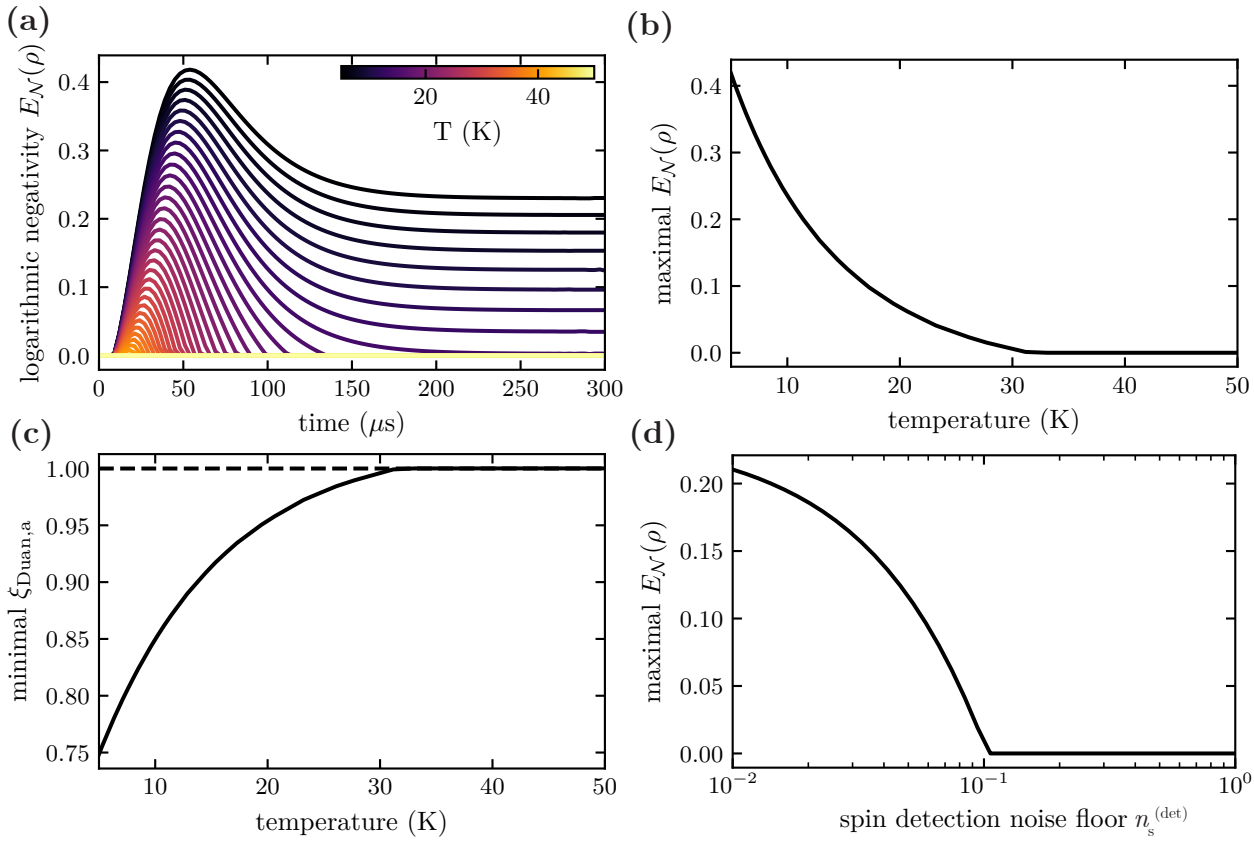

Figure 4.2.4: Results of the parametric-gain interaction: (a) shows the logarithmic negativity of the covariance matrix as a function of time for different membrane environment temperatures. In (b) the maximum entanglement obtained is shown as a function of temperature. In (c) the Duan criterion is evaluated for the same simulation. (d) shows the logarithmic negativity that can be measured for the system with a membrane at $T = 10\,\mathrm{K}$ and detection noise in the spin detection. Here, the detection noise floor $n_{\mathrm{s}}^{(det)}$ is normalised to a single spin excitation.

4.3 Experimental Implementation of the Coupling Loop

In this section, the experimental implementation of the coupling loop is discussed. A detailed schematic of the experimental setup is shown in figure 4.3.1, where key building blocks of the loop geometry are highlighted. The following sections elaborate on the experimental implementation of these building blocks. First, the optomechanical interface is discussed in subsection 4.3.1. Next, in subsection 4.3.2, the experimental implementation of the polarisation interferometer is shown, which has previously been discussed theoretically in section 4.2.2. In the theory section at the beginning of this chapter, we have seen that the loop phase is crucial for the nature of the spin-membrane interaction. How this loop phase is implemented in our experiment is presented in section 4.3.3. In the loop, the spin interacts twice with the light. The implementation of this double pass is discussed in section 4.3.4. The light of the two spin-light interactions interferes. The phase difference of the light of these two spin-light interactions is actively stabilised, which is introduced in section 4.3.5. Finally, the in-loop spin detection is introduced in section 4.3.6.

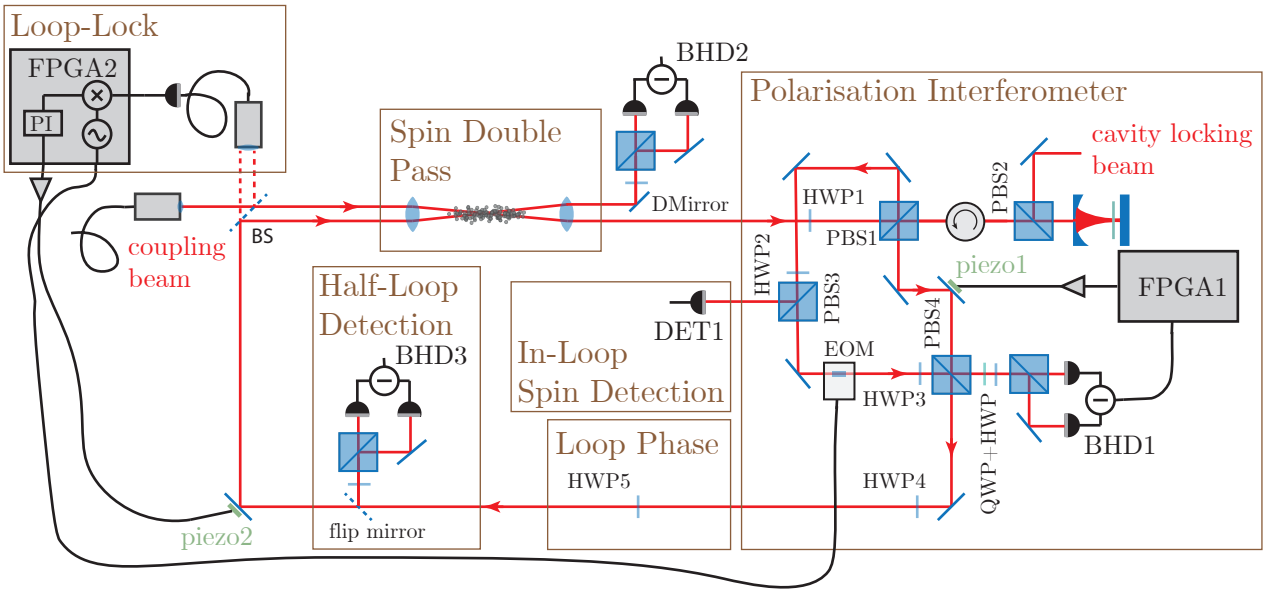

Figure 4.3.1: Sketch of the coupling loop with detailed representation of the polarisation interferometer, the loop phase lock, and the in-loop spin detection.

4.3.1 Optomechanical Interface

The optomechanical interface has already been introduced in chapter 3. Here we give a short summary of how the cavity is used in the coupling experiments. For this, we consider the nano-pillar membrane described in section 3.3. The membrane is embedded in a single-sided cavity with a linewidth of $\kappa = 2\pi \times 94\,\mathrm{MHz}$. Two orthogonally polarised beams interface the cavity: (1) the coupling beam, more precisely the cavity arm of the polarisation interferometer, and (2) the locking beam. The two beams are combined at the last PBS before the cavity (PBS2 in figure 4.3.1). Both beams are derived from the same titanium-sapphire laser[2] and are frequency shifted and switched by individual AOMs (shown

[2]MSquared SolsTiS 5000 PSX XF laser system

in figure 3.3.2). The AOM of the the locking beam is driven at 100 MHz by a fixed frequency VCO[3]. A function generator[4] is used to provide the frequency for the coupling beam AOM, which is set to 105 MHz for the coupling experiment. For both AOMs, the first positive deflection is used so that the coupling beam is blue-detuned by 5 MHz from the locking beam. The length of the cavity is stabilised by a PDH lock (using the locking beam, shown in figure 3.3.2) so that the locking beam is about -5 MHz red detuned from the cavity resonance and the coupling beam is approximately in resonance with the cavity. In practice, the lock point is set so that the coupling beam is slightly red-detuned to ensure the stability of the cavity. In the presence of the locking beam (10 µW), the membrane is broadened from $2\pi \times 152$ mHz (at room temperature) to $2\pi \times 56$ Hz. The coupling beam (200 µW) further broadens the membrane mode to $2\pi \times 480$ Hz. This reduces the occupation of the membrane vibrational mode from $n_{\mathrm{th}} = 2.7 \times 10^6$ to $n_{\mathrm{opt}} = 860$.

4.3.2 Lock of the Polarisation Interferometer

The cavity is interfaced by one arm of a polarisation interferometer as described in section 4.2.2. The polarisation interferometer converts signals encoded in the polarisation degree of freedom onto a phase or amplitude modulation and back again. At the output of the polarisation interferometer, the vibrations of the membrane should have been mapped onto the $\hat{S}_z$-component of the Stokes vector so that it can act on the spin. In order to ensure that the mechanical state of the membrane is mapped onto the circular polarisation of the light, the interferometer has to be stabilised at a phase difference between the two interferometer arms of $\Delta\phi = 0$. Locking this phase is achieved by splitting off about 3 % of both interferometer arms at the PBS4, where the two arms of the interferometer are recombined (shown in figures 4.2.1 and 4.3.1). The leak is detected by a balanced homodyne detection (BHD1). Using a normal polarisation homodyne detection for BHD1 (with just a HWP), the phase $\Delta\phi = 0$ would correspond to a maximum or a minimum of the detected sinusoidal interference (because the detected signal is then $D \propto \cos(\Delta\phi)$). If instead we use a QWP and a HWP in succession, we can tune the phase of the sinusoidal interference. The polarisation state of the light after the PBS4 can be written as a Jones vector $(\hat{a}_1, \hat{a}_2 \exp(\mathrm{i}\Delta\Phi))$, where $\hat{a}_1$ is the annihilation operator of light coming from the cavity arm of the interferometer and is horizontally polarised and $\hat{a}_2$ is the annihilation operator of light coming from the local oscillator arm of the interferometer and is vertically polarised. The detected signal of the homodyne detector is given by

$$
\begin{aligned}
D &= \langle \hat{a}^\dagger_{\mathrm{det}+} \hat{a}_{\mathrm{det}+} - \hat{a}^\dagger_{\mathrm{det}-} \hat{a}_{\mathrm{det}-} \rangle / 2 && (4.3.1)\\
&= \langle \hat{a}_1^\dagger \hat{a}_1 - \hat{a}_2^\dagger \hat{a}_2 \rangle (\cos(4\theta_{\mathrm{HWP}}) + \cos(4(\theta_{\mathrm{HWP}} - \theta_{\mathrm{QWP}})))\\
&\quad + \langle \hat{a}_1^\dagger \hat{a}_2 \mathrm{e}^{\mathrm{i}\Delta\Phi} + a_2^\dagger \hat{a}_1 \mathrm{e}^{-\mathrm{i}\Delta\Phi} \rangle (\sin(4\theta_{\mathrm{HWP}}) + \sin(4(\theta_{\mathrm{HWP}} - \theta_{\mathrm{QWP}})))\\
&\quad + \mathrm{i} \langle \hat{a}_1^\dagger \hat{a}_2 \mathrm{e}^{\mathrm{i}\Delta\Phi} - a_2^\dagger \hat{a}_1 \mathrm{e}^{-\mathrm{i}\Delta\Phi} \rangle \sin(4\theta_{\mathrm{HWP}} - 2\theta_{\mathrm{QWP}}) && (4.3.2)\\
&= (\alpha^2 - \beta^2)(\cos(4\theta_{\mathrm{HWP}}) + \cos(4(\theta_{\mathrm{HWP}} - \theta_{\mathrm{QWP}})))\\
&\quad + \frac{\alpha\beta}{2} \cos(\Delta\Phi)(\sin(4\theta_{\mathrm{HWP}}) + \sin(4(\theta_{\mathrm{HWP}} - \theta_{\mathrm{QWP}})))\\
&\quad - \frac{\alpha\beta}{2} \sin(\Delta\Phi) \sin(4\theta_{\mathrm{HWP}} - 2\theta_{\mathrm{QWP}}) && (4.3.3)
\end{aligned}
$$

[3] Voltage Controlled Oscillator, Crystek, CRBSCS-01-100.000, sine-wave output at 100 MHz with a frequency stability of ±25 ppm

[4] Rhode&Schwarz signal generator: SMB 100A

where $\langle \hat{a}^\dagger_{\mathrm{det}\pm} \hat{a}_{\mathrm{det}\pm} \rangle$ is the flux in front of each detector, θ_{QWP} is the angle of the QWP, and θ_{HWP} is the angle of the HWP. The expectation values $\alpha = \langle \hat{a}_1 \rangle$ and $\beta = \langle \hat{a}_2 \rangle$ are calculated for a coherent state of light. In order to stabilise the interferometer around $\Delta\phi = 0$, the waveplates are set to $4\theta_{\mathrm{HWP}} - 2\theta_{\mathrm{QWP}} = \pi/2$ and an error signal $D = -\alpha\beta \sin(\Delta\phi)/2$ is obtained. The error signal, which is linear around $\Delta\phi = 0$, is given as input to a digital lockbox [73]. The PI control of this digital lockbox is used to send a feedback signal to a high-voltage amplifier[5], which drives the piezo1 used to modulate the path length of the cavity arm of the interferometer and as such the relative phase between both interferometer arms.

Experimentally, the QWP and the HWP of the polarisation interferometer homodyne detection are optimised by detecting the interference signal at the balanced homodyne detection BHD3, which can be accessed via a flip mirror. For the coarse adjustment, the piezo1 is scanned and the waveplates are set so that the sinusoidal signals of the BHD1 and BHD3 are in quadrature with respect to each other. To fine-tune the QWP and HWP, an iterative process has proven to be most efficient: the membrane signal (or an EOM modulation, using the EOM in the interferometer) on the BHD3 should be minimised while the polarisation interferometer is locked (a phase modulation on one of the interferometer arms should be mapped on $\hat{S}_z$, which cannot be detected by BHD3), and the sinusoidal signal on the BHD1 should be centred around zero while piezo1 is scanned.

The coupling beam is turned off during some stages of the sequence to avoid heating the trapped atoms. The lock is turned off during these stages. To ensure a stable operation of the polarisation interferometer during the spin-membrane interaction time, the coupling beam and the lock are turned on for 4.5 ms before the spin-pumping stage. The lock is then on hold again for 1.5 ms, during which the internal state of the atoms is prepared by spin-pumping, before the coupling beam is switched on again to couple the spin and the membrane.

4.3.3 Implementation of the Loop Phase

In order to mediate Hamiltonian interactions between the spin and the membrane, it turns out that the sign of the quantum signal on the carrier has to be inverted before the second interaction with the spin [37]. More generally, this corresponds to a phase shift of $\phi = \pi$ of the quantum signal on the carrier. This so-called loop phase changes the optical quadratures $\hat{X}_{\mathrm{L}} \to -\hat{X}_{\mathrm{L}}$ and $\hat{P}_{\mathrm{L}} \to -\hat{P}_{\mathrm{L}}$. In our implementation of the looped, cascaded system, the quantum signal is encoded in the polarisation state of the light. Assuming that the light is polarised along $\hat{S}_x$, the quadratures can be written as Stokes vector components $\hat{X}_{\mathrm{L}} \approx \hat{S}_y/\sqrt{\bar{S}_0}$ and $\hat{P}_{\mathrm{L}} \approx \hat{S}_z/\sqrt{\bar{S}_0}$. Changing the loop phase is therefore equivalent to a rotation of the polarisation. To implement a phase $\phi = \pi$ we use a HWP with the fast axis aligned with the local oscillator of the light $\hat{S}_x$. Using a stack of QWP - HWP - QWP one could set an arbitrary loop phase, as shown in [68].

4.3.4 Double Pass of the Spin Ensemble

In our loop design, the spin is interfaced twice. This double pass is implemented experimentally by having a small angle between the first and the second pass at the position of the atomic cloud (see figure 4.3.2). This angle is set by aligning the two beams parallel at a distance of $2d$ in front of the lens ($f = 200$ mm) which focuses the beams onto the atomic cloud. This lens transforms the parallel offset of the beams into

[5] Homebuilt high voltage amplifier by our workshop: SP908, up to ±100 V

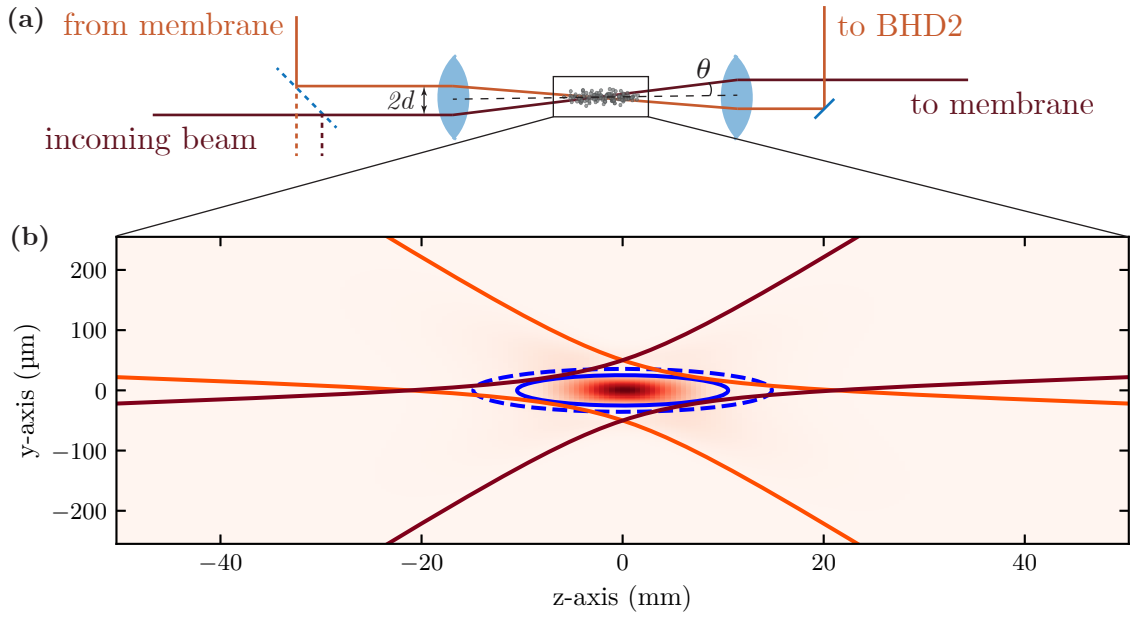

Figure 4.3.2: Schematics of the double interaction of the atomic cloud: (a) shows the beam path of the coupling beam interfacing the atomic cloud twice. The beams cross with an angle 2θ at the position of the atoms, which is shown in more details in (b). Here, the $1/e^2$ waist of the beams is shown by the dark red (first interaction) and orange (second interaction) solid lines. The blue lines show the $1/e$ (solid) and the $1/e^2$ (dashed) waist of the atomic cloud. The colour-map shows the intensity of the total optical field.

a relative angle of $2\theta = 2d/f$. After the atomic cloud, there is a second $f = 200\,\text{mm}$ lens which collimates the beam again at a relative distance of $2d$ between the beams.

The distance d between the two beams is a trade-off between two conflicting requirements. On the one hand, the distance between the beams has to be large enough to separate the beams after the second lens. On the other hand, the angle on the atoms has to be small enough so that the two passes address the same spin wave, see equation (4.2.21). In [68], this trade-off is studied in detail, both theoretically and experimentally. It turns out, that choosing a displacement similar to the beam waist in front of the first lens $d = w$ is a good compromise.

From the basic formulae given in section 4.2.2, the parameters for our coupling setup are calculated below. In our current setup, the beams in front of the first lens have a waist of 1 mm. So we chose a displacement of $d = \pm 1\,\text{mm}$ from the central axis for the two passes and get a relative angle of $2\theta = 2d/f = 0.01$ and a $1/e^2$ beam waist (radius) of $w_0 = 50\,\mu\text{m}$ at the position of the atoms. Calculating the overlap integrals for our cloud geometry, we obtain geometry factors of $\langle \text{Re}(\beta_{\text{fst}})^2 \rangle_{N_a} = 0.53$, $\langle \text{Re}(\beta_{\text{snd}})^2 \rangle_{N_a} = 0.48$ for the desired coupling and $\langle \text{Im}(\beta_{\text{fst}})^2 \rangle_{N_a} = 0.05$, $\langle \text{Im}(\beta_{\text{snd}})^2 \rangle_{N_a} = 0.05$ for the undesired coupling (considering a transmission of $\eta = 0.9$). These numbers have to be compared with the geometry factor of the single-pass 3D-interaction without angle $\langle \eta_s^2 \rangle_{N_a} = 0.33$ (described in section 2.4). For the double pass with angle, the atomic cloud is addressed with two beams, but the mode matching is worse than for the single pass. It turns out that the measurement rate is higher in the two-beam configuration than with one on-axis probe. However, the decoherence is much greater for the double pass than for the single pass. The light-induced spin decoherence depends on the local light intensity, which is on average by a factor $\sim (1 + \eta^2)^2 = 3.24$ larger than for the single pass without angle.

In the following, the coupling to the $\hat{S}_y$ Stokes vector component is neglected because it is small. The

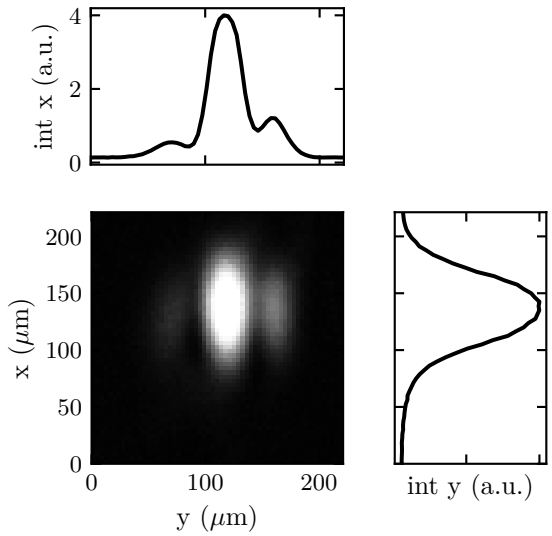

Figure 4.3.3: Interference fringe of the first and the second pass measured at the focus of the coupling laser using a mirror leak. The image has been integrated along the x- and y-axis to obtain the projections along these axes. The spatial interference is along the y-axis. In this image, the displacement between the beams is greater than in the final experiment, and the difference between two maxima is about $\Delta y = 45\,\mu\text{m}$. Along the x-axis, the beams have a Gaussian profile with a waist of 50 µm.

overlap between the two spin waves is very large $\eta_{\text{ol}} = 0.97$, so we can assume that the same spin waves are addressed by both interactions.

4.3.5 Stabilisation of the Optical Phase of the Loop

For the double pass of the atomic spin, the relative optical phase of the two passes is relevant, as can be seen from the double pass Hamiltonians given in equations (4.2.18) and (4.2.19). The two passes need to constructively interfere at the position of the atoms to maximise the prefactor of the double-pass spin-light Hamiltonian. It is therefore necessary to stabilise the optical path length of the loop. To do this, the phase of one of the polarisation interferometer arms is modulated by an EOM at 50 kHz (shown in figure 4.3.1). By combining the two arms of the polarisation interferometer on the PBS4, this phase modulation is converted into a polarisation modulation. The returning light of the second pass is combined with the first pass on a 98:2 beam splitter (BS) before being sent to the atoms. The two beams are combined so that they are parallel at a distance of 2 mm (see last subsection). Most of the light from the second pass is reflected at the BS and sent to the atoms. However, a small fraction is transmitted and focused onto a fibre. From the first pass, 98 % of the light is reflected at the BS and focused onto the same fibre. At the focus, the two beams overlap and thus interfere. This interference signal is modulated due to the polarisation modulation of the second pass generated by the EOM. The modulated interference signal is measured on a photodiode. A FPGA board demodulates the signal and feeds it back to the piezo2 to control the length and thereby the optical phase of the loop.

The light in the other BS output is focused onto the atomic cloud by a 200 mm lens. The leakage of

a mirror after the lens (not shown in figure 4.3.1) is used to monitor the interference pattern by imaging the two beams with a CCD camera[6] (an example shown in figure 4.3.3). For small angles $\theta \ll 1$ and weakly focused beams, the interference at the focus of the laser is given by

$$I(x, y, z = 0) = |u_{\mathrm{fst}}(x, y, z = 0) + \eta^2 u_{\mathrm{snd}}(x, y, z = 0)|^2 \tag{4.3.4}$$

$$\approx (1 + \eta^2)^2 \, \mathrm{e}^{-2\frac{x^2+y^2}{w_0^2}} \cos^2\left(2\pi \frac{y\theta}{\lambda}\right). \tag{4.3.5}$$

The distance between the first and the second maximum of the interference fringe is then $\Delta y = \lambda/(2\theta) = 78\,\mu\mathrm{m}$. By checking the distance between the maximum and the first order interference fringes, the angle between the beams can be estimated.

4.3.6 In-Loop Measurement of the Spin State

In the hybrid experiment, the spin signal is measured in-loop by detecting 8 % of the light of the local oscillator arm of the polarisation interferometer (see figure 4.3.1). By detecting the light in the loop, the actual losses in the loop are increased. Therefore, only a few percent of the light is split off on the PBS3 for detection. It is very convenient to have a detector that detects only the spin signal and no signal from the membrane. However, because only a small fraction of the light can be detected and no homodyne measurement can be performed at this position of the loop, the signal-to-noise ratio of the measurement is limited. The shot noise in the detection can be normalised to a single spin excitation, from which we obtain a minimal noise level of about $n_{\mathrm{s}}^{(\mathrm{det})} = 50$. Thus, as soon as we move towards the quantum-limited operation of the hybrid experiment, the signal-to-noise ratio of this detection is too small.

4.4 Experimental Characterisation of the Double Pass of the Spin

The membrane oscillator is interfaced only once in our implementation of the hybrid coupling. Therefore, the description of the membrane oscillator given in chapter 3 does not need to be modified much when integrating the membrane into the loop (see section 4.2.2). This is not the case for the spin oscillator: By coupling the spin with two beams at an angle, the description of the spin interface changes, as described in section 4.3.4. As a first approximation, we can simply modify the spin-light coupling rate and the spin damping rate and consider a new effective spin oscillator. The experimental characterisation of this new spin-oscillator is shown in the following sections. Furthermore, the backaction acting on the spin is cancelled by the second interaction with the light. In section 4.4.3, the characterisation of the backaction cancellation of the spin is shown.

However, it should be noted that this does not fully describe the spin-light interface. In section 4.3.4, it is shown theoretically that due to the spin-light interface where two beams pass the spin at a relative angle, the spin couples not only to $\hat{P}_{\mathrm{L}}$ but also to $\hat{X}_{\mathrm{L}}$. In the loop, this leads to a self-interaction of the spin as described in [68]. In our case, this coupling to $\hat{X}_{\mathrm{L}}$ is weak due to the very small angle between the two beams. Therefore, this undesired coupling contribution is neglected in the following. In future experiments, the coupling to $\hat{X}_{\mathrm{L}}$ could be used to engineer a self-interaction of the spin by setting a larger angle between the two beams.

[6] Flir Cameleon3 USB3, CM3-U3-13S2M-CS: resolution: 1288×964, pixel size: $3.75\,\mu\mathrm{m}$

4.4.1 New Effective Spin Length

The calibration of the spin signal in the loop geometry consists of several measurements. First, the effective spin-light interaction for the new geometry with the angle between the atomic cloud and the probe beam is characterised. Then the in-loop detection is calibrated with respect to the homodyne detection used for the spin characterisation in chapter 2. Finally, the effect of a second spin-light interaction on the detection after the first spin-light interaction is characterised.

The new effective spin length for an interaction with an angle is characterised by repeating the calibration experiment described in section 2.3.4 for the new geometry. It turns out that the effective (mean) spin length is reduced by 10 % if the spin is interfaced with an angle compared to the interaction without an angle. This is a smaller reduction than expected from theory: the spin-light interaction for the measurement of the mean spin scales with the average intensity of the light, as shown in section 2.4.2. For a beam without an angle, the average intensity is given by $\langle \eta_\mathrm{s} \rangle = 0.53$ (see table 2.4.2) while for a beam with an angle the average intensity (at the position of the atoms) is given by $\langle |u_\mathrm{fst}|^2 \rangle_{N_\mathrm{a}} = 0.41$ (compare to section 4.3.4), giving a reduction of 23 %. The deviation from the theoretical model could be due to an overestimation of the length of the atomic cloud or a miscalibration of the angle between the laser beam and the atomic cloud axis.

The second step is to calibrate the in-loop detection. In the spin calibration experiments shown in chapter 2, the light is detected after the interaction with the spin. If we consider the loop geometry, the spin must be detected elsewhere. Therefore, a leak of the local oscillator arm of the polarisation interferometer is used for detection (shown in figure 4.3.1 as DET1 and described in section 4.3.6). To calibrate the in-loop detection, we compare the measurement result of the same experimental sequence for the detection after the interaction with the spin (as in chapter 2) with the in-loop detection. We obtain that the in-loop signal is smaller by a factor of 0.018 than the single-pass spin detection, which is the expected reduction factor considering the splitting ratio of the polarisation interferometer (at PBS1 in figure 4.3.1) and the pick-up ratio of the local oscillator (at PBS3).

From the theory, we expect that the spin signal on the light increases when adding a second local oscillator at an angle from $\langle |u_\mathrm{fst}|^2 \rangle_{N_\mathrm{a}} = 0.41$ to $\langle \mathrm{Re}(\beta_\mathrm{fst}) \rangle_{N_\mathrm{a}} = 0.58$ (as derived in section 4.3.4). In the experiment, however, we do not see this amplification of the spin signal of the first interaction when the spin is interfaced with a second beam at a different angle, independent of the loop phase. This deviation from theory is not yet fully understood. One possible explanation could be that the spin decoherence increases significantly when the second interaction is added (see below), potentially reducing the initial spin signal. However, further investigation is needed to fully understand the double-pass interface of the atomic spin.

In this section only the effective length of the mean spin is discussed, but not the variance of the effective spin oscillator. In the future, a full characterisation of the spin noise should be considered in order to complete the characterisation of the spin oscillator in the double-pass configuration.

4.4.2 Spin Decoherence Rate

The hybrid experiment is performed in the regime of high spin cooperativity. For high cooperativity, it is useful to work in the regime where the spin linewidth is mainly determined by the interaction with the light and not by magnetic field inhomogeneities or other decay channels. Thus, we can consider the

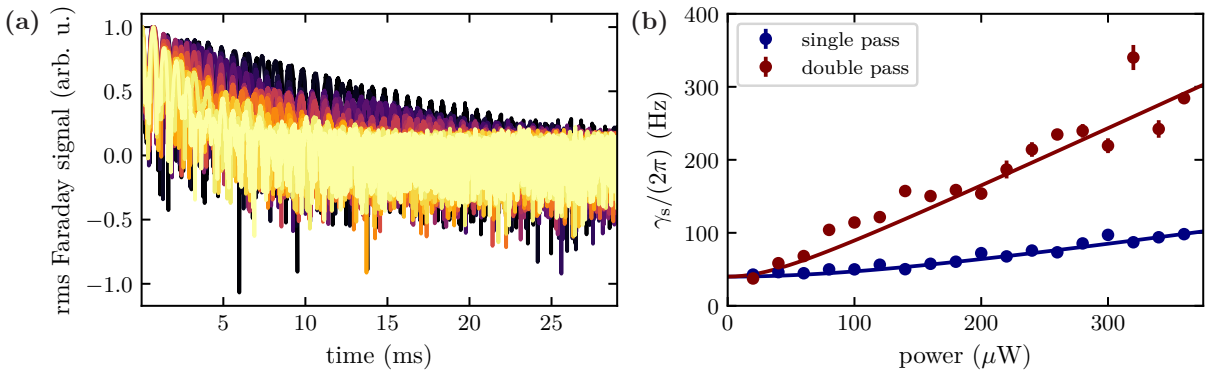

Figure 4.4.1: Decay of the atomic spin signal in the double-pass configuration: (a) shows the demodulated rms spin signal on the light for different optical powers of the coupling beam. The quadratic Zeeman splitting leads to an oscillating signal. The maxima of the oscillations are fitted with an exponential decay to extract a spin linewidth γ_s, which is plotted in (b). In (b) the fitted spin linewidths are plotted as a function of the coupling beam power P. A linear function with an offset $\gamma_s(P) = \sqrt{C^2 + (AP)^2}$ is fitted to the data. The fit yields decay constants of $A = 2\pi \times 0.25\,\mathrm{Hz\,\mu W^{-1}}$ for the single pass and $A = 2\pi \times 0.80\,\mathrm{Hz\,\mu W^{-1}}$ for the double pass.

interaction with the light as the primary source of spin broadening. In the double-pass configuration, the local intensity of the light is a factor $(1+\eta^2)^2 = 3.24$ higher than without the second pass.

In order to measure the spin decay, the spin is excited by a short (60 µs) rf pulse. The coupling beam is then switched on. For the single-pass configuration, the spin is directly measured after the first interaction. In the double-pass configuration, the light is sent further to the polarisation interferometer after the first interaction with the spin. The membrane cavity is far detuned from the coupling beam ($|\Delta_c| \gg \kappa$) so that the light is reflected at the first cavity mirror and does not interact with the membrane. The measurements presented here are performed at $\phi = 0$ loop phase so that there is no signal cancellation for the spin signal (and the signal-to-noise ratio is large). The Faraday signal is measured after the second pass by homodyne detection, demodulated by a lockin amplifier, and fitted with an exponential decay (shown in figure 4.4.1 (a)). The fitted decay rates are shown in figure 4.4.1 (b). The decay rates depend linearly on the power of the coupling beam, as expected from theory. The spin decay in the single-pass configuration agrees with the calibration shown in section 2.6.3. The spin decay in the double-pass configuration is on average a factor 3.20 larger than in the single-pass configuration. This is in good agreement with our theoretical expectation.

Control of the Spin Damping Rate

In our experiment, we can actively control the spin damping rate γ_s. This proves to be an important parameter for changing the hybrid dynamics of the system. Thereby, controlling the damping rate can be used to manipulate the membrane, as it will be shown in chapter 5.

In addition to the intrinsic damping of the spin by the coupling beam, the damping rate can be increased by switching on a pumping beam. This is done by applying a circularly polarised beam resonant with the $|f = 2\rangle \leftrightarrow |f' = 2\rangle$-transition. The beam propagates along the x-axis (along which the spin is polarised prior to the experiment) and thus pumps the internal atomic state into the $|f = 2, m_f = -2\rangle$-state (the same beam as used for the spin preparation). In the oscillator picture, this pump beam is

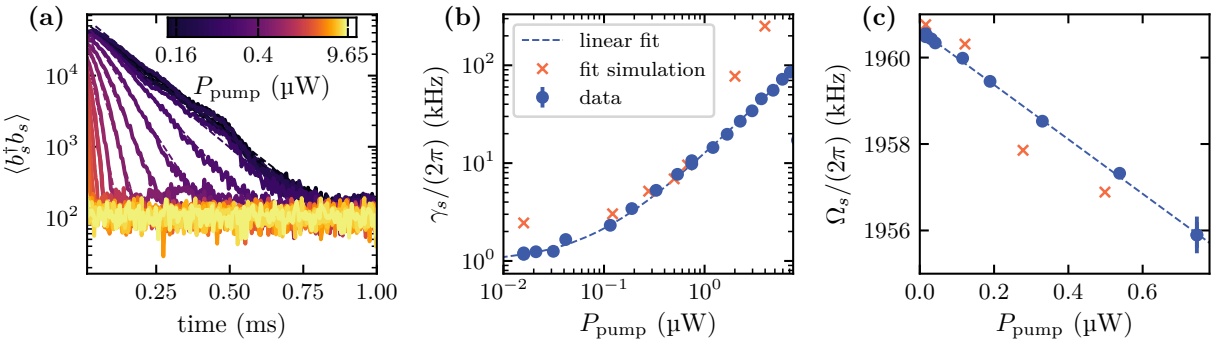

Figure 4.4.2: Measurement of the spin in the absence of coupling to the membrane after excitation by a weak rf pulse: (a) Time trace of double-pass measurement of the spin with different pump powers (range from 0 to 10 µW). The dashed lines show fits with an exponential decay. The spin linewidth (b) and spin frequency (c) are plotted as a function of the pump power. The crosses show the fit parameters extracted from figure 5.3.1 (a), which were used as input for the simulations.

an effective cooling force acting on the spin oscillator because it restores the initial low entropy state of the oscillator. In addition to the cooling force, the circularly polarised pump light creates an effective magnetic field for the spins. This leads to a shift of the resonance frequency of the spin oscillator in the presence of the pump light.

In order to measure the damping rate and the resonance frequency of the spin oscillator in the presence of all lasers but without coupling to the membrane, we detune the coupling laser from the cavity resonance ($|\Delta_c| \gg \kappa$). The laser thus is reflected from the incoupling mirror of the cavity and only the spin is probed. For the calibration measurements, the spin is coherently excited by a weak rf pulse. The spin signal is measured by detecting the signal remaining on the light after the second pass. It is normalised to spin occupation numbers (shown in figure 4.4.2 (a)).

The damping rate γ_s is extracted from the exponential fit to the temporal dynamics (see figure 4.4.2 (b)) and the spin resonance frequency Ω_s is extracted from a Lorentzian fit to the spectrum (see figure 4.4.2 (c)). For optical pump power larger than $P_{\mathrm{pump}} > 0.7\,\mu\mathrm{W}$, the spectra are too broad to provide reasonable fit results (and are therefore not shown in figure 4.4.2 (c)). Additionally to this calibration, the spin damping rate and the resonant frequency are fitted from the coupled dynamics described in chapter 5. In figure 4.4.2 (b) and (c), the fit parameters for the coupled dynamics are shown.

4.4.3 Spin Signal Cancellation

In order to have a Hamiltonian spin-membrane interaction, we need to ensure that as little signal as possible leaks out of the hybrid system. For this reason, the spin is interfaced twice, where the second interaction is the time-reversal of the first one. By changing the phase of the quantum signal in the loop, the second interaction undoes the effect of the first interaction. In this way, the quantum backaction of the light on the spin is cancelled. The backaction cancellation is limited by the losses in the loop, the finite loop delay, and the fact that the two spin-light interactions do not couple exactly the same spin waves.

By measuring the outgoing light after the second spin interaction, these limitations can be quantified and compared with the theory of cascaded quantum systems [37]. Neglecting the membrane for the

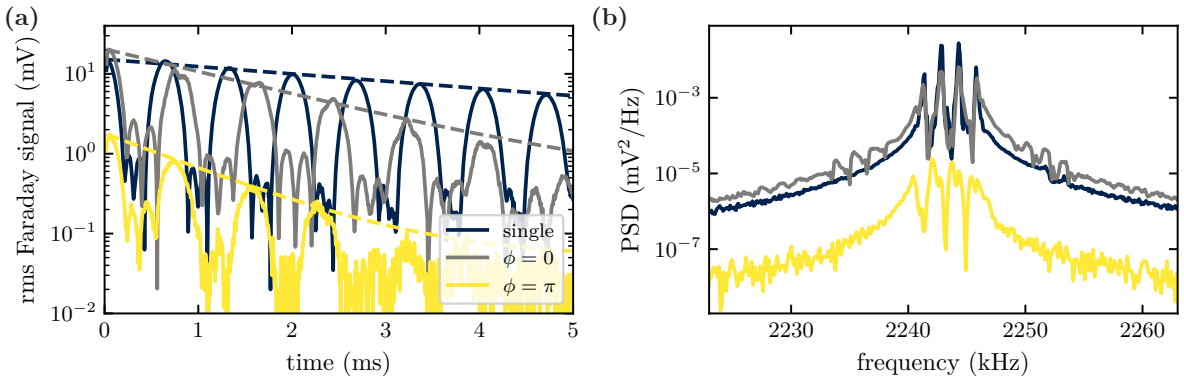

Figure 4.4.3: Demodulated time trace (a) and spectrum (b) of the spin signal for different loop configurations. The yellow curve shows the measurement of the spin signal at the end of the loop with a loop phase of $\phi = \pi$. The signal is strongly suppressed compared to the 0-phase shift which is shown in grey. The dark-blue trace shows the single pass where the second pass does not pass the atomic cloud. In all traces, the quadratic Zeeman effect leads to a decay and revival of the envelope rms function. An exponential decay is fitted to the maxima of this oscillating signal.

moment, the X-quadrature of the light after the two spin-light interactions can be written as

$$\hat{X}_{\mathrm{L}}^{(\mathrm{out})}(t) = \eta^2 \hat{X}_{\mathrm{L}}^{(\mathrm{in})}(t) + \sqrt{1-\eta^4}\hat{X}^{(\nu)}(t) \tag{4.4.1}$$

$$+ 2\eta^2\sqrt{\Gamma_{\mathrm{s}}}\left(\hat{X}_{\mathrm{s}}(t)\left(1+\cos(\phi)\cos(2\Omega_{\mathrm{s}}\tau)\right) - \hat{P}_{\mathrm{s}}(t)\cos(\phi)\sin(2\Omega_{\mathrm{s}}\tau)\right). \tag{4.4.2}$$

where ϕ is the loop phase, the first line describes the input noise of the light and the noise due to optical losses, while the second line describes the spin signal on the light. To measure the signal interference of the two passes, we apply a classical rf drive to the spin ensemble so that we can neglect the quantum noise terms and write $\langle \hat{X}_{\mathrm{s}}(t)\rangle \approx A\sin(\Omega_{\mathrm{s}}t)$ and $\langle \hat{P}_{\mathrm{s}}(t)\rangle \approx A\cos(\Omega_{\mathrm{s}}t)$. The measured $\langle \hat{X}_{\mathrm{L}}^{(\mathrm{out})}(t)\rangle$ is demodulated at the spin frequency and the rms value is calculated, which in the case of a classical signal is given by

$$\langle \hat{X}_{\mathrm{L}}^{(\mathrm{out})}\rangle_{\mathrm{rms}} \approx \sqrt{2}\eta^2\sqrt{\Gamma_{\mathrm{s}}}A\sqrt{1+\cos^2(\phi)+2\cos(\phi)\cos(2\Omega_{\mathrm{s}}\tau)}. \tag{4.4.3}$$

By changing the loop phase and comparing the measurement results, one cannot measure the losses in the loop, because the local oscillator and the spin signal are both subjected to the same losses in the loop. What can be quantified is the imperfect cancellation due to the delay and due to different spin-light interaction rates in the two passes. In our experiment, we have a round trip length of about $2\tau c = 4\,\mathrm{m}$ and we prepare the spin oscillator at $\Omega_{\mathrm{s}} = 2\pi \times 2.245\,\mathrm{MHz}$. This leads to an expected spin signal suppression of $\langle \hat{X}_{\mathrm{L}}^{(\mathrm{out})}\rangle_{\phi=0}/\langle \hat{X}_{\mathrm{L}}^{(\mathrm{out})}\rangle_{\phi=\pi} = 10.6$. A measurement of the spin signal for different loop phases is shown in figure 4.4.3. The measured signal cancellation is about what we expect $\langle \hat{X}_{\mathrm{L}}^{(\mathrm{out})}\rangle_{\phi=0}/\langle \hat{X}_{\mathrm{L}}^{(\mathrm{out})}\rangle_{\phi=\pi} = 11.8$.

The optical losses in the loop can be measured directly by measuring the power of the light at different positions in the loop. The round trip transmission in the loop is $\eta^4 = 0.64$. So the backaction cancellation on the spin is about $1-\eta^4 = 0.36$.

4.5 Conclusion

In this chapter the theoretical concept and the experimental implementation of a coupling loop between the atoms and the membrane is established. It is shown that for our set of parameters (presented in chapter 2 and 3 and summarised in table 4.2.1), quantum coherent coupling between the two systems is expected. Furthermore, it is shown that this quantum coherent coupling can be used to entangle the spin and the membrane.

The coupling of the systems requires stabilising the polarisation interferometer, which converts the signal from the polarisation state of the light to the amplitude and phase of the light and back again, and the total loop phase of the coupling loop. Both locks are presented here. In the loop, the spin is interfaced two times. In order to separate the light from both passes, an angle is implemented in between the two passes of the spin. This angle and the two passes change the spin-light interaction. Therefore, the interaction strength of the spin-light interface is calibrated again for the geometry of the spin interface. In theory, we would expect a larger spin signal because of the two passes of the light. But in the experiment, this is not observed.

Nevertheless, the requirements for performing quantum coherent coupling experiments are fulfilled. The next two chapters report on the coupling between the collective atomic spin and the mechanical oscillator.

Chapter 5

Coherent Feedback Cooling of a Nanomechanical Membrane with Atomic Spins

The mechanism of remote coupling between the collective spin of an atomic ensemble and a nanomechanical membrane was introduced in the previous chapter. In this chapter this spin-membrane coupling is used for coherent feedback cooling of the phononic bandgap shielded membrane. Coherent control of this system allows to explore different cooling regimes: for strong spin-membrane coupling, state swaps are observed which reduce the steady-state membrane temperature via spin damping. Applying additional spin pumping results in the transition to a regime of continuous, overdamped cooling. Making use of the full coherent control offered by the hybrid system, we perform spin-membrane state swaps combined with stroboscopic spin pumping to cool the membrane in a room-temperature environment to $T = 216\,\mathrm{mK}$ ($\bar{n}_\mathrm{m} = 2.3 \times 10^3$ phonons) in $200\,\mu\mathrm{s}$. Furthermore the effects of the loop delay in the coherent feedback loop on the cooling performance are studied. Starting from a cryogenically precooled membrane, this method would enable cooling of the mechanical oscillator close to its quantum mechanical ground state and the preparation of nonclassical states.

For this chapter, the phononic bandgap shielded membrane was used, introduced in section 3.2. The following chapter was published in [30]. Only a few changes were made for better integration into this thesis.

5.1 Introduction

Hybrid quantum systems in which a mechanical oscillator is coupled to a spin are a promising platform for fundamental quantum science as well as for quantum sensing [9, 11, 157]. The interest in such systems derives from the fact that the spin – a genuinely quantum-mechanical object – can be used to control, read-out, and lend new functionality to the much more macroscopic mechanical device. Recently, different

spin-mechanics interfaces have been realised, involving the coupling of a mechanical oscillator to (pseudo-)spin systems such as atomic ensembles [25, 27, 28, 29, 31, 68], quantum dots [18, 19], superconducting qubits [20, 158, 159], or impurity spins in solids [10, 14, 17, 160], using light-, strain-, or magnetically-mediated interactions.

Coherent feedback is an intriguing concept that can be studied with such systems [39, 64]. In coherent feedback, a quantum system is controlled through its interaction with another one, in such a way that quantum coherence is preserved. In contrast to measurement-based feedback [144], coherent feedback does not rely on measurements, thus avoiding the associated backaction and decoherence. Coherent feedback can under certain conditions outperform measurement-based feedback in tasks such as cooling of resonators [161, 162], and it has been implemented in solid state systems to enhance the coherence time of a qubit [163]. In optomechanical systems, it has been theoretically studied as a way to generate large nonlinearities at the single photon level [164, 165], to enhance optomechanical cooling and state transfer [166], as well as for entanglement generation [166, 167, 168].

In the context of spin-mechanics interfaces, the mechanical oscillator can act as the system to be controlled, i.e. the *plant*, which is coupled to a noisy thermal bath, and the spin system as the *controller*, coupled to a zero-temperature bath. Coherent feedback is achieved by coupling the two systems, thus reducing the noise in the mechanical system by transferring it to the spin, where it is dissipated. Additional coherent control of the spin enhances the cooling performance.

Hybrid systems combining atomic ensembles and mechanical oscillators have been used for sympathetic cooling by coupling the mechanical vibrations of a membrane to the centre-of-mass oscillation of cold atoms in an optical lattice [27, 28]. In these systems the atomic motion was strongly damped and did not offer the possibility for coherent control. In contrast, collective spin states of atomic ensembles offer long coherence times and a versatile quantum toolbox exists that provides sophisticated techniques for ground-state cooling and quantum control [13, 52]. This makes it possible to use the atomic spin as a coherent feedback controller, which can be employed to efficiently cool and control the mechanical oscillator [51], e.g., via a state-swap [169].

Here, we demonstrate coherent feedback control of a nanomechanical membrane oscillator with the collective spin of an atomic ensemble and employ it to cool the membrane. For this, we exploit the coherent control offered by our recently demonstrated spin-membrane interface, where light mediates strong coupling between the two systems [29]. Using optical pumping on an internal atomic transition we can modify the spin damping rate and study the membrane cooling performance in different regimes. We show that coherent state swaps alternated with spin pumping pulses allow us to extract the noise from the mechanical system in an efficient way, providing the largest cooling rate and reaching the phonon steady-state faster than for continuous cooling. Finally, we study the effect of feedback delay onto the steady-state temperature of the membrane in the light-mediated coupling between the mechanical and spin systems. Our observations agree well with a theoretical model.

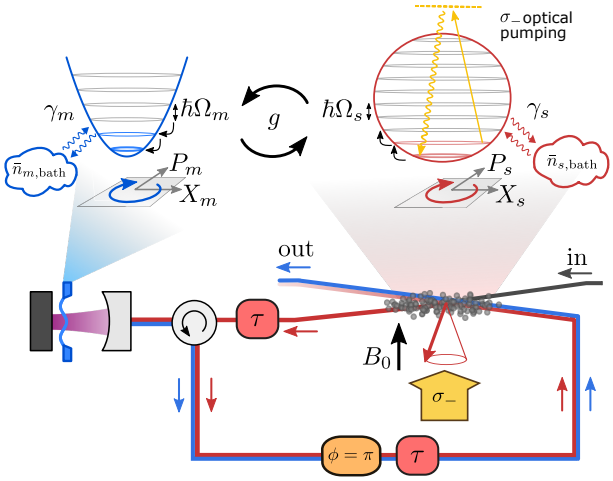

Figure 5.2.1: Sketch of the light-mediated spin-membrane coupling. Light interacts first with the spin, then with the membrane, and then again with the spin. The propagation of the light leads to a feedback delay τ. On the way back from the membrane to the spin, a π-phase is imprinted on the light, rendering the spin-membrane interaction effectively Hamiltonian for zero-delay $\tau = 0$. The systems can be approximated by harmonic oscillators of frequencies Ω_m and Ω_s with damping rates γ_m and γ_s coupling them to a bath with $\bar{n}_{m,\mathrm{bath}}$ and $\bar{n}_{s,\mathrm{bath}}$ phonons, respectively. The oscillators are coupled at a rate g. The spin damping rate can be increased by applying a σ_--polarized pumping laser.

5.2 Setup

Our hybrid system consists of a mechanical oscillator and a collective atomic spin coupled by laser light over a distance of 1 meter in a loop geometry (figure 5.2.1). The mechanical oscillator is the (2, 2) square drum mode of a silicon-nitride membrane [170], which has a vibrational frequency $\Omega_\mathrm{m} = 2\pi \times 1.957\,\mathrm{MHz}$ and an intrinsic quality factor $Q_\mathrm{m} = 1.4 \times 10^6$ (see section 3.2 for details). The membrane is placed in a single-sided optical cavity of linewidth $\kappa = 2\pi \times 77\,\mathrm{MHz}$, which enhances the optomechanical coupling to external fields. The cavity is driven by an auxiliary laser beam (not shown in figure 5.2.1) that is red-detuned from the cavity resonance, providing some initial cavity optomechanical cooling of the membrane to 2×10^5 phonons [54]. The reflection of this beam is used to stabilize the cavity length and read out the membrane displacement via homodyne detection (detailed in section 3.1.3).

The collective spin is realised with an ensemble of 1.3×10^7 cold ^{87}Rb atoms confined in an optical dipole trap. Strong coupling of the atomic ensemble to the light is ensured by its large optical depth $d_0 \approx 300$. The atomic spins are optically pumped into the hyperfine ground state $|F = 2, m_F = -2\rangle$ with respect to a static magnetic field $B_0 = 2.8\,\mathrm{G}$ perpendicular to the propagation direction of the coupling laser. The Larmor frequency $\Omega_\mathrm{s} \propto B_0$ is tuned into resonance with the membrane frequency Ω_m. The spin precession is measured after the first interaction with the coupling laser by picking up a small fraction of the light (calibration shown in section 2.6 and 4.4.1). The small-amplitude dynamics of the transverse spin components can be described by a harmonic oscillator of frequency Ω_s using the Holstein-Primakoff approximation [13].

A coupling laser beam interacts first with the spin, then with the membrane, and once again with the spin, as sketched in figure 5.2.1 and detailed in [29]. The coupling beam with 1 mW optical power is slightly red-detuned with respect to the membrane cavity and $-2\pi \times 40\,\mathrm{GHz}$ red-detuned from the ^{87}Rb D_2-line. It cools the membrane further to $\bar{n}_{m,\mathrm{bath}} = 2.0 \times 10^4$ phonons, which broadens its linewidth to

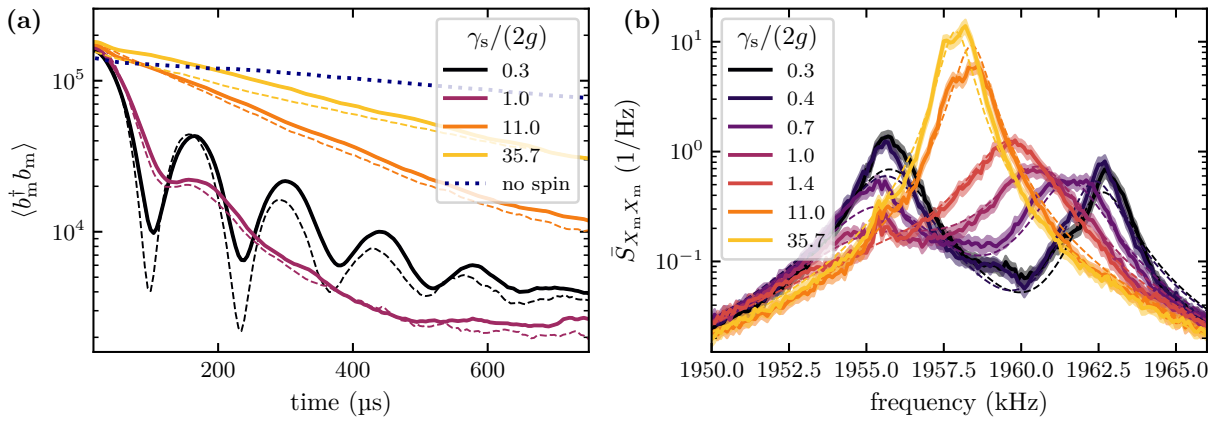

Figure 5.3.1: (a): Time traces of the membrane occupation number after turning on the coupling to the atoms. The different traces show measurements with different spin damping rates γ_s. The dashed lines correspond to the simulation described in the text based on equations (5.5.1) and (5.5.2). The dotted line shows the membrane dynamics without atoms but with the coupling beam turned on. (b): Power spectral density of the membrane displacement. The dashed lines show a global fit to the data with the initial phonon occupation $\langle b_i^\dagger b_i \rangle (t = 0)$, Ω_m, τ, g, and the detector shot noise level as global fit parameters and Ω_s and γ_s as individual fit parameters. All other parameters were taken from independent calibrations. In (a) and (b), solid lines correspond to the mean and shaded areas to the standard deviation of 355 measurements.

$\gamma_m = 2\pi \times 262\,\mathrm{Hz}$. In presence of the coupling beam, the spin linewidth is $\gamma_s = 2\pi \times 2.2\,\mathrm{kHz}$. In the first spin-light interaction, the $\hat{X}_s$ quadrature of the atomic spin is imprinted onto the coupling beam via the Faraday interaction [13], resulting in a modulation of the radiation-pressure force on the membrane. Likewise, the membrane displacement $\hat{X}_m$ modulates the light reflected from the cavity [54] which then creates a torque on the spin in the second interaction. On the way back from the membrane to the spin, the optical field carrying the spin and membrane signals is phase-shifted by π such that the effective spin-membrane interaction is predominantly Hamiltonian and the backaction of the light on the spin is suppressed [37]. Tracing out the light field and neglecting the propagation delay for the moment, the resonant part of the effective spin-membrane interaction is described by a beam-splitter Hamiltonian $\hat{H}_{BS} = \hbar g(\hat{b}_s^\dagger \hat{b}_m + \hat{b}_m^\dagger \hat{b}_s)$, where $\hat{b}_m$ ($\hat{b}_s$) is the annihilation operator of a membrane (spin) excitation and g is the effective spin-membrane coupling rate [29].

5.3 Continuous Cooling

Recently, we demonstrated strong coupling with this spin-membrane interface, i.e. $2g > (\gamma_s + \gamma_m) \approx \gamma_s$ [29]. Strong coupling is manifested by the hybridization of the membrane and spin modes which leads to a normal mode splitting of $2g = 2\pi \times 6.8\,\mathrm{kHz}$ in the spectrum as shown in figure 5.3.1 (b). In the time domain, strong coupling gives rise to state swaps between the spin and the membrane at the coupling rate g. In figure 5.3.1 (a) we show the time evolution of the membrane occupation number after switching on the coupling beam. For $2g > \gamma_s$, the thermally excited membrane swaps its state with the spin, which is initially prepared close to its ground-state, in half a period $T_\pi = \pi/g$ of the energy exchange oscillations. After another half period, the thermal state is swapped back onto the membrane but the phonon number is reduced due to the damping that occurred in the spin system, whose linewidth is larger than that of

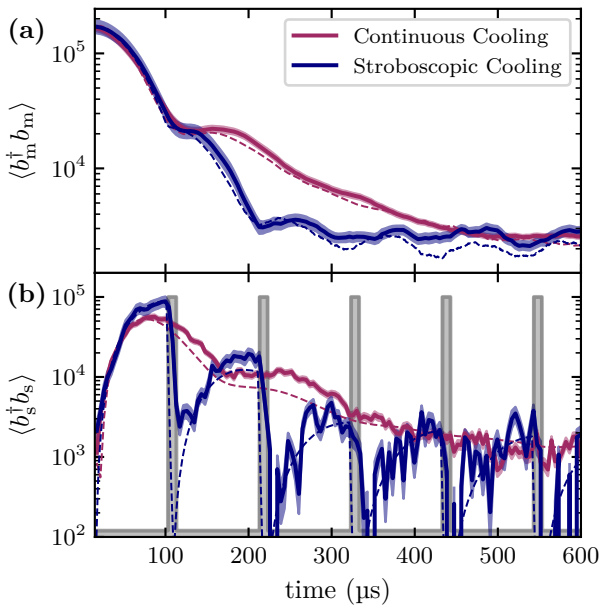

Figure 5.4.1: (a) Membrane and (b) spin occupation numbers for continuous cooling at $\gamma_s = 2g$ and stroboscopic cooling at $\gamma_s = 0.6g$. The gray shaded areas indicate the spin pumping pulses (where $\gamma_s \approx 60g$). Solid lines and shaded areas correspond to the mean and standard deviation of 70 measurements and dashed lines correspond to a simulation.

the membrane. The oscillations dephase after approximately 1 ms and a steady state with a membrane occupation of $\bar{n}_{m,\mathrm{ss}} \approx 2.3 \times 10^3$ phonons is reached, corresponding to a temperature decrease by two orders of magnitude compared to the initial state. In this process the membrane is predominantly cooled via its coupling to the cold and damped spin, reaching a temperature one order of magnitude lower than in the presence of the optomechanical cooling beams alone.

We now study the effect of increasing the spin damping rate γ_s on the coupled dynamics. To increase γ_s we apply a σ_--polarized pump laser along the polarization axis of the spin (calibration in section 4.4.2). As can be seen in figure 5.3.1 (a), increasing γ_s first enhances the membrane cooling, until the overdamped regime $\gamma_s \gg 2g$ is reached where the membrane couples incoherently to a quasi-continuum of cold spin fluctuations. The membrane decay is then governed by Fermi's golden rule, with the occupation number decreasing at the sympathetic cooling rate $\gamma_{\mathrm{sym}} \approx 4g^2/\gamma_s$, i.e. the cooling becomes less effective as γ_s is increased further. In this weak-coupling regime, the modes decouple and the membrane spectrum shows a single Lorentzian peak, broadened by the interaction with the spin, see figure 5.3.1 (b).

5.4 Stroboscopic Cooling

Previous experiments, which coupled a membrane to the motion of cold atoms [27, 28], lacked both strong coupling and coherent control over the atoms. In contrast, our strongly coupled spin-membrane system allows us to implement more elaborate coherent control schemes. In particular, we can combine strong coupling and strong spin damping in a stroboscopic fashion in order to cool the membrane much faster than in the continuous cooling case discussed above. In figure 5.4.1 we show a comparison between stroboscopic and continuous cooling, where time traces for (a) the membrane occupation number and (b) the spin occupation number are shown. In the stroboscopic sequence we perform a coherent π-pulse

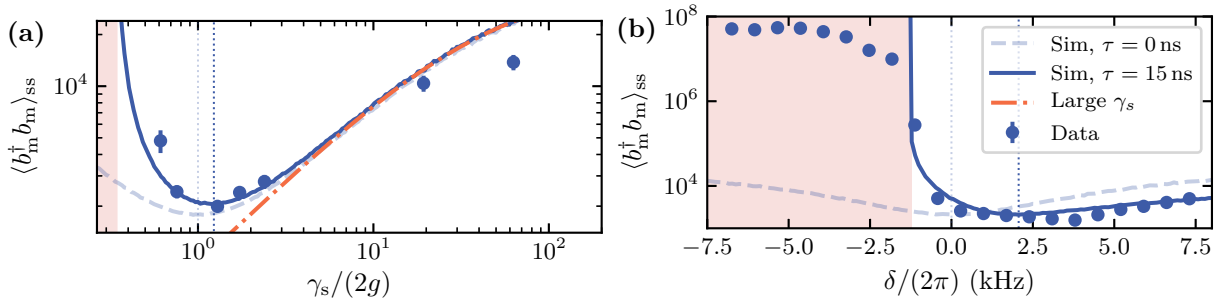

Figure 5.4.2: Steady state occupation of the membrane as a function of (a) spin damping rate γ_s (at resonance, $\delta = 0$) and (b) spin-membrane detuning $\delta = \Omega_s - \Omega_m$ at $\gamma_s = 0.6g$. The solid (dashed) blue line shows the result of the simulation with (without) delay. In (a), the red dashed-dotted line indicates the steady-state number given by the rate in equation (5.6.1) with $\tau = 15\,\mathrm{ns}$. The red shaded area shows the region for which the dynamics is found to be unstable using the Routh-Hurwitz criterion. For this measurement, $\bar{n}_{m,\mathrm{bath}} \approx 4.0 \times 10^4$ phonons and $\gamma_m = 2\pi \times 94\,\mathrm{Hz}$ (independently calibrated without atoms).

($T_{\mathrm{pulse}} = 100\,\mu\mathrm{s}$, $\gamma_s = 0.6g$) to swap membrane and spin states. Afterwards, we apply an optical pumping pulse of duration $T_{\mathrm{pump}} = 10\,\mu\mathrm{s}$ which increases the spin damping rate to $\gamma_s \approx 60g$ and depletes the spin occupation on a timescale much shorter than the state swap (gray pulses in figure 5.4.1 (b)). During the pumping pulse the coupling is kept on. Since the spin is reinitialised close to the ground state, the next coherent state swap does not transfer thermal energy back to the membrane but only cools it further. It takes two to three such iterations of a coherent π-pulse followed by a spin pumping pulse to reach the steady state (see figure 5.4.1). Using this simple sequence, we can reach the membrane steady state temperature of 216 mK ($\bar{n}_{m,\mathrm{ss}} = 2.3 \times 10^3$ phonons) in around 200 µs, approximately a factor of two faster than for continuous cooling. This exemplarily shows the advantage of a coherent feedback controller, which enables faster cooling than if the membrane is coupled with a similar rate to an incoherent, overdamped system.

5.5 Theoretical Model

Further insight into the dynamics is gained by solving the equations of motion for the coupled spin-membrane system [29],

$$\ddot{X}_m + \gamma_m \dot{X}_m + \Omega_m^2 X_m = -2g\Omega_m X_s(t-\tau) + \Omega_m \mathcal{F}_m, \tag{5.5.1}$$

$$\ddot{X}_s + \gamma_s \dot{X}_s + \Omega_s^2 X_s = -2g\Omega_s X_m(t-\tau) + \Omega_s \mathcal{F}_s, \tag{5.5.2}$$

where terms on the left-hand-side describe the internal dynamics of the damped oscillators and the first term on the right-hand-side describes the state swap dynamics including a propagation delay τ between the spin and the membrane. We included the generalized Langevin forces $\mathcal{F}_m$ and $\mathcal{F}_s$ that capture stochastic force terms due to quantum fluctuations, thermal and measurement backaction noise (detailed in appendix F).

We used the following procedures to simulate our experimental results: for the continuous cooling measurements, we first fitted the spectra for different γ_s in figure 5.3.1 (b) globally using a coupled-mode model (fit function given as equation (4.2.45)). From this fit, the extracted τ and Ω_m were used as the

input parameters for the simulation. We adapted the technique described in [171] to numerically solve the equations of motion (5.5.1) and (5.5.2) and compare the solution to our data (more details are given in appendix F). To generate each time trace in figure 5.3.1 (a) (dashed lines) we fitted the numerical solution to our data with only γ_s and Ω_s as free parameters. The fit results show a systematic shift of Ω_s with increasing spin pumping power, likely due to the light shift induced by the circularly polarised pumping laser (figure 4.4.2), and γ_s was observed to be larger than in the independent calibration shown in section 4.4.2.

For the stroboscopic cooling measurements, we took the fit parameters from the continuous cooling measurement and ran the simulation with a time dependent spin damping rate which was taken to be $\gamma_\mathrm{s} = 0.6g$ during the state swaps and $\gamma_\mathrm{s} = 60g$ during the pumping pulses. The fit is shown for membrane and spin in figure 5.4.1 as a dashed line. The good agreement between fit and data shows that our model includes all the relevant factors which govern the coupled dynamics.

5.6 Delayed Feedback

Our hybrid spin-membrane system constitutes a coherent feedback network [162], in which delayed feedback can give rise to instabilities [50, 172, 173]. In our experiment, such instabilities show up as a spontaneous coupled oscillation of spin and membrane, which we observe for certain values of the spin-membrane detuning $\delta = \Omega_\mathrm{s} - \Omega_\mathrm{m}$. Even at resonance, we have to include the feedback delay to predict the experimentally measured steady state occupation of the membrane accurately. In figure 5.4.2 we plot the measured and simulated occupation numbers of the membrane in steady state as a function of γ_s (shown in figure 5.4.2 (a)) and δ (shown in figure 5.4.2 (b)). At resonance and for $\Omega_\mathrm{m}\tau \ll 1$ (as in our system), the effect of the feedback delay is most apparent in the limit of small γ_s. The model without delay (light-blue dashed line) predicts a significantly smaller occupation number compared to both what we observe in experiments and what is predicted by our model including the feedback delay (blue solid line). In the large γ_s limit, the sympathetic cooling rate is modified to

$$\gamma_\mathrm{sym} \approx \frac{4g^2}{4\delta^2 + \gamma_\mathrm{s}^2}\left[\gamma_\mathrm{s}\cos(2\Omega_\mathrm{m}\tau) + 2\delta\sin(2\Omega_\mathrm{m}\tau)\right] \tag{5.6.1}$$

(see section 4.2.3 for derivation). In this limit, the steady state occupation is given asymptotically by $\langle b_\mathrm{m}^\dagger b_\mathrm{m}\rangle_\mathrm{ss} = \bar{n}_\mathrm{m,bath}\gamma_\mathrm{m}/(\gamma_\mathrm{m} + \gamma_\mathrm{sym})$, shown as the red dashed-dotted line in figure 5.4.2 (a). The theory of coupled oscillators without delay predicts optimal sympathetic cooling at the critical damping of $\gamma_\mathrm{s} = 2g$ (faded vertical dotted line in figure 5.4.2). Including the feedback delay in the model, the minimal occupation number shifts to larger γ_s (dark vertical dotted line), because the self-oscillations have to be compensated by a higher spin damping rate. The experimental data confirms this theoretical prediction.

Furthermore, we find that the presence of delay lifts the symmetry in δ, as inferred theoretically from equation (see 5.6.1) for large γ_s and shown both experimentally and theoretically in figure 5.4.2 (b) for small $\gamma_\mathrm{s} = 0.6g$. We see that the minimal steady state occupation of the membrane is obtained for positive detuning δ, i.e. $\Omega_\mathrm{s} > \Omega_\mathrm{m}$, which is true in general for a feedback system with a delay of $\tau < \pi/(2\Omega_\mathrm{m})$. For large enough negative δ, we observe that the coupling drives the system into limit cycle oscillations, see figure 5.4.2 (b). With our model we can attribute these self-oscillations to the feedback delay. In this self-driven regime, the resulting membrane occupation of 6.8×10^7 exceeds the spin length by around a factor of three. The emergence of such instabilities can be characterised using the Routh-Hurwitz stability

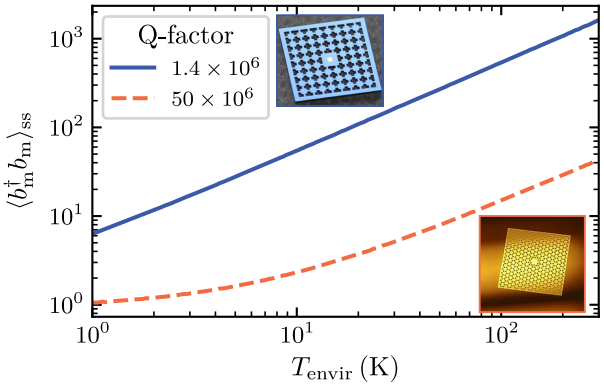

Figure 5.6.1: Simulated steady state occupation of membranes for varying cryostat temperature and different mechanical Q_m factors. Here, $\gamma_\mathrm{s} = 2g$, $\delta = 0$ and $\tau = 15\,\mathrm{ns}$. The insets show the current membrane with phononic shield used in these experiments and a soft-clamped membrane for which $Q_\mathrm{m} \approx 5 \times 10^7$.

criterion [147], which indicates whether the real part of one of the normal modes of the system reverses its sign (shown in section 4.2.3). In figure 5.4.2 we indicate such unstable regions for our coupled system by a shaded area. Our calculations show that the precise value of δ at which the driving due to the loop delay exceeds the damping of the coupled system depends on γ_s. Even at resonance (see figure 5.4.2 (a)) self-oscillations are predicted for small enough γ_s.

The propagation delay is an interesting tuning knob for coherent feedback experiments, which gives access to Hamiltonian and dissipative dynamics: We can induce self-oscillations of the system, tune the dependence of the steady state on system parameters such as damping rate and detuning, or even render the delay negligible by tuning $2\Omega_\mathrm{m}\tau$ to a multiple of 2π.

5.7 Discussion

In our experiment, the cooling rate of the membrane due to its coupling to the spin exceeds the cavity-optomechanical cooling rate by more than one order of magnitude. The lowest achievable phonon occupation of the membrane is thus given by the competition of cooling the membrane with the spin and heating due to its coupling to the room-temperature environment. In figure 5.6.1 we show the expected membrane steady state occupation for varying environment temperature and two different membrane designs. In this calculation we include the cavity-optomechanical cooling of the membrane (which has a negligible effect), the light-mediated coupling to the spin including backaction of the light, as well as thermal and quantum mechanical ground state fluctuations of both systems. The higher quality factors $Q_\mathrm{m} > 5 \times 10^7$ of soft-clamped membranes [56, 132] would reduce the thermal decoherence rate by a factor 25 and allow us to prepare the mechanical oscillator close to its ground state in a 4 K environment. These technical improvements would realise a mechanical oscillator whose phonon occupation is limited by quantum backaction instead of thermal noise. While in the current coupling scheme the double pass eliminates backaction on the atomic spin, a large membrane quantum cooperativity $C_m > 1$ would favour a double pass scheme with coherent cancellation of quantum backaction on the membrane. This would lead to a higher quantum cooperativity for the spin-membrane coupling [37]. Further, the feedback control of the membrane could be improved by increasing the quantum cooperativity of the spin system. This involves

gaining a better understanding of the spin decoherence sources and achieving a larger spin-light coupling rate.

In this work we implemented a relatively simple coherent feedback sequence based on coherent state swaps of pulse area π interleaved with short spin pumping pulses. In the future, it would be interesting to explore more elaborate feedback sequences to optimize the cooling in a specific situation. For example, the duty cycle of the stroboscopic cooling sequence could be changed over time to cool a mechanical oscillator with a high initial occupation that exceeds the spin length. Initially, short coupling pulses of pulse area $\ll \pi$ could remove excitations without saturating the spin, and once the phonon number is sufficiently reduced, the pulse area could be increased to minimize the final temperature.

Our coherent feedback cooling scheme is a rather general technique that can be applied to any physical system with a strong light-matter interface. This includes cavity optomechanical systems or mechanical oscillators without an optical cavity. Moreover, similar cooling schemes could be implemented in the microwave domain with electromechanical oscillators [159] coupled to solid-state spin systems.

The coherent control and bidirectional Hamiltonian coupling employed in this work pave the way towards more elaborate quantum protocols such as the generation of non-classical mechanical states via state swaps [169] as well as further studies of coherent feedback in the quantum regime [39, 64, 144, 161].

Chapter 6

Towards Quantum Coherent Coupling of a Mechanical Oscillator and an Atomic Spin

The coupling of a nano-pillar membrane in a 10 K environment to the collective spin of an atomic cloud theoretically allows one to reach the regime of the quantum coherent coupling. In this regime, the atomic spin could be used to sympathetically cool the membrane mode to the vibrational ground state. Moreover, the atomic spin and the membrane could be entangled.

In this chapter, preliminary results on the coupling between the nano-pillar membrane and the collective atomic spin are presented. We observe strong coupling between the two systems at both room temperature and cryogenic temperatures. This provides a promising starting point for the operation of the hybrid system in the quantum coherent coupling regime.

In the previous chapter, strong coupling between the collective atomic spin and the phononic bandgap shielded membrane in a room temperature environment was used for coherent feedback experiments. The interaction presented in the last chapter is not yet in the quantum coherent coupling regime [30]. The main limitation to reach the quantum coherent coupling regime is the fact that the membrane is strongly driven by thermal noise [68, 69]. In order to overcome this limitation, the phononic bandgap shielded membrane has been replaced by a nano-pillar membrane, which increases the mechanical Q-factor of the optomechanical system by more than an order of magnitude. In addition, the membrane is installed in a cavity that is mechanically stable when cooled to cryogenic temperatures (unlike the cavity used previously in [29, 30, 68, 69]), allowing coupling experiments to be performed with the membrane environment cooled to cryogenic temperatures. Furthermore, the optimisation of the geometry of the atomic cloud and the homogeneity of the magnetic field across the atomic cloud results in a longer coherence time of the atomic spin.

Using the nano-pillar membrane at cryogenic temperatures, it seems feasible to perform coupling experiments in the quantum coherent coupling regime. This allows the mechanical oscillator to be cooled sympathetically by the atoms to the mechanical ground state and the atoms to be entangled with the

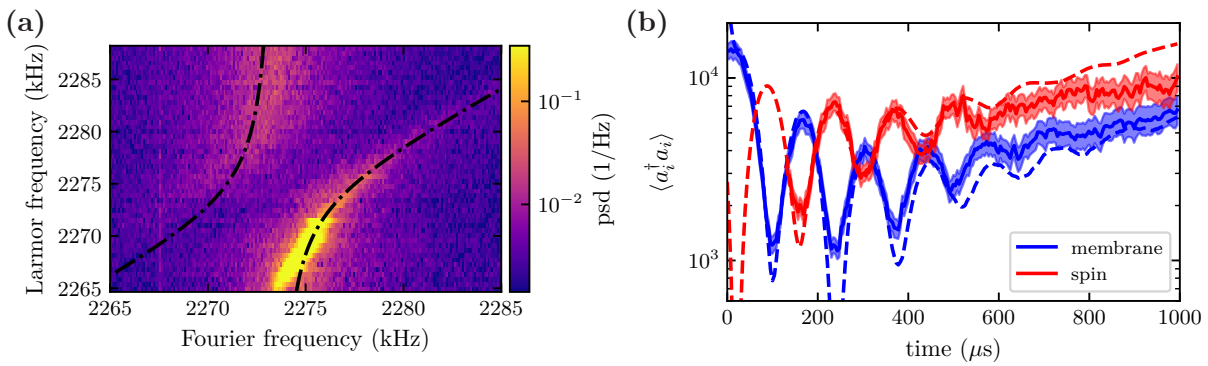

Figure 6.1.1: Room temperature measurement of the membrane and the spin coupled by a beam-splitter Hamiltonian: (a) The Larmor frequency of the spin Ω_s is tuned across the membrane resonance frequency Ω_m. For each detuning $\delta = \Omega_s - \Omega_m$ between the spin and the membrane, the PSD of the homodyne measurement of the membrane is calculated and plotted here. The eigenfrequencies of the coupled system, given by equation (4.2.53), are plotted to the data as a guide to the eye. (b) Time trace of the spin and the membrane occupation in a coupling experiment. The spin is slightly detuned from the membrane. The solid line shows the average over 100 measurements, the shaded areas the standard error. The dashed line shows a simulation of the spin-membrane coupling experiment with $\delta = 2\pi \times 3.5\,\mathrm{kHz}$, $\gamma_m = 2\pi \times 100\,\mathrm{Hz}$, $\gamma_s = 2\pi \times 1.2\,\mathrm{kHz}$ and $2g = 2\pi \times 6.4\,\mathrm{kHz}$. The measurement of the spin system did not work during the first 140 µs.

membrane, as shown theoretically in chapter 4. In this chapter, first coupling experiments between the two optimised systems are presented. First, experiments using the beam-splitter interaction are presented: In section 6.1 it is shown that the two systems are indeed strongly coupled at room temperature. This coupling can be used to coherently cool the membrane to $n_m \approx 50$ phonons in a cryogenic environment, which is discussed in section 6.2. This is more than an order of magnitude colder than for the experiments presented in the previous chapter reaching $n_m \approx 2.3 \times 10^3$ in a room temperature environment. For the experiments in section 6.3, the spin is implemented as a negative mass oscillator resulting in a parametric-gain interaction between the two systems. Finally, in section 6.4, the main limitations of the experimental setup in its current state are discussed and some ideas to overcome them are proposed.

6.1 Normal Mode Splitting

We couple the new nano-pillar membrane and the spin in the new dipole trap configuration by a beam-splitter interaction (see section 4.2.3) at room temperature to show strong coupling between the systems.

In the experiment the spin is polarised antiparallel to the magnetic field, so that it can be approximated by a positive mass oscillator (see section 2.7). In this regime, the interaction between the two systems can be described as a beam-splitter interaction (as described in section 4.2.3). One of the signatures of strong coupling between two systems is the hybridisation of the modes: If the two oscillators are resonant, the eigenmodes of the strongly coupled system hybridise into two collective modes, which is quantitatively described in equation (4.2.53). The spin resonance frequency is given by the Larmor frequency which is defined by the magnetic field. In a first experiment, the spin resonance is tuned across the mechanical resonance. The result is shown in figure 6.1.1 (a). At the spin-membrane resonance, the two eigenmodes of the coupled system are split by about $2g = 2\pi \times 6.4\,\mathrm{kHz}$.

Compared to the coupled dynamics presented in chapter 5, the linewidth of both oscillators is narrower

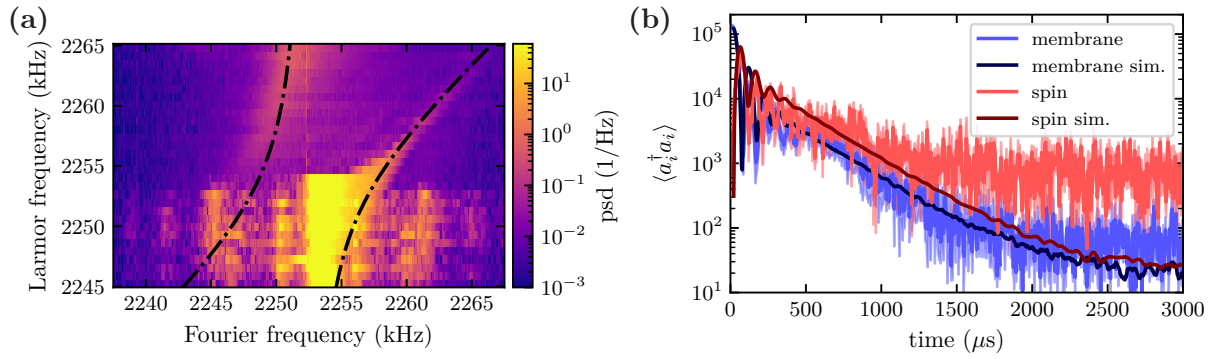

Figure 6.2.1: Experiments with a beam-splitter interaction between the collective spin of the atomic cloud and the nano-pillar membrane in a 60 K environment: (a) The spin resonance is tuned over the membrane resonance. To the data, the eigenfrequencies of the coupled system are plotted as a guide to the eye, given by equation (4.2.53). (b) Time trace of spin and membrane occupation in a coupling experiment. The spin is detuned from the membrane by $\delta = 2\pi \times 3.8\,\mathrm{kHz}$. The solid light lines show the average over 3 measurements, the shaded areas the standard error. The shot noise limits the sensitivity of the spin detection to $n_\mathrm{s}^{(\mathrm{det})} = 10^3$. The dark lines show a simulation of the spin-membrane coupling experiment with $\delta = 2\pi \times 3.8\,\mathrm{kHz}$, $\gamma_\mathrm{m} = 2\pi \times 1000\,\mathrm{Hz}$, $\gamma_\mathrm{s} = 2\pi \times 3.0\,\mathrm{kHz}$ and $2g = 2\pi \times 9.6\,\mathrm{kHz}$.

and the relative loop delay $\bar{\Omega}\tau/(2\pi)$ is larger (due to the larger mean resonance frequency $\bar{\Omega}$). The system is therefore less stable, as expected from the analysis of the Hurwitz criterion introduced in section 4.2.3. If the spin frequency is smaller than the membrane frequency, the hybrid system is unstable and self-driven. But even if the spin frequency is slightly larger than the membrane frequency, the coupled system is driven because of the finite propagation delay of the light, as shown in figure 6.1.1 (b). In order to run the experiment at resonance without driven self-oscillations, we need to broaden the spin or the membrane oscillator more strongly. For future experiments, it would be possible to broaden the membrane much more and thereby pre-cool the mechanical oscillator, which could be an advantage for the experiment.

Comparing the observed spectrum with the calculated eigenfrequencies (given by equations (4.2.53)), we observed a deviation from theory when the system is self-driven. The self-driven hybrid system seems to oscillate at the membrane resonance frequency rather than the eigenfrequency of the coupled system. This is true for both beam-splitter coupling experiments, for the room temperature experiment shown in figure 6.1.1 (a) and even more clearly for the experiment at a cryostat temperature of 60 K shown in figure 6.2.1 (a). The simulation of the hybrid system (presented in appendix F) does not reproduce this feature and so far we do not understand it.

6.2 Coherent Cooling Experiment

Using the spin as a feedback controller, the membrane can be cooled coherently by coupling the oscillators with a beam-splitter interaction (as shown in chapter 5). Here, the optomechanical system is placed in a cryostat at a temperature of 60 K to reduce the stochastic drive of the thermal environment and reach a lower phonon occupation. The beam-splitter experiment discussed in the previous section is repeated with the membrane in the cold environment. Again the spin resonance is scanned over the mechanical resonance and we observe normal mode splitting of the hybridised modes (see figure 6.2.1 (a)). As at room temperature, strong coupling between the membrane and the spin is observed at a cryogenic temperature

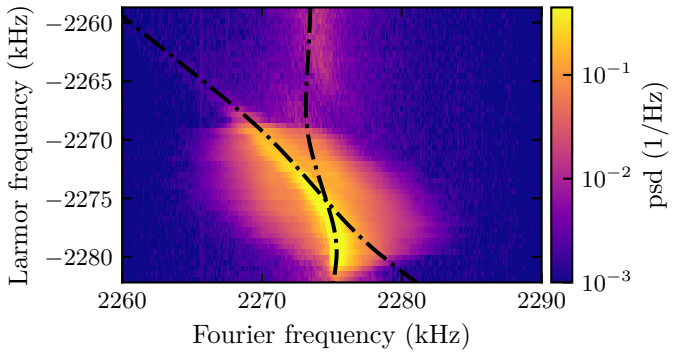

Figure 6.3.1: Homodyne measurement of the membrane oscillator at room temperature coupled to the spin oscillator by a parametric-gain interaction: The spin resonance frequency is tuned across the membrane resonance frequency. The PSD of the membrane homodyne measurement is shown for different detunings. The eigenfrequencies of the coupled system are plotted to the data as a guide to the eye. The normal modes are given by equation (6.3.1) with $2g = 2\pi \times 3.6\,\mathrm{kHz}$, $\Omega_\mathrm{m} = 2\pi \times 2.276\,\mathrm{MHz}$, and $\tau = 15\,\mathrm{ns}$.

of 60 K. We want to evaluate how much the membrane oscillator can be cooled sympathetically. This is done by analysing the time traces of the oscillators. An example is shown in figure 6.2.1 (b). Note that the spin detection is limited to $n_\mathrm{s}^{(\mathrm{det})} < 10^3$ by shot noise of the light. The membrane detection, on the other hand, can resolve much lower phonon numbers: We measure steady state membrane occupation of $n_\mathrm{m} \approx 50$.

The simulated number of phonons on the membrane mode in steady state is $n_\mathrm{m} = 19$, which is more than a factor of two lower than the measured occupation. The experimental sequence has been analysed and it has been found that the switching on of the coupling beam drives the membrane strongly. A new sequence is now programmed to avoid this driving.

6.3 Parametric-Gain Interaction

Our versatile setup allows us to change the effective coupling from a beam-splitter interaction to a parametric-gain interaction. This is done by inverting the mean spin polarisation with respect to the magnetic field [29]. The inverted spin can be approximated by a negative frequency harmonic oscillator. The resulting parametric-gain Hamiltonian is given in section 4.2.4. As in the previous section, the spin resonance is tuned across the membrane resonance. The results of such spectroscopy are shown in figure 6.3.1. The eigenmodes of the coupled system are given by

$$\Omega_\pm + \mathrm{i}\frac{\gamma_\pm}{2} = \bar{\Omega} + \mathrm{i}\frac{\gamma_\mathrm{m} + \gamma_\mathrm{s}}{4} \pm \sqrt{\left(\frac{\delta}{2} + \mathrm{i}\frac{\gamma_\mathrm{m} - \gamma_\mathrm{s}}{4}\right)^2 - g^2 \mathrm{e}^{\mathrm{i}2\bar{\Omega}\tau}} \tag{6.3.1}$$

where $\bar{\Omega} = (|\Omega_\mathrm{s}| + \Omega_\mathrm{m})/2$ is the mean resonance frequency, $\delta = |\Omega_\mathrm{s}| - \Omega_\mathrm{m}$ is the detuning between the systems and τ is the light propagation delay between the spin and the membrane. The calculated eigenfrequencies are shown in figure 6.3.1 as dash-dotted lines. In our experiment, the delay is small $\tau \ll \pi/\bar{\Omega}$. In this limit the coupling leads to normal-mode attraction. For one single frequency the modes are degenerate. Without propagation delay, the modes would be degenerate at resonance but

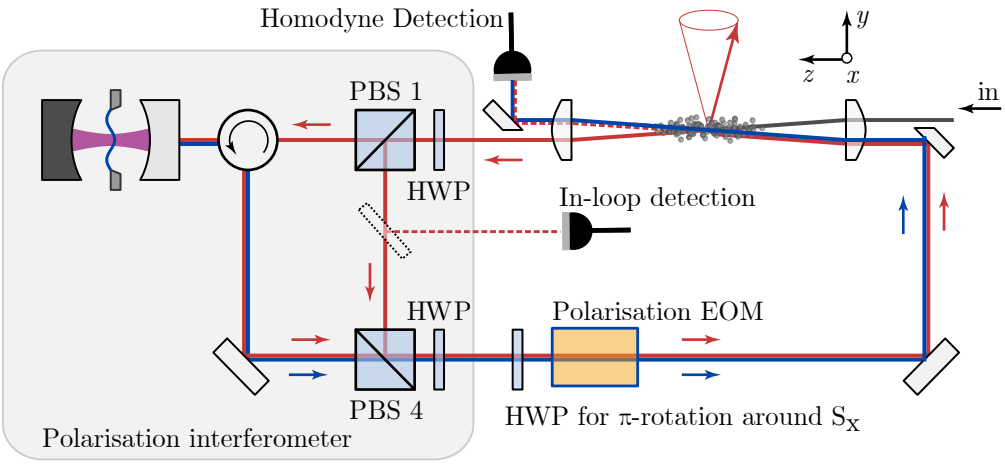

Figure 6.3.2: Experimental scheme for hybrid coupling. The inclusion of an EOM in the loop allows us to change the loop phase in a time-controlled manner during the experiment. Switching the loop phase from π to zero changes the interaction from Hamiltonian to dissipative. In this way the backaction cancellation of the spin signal can be switched off and the spin signal can be detected by the homodyne detector at the end of the loop.

including the propagation delay this is reached at $\delta > 0$. In the limit of similar damping rates of both oscillators and no detuning, the damping rate can be written as $\gamma_\pm = \bar{\gamma} \pm 2g$ where $\bar{\gamma} = (\gamma_\mathrm{m} + \gamma_\mathrm{s})/2$ is the mean damping rate. In the strong coupling regime this corresponds to a strongly damped mode γ_+ and an amplified mode $\gamma_- < 0$. It turns out that these normal modes correspond to the squeezed and anti-squeezed coupled modes [68].

Comparing the measured spectra with the theoretical normal mode analysis, we observe that the coupling rate g in this experiment is smaller by a factor of 2 compared to the coupling experiments with a beam-splitter interaction. In the past we have observed that the spin polarisation is worse for the inverted spin, but this did only reduce the coupling rate by a factor of 1.4 [29]. So far we do not know why the coupling rate is reduced so much for the parametric-gain interaction.

The parametric-gain interaction can be used to squeeze the thermal state of the membrane in a room temperature environment, as shown in [29]. If the membrane is cryogenically cooled to 10 K, we expect quantum entanglement generation between the two systems. However, in order to observe this entanglement, both systems must be detected with a signal-to-noise ratio exceeding unity for the single phonon (see figure 4.2.4 for a simulation).

6.3.1 Improving the Detection Efficiency

The main limitation in detecting entanglement between the spin and the membrane is the noise in the spin detection. If configured for Hamiltonian interaction between the membrane and the spin, the spin signal on the light is cancelled. Thus, there is little spin information on the outgoing light after the loop is completed (mainly due to the loop delay). Therefore, the spin is measured with an in-loop measurement by splitting off a small part of the light from the local oscillator arm of the polarisation interferometer (shown in figure 6.3.2). This detection suffers from two shortcomings: (1) The splitting ratio on the PBS1 is set to 20:80 (for optimal coupling, a splitting ratio of 50:50 would be optimal, but then the membrane would be maximally driven by amplitude noise, see section 4.2.2). Therefore, the spin signal on the local

oscillator arm of the polarisation interferometer is small and the signal-to-noise ratio is unfavourable. (2) In addition, by detecting a small leak of only one arm of the polarisation interferometer, we do not perform a homodyne measurement and therefore the intensity noise of the laser cannot be cancelled. This reduces the signal-to-noise ratio of the detection compared to a homodyne detection.

One way to improve spin detection would be to split the sequence temporally in two parts: First, the spin and the membrane interact through a Hamiltonian coupling. This part could be used, for example, to entangle the spin and the membrane by a coherent interaction. Then the loop phase is changed from π to zero, changing the interaction from Hamiltonian to dissipative. For a loop phase of $\phi = 0$, there is no backaction cancellation of the spin [29]. Thus, the spin oscillator can be measured with high sensitivity using the homodyne detection at the end of the loop (see figure 6.3.2). Experimentally, the loop phase can be changed by adding a polarisation EOM to the loop. This polarisation EOM acts as a tunable, time-controlled waveplate.

6.4 Summary and Outlook

In this chapter, first coupling experiments with the new nano-pillar membrane are presented. Strong coupling between the membrane and the collective spin of an atomic cloud is shown in this new configuration. This coupling can be used to cool the membrane in a cryogenic environment of 60 K to 50 phonons, compared to 2.3×10^3 in the previous chapter. Furthermore, some results of the parametric-gain interaction are shown and discussed.

In a next series of experiments, even lower cryostat temperatures could be used to perform coupling experiments in the regime of quantum coherent coupling. In this regime it will be essential to improve the spin detection, as discussed in the last paragraph. In addition, we can envisage more complex sequences that make full use of our versatile coupling setup.

For optimal spin-membrane entanglement, the membrane should be as cold as possible. With the current cavity, the membrane cannot be cooled using standard cavity cooling to a phonons occupation lower than $n_\mathrm{m} \approx 11$. Instead the spin could be used to prepare a cold membrane state by sympathetic cooling. This poses an additional challenge: First, the spin must be implemented as positive frequency oscillator to sympathetically cool the membrane, and then as negative frequency oscillator to implement the parametric-gain Hamiltonian. The change from positive to negative frequency oscillator is usually achieved by inverting the magnetic field. However, the magnetic field is slow compared to the coherence time of the coupled system. Therefore the following sequence is proposed (depicted in figure 6.4.1): (1) The atomic spin is prepared along $-x$ antiparallel to a magnetic field along B_x (as for a normal experiment with the spin as a positive frequency oscillator). (2) The magnetic field is slowly rotated from B_x to $-B_x$ so that the spin follows adiabatically. The spin is still a positive frequency oscillator (because its orientation with respect to the magnetic field has not changed), but is now rotated by π with respect to the initial spin. (3) The coupling between the spin and the membrane with a loop phase $\phi = \pi$ is switched on by switching on the coupling laser. The beam-splitter interaction between the spin and the membrane cools the membrane sympathetically close to the ground state. (4) A short spin-pumping pulse is applied. The spin is again prepared along $-x$ but now parallel to the magnetic field pointing along $-B_x$. The spin is now an effective negative frequency oscillator. (5) The coupling between the spin and the pre-cooled membrane is turned on by switching on the coupling beam. Since the inverted spin acts as negative frequency oscillator, the coupling Hamiltonian is effectively a parametric-gain interaction

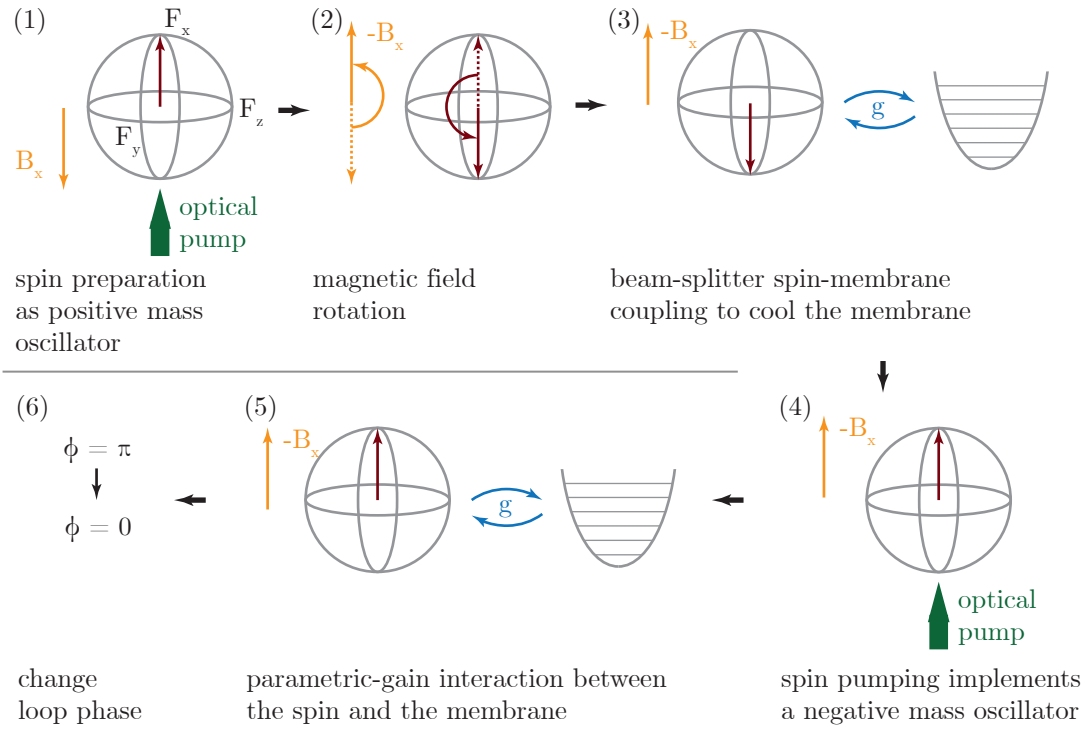

Figure 6.4.1: Proposed sequence for the coupling experiment. First the atomic spin is used to sympathetically cool the membrane oscillator (step (3)) by applying a beam-splitter coupling. Then the membrane is entangled with the spin by a parametric-gain interaction between the systems (step (5)). Finally, the loop phase is changed to obtain a good readout of the spin (step (6)). Details are given in the text.

that entangles the spin and the membrane. (6) Finally the loop phase is switched from $\phi = \pi$ to $\phi = 0$ in order to read out the spin state with high sensitivity (as described in section 6.3.1).

Chapter 7

Conclusion and Outlook

7.1 Conclusion

This thesis presents the hybrid, light-mediated coupling between the collective spin of an atomic ensemble and a mechanical oscillator. One of the main achievements of this work, was to upgrade the system from the classical regime, where strong coupling between the two systems was observed [29, 30, 68, 69], towards the quantum coherent coupling regime. For this both individual systems were improved:

Spin System: The collective spin of cold atomic ensembles is a well-established quantum system with a large toolbox for initiation and manipulation. However, operation of the atomic spin in the quantum regime had not been achieved so far in our experiment [68, 69]. In this thesis the loading of a dipole trap that is well mode-matched to the coupling laser is presented. The experimentally relevant three-dimensional Faraday interaction, coupling the spin to the polarisation state of the light, is modelled and compared with calibration measurements. It is shown that for certain parameters, the spin-light interface can be operated with high cooperativity $C_\mathrm{s} > 1$ in a quantum backaction-noise-dominated regime. This places the spin-light interface in the quantum regime, a crucial prerequisite to quantum coherently couple the spin system remotely to another system.

Optomechanical System: In the optomechanical system, the membrane with a phononic bandgap shield in the frame has been replaced by a nano-pillar membrane. The nano-pillar membrane has a mechanical Q-factor of $Q_\mathrm{m} = 5.1 \times 10^7$ at a temperature of 10 K which is more than an order of magnitude larger than the Q-factor of the phononic bandgap shielded membrane. In addition, the cavity design has been adapted to allow the membrane to be cryogenically cooled to 10 K without missaligning [124]. In this new configuration, the vibrational state of the membrane can be optically cooled to the cavity dynamical backaction cooling limit of $n_\mathrm{m} \approx 11$ phonons and the optomechanical interface is operated in the regime of high quantum cooperativity $C_\mathrm{m} > 1$. Thus, the second system can be also operated in the quantum regime where hybrid experiments in the regime of quantum coherent coupling are feasible.

Coherent Feedback Cooling: In a first series of hybrid experiments performed during this thesis [30], the strong coupling between the atomic spin and the phononic bandgap shielded membrane [29] was used to implement a coherent feedback loop using the atoms as a coherent controller for the membrane.

In contrast to measurement based feedback, in coherent feedback, the feedback is applied by another quantum system [39, 64], avoiding measurement and the associated decoherence [39]. In our experiment, we employed coherent feedback to remotely cool the membrane from room temperature to 216 mK using the collective spin of the atomic ensemble as controller [30].

Towards Quantum Coherent Coupling: In a second series of hybrid experiments, the nano-pillar membrane was operated in a cryogenic environment. First experiments show strong coupling between the two systems at cryogenic temperatures. Further experiments with the current hybrid system will allow to reach the regime of quantum coherent coupling, which is the next outstanding goal. In the following, we will outline further improvements and experimental steps to reach this goal.

7.2 Outlook

The improvements of the individual systems make it possible to operate both systems in the regime of high quantum cooperativity. Still, there are some remaining open questions and some more ideas to improve the individual systems:

Spin System: Even though the spin system can be operated at high quantum cooperativity and the spin dynamics has been studied in depth during this work, certain aspects of the spin dynamics are not fully understood yet: The decay of the atomic spin is larger than expected from a single-atom theory. In order to model the spin decoherence more realistically, the collective scattering to higher order optical modes should be considered, which has not been quantitatively studied in this thesis. Furthermore, for certain sets of probe parameters a coherent light-induced driving of the atomic spin is observed which cannot be explained by single-atom physics. The non-linear scaling of this driving with the number of atoms in the cloud suggests that it is caused by the collective dynamics of the atomic cloud rather than a single-atom effect. In the literature, models for collective scattering of cold atomic ensembles have been proposed that go beyond the description presented in this thesis and take into account inhomogeneous excitation along the atomic cloud [174] or significant atom-atom correlations induced by the interaction with light [175]. For a better understanding of the spin-light interface in our experiment, these theoretical models could be adapted to our experimental situation and may give some understanding of the observed spin dynamics.

Membrane System: Further improvements of the optomechanical system seem feasible: the mechanical Q-factor of our current membrane is $Q_\mathrm{m} = 5.1 \times 10^7$ which is still at the lower end of the state-of-the-art membranes [55]. Moreover, the cavity noise could be reduced by using cavity mirrors with a phononic bandgap [63], which might be interesting to increase the stability of the cavity for experiments at room temperature. Another interesting way to proceed would be to increase the reflectivity of the membrane by engineering a photonic crystal at the defect of the membrane [142]. This would allow us to reduce the requirements for the cavity or to remove it altogether [176] and perform cavity-free hybrid spin-mechanical experiments.

Coupled System: The light-mediated coupling of the spin and the membrane in the current experimental setup should allow the membrane mode to be cooled sympathetically to the vibrational ground

state $n_\mathrm{m} < 1$. In order to verify the number of excitations of the membrane vibrational mode, a heterodyne measurement of the membrane oscillator should be installed [112]. This allows to perform essentially calibration-free and more accurate measurement of the membrane occupation. Moreover, entanglement between the spin and the membrane could, in principle, be generated using the current experimental parameters. The parametric-gain Hamiltonian creates and annihilates collective spin-membrane excitations. In order to observe the entanglement, the signal-to-noise ratio of the spin detection has to be improved. Thus, for witnessing the interesting dynamics which can be engineered in our hybrid system, the individual detections of both systems have to be improved.

In addition to entanglement generation between the systems and ground state cooling of the membrane with the atoms, our versatile hybrid system can be employed in future experiments to study many other regimes and effects. There are many tuning parameters which allows us to enter diverse coupling regimes, such as the loop phase, the propagation delay in the loop, the linewidth of the individual systems, the detuning between the spin and the membrane, and the relative orientation of the spin with respect the magnetic field (implementing a positive or a negative frequency oscillator), most of which can be accessed in a time-controlled manner. Some of these coupling regimes are discussed in the following paragraphs:

Dissipative Coupling

The hybrid setup could be used to study dissipative collective dynamics in remote hybrid systems. For an arbitrary loop phase, the Hamiltonian coupling mediated by the light is given by

$$\hat{H}_\mathrm{eff} = \hbar(1-\cos\phi)g\hat{X}_\mathrm{s}\hat{X}_\mathrm{m} + \hbar 2\sin(\phi)\Gamma_\mathrm{s}\hat{X}_\mathrm{s}^2 \tag{7.2.1}$$

and the collective jump operator governing the dissipative dynamics by

$$\hat{J} = \sqrt{2\Gamma_\mathrm{m}}\hat{X}_\mathrm{m} + \mathrm{i}(1+\mathrm{e}^{\mathrm{i}\phi})\sqrt{2\Gamma_\mathrm{s}}\hat{X}_\mathrm{s} \tag{7.2.2}$$

where neither losses nor the loop delay are considered [37], see appendix G for details. If the loop phase is set to $\phi = \pi$, the coupling is Hamiltonian and the backaction of the light acting on the spin is cancelled, i.e. the jump operator does not act on the spin. However, if the loop phase is set to $\phi = 0$, the coupling between the spin and the membrane is fully dissipative (for a small loop delay τ). This leads to the appearance of exceptional points in the spectrum [68]. If, in addition to a loop phase of $\phi = 0$, the total loop delay τ_ss (i.e. the propagation time of the light between the two interactions with the spin) is engineered to be $\Omega_\mathrm{s}\tau_\mathrm{ss} = \pi$, the backaction of the light on the spin can again be suppressed (see equation (G.3.8) for details). In this scenario, the complex phase of the coupling could be tuned by adjusting the relative delay in the spin-membrane or the membrane-spin path. For similar path lengths in both paths (spin-membrane and membrane-spin), we get a self-amplification or a self-damping as result of the hybrid dynamics, i.e. $\dot{\hat{b}}_\mathrm{s} \propto \pm g\hat{b}_\mathrm{m}$ and $\dot{\hat{b}}_\mathrm{m} \propto \pm g\hat{b}_\mathrm{s}$. The loop delay can be engineered easily by coupling the light into optical fibres. The induced coupled dynamics can be interesting to study dissipative amplification in coupled systems. Moreover, we can use the dissipative interaction between the systems to cool the membrane oscillator and compare the cooling process to the cooling by a Hamiltonian coupling which we have shown in [30].

Non-Reciprocal Coupling

There is a growing interest in the non-reciprocal dynamics of hybrid quantum systems [177]. Cascaded quantum systems are non-reciprocal by default; on the contrary, the cascaded system must be engineered with great care, to obtain a bidirectional Hamiltonian interaction [37]. Therefore, cascaded quantum systems are a natural choice for testing non-reciprocal quantum protocols. If the loop phase of the remote interaction is set to $\phi = \pi/2$, the interaction between the spin and the membrane is non-reciprocal, i.e. the spin can drive the membrane but not vice versa. This can be best seen in the equations of motion, derived in appendix G, given by

$$\dot{\hat{b}}_\mathrm{s} = \mathcal{L}_0\hat{b}_\mathrm{s} + \mathrm{i}2\Gamma_\mathrm{s}\sqrt{2}\hat{X}_\mathrm{s}(t-\tau_\mathrm{ss}) - \mathrm{i}\sqrt{2\Gamma_\mathrm{s}}\left(\hat{P}_\mathrm{in}(\xi_1) - \hat{X}_\mathrm{in}(\xi_3)\right) \tag{7.2.3}$$

$$\dot{\hat{b}}_\mathrm{m} = \mathcal{L}_0\hat{b}_\mathrm{m} - \mathrm{i}g\sqrt{2}\hat{X}_\mathrm{s}(t-\tau_\mathrm{sm}) - \mathrm{i}\sqrt{2\Gamma_\mathrm{m}}\hat{X}_\mathrm{in}(\xi_2), \tag{7.2.4}$$

where the first term in each line describes the local dynamics, the second term the coupling due to the loop and the third term the backaction of the light acting on the systems. Here, τ_sm (τ_ss) is the propagation delay between the first spin interaction and the membrane interaction (second spin interaction). For the further discussion, we will distinguish between the dynamics for the spin acting as a positive and as a negative frequency oscillator:

Non-reciprocal Quantum Battery: For a spin acting as a positive frequency oscillator, the coupled dynamics of the expectation values in a frame rotating at the spin frequency is given by (derived in appendix G.3)

$$\langle\dot{\hat{b}}_\mathrm{s}\rangle = -\frac{\gamma_\mathrm{s}}{2}\langle\hat{b}_\mathrm{s}\rangle + \mathrm{i}\mathrm{e}^{\mathrm{i}\Omega_\mathrm{s}\tau_\mathrm{ss}}2\Gamma_\mathrm{s}\langle\hat{b}_\mathrm{s}\rangle \tag{7.2.5}$$

$$\langle\dot{\hat{b}}_\mathrm{m}\rangle = \mathrm{i}\delta\langle\hat{b}_\mathrm{m}\rangle - \frac{\gamma_\mathrm{s}}{2}\langle\hat{b}_\mathrm{m}\rangle + \mathrm{i}\mathrm{e}^{\mathrm{i}\Omega_\mathrm{s}\tau_\mathrm{sm}}g\langle\hat{b}_\mathrm{s}\rangle \tag{7.2.6}$$

where $\delta = \Omega_\mathrm{s} - \Omega_\mathrm{m}$ is the detuning between the two systems, τ_ss is the time for the light to complete the loop and τ_sm the time for the light to travel from the spin to the membrane. In this equation, we see again the non-reciprocal nature of the coupling: While the membrane is driven by the spin, the spin is not influenced by the membrane. By tuning the delay between spin and the membrane to $\Omega_\mathrm{s}\tau_\mathrm{sm} = \pi/2$ and matching the linewidth of the systems, the dynamics of a *dissipative isolator* [178] can be obtained (in equations (G.3.14) and (G.3.14) the quantum noise is included). By driving the spin system (e.g. with a rf coil), the dynamics of a *non-reciprocal quantum battery* [179] is obtained. In this implementation, the spin acts as the charger and the membrane as the quantum battery. In a non-reciprocal quantum battery, the charger (spin) is driven, but the battery (membrane) ends up in a higher energy state than the charger. Using the quantum protocol presented in [179], the energy dissipation to the environment is reduced compared to a classical charging process. The full analysis of our system including the backaction noise is given in appendix G.

Directional Phase-Preserving Quantum Amplifier: If on the other hand the spin acts as a negative frequency oscillator, the coupled dynamics is given by (derived in appendix G.3)

$$\langle\dot{\hat{b}}_\mathrm{s}\rangle = -\frac{\gamma_\mathrm{s}}{2}\langle\hat{b}_\mathrm{s}\rangle + \mathrm{i}e^{\mathrm{i}\Omega_\mathrm{s}\tau_\mathrm{ss}}2\Gamma_\mathrm{s}\langle\hat{b}_\mathrm{s}^\dagger\rangle \tag{7.2.7}$$

$$\langle\dot{\hat{b}}_\mathrm{m}\rangle = \mathrm{i}\delta\langle\hat{b}_\mathrm{m}\rangle - \frac{\gamma_\mathrm{s}}{2}\langle\hat{b}_\mathrm{m}\rangle + \mathrm{i}e^{\mathrm{i}\Omega_\mathrm{s}\tau_\mathrm{sm}}g\langle\hat{b}_\mathrm{s}^\dagger\rangle \tag{7.2.8}$$

where the detuning is given by $\delta = |\Omega_\mathrm{s}| - \Omega_\mathrm{m}$. By tuning the propagation delays between the spin and the membrane to $\Omega_\mathrm{s}\tau_\mathrm{sm} = \pi/2$, the dynamics of a *directional phase-preserving quantum amplifier* can be implemented [178]. Here, the first spin-light interaction and the membrane-light interaction establish a unidirectional coupling from the spin to the membrane. The loop phase can be set to $\phi = \pi/2$ so that in the second spin-light interaction the spin is driven by the same noise quadrature as the membrane, so that a common reservoir for the two oscillators is established. A rigorous analysis of the noise processes needs still to be done.

In the future, our versatile coupled system will allow us to demonstrate some of the protocols proposed for non-reciprocal quantum devices [178, 179].

Self Interaction of a Single System

The use of light to mediate interactions between different, remote systems has inspired the development of systems in which light mediates the self-interaction of a single system. Thereby, the light interacts with the system multiple times without any measurements in between, implementing a coherent optical feedback loop. By manipulating the phase and the delay of the loop, the coherent feedback can be used to control the system. In our laboratory we have performed a series of coherent feedback experiments, cooling a membrane oscillator close to the mechanical ground state [65]. The scheme of this experiment is shown in figure 7.2.1 (a).

In a similar way, the spin oscillator could be manipulated by optical coherent feedback. This could be done using the existing loop, but without interfacing the membrane oscillator [37] (i.e. $\Gamma_\mathrm{m} = 0$, scheme shown in figure 7.2.1 (b)). The self-interacting term of the coupling Hamiltonian is proportional to $\hat{H}_\mathrm{eff} \propto \hat{X}_\mathrm{s}^2$ and could therefore potentially be used to squeeze the spin oscillator. For a precessing spin, the effective spin self-interaction Hamiltonian is given by

$$\hat{H}_\mathrm{eff} = \hbar 2\Gamma_\mathrm{s}\sin(\phi)\left(\hat{b}_\mathrm{s}\hat{b}_\mathrm{s}^\dagger + \hat{b}_\mathrm{s}^\dagger\hat{b}_\mathrm{s} + \hat{b}_\mathrm{s}\hat{b}_\mathrm{s}e^{-\mathrm{i}2\Omega_\mathrm{s}\tau} + \hat{b}_\mathrm{s}^\dagger\hat{b}_\mathrm{s}^\dagger e^{\mathrm{i}2\Omega_\mathrm{s}\tau}\right). \tag{7.2.9}$$

The first two terms of this Hamiltonian correspond to a shift in the oscillation frequency of the spin. The last two terms cause a one-axis twisting dynamics, but rotate at twice the spin frequency. By modulating the loop phase at twice the spin frequency $\phi = \pi + \phi_1\cos(2\Omega_\mathrm{s}t)$, an effective spin squeezing Hamiltonian is obtained

$$\hat{H}_\mathrm{eff} = \hbar\Gamma_\mathrm{s}\frac{\phi_1}{2}\left(\hat{b}_\mathrm{s}\hat{b}_\mathrm{s} + \hat{b}_\mathrm{s}^\dagger\hat{b}_\mathrm{s}^\dagger\right). \tag{7.2.10}$$

Taking into account the decoherence of the system, the amount of squeezing can be calculated (explicitly done in appendix H). The modulation amplitude ϕ_1 can be optimised to obtain maximal squeezing, given by

$$\xi^2_\mathrm{min} = \frac{\sqrt{1+2\eta C_\mathrm{s}(1+2C_\mathrm{s}(1-\eta))}-1}{\eta C_\mathrm{s}} \xrightarrow{\eta=1} \frac{\sqrt{1+2C_\mathrm{s}}-1}{C_\mathrm{s}} \tag{7.2.11}$$

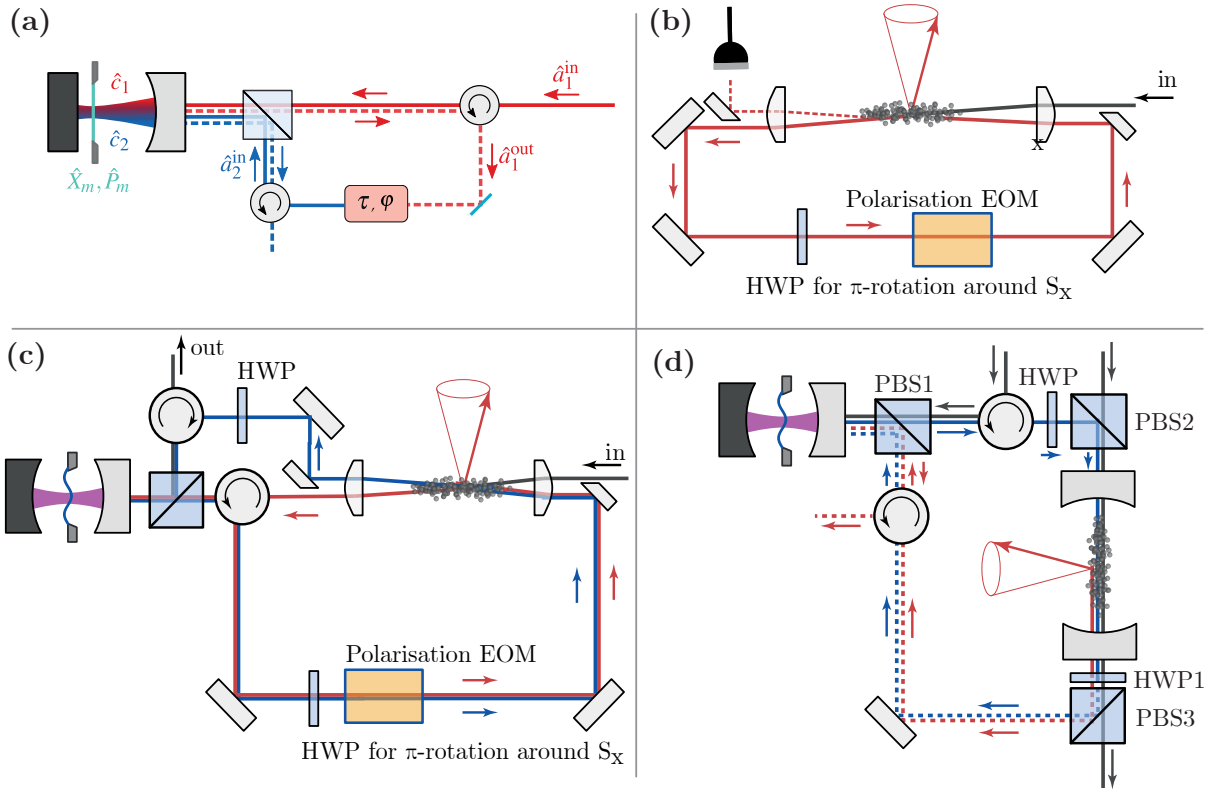

Figure 7.2.1: Different coupling setups for coherent coupling or feedback experiments: (a) The setup for the optical feedback on the membrane [65], figure taken from [124]. The light interacts with the membrane twice. Between the two interactions, the delay and the phase of the light can be changed. (b) The corresponding setup for a coherent, optical feedback on the atomic spin. After the first interaction with the atomic spin the light is sent back to the atoms. In between, the loop phase can be modulated around a mean loop phase $\phi = \pi$ (set by the HWP) using an EOM. (c) The coupling experiment in a spin-membrane-spin-membrane configuration. In contrast to the coupling experiments described in this thesis, this scheme allows the cancellation of the backaction on the membrane and the spin. (d) Proposal for an experiment in which the membrane interacts twice with the light while the atomic spin interacts only once. After the first interaction with the membrane, the light is combined with a second local oscillator on PBS2 converting the phase modulation into a polarisation modulation. This allows the membrane to act on the spin. After interacting with the spin, a half waveplate is placed to set the loop phase $\phi = \pi$. The polarisation state of the light is then mapped back to the phase space of the light by PBS3. In a second interaction with the membrane, the spin signal acts on the membrane and the backaction of the light on the membrane is cancelled.

where $C_s = 2\Gamma_s/\gamma_s$ is the cooperativity of the spin system and η is the (amplitude) loop transmission. The losses in the loop drastically limit the amount of squeezing. With this protocol, there is no more squeezing for loop transmission $\eta < 0.8$ independent of the spin cooperativity. Achieving large enough loop transmissions may be impossible for the current loop design, but without the membrane cavity in the loop, a very high transmission through the loop is expected. Still, in this scheme, the optimal squeezing is always a trade-off between the squeezing dynamics and the backaction driving the spin. However, this can be solved if a third atom-light interaction is engineered, as proposed by Wang et al. [180]. With only two interactions, either the backaction acting on the spin can be cancelled or the squeezing Hamiltonian can be implemented. By adding a third atom-light interaction, the loop phase between the interaction can be set such that there is a squeezing interaction and the backaction is cancelled.

There have also been proposals to use a spin ensemble to squeeze the polarisation state of the light by passing it twice [181]. In the proposal by Sherson et al. [181], the spin ensemble must be passed from orthogonal directions in order to couple two different spin quadratures to the light. With our elongated atomic cloud, this seems to be impossible to implement. But instead of passing from two orthogonal directions, a loop delay of $\tau\Omega_s = \pi/2$ could be added. This allows the coupling to two orthogonal spin quadratures and thus to implement a similar light squeezing scheme as proposed in [181].

Fully Closed Loop

In the current loop design, the spin is interfaced twice while the membrane is interfaced only once. Therefore, the backaction is only cancelled for the spin but not for the membrane. In a future upgrade of the experiment, the loop could be closed for the membrane as well so that the backaction acting on the membrane could be cancelled (scheme shown in figure 7.2.1 (c)). The technique of interfacing the membrane twice has been successfully implemented in our laboratory by using two orthogonal polarisations [65]. In our current experiment, the second polarisation in the cavity is used to lock the cavity and to read out the membrane state. In order to still use a separate lock and read-out beam, this beam could be detuned by several nanometres from the coupling beam so that the two beams can be combined using a dichroic mirror, addressing different longitudinal cavity mode. In this case, both beams must be locked to a common frequency reference in order to couple them to different modes of the same cavity. This frequency reference could be the in-house frequency comb stabilised to a stable frequency reference [74] or a transfer cavity.

Coupling Beyond Harmonic Oscillators

For the hybrid experiments in this thesis, the collective atomic spin is approximated as a harmonic oscillator. Since the tilt of the spin is small, the nonlinearity of the atomic spin system is not significant so far. However, there is a great interest in developing nonlinear coupling terms for mechanical oscillators [182].

In order to increase the non-linearity of the spin system, a smaller atomic cloud could be used. The reduced coupling strength could be compensated by placing the atomic cloud in a cavity. However, the use of a cavity makes it difficult to engineer the double-pass geometry with two beams passing the atomic cloud at a small angle. Alternatively, the spin could be passed only once, while the double-pass is implemented on the membrane (proposal shown in figure 7.2.1 (d)). In this way, it might be feasible to use the atomic spin as a non-linear medium to manipulate the state of the membrane.

Coupling of Other Quantum Systems

The general coupling scheme used in this thesis is versatile and can be applied to any system that can be strongly coupled to light [37]. This allows the coherent interaction to be used to prepare or coherently manipulate quantum systems by coupling them to a well established quantum system.

For example, the coherent feedback technique could be of interest for levitated nanoparticles [183]. The use of coherent feedback cooling techniques could potentially reduce the laser power required and thus the internal temperature of the nanoparticle [184], which currently limits the coherence of the centre-of-mass motion due to the black-body emission of the nanoparticle [185].

Furthermore, the engineering of coherent links between systems could have interesting applications in the engineering of hybrid quantum networks [186]. Different superconducting qubits in different dilution refrigerators could be coherently coupled using similar techniques in the microwave domain [36, 48]. Moreover, the general coupling scheme could be used to coherently interconnect multiple quantum devices, including sensing probes, quantum processors and readout systems. First experiments of coupling schemes similar to ours, which couple more than two quantum systems, have recently been proposed [187, 188].

Moreover, the coupling scheme presented in this thesis is not limited to photons as carriers. There is a growing interest and expertise in the engineering of phononic structures [189, 190]. Coherent interaction between mechanical systems could be mediated by phonons propagating in a phononic crystal waveguide [191]. The versatile coupling scheme presented and experimentally implemented in this thesis provides an interesting starting point and inspiration for further experiments, engineering quantum coherent interactions between remote systems mediated by a propagating field.

Acknowledgements

I would like to express my deepest gratitude to the many persons who have supported me and contributed, both directly and indirectly, to the completion of this thesis.

First, I am incredibly grateful to Philipp Treutlein for the opportunity to work under his guidance. His invaluable input during discussions, his patience, and his effort to explain complex concepts in a pedagogical manner have been very important to my understanding. I deeply appreciate his enthusiasm for quantum physics in general and our project in particular, which has been a constant source of inspiration.

I would also like to thank Patrick Maletinsky for serving as my second supervisor. His insightful questions and fresh perspective during discussions have been very helpful. I am very grateful to Witlef Wieczorek for kindly reviewing my thesis.

A heartfelt thank you to the membrane team: James (Chun Tat) Ngai, Manel Bosch Aguilera, and Maryse Ernzer. Working alongside you has been an absolute joy. I deeply appreciate your contributions, the time we spent together in the lab and office, and all the moments we shared—whether they were filled with joy or frustration. Thank you, James, for often pushing me to see things from new perspectives, for sharing the struggles with low atom numbers, and for celebrating with me when we first observed light squeezing. Manel, your discussions and advice have been invaluable—whether or not they solved the problem at hand, they always reminded me that I wasn't alone in facing challenges. Thank you very, very much, for reading and providing feedback on this thesis! Maryse, it was a true pleasure to have you on the team, and I'm grateful for our shared experiences. In the same spirit, I want to thank Florian Goschin for visiting our experiment and work with me on the dipole trap. Thank you for your energy, joy and enthusiasm. I enjoyed it much to work with you. I am looking forward to working more with Alexandre Huot de Saint-Albin and Alvaro Mitchell Galvao de Melo on our experiment.

A special thanks to Thomas Karg and Baptiste Gouraud for introducing me to experimental quantum optics and atomic physics, and for your careful work on the experiment, from which I benefited greatly. Your guidance and explanations were key to helping me understand the complexities of our setup.

I am also thankful for the opportunity to collaborate with Patrick Potts, Matteo Brunelli, and Christoph Bruder. Thank you for the stimulating discussions, the theoretical insights, and for offering different perspectives on the same physics. I truly appreciated the positive atmosphere throughout.

Our work in optomechanics relied heavily on the expertise of our collaborators who fabricated the remarkable membranes we used. I would like to extend my gratitude to Luiz Couto Correa Pinto Filho from Ulrik Lund Andersen's group, and everyone involved in fabricating the nano-pillar membranes. Luiz, thank you for visiting our lab, collaborating on the membrane part of the experiment, and delivering these extraordinary membranes. Additionally, I would like to thank Klaus Gärtner, Jin Chang, and Simon Gröblacher for their long-standing collaboration and for producing such incredible membranes. I'm confident they will enable groundbreaking experiments in the near future.

A sincere thank you to Michael Vogelpohl for developing the core of the simulation that helped us better understand the atomic dynamics under probe light. This simulation was essential for diving deeper into the spin dynamics of our system.

I am also grateful to the mechanics and electronics workshops at the physics department. Your support has been invaluable. Thank you, Michael Steinacher and Sascha Linder, for your friendly demeanor, patience, and for walking me through even the simplest concepts in electronics. Your development of new current sources and assistance with numerous broken devices was a huge help. Thanks to Sascha Martin and the team for fabricating the various components for our experiments, and to Dominik Sifrig for consistently ensuring we had the liquid helium we needed, whether scheduled or not.

I also wish to thank the members of the Treutlein group, with whom I've shared countless coffee breaks, hikes, lunches, and swims in the Rhein. Thank you for the conversations and camaraderie, particularly Gianni Buser, Paolo Colciaghi, Björn Cotting, Matteo Fadel, Suyash Gaikwad, Jiajie Guo, Lex Joosten, Simon Josephy, Yifan Li, Roberto Mottola, Haroon Saeed, Madhavakkannan Saravanan, Yongqi Shi, Fabrizio Volante, and Tilman Zibold.

To my family, friends, and everyone who has been part of my life over the past five years—thank you for enriching my journey. My deepest gratitude goes to my parents. Mami and Papi, you are two of the main reasons I was able to write this thesis! To Anja, your support has meant the world to me. Thank you for your understanding and for standing by my side. Words cannot express how much your presence during this time has meant to me, no matter if it was a good or a bad time.

Finally, I would like to take a moment to reflect on a broader perspective: It is a privilege to have been raised and educated by so many wonderful people and to have had the opportunity to pursue curiosity-driven science. I recognise how rare and precious this privilege is, and I am profoundly grateful to all those who have made it possible and to the God in whom I believe. It is in this spirit that I dedicate this work to those who not only appreciate this gift but also understand the responsibility that comes with it. I am deeply thankful to all those who go to places that (at first glance) seem less favourable and less bright, and work to extend this precious privilege so that in the future even more people can live in dignity, righteous peace, reasonable prosperity and the freedom to express their creativity.

Appendix A

Phase Loop Lock for Second Repump Laser

In this appendix, the implementation of the phase loop lock is described in more details. In our experiment, the phase loop lock is used to lock the frequency of a second repump laser. Potentially, a similar lock could be used in the future to lock the light of the Ti:Saph to the frequency comb which is available in our laboratory.

To maximise the number of atoms, we have realised that it would be advantageous to have more power from the repump laser than could be provided by the butterfly diode. We have therefore implemented a second laser at the frequency of the $F = 1 \leftrightarrow F' = 2$ transition. This second laser is locked to the first repump laser by a frequency offset lock. The offset lock is implemented as a phase loop lock (see figure A.0.1), inspired by Appel et al. [72]. In the experiment, the light from both lasers is combined on a fibre coupled beam splitter and measured on a photodiode[1]. The signal from the photodiode is split into a dc and a rf component by a bias-tee[2]. The dc component can be used to improve coupling into the fibre in the future. A directional coupler[3] is added to the rf output of the bias-tee to monitor the beat note. After the directional coupler, the beat note has an amplitude of about 0 dBm which is compatible with the input power required for the evaluation board[4].

The evaluation board contains a digital phase detector. Here we use the *ADF4002* chip, which has an input frequency range between 5 MHz and 400 MHz. If a lock at a higher beat-note frequency (up to 7 GHz) is required, the board *ADF4107* can be used [72, 192]. The *ADF4002* chip on the evaluation board contains a programmable reference divider which can be used to compare the beat-note frequency with a reference frequency multiplied by a fraction N/R, where N is an integer between 1 and 8191 and R is an integer between 1 and 16'383. In our case, we use the $f_{\text{ref}} = 10\,\text{MHz}$ clock of the experiment as the reference frequency to create a lock at $f_{\text{lock}} = 10\,\text{MHz} \cdot 392/50 = 78.4\,\text{MHz}$. Using the system

[1] Amplified photodiode, *Thorlabs, PDA10A2*; $f_{\text{bw}} = 150\,\text{MHz}$

[2] Bias-tee, *MiniCircuits, ZX85-12-S+*

[3] Directional Coupler, *MiniCircuits, ZFDC-20-5-S+*

[4] Evaluation board, *Analog Devices, EVAL-ADF4002*; frequency range: 5 MHz to 400 MHz; input power: −5 dBm to 5 dBm

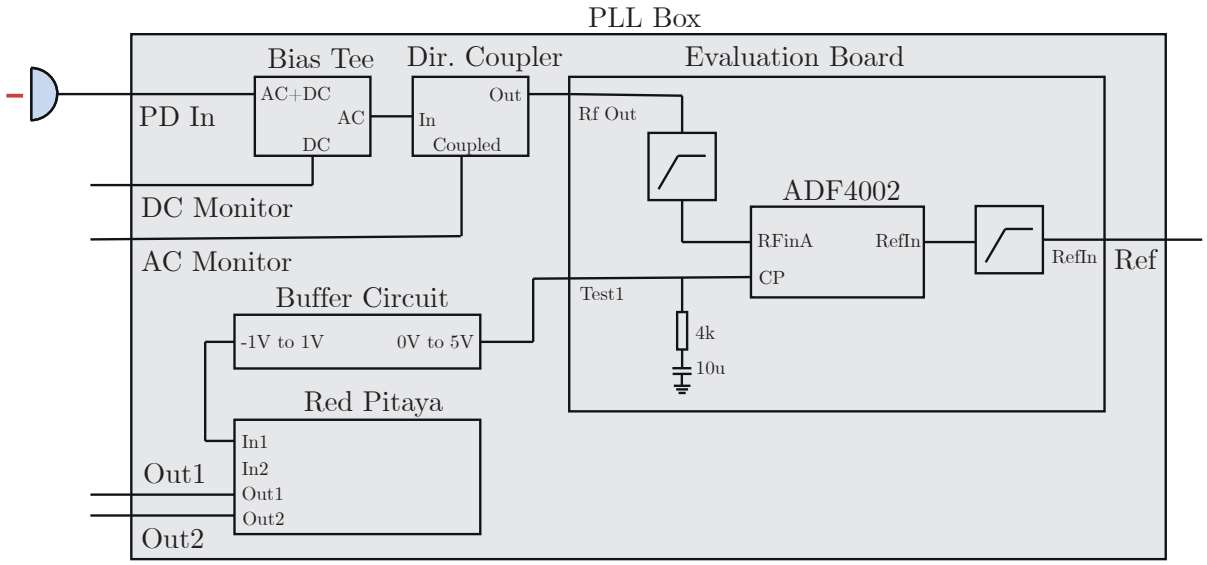

Figure A.0.1: Schematic of our PLL box which is used to generate an offset lock to lock the second repump laser.

demonstration platform board[5] and a software provided by *Analog Devices*, the *ADF4002* can be easily programmed (see figure A.0.3 (a)). It should be noted that the *ADF4002* does not save the configurations. Therefore, after each power cut, the *ADF4002* must be reprogrammed.

The *ADF4002* chip has a charge pump output which outputs 5 mA if the beat-note frequency is lower than the programmed frequency value and 625 μA if the beat-note frequency is higher than the programmed frequency. We have modified the evaluation board so that the output of the charge pump is connected to ground via a 4 kΩ resistor and a 10 µF capacitor in series. This converts the current to an output voltage of 0 V or 5 V depending on the beat-note frequency. A buffer circuit is used to shift this modulation to −1 V to 1 V which is then used as an error signal for a PI lock implemented on a *Red Pitaya* [73].

The slope of the error signal (the step function between −1 V and 1 V) is much steeper than the bandwidth of the feedback loop to the laser. Therefore the error signal is always given by the maximum error (i.e. −1 V or 1 V). The lock parameters must be configured to prevent large oscillations around the target frequency. We have programmed the lockbox on the *Red Pitaya* to apply a slow, low-pass filtered I-gain to the piezo of the ECDL laser. We chose a very high I-gain, ensuring that with only the I-gain, the frequency undergoes large, slow oscillations. In addition, a high-pass filtered signal is fed back to the laser current as P-gain. The maximum amplitude of this P-gain is reduced so that the corrections are small even when the error signal is at maximum error (see figure A.0.3 (b) for the parameter). This minimises the oscillations around the target frequency.

[5]System demonstration platform, *Analog Devices, SDS-S*

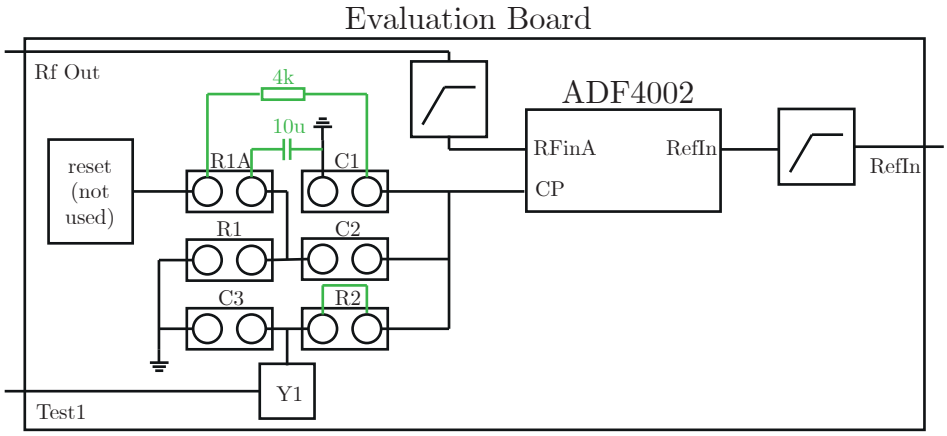

Figure A.0.2: Schematic of the evaluation board. The green jumpers are noted which are used for our PLL.

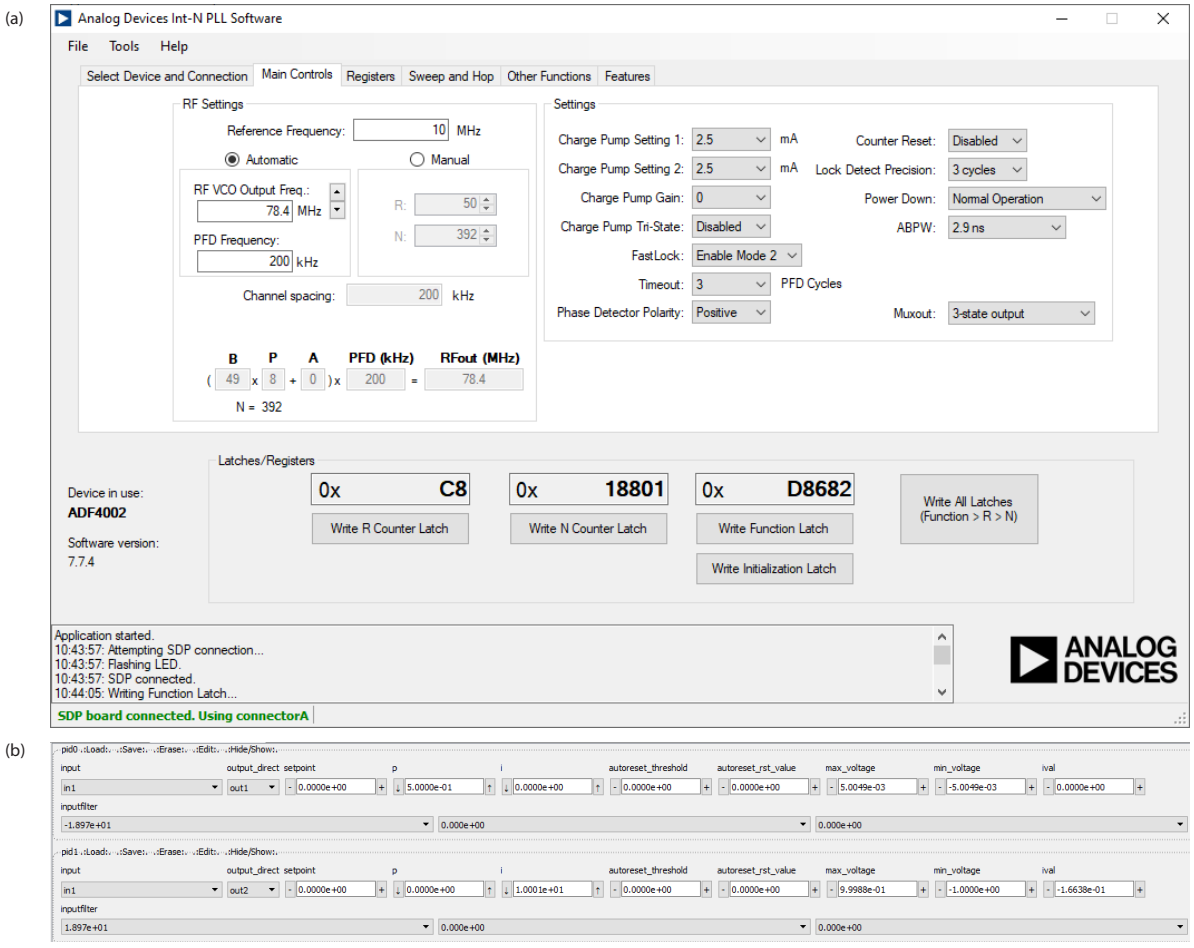

Figure A.0.3: Graphical interface of the digital control of (a) the *ADF4002* board and (b) the *Red Pitaya* interface [73] with the values used in the experiment.

Appendix B

Derivation of the Atom-Light Coupling Hamiltonian and Some More Examples

---

In this appendix, a more complete derivation of the atom-light coupling is given, starting from the well-known dipole Hamiltonian. Furthermore, the explicit elimination of the excited state is shown. The equations derived here are used in section 2.2.

The derivations in this appendix follow to a large extent the definitions given in [102]. The obtained results for the Rubidium atom are compared with the results presented in [110, 114] and found to be consistent.

B.1 The optical field

Before describing the atom-light interaction, in this section the electromagnetic field is defined. We assume that we have only one paraxial mode of the electromagnetic field which is described by the unitless mode function $u(\mathbf{r})$. Following the slowly varying envelope approximation we get

$$\hat{\mathbf{E}}(\mathbf{r},t) = \mathcal{E}_0 \left((\hat{a}_H(z,t)\mathbf{e}_H + \hat{a}_V(z,t)\mathbf{e}_V)u(\mathbf{r})\mathrm{e}^{\mathrm{i}(k_0 z - \omega_\mathrm{L} t)} + (\hat{a}_H^\dagger(z,t)\mathbf{e}_H^* + \hat{a}_V^\dagger(z,t)\mathbf{e}_V^*)u^*(\mathbf{r})\mathrm{e}^{-\mathrm{i}(k_0 z - \omega_\mathrm{L} t)} \right), \tag{B.1.1}$$

where $\mathcal{E}_0 = \sqrt{\frac{\hbar\omega_\mathrm{L}}{2\epsilon_0 c A}}$ is the vacuum electric field density (per $s^{-1/2}$ bandwidth, units of $V\sqrt{s}/m$), A is the cross-section area of the optical mode, $\hat{a}_H$ ($\hat{a}_V$) annihilation operators of the horizontally (vertically) polarised field (units of $s^{-1/2}$), $k_0 = 2\pi/\lambda$ the wave vector of the field, ω_L the angular frequency of the field, λ the wavelength of the field, c the speed of light and ϵ_0 the vacuum permittivity. The electric field operators can be rewritten in terms of the circularly polarised field components by defining a spherical basis

$$\mathbf{e}_+ = -\frac{1}{\sqrt{2}}(\mathbf{e}_H + \mathrm{i}\mathbf{e}_V), \qquad \mathbf{e}_- = \frac{1}{\sqrt{2}}(\mathbf{e}_H - \mathrm{i}\mathbf{e}_V), \tag{B.1.2}$$

and the corresponding annihilation operators of the circularly polarised field [102, 108]

$$\hat{a}_+ = -\frac{1}{\sqrt{2}}(\hat{a}_H + \mathrm{i}\hat{a}_V), \qquad \hat{a}_- = \frac{1}{\sqrt{2}}(\hat{a}_H - \mathrm{i}\hat{a}_V). \tag{B.1.3}$$

In the spherical basis, the dot product is given by [102]

$$\mathbf{A}\cdot\mathbf{B} = \sum_q (-1)^q A_q B_{-q}. \tag{B.1.4}$$

The free-space electric field can be separated in rotating and counter-rotating terms $\hat{\mathbf{E}}(\mathbf{r},t) = \hat{\mathbf{E}}^{(+)}(\mathbf{r},t) + \hat{\mathbf{E}}^{(-)}(\mathbf{r},t)$ [103]. In the spherical coordinate system, the electric field reads as

$$\hat{\mathbf{E}}^{(-)}(\mathbf{r},t) = -\mathcal{E}_0(\hat{a}_-^\dagger(z,t)\mathbf{e}_+^* + \hat{a}_+^\dagger(z,t)\mathbf{e}_-^*)u^*(\mathbf{r})\mathrm{e}^{-\mathrm{i}(k_0 z-\omega_\mathrm{L}t)}, \tag{B.1.5}$$

$$\hat{\mathbf{E}}^{(+)}(\mathbf{r},t) = -\mathcal{E}_0(\hat{a}_-(z,t)\mathbf{e}_+ + \hat{a}_+(z,t)\mathbf{e}_-)u(\mathbf{r})\mathrm{e}^{\mathrm{i}(k_0 z-\omega_\mathrm{L}t)}. \tag{B.1.6}$$

The creation and annihilation operators of the light field are given in units of $s^{-1/2}$ and have the following commutation relations

$$[\hat{a}_\alpha(\xi), \hat{a}_{\alpha'}^\dagger(\xi')] = [\hat{a}_\alpha(z,t), \hat{a}_{\alpha'}^\dagger(z',t')] = c\delta_{\alpha\alpha'}\delta(z-z'-c(t-t')) = \delta_{\alpha\alpha'}\delta(t-t'-(z-z')/c), \tag{B.1.7}$$

$$[\hat{a}_\alpha^\dagger(z,t), \hat{a}_{\alpha'}^\dagger(z',t')] = [\hat{a}_\alpha(z,t), \hat{a}_{\alpha'}(z',t')] = 0, \tag{B.1.8}$$

where z is the position coordinate along the propagation direction of the light and t is the time dependency of the slowly varying envelope function of the electromagnetic field. Note that unlike the electric field the creation and annihilation operators do not oscillate at the optical frequency. In the following, I will omit the time dependency on the slowly varying envelope function. From the creation and annihilation operators, the total photon flux can be calculated by

$$\Phi_\mathrm{L}(\xi) = \langle \hat{a}_+^\dagger(\xi)\hat{a}_+(\xi) + \hat{a}_-^\dagger(\xi)\hat{a}_-(\xi)\rangle = \langle \hat{a}_H^\dagger(\xi)\hat{a}_H(\xi) + \hat{a}_V^\dagger(\xi)\hat{a}_V(\xi)\rangle. \tag{B.1.9}$$

The total light power is then given by $P = \Phi_\mathrm{L}\hbar\omega_\mathrm{L}$. For a free space electromagnetic field, the local intensity can be expressed as [102, 103]

$$I(\mathbf{r}) = c\epsilon_0\langle|\hat{\mathbf{E}}(\mathbf{r},t)|^2\rangle_t = 2c\epsilon_0\langle\hat{\mathbf{E}}^{(-)}(\mathbf{r},t)\cdot\hat{\mathbf{E}}^{(+)}(\mathbf{r},t)\rangle = \frac{\hbar\omega_\mathrm{L}}{A}|u(\mathbf{r})|^2\Phi_\mathrm{L}(\xi) = \frac{P(\xi)}{A}|u(\mathbf{r})|^2. \tag{B.1.10}$$

Here, the intensity is the average over one oscillation period of the optical field.

B.1.1 Gaussian Beam

Assumed that we have a Gaussian beam, the mode function of the light is given by

$$u_{00}(r,\phi,z) = \frac{w_0}{w(z)}\exp\left(-\frac{r^2}{w(z)^2} + \mathrm{i}k_0\frac{r^2}{2R(z)} - \mathrm{i}\Phi(z)\right), \tag{B.1.11}$$

where we have defined

$$w(z) = w_0\sqrt{1+\left(\frac{z}{z_\mathrm{R}}\right)^2}, \tag{B.1.12}$$

$$R(z) = \frac{z^2+z_\mathrm{R}^2}{z}, \tag{B.1.13}$$

$$\Phi(z) = \arctan\left(\frac{z}{z_\mathrm{R}}\right), \tag{B.1.14}$$

where the Rayleigh length is given by $z_\mathrm{R} = \pi w_0^2/\lambda$, with the waist w_0 and the wavelength λ. The intensity profile of the Gaussian mode is given by

$$|u_{00}(r,\phi,z)|^2 = \frac{z_\mathrm{R}^2}{z^2+z_\mathrm{R}^2}\exp\left(-\frac{2r^2}{w(z)^2}\right). \tag{B.1.15}$$

We see that the normalisation of the mode is chosen that we have at the peak $u_{00}(0,\phi,0) = 1$. In order to obtain the cross-section area of the optical mode, we integrate the Gaussian beam in the transverse direction. We see that

$$A = \int_0^\infty\int_0^{2\pi} u_{00}^*(r,\phi,z)u_{00}(r,\phi,z)\mathrm{d}\phi r\mathrm{d}r = \frac{\pi w(z)^2}{2} \underset{z=0}{\to} \frac{\pi w_0^2}{2}. \tag{B.1.16}$$

Now we plug this area into the definition of intensity given in equation B.1.10 and get

$$I(\mathbf{r}) = \frac{2P}{\pi w_0^2}|u_{00}(\mathbf{r})|^2. \tag{B.1.17}$$

Here, we directly see that the peak intensity is indeed $I_0 = 2P/(\pi w_0^2)$ while the average intensity of the beam is obtained by integrating the intensity over the transverse plane and proves to be a factor two smaller $\bar{I} = P/(\pi w_0^2)$.

B.1.2 Top Hat Beam

On the other side, we can model a homogeneous light distribution by assuming a top hat beam. The mode function of an idealised laser beam with a top hat beam profile of radius w_0 is given by

$$u(r,\phi,z) = \Theta(w_0 - r), \tag{B.1.18}$$

where $\Theta(x)$ is the Heaviside step function which is zero for $x < 0$ and one else. Again, the cross-section area of the optical mode can be obtained by integrating over the transverse plane

$$A = \int_0^\infty\int_0^{2\pi} \Theta(w_0-r)^2\mathrm{d}\phi r\mathrm{d}r = \pi w_0^2. \tag{B.1.19}$$

The intensity profile is homogeneous inside the beam and given by

$$I(\mathbf{r}) = \frac{P}{\pi w_0^2}\Theta(w_0 - r). \tag{B.1.20}$$

We see that the intensity of the top hat laser beam is the same as the mean intensity of the Gaussian laser beam for the same laser power P (and accordingly the same total flux). In the following, we see that the coupling of an atom to the light-field depends on the flux, the position of the atom and the cross section area. The mode functions of the laser beam is normalised such that at the peak intensity $u = 1$. Thus, the beam geometry is mainly contained in the cross-section area.

B.2 Dipole Hamiltonian

In this section, the derivation given in the first part of section 2.2 is given but in more details. Again, we start at the electric dipole Hamiltonian given by

$$\hat{H}_{\text{int}} = -\hat{\mathbf{d}} \cdot \hat{\mathbf{E}}(\mathbf{r}, t) = -e\hat{\mathbf{r}}_e \cdot \hat{\mathbf{E}}(\mathbf{r}, t), \tag{B.2.1}$$

where $\hat{\mathbf{r}}_e$ is the position operator of the electron (units of m) and $\mathbf{r}$ is the classical position of the nucleus of the atom. Here we have applied the dipole approximation. The dipole operator $\hat{\mathbf{d}}$ (and similarly the position operator $\hat{\mathbf{r}}_e$) can be decomposed in positive and negative rotating terms

$$\hat{\mathbf{d}} = \hat{\mathbf{d}}^{(+)} + \hat{\mathbf{d}}^{(-)}. \tag{B.2.2}$$

This works, since the dipole operator does not couple states within the ground state manifold or the excited state manifold. We defined $\hat{\mathbf{d}}^{(+)} = \hat{P}_g \hat{\mathbf{d}} \hat{P}_e$ as the operator changing the atomic state from the excited state manifold to the ground state manifold and $\hat{\mathbf{d}}^{(-)} = \hat{P}_e \hat{\mathbf{d}} \hat{P}_g$ doing the opposite. Here, P_g (P_e) is the projector into the atomic ground (excited) state manifold. Next we assume that the optical frequency ω_{L} is close to the atomic transition of interest at a frequency ω_0. We go to a frame which rotates at the optical frequency. In this regime, we can apply the rotating wave approximation and neglect the fast rotating terms $\hat{\mathbf{d}}^{(+)} \cdot \hat{\mathbf{E}}^{(+)}(\mathbf{r}, t)$ and $\hat{\mathbf{d}}^{(-)} \cdot \hat{\mathbf{E}}^{(-)}(\mathbf{r}, t)$. We get

$$\hat{H}_{\text{int}} \approx -\hat{\mathbf{d}}^{(+)} \cdot \hat{\mathbf{E}}^{(-)}(\mathbf{r}) - \hat{\mathbf{d}}^{(-)} \cdot \hat{\mathbf{E}}^{(+)}(\mathbf{r}). \tag{B.2.3}$$

We can write the Hamiltonian in the spherical basis (the scalar product is defined in equation B.1.4) and get [102]

$$\hat{H}_{\text{int}} \approx -e \sum_q (-1)^q \left(\hat{r}_q^{(+)} \cdot \hat{E}_{-q}^{(-)}(\mathbf{r}_i) + \hat{r}_q^{(-)} \cdot \hat{E}_{-q}^{(+)}(\mathbf{r}_i) \right). \tag{B.2.4}$$

This Hamiltonian can be written in the basis of the hyperfine states as

$$\begin{aligned} \hat{H}_{\text{int}} \approx -e \sum_q \sum_{f, m_f, f', m_{f'}} (-1)^q \Bigg(& \langle f, m_f | \hat{r}_q | f', m_{f'} \rangle | f, m_f \rangle \langle f', m_{f'} | \hat{E}_{-q}^{(-)}(\mathbf{r}_i) \\ & + \langle f', m_{f'} | \hat{r}_q | f, m_f \rangle | f', m_{f'} \rangle \langle f, m_f | \hat{E}_{-q}^{(+)}(\mathbf{r}_i) \Bigg). \end{aligned} \tag{B.2.5}$$

We rewrite the interaction Hamiltionian in terms of atomic lowering operator $\hat{\sigma}_q$ and raising operator $\hat{\sigma}_q^\dagger$ [102]

$$\hat{H}_{\text{int}} = \hbar \tilde{\Omega}_{jj'} \sum_{q \in (1,-1)} \hat{a}_{-q} \hat{\sigma}_q^\dagger u(\mathbf{r}_i) \exp(\mathrm{i}(k_0 z - \Delta t)) + \text{h.c.}, \tag{B.2.6}$$

where the detuning between the atomic resonance and the probe field is given by $\Delta = \omega_{\mathrm{L}} - \omega_0$ and the atomic lowering operator as

$$\hat{\sigma}_q = \sum_{f,m_f,f',m_{f'}} \frac{\langle f, m_f | e\hat{r}_q | f', m'_f \rangle}{\langle j || e\hat{r}_q || j' \rangle} |f, m_f\rangle\langle f', m_{f'}| \tag{B.2.7}$$

and the transition strength by

$$\tilde{\Omega}_{jj'} = -\mathcal{E}_0 \langle j || e\hat{\mathbf{r}}_e || j' \rangle / \hbar = -\sqrt{\frac{\omega}{2\hbar\epsilon_0 cA}} \langle j || e\hat{\mathbf{r}}_e || j' \rangle, \tag{B.2.8}$$

where the transition strength $\tilde{\Omega}_{jj'}$ has units of $\mathrm{s}^{-1/2}$ such that multiplied with the light annihilation operator $\hat{a}_q$ which has units of $1/\sqrt{s}$ we get units of angular frequency. Here, it should be noted that the operator $\hat{\sigma}_1^\dagger$ drives the σ^--transition which lowers the angular momentum by one $m'_f = m_f - 1$, while the operator $\hat{\sigma}_{-1}^\dagger$ drives the σ^+-transition which increases the angular momentum by one $m'_f = m_f + 1$ [102]. The sign convention of the q coordinate results from the definition of the spherical basis. The atomic lowering operator $\hat{\sigma}_q$ can be evaluated by looking at the matrix elements explicitly. We can factor out the angular dependence and write the matrix element as product of a Clebsch-Gordan coefficient and a reduced matrix element as [105, 107, 108]

$$\begin{aligned} \langle f, m_f | e\hat{r}_q | f', m'_f \rangle =& \langle f || e\hat{\mathbf{r}}_e || f' \rangle (-1)^{f'-1+m_f} \sqrt{2f+1} \begin{pmatrix} f' & 1 & f \\ m_{f'} & q & -m_f \end{pmatrix} && \text{(B.2.9)} \\ =& \langle f || e\hat{\mathbf{r}}_e || f' \rangle \langle f', m_{f'}; 1, q | f, m_f \rangle, && \text{(B.2.10)} \end{aligned}$$

where $\langle f', m_{f'}; 1, q | f, m_f \rangle$ is a Clebsch-Gordan coefficient and

$$\langle f || e\hat{\mathbf{r}}_e || f' \rangle = \langle j || e\hat{\mathbf{r}}_e || j' \rangle (-1)^{f'+j+1+i} \sqrt{(2f'+1)(2j+1)} \begin{Bmatrix} j & j' & 1 \\ f' & f & i \end{Bmatrix}, \tag{B.2.11}$$

where the numerical value of $\langle j || e\hat{\mathbf{r}}_e || j' \rangle$ is known in literature ([105]: D2-line: $\langle j = 1/2 || e\hat{\mathbf{r}}_e || j' = 3/2 \rangle = 3.58424 \cdot 10^{-29}\mathrm{Cm}$, D1-line: $\langle j = 1/2 || e\hat{\mathbf{r}}_e || j' = 1/2 \rangle = 2.5377 \cdot 10^{-29}\mathrm{Cm}$). In the following we assume that the probe light propagates along the z-axis, so that the contribution from $q = 0$ (which is due to electric fields aligned with the quantisation axis) can be omitted. We have

$$\hat{H}_{\mathrm{int}} = \hbar\tilde{\Omega}_{jj'} \left(\hat{a}_- \hat{\sigma}_1^\dagger + \hat{a}_+ \hat{\sigma}_{-1}^\dagger \right) u(\mathbf{r}_i) \exp(i(k_0 z - \Delta t)) + \mathrm{h.c.}, \tag{B.2.12}$$

which is the Hamiltonian given in equation (2.2.5). Note, that in the spherical basis defined here, the transitions with $\hat{\sigma}_{-1}$ correspond the the so-called σ^+-transitions and couple a ground state m_f to an excited state with $m'_f = m_f + 1$. Similarly, the terms with the atomic lowering operator $\hat{\sigma}_{+1}$ couples transitions with $m'_f = m_f - 1$, which is referred to as σ^--transition [105].

Natural Decay: Like $\tilde{\Omega}_{jj'}$, the natural population decay constant γ_{Rb} depends on the transition strength $\langle j || e\hat{\mathbf{r}}_e || j' \rangle$. It is given by [105]

$$\gamma_{\mathrm{Rb}} = \frac{\omega_0^3}{3\pi\epsilon_0\hbar c^3} \frac{2j+1}{2j'+1} |\langle j || e\hat{\mathbf{r}}_e || j' \rangle|^2. \tag{B.2.13}$$

Thus, one can express the rate $|\tilde{\Omega}_{jj'}|^2$ in terms of the natural linewidth

$$|\Omega_{jj'}|^2 = \frac{2j'+1}{2j+1}\frac{3\lambda^2}{8\pi A}\gamma_{\mathrm{Rb}} = \frac{2j'+1}{2j+1}\frac{\sigma_0}{4A}\gamma_{\mathrm{Rb}}, \tag{B.2.14}$$

where $\sigma_0 = 3\lambda^2/(2\pi)$ is the resonant atomic cross-section [105]. The jump operators for the natural decay are given by [102]

$$J_{\sigma^+} = \sqrt{\gamma_{\mathrm{Rb}}\frac{2j'+1}{2j+1}}\sigma_{-1}, \qquad J_{\pi} = \sqrt{\gamma_{\mathrm{Rb}}\frac{2j'+1}{2j+1}}\sigma_{0}, \qquad J_{\sigma^-} = \sqrt{\gamma_{\mathrm{Rb}}\frac{2j'+1}{2j+1}}\sigma_{1}, \tag{B.2.15}$$

where the indices of the jump operator denote the polarisation of the emitted photon (and do not give the coordinate q).

B.2.1 Effective Two Level Atom

In a first section, the well known model of a two-level atom is considered. For this we assume that we have an atom with no nuclear spin, i.e. $i = 0$, a ground state with $j = 0$ and an excited state with $j' = 1$ (and thus $f = 0$, $f' = 1$) and drive the atom with circularly polarised light. Like this, effectively only two of the four levels are coupled. But before considering the dynamics of the atom coupled by a circularly polarised beam, we calculate the atomic interaction with light having an arbitrary polarisation. For this situation, we have

$$\hat{\sigma}_1 = \mu^*|g\rangle\langle e_{-1}|, \tag{B.2.16}$$

$$\hat{\sigma}_0 = -\mu^*|g\rangle\langle e_0|, \tag{B.2.17}$$

$$\hat{\sigma}_{-1} = \mu^*|g\rangle\langle e_1|, \tag{B.2.18}$$

where $\mu = 1/\sqrt{3}$. Here one can easily see that $\hat{\sigma}_1$ drives the σ^--transition while $\hat{\sigma}_{-1}$ addresses the σ^+-transition. The light-atom Hamiltonian is then given by

$$\hat{H}_{\mathrm{int}} = \hbar\tilde{\Omega}\mu\left(\hat{a}_-|e_{-1}\rangle\langle g| + \hat{a}_+|e_1\rangle\langle g|\right)u(\mathbf{r}_i)\exp(\mathrm{i}(k_0 z - \omega_{\mathrm{L}}t)) + \mathrm{h.c.} \tag{B.2.19}$$

where we have defined the transition strength $\tilde{\Omega} = \tilde{\Omega}_{0,1} = \sqrt{3\gamma_{\mathrm{Rb}}\sigma_0/(4A)}$. The jump operators are given for this specific atom by

$$J_{\sigma^-} = \sqrt{3\gamma_{\mathrm{Rb}}}\mu^*|g\rangle\langle e_{-1}| = \sqrt{\gamma_{\mathrm{Rb}}}|g\rangle\langle e_{-1}|, \tag{B.2.20}$$

$$J_{\pi} = -\sqrt{3\gamma_{\mathrm{Rb}}}\mu^*|g\rangle\langle e_0| = \sqrt{\gamma_{\mathrm{Rb}}}|g\rangle\langle e_0|, \tag{B.2.21}$$

$$J_{\sigma^+} = \sqrt{3\gamma_{\mathrm{Rb}}}\mu^*|g\rangle\langle e_1| = \sqrt{\gamma_{\mathrm{Rb}}}|g\rangle\langle e_1|. \tag{B.2.22}$$

We go to a rotating frame with respect to the light field. Thus, the atomic Hamiltonian is expressed as

$$\hat{H}_0 = -\hbar\sum_m \Delta_m|e_m\rangle\langle e_m|. \tag{B.2.23}$$

where Δ_m is the detuning to a specific excited state $|e_m\rangle$. For simplicity, we assume that $|u(\mathbf{r})| = 1$. The evolution of the excited states is given by (the Lindblad equation for operators is different than for

states)

$$\frac{\mathrm{d}}{\mathrm{d}t}|e_m\rangle\langle e_{m'}| = \frac{1}{\mathrm{i}\hbar}[\hat{H}_0 + \hat{H}_{\mathrm{int}}, |e_m\rangle\langle e_{m'}|] + \sum_k \left(\hat{J}_k^\dagger |e_m\rangle\langle e_{m'}|\hat{J}_k - \frac{1}{2}\{\hat{J}_k^\dagger \hat{J}_k, |e_m\rangle\langle e_{m'}|\}\right) \tag{B.2.24}$$

$$\begin{aligned} &= \mathrm{i}(-\Delta_{m'}|e_m\rangle\langle e_{m'}| + \Delta_m|e_m\rangle\langle e_{m'}|) - \mathrm{i}\tilde{\Omega}\mu^*\left(\hat{a}_-^\dagger|g\rangle\langle e_{m'}|\delta_{m,-1} + \hat{a}_+^\dagger|g\rangle\langle e_{m'}|\delta_{m,1}\right) \\ &\quad + \mathrm{i}\tilde{\Omega}\mu\left(\hat{a}_-|e_{m'}\rangle\langle g|\delta_{m,-1} + \hat{a}_+|e_{m'}\rangle\langle g|\delta_{m,1}\right) \\ &\quad - \frac{\gamma_{\mathrm{Rb}}}{2}\Bigg[\left(|e_{-1}\rangle\langle e_{m'}|\delta_{m,-1} + |e_m\rangle\langle e_{-1}|\delta_{m',1}\right) \end{aligned} \tag{B.2.25}$$

$$\quad + \left(|e_0\rangle\langle e_{m'}|\delta_{m,0} + |e_m\rangle\langle e_0|\delta_{m',0}\right) + \left(|e_1\rangle\langle e_{m'}|\delta_{m,1} + |e_m\rangle\langle e_1|\delta_{m',1}\right)\Bigg].$$

For the populations (i.e. $m = m'$), this simplifies to

$$\frac{\mathrm{d}}{\mathrm{d}t}|e_m\rangle\langle e_m| = -\mathrm{i}\tilde{\Omega}\mu^*\left(\hat{a}_-^\dagger|g\rangle\langle e_m|\delta_{m,-1} + \hat{a}_+^\dagger|g\rangle\langle e_m|\delta_{m,1}\right) \tag{B.2.26}$$

$$+ \mathrm{i}\tilde{\Omega}\mu\left(\hat{a}_-|e_m\rangle\langle g|\delta_{m,-1} + \hat{a}_+|e_m\rangle\langle g|\delta_{m,1}\right) - \gamma_{\mathrm{Rb}}|e_m\rangle\langle e_m|. \tag{B.2.27}$$

The evolution of the ground state is given by

$$\frac{d}{dt}|g\rangle\langle g| = -\mathrm{i}\tilde{\Omega}\mu\left(\hat{a}_-|e_{-1}\rangle\langle g| + \hat{a}_+|e_1\rangle\langle g|\right) + \mathrm{i}\tilde{\Omega}\mu^*\left(\hat{a}_-^\dagger|g\rangle\langle e_{-1}| + \hat{a}_+^\dagger|g\rangle\langle e_1|\right) + \gamma_{\mathrm{Rb}}\sum_m |e_m\rangle\langle e_m|. \tag{B.2.28}$$

And the evolution of the coherences is given by

$$\frac{d}{dt}|e_m\rangle\langle g| = \mathrm{i}\Delta_m|e_m\rangle\langle g| + \mathrm{i}\tilde{\Omega}\mu^*\left(\hat{a}_-^\dagger|e_m\rangle\langle e_{-1}| + \hat{a}_+^\dagger|e_m\rangle\langle e_1|\right) \tag{B.2.29}$$

$$- \mathrm{i}\tilde{\Omega}\mu^*\left(\hat{a}_-^\dagger|g\rangle\langle g|\delta_{m,-1} + \hat{a}_+^\dagger|g\rangle\langle g|\delta_{m,1}\right) - \frac{\gamma_{\mathrm{Rb}}|\mu|^2}{2}|e_m\rangle\langle g|. \tag{B.2.30}$$

In order to implement a two level atom, we consider circularly polarised light, such that only one excited state is addressed. We approximate the driving field by a classical field such that $\hat{a}_+ \to \sqrt{\Phi_{\mathrm{L}}}$ and $\hat{a}_- \to 0$. The classical field couples the ground state to the $m = 1$ excited state (σ^+-transition). In this model, the Rabi frequency is defined as $\Omega_R = 2\mu\tilde{\Omega}\sqrt{\Phi_{\mathrm{L}}}$, so that we obtain the textbook result

$$\dot{\rho}_{e_1,e_1} = \frac{\mathrm{i}}{2}(\Omega_R^*\rho_{e_1,g} - \Omega_R\rho_{g,e_1}) - \gamma_{\mathrm{Rb}}\rho_{e_1,e_1}, \tag{B.2.31}$$

$$\dot{\rho}_{e_1,g} = \frac{\mathrm{i}}{2}\Omega_R(\rho_{e_1,e_1} - \rho_{g,g}) - \left(\frac{\gamma_{\mathrm{Rb}}}{2} - \mathrm{i}\Delta_1\right)\rho_{e_1,g}, \tag{B.2.32}$$

$$\dot{\rho}_{g,e_1} = \dot{\rho}_{e_1,g}^*, \tag{B.2.33}$$

$$\dot{\rho}_{g,g} = -\dot{\rho}_{e_1,e_1}. \tag{B.2.34}$$

In the steady state (i.e. $\dot{\rho}_{i,j} = 0$), the atom is in the states of interest (i.e. $\rho_{e_1,e_1} + \rho_{g,g} = 1$), and we get

$$\rho_{g,e_1,\mathrm{ss}} = \frac{\tilde{\Omega}\mu^*\sqrt{\Phi_{\mathrm{L}}}}{\Delta_1 - \mathrm{i}\gamma_{\mathrm{Rb}}/2}\left(\rho_{e_1,e_1} - \rho_{g,g}\right) = -\frac{\Omega_R^*}{2\Delta_1 - \mathrm{i}\gamma_{\mathrm{Rb}}/2}\left(\rho_{e_1,e_1} - \rho_{g,g}\right), \tag{B.2.35}$$

$$\rho_{e_1,e_1,\mathrm{ss}} = \frac{|\mu|^2\Phi_{\mathrm{L}}|\tilde{\Omega}|^2}{\Delta_1^2 + (\gamma_{\mathrm{Rb}}/2)^2 + 2|\mu|^2\Phi_{\mathrm{L}}|\tilde{\Omega}|^2} = \frac{|\Omega_R|^2}{4\Delta_1^2 + \gamma_{\mathrm{Rb}}^2 + 2|\Omega_R|^2}. \tag{B.2.36}$$

The total photon scattering rate is given by

$$\gamma_{\mathrm{sc}} = \gamma_{\mathrm{Rb}}\rho_{e_1,e_1,\mathrm{ss}} = \frac{\gamma_{\mathrm{Rb}}\Phi_{\mathrm{L}}|\tilde{\Omega}|^2/3}{\Delta_1^2 + (\gamma_{\mathrm{Rb}}/2)^2 + 2\Phi_{\mathrm{L}}|\tilde{\Omega}|^2/3} \xrightarrow{\Delta_1 \gg \gamma_{\mathrm{Rb}}} \frac{\sigma_0}{A}\left(\frac{\gamma_{\mathrm{Rb}}}{2\Delta_1}\right)^2 \Phi_{\mathrm{L}}. \tag{B.2.37}$$

This is exactly the scattering rate which is expected for a two-level atom [68, 105].

B.2.2 Adiabatic Elimination of the Excited State for an Atom with a Spin-1/2 Ground State

Here, the explicit procedure of the adiabatic elimination of the atom given in section 2.2.1 is given. If the interaction Hamiltonian given in equation (2.2.13) is small because the optical field is far detuned, we can assume that the excited state manifold is not occupied. Thus, it make sense to adiabatically eliminate the excited states. For this, we have to write all elements of the interaction Hamiltonian as matrix elements$|g_m\rangle\langle g_{m'}|$. For this derivation, we assume for simplicity that the mode function is unity at the position of the atom $u(\mathbf{r}) = 1$. Here, we start by calculating the time evolution of the coherence $|g_m\rangle\langle e_{m'}|$, which is given by

$$\begin{aligned}\frac{\mathrm{d}}{\mathrm{d}t}|g_m\rangle\langle e_{m'}| = {}& \mathrm{i}\Delta_{m'}|g_m\rangle\langle e_{m'}| - i\tilde{\Omega}\Big(\mu\hat{a}_+(|e_{3/2}\rangle\langle e_{m'}|\delta_{m,1/2} - |g_m\rangle\langle g_{1/2}|\delta_{m',3/2}) \\ &+ \nu\hat{a}_+(|e_{1/2}\rangle\langle e_{m'}|\delta_{m,-1/2} - |g_m\rangle\langle g_{-1/2}|\delta_{m',1/2}) \\ &+ \nu\hat{a}_-(|e_{-1/2}\rangle\langle e_{m'}|\delta_{m,1/2} - |g_m\rangle\langle g_{1/2}|\delta_{m',-1/2}) \\ &+ \mu\hat{a}_-(|e_{-3/2}\rangle\langle e_{m'}|\delta_{m,-1/2} - |g_m\rangle\langle g_{-1/2}|\delta_{m',-3/2})\Big)\exp(\mathrm{i}(k_0 z - \Delta t)).\end{aligned} \tag{B.2.38}$$

where we have defined the transition strength as $\tilde{\Omega} = \tilde{\Omega}_{1/2,3/2} = \sqrt{\gamma_{\mathrm{Rb}}\sigma_0/(2A)}$ (units of $\mathrm{s}^{-1/2}$). We assume that the coherence is in a steady state (i.e. $\frac{\mathrm{d}}{\mathrm{d}t}|g_m\rangle\langle e_{m'}| = 0$) and that the excited states are not occupied $|e_m\rangle\langle e_{m'}| = 0$. We get

$$\begin{aligned}|g_m\rangle\langle e_{m'}| = {}& \frac{\tilde{\Omega}}{\Delta_{m'}}\exp(\mathrm{i}(k_0 z - \Delta t))\left(\mu|g_m\rangle\langle g_{1/2}|\delta_{m',3/2} + \nu|g_m\rangle\langle g_{-1/2}|\delta_{m',1/2}\right)\hat{a}_+ \\ &+ \frac{\tilde{\Omega}}{\Delta_{m'}}\exp(\mathrm{i}(k_0 z - \Delta t))\left(\nu|g_m\rangle\langle g_{1/2}|\delta_{m',-1/2} + \mu|g_m\rangle\langle g_{-1/2}|\delta_{m',-3/2}\right)\hat{a}_-.\end{aligned} \tag{B.2.39}$$

This expression can be introduced into the expression for the interaction Hamiltonian (given in equation (2.2.13)). Further, we assume that all detunings $\Delta_m = \Delta$ are the same. We get

$$\hat{H}_{\mathrm{int}} \approx \frac{\hbar|\tilde{\Omega}|^2}{\Delta}\left[(\hat{a}_-^\dagger\hat{a}_-|\nu|^2 + \hat{a}_+^\dagger\hat{a}_+|\mu|^2)|g_{1/2}\rangle\langle g_{1/2}| + (\hat{a}_-^\dagger\hat{a}_-|\mu|^2 + \hat{a}_+^\dagger\hat{a}_+|\nu|^2)|g_{-1/2}\rangle\langle g_{-1/2}|\right] + \mathrm{h.c.} \tag{B.2.40}$$

$$= \frac{2\hbar|\tilde{\Omega}|^2}{\Delta}\left[(\hat{a}_-^\dagger\hat{a}_-|\nu|^2 + \hat{a}_+^\dagger\hat{a}_+|\mu|^2)|g_{1/2}\rangle\langle g_{1/2}| + (\hat{a}_-^\dagger\hat{a}_-|\mu|^2 + \hat{a}_+^\dagger\hat{a}_+|\nu|^2)|g_{-1/2}\rangle\langle g_{-1/2}|\right]. \tag{B.2.41}$$

The atomic Hamiltonian can be re-expressed in terms of the groundstate by writing the excited state populations as $|e_i\rangle\langle e_i| = |e_i\rangle\langle g_j|g_j\rangle\langle e_i|$ (where we can chose an $j \in (-1/2, 1/2)$) and write

$$\hat{H}_0 = -\hbar \sum_i \Delta_i |e_i\rangle\langle g_{1/2}|g_{1/2}\rangle\langle e_i| \tag{B.2.42}$$

$$\approx -\frac{\hbar|\tilde{\Omega}|^2}{\Delta}|u(\mathbf{r}_i)|^2\Big(|\mu|^2|g_{-1/2}\rangle\langle g_{-1/2}|\hat{a}_-^\dagger\hat{a}_- + |\nu|^2|g_{1/2}\rangle\langle g_{1/2}|\hat{a}_-^\dagger\hat{a}_- + |\nu|^2|g_{-1/2}\rangle\langle g_{-1/2}|\hat{a}_+^\dagger\hat{a}_+ + |\mu|^2|g_{1/2}\rangle\langle g_{1/2}|\hat{a}_+^\dagger\hat{a}_+\Big). \tag{B.2.43}$$

If we then add the atomic Hamiltonian to the interaction Hamiltonian we get an effective Hamiltonian

$$\hat{H}_{\text{eff}} = \hat{H}_0 + \hat{H}_{\text{int}} \tag{B.2.44}$$

$$= \frac{\hbar|\tilde{\Omega}|^2}{\Delta}\left[(\hat{a}_-^\dagger\hat{a}_-|\nu|^2 + \hat{a}_+^\dagger\hat{a}_+|\mu|^2)|g_{1/2}\rangle\langle g_{1/2}| + (\hat{a}_-^\dagger\hat{a}_-|\mu|^2 + \hat{a}_+^\dagger\hat{a}_+|\nu|^2)|g_{-1/2}\rangle\langle g_{-1/2}|\right] \tag{B.2.45}$$

$$\approx \hbar\alpha_0 \mathbb{1}_g \hat{S}_0 + \hbar\alpha_1 \hat{f}_z\hat{S}_z, \tag{B.2.46}$$

with

$$\alpha_0 = \frac{|\tilde{\Omega}|^2}{\Delta}(|\nu|^2 + |\mu|^2), \tag{B.2.47}$$

$$\alpha_1 = \frac{2|\tilde{\Omega}|^2}{\Delta}(|\mu|^2 - |\nu|^2). \tag{B.2.48}$$

Here, we have assumed that the number of photons is large in both circular polarisation states so that we can approximate $\hat{a}_q^\dagger\hat{a}_q \approx \hat{a}_q\hat{a}_q^\dagger$. If this is not the case, one has to sort out exactly, how the operators should be ordered. We can plug in the values for the Clebsch-Gordan coefficients $\mu = \sqrt{1/2}$ and $\nu = \sqrt{1/6}$ and find that $\alpha_0 = \alpha_1 = 2|\tilde{\Omega}|^2/(3\Delta) = \sigma_0\gamma_{\text{Rb}}/(3A\Delta) = \sigma_\pi\gamma_{\text{Rb}}/(2A\Delta)$.

B.2.3 Quantum Limited Spin-Light Interface

For the atomic spin, the common uncertainty relations of a quantum mechanical spin are valid, which can be derived from the commutation relations of a spin given by $[\hat{f}_j, \hat{f}_k] = \mathrm{i}\epsilon_{jkl}\hat{f}_l$. For here, assume that the spin is well polarised along the x-axis, such that the collective spin along the x-axis can be approximated classically by $\bar{F}_x = fN_a$ where f is the hyperfine quantum number. The uncertainty relation for the transversal axis is then given by $[\hat{F}_y, \hat{F}_z] = \mathrm{i}fN_a$.

Furthermore, we assume that the incoming light is linearly polarised along the horizontal axis. Similarly to the spin, we can then approximate $\hat{S}_x$ as classical mean value $\bar{S}_x = \Phi_{\text{L}}/2$ and write the uncertainty relation of the transversal components as $[\hat{S}_y(t), \hat{S}_z(t')] = \mathrm{i}\bar{S}_x\delta(t-t')$. Here, the spin noise mapped on the light is derived including the backaction of the light onto the atomic spin. For this, the Heisenberg equations of motion of the spin in a magnetic field are rewritten with all noise terms [111]

$$\frac{\mathrm{d}}{\mathrm{d}t}\hat{F}_y(t) = -\Omega_{\text{s}}\hat{F}_z(t) - \frac{\gamma_{\text{s}}}{2}\hat{F}_y(t) + \hat{h}_y(t) + \alpha_1\bar{F}_x\hat{S}_z(t), \tag{B.2.49}$$

$$\frac{\mathrm{d}}{\mathrm{d}t}\hat{F}_z(t) = \Omega_{\text{s}}\hat{F}_y(t) - \frac{\gamma_{\text{s}}}{2}\hat{F}_z(t) + \hat{h}_z(t), \tag{B.2.50}$$

where the first term is the Larmor precession in the magnetic field, the second defines the spin decay with decay constant γ_{s} which comes from the interaction with the light and incoherent processes as

magnetic field fluctuations. The spin decay gives rise to Langevin forces terms $\hat{h}_i(t)$ which are necessary to preserve noise statistics according to the fluctuation dissipation theorem [111]. The last term of the equation (B.2.49) shows the spin driven by the circular polarised light via the Faraday interaction. The noise of the spin is easiest assessed in the spectral domain, thus it is worth to Fourier-transform the equations motion and insert it into the input-output relation of the light (see equation (2.2.32)), yielding

$$\hat{S}_y^{(\mathrm{out})}(\omega) = \hat{S}_y^{(\mathrm{in})}(\omega) + \alpha_1 \bar{S}_x \cdot \frac{(\gamma_\mathrm{s}/2 - \mathrm{i}\omega)\hat{h}_z(\omega) + \Omega_\mathrm{s}[\hat{h}_y(\omega) + \alpha_1 \bar{F}_x \hat{S}_z^{(in)}(\omega)]}{(\Omega_\mathrm{s} - \omega)(\Omega_\mathrm{s} + \omega) + (\gamma_\mathrm{s}/2)^2 - \mathrm{i}\gamma_\mathrm{s}\omega}. \tag{B.2.51}$$

The light is detected by a polarisation homodyne detection, as introduced in section 2.3.3. Here, we assume the general case for an arbitrary homodyne angle θ

$$\hat{S}_\theta = \cos(4\theta)\hat{S}_y + 2\sin(4\theta)\hat{S}_z. \tag{B.2.52}$$

The power spectral density is then given by

$$\begin{aligned} S_{S_\theta S_\theta}(\omega) &= \int_{-\infty}^{\infty} \langle \hat{S}_\theta^{(\mathrm{out})\dagger}(-\omega)\hat{S}_\theta^{(\mathrm{out})}(\omega')\rangle d\omega' \\ &= \int_{-\infty}^{\infty} \big[\cos^2(4\theta)\langle \hat{S}_y^{(\mathrm{out})}(\omega)\hat{S}_y^{(\mathrm{out})}(\omega')\rangle + \sin^2(4\theta)\langle \hat{S}_z^{(\mathrm{out})}(\omega)\hat{S}_z^{(\mathrm{out})}(\omega')\rangle \\ &\quad - \sin(4\theta)\cos(4\theta)(\langle \hat{S}_y^{(\mathrm{out})}(\omega)\hat{S}_z^{(\mathrm{out})}(\omega')\rangle + \langle \hat{S}_z^{(\mathrm{out})}(\omega)\hat{S}_y^{(\mathrm{out})}(\omega')\rangle)\big] d\omega'. \end{aligned} \tag{B.2.53}$$

In the main text, the result for the integral of $\langle \hat{S}_y^{(\mathrm{out})}(\omega)\hat{S}_y^{(\mathrm{out})}(\omega')\rangle$ is derived (see equation (2.2.49)). The PSD of $\hat{S}_z^{(\mathrm{out})}(\omega)$ is easy to calculate. The Faraday interaction does not influence the circular component of the light, i.e. $\hat{S}_z^{(\mathrm{out})}(\omega) = \hat{S}_z^{(\mathrm{in})}(\omega)$. Because the incoming light is in a coherent state, we obtain

$$\langle \hat{S}_z^{(\mathrm{out})}(\omega)\hat{S}_z^{(\mathrm{out})}(\omega')\rangle = \delta(\omega + \omega')\frac{\bar{S}_x}{2}. \tag{B.2.54}$$

The third term of equation (B.2.53) can be calculated, using equation (B.2.51) for $S_y^{(\mathrm{out})}$. Further we assume, that the shot noise and the spin noise are not correlated, i.e. $\langle \hat{S}_z \hat{f}_i\rangle = 0\ \forall i,j \in \{x,y,z\}$, and obtain

$$\langle \hat{S}_z^{(\mathrm{out})}(\omega)\hat{S}_y^{(\mathrm{out})}(\omega')\rangle = \langle \hat{S}_z^{(\mathrm{in})}(\omega)\hat{S}_y^{(\mathrm{in})}(\omega')\rangle + \alpha_1 \bar{S}_x \frac{\Omega_\mathrm{s}\alpha_1 \bar{F}_x \langle S_z^{(\mathrm{in})}(\omega) S_z^{(\mathrm{in})}(\omega')\rangle}{(\Omega_\mathrm{s} - \omega')(\Omega_\mathrm{s} + \omega') + (\gamma_\mathrm{s}/2)^2 - \mathrm{i}\gamma_\mathrm{s}\omega'} \tag{B.2.55}$$

$$= -\frac{\mathrm{i}\bar{S}_x}{2}\delta(\omega + \omega') + \alpha_1 \bar{S}_x \frac{\frac{1}{2}\Omega_\mathrm{s}\alpha_1 \bar{F}_x \bar{S}_x \delta(\omega + \omega')}{(\Omega_\mathrm{s} - \omega')(\Omega_\mathrm{s} + \omega') + (\gamma/2)^2 - \mathrm{i}\gamma_\mathrm{s}\omega'}. \tag{B.2.56}$$

By summing the two cross terms of equation (B.2.53) and integrate over ω', we obtain the third term of equation (B.2.53)

$$\begin{aligned} &\int_{-\infty}^{\infty} \big[\langle \hat{S}_z^{(\mathrm{out})}(\omega)\hat{S}_y^{(\mathrm{out})}(\omega')\rangle + \langle \hat{S}_y^{(\mathrm{out})}(\omega)\hat{S}_z^{(\mathrm{out})}(\omega')\rangle\big] d\omega' \\ &\qquad = \frac{(\alpha_1 \bar{S}_x)^2 \Omega_\mathrm{s} \bar{F}_x (\Omega_\mathrm{s}^2 - \omega^2 + (\gamma_\mathrm{s}/2)^2)}{((\Omega_\mathrm{s} - \omega)(\Omega_\mathrm{s} + \omega) + (\gamma_\mathrm{s}/2)^2)^2 + (\gamma_\mathrm{s}\omega)^2} \end{aligned} \tag{B.2.57}$$

Plugging this expression and equation (2.2.49) into equation (B.2.53), we get the expression for the

spectrum

$$\begin{aligned}\bar{S}_{S_\theta S_\theta}(\omega) =& \frac{\bar{S}_x}{2} + \frac{(\alpha_1 \bar{S}_x)^2 \cos(4\theta)}{((\Omega_\mathrm{s}-\omega)(\Omega_\mathrm{s}+\omega)+(\gamma_\mathrm{s}/2)^2)^2+(\gamma_\mathrm{s}\omega)^2} \\ &\cdot \Bigg(\cos(4\theta)\left((\gamma_\mathrm{s}/2)^2+\omega^2+\Omega_\mathrm{s}^2)\gamma|F_x|/2 + \frac{\Omega_\mathrm{s}^2\alpha_1^2\bar{F}_x^2\bar{S}_x}{2}\right) \\ &- \sin(4\theta)(\Omega_\mathrm{s}^2-\omega^2+(\gamma_\mathrm{s}/2)^2)\Omega_\mathrm{s}\bar{F}_x\Bigg).\end{aligned} \tag{B.2.58}$$

Using the narrow band approximation $\gamma_\mathrm{s} \ll |\Omega_\mathrm{s}-\omega| \ll \Omega_\mathrm{s}$, this expression can be simplified to

$$\begin{aligned}\bar{S}_{S_\theta S_\theta}(\omega) \approx \frac{\bar{S}_x}{2} + \frac{(\frac{1}{2}\alpha_1\bar{S}_x)^2}{(\Omega_\mathrm{s}-\omega)^2+(\gamma_\mathrm{s}/2)^2} \cdot \Bigg(&\cos^2(4\theta)\left(\gamma|F_x| + \frac{(\alpha_1\bar{F}_x)^2\bar{S}_x}{2}\right) \\ &-2\sin(4\theta)\cos(4\theta)(\Omega_\mathrm{s}-\omega)\bar{F}_x\Bigg).\end{aligned} \tag{B.2.59}$$

This equation is used in section 2.6.4 to fit the squeezing data. Setting the homodyne angle $\theta = 0$, the result given in equation (2.2.49) is obtained.

B.2.4 Formalism for the Adiabatic Elimination of Excited States

Reiter *et al.* [113] provided a general approach to calculating the effective Hamiltonian and effective jump operators by adiabatic elimination of the excited state. The procedure is outlined in brief herewith: If there is a quantum system with two distinct subspaces and the coupling between these subspaces is perturbative, the dynamics of the system can be simplified. To do this, we assume that the dynamics of the full system is described by a master equation

$$\dot{\hat{\rho}} = \frac{1}{\mathrm{i}\hbar}[\hat{H},\rho] + \sum_k \hat{J}_k\rho\hat{J}_k^\dagger - \frac{1}{2}\{\hat{J}_k^\dagger\hat{J}_k,\hat{\rho}\}, \tag{B.2.60}$$

where $\hat{H}$ is the Hamiltonian of the system and $\hat{J}_k$ are jump operators modelling a coupling to a Markovian bath. In the following, we want to write the effective ground-state Hamiltonian of the system. To do this we need to structure the Hamiltonian of the system into two subspaces. We define $\hat{P}_\mathrm{g}$ as the projector on the ground states and $\hat{P}_\mathrm{e}$ as the projector on the excited states. The Hamiltonian can be decomposed into the following parts

$$\hat{H} = \hat{H}_\mathrm{g} + \hat{H}_\mathrm{e} + \hat{V}_+ + \hat{V}_-, \tag{B.2.61}$$

where $\hat{H}_\mathrm{g} = P_\mathrm{g}\hat{H}P_\mathrm{g}$ is the ground-state Hamiltonian, $\hat{H}_\mathrm{e} = P_\mathrm{e}\hat{H}P_\mathrm{e}$ is the excited-state Hamiltonian, and $\hat{V}_+ = P_\mathrm{e}\hat{H}P_\mathrm{g}$ and $\hat{V}_- = P_\mathrm{g}\hat{H}P_\mathrm{e}$ are the parts of the Hamiltonian that couple the ground state manifold and excited-state manifold. We assume that $\hat{H}_\mathrm{g}$ can be diagonalised as $\hat{H}_\mathrm{g} = \sum_l E_l\hat{P}_l$ where $\hat{P}_l$ is a projector for one eigenstate in the ground state manifold. For each ground-state projector $\hat{P}_l$, we can define a non-Hermitian Hamiltonian

$$\hat{H}_\mathrm{NH}^{(l)} = \hat{H}_\mathrm{e} - \frac{\mathrm{i}\hbar}{2}\sum_k \hat{J}_k^\dagger\hat{J}_k - E_l\hat{P}_\mathrm{e}. \tag{B.2.62}$$

This non-hermitian Hamiltonian has only non-zero entries in the excited-state subspace. The quasi-inverse of this Hamiltonian is defined as $(\hat{H}_{\mathrm{NH}}^{(l)})^{-1}\hat{H}_{\mathrm{NH}}^{(l)} = \hat{P}_{\mathrm{e}}$. Doing the adiabatic elimination of the excited state, the effective ground state dynamics is again given by a master equation

$$\dot{\hat{\rho}} = \frac{1}{\mathrm{i}\hbar}[\hat{H}_{\mathrm{eff}}, \hat{\rho}] + \sum_k \hat{J}_{k,\mathrm{eff}}\hat{\rho}\hat{J}_{k,\mathrm{eff}}^{\dagger} - \frac{1}{2}\{\hat{J}_{k,\mathrm{eff}}^{\dagger}\hat{J}_{k,\mathrm{eff}}, \hat{\rho}\}, \tag{B.2.63}$$

where the effective operators are defined as

$$\hat{H}_{\mathrm{eff}} = -\frac{1}{2}\left(\hat{V}_{-}\sum_l (\hat{H}_{\mathrm{NH}}^{(l)})^{-1}\hat{V}_{+}^{(l)} + \mathrm{h.c.}\right) + \hat{H}_{\mathrm{g}}, \tag{B.2.64}$$

$$\hat{J}_{k,\mathrm{eff}} = \hat{J}_k \sum_l (\hat{H}_{\mathrm{NH}}^{(l)})^{-1}\hat{V}_{+}^{(l)}, \tag{B.2.65}$$

and $\hat{V}_{+}^{(l)} = \hat{V}_{+}\hat{P}_l$. If the ground-state manifold can be assumed to be degenerate, the equations can be simplified. In the course of this work, this formalism has been implemented both analytically and numerically to calculate the spin dynamics.

B.2.5 Effective Hamiltonian of an Atom with a Spin-1 Ground State

In order to study the decay to a different hyperfine state, we consider a slightly more complicated atom. We assume that we have an atom with nuclear spin $i = 1/2$, a ground-state manifold with $j = 1/2$ and an excited-state manifold of $j' = 1/2$. In the ground-state manifold we have in total four levels, one with $f = 0$ and with with $f = 1$. We assume that the hyperfine splitting of the ground-state is A_{HF} while we neglect the hyperfine splitting of the excited state.

After the adiabatic elimination of the excited state, we get

$$\begin{aligned}\hat{H}_{\mathrm{eff}} =& -\hbar(\Delta_{\mathrm{hf}} + \alpha_{0,f=0}\hat{S}_0)|0,0\rangle\langle 0,0| \\ &+ \hbar\alpha_{0,f=1}\hat{S}_0\mathbb{1}_{f=1} + \hbar\alpha_1\hat{S}_z\hat{f}_z, \\ &+ \hbar\alpha_{f=0,f=1}\hat{S}_z(|0,0\rangle\langle 1,0| + |1,0\rangle\langle 0,0|),\end{aligned} \tag{B.2.66}$$

with

$$\alpha_{0,f} = \frac{\gamma_{\mathrm{Rb}}\sigma_\pi\Delta_f}{4A(\Delta_f^2 + (\gamma_{\mathrm{Rb}}/2)^2)}, \tag{B.2.67}$$

$$\alpha_1 = \frac{\gamma_{\mathrm{Rb}}\sigma_\pi\Delta_{f=1}}{4A(\Delta_{f=1}^2 + (\gamma_{\mathrm{Rb}}/2)^2)} = \alpha_{0,f=1} \tag{B.2.68}$$

$$\alpha_{f=0,f=1} = \frac{\gamma_{\mathrm{Rb}}\sigma_\pi(\Delta_{f=0} + \Delta_{f=1})}{8A\Delta_{f=0}\Delta_{f=1}}, \tag{B.2.69}$$

where the detuning from the $f = 0$ is off from the detuning to the $f = 1$ by the hyperfine splitting, i.e. $\Delta_{f=0} = \Delta_{f=1} - \Delta_{\mathrm{hf}}$.

B.2.6 Model of the D2-line of Rubidium-87

In this section, the more evolved formula for section 2.2.3 are given. Parts of this derivation are already given in [79]. The results given here follow directly from the derivation given earlier in this section but

consider the more complicated structure of the D2-line of Rubidium. The light-matter interaction is given by $\hat{H}_I = -\hat{\mathbf{d}} \cdot \hat{\mathbf{E}}$. The electric field can be separated into rotating and counter-rotating terms. For an electromagnetic field far detuned from the atomic transition, the light-matter Hamiltonian can be approximated with a rotating wave approximation and a perturbation expansion (following the derivation described in [13, 107, 110]). For one atom, it can be written as

$$\hat{H}_I = \sum_{f,f'} \hat{\mathbf{E}}^{(-)}(\mathbf{r}_i, t) \frac{\hat{\boldsymbol{\alpha}}_{f,f'}}{\hbar \Delta_{f,f'}} \hat{\mathbf{E}}^{(+)}(\mathbf{r}_i, t), \tag{B.2.70}$$

where the hyperfine states of the ground state are given by f, the hyperfine states of the excited state are given by f', $\Delta_{f,f'} = \omega - \omega_{f,f'}$ is the detuning of the light from the transition of the two corresponding states, $\mathbf{r}_i$ is the position of the atom, and the atomic polarisability tensor is given by [106, 110, 115]

$$\hat{\boldsymbol{\alpha}}_{f,f'} = \hat{P}_f \hat{\mathbf{d}} \hat{P}_{f'} \hat{\mathbf{d}}^\dagger \hat{P}_f, \tag{B.2.71}$$

where $\hat{P}_f$ ($\hat{P}_{f'}$) is the projector onto the ground hyperfine state (excited hyperfine state). This polarisation tensor can be understood intuitively: $\hat{P}_{f'} \hat{\mathbf{d}}^\dagger \hat{P}_f$ is a virtual excitation of the atom. This virtual excitation of the atom is destroyed again by the term $\hat{P}_f \hat{\mathbf{d}} \hat{P}_{f'}$. Thus, the polarisation tensor describes this off-resonant two-photon transition between different ground states of the atom. The polarisability tensor can be decomposed in three parts, for which the first $\hat{\boldsymbol{\alpha}}^{(0)}_{f,f'}$ transforms as a scalar, the second $\hat{\boldsymbol{\alpha}}^{(1)}_{f,f'}$ transforms as a vector, and the third $\hat{\boldsymbol{\alpha}}^{(2)}_{f,f'}$ transforms as a rank-2 symmetrical tensor in SO(3) [110]

$$\hat{\boldsymbol{\alpha}}_{f,f'} = \hat{\boldsymbol{\alpha}}^{(0)}_{f,f'} \oplus \hat{\boldsymbol{\alpha}}^{(1)}_{f,f'} \oplus \hat{\boldsymbol{\alpha}}^{(2)}_{f,f'}. \tag{B.2.72}$$

Therefore the polarisability Hamiltonian can be decomposed in a scalar, a vector and a tensor component:

$$\hat{H}_I = \hat{H}_I^{(0)} + \hat{H}_I^{(1)} + \hat{H}_I^{(2)}, \tag{B.2.73}$$

where

$$\hat{H}_I^{(k)} = \sum_{f,f'} \hat{\mathbf{E}}^{(-)}(\mathbf{r}_i, t) \frac{\hat{\boldsymbol{\alpha}}^{(k)}_{f,f'}}{\hbar \Delta_{f,f'}} \hat{\mathbf{E}}^{(+)}(\mathbf{r}_i, t). \tag{B.2.74}$$

The decomposition can be followed in [110] explicitly. For one atom in a given hyperfine ground state ($f = 1$ or $f = 2$), the three decomposed Hamiltonians can be written in a new form [110]. In the following, we consider that the light propagates along the z-axis

$$\hat{H}_{0,f} = \hbar \alpha_{f,0} |u(\mathbf{r}_i)|^2 \hat{S}_0 \hat{\mathbb{1}}_f, \tag{B.2.75}$$

$$\hat{H}_{1,f} = \hbar \alpha_{f,1} |u(\mathbf{r}_i)|^2 \hat{S}_z \hat{f}_z, \tag{B.2.76}$$

$$\hat{H}_{2,f} = \hbar \alpha_{f,2} |u(\mathbf{r}_i)|^2 (\hat{S}_x (\hat{f}_x^2 - \hat{f}_y^2) + \hat{S}_y (\hat{f}_x \hat{f}_y + \hat{f}_y \hat{f}_x) + \frac{1}{3} \hat{S}_0 [3\hat{f}_z^2 - f(f+1)\hat{\mathbb{1}}_f]). \tag{B.2.77}$$

We call the dimensionless scaling factors $\alpha_{f,k}$ of the interaction Hamiltonians (equations B.2.75-B.2.77) *atomic polarisability constants*. They depend on the hyperfine ground state f and the detuning Δ. Here, the detuning Δ is defined as the detuning from the frequency difference between the $f = 2$ ($f = 1$) state and the middle of the excited state manifold (*i.e.* detuning from $\omega = 384.227\,921\,\text{THz}$ for $f = 2$ and $\omega = 384.234\,755\,\text{THz}$ for $f = 1$). The detuning to a specific hyperfine state is given by: $\Delta_{f,f'} = \Delta - \Delta_{f'}$

where $\Delta_{f'}$ is the frequency difference between an excited hyperfine state and our arbitrary chosen middle of the excited state manifold. For simplicity, we define the dimensionless coupling parameter of two defined hyperfine states

$$\alpha_f^{f'}(\Delta) = \frac{3}{2}\frac{\Delta_{f,f'}\Delta}{(\gamma_{\mathrm{Rb}}^2/4 + \Delta_{f,f'}^2)}(2j'+1)\begin{Bmatrix} j' & f' & i \\ f & j & 1 \end{Bmatrix}^2, \tag{B.2.78}$$

where "{ }" is the Wigner 6-j symbol. For large detuning, the fraction yields unity and the coupling parameter $\alpha_f^{f'}$ is approximately independent of the exact frequency of the light. With this definition, the scalar atomic polarisability constant can be written as:

$$\alpha_{f,0} = \frac{\lambda^2}{2\pi A}\cdot\frac{\gamma_{\mathrm{Rb}}}{\Delta}\cdot a_f^{(0)}(\Delta), \tag{B.2.79}$$

with

$$a_f^{(0)}(\Delta) = \frac{1}{3}\cdot(-1)^{2f}\sum_{f'}\alpha_f^{f'}(\Delta)\cdot[(2f-1)\delta_{f'}^{f-1} + (2f+1)\delta_{f'}^{f} + (2f+3)\delta_{f'}^{f+1}] \quad \underrightarrow{\Delta\to\infty} \quad 1, \tag{B.2.80}$$

where δ_l^j is the Kronecker delta. In the limit of large detuning ($|\Delta| \gg \Gamma_{Rb}$, $\Delta \cong \Delta_{F,F'}$), the factor $a_f^{(0)}(\Delta) = 1$ reduces to unity. The scalar polarisability constant thus scales with $\alpha_{f,0} \propto 1/(\Delta w_0^2)$. The vector polarisability constant is given by

$$\alpha_{f,1} = \frac{\lambda^2}{8\pi A}\cdot\frac{\Gamma_{Rb}}{\Delta}\cdot a_f^{(1)}(\Delta), \tag{B.2.81}$$

with

$$a_f^{(1)}(\Delta) = 2\cdot(-1)^{2f}\sum_{f'}\alpha_f^{f'}(\Delta)\cdot[-\frac{2f-1}{f}\delta_{f'}^{f-1} - \frac{2f+1}{f(f+1)}\delta_{f'}^{f} + \frac{2f+3}{f+1}\delta_{f'}^{f+1}] \quad \underrightarrow{\Delta\to\infty} \quad 1, \tag{B.2.82}$$

where the scaling for large detuning is the same as for the scalar polarisability constant but the pre-factors are smaller by a factor of 4. The tensor polarisability constant is given by

$$\alpha_{f,2} = \frac{\lambda^2}{8\pi A}\cdot\frac{\Gamma_{Rb}}{\Delta}\cdot a_f^{(2)}(\Delta), \tag{B.2.83}$$

with

$$a_f^{(2)}(\Delta) = 2\cdot(-1)^{2f}\sum_{f'}\alpha_f^{f'}(\Delta)\cdot[\frac{1}{f}\delta_{f'}^{f-1} - \frac{2f+1}{f(f+1)}\delta_{f'}^{f} + \frac{1}{f+1}\delta_{f'}^{f+1}] \quad \underrightarrow{\Delta\to\infty} \quad 0. \tag{B.2.84}$$

For large detuning, transitions to different excited state hyperfine levels interfere destructively for the tensor interaction, such that $a_{f,2}$ tends to zero. This destructive interference results in a different scaling of the tensor polarisability constant with detuning than of the vector and scalar polarisability constants. For a large detuning, the scalar and vector polarisability constants scale approximately with $\alpha_{f,0}, \alpha_{f,1} \propto 1/\Delta$ while the tensor polarisability constant scales with $\alpha_{f,2} \propto 1/\Delta^2$. By choosing a detuning, a Hamiltonian can be designed with different ratios between the vector and the tensor interaction Hamiltonian [115].

Appendix C

Fourier Transformation, Power Spectral Density and the Autocorrelation Function

In this appendix the definition of the Fourier transform and the power spectral density (PSD) is given. Furthermore, the autocorrelation function is introduced and it is shown how the variance of a signal can be calculated by integrating over the PSD. In the second part, the implementation of the PSD in Python is shown.

C.1 Fourier Transform

In this work, the Fourier transform is defined as,

$$h(\omega) = \mathcal{FT}(h(t)) = \frac{1}{\sqrt{2\pi}} \int h(t) \mathrm{e}^{\mathrm{i}\omega t} \mathrm{d}t, \tag{C.1.1}$$

$$h(t) = \mathcal{FT}^{-1}(h(\omega)) = \frac{1}{\sqrt{2\pi}} \int h(\omega) \mathrm{e}^{-\mathrm{i}\omega t} \mathrm{d}\omega. \tag{C.1.2}$$

Using this definition, the Fourier transform of the derivatives are given by $\mathcal{FT}(\frac{\mathrm{d}h(t)}{\mathrm{d}t}) = -\mathrm{i}\omega h(\omega)$ and $\mathcal{FT}^{-1}(\frac{\mathrm{d}h(\omega)}{\mathrm{d}\omega}) = \mathrm{i}\omega h(t)$. In this thesis, the operators for the free-space field are often given with respect to space coordinates instead of time. Accordingly, the Fourier transformation has to be written slightly differently: If we have an operator $\hat{a}(\xi)$ which depends on the position $\xi = z - ct$, the Fourier transform is defined by

$$\hat{a}(\omega) = \int \frac{\mathrm{d}\xi}{c\sqrt{2\pi}} \hat{a}(\xi) e^{\mathrm{i}\omega\xi/c}, \tag{C.1.3}$$

$$\hat{a}(\xi) = \int \frac{\mathrm{d}\omega}{\sqrt{2\pi}} \hat{a}(\omega) e^{-\mathrm{i}\omega\xi/c}, \tag{C.1.4}$$

where c is the speed of light.

Fourier transform of operators and their complex conjugate: Let us assume that we have an operator $\hat{O}(t)$ which is non-hermitian. The Fourier transform of this operator is given by

$$\hat{O}(\omega) = \frac{1}{\sqrt{2\pi}} \int \hat{O}(t) \mathrm{e}^{\mathrm{i}\omega t} \mathrm{d}t, \tag{C.1.5}$$

$$\hat{O}(t) = \frac{1}{\sqrt{2\pi}} \int \hat{O}(\omega) \mathrm{e}^{-\mathrm{i}\omega t} \mathrm{d}\omega. \tag{C.1.6}$$

In this thesis, we represent the adjoint of $\hat{O}(\omega)$ as $\hat{O}^\dagger(\omega)$. In certain publication the adjoint operator of $\hat{O}(\omega)$ is written as $[\hat{O}(\omega)]^\dagger$ (and there is a difference between $[\hat{O}(\omega)]^\dagger$ and $\hat{O}^\dagger(\omega)$) but for simplicity we stick with the shorter form. The Fourier transform of operators and complex conjugated operators are then given as

$$\mathcal{FT}(\hat{O}(t)) = \hat{O}(\omega), \tag{C.1.7}$$

$$\mathcal{FT}(\hat{O}^\dagger(t)) = \hat{O}^\dagger(-\omega). \tag{C.1.8}$$

For an operator $\hat{O}(t)$ which is hermitian in the time domain, we get for the corresponding operator $\hat{O}(\omega)$ in the frequency domain

$$\hat{O}^\dagger(\omega) = \left[\int \hat{O}(t) e^{\mathrm{i}\omega t} \frac{\mathrm{d}t}{\sqrt{2\pi}} \right]^\dagger = \int \hat{O}(t) e^{-\mathrm{i}\omega t} \frac{\mathrm{d}t}{\sqrt{2\pi}} = \hat{O}(-\omega). \tag{C.1.9}$$

Thus, the Fourier transform of a hermitian operator is not hermitian any more, i.e. $\hat{O}^\dagger(-\omega) = \hat{O}(\omega)$.

C.2 Power Spectral Density

The power spectral density (PSD) of a signal $h(t)$ is defined by [112]

$$S_{hh}(\omega) = \lim_{\tau \to \infty} \frac{1}{\tau} \langle h_\tau^*(\omega) h_\tau(\omega) \rangle. \tag{C.2.1}$$

Here, h_τ is the windowed Fourier transform of $h(t)$

$$h_\tau(\omega) = \frac{1}{\sqrt{2\pi}} \int_{-\tau/2}^{\tau/2} h(t) \mathrm{e}^{\mathrm{i}\omega t} \mathrm{d}t. \tag{C.2.2}$$

The symmetrised power spectral density $\bar{S}_{hh}(\omega)$ of a signal h is given by the average over positive and negative frequency components of the power spectral density

$$\bar{S}_{hh}(\omega) = \frac{S_{hh}(\omega) + S_{hh}(-\omega)}{2} \tag{C.2.3}$$

where $\omega > 0$. In this work, we consider often the PSD of (expectation values of) operators. The definition of the PSD can be applied to operators. The quantum power spectral density of a general operator $\hat{O}$ is given by [112]

$$S_{OO}(\omega) = \lim_{\tau \to \infty} \frac{1}{\tau} \langle \hat{O}_\tau^\dagger(\omega) \hat{O}_\tau(\omega) \rangle, \tag{C.2.4}$$

where again $O_\tau(\omega)$ is the Fourier transform of $\hat{O}(t)$ sampled over the time period τ. For an operator with stationary statistics, the Wiener-Khinchin theorem states [112] a direct relation between the PSD of a variable and its autocorrelation function (defined later in equation (C.3.1)) in the time domain,

$$S_{OO}(\omega) = \int_{-\infty}^{\infty} \langle \hat{O}^\dagger(t+\tau)\hat{O}(t)\rangle_{t=0} \mathrm{e}^{\mathrm{i}\omega\tau} \mathrm{d}\tau. \tag{C.2.5}$$

By using the properties of the Fourier transform, we can derive

$$\begin{aligned} S_{OO}(\omega) &= \int_{-\infty}^{\infty} \langle \hat{O}^\dagger(t)\hat{O}(0)\rangle \mathrm{e}^{\mathrm{i}\omega t} \mathrm{d}t & \text{(C.2.6)}\\ &= \int_{-\infty}^{\infty} \frac{\mathrm{d}\omega'}{\sqrt{2\pi}} \int_{-\infty}^{\infty} \frac{\mathrm{d}\omega''}{\sqrt{2\pi}} \int_{-\infty}^{\infty} \mathrm{d}t \langle \hat{O}^\dagger(\omega'')\mathrm{e}^{\mathrm{i}\omega'' t}\hat{O}(\omega')\rangle \mathrm{e}^{\mathrm{i}\omega t} & \text{(C.2.7)}\\ &= \int_{-\infty}^{\infty} \frac{\mathrm{d}\omega'}{\sqrt{2\pi}} \int_{-\infty}^{\infty} \frac{\mathrm{d}\omega''}{\sqrt{2\pi}} \int_{-\infty}^{\infty} \mathrm{d}t \mathrm{e}^{\mathrm{i}(\omega+\omega'')t} \langle \hat{O}^\dagger(\omega'')\hat{O}(\omega')\rangle & \text{(C.2.8)}\\ &= \int_{-\infty}^{\infty} \mathrm{d}\omega' \langle \hat{O}^\dagger(-\omega)\hat{O}(\omega')\rangle. & \text{(C.2.9)} \end{aligned}$$

From the third line to the fourth line, we have used that $\int_{-\infty}^{\infty} \exp(\mathrm{i}(\omega+\omega'')t)\mathrm{d}t = 2\pi\delta(\omega+\omega'')$. For a hermitian operator (in the time domain) we have seen that $\hat{O}(\omega) = \hat{O}^\dagger(-\omega)$. And finally we get

$$S_{OO}(\omega) = \int_{-\infty}^{\infty} \langle \hat{O}(\omega)\hat{O}(\omega')\rangle \mathrm{d}\omega' \tag{C.2.10}$$

This from of writing the PSD is much more handy to use than the standard form with $\hat{O}_\tau(\omega)$ given in equation (C.2.4).

C.3 Autocorrelation function and Variance

The autocorrelation function of the stationary noise process $V(t)$ is defined as

$$G_{VV}(t-t') = \langle V(t)V(t')\rangle. \tag{C.3.1}$$

The variance of a noise process $V(t)$ with zero mean ($\langle V(t)\rangle_t = 0$) is then given by the autocorrelation at zero time delay

$$\mathrm{var}(V) = \langle V^2\rangle = G_{VV}(0). \tag{C.3.2}$$

From equation (C.2.5) we see that the PSD can be directly written as integral over the autocorrelation function

$$S_{VV}(\omega) = \int_{-\infty}^{\infty} \mathrm{e}^{\mathrm{i}\omega\tau} G_{VV}(\tau)\mathrm{d}\tau. \tag{C.3.3}$$

Similarly, we can write the autocorrelation function as the Fourier transform the PSD. For deriving the exact relation, we integrate over the PSD and get

$$\begin{aligned} \frac{1}{2\pi}\int_{-\infty}^{\infty} \mathrm{e}^{-\mathrm{i}\omega t} S_{VV}(\omega)\mathrm{d}\omega &= \frac{1}{2\pi}\int_{-\infty}^{\infty} \mathrm{d}\omega \int_{-\infty}^{\infty} \mathrm{d}\tau \mathrm{e}^{-\mathrm{i}\omega t}\mathrm{e}^{\mathrm{i}\omega\tau} G_{VV}(\tau) & \text{(C.3.4)}\\ &= \int_{-\infty}^{\infty} \mathrm{d}\tau G_{VV}(\tau)\delta(\tau - t) = G_{VV}(t). & \text{(C.3.5)} \end{aligned}$$

Summarising we have

$$G_{VV}(t) = \frac{1}{2\pi}\int_{-\infty}^{\infty} \mathrm{e}^{-\mathrm{i}\omega t} S_{VV}(\omega)\mathrm{d}\omega. \tag{C.3.6}$$

For the variance, we can just set $t = 0$ and get

$$\mathrm{var}(V) = G_{VV}(0) = \frac{1}{2\pi}\int_{-\infty}^{\infty} S_{VV}(\omega)\mathrm{d}\omega. \tag{C.3.7}$$

Note that in these relations involving the integrals of the PSD, the prefactor $1/(2\pi)$ appears and not the prefactor $1/\sqrt{2\pi}$ as in the definition of the Fourier transform.

C.4 Implementation in Python

Fast Fourier Transform: In contrast to the formulas in the last few paragraphs, in real life we do not have infinite time traces. Additionally, the measured data is digital, which means that we obtain discrete data points at a sampling rate f_{sample} for a total time $t_{\max}$, which then results in an array $F(k)$ with $n = f_{\mathrm{sample}} t_{\max}$ entries. We use the fast Fourier transform in order to calculate later the PSD. In python, the fast Fourier transform `fft[z]`[1] is defined by

$$\tilde{F}(l) = \sum_{k=0}^{n-1} F(k)\, \mathrm{e}^{-\mathrm{i}2\pi lk/n}, \tag{C.4.3}$$

where $\tilde{F}(l)$ is the lth entry of Fourier transform of $F(k)$. Each entry of the array $\tilde{F}(l)$ corresponds to the fast Fourier transform value at a frequency $f_l = l/t_{\max}$. The resolution bandwidth is given by the finite length of the data set, $\mathrm{RBW} = f_{\mathrm{sample}}/n$. In the following, we would like to relate this discrete Fourier transform to the continuous one. For this, we can define the times at which the data points are taken as $t_k = kt_{\max}/n$ and the inverse sampling rate as $\delta t = t_{k+1} - t_k = t_{\max}/n = 1/f_{\mathrm{sample}}$. Then we can multiply the expression by $1 = (t_{k+1} - t_k)/\delta t$

$$\tilde{F}(l) = \frac{1}{\delta t}\sum_{k=0}^{n-1}(t_{k+1} - t_k) F(k)\, \mathrm{e}^{-\mathrm{i}2\pi l t_k/t_{\max}}. \tag{C.4.4}$$

Further, we can define the Fourier frequencies as $f_l = l/t_{\max} = f_{\mathrm{sample}} l/n$ and continuous functions such that $f(t_k) = F(k)$ and $\tilde{f}(f_l) = F(l)$. We get

$$\tilde{f}(f_l) = \frac{1}{\delta t}\sum_{k=0}^{n-1}(t_{k+1} - t_k) f(t_k)\, \mathrm{e}^{-\mathrm{i}2\pi f_l t_k}. \tag{C.4.5}$$

[1] Using the `fft` function, a discrete Fourier transform is calculated

$$\texttt{fft[z]} = \sum_{k=0}^{n-1} z[k]\cdot e^{-ilk2\pi/n},\ l = 0 \ldots n-1. \tag{C.4.1}$$

The corresponding frequencies can be calculated with the `fftfreq` function:

$$\texttt{fftfreq[n, dt]} = \frac{1}{\texttt{n dt}} \cdot \begin{cases} 0, 1, ..., \texttt{n}/2 - 1, -\texttt{n}/2, ..., -1 & \texttt{if n is even} \\ 0, 1, ..., (\texttt{n}-1)/2, -(\texttt{n}-1)/2, ..., -1 & \texttt{if n is odd} \end{cases} \tag{C.4.2}$$

where `dt` is the inverse of the sampling frequency and `n` the number of samples. We see that the frequencies are not ordered form the minimal value to the maximal value. Thus, we use the function `fftshift`, which shifts the zero-frequency component to the center of the spectrum.

This already looks like a Riemann sum. Taking the limit of this sum for large $n \to \infty$ as

$$\lim_{n\to\infty} \tilde{f}(f_l) = f_{\text{sample}} \int_0^{t_{\max}} f(t)\, \mathrm{e}^{-\mathrm{i}2\pi f t} \mathrm{d}t \tag{C.4.6}$$

which is the Fourier transform to frequencies instead of angular frequencies as it was defined in the last paragraphs. This has to be considered when calculating the PSD. Similarly to this, the back-transformation can be compared to the continuous Fourier transform. The inverse Fourier transform is defined as

$$F(k) = \frac{1}{n} \sum_{l=0}^{n-1} \tilde{F}(l) \cdot e^{\mathrm{i}2\pi l k/n}. \tag{C.4.7}$$

We use that the frequency spacing is given by the resolution bandwidth $f_{l+1} - f_l = f_{\text{sample}}/n$ and get

$$\lim_{n\to\infty} f(t_k) = \frac{1}{f_{\text{sample}}} \int_{-f_{\text{sample}}/2}^{f_{\text{sample}}/2} \tilde{f}(f)\, \mathrm{e}^{\mathrm{i}2\pi f t} \mathrm{d}t. \tag{C.4.8}$$

Because in this definition, we transform back and forth from time to frequency (and not angular frequency), there is no factor of 2π appearing.

In our analysis, we use the the `scipy.fftpack` package of python. Using the `fft` function, a discrete Fourier transform is calculated, while the corresponding frequencies can be calculated with the `fftfreq` function.

Power Spectral Density: From the fast Fourier transform, the PSD can be calculated. In order to show the definition of the power spectral density, we define an example data set by

```
### Example Data
t_max = 5e-3                    #s time window
dt = 1e-7                       #s time spacing, inverse of the sampling rate
f_res = 1e6                     #Hz resonance frequency
gamma = 2*np.pi*1e3             # Linewidth in radial frequency

n = int(t_max/dt) + 1 # add one such that n is odd. Simplifies the example.
t = np.linspace(0, t_max, n)
X = np.cos(2*np.pi*f_res*t)*np.exp(-gamma*t/2)
```

The PSD is defined in equation (C.2.1). In order to estimate the PSD, the discrete Fourier transform is used, more precisely

$$S_{XX}(\Omega) = \lim_{\tau\to\infty} \frac{1}{\tau} |X_\tau(\omega)|^2 \to S_{XX}(f) = \frac{1}{\tau} |X_{\text{dis}}(m)/f_{\text{sample}}|^2 = |X_{\text{dis}}(m)|^2 \frac{\delta t}{n} \tag{C.4.9}$$

where $X_{\text{dis}}(\omega)$ is the discrete (fast) Fourier transform as defined in the last paragraph and we have used that the probe duration times the sampling rate is the number of samples $\tau f_{\text{sample}} = n$ and that $\delta t = 1/f_{\text{sample}}$ is the inverse of the sampling rate. Here, it is important to note that changing from $S_{XX}(\Omega)$ to $S_{XX}(f)$ is not just changing the variable of the argument of the function but changing the

function itself[2]. In order to obtain the power, we have to multiply $S_{XX}(\Omega)$ by an angular frequency (in s^{-1}) while $S_{XX}(f)$ has to be multiplied by a frequency (in Hz). The PSD of this signal `X` can then be calculated with

```
### Calculate PSD of the signal:
fft_z = fft(X)                          # Calculate the fast Fourier transform
f = fftfreq(n, d=dt)                    # Get the frequency axis
f = fftshift(f)                         # Reorder the entries of the frequency axis.
fft_z = fftshift(fft_z)                 # Reorder the entries of the fft axis.
psd = abs(fft_z)**2*dt/float(n) # Calculate the PSD

### Symmetrise PSD:
psd_sym = (psd + psd[::-1])/2
psd_sym = psd_sym[f>0]  # For the symmetrised PSD only keep pos frequencies
f_sym = f[f>0]          # For the symmetrised PSD only keep pos frequencies
```

In order to get the variance from this PSD, we have to consider that the integration over frequency is different than the integration over angular frequency. Including all factors, we get

$$\mathrm{var}(V) = G_{VV}(0) = \int_{-\infty}^{\infty} S_{VV}(f)\mathrm{d}f. \tag{C.4.14}$$

In our experiments we mostly observe a fast oscillating signal. Therefore our measurements are done by using a lockin amplifier or a spectrum analyser in the IQ-mode. Thereby, we obtain the demodulated in-phase and quadrature signal, as explained in section 2.3.3. For here we assume that the lockin amplifier demodulates the data at the `f_demod`. Here, we have to implement this demodulation by hand, using

```
def moving_average(x, w):
    return np.convolve(x, np.ones(w), 'valid') / w

### Demodulation of the signal:
f_demod = f_res
t_demod = moving_average(t, 100)
I_trace = moving_average(np.sqrt(2)*X*np.cos(2*np.pi*f_demod*t), 100)
Q_trace = moving_average(np.sqrt(2)*X*np.sin(2*np.pi*f_demod*t), 100)
```

[2]We define the Fourier transform for the conversion from time to frequency to match better, what we numerically calculate in the Python code. For here, the Fourier transform is given as

$$h(f) = \int h(t)\mathrm{e}^{\mathrm{i}2\pi ft}\mathrm{d}t, \tag{C.4.10}$$

$$h(t) = \int h(f)\mathrm{e}^{-\mathrm{i}2\pi t}\mathrm{d}f. \tag{C.4.11}$$

The definition of the PSD in frequency units is not much different than for angular frequencies. We can write

$$S_{hh}(f) = \int_{-\infty}^{\infty} \langle h(t)h(0)\rangle \mathrm{e}^{\mathrm{i}2\pi ft}\mathrm{d}t = \int_{-\infty}^{\infty} \langle h(f)h(f')\rangle \mathrm{d}f'. \tag{C.4.12}$$

To derive the last term, consider that the argument of the Dirac function transforms as $\delta(2\pi(f''-f)) = \delta(f''-f)/(2\pi)$. With this, we can derive the autocorrelation function

$$G_{hh}(t) = \int_{-\infty}^{\infty} \mathrm{e}^{-\mathrm{i}2\pi ft} S_{hh}(f)\mathrm{d}f. \tag{C.4.13}$$

```
Z_trace = I_trace + 1j*Q_trace
dt_demod = np.mean(np.diff(t_demod))
n_demod = len(t_demod)
```

In our normal analysis routine, the PSD of the demodulated data is calculated by using thte same functions as already introduced on top, more precisely by the following code:

```
### Calculate PSD of demodulated signal:
fft_demod = fft(Z_trace)
psd_demod = abs(fft_demod)**2*dt_demod/n_demod
f1= fftfreq(n_demod, d=dt_demod)

psd_demod = fftshift(psd_demod)
f1 = fftshift(f1) + f_demod
```

Here in the last line, the frequency is shifted by the demodulation frequency to obtain the non-demodulated frequencies. Comparing the symmetric PSD `psd_sym` and the PSD from the demodulated data `psd_demod`, we observe that they differ by a factor of two. In order to obtain the symmetrised PSD as defined in equation (C.2.3), the PSD from the demodulated data has to be divided by two, `psd_sym` = `psd_demod`/2. This factor of two has to be taken into account when calculating i.e. the number of excitations of a system.

Appendix D

Some Derivation of the 3D Spin-Light-Interface

In this appendix, the derivation and some more formula for the collective scattering of an atomic cloud are provided.

D.1 Laguerre-Gaussian Modes

In the following, we need to have a basis for the modes of the light. In the paraxial approximation, the classical electric field of the light can be written as [94]

$$\mathbf{E}_{pl}(r,\phi,z) = \frac{1}{2}\vec{\epsilon}_L E_{pl}(r,\phi,z)e^{-i\omega t+ik_0 z} + c.c. \tag{D.1.1}$$

$$= \frac{1}{2}\vec{\epsilon}_L \mathcal{E}\tilde{u}_{pl}(r,\phi,z)\exp(-i\omega t) + c.c. \tag{D.1.2}$$

where $\vec{\epsilon}_L$ is the polarisation unit vector, $\mathcal{E} = 2\mathcal{E}_0\sqrt{\Phi_L} = \sqrt{2P/(\varepsilon_0 cA)}$ is the amplitude of the electrical field with the vacuum electric field density $\mathcal{E}_0 = \sqrt{\hbar\omega_{\mathrm{L}}/(2\varepsilon_0 cA)}$, the photon flux Φ_L, the mode area $A = \pi w_0^2/2$, the speed of light c, the power P and the vacuum permittivity ε_0. $E_{pl}(r,\phi,z) = \mathcal{E}u_{pl}(r,\phi,z)$ is the local electric field. Here, the mode function contain one more phase factor, namely $\tilde{u}_{pl} = u_{pl}\exp(+ik_0 z)$. For a system which is cylindrical symmetric, it proves to be useful to use the Laguerre-Gaussian modes given by [85]

$$u_{pl}(r,\phi,z) = \sqrt{\frac{p!}{(p+|l|)!}}\frac{w_0}{w(z)}\left(\frac{\sqrt{2}r}{w(z)}\right)^{|l|} L_p^{|l|}\left(\frac{2r^2}{w(z)^2}\right) \cdot \exp\left(-\frac{r^2}{w(z)^2} + ik_0\frac{r^2}{2R(z)} - il\phi - i(l+2p+1)\Phi(z)\right), \tag{D.1.3}$$

where we have defined

$$w(z) = w_0\sqrt{1+\left(\frac{z}{z_R}\right)^2}, \tag{D.1.4}$$

$$R(z) = \frac{z^2+z_R^2}{z}, \tag{D.1.5}$$

$$\Phi(z) = \arctan\left(\frac{z}{z_R}\right) \tag{D.1.6}$$

and the wavevector $k_0 = 2\pi/\lambda$, the Rayleigh length $z_R = \pi w_0^2/\lambda$, the wavelength λ and the waist w_0. Here, $p \geq 0$ is the radial index and l the azimuthal index which can be positive, negative or zero. Both indices are integers. $L_p^l(x)$ is the generalised Laguerre polynomial given by

$$L_p^{|l|}(x) = \frac{x^{-|l|}e^x}{p!}\frac{d^p}{dx^p}\left(e^{-x}x^{p+|l|}\right). \tag{D.1.7}$$

The normalisation is chosen such that the modes for $l = 0$ are unity in the focus, i.e. $u_{p0}(0,\phi,0) = 1$. Integrating radially over the intensity yields then

$$A = \int_0^\infty \int_0^{2\pi} u_{pl}^*(r,\phi,z)u_{p'l'}(r,\phi,z)\mathrm{d}\phi r\mathrm{d}r = \frac{\pi w_0^2}{2}\delta_{p,p'}\delta_{l,l'} \tag{D.1.8}$$

which is the effective beam area of the laser beam. For future calculations it might be useful to consider the following relations [85]:

$$\sum_{p,l} u_{pl}^*(r,\phi,z)u_{pl}(r',\phi',z) = A\delta(\mathbf{r}_\perp - \mathbf{r}'_\perp) = A\frac{\delta(r-r')}{r}\delta(\phi-\phi'), \tag{D.1.9}$$

$$\sum_{p,l} u_{pl}^*(r,\phi,z)u_{pl}(r',\phi',z') = A\frac{-ik_0}{2\pi(z-z')}\exp\left(\frac{ik_0|\mathbf{r}_\perp - \mathbf{r}'_\perp|^2}{2(z-z')}\right), \tag{D.1.10}$$

$$= A\frac{-ik_0}{2\pi(z-z')}\exp\left(\frac{ik_0(r^2+r'^2-2rr'\cos(\phi-\phi'))}{2(z-z')}\right). \tag{D.1.11}$$

Zero'th Order Mode: The fundamental mode of the Laguerre-Gaussian mode is indeed the Gaussian TEM_{00}, namely

$$u_{00}(r,\phi,z) = \frac{w_0}{w(z)}\exp\left(-\frac{r^2}{w(z)^2} + ik_0\frac{r^2}{2R(z)} - i\Phi(z)\right). \tag{D.1.12}$$

The intensity profile of the fundamental mode is given by

$$\beta_{00}(r,\phi,z) = |u_{00}(r,\phi,z)|^2 = \frac{z_R^2}{z^2+z_R^2}\exp\left(-\frac{2r^2}{w(z)^2}\right). \tag{D.1.13}$$

D.2 Classical Model of Scattering of Light one Atom

This section follows the classical description of light-atom interaction given in [94]. In the following we assume that the driving field is in the fundamental $(p,l) = (0,0)$ mode and denote the incoming amplitude with $\mathcal{E} = \mathcal{E}_{\mathrm{in}}$. The atomic dipole moment induced by the field is consequently given by

$$\mathbf{p} = \frac{1}{2}\mathbf{e}pe^{-i\omega t} + c.c. \tag{D.2.1}$$

with the amplitude of the induced dipole $p = \alpha E_{00}\exp(ik_0 z)$. Here, the atomic polarisability reads

$$\alpha = 6\pi\epsilon_0 c^3 \frac{\gamma_{\mathrm{Rb}}/\omega_0^2}{\omega_0^2 - \omega^2 - i(\omega^3/\omega_0^2)\gamma_{\mathrm{Rb}}} \tag{D.2.2}$$

$$\approx 6\pi\epsilon_0 \frac{c^3}{\omega^3}\left(\frac{-2\gamma_{\mathrm{Rb}}\Delta}{\gamma_{\mathrm{Rb}}^2 + 4\Delta^2} + i\frac{\gamma_{\mathrm{Rb}}^2}{\gamma_{\mathrm{Rb}}^2 + 4\Delta^2}\right), \tag{D.2.3}$$

where ω_0 is the atomic resonance frequency [94]. In the second line, the narrow bandwidth approximation was applied, i.e. $\omega \approx \omega_0 \gg \Delta, \gamma_{\mathrm{Rb}}$ where the detuning is given by $\Delta = \omega - \omega_0$. We can write the dimensionless atomic polarisability constant as

$$\beta = \frac{k_0}{2A}\frac{\alpha}{\epsilon_0} = \frac{\sigma_0}{2A}\left(\frac{-2\gamma_{\mathrm{Rb}}\Delta}{\gamma_{\mathrm{Rb}}^2 + 4\Delta^2} + i\frac{\gamma_{\mathrm{Rb}}^2}{\gamma_{\mathrm{Rb}}^2 + 4\Delta^2}\right). \tag{D.2.4}$$

where $\sigma_0 = 3\lambda^2/(2\pi) = P_{\mathrm{rad}}/I_{\mathrm{in}}$ is the single atom cross-section. For an atom at the origin (i.e. $u(0,0,0) = 1$), the emitted radiation at a distance $R \gg \lambda$ is given by [94]

$$E_{\mathrm{rad}}(R,\theta) = \frac{k_0^2\sin(\theta)}{4\pi\epsilon_0}\frac{e^{ik_0 R}}{R}\alpha\mathcal{E}_{\mathrm{in}} = \sin(\theta)\frac{Ak_0}{2\pi}\frac{e^{ik_0 R}}{R}\beta\mathcal{E}_{\mathrm{in}}, \tag{D.2.5}$$

where $R = \sqrt{r^2 + z^2}$ is the distance of the observer to the atom and θ is the angle with respect to the polarisation $\vec{\epsilon}_L$. The total scattering can be calculated by integrating the scattered intensity $I_{\mathrm{rad}}(R,\theta) = \epsilon_0 c|E_{\mathrm{rad}}(R,\theta)|^2/2$. We obtain

$$P_{\mathrm{rad}} = \int_0^{\pi}\int_0^{2\pi} I_{\mathrm{rad}}(R,\theta)R^2\sin(\theta)\mathrm{d}\phi\mathrm{d}\theta \tag{D.2.6}$$

$$= \frac{\sigma_0}{2A}\frac{\gamma_{\mathrm{Rb}}^2}{\gamma_{\mathrm{Rb}}^2 + 4\Delta^2}|\mathcal{E}_{\mathrm{in}}|^2\varepsilon_0 cA = \frac{\sigma_0}{2A}\frac{\gamma_{\mathrm{Rb}}^2}{\gamma_{\mathrm{Rb}}^2 + 4\Delta^2}2P_{\mathrm{in}}. \tag{D.2.7}$$

From this, we can calculate the amplitude of the radiated field, namely

$$|\mathcal{E}_{\mathrm{rad}}| = \sqrt{\frac{2P_{\mathrm{rad}}}{\varepsilon_0 cA}} = |\mathcal{E}_{\mathrm{in}}|\frac{|\alpha|k_0^2}{\epsilon_0\sqrt{6\pi A}}. \tag{D.2.8}$$

In this derivation, we have lost the information about the phase. We define the mode-function of the radiated light by

$$\tilde{u}_{\mathrm{rad}}(r,z) = \frac{E_{\mathrm{rad}}}{\mathcal{E}_{\mathrm{rad}}} = \sin(\theta)\frac{Ak_0}{2\pi}\frac{e^{ik_0 R}}{R}\beta\frac{\mathcal{E}_{\mathrm{in}}}{\mathcal{E}_{\mathrm{rad}}}. \tag{D.2.9}$$

For an observer at a large distant but on axis with the propagation of the laser light, we can approximate $\sin\theta \approx 1$ and $\exp(ikR)/R \approx \exp(ik_0 z + ik_0 r^2/(2z))/z$. We get

$$u_{\mathrm{rad}} = \frac{k_0^2}{4\pi\epsilon_0}\frac{e^{ik_0\frac{r^2}{2z}}}{z}\alpha\frac{\mathcal{E}_{\mathrm{in}}}{\mathcal{E}_{\mathrm{rad}}} = \frac{Ak_0}{2\pi}\frac{e^{ik_0\frac{r^2}{2z}}}{z}\beta\frac{\mathcal{E}_{\mathrm{in}}}{\mathcal{E}_{\mathrm{rad}}}. \tag{D.2.10}$$

Next, we want to calculate how much of the light is scattered into a certain mode. We have

$$\frac{\mathcal{E}_{pl}}{\mathcal{E}_{\mathrm{rad}}} = \frac{1}{A}\int_0^{\infty}\int_0^{2\pi} u_{pl}^* u_{\mathrm{rad}} d\phi r dr \tag{D.2.11}$$

In order to do this integration explicitly, we approximate the Laguerre-Gauss mode in the far distance. For this, we take $z \gg z_R$ such that $\Phi(z) \approx \pi/2$, $w(z) \approx w_0 z/z_R$, and $R(z) = z$. The Laguerre-Gauss modes simplify to

$$\begin{aligned} u_{pl}(r,\phi,z) =& \sqrt{\frac{p!}{(p+|l|)!}} \frac{z_R}{z} \left(\frac{\sqrt{2} r z_R}{w_0 z}\right)^{|l|} L_p^{|l|}\left(\frac{2r^2 z_R^2}{w_0^2 z^2}\right) \\ & \cdot \exp\left(-\frac{r^2 z_R^2}{w_0^2 z^2} + ik\frac{r^2}{2z} - il\phi - i(l+2p+1)\frac{\pi}{2}\right) \end{aligned} \tag{D.2.12}$$

The scattering into the fundamental yields [94]

$$\frac{\mathcal{E}_{00}}{\mathcal{E}_{\text{rad}}} = \frac{1}{A}\int_0^\infty \int_0^{2\pi} u_{00}^* u_{\text{rad}} d\phi r dr \tag{D.2.13}$$

$$= \frac{2\pi}{A}\int_0^\infty \frac{z_R}{z} \exp\left(-\frac{r^2 z_R^2}{w_0^2 z^2} - \mathrm{i}k\frac{r^2}{2z} + \mathrm{i}\frac{\pi}{2}\right) \frac{k_0^2}{4\pi\epsilon_0} \frac{e^{\mathrm{i}k_0 \frac{r^2}{2z}}}{z} \alpha \frac{\mathcal{E}_{\text{in}}}{\mathcal{E}_{\text{rad}}} r dr \tag{D.2.14}$$

$$\Leftrightarrow \frac{\mathcal{E}_{00}}{\mathcal{E}_{\text{in}}} = \mathrm{i}\frac{2\pi}{A}\int_0^\infty \frac{z_R}{z} \exp\left(-\frac{r^2 z_R^2}{w_0^2 z^2}\right) \frac{k_0^2}{4\pi\epsilon_0} \frac{1}{z} \alpha r dr \tag{D.2.15}$$

$$= \mathrm{i}\frac{k_0}{2A}\frac{\alpha}{\epsilon_0} = \mathrm{i}\beta. \tag{D.2.16}$$

where in the last line we used that $w_0^2 = z_R\lambda/\pi$ and $k_0 = 2\pi/\lambda$. From this we can define the single atom cooperativity by

$$C = \frac{2P_{00}}{P_{\text{rad}}} = \frac{2|\mathcal{E}_{00}|^2}{|\mathcal{E}_{\text{rad}}|^2} = \frac{6\pi}{k_0^2 A} = \frac{\sigma_0}{A}, \tag{D.2.17}$$

where $\sigma_0 = 3\lambda^2/(2\pi)$ is the single atom cross-section. This cooperativity is given in equation (8) of [94] and accounts for scattering both, in forward and in backward direction. This derivation does not seem to be very solid on first sight: first we make the approximation for small r and then we integrate the variable r from zero to infinity. If we integrate r just to a cut-off radius R instead of to infinity, we would have to correct the upper result by a factor

$$1 - \exp\left(-\frac{R^2 z_R^2}{w_0^2 z^2}\right) = 1 - \exp\left(-\frac{R^2}{z^2}\frac{3A}{4\sigma_0}\right). \tag{D.2.18}$$

Thus, as long as the beam area A is much larger that the single atom cross-section σ_0, R can be still significantly smaller than z without changing the result much. Thus, the assumptions for small $r \ll z$ is not violated too much by integrating r to infinity.

D.3 Derivation of the Power Spectral Density for the Collective Scattering

For inhomogeneous coupling the spin-light interaction Hamiltonian reads as

$$H_{\text{int}} = \hbar\alpha_1 \hat{S}_z \sum_{i=1}^{N_a} \eta_{\text{s}}^{(i)} \hat{f}_z^{(i)}. \tag{D.3.1}$$

For every single spin, the equation of motion can be calculated by assuming that they commute

$$\frac{d}{dt}\hat{f}_y^{(i)}(t) = -\Omega_\mathrm{s}\hat{f}_z^{(i)}(t) - \frac{\gamma_\mathrm{s}}{2}\hat{f}_y^{(i)}(t) + \hat{h}_y^{(i)}(t) + \alpha_1\eta_\mathrm{s}^{(i)}\hat{f}_x^{(i)}(t)\hat{S}_z(t), \tag{D.3.2}$$

$$\frac{d}{dt}\hat{f}_z^{(i)}(t) = \Omega_\mathrm{s}\hat{f}_y^{(i)}(t) - \frac{\gamma_\mathrm{s}}{2}\hat{f}_z^{(i)}(t) + \hat{h}_z^{(i)}(t), \tag{D.3.3}$$

where the first term corresponds to the rotation around the magnetic field at Larmor frequency Ω_s and the second term describes the spin decay. In order to preserve the noise statistics in presence of the decay term, we have included the Langevin forces $\hat{h}_y$ and $\hat{h}_z$ [111]. The last term of the first line is the spin-light coupling. To solve this system of equation, we transform these equations to the frequency space

$$\hat{f}_z^{(i)}(\omega) = \frac{(\gamma_\mathrm{s}/2 - i\omega)\hat{h}_z^{(i)}(\omega) + \Omega_\mathrm{s}[\hat{h}_y^{(i)}(\omega) + \alpha_1\eta_\mathrm{s}^{(i)}\hat{f}_x^{(i)}(\omega)\hat{S}_z(\omega)]}{\Omega_\mathrm{s}^2 - \omega^2 + (\gamma_\mathrm{s}/2)^2 - 2\mathrm{i}\gamma_\mathrm{s}\omega}. \tag{D.3.4}$$

This result can be plugged into the input-output relation of light. We obtain

$$\hat{S}_y^{(out)}(\omega) = \hat{S}_y^{(in)}(\omega) + \alpha_1\hat{S}_x^{(in)}(\omega)\sum_{i=1}^{N_a}\eta_\mathrm{s}^{(i)}\hat{f}_z^{(i)}(\omega) \tag{D.3.5}$$

$$= \hat{S}_y^{(in)}(\omega) + \alpha_1\hat{S}_x^{(in)}(\omega)\sum_{i=1}^{N_a}\eta_\mathrm{s}^{(i)}\frac{(\gamma_\mathrm{s}/2 - i\omega)\hat{h}_z^{(i)}(\omega) + \Omega_\mathrm{s}[\hat{h}_y^{(i)}(\omega) + \alpha_1\eta_\mathrm{s}^{(i)}\hat{f}_x^{(i)}(\omega)\hat{S}_z(\omega)]}{\Omega_\mathrm{s}^2 - \omega^2 + (\gamma_\mathrm{s}/2)^2 - 2\mathrm{i}\gamma_\mathrm{s}a\omega}. \tag{D.3.6}$$

The spectrum can be calculated by using the following expectation values

$$\langle\hat{S}_y^{(in)}(\omega)\hat{S}_y^{(in)}(\omega')\rangle = \langle\hat{S}_z^{(in)}(\omega)\hat{S}_z^{(in)}(\omega')\rangle = \delta(\omega+\omega')\frac{\bar{S}_x}{2}, \tag{D.3.7}$$

$$\langle\hat{h}_y^{(i)}(\omega)\hat{h}_y^{(j)}(\omega')\rangle = \langle\hat{h}_z^{(i)}(\omega)\hat{h}_z^{(j)}(\omega')\rangle = \delta(\omega+\omega')\delta_{ij}\frac{\gamma_\mathrm{s}}{2}|\bar{f}_x^{(i)}|, \tag{D.3.8}$$

$$\langle\hat{h}_y^{(i)}(\omega)\hat{h}_z^{(j)}(\omega')\rangle = -\langle\hat{h}_z^{(i)}(\omega)\hat{h}_y^{(j)}(\omega')\rangle = \delta(\omega+\omega')\delta_{ij}\mathrm{i}\frac{\gamma_\mathrm{s}}{2}\bar{f}_x^{(i)}. \tag{D.3.9}$$

Furthermore, we assume that spins and light are well polarised such that we can write $\hat{S}_x^{(\mathrm{in})}(\omega) = \bar{S}_x$ and $\hat{f}_x^{(i)}(\omega) = \bar{f}_x$. In order to calculate these equations, we have assumed that $\langle\hat{f}_x^{(i)}\rangle$ is not changed over time (for further details, see Appendix G in [111]). The symmetrised power spectral density is then:

$$\bar{S}_{S_yS_y}(\omega) = \frac{\bar{S}_x}{2} + \frac{(\alpha_1\bar{S}_x/2)^2}{(\Omega_\mathrm{s}-\omega)^2 + (\gamma_\mathrm{s}/2)^2}\cdot\left(\sum_{i=1}^{N_a}\gamma_\mathrm{s}\eta_\mathrm{s}^{(i)2}|\bar{f}_x^{(i)}| + \sum_{i=1}^{N_a}\sum_{j=1}^{N_a}\alpha_1^2\eta_\mathrm{s}^{(i)2}\eta_\mathrm{s}^{(j)2}\bar{f}_x^{(i)}\bar{f}_x^{(j)}\bar{S}_x/2\right), \tag{D.3.10}$$

where we applied the narrow bandwidth approximation. Further, we see that for the noise $\hat{F}_x$ cannot be just replaced by $\hat{\tilde{F}}_x$ to obtain similar equations as for homogeneous coupling. To obtain the same equation as for homogeneous coupling but with effective parameters, we have two options: either we only normalise the polarisability constant or we adapt the spin operator and adapt the polarisability constant.

Renormalise the Spin Operators and the Polarisability Constant: Having this an expression for the PSD, effective spin operators can be defined. The effective atomic operators of higher order

(similar to [85]) are defined as

$$\hat{F} \longrightarrow \hat{\tilde{F}}^{(n)} = \sum_{i=1}^{N_a} \left(\frac{\eta_{\mathrm{s}}^{(i)}}{\eta_{\mathrm{s,eff}}} \right)^n \hat{f}^{(i)} \tag{D.3.11}$$

and the effective atomic polarisabiliy

$$\alpha_1 \longrightarrow \tilde{\alpha}_1 = \alpha_1 \cdot \eta_{\mathrm{s,eff}}. \tag{D.3.12}$$

The higher order effective atomic operators fulfil the spin commutation relation only if we assume that all spins are identical (i.e. $\hat{f} = \hat{f}^{(i)}\ \forall i$). This is a good assumption for a well polarised cloud of spins. In the case of this normalisation convention, we get the Hamiltonian

$$\hat{H} = \hbar \tilde{\alpha}_1 \hat{\tilde{F}}_z^{(1)} \hat{S}_z \tag{D.3.13}$$

and the spectrum of the outgoing light reads as

$$\bar{S}_{S_y S_y}(\omega) \approx \frac{\bar{S}_x}{2} + \frac{(\tilde{\alpha}_1 \bar{S}_x/2)^2}{(\Omega_{\mathrm{s}} - \omega)^2 + \gamma_{\mathrm{s}}^2/4} \cdot \left(\gamma_{\mathrm{s}} |\bar{\tilde{F}}_x^{(2)}| + \frac{\tilde{\alpha}_1^2 \bar{\tilde{F}}_x^{(2)2} \bar{S}_x}{2} \right). \tag{D.3.14}$$

We can futher simplify this expression by defining a measurement rate of second order

$$\tilde{\Gamma}_{\mathrm{s}}^{(2)} = \frac{\tilde{\alpha}_1^2 \bar{\tilde{F}}_x^{(2)} \bar{S}_x}{4} = \frac{\alpha_1^2 \bar{S}_x}{4} \sum_{i=1}^{N_a} \eta_s^{(i)2} \bar{f}_x \approx \frac{\alpha_1^2 \bar{S}_x \bar{f} N_a \langle \eta_s^2 \rangle}{4}. \tag{D.3.15}$$

For the last expression we have assumed that the spins are well polarised along the x-axis. Inserting this into the expression for the PSD, we get our usual expression for the spectrum (assumed that $\bar{\tilde{F}}_x^{(2)} > 0$)

$$\frac{\bar{S}_{S_y S_y}(\omega)}{\bar{S}_x} \approx \frac{1}{2} + \frac{\tilde{\Gamma}_{\mathrm{s}}^{(2)}}{(\Omega_{\mathrm{s}} - \omega)^2 + \gamma_{\mathrm{s}}^2/4} \cdot \left(\gamma_{\mathrm{s}} + 2\tilde{\Gamma}_{\mathrm{s}}^{(2)} \right). \tag{D.3.16}$$

Assumed that all spins are identical, i.e. $\hat{f} = \hat{f}^{(i)}\ \forall i$, the first order and second order spin operators are equal

$$\hat{\tilde{F}}^{(2)} = \hat{\tilde{F}}^{(1)}. \tag{D.3.17}$$

This is not the case for higher order spin operators any more.

Variance of the Measurement Record

In most measurements, we can measure the variance of the Faraday measurement. It is directly obtained from integrating over the spectrum over the bandwidth Δ_{bw}, yielding

$$\mathrm{var}(\hat{S}_y) = 2 \int_{\omega_L - \Delta_{\mathrm{bw}}/2}^{\omega_L + \Delta_{\mathrm{bw}}/2} \bar{S}_{S_y S_y}(\omega) \frac{\mathrm{d}\omega}{2\pi} = \bar{S}_x \frac{\Delta_{\mathrm{bw}}}{2\pi} + \frac{\tilde{\alpha}_1^2 \bar{S}_x^2}{4} \left(2|\bar{F}_x^{(2)}| + \frac{\tilde{\alpha}_1^2 \bar{F}_x^{(2)2} \bar{S}_x}{\gamma_{\mathrm{s}}} \right). \tag{D.3.18}$$

If we define a Faraday angle as $\hat{\theta} = \hat{S}_y/(2\bar{S}_x)$, we can write the variance of this Faraday angle as

$$\mathrm{var}(\hat{\theta}) = \frac{\mathrm{var}(\hat{S}_y)}{4\bar{S}_x^2} = \frac{\Delta_{\mathrm{bw}}}{2\pi} \frac{1}{4\bar{S}_x} + \frac{\tilde{\alpha}_1^2 |\bar{F}_x^{(2)}|}{8} + \frac{(\tilde{\alpha}_1^2 \bar{F}_x^{(2)})^2 \bar{S}_x}{16\gamma_{\mathrm{s}}}. \tag{D.3.19}$$

D.4 Calculating Overlap Integrals for an Atomic Cloud

For performing some overlap calculations, it is assumed that all spins are identical and that the sum can be approximated by an integral, thereby loosing the randomness of the atomic position. Furthermore, the atomic cloud is approximated as 3D-Gaussian distribution

$$n(r,z) = N_a \sqrt{\frac{1}{\pi^3 w_{a,r}^4 w_{a,z}^2}} \exp\left(-\frac{r^2}{w_{a,r}^2}\right) \exp\left(-\frac{z^2}{w_{a,z}^2}\right), \tag{D.4.1}$$

as derived in section 1.6.1 for a dipole trapped cloud. For a Gaussian beam,

$$I(r,z) = I_0 |u_{00}(z,r)|^2 = I_0 \left(\frac{w_0}{w(z)}\right)^2 \exp\left(\frac{-2r^2}{w(z)^2}\right), \tag{D.4.2}$$

we obtain

$$\langle \eta_s \rangle = \frac{1}{2}\sqrt{\pi} \exp\left(\frac{2z_R^2}{w_{a,z}^2 D}\right) \sqrt{2D} \frac{z_R}{w_{a,z}} \mathrm{Erfc}\left(\frac{z_R\sqrt{2}}{w_{a,z}\sqrt{D}}\right), \tag{D.4.3}$$

with

$$D = \frac{2w_0^2}{w_0^2 + 2w_{a,r}^2}. \tag{D.4.4}$$

In the limit of a long Rayleigh length, $z_\mathrm{R} \gg w_{a,z}$, this reduces to $\langle \eta_\mathrm{s} \rangle = D/2$ (limit of large Fresnel number $F = w_0^2/(\lambda w_{a,z})$). To simplify the expression of the second order integral, we assume that $D = 1$. We get

$$\langle \eta_s^2 \rangle = \frac{z_R}{2w_{a,z}}\sqrt{\pi} \left(\exp\left(\frac{z_R}{\sqrt{2}w_{a,z}}\right) \mathrm{Erfc}\left(\frac{z_R}{w_{a,z}}\right) - \frac{1}{\sqrt{3}} \exp\left(\frac{3z_R}{\sqrt{2}w_{a,z}}\right) \mathrm{Erfc}\left(\frac{\sqrt{3}z_R}{w_{a,z}}\right)\right), \tag{D.4.5}$$

which reduces to $\langle \eta_s^2 \rangle = 1/3$ for a large Rayleigh length. In this limit, we get $\hat{\mathbf{F}}^{(1)} = \hat{\mathbf{F}}^{(2)} = 3\hat{\mathbf{F}}/4$ and $\tilde{\alpha}_1 = 2\alpha_1/3$. In theory, this limit is described as the limit in which the 1D- approximation is still valid [13].

Appendix E

Derivation of Ponderomotive Squeezing of the Light by the Optomechanical System

---

The mechanism of ponderomotive squeezing was predicted early in 1994 [136, 137]. Nearly twenty years later, it was experimentally demonstrated for a silicon nitride membrane [120] and a for a wave-guide resonator [193]. Since then, it serves as benchmark for a mechanical oscillator in the quantum regime. Ponderomotive squeezing of the light was shown using diverse mechanical systems, including wave-guide resonators [193], a single levitated nano-particle [194] and a silicon nitride membrane in a room-temperature environment [63]. In chapter 3, ponderomotive squeezing of the light is shown. Here, the theoretical model used in figure 3.3.5 to compare to the theory is derived.

The linearised Hamiltonian describing the optomechanical interaction between the membrane and the cavity photons is given by [54] (see equation (3.1.6))

$$\hat{H}_{\mathrm{om}} = -\hbar g_0 \sqrt{n_c}\sqrt{2}\hat{X}_m \left(\hat{c} + \hat{c}^\dagger\right), \tag{E.0.1}$$

where $n_c = \langle \hat{c}^\dagger \hat{c} \rangle$ is the average number of photons in the cavity. From this Hamiltonian, the following equations of motion can be derived,

$$\partial_t \hat{X}_{\mathrm{m}} = \Omega_{\mathrm{m}} \hat{P}_{\mathrm{m}}, \tag{E.0.2}$$

$$\partial_t \hat{P}_{\mathrm{m}} = -\Omega_{\mathrm{m}} \hat{X}_{\mathrm{m}} - \gamma_{\mathrm{m}} \hat{P}_{\mathrm{m}} - \sqrt{2}\left(g^* \hat{c} + g\hat{c}^\dagger\right) + \sqrt{2\gamma_{\mathrm{m}}}\hat{P}_{\mathrm{th}}, \tag{E.0.3}$$

$$\partial_t \hat{c} = \left(\mathrm{i}\Delta_{\mathrm{c}} - \frac{\kappa}{2}\right)\hat{c} - \sqrt{\kappa\eta}\hat{a}^{(\mathrm{in})} - \mathrm{i}\sqrt{2} g \hat{X}_{\mathrm{m}}. \tag{E.0.4}$$

Here, we have defined a more general optomechanical coupling strength $g = g_0 \alpha_L \sqrt{\kappa\eta}/(\kappa/2 - \mathrm{i}\Delta)$ which takes the phase difference between the incoming field and the cavity field due to the cavity detuning into account. Furthermore, the cavity incoupling efficiency is given as $\eta = \kappa_1/\kappa$. In the frequency domain,

the cavity field is given by

$$\hat{c}(\omega) = -\chi_{\mathrm{c}}(\omega)\left(\sqrt{\kappa\eta}\hat{a}^{(\mathrm{in})}(\omega) + \mathrm{i}\sqrt{2}g\hat{X}_{\mathrm{m}}(\omega)\right), \tag{E.0.5}$$

where the cavity susceptibility is defined as

$$\chi_{\mathrm{c}}(\omega) = \frac{1}{\kappa/2 - \mathrm{i}(\omega + \Delta_{\mathrm{c}})}. \tag{E.0.6}$$

The ponderomotive squeezing affects the outgoing light, thus we derive the outgoing light quadratures. The outgoing light is given by the incoming field plus the effect of the cavity on the light

$$\hat{X}_{\mathrm{L}}^{(\mathrm{out})} = \hat{X}_{\mathrm{L}}^{(\mathrm{in})} + \sqrt{\kappa\eta}\hat{X}_{\mathrm{c}}, \tag{E.0.7}$$

$$\hat{P}_{\mathrm{L}}^{(\mathrm{out})} = \hat{P}_{\mathrm{L}}^{(\mathrm{in})} + \sqrt{\kappa\eta}\hat{P}_{\mathrm{c}}, \tag{E.0.8}$$

with the incoming light quadratures defined as

$$\hat{X}_{\mathrm{L}}^{(\mathrm{in})} = \frac{1}{\sqrt{2}}(\hat{a}^{(\mathrm{in})\dagger} + \hat{a}^{(\mathrm{in})}), \quad \hat{P}_{\mathrm{L}}^{(\mathrm{in})} = \frac{\mathrm{i}}{\sqrt{2}}(\hat{a}^{(\mathrm{in})\dagger} - \hat{a}^{(\mathrm{in})}), \tag{E.0.9}$$

and the cavity quadratures as

$$\hat{X}_{\mathrm{c}} = \frac{1}{\sqrt{2}}(\hat{c}^{\dagger} + \hat{c}), \quad \hat{P}_{\mathrm{c}} = \frac{\mathrm{i}}{\sqrt{2}}(\hat{c}^{\dagger} - \hat{c}). \tag{E.0.10}$$

Plugging the expression from above in the equation for the outgoing light quadratures, we obtain

$$\hat{X}_{L}^{(\mathrm{out})}(\omega) = -\kappa\eta\xi_{-}(\omega)\hat{P}_{\mathrm{L}}^{(\mathrm{in})} + (1 - \kappa\eta\xi_{+}(\omega))\hat{X}_{\mathrm{L}}^{(\mathrm{in})} - \eta\kappa\mathcal{R}_{-}(\omega)g_0\alpha_L\hat{X}_{\mathrm{m}}(\omega), \tag{E.0.11}$$

$$\hat{P}_{L}^{(\mathrm{out})}(\omega) = \kappa\eta\xi_{-}(\omega)\hat{X}_{\mathrm{L}}^{(\mathrm{in})} + (1 - \kappa\eta\xi_{+}(\omega))\hat{P}_{\mathrm{L}}^{(\mathrm{in})} - \eta\kappa\mathcal{R}_{+}(\omega)g_0\alpha_L\hat{X}_{\mathrm{m}}(\omega), \tag{E.0.12}$$

where we defined

$$\xi_{+}(\omega) = \frac{\chi_{\mathrm{c}}(\omega) + \chi_{\mathrm{c}}^{*}(-\omega)}{2}, \tag{E.0.13}$$

$$\xi_{-}(\omega) = \mathrm{i}\frac{\chi_{\mathrm{c}}(\omega) - \chi_{\mathrm{c}}^{*}(-\omega)}{2}, \tag{E.0.14}$$

$$\mathcal{R}_{+}(\omega) = \left(\chi_{\mathrm{c}}(0)\chi_{\mathrm{c}}(\omega) + \chi_{\mathrm{c}}^{*}(0)\chi_{\mathrm{c}}^{*}(-\omega)\right), \tag{E.0.15}$$

$$\mathcal{R}_{-}(\omega) = \mathrm{i}\left(\chi_{\mathrm{c}}(0)\chi_{\mathrm{c}}(\omega) - \chi_{\mathrm{c}}^{*}(0)\chi_{\mathrm{c}}^{*}(-\omega)\right). \tag{E.0.16}$$

The mechanical quadrature can be rewritten in the frequency domain as

$$\hat{X}_{\mathrm{m}}(\omega) = \chi_{\mathrm{m,eff}}(\omega)\left[\eta\kappa\alpha_L g_0\left(\mathcal{R}_{+}(\omega)\hat{X}_{\mathrm{L}}^{(\mathrm{in})} + \mathcal{R}_{-}(\omega)\hat{P}_{\mathrm{L}}^{(\mathrm{in})}\right) + \sqrt{2\gamma_{\mathrm{m}}}\hat{P}_{\mathrm{th}}\right], \tag{E.0.17}$$

where the effective susceptibility is given by

$$\chi_{\mathrm{m,eff}}(\omega)^{-1} = \frac{1}{\Omega_{\mathrm{m}}}\left(\Omega_{\mathrm{m}}^2 - \omega^2 - \mathrm{i}\gamma_{\mathrm{m}}\omega - 4|g|^2\Omega_{\mathrm{m}}\xi_{-}(\omega)\right). \tag{E.0.18}$$

The homodyne detection signal is given by [65]

$$\hat{D}(\omega) = \sqrt{2}\alpha_{\mathrm{LO}}\sqrt{\eta_{\mathrm{det}}}\left(\cos(\phi)\hat{X}_L^{(\mathrm{out})}(\omega) + \sin(\phi)\hat{P}_L^{(\mathrm{out})}(\omega)\right), \tag{E.0.19}$$

where ϕ is the homodyne angle that allows us to adjust the detected light quadrature. Expressing $\hat{D}(\omega)$ in terms of the input light quadratures and the thermal drive of the membrane, we obtain

$$\begin{aligned}\frac{\hat{D}(\omega)}{\sqrt{2}\alpha_{\mathrm{LO}}\sqrt{\eta_{\mathrm{det}}}} = \hat{X}_L^{(\mathrm{in})}\Big[&\cos(\phi) - \kappa\eta\left(\cos(\phi)\xi_+(\omega) - \sin(\phi)\xi_-(\omega)\right)\\ &- (\kappa\eta\alpha_L g_0)^2\chi_{\mathrm{m}}(\omega)\left(\cos(\phi)\mathcal{R}_-(\omega)\mathcal{R}_+(\omega) + \sin(\phi)\mathcal{R}_+(\omega)^2\right)\Big]\\ +\hat{P}_L^{(\mathrm{in})}\Big[&\sin(\phi) - \kappa\eta\left(\cos(\phi)\xi_-(\omega) + \sin(\phi)\xi_+(\omega)\right)\\ &- (\kappa\eta\alpha_L g_0)^2\chi_{\mathrm{m}}(\omega)\left(\cos(\phi)\mathcal{R}_-(\omega)^2 + \sin(\phi)\mathcal{R}_-(\omega)\mathcal{R}_+(\omega)\right)\Big]\\ +\hat{P}_{\mathrm{th}}\Big[&\eta\kappa\alpha_L g_0\sqrt{2\gamma_{\mathrm{m}}}\chi_{\mathrm{m}}\left(\cos(\phi)\mathcal{R}_-(\omega) + \sin(\phi)\mathcal{R}_+(\omega)\right)\Big].\end{aligned} \tag{E.0.20}$$

As it is written here, the output light depends on the input noise of the light and the thermal noise of the membrane. The correlators of the stochastic noise terms are given by

$$\langle\hat{X}_L^{(\mathrm{in})}(\omega)\hat{X}_L^{(\mathrm{in})}(\omega')\rangle = \langle\hat{P}_L^{(\mathrm{in})}(\omega)\hat{P}_L^{(\mathrm{in})}(\omega')\rangle = \frac{1}{2}\delta(\omega+\omega'), \tag{E.0.21}$$

$$\langle\hat{X}_L^{(\mathrm{in})}(\omega)\hat{P}_L^{(\mathrm{in})}(\omega')\rangle = -\langle\hat{P}_L^{(\mathrm{in})}(\omega)\hat{X}_L^{(\mathrm{in})}(\omega')\rangle = \frac{\mathrm{i}}{2}\delta(\omega+\omega'), \tag{E.0.22}$$

$$\langle\hat{P}_{\mathrm{th}}^{(\mathrm{in})}(\omega)\hat{P}_{\mathrm{th}}^{(\mathrm{in})}(\omega')\rangle = \left(\bar{n}_{\mathrm{th}} + \frac{1}{2}\right)\delta(\omega+\omega'), \tag{E.0.23}$$

while the thermal noise and the optical input noise do not correlate. We can write this expression as $\hat{D}(\omega) = A(\omega)\hat{X}_L^{(\mathrm{in})} + B(\omega)\hat{P}_L^{(\mathrm{in})} + C(\omega)\hat{P}_{\mathrm{th}}$. The symmetrised power spectral density of the detected field is then given by

$$\bar{S}_{DD}(\omega) = |A(\omega)|^2\bar{S}_{XX}^{(\mathrm{in})} + |B(\omega)|^2\bar{S}_{PP}^{(\mathrm{in})} + |C(\omega)|^2\bar{S}_{PP}^{(\mathrm{th})}. \tag{E.0.24}$$

where the individual noise power spectral densities are given by

$$\bar{S}_{XX}^{(\mathrm{in})} = \bar{S}_{PP}^{(\mathrm{in})} = \frac{1}{2} \qquad \text{and} \qquad \bar{S}_{PP}^{(\mathrm{th})} = n_{\mathrm{th}} + \frac{1}{2}. \tag{E.0.25}$$

This equation is used to fit the data in figure 3.3.5.

Resonantly Driven Cavity: In order to gain a intuitive understanding of this term, we consider the resonantly driven cavity. If the cavity is resonant, this equation simplifies significantly to

$$\begin{aligned}\frac{\hat{D}(\omega)}{\sqrt{2}\alpha_{\mathrm{LO}}\sqrt{\eta_{\mathrm{det}}}} = \hat{X}_L^{(\mathrm{in})}\Big[&\cos(\phi)(1 - \kappa\eta\xi_+(\omega)) - (\kappa\eta\alpha_L g_0)^2\chi_{\mathrm{m}}(\omega)\sin(\phi)\mathcal{R}_+(\omega)^2\Big]\\ +\hat{P}_L^{(\mathrm{in})}\Big[&\sin(\phi)(1 - \kappa\eta\xi_+(\omega))\Big]\\ +\hat{P}_{\mathrm{th}}\Big[&\eta\kappa\alpha_L g_0\sqrt{2\gamma_{\mathrm{m}}}\chi_{\mathrm{m}}(\omega)\sin(\phi)\mathcal{R}_+(\omega)\Big].\end{aligned} \tag{E.0.26}$$

which can be re-expressed as

$$\begin{aligned}\frac{\hat{D}(\omega)}{\sqrt{2}\alpha_{\mathrm{LO}}\sqrt{\eta_{\mathrm{det}}}} =& \hat{X}_L^{(\mathrm{in})}\left[(1-\chi_{\mathrm{c}}(\omega)\kappa\eta)\cos(\phi)+4g_{\mathrm{om}}^2\kappa\eta\chi_{\mathrm{m}}(\omega)\chi_{\mathrm{c}}^2(\omega)\sin(\phi)\right]\\ &+\hat{P}_L^{(\mathrm{in})}\left[(1-\chi_{\mathrm{c}}(\omega)\kappa\eta)\sin(\phi)\right]\\ &+\hat{P}_{\mathrm{th}}\left[2g_{\mathrm{om}}\sqrt{\kappa\eta}\chi_{\mathrm{m}}(\omega)\chi_{\mathrm{c}}(\omega)\sqrt{2\gamma_{\mathrm{m}}}\sin(\phi)\right].\end{aligned} \tag{E.0.27}$$

For a cavity with a very large linewidth $\kappa \gg \Omega_m$ around the membrane resonance $\Omega_m/\omega \simeq 1$, one can write $|\chi_c|^2 \to 4/\kappa^2$. Using this, we can calculate a very simple expression for the symmetrised power spectral density. Here, we apply the Lorentzian approximation and evaluate the power spectral density at $\omega \approx \Omega_m$ to get

$$\begin{aligned}\frac{\bar{S}_{DD}}{2|\alpha_{\mathrm{LO}}|^2\eta_{\mathrm{det}}} =& \frac{1}{2}-(1-\eta)\eta\left(\frac{\kappa}{2}\right)^2|\chi_{\mathrm{c}}(\omega)|^2\\ &+\sin(\phi)\cos(\phi)4g_{\mathrm{om}}^2\eta\kappa|\chi_{\mathrm{m}}(\omega)|^2|\chi_{\mathrm{c}}(\omega)|^4\\ &\quad\cdot\left[\gamma_{\mathrm{m}}\kappa(1-\eta)(\Delta_{\mathrm{c}}-\omega)+2\left((2\eta-1)\left(\frac{\kappa}{2}\right)^2+(\Delta-\omega)^2\right)(\omega-\Omega_{\mathrm{m}})\right]\\ &+\sin^2(\phi)8g_{\mathrm{om}}^4\kappa^2\eta^2|\chi_{\mathrm{m}}(\omega)|^2|\chi_{\mathrm{c}}(\omega)|^4\\ &+\sin^2(\phi)8\gamma_{\mathrm{m,th}}g_{\mathrm{om}}^2\kappa\eta|\chi_{\mathrm{m}}(\omega)|^2|\chi_{\mathrm{c}}(\omega)|^2.\end{aligned} \tag{E.0.28}$$

If we neglect the losses $\eta = 1$, this simplifies to

$$\begin{aligned}\frac{\bar{S}_{DD}}{2|\alpha_{\mathrm{LO}}|^2\eta_{\mathrm{det}}} =& \frac{1}{2}\\ &+8g_{\mathrm{om}}^2\kappa|\chi_{\mathrm{m}}(\omega)|^2|\chi_{\mathrm{c}}(\omega)|^2(\omega-\Omega_{\mathrm{m}})\sin(\phi)\cos(\phi)\\ &+8g_{\mathrm{om}}^4\kappa^2|\chi_{\mathrm{m}}(\omega)|^2|\chi_{\mathrm{c}}(\omega)|^4\sin^2(\phi)\\ &+8\gamma_{\mathrm{m,th}}g_{\mathrm{om}}^2\kappa|\chi_{\mathrm{m}}(\omega)|^2|\chi_{\mathrm{c}}(\omega)|^2\sin^2(\phi).\end{aligned} \tag{E.0.29}$$

If we further assume that the cavity linewidth is large, $\kappa \gg \omega$, we can simplify $\kappa|\chi_{\mathrm{c}}(\omega)| \to 2$ and get

$$\frac{\bar{S}_{DD}}{2|\alpha_{\mathrm{LO}}|^2\eta_{\mathrm{det}}} = \frac{1}{2}+8\Gamma_{\mathrm{m}}|\chi_{\mathrm{m}}(\omega)|^2\Big[(\omega-\Omega_{\mathrm{m}})\sin(\phi)\cos(\phi)+(\Gamma_{\mathrm{m}}+\gamma_{\mathrm{m,th}})\sin^2(\phi)\Big]. \tag{E.0.30}$$

This is the formula given in equation (3.3.1).

Appendix F

Simulation of the Spin-Membrane Dynamics for the Beam-Splitter Interaction

The simulation of the coupled spin-membrane dynamic is described. For this we closely follow the algorithm presented in [171]. The following appendix is published as appendix of [30].

In this appendix, we provide some details on the simulation method we used to solve the stochastic equations of motion equations (5.5.1) and (5.5.1) (and similarly of equation (4.2.36) and (4.2.37)) for the spin-membrane system. This simulation follows closely the algorithm presented in [171]. For the simulation, we rewrite the equations of motion as four coupled first-order differential equations for $\tilde{X}_j$ and $\tilde{P}_j$, with $j \in (\mathrm{m}, \mathrm{s})$ in a frame rotating at the membrane frequency Ω_m (operators in the rotating frame are denoted with a tilde) and apply the rotating wave approximation (RWA). In the limit where the propagation delay is small compared to other timescales involved in the coupled dynamics (i.e. $\tau \ll \gamma_j^{-1}, g^{-1}, \delta^{-1}$), the change of the oscillator quadratures during the time τ can be neglected in the rotating frame i.e. $\tilde{X}_j(t) \approx \tilde{X}_j(t-\tau)$ and $\tilde{P}_j(t) \approx \tilde{P}_j(t-\tau)$. The equations of motion then read

$$\frac{\mathrm{d}}{\mathrm{d}t}\begin{pmatrix} \tilde{X}_\mathrm{m}(t) \\ \tilde{P}_\mathrm{m}(t) \\ \tilde{X}_\mathrm{s}(t) \\ \tilde{P}_\mathrm{s}(t) \end{pmatrix} = -\mathbf{M}\begin{pmatrix} \tilde{X}_\mathrm{m}(t) \\ \tilde{P}_\mathrm{m}((t) \\ \tilde{X}_\mathrm{s}(t) \\ \tilde{P}_\mathrm{s}(t) \end{pmatrix} + \begin{pmatrix} -\sin\left(\Omega_\mathrm{m}(t)\right)\mathcal{F}_\mathrm{m}(t) \\ \cos\left(\Omega_\mathrm{m}(t)\right)\mathcal{F}_\mathrm{m}(t) \\ -\sin\left(\Omega_\mathrm{m}(t)\right)\mathcal{F}_\mathrm{s}(t) \\ \cos\left(\Omega_\mathrm{m}(t)\right)\mathcal{F}_\mathrm{s}(t) \end{pmatrix}, \tag{F.0.1}$$

where we have split the dynamics into the 4×4 dynamical matrix

$$\mathbf{M} = \begin{pmatrix} \gamma_\mathrm{m}/2 & 0 & -g\sin\left(\Omega_\mathrm{m}\tau\right) & -g\cos\left(\Omega_\mathrm{m}\tau\right) \\ 0 & \gamma_\mathrm{m}/2 & g\cos\left(\Omega_\mathrm{m}\tau\right) & -g\sin\left(\Omega_\mathrm{m}\tau\right) \\ -g\sin\left(\Omega_\mathrm{m}\tau\right) & -g\cos\left(\Omega_\mathrm{m}\tau\right) & \gamma_\mathrm{s}/2 & -\delta \\ g\cos\left(\Omega_\mathrm{m}\tau\right) & -g\sin\left(\Omega_\mathrm{m}\tau\right) & \delta & \gamma_\mathrm{s}/2 \end{pmatrix}, \tag{F.0.2}$$

and a stochastic part, given by the generalized noise forces $\mathcal{F}_j(t) = \sqrt{2\gamma_j}F_j^{(\mathrm{tot})}(t)$. The total force noise $\mathcal{F}_j^{(\mathrm{tot})}(t)$ includes the thermal noise $F_j^{(\mathrm{th})}(t)$ and the backaction noise $F_j^{(\mathrm{ba})}(t)$ which itself depends on the optical vacuum noise $F_j^{(\mathrm{in})}(t)$. Thus, it is given by

$$F_j^{(\mathrm{tot})}(t) = F_j^{(\mathrm{th})}(t) + F_j^{(\mathrm{ba})}(t) = F_j^{(\mathrm{th})}(t) + \sqrt{\frac{2\Gamma_j}{\gamma_j}}F_j^{(\mathrm{in})}(t), \tag{F.0.3}$$

where Γ_j is the measurement rate of the individual system. The noise terms $F_j^{(\nu)}(t)$, $\nu \in (\mathrm{th}, \mathrm{in})$ can be expressed explicitly in terms of the product of a noise amplitude and a zero mean, delta correlated noise $f_j^{(\nu)}(t)$

$$F_j^{(\mathrm{th})}(t) = \sqrt{\bar{n}_{j,\mathrm{bath}} + \frac{1}{2}}f_j^{(\mathrm{th})}(t), \tag{F.0.4}$$

$$F_{\mathrm{m}}^{(\mathrm{in})}(t) = \sqrt{\frac{\eta^2}{2}}f_{\mathrm{m}}^{(\mathrm{in})}(t), \tag{F.0.5}$$

$$F_{\mathrm{s}}^{(\mathrm{in})}(t) = \sqrt{\frac{1-\eta^4}{2}}f_{\mathrm{s}}^{(\mathrm{in})}(t), \tag{F.0.6}$$

where $\eta^2 \approx 0.8$ is the power transmission coefficient of the light between the spin and the membrane and $\bar{n}_{j,\mathrm{bath}}$ is the number of thermal phonons in the individual system. The thermal noise amplitude is calculated from the fluctuation dissipation theorem while for the derivation of the backaction noise we refer to [37]. The number of thermal phonons of the membrane $\bar{n}_{\mathrm{m,bath}}$ is measured by homodyne detection in presence of all laser beams but without loading the atoms. This calibrated value agrees very well with an estimation from comparing the spectral linewidth in presence of the cooling and coupling beams with the spectral linewidth of the uncooled membrane and the calculated room temperature occupation of the membrane. We assume the spin pumping to be perfect such that the spin oscillator environment is in its quantum mechanical ground state (i.e. $\bar{n}_{\mathrm{s,bath}} = 0$).

The approach given in [171] allows for an exact simulation of the stochastic dynamics for a single oscillator for arbitrary time steps, which we extend to the case of two coupled oscillators with delay. This is done by calculating for each time step the coherent evolution and the noise separately:

$$\begin{pmatrix} \tilde{X}_{\mathrm{m}}(t_{i+1}) \\ \tilde{P}_{\mathrm{m}}(t_{i+1}) \\ \tilde{X}_{\mathrm{s}}(t_{i+1}) \\ \tilde{P}_{\mathrm{s}}(t_{i+1}) \end{pmatrix} = \mathrm{e}^{-\mathbf{M}\Delta t} \begin{pmatrix} \tilde{X}_{\mathrm{m}}(t_i) \\ \tilde{P}_{\mathrm{m}}(t_i) \\ \tilde{X}_{\mathrm{s}}(t_i) \\ \tilde{P}_{\mathrm{s}}(t_i) \end{pmatrix} + \begin{pmatrix} \Delta\tilde{X}_{\mathrm{m}}^{t_i\to t_{i+1}} \\ \Delta\tilde{P}_{\mathrm{m}}^{t_i\to t_{i+1}} \\ \Delta\tilde{X}_{\mathrm{s}}^{t_i\to t_{i+1}} \\ \Delta\tilde{P}_{\mathrm{s}}^{t_i\to t_{i+1}} \end{pmatrix}, \tag{F.0.7}$$

where $\Delta t = t_{i+1} - t_i$ is one simulation time step, and $\Delta\tilde{X}_j^{t_i\to t_{i+1}}$, $\Delta\tilde{P}_j^{t_i\to t_{i+1}}$ are terms for the stochastic noise which enters the system in between time t_i and t_{i+1}. We performed the simulation at time steps comparable to the oscillation period Ω_{m}^{-1}. Thus, the noise terms $\Delta\tilde{X}_j^{t_i\to t_{i+1}}$ and $\Delta\tilde{P}_j^{t_i\to t_{i+1}}$ are correlated which is taken into account by following the calculation of noise variances and covariances in [171]. Because the coupling between the two oscillators is much slower than the simulation time step $g \ll \Omega_{\mathrm{m}} \approx \Delta t^{-1}$ we neglect the correlation of noise building up between the oscillators during one simulation step. Thus, we can treat the noise of both oscillators separately. In order to simulate the system more efficiently, we perform the simulation in time steps of multiples of one frame rotation $\Delta t = k \cdot 2\pi/\Omega_{\mathrm{m}}$, $k = 1, 2, 3...$ such that the noise amplitudes [proportional to $\sin(\Omega_{\mathrm{m}}t), \cos(\Omega_{\mathrm{m}}t)$, see equation (F.0.1)] are

the same for each step of the simulation. This way, the noise amplitude have only to be calculated once, while the stochastic term has to be sampled for every single step.

Appendix G

Coupling Dynamics for an Arbitrary Loop Phase

In chapter 4 the light-mediated coupling between the spin and the membrane with a loop phase $\phi = \pi$ and a small propagation delay is discussed. In this appendix the coupling is generalised for an arbitrary loop phase and larger propagation delays. These new coupling regimes could be implemented in our experiment in the future.

Part of this appendix is copied from [37], but is restated here for completeness.

In section 4.2.1 the theory of remotely coupled systems mediated by a travelling light field is introduced (which is given in [37]). Here, we use this theory to derive the propagator and the equations of motion of the membrane and spin system coupled with arbitrary loop phase and loop delay. The dynamics shown in chapter 4 is then one special case of the dynamics presented in this appendix.

G.1 Coupling Hamiltonian

In a first step, the propagator of the coupled system is derived for an arbitrary loop phase. Assuming that the light interacts in a loop first with the spin, then with the membrane and finally after adding a loop-phase ϕ again with the spin, the interaction operators can be defined as $\hat{B}_1 = \mathrm{i}\hat{X}_\mathrm{s}$, $\hat{B}_2 = \hat{X}_\mathrm{m}$ and $\hat{B}_3 = \mathrm{i}\exp(\mathrm{i}\phi)\hat{X}_\mathrm{s}$ (where the $\hat{B}_j$ are defined in equation (4.2.1) and the interaction Hamiltonians for the spin-light interaction and the membrane-light interaction are introduced in section 4.2.2). Furthermore, we assume that the propagation delay is much smaller than any dynamics of the oscillator other than the oscillation period (i.e. $\tau \ll \gamma_j^{-1}, g^{-1}, |\delta|^{-1}$), so that we can use equation (4.2.25) to account for the propagation delay. The propagator of the system can be written as

$$\begin{aligned}\hat{A} =& \mathrm{i}g\left(\mathrm{e}^{\mathrm{i}\phi}\cos(\Omega_\mathrm{s}\tau_\mathrm{ms})\hat{X}_\mathrm{s}\hat{X}_\mathrm{m} + \mathrm{e}^{\mathrm{i}\phi}\sin(\Omega_\mathrm{s}\tau_\mathrm{ms})\hat{P}_\mathrm{s}\hat{X}_\mathrm{m} - \cos(\Omega_\mathrm{m}\tau_\mathrm{sm})\hat{X}_\mathrm{s}\hat{X}_\mathrm{m} - \sin(\Omega_\mathrm{m}\tau_\mathrm{sm})\hat{X}_\mathrm{s}\hat{P}_\mathrm{m}\right) \\ &+ 2\Gamma_\mathrm{s}\left(\eta^2\mathrm{e}^{-\mathrm{i}\phi}\cos(\Omega_\mathrm{s}\tau_\mathrm{ss})\hat{X}_\mathrm{s}^2 + \eta^2\mathrm{e}^{-\mathrm{i}\phi}\sin(\Omega_\mathrm{s}\tau_\mathrm{ss})\hat{X}_\mathrm{s}\hat{P}_\mathrm{s} + \hat{X}_\mathrm{s}^2\right) + \Gamma_\mathrm{m}\hat{X}_\mathrm{m}^2, \end{aligned} \tag{G.1.1}$$

where the coupling rate is given as $g = \eta\sqrt{\Gamma_\mathrm{s}\Gamma_\mathrm{m}}$. We assume that the optical transmission on both paths (spin-membrane and membrane-spin) is given by η. The propagation delay from the spin to the membrane is given by τ_sm, from the membrane to the spin by τ_ms and to complete the full loop by $\tau_\mathrm{ss} = \tau_\mathrm{sm} + \tau_\mathrm{ms}$. From the propagator, the Hamiltonian of the system can be calculated. We obtain

$$\begin{aligned}\hat{H}_\mathrm{int} =&\hbar\frac{g}{2}\left(\left(\cos(\Omega_\mathrm{s}\tau_\mathrm{ms})\cos(\phi) - \cos(\Omega_\mathrm{m}\tau_\mathrm{sm})\right)\hat{X}_\mathrm{s}\hat{X}_\mathrm{m} + \sin(\Omega_\mathrm{s}\tau_\mathrm{ms})\cos(\phi)\hat{P}_\mathrm{s}\hat{X}_\mathrm{m} - \sin(\Omega_\mathrm{m}\tau_\mathrm{sm})\hat{X}_\mathrm{s}\hat{P}_\mathrm{m}\right)\\ &- \hbar\Gamma_\mathrm{s}\eta^2\sin(\phi)\left(\cos(\Omega_\mathrm{s}\tau_\mathrm{ss})\hat{X}_\mathrm{s}^2 + \sin(\Omega_\mathrm{s}\tau_\mathrm{ss})\hat{X}_\mathrm{s}P_\mathrm{s}\right).\end{aligned} \tag{G.1.2}$$

For the dissipator of the system, we get

$$\begin{aligned}\Lambda_\mathrm{eff} =& -2g\sin(\phi)\cos(\Omega_\mathrm{s}\tau_\mathrm{ms})\hat{X}_\mathrm{s}X_\mathrm{m} - 2g\sin(\phi)\sin(\Omega_\mathrm{s}\tau_\mathrm{ms})\hat{P}_\mathrm{s}X_\mathrm{m}\\ &+ 4\Gamma_\mathrm{s}\left(\eta^2\cos(\phi)\cos(\Omega_\mathrm{s}\tau_\mathrm{ss}) - 1\right)\hat{X}_\mathrm{s}^2 + 4\Gamma_\mathrm{s}\eta^2\cos(\phi)\sin(\Omega_\mathrm{s}\tau_\mathrm{ss})\hat{X}_\mathrm{s}\hat{P}_\mathrm{s} + 2\Gamma_\mathrm{m}\hat{X}_\mathrm{m}^2.\end{aligned} \tag{G.1.3}$$

G.2 Equations of Motion in Cascaded Systems

Before we derive the equations of motion for our coupled systems, we briefly review the equations of motion for a general cascaded system, given in [37]. If we have a looped, cascaded system, the dynamics of the systems can be described by the Hamiltonian given in equation (4.2.1). From this Hamiltonian, the equation of motion of the operators of one of the systems can be calculated [37]

$$\dot{\hat{b}}_i = \mathcal{L}_0\hat{b}_i - \mathrm{i}\sum_{j=1}^{n}\sqrt{2\Gamma_j}\left([\hat{b}_i, \hat{B}_j^\dagger]\hat{a}(\xi_j) + \hat{a}^\dagger(\xi_j)[\hat{b}_i, \hat{B}_j]\right), \tag{G.2.1}$$

where the Liouvillian $\mathcal{L}_0 b_i$ captures all the internal dynamics of the system i. The light at a given position ξ in the loop is given by [37]

$$\hat{a}(\xi, t) = \hat{a}_\mathrm{in}(\xi, t) - \mathrm{i}\sum_{j=1}^{n}\sqrt{2\Gamma_j}\hat{B}_j(t - (\xi - \xi_j)/c)\Theta(\xi - \xi_j), \tag{G.2.2}$$

where Θ is the Heaviside step function defined by $\Theta(x) = 1$ for $x > 0$, $\Theta(x) = 0$ for $x < 0$, and $\Theta(0) = 1/2$. Including this into the equation of motion of the system annihilation operator, we get [37]

$$\begin{aligned}\dot{\hat{b}}_i =&\mathcal{L}_0\hat{b}_i - \mathrm{i}\sum_{j=1}^{n}\sqrt{2\Gamma_j}\left([\hat{b}_i, \hat{B}_j^\dagger]\hat{a}_\mathrm{in}(\xi_j) + \hat{a}_\mathrm{in}^\dagger(\xi_j)[\hat{b}_i, \hat{B}_j]\right)\\ &- \sum_{j=1}^{n}\sum_{k\le j}\sqrt{4\Gamma_j\Gamma_k}\Theta(\xi_j - \xi_k)\left([\hat{b}_i, \hat{B}_j^\dagger(t)]\hat{B}_k(t - \tau_{jk}) - \hat{B}_k^\dagger(t - \tau_{jk})[\hat{b}_i, \hat{B}_j]\right),\end{aligned} \tag{G.2.3}$$

where $\tau_{jk} = (\xi_j - \xi_k)/c$ is the propagation delay of the optical field going from interaction j to interaction k. In this equation, the first line describes the internal dynamics of the system and the driving by the input light while the second line describes the mediated interactions between different systems coupled to the light and the light-mediated self-interaction.

G.3 Loop on the Spin System

We assume that we have two systems, a membrane and a spin. We interact with the spin two times while there is only one interaction with the membrane, as described in chapter 4. However, unlike chapter 4, we derive the dynamics for an arbitrary loop phase ϕ. The interaction operators with the light are given by $\hat{B}_1 = \mathrm{i}\hat{X}_\mathrm{s}$, $\hat{B}_2 = \hat{X}_\mathrm{m}$ and $\hat{B}_3 = \mathrm{i}\exp(\mathrm{i}\phi)\hat{X}_\mathrm{s}$ [29] (where the $\hat{B}_j$ are defined in equation (4.2.1) and the interaction Hamiltonians for the spin-light interaction and the membrane-light interaction are introduced in section 4.2.2). Calculating the propagation of the system operator, we get

$$\begin{aligned}\dot{\hat{b}}_\mathrm{s} =&\mathcal{L}_0\hat{b}_\mathrm{s} - \sqrt{\Gamma_\mathrm{s}}\left(\hat{a}_\mathrm{in}(\xi_1) - \hat{a}^\dagger_\mathrm{in}(\xi_1) + \mathrm{e}^{-\mathrm{i}\phi}\hat{a}_\mathrm{in}(\xi_3) - \mathrm{e}^{\mathrm{i}\phi}\hat{a}^\dagger_\mathrm{in}(\xi_3)\right)\\ &+ \mathrm{i}2\Gamma_\mathrm{s}\sin(\phi)\sqrt{2}\hat{X}_\mathrm{s}(t-\tau_\mathrm{ss})\\ &- \mathrm{i}\sqrt{4\Gamma_\mathrm{s}\Gamma_\mathrm{m}}\cos(\phi)\sqrt{2}\hat{X}_\mathrm{m}(t-\tau_\mathrm{ms}).\end{aligned} \tag{G.3.1}$$

The first line of this equation describes the internal dynamics of the spin system and the stochastic driving by the probe light. The second line shows the self-interaction of the spin and the third line shows the coupling between the spin and the membrane. The equation of motion for the membrane is similar

$$\begin{aligned}\dot{\hat{b}}_\mathrm{m} =&\mathcal{L}_0\hat{b}_\mathrm{m} - \mathrm{i}\sqrt{\Gamma_\mathrm{m}}\left(\hat{a}^\dagger_\mathrm{in}(\xi_2) + \hat{a}_\mathrm{in}(\xi_2)\right)\\ &- \mathrm{i}\sqrt{4\Gamma_\mathrm{s}\Gamma_\mathrm{m}}\sqrt{2}\hat{X}_\mathrm{s}(t-\tau_\mathrm{sm}),\end{aligned} \tag{G.3.2}$$

except that it does not depend on the loop phase ϕ and there is no self-interaction because the membrane is interfaced only once. For this appendix, we model the local dynamics of the systems as a decaying oscillator, so that

$$\mathcal{L}_0\hat{b}_i = -\mathrm{i}\Omega_i\hat{b}_i - \frac{\gamma_i}{2}\hat{b}_i + \sqrt{\gamma_i}\hat{b}^{(\mathrm{th})}_i, \tag{G.3.3}$$

where the last term is the thermal drive due to the coupling to the environment with $\langle\hat{b}^{(\mathrm{th})\dagger}_i(t)b^{(\mathrm{th})}_i(t')\rangle = \bar{n}_i\delta(t-t')$ and $\langle\hat{b}^{(\mathrm{th})}_i(t)b^{(\mathrm{th})\dagger}_i(t')\rangle = (\bar{n}_i+1)\delta(t-t')$ and $\bar{n}_i$ is the thermal occupation of the environment. Note that the input noise $\hat{b}^{(\mathrm{th})}_i$ has units of $\mathrm{s}^{-1/2}$ while the system annihilation operator $\hat{b}_i$ is unitless.

G.3.1 Dynamics for a Positive Frequency Spin

In order to simplify the equations of motion, we move to a rotating frame at the spin oscillation frequency, i.e. $\hat{b}_i \to \hat{b}_i\exp(-\mathrm{i}\Omega_\mathrm{s}t)$. If the spin is acting as a positive frequency oscillator, we get

$$\begin{aligned}\dot{\hat{b}}_\mathrm{s} =&\sqrt{\Gamma_\mathrm{s}}\mathrm{e}^{-\mathrm{i}\Omega_\mathrm{s}t}\left(\hat{a}_\mathrm{in}(\xi_1)\left[1+\mathrm{e}^{\mathrm{i}(-\phi+\Omega_\mathrm{s}\tau_\mathrm{ss})}\right] - \hat{a}^\dagger_\mathrm{in}(\xi_1)\left[1+\mathrm{e}^{\mathrm{i}(\phi+\Omega_\mathrm{s}\tau_\mathrm{ss})}\right]\right) + \sqrt{\gamma_\mathrm{s}}\hat{b}^{(\mathrm{th})}_\mathrm{s}\\ &- \frac{\gamma_\mathrm{s}}{2}\hat{b}_\mathrm{s} + \mathrm{i}\mathrm{e}^{\mathrm{i}\Omega_\mathrm{s}\tau_\mathrm{ss}}\sin(\phi)2\Gamma_\mathrm{s}\hat{b}_\mathrm{s} - \mathrm{i}\mathrm{e}^{\mathrm{i}\Omega_\mathrm{s}\tau_\mathrm{ms}}\cos(\phi)\sqrt{4\Gamma_\mathrm{s}\Gamma_\mathrm{m}}\hat{b}_\mathrm{m},\end{aligned} \tag{G.3.4}$$

$$\begin{aligned}\dot{\hat{b}}_\mathrm{m} =&\mathrm{i}\sqrt{\Gamma_\mathrm{m}}\mathrm{e}^{-\mathrm{i}\Omega_\mathrm{s}t}\left(\hat{a}_\mathrm{in}(\xi_2) + \hat{a}^\dagger_\mathrm{in}(\xi_2)\right) + \sqrt{\gamma_\mathrm{m}}\hat{b}^{(\mathrm{th})}_\mathrm{m}\\ &+ \mathrm{i}\delta\hat{b}_\mathrm{m} - \frac{\gamma_\mathrm{m}}{2}\hat{b}_\mathrm{m} - \mathrm{i}\mathrm{e}^{\mathrm{i}\Omega_\mathrm{s}\tau_\mathrm{sm}}\sqrt{4\Gamma_\mathrm{s}\Gamma_\mathrm{m}}\hat{b}_\mathrm{s},\end{aligned} \tag{G.3.5}$$

where $\delta = \Omega_\mathrm{s} - \Omega_\mathrm{m}$ is the detuning between the two systems. The fast rotating terms are neglected. In both equations of motion, the first line is the stochastic drive due to the backaction of the light and the coupling to the environment while the second line describes the mean dynamics of the system.

Loop Phase of $\phi = \pi$ and no Loop Delay: The backaction of the spin can be cancelled if the loop phase is set to $\phi = \pi$ and there is no loop delay. The equation of motion is then given by

$$\dot{\hat{b}}_{\mathrm{s}} = -\frac{\gamma_{\mathrm{s}}}{2}\hat{b}_{\mathrm{s}} + \sqrt{\gamma_{\mathrm{s}}}\hat{b}_{\mathrm{s}}^{(\mathrm{th})} + \mathrm{i}\sqrt{4\Gamma_{\mathrm{s}}\Gamma_{\mathrm{m}}}\hat{b}_{\mathrm{m}}, \tag{G.3.6}$$

$$\begin{aligned}\dot{\hat{b}}_{\mathrm{m}} =& \mathrm{i}\sqrt{\Gamma_{\mathrm{m}}}\mathrm{e}^{-\mathrm{i}\Omega_{\mathrm{s}}t}\left(\hat{a}_{\mathrm{in}}(\xi_2) + \hat{a}_{\mathrm{in}}^{\dagger}(\xi_2)\right) + \sqrt{\gamma_{\mathrm{m}}}\hat{b}_{\mathrm{m}}^{(\mathrm{th})} \\ &+ \mathrm{i}\delta\hat{b}_{\mathrm{m}} - \frac{\gamma_{\mathrm{m}}}{2}\hat{b}_{\mathrm{m}} - \mathrm{i}\sqrt{4\Gamma_{\mathrm{s}}\Gamma_{\mathrm{m}}}\hat{b}_{\mathrm{s}}.\end{aligned} \tag{G.3.7}$$

This case is discussed in depth in chapter 4.

Loop Phase of $\phi = 0$ and Loop Delay of $\Omega_{\mathrm{s}}\tau_{\mathrm{ss}} = \pi$: Alternatively, the backaction on the spin can be cancelled by setting a phase of $\phi = 0$ but engineering a loop delay of $\Omega_{\mathrm{s}}\tau_{\mathrm{ss}} = \pi$. In this way the spin oscillator precesses by half a period in the time it takes the light to pass through the loop, and therefore the two interactions with the light interfere destructively. We get

$$\dot{\hat{b}}_{\mathrm{s}} = -\frac{\gamma_{\mathrm{s}}}{2}\hat{b}_{\mathrm{s}} + \sqrt{\gamma_{\mathrm{s}}}\hat{b}_{\mathrm{s}}^{(\mathrm{th})} - \mathrm{i}\mathrm{e}^{\mathrm{i}\Omega_{\mathrm{s}}\tau_{\mathrm{ms}}}\sqrt{4\Gamma_{\mathrm{s}}\Gamma_{\mathrm{m}}}\hat{b}_{\mathrm{m}}, \tag{G.3.8}$$

$$\begin{aligned}\dot{\hat{b}}_{\mathrm{m}} =& \mathrm{i}\sqrt{\Gamma_{\mathrm{m}}}\mathrm{e}^{-\mathrm{i}\Omega_{\mathrm{s}}t}\left(\hat{a}_{\mathrm{in}}(\xi_2) + \hat{a}_{\mathrm{in}}^{\dagger}(\xi_2)\right) + \sqrt{\gamma_{\mathrm{m}}}\hat{b}_{\mathrm{m}}^{(\mathrm{th})} \\ &+ \mathrm{i}\delta\hat{b}_{\mathrm{m}} - \frac{\gamma_{\mathrm{m}}}{2}\hat{b}_{\mathrm{m}} - \mathrm{i}\mathrm{e}^{\mathrm{i}(\pi-\Omega_{\mathrm{s}}\tau_{\mathrm{ms}})}\sqrt{4\Gamma_{\mathrm{s}}\Gamma_{\mathrm{m}}}\hat{b}_{\mathrm{s}}.\end{aligned} \tag{G.3.9}$$

If the delay is mainly implemented on one of the paths, then this interaction is the same as the interaction for a loop phase of $\phi = \pi$ and without delay $\tau_{\mathrm{ss}} = 0$. But if the delay is on both the spin-membrane and the membrane-spin paths, then the complex phase of the interaction term changes. For example, if the delay is engineered to be on both paths equally $\Omega_{\mathrm{s}}\tau_{\mathrm{ms}} = \Omega_{\mathrm{s}}\tau_{\mathrm{sm}} = \pi/2$, we get

$$\dot{\hat{b}}_{\mathrm{s}} = -\frac{\gamma_{\mathrm{s}}}{2}\hat{b}_{\mathrm{s}} + \sqrt{\gamma_{\mathrm{s}}}\hat{b}_{\mathrm{s}}^{(\mathrm{th})} + g\hat{b}_{\mathrm{m}}, \tag{G.3.10}$$

$$\begin{aligned}\dot{\hat{b}}_{\mathrm{m}} =& \mathrm{i}\sqrt{\Gamma_{\mathrm{m}}}\mathrm{e}^{-\mathrm{i}\Omega_{\mathrm{s}}t}\left(\hat{a}_{\mathrm{in}}(\xi_2) + \hat{a}_{\mathrm{in}}^{\dagger}(\xi_2)\right) + \sqrt{\gamma_{\mathrm{m}}}\hat{b}_{\mathrm{m}}^{(\mathrm{th})} \\ &+ \mathrm{i}\delta\hat{b}_{\mathrm{m}} - \frac{\gamma_{\mathrm{m}}}{2}\hat{b}_{\mathrm{m}} + g\hat{b}_{\mathrm{s}}.\end{aligned} \tag{G.3.11}$$

which is a self-amplification of the systems.

Dissipative Isolator for Loop Phase of $\phi = \pi/2$ and Loop Delay of $\Omega_{\mathrm{s}}\tau_{\mathrm{sm}} = \pi/2$: In our system, the dynamics of a *dissipative isolator* [178] can be obtained if we consider a loop phase of $\phi = \pi/2$ and a loop delay of $\Omega_{\mathrm{s}}\tau_{\mathrm{sm}} = \pi/2$. The dynamics reads

$$\dot{\hat{b}}_{\mathrm{s}} = -\frac{\gamma_{\mathrm{s}}}{2}\hat{b}_{\mathrm{s}} + \sqrt{\gamma_{\mathrm{s}}}\hat{b}_{\mathrm{s}}^{(\mathrm{th})} + \mathrm{i}2\Gamma_{\mathrm{s}}\hat{b}_{\mathrm{s}}(t-\tau_{\mathrm{ss}}) - \mathrm{i}\sqrt{2\Gamma_{\mathrm{s}}}(\hat{P}_{\mathrm{in}}(\xi_1) - \hat{X}_{\mathrm{in}}(\xi_3)), \tag{G.3.12}$$

$$\dot{\hat{b}}_{\mathrm{m}} = -\frac{\gamma_{\mathrm{m}}}{2}\hat{b}_{\mathrm{m}} + \sqrt{\gamma_{\mathrm{m}}}\hat{b}_{\mathrm{m}}^{(\mathrm{th})} + g\hat{b}_{\mathrm{s}} - \mathrm{i}\sqrt{2\Gamma_{\mathrm{m}}}\hat{X}_{\mathrm{in}}(\xi_2) \tag{G.3.13}$$

where we have used that $\hat{b}_{\mathrm{m}}(t-\tau_{\mathrm{ms}}) = \hat{b}_{\mathrm{m}}(t)\mathrm{e}^{\mathrm{i}\Omega_{\mathrm{m}}\tau_{\mathrm{ms}}}$. The reservoir of the spin-oscillator can be engineered by tuning the propagation delay τ_{ss}. As such, a common driving force of spin and membrane can be

implemented. If the second spin-light interaction is blocked, we obtain

$$\dot{\hat{b}}_{\mathrm{s}} = -\frac{\gamma_{\mathrm{s}}}{2}\hat{b}_{\mathrm{s}} + \sqrt{\gamma_{\mathrm{s}}}\hat{b}_{\mathrm{s}}^{(\mathrm{th})} - \mathrm{i}\sqrt{2\Gamma_{\mathrm{s}}}\hat{P}_{\mathrm{in}}(\xi_1), \tag{G.3.14}$$

$$\dot{\hat{b}}_{\mathrm{m}} = -\frac{\gamma_{\mathrm{m}}}{2}\hat{b}_{\mathrm{m}} + \sqrt{\gamma_{\mathrm{m}}}\hat{b}_{\mathrm{m}}^{(\mathrm{th})} + g\hat{b}_{\mathrm{s}} - \mathrm{i}\sqrt{2\Gamma_{\mathrm{m}}}\hat{X}_{\mathrm{in}}(\xi_2). \tag{G.3.15}$$

If the linewidths γ_i and the measurement rates Γ_i of the individual systems are matched, we obtain the dynamics that is very close to the one given in [178], equation (31) with $J = \mathrm{i}\Gamma/2$. But having a second spin interaction opens some interesting possibilities: By changing the loop delay $\Omega_{\mathrm{s}}\tau_{\mathrm{ss}}$, different forms of self-interaction of the spin can be engineered $\mathrm{i}2\Gamma_{\mathrm{s}}\hat{b}_{\mathrm{s}}(t-\tau_{\mathrm{ss}}) \to \mathrm{i}2\Gamma_{\mathrm{s}}\hat{b}_{\mathrm{s}}\mathrm{e}^{\mathrm{i}\Omega_{\mathrm{s}}\tau_{\mathrm{ss}}}$.

G.3.2 Dynamics for a Negative Frequency Spin

We repeat the calculations presented in the last section for a negative frequency spin-oscillator: Again we go to a rotating frame at the spin oscillation frequency, i.e. $\hat{b}_i \to \hat{b}_i \exp(-\mathrm{i}\Omega_{\mathrm{s}}t)$. If the spin is a negative frequency oscillator, we get

$$\begin{aligned}\dot{\hat{b}}_{\mathrm{s}} =& \sqrt{\Gamma_{\mathrm{s}}}\mathrm{e}^{-\mathrm{i}\Omega_{\mathrm{s}}t}\left(\hat{a}_{\mathrm{in}}(\xi_1)\left[1+\mathrm{e}^{\mathrm{i}(-\phi+\Omega_{\mathrm{s}}\tau_{\mathrm{ss}})}\right] - \hat{a}_{\mathrm{in}}^{\dagger}(\xi_1)\left[1+\mathrm{e}^{\mathrm{i}(\phi+\Omega_{\mathrm{s}}\tau_{\mathrm{ss}})}\right]\right) + \sqrt{\gamma_{\mathrm{s}}}\hat{b}_{\mathrm{s}}^{(\mathrm{th})} \\ &- \frac{\gamma_{\mathrm{s}}}{2}\hat{b}_{\mathrm{s}} + \mathrm{i}\mathrm{e}^{\mathrm{i}\Omega_{\mathrm{s}}\tau_{\mathrm{ss}}}\sin(\phi)2\Gamma_{\mathrm{s}}\hat{b}_{\mathrm{s}} - \mathrm{i}\mathrm{e}^{\mathrm{i}\Omega_{\mathrm{s}}\tau_{\mathrm{ms}}}\cos(\phi)\sqrt{4\Gamma_{\mathrm{s}}\Gamma_{\mathrm{m}}}\hat{b}_{\mathrm{m}}^{\dagger}, \end{aligned}\tag{G.3.16}$$

$$\begin{aligned}\dot{\hat{b}}_{\mathrm{m}} =& \sqrt{\Gamma_{\mathrm{m}}}\mathrm{e}^{-\mathrm{i}\Omega_{\mathrm{s}}t}\left(\hat{a}_{\mathrm{in}}(\xi_2) + \hat{a}_{\mathrm{in}}^{\dagger}(\xi_2)\right) + \sqrt{\gamma_{\mathrm{m}}}\hat{b}_{\mathrm{m}}^{(\mathrm{th})} \\ &+ \mathrm{i}\delta\hat{b}_{\mathrm{m}} - \frac{\gamma_{\mathrm{m}}}{2}\hat{b}_{\mathrm{m}} - \mathrm{i}\mathrm{e}^{\mathrm{i}\Omega_{\mathrm{s}}\tau_{\mathrm{sm}}}\sqrt{4\Gamma_{\mathrm{s}}\Gamma_{\mathrm{m}}}\hat{b}_{\mathrm{s}}^{\dagger}, \end{aligned}\tag{G.3.17}$$

where $\delta = |\Omega_{\mathrm{s}}| - \Omega_{\mathrm{m}}$ is the detuning between the two systems. The fast rotating terms are neglected.

Directional Phase-Preserving Quantum Amplifier: In order to implement a *directional phase-preserving quantum amplifier* [178], the loop phase is set to $\phi = \pi/2$, the delay on the the path from the spin to the membrane is set to $\Omega_{\mathrm{s}}\tau_{\mathrm{sm}} = \pi/2$ and the propagation delay on the path from the membrane to the spin is small such that we approximate $\Omega_{\mathrm{s}}\tau_{\mathrm{ss}} = \pi/2$. Furthermore, we assume that the oscillators are resonant, $\delta = 0$, and convert the input noise to the rotating frame at Ω_{s}

$$\dot{\hat{b}}_{\mathrm{s}} = \sqrt{2\Gamma_{\mathrm{s}}}\left(\mathrm{i}\hat{P}_{\mathrm{in}}(\xi_1) + \hat{X}_{\mathrm{in}}(\xi_1)\right) + \sqrt{\gamma_{\mathrm{s}}}\hat{b}_{\mathrm{s}}^{(\mathrm{th})} - \frac{\gamma_{\mathrm{s}}}{2}\hat{b}_{\mathrm{s}} - 2\Gamma_{\mathrm{s}}\hat{b}_{\mathrm{s}}, \tag{G.3.18}$$

$$\dot{\hat{b}}_{\mathrm{m}} = \sqrt{2\Gamma_{\mathrm{m}}}\hat{X}_{\mathrm{in}}(\xi_2) + \sqrt{\gamma_{\mathrm{m}}}\hat{b}_{\mathrm{m}}^{(\mathrm{th})} - \frac{\gamma_{\mathrm{m}}}{2}\hat{b}_{\mathrm{m}} + g\hat{b}_{\mathrm{s}}^{\dagger}. \tag{G.3.19}$$

These equations are very close to the equations of motions given in [178] for a *directional phase-preserving quantum amplifier*, only that the linewidths of the oscillators must be matched.

Appendix H

Optical Coherent Feedback on a Spin-Oscillator

The looped cascaded setup can be used mediate a spin self-interaction. A one-axis twisting Hamiltonian can be engineered by feeding back the outgoing light field after a first interaction with a spin-oscillator to the spin-oscillator. In between the two interaction we can modify the light by adding a propagation delay and a loop phase. For a one-axis twisting Hamiltonian the loop phase between the two interactions has to be modulated at twice the oscillator frequency. In this appendix the dynamics of the spin system in such a feedback loop is derived.

We assume a single (spin) oscillator that is coupled twice to the light. The general coupling theory given in [37] and introduced in section 4.1 is applied. Between the two interactions, the light is modified by adding a loop phase ϕ and delayed by τ. In this scenario the interaction operators are given by $\hat{B}_1(t) = \mathrm{i}\hat{X}(t)$ and $\hat{B}_2(t) = \mathrm{i}e^{\mathrm{i}\phi}\hat{X}(t)$ (see section 4.2.1 for details).

H.1 Derivation of the Susceptibility of the Oscillator

Feeding back the optical signal of an oscillator to the oscillator itself can change the damping rate and the resonance frequency of the oscillator [37, 65]. In order to quantify this effect, we derive the susceptibility of the oscillator when interfaced twice. The first step is to calculate the field operators at the coordinates of the interaction. For that, the parameters and operators $\hat{B}_{1,2}$ are substituted into the equation G.2.2. The light operator is given by

$$\hat{a}(\xi_1, t) = \hat{a}_{\mathrm{in}}(\xi_1, t) + \sqrt{\frac{\Gamma}{2}}\hat{X}(t) \tag{H.1.1}$$

at the first interaction coordinate ξ_1 and

$$\hat{a}(\xi_2, t) = \hat{a}_{\mathrm{in}}(\xi_2, t) + \sqrt{2\Gamma}\hat{X}(t-\tau) + \sqrt{\frac{\Gamma}{2}}e^{i\phi}\hat{X}(t) \tag{H.1.2}$$

at the second interaction coordinate ξ_2. Here we have defined the round trip time $\tau = (\xi_2 - \xi_1)/c$. These operators are inserted into the equations of motion for the system quadratures $\hat{X}(t)$ and $\hat{P}(t)$. Since $\hat{X}(t)$ commutes with itself, the propagation of $\hat{X}(t)$ is given by the system dynamics

$$\dot{\hat{X}}(t) = \mathcal{L}_0\hat{X}(t) = \Omega\hat{P}(t) - \frac{\gamma}{2}\hat{X}(t) + \sqrt{\gamma}\hat{X}^{(\mathrm{th})}(t) \tag{H.1.3}$$

where $\hat{X}^{(\mathrm{th})}$ is the stochastic drive from the thermal environment. The light interacts with the P-quadrature, so this is more developed. It reads

$$\dot{\hat{P}}(t) = \mathcal{L}_0\hat{P}(t) - \mathrm{i}\sum_{j=1,2}\sqrt{\Gamma_j}([\hat{P}(t), \hat{B}_j^\dagger(t)]\hat{a}(\xi_j, t) + \hat{a}^\dagger(\xi_j, t)[\hat{P}(t), \hat{B}_j(t)]). \tag{H.1.4}$$

As for the X-quadrature, the local dynamics is given by $\mathcal{L}_0\hat{P} = -\Omega\hat{X} - \frac{\gamma}{2}\hat{P} + \sqrt{\gamma}\hat{P}^{(\mathrm{th})}$. The equation of motion of the P-quadrature can be simplified to

$$\dot{\hat{P}}(t) = -\Omega\hat{X}(t) - \frac{\gamma}{2}\hat{P}(t) + 4\Gamma\sin(\phi)\hat{X}(t-\tau) + \sqrt{\gamma}\hat{P}^{(\mathrm{th})} + \mathrm{i}\sqrt{2\Gamma}\hat{F}_L(t) \tag{H.1.5}$$

where we have assumed the same measurement rates for both interactions $\Gamma_i = \Gamma$ and we have defined the optical force on the system by

$$\hat{F}_L(t) = \hat{a}_{\mathrm{in}}(\xi_1, t) - \hat{a}_{\mathrm{in}}^\dagger(\xi_1, t) + e^{-\mathrm{i}\phi}\hat{a}_{\mathrm{in}}(\xi_2, t) - e^{\mathrm{i}\phi}\hat{a}_{\mathrm{in}}^\dagger(\xi_2, t) \tag{H.1.6}$$

$$= \hat{a}_{\mathrm{in}}(\xi_2 - \tau c, t) - \hat{a}_{\mathrm{in}}^\dagger(\xi_2 - \tau c, t) + e^{-\mathrm{i}\phi}\hat{a}_{\mathrm{in}}(\xi_2, t) - e^{\mathrm{i}\phi}\hat{a}_{\mathrm{in}}^\dagger(\xi_2, t). \tag{H.1.7}$$

We want to solve this system of two coupled equations. In order to do this, it is easier to transform the equations into the frequency domain. We obtain

$$-\mathrm{i}\omega\hat{X}(\omega) = \Omega\hat{P}(\omega) - \frac{\gamma}{2}\hat{X}(\omega) + \sqrt{\gamma}\hat{X}^{(\mathrm{th})}(\omega), \tag{H.1.8}$$

$$-\mathrm{i}\omega\hat{P}(\omega) = -\Omega\hat{X}(\omega) - \frac{\gamma}{2}\hat{P}(\omega) + 4\Gamma\sin(\phi)e^{\mathrm{i}\omega\tau}\hat{X}(\omega) + \sqrt{\gamma}\hat{P}^{(\mathrm{th})}(\omega) + \mathrm{i}\sqrt{2\Gamma}\hat{F}_L(\omega), \tag{H.1.9}$$

with

$$\hat{F}_L(\omega) = \hat{a}_{\mathrm{in}}(\omega)(e^{\mathrm{i}\omega\tau} + e^{-\mathrm{i}\phi}) - \hat{a}_{\mathrm{in}}^\dagger(\omega)(e^{\mathrm{i}\omega\tau} + e^{\mathrm{i}\phi}). \tag{H.1.10}$$

Solving this system of equations for $X(\omega)$, we get

$$\hat{X}(\omega) = \mathrm{i}\frac{\Omega}{\Omega^2 - \omega^2 + (\gamma/2)^2 - \mathrm{i}\omega\gamma - 4\Omega\Gamma\sin(\phi)e^{\mathrm{i}\omega\tau}}\sqrt{2\Gamma}\hat{F}_L(\omega). \tag{H.1.11}$$

This is again a Lorentzian peak with a modified damping rate and a shifted resonance frequency. The frequency shift is given by

$$\delta\Omega = -2\Gamma\sin(\phi)\cos(\Omega\tau), \tag{H.1.12}$$

and the change in damping rate by

$$\delta\gamma = -4\Gamma\sin(\phi)\sin(\Omega\tau). \tag{H.1.13}$$

Depending on the delay and phase, this can lead to a broadening or narrowing of the oscillator.

H.2 Derivation of the Effective Hamiltonian and Dissipator

The effective dynamics of the spin is fully described by the propagation operator $\hat{A}$, which is defined in [37] equations (12) and (13). Here, we have two interactions with the light field $\hat{B}_1 = \mathrm{i}\hat{X}$ and $\hat{B}_2 = \mathrm{i}\hat{X}\exp(\mathrm{i}\phi)$, both with the same coupling strength $g_1 = g_2 = \sqrt{2\Gamma}$. Inserting this into the general equation given in [37], we get

$$\hat{A} = 2\Gamma\left(\mathrm{e}^{-\mathrm{i}\phi}\tilde{X}(t)\tilde{X}(t-\tau) + \tilde{X}(t)\tilde{X}(t)\right). \tag{H.2.1}$$

First we look at the Hamiltonian part of this propagation. The effective Hamiltonian is proportional to the imaginary part of $\hat{A}$. It is given by

$$\hat{H}_{\mathrm{eff}} = \frac{\hbar}{2\mathrm{i}}(\hat{A} - \hat{A}^\dagger) = -\mathrm{i}\hbar\Gamma\left(\mathrm{e}^{-\mathrm{i}\phi}\tilde{X}(t)\tilde{X}(t-\tau) - \mathrm{e}^{\mathrm{i}\phi}\tilde{X}(t-\tau)\tilde{X}(t)\right) \tag{H.2.2}$$

and the dissipative part by

$$\hat{\Lambda}_{\mathrm{eff}} = \hat{A} + \hat{A}^\dagger = 2\Gamma\left(\mathrm{e}^{-\mathrm{i}\phi}\tilde{X}(t)\tilde{X}(t-\tau) + 2\tilde{X}(t)^2 + \mathrm{e}^{\mathrm{i}\phi}\tilde{X}(t-\tau)\tilde{X}(t)\right). \tag{H.2.3}$$

In the interaction picture, the propagation of the operators is split into two parts. The quadrature operator can be written in terms of the ladder operators in the Schrödinger picture with their evolution, namely

$$\tilde{X}(t) = \frac{1}{\sqrt{2}}\left(\hat{b}\mathrm{e}^{-\mathrm{i}\Omega t} + \hat{b}^\dagger\mathrm{e}^{\mathrm{i}\Omega t}\right)\mathrm{e}^{-\gamma t/2}. \tag{H.2.4}$$

Here we have included both local Hamiltonian dynamics and local decoherence. To write the effective Hamiltonian, only need to include the local Hamiltonian dynamics, not the decoherence part. The effective Hamiltonian is

$$\begin{aligned}\hat{H}_{\mathrm{eff}} =& -\frac{\mathrm{i}\hbar\Gamma}{2}\big[\mathrm{e}^{-\mathrm{i}\phi}\left(\hat{b}\hat{b}\mathrm{e}^{-\mathrm{i}2\Omega t}\mathrm{e}^{\mathrm{i}\Omega\tau} + \hat{b}\hat{b}^\dagger\mathrm{e}^{-\mathrm{i}\Omega\tau} + \hat{b}^\dagger\hat{b}\mathrm{e}^{\mathrm{i}\Omega\tau} + \hat{b}^\dagger\hat{b}^\dagger\mathrm{e}^{\mathrm{i}2\Omega t}\mathrm{e}^{-\mathrm{i}\Omega\tau}\right) \\ &- \mathrm{e}^{\mathrm{i}\phi}\left(\hat{b}\hat{b}\mathrm{e}^{-\mathrm{i}2\Omega t}\mathrm{e}^{\mathrm{i}\Omega\tau} + \hat{b}\hat{b}^\dagger\mathrm{e}^{\mathrm{i}\Omega\tau} + \hat{b}^\dagger\hat{b}\mathrm{e}^{-\mathrm{i}\Omega\tau} + \hat{b}^\dagger\hat{b}^\dagger\mathrm{e}^{\mathrm{i}2\Omega t}\mathrm{e}^{-\mathrm{i}\Omega\tau}\right)\big] \qquad \text{(H.2.5)} \\ =& -\hbar\Gamma\big[\sin(\phi)\left(\hat{b}\hat{b}\mathrm{e}^{-\mathrm{i}2\Omega t}\mathrm{e}^{\mathrm{i}\Omega\tau} + \hat{b}^\dagger\hat{b}^\dagger\mathrm{e}^{\mathrm{i}2\Omega t}\mathrm{e}^{-\mathrm{i}\Omega\tau}\right) \\ &+ \sin(\phi+\Omega\tau)\hat{b}\hat{b}^\dagger + \sin(\phi-\Omega\tau)\hat{b}^\dagger\hat{b}\big], \qquad \text{(H.2.6)}\end{aligned}$$

and the dissipative part reads

$$\begin{aligned}\hat{\Lambda}_{\mathrm{eff}} =& 4\Gamma\Big[\cos^2\left(\frac{\phi}{2}\right)\left(\hat{b}\hat{b}\mathrm{e}^{-\mathrm{i}2\Omega t}\mathrm{e}^{\mathrm{i}\Omega\tau} + \hat{b}^\dagger\hat{b}^\dagger\mathrm{e}^{\mathrm{i}2\Omega t}\mathrm{e}^{-\mathrm{i}\Omega\tau}\right) \\ &+ \cos^2\left(\frac{\phi+\Omega\tau}{2}\right)\hat{b}\hat{b}^\dagger + \cos^2\left(\frac{\phi-\Omega\tau}{2}\right)\hat{b}^\dagger\hat{b}\Big]. \end{aligned}\tag{H.2.7}$$

In the following we consider these operators in four different regimes, which we can access by changing the loop phase ϕ and the loop delay τ. In all the each regime we expect a unique coupled dynamics:

Pure Frequency Shift for $\phi = \pi/2$; $\Omega\tau = m \cdot 2\pi$: If the detuning is negligible and we set the phase to $\pi/2$, we can apply the rotating wave approximation (RWA) and rewrite the Hamiltonian and

the dissipation in the form of

$$\hat{H}_{\text{eff}} \approx -\hbar\Gamma(\hat{b}\hat{b}^\dagger + \hat{b}^\dagger\hat{b}) = -\hbar\Gamma(2\hat{b}^\dagger\hat{b} + 1), \tag{H.2.8}$$

$$\hat{\Lambda}_{\text{eff}} \approx 2\Gamma(\hat{b}\hat{b}^\dagger + \hat{b}^\dagger\hat{b}) = 2\Gamma(2\hat{b}^\dagger\hat{b} + 1). \tag{H.2.9}$$

This corresponds to a frequency shift of Γ and an increased damping of the spin system.

Suppress Hamiltonian Dynamics for $\phi = 0$; $\Omega\tau = \pi/2$: If we apply no phase, but only a delay of $\pi/2$, we get the following Hamiltonian and dissipator in the RWA

$$\hat{H}_{\text{eff}} \approx \hbar\Gamma(\hat{b}\hat{b}^\dagger - \hat{b}^\dagger\hat{b}) = \hbar\Gamma, \tag{H.2.10}$$

$$\hat{\Lambda}_{\text{eff}} \approx 2\Gamma(\hat{b}\hat{b}^\dagger + \hat{b}^\dagger\hat{b}) = 2\Gamma(2\hat{b}^\dagger\hat{b} + 1). \tag{H.2.11}$$

In this regime, the Hamiltonian part is just a constant offset that does not change the dynamics.

Parametric-Gain Hamiltonian for $\phi = \pi + \phi_1\cos(2\Omega t)$; $\Omega\tau = m\cdot 2\pi$: More interesting parts of the coupling can be implemented by modulating the phase. Here we assume that the amplitude of the drive ϕ_1 is small, so that we can approximate $\sin(\pi + \phi_1\cos(2\Omega t)) \approx -\phi_1\cos(2\Omega t)$ and $\cos^2((\pi + \phi_1\cos(2\Omega t))/2) \approx \phi_1^2\cos^2(2\Omega t)/4$. Assuming that the delay is negligible, we get

$$\hat{H}_{\text{eff}} \approx \hbar\Gamma\frac{\phi_1}{2}(\hat{b}\hat{b} + \hat{b}^\dagger\hat{b}^\dagger) = \hbar\Gamma\frac{\phi_1}{2}(\hat{X}^2 - \hat{P}^2), \tag{H.2.12}$$

$$\hat{\Lambda}_{\text{eff}} \approx \Gamma\frac{\phi^2}{2}(\hat{b}\hat{b} + \hat{b}^\dagger\hat{b}^\dagger + \hat{b}^\dagger\hat{b} + \hat{b}\hat{b}^\dagger) = \Gamma\phi^2\hat{X}^2. \tag{H.2.13}$$

This Hamiltonian leads to a squeezing of the $(X+P)$-quadrature and an anti-squeezing of the $(X-P)$-quadrature, or vice versa.

Dynamic for a Modulation of the Measurement Rate $\Gamma = \Gamma_1\cos^2(\omega + \varphi)$: Instead of the in-loop phase, we can modulate the measurement rate by modulating the power of the coupling beam. This results in a dynamic governed by

$$\begin{aligned}\hat{A} \approx \frac{\Gamma_1}{4}\Big(&\hat{b}\hat{b}\mathrm{e}^{-2\mathrm{i}\varphi}\left(\mathrm{e}^{-\mathrm{i}\phi+\mathrm{i}\Omega\tau}+1\right) + \hat{b}^\dagger\hat{b}^\dagger\mathrm{e}^{2\mathrm{i}\varphi}\left(\mathrm{e}^{-\mathrm{i}\phi-\mathrm{i}\Omega\tau}+1\right)\\ &+ 2\hat{b}\hat{b}^\dagger\left(\mathrm{e}^{-\mathrm{i}\phi-\mathrm{i}\Omega\tau}+1\right) + 2\hat{b}^\dagger\hat{b}\left(\mathrm{e}^{-\mathrm{i}\phi+\mathrm{i}\Omega\tau}+1\right)\Big).\end{aligned} \tag{H.2.14}$$

This gives a Hamiltonian and a dissipator of

$$\begin{aligned}\hat{H}_{\text{eff}} \approx -\hbar\frac{\Gamma_1}{4}\Big(&\sin(\phi)\left(\hat{b}\hat{b}\mathrm{e}^{-2\mathrm{i}\varphi+\mathrm{i}\Omega\tau} + \hat{b}^\dagger\hat{b}^\dagger\mathrm{e}^{2\mathrm{i}\varphi-\mathrm{i}\Omega\tau}\right)\\ &+ 2\hat{b}\hat{b}^\dagger\sin(\phi+\Omega\tau) + 2\hat{b}^\dagger\hat{b}\sin(\phi-\Omega\tau)\Big),\end{aligned} \tag{H.2.15}$$

$$\begin{aligned}\Lambda_{\text{eff}} \approx -\hbar\frac{\Gamma_1}{2}\Big(&(1+\cos(\phi))\left(\hat{b}\hat{b}\mathrm{e}^{-2\mathrm{i}\varphi+\mathrm{i}\Omega\tau} + \hat{b}^\dagger\hat{b}^\dagger\mathrm{e}^{2\mathrm{i}\varphi-\mathrm{i}\Omega\tau}\right)\\ &+ 2\hat{b}\hat{b}^\dagger(1+\cos(\phi+\Omega\tau)) + 2\hat{b}^\dagger\hat{b}(1+\cos(\phi-\Omega\tau))\Big).\end{aligned} \tag{H.2.16}$$

So we can construct a squeezing Hamiltonian $\propto bb + b^\dagger b^\dagger$ by setting a loop phase of $\phi \neq m\pi\ \forall\ m$. For complete backaction cancellation we need to set $\phi = \pi$. So we have to operate in a regime close to $\phi = \pi$

so that the backaction noise does not dominate, but there is still a squeezing Hamiltonian. For small $\phi_\pi = \phi - \pi$ and if we neglect the delay $\tau = 0$ and set $\varphi = 0$, we get

$$\hat{H}_{\text{eff}} \approx \hbar \frac{\Gamma_1}{4} \phi_\pi \left(\hat{b}\hat{b} + \hat{b}^\dagger \hat{b}^\dagger \ + 2\hat{b}\hat{b}^\dagger + 2\hat{b}^\dagger \hat{b} \right), \tag{H.2.17}$$

$$\hat{\Lambda}_{\text{eff}} \approx -\hbar \frac{\Gamma_1}{2} \phi_\pi^2 \left(\hat{b}\hat{b} + \hat{b}^\dagger \hat{b}^\dagger + 2\hat{b}\hat{b}^\dagger + 2\hat{b}^\dagger \hat{b} \right). \tag{H.2.18}$$

H.3 Calculate Propagation of the Density Operator

Now that we have seen the Hamiltonian and the dissipator of the system, we want to calculate the propagation of the density operator. To do this, we can use the propagator given in [37]

$$\dot{\tilde{\rho}} = -\hat{A}\tilde{\rho} - \tilde{\rho}\hat{A} + \mathcal{J}\tilde{\rho}. \tag{H.3.1}$$

In the last section we already derived an expression for $\hat{A}$ which we recall here as

$$\hat{A} = 2\Gamma \left(e^{-i\phi} \tilde{X}(t) \tilde{X}(t-\tau) + \tilde{X}(t)\tilde{X}(t) \right) \tag{H.3.2}$$

$$\begin{aligned} &= \Gamma \Big(\hat{b}\hat{b} \mathrm{e}^{2\mathrm{i}\Omega t} \left(\mathrm{e}^{-\mathrm{i}\phi} \mathrm{e}^{\mathrm{i}\Omega\tau} + 1 \right) + \hat{b}^\dagger \hat{b}^\dagger \mathrm{e}^{-2\mathrm{i}\Omega t} \left(\mathrm{e}^{-\mathrm{i}\phi} \mathrm{e}^{-\mathrm{i}\Omega\tau} + 1 \right) \\ &\quad + \hat{b}\hat{b}^\dagger \left(\mathrm{e}^{-\mathrm{i}\phi} \mathrm{e}^{-\mathrm{i}\Omega\tau} + 1 \right) + \hat{b}^\dagger \hat{b} \left(\mathrm{e}^{-\mathrm{i}\phi} \mathrm{e}^{\mathrm{i}\Omega\tau} + 1 \right) \Big), \end{aligned} \tag{H.3.3}$$

where we have used the time-dependent form of $\tilde{X}(t) = \left(\hat{b} e^{i\Omega t} + \hat{b}^\dagger e^{-i\Omega t} \right) / \sqrt{2}$. The jump term can be calculated from formula (14) and (15) of [37], which yields

$$\mathcal{J}\tilde{\rho} = 2\Gamma \left(\hat{X}(t-\tau)\tilde{\rho}\hat{X}(t) \mathrm{e}^{-\mathrm{i}\phi} + \hat{X}(t)\tilde{\rho}\hat{X}(t-\tau)\mathrm{e}^{\mathrm{i}\phi} + 2\hat{X}(t)\tilde{\rho}\hat{X}(t) \right) \tag{H.3.4}$$

$$\begin{aligned} &= 2\Gamma \Big(\hat{b}\tilde{\rho}\hat{b} \left(\mathrm{e}^{2\mathrm{i}\Omega t} \left(\mathrm{e}^{\mathrm{i}\Omega\tau} \cos(\phi) + 1 \right) \right) + \hat{b}^\dagger \tilde{\rho} \hat{b}^\dagger \left(\mathrm{e}^{-2\mathrm{i}\Omega t} \left(\mathrm{e}^{-\mathrm{i}\Omega\tau} \cos(\phi) + 1 \right) \right) \\ &\quad + \hat{b}\tilde{\rho}\hat{b}^\dagger \left(\cos(\Omega\tau - \phi) + 1 \right) + \hat{b}^\dagger \tilde{\rho} \hat{b} \left(\cos(\Omega\tau + \phi) + 1 \right) \Big). \end{aligned} \tag{H.3.5}$$

Parametric-Gain Hamiltonian for $\phi = \pi + \phi_1 \cos(2\Omega t)$; $\Omega\tau = m \cdot 2\pi$: We want to consider the case for which we have the most interesting dynamics. If we modulate the phase with $\phi = \pi + \phi_1 \cos(2\Omega t)$ we get $\cos(\phi) \approx -1 + \phi_1^2/4(1 + \cos(4\Omega t))$ and $\exp(-\mathrm{i}\phi) \approx -1 - \mathrm{i}\phi_1 \cos(2\Omega t) + \phi_1^2(1 + \cos(4\Omega t)/4)$ up to the second order. Substituting this into the expressions above and doing the RWA, we get

$$\hat{A} = \frac{\Gamma}{2} \left(-\mathrm{i}\phi_1 (\hat{b}\hat{b} + \hat{b}^\dagger \hat{b}^\dagger) + \frac{\phi_1^2}{2} (\hat{b}\hat{b}^\dagger + \hat{b}^\dagger \hat{b}) \right), \tag{H.3.6}$$

$$\mathcal{J}\tilde{\rho} = \frac{\Gamma}{2} \phi_1^2 \left(\hat{b}\tilde{\rho}\hat{b}^\dagger + \hat{b}^\dagger \tilde{\rho} \hat{b} \right), \tag{H.3.7}$$

which leads to a dynamics of the state of the system described by the equation of motion of the density operator

$$\dot{\tilde{\rho}} = \frac{1}{\mathrm{i}\hbar} [\hat{H}_{\text{eff}}, \tilde{\rho}] + \frac{\Gamma\phi_1^2}{2} \mathcal{D}[\hat{b}]\tilde{\rho} + \frac{\Gamma\phi_1^2}{2} \mathcal{D}[\hat{b}^\dagger]\tilde{\rho}, \tag{H.3.8}$$

where the dissipation superoperator is given by $\mathcal{D}(\hat{J})\rho = \hat{J}\rho\hat{J}^\dagger - (\hat{J}^\dagger\hat{J}\rho + \rho\hat{J}^\dagger\hat{J})/2$ and the effective Hamiltonian by

$$\hat{H}_{\text{eff}} = \frac{\hbar\Gamma}{2}\phi_1(\hat{b}\hat{b} + \hat{b}^\dagger\hat{b}^\dagger) \tag{H.3.9}$$

as derived in the last section.

H.4 Calculate Gaussian Dynamics

In order to calculate the amount of squeezing induced by this interaction, the Gaussian dynamics of the system is calculated. We consider the same interactions with the light field $\hat{B}_1 = \mathrm{i}\hat{X}$ and $\hat{B}_2 = \mathrm{i}\hat{X}\exp(\mathrm{i}\phi)$ as before. Again we assume that both interaction have the same coupling strength $g_1 = g_2 = \sqrt{2\Gamma}$. Here we assume that, we have the transmission (amplitude) η between the interactions. Inserting this into the general equation given in equation 4.2.5 gives us

$$\dot{\tilde{\rho}} = -2\Gamma e^{-i\phi}\eta[\tilde{X}(t), \tilde{X}(t-\tau)\tilde{\rho}] - 2\Gamma[\tilde{X}(t), \tilde{X}(t)\tilde{\rho}] + \text{h.c.} \tag{H.4.1}$$

In the following we convert this expression to the Schrödinger picture and yield

$$\begin{aligned}\dot{\rho} = &-\mathrm{i}\frac{\Omega}{2}\Big([\hat{X}(t), \hat{X}(t)\rho] + [\hat{P}(t), \hat{P}(t)\rho]\Big) - \frac{\gamma(2\bar{n}+1)}{4}\Big([\hat{X}(t), \hat{X}(t)\rho] + [\hat{P}(t), \hat{P}(t)\rho]\Big) \\ &- \frac{\mathrm{i}\gamma}{4}\Big([\hat{X}(t), \hat{P}(t)\rho] - [\hat{P}(t), \hat{X}(t)\rho]\Big) \\ &- 2\Gamma e^{-i\phi}\eta[\hat{X}(t), \hat{X}(t-\tau)\rho] - 2\Gamma[\hat{X}(t), \hat{X}(t)\rho] + \text{h.c.}\end{aligned} \tag{H.4.2}$$

We assume that we can write $\hat{X}(t-\tau) = \hat{X}(t)\cos(\Omega\tau) - \hat{P}(t)\sin(\Omega\tau)$ which holds for high-Q oscillators. Next we write the equation of motion as a function of quadratures in a rotating frame at frequency ω. We get

$$\begin{aligned}\dot{\breve{\rho}} = &-\left(\mathrm{i}\frac{\Omega-\omega}{2} + \frac{\gamma(2\bar{n}+1)}{4}\right)\Big([\hat{X}, \hat{X}\breve{\rho}] + [\hat{P}, \hat{P}\breve{\rho}]\Big) \\ &- \frac{\mathrm{i}\gamma}{4}\Big([\hat{X}, \hat{P}\breve{\rho}] - [\hat{P}, \hat{X}\breve{\rho}]\Big) \\ &- 2\Gamma\left(\eta e^{-\mathrm{i}\phi}\cos(\Omega\tau) + 1\right)\Bigg(\cos^2(\omega t)[\hat{X}, \hat{X}\breve{\rho}] \\ &\quad + \cos(\omega t)\sin(\omega t)\Big([\hat{P}, \hat{X}\breve{\rho}] + [\hat{X}, \hat{P}\breve{\rho}]\Big) + \sin^2(\omega t)[\hat{P}, \hat{P}\breve{\rho}]\Bigg) \\ &+ 2\Gamma\eta e^{-i\phi}\sin(\Omega\tau)\Bigg(\cos^2(\omega t)[\hat{X}, \hat{P}\breve{\rho}] \\ &\quad - \cos(\omega t)\sin(\omega t)\Big([\hat{X}, \hat{X}\breve{\rho}] - [\hat{P}, \hat{P}\breve{\rho}]\Big) - \sin^2(\omega t)[\hat{P}, \hat{X}\breve{\rho}]\Bigg) + \text{h.c.}\end{aligned} \tag{H.4.3}$$

In the following we assume that there is no detuning between the rotating frame and the oscillator frequency, i.e. $\delta = \Omega - \omega = 0$.

Parametric-Gain Hamiltonian for $\phi = \pi + \phi_1\cos(2\omega t)$; $\Omega\tau = m\cdot 2\pi$: Here we assume that the amplitude of the drive ϕ_1 is small so that we can approximate $\exp(\mathrm{i}\pi + \mathrm{i}\phi_1\cos(2\omega t)) \approx -1 + i\phi_1\cos(2\omega t) +$

$\phi_1^2 \cos^2(2\omega t)/2$. Assuming that the delay is negligible, we get

$$\begin{aligned}\dot{\breve{\rho}} =& -\frac{\gamma(2\bar{n}+1)}{4}\left([\hat{X},\hat{X}\breve{\rho}]+[\hat{P},\hat{P}\breve{\rho}]\right)-\frac{\mathrm{i}\gamma}{4}\left([\hat{X},\hat{P}\breve{\rho}]-[\hat{P},\hat{X}\breve{\rho}]\right)\\ &+\eta\frac{\mathrm{i}\phi_1\Gamma}{2}\left([\hat{X},\hat{X}\breve{\rho}]-[\hat{P},\hat{P}\breve{\rho}]\right)-\Gamma\left(1-\eta+\eta\frac{\phi_1^2}{4}\right)\left([\hat{X},\hat{X}\breve{\rho}]+[\hat{P},\hat{P}\breve{\rho}]\right)+\text{h.c.}\end{aligned} \tag{H.4.4}$$

In order to see squeezing, we need to consider a superposition of $\hat{X}$ and $\hat{P}$. Therefore we introduce two rotated quadratures $\hat{X}_\alpha = \hat{X}\cos(\alpha) - \hat{P}\sin(\alpha)$ and $\hat{P}_\alpha = \hat{P}\cos(\alpha) + \hat{X}\sin(\alpha)$. The equation of motion can be written in terms of these new quadratures, namely

$$\begin{aligned}\dot{\breve{\rho}} =& -\left(\frac{\gamma(2\bar{n}+1)}{4}+\Gamma\left(1-\eta+\eta\frac{\phi_1^2}{4}\right)\right)\left([\hat{X}_\alpha,\hat{X}_\alpha\breve{\rho}]+[\hat{P}_\alpha,\hat{P}_\alpha\breve{\rho}]\right)-\frac{\mathrm{i}\gamma}{4}\left([\hat{X}_\alpha,\hat{P}_\alpha\breve{\rho}]-[\hat{P}_\alpha,\hat{X}_\alpha\breve{\rho}]\right)\\ &+\eta\frac{\mathrm{i}\phi_1\Gamma}{2}\Big(\cos(2\alpha)\left([\hat{X}_\alpha,\hat{X}_\alpha\breve{\rho}]-[\hat{P}_\alpha,\hat{P}_\alpha\breve{\rho}]\right)-\sin(2\alpha)\left([\hat{X}_\alpha,\hat{P}_\alpha\breve{\rho}]+[\hat{P}_\alpha,\hat{X}_\alpha\breve{\rho}]\right)\Big)+\text{h.c.}\end{aligned} \tag{H.4.5}$$

From this equation the drift matrix F and the diffusion matrix N can be calculated similarly to section 4.2.4. It turns out that the maximum squeezing can be observed for a linear combination of quadratures with equal weight, for example for $\alpha = \pi/4$. For this angle the matrices are given by

$$F = \begin{pmatrix}-\gamma/2+\eta\Gamma\phi_1 & 0\\ 0 & -\gamma/2-\eta\Gamma\phi_1\end{pmatrix} \tag{H.4.6}$$

and

$$N = \begin{pmatrix}\gamma(\bar{n}+1/2)+2\Gamma(1-\eta+\eta\phi_1^2/4) & 0\\ 0 & \gamma(\bar{n}+1/2)+2\Gamma(1-\eta+\eta\phi_1^2/4)\end{pmatrix}. \tag{H.4.7}$$

From these two matrices the dynamics and the steady state can be calculated. First we consider the steady state and obtain

$$\langle\hat{X}^2_{\pi/4}\rangle_{\text{ss}} - \langle\hat{X}_{\pi/4}\rangle^2_{\text{ss}} = \frac{\gamma(\bar{n}+1/2)+2\Gamma((1-\eta)+\eta\phi_1^2/4)}{\gamma-\eta 2\Gamma\phi_1}, \tag{H.4.8}$$

$$\langle\hat{P}^2_{\pi/4}\rangle_{\text{ss}} - \langle\hat{P}_{\pi/4}\rangle^2_{\text{ss}} = \frac{\gamma(\bar{n}+1/2)+2\Gamma((1-\eta)+\eta\phi_1^2)/4}{\gamma+\eta 2\Gamma\phi_1}. \tag{H.4.9}$$

In the case where the damping is dominated by spontaneous scattering we can assume that $n = 0$ and $\gamma = 2\Gamma/C$ where C is the cooperativity. For the squeezed quadrature we get

$$\langle\hat{P}^2_{\pi/4}\rangle_{\text{ss}} - \langle\hat{P}_{\pi/4}\rangle^2_{\text{ss}} = \frac{1+2C((1-\eta)+\eta\phi_1^2/4)}{2(1+\eta C\phi_1)}. \tag{H.4.10}$$

We can define a squeezing parameter as

$$\xi^2 = \frac{\langle\hat{P}^2_{\pi/4}\rangle_{\text{ss}}}{\langle\hat{P}_0^2\rangle} = \frac{1+2C((1-\eta)+\eta\phi_1^2/4)}{1+\eta C\phi_1} \tag{H.4.11}$$

and minimise it with respect to the modulation amplitude ϕ_1

$$\xi^2_{\text{min}} = \frac{\sqrt{1+2\eta C(1+2C(1-\eta))}-1}{\eta C}. \tag{H.4.12}$$

We see that the loss actually strictly limits the maximum steady state squeezing achievable, even for arbitrarily large cooperativity

$$\lim_{C\to\infty} \xi^2_{\min} = 2\sqrt{\frac{1-\eta}{\eta}}. \tag{H.4.13}$$

This might be a challenge for actual implementation, because to have squeezing one needs a loop transmission of $\eta > 4/5$.

Bibliography

[1] Antonio Acín, Immanuel Bloch, Harry Buhrman, Tommaso Calarco, Christopher Eichler, Jens Eisert, Daniel Esteve, Nicolas Gisin, Steffen J. Glaser, Fedor Jelezko, Stefan Kuhr, Maciej Lewenstein, Max F. Riedel, Piet O. Schmidt, Rob Thew, Andreas Wallraff, Ian Walmsley, and Frank K. Wilhelm. "The quantum technologies roadmap: a European community view". In: *New Journal of Physics* 20.8 (Aug. 2018), p. 080201. DOI: 10.1088/1367-2630/aad1ea (cit. on p. 1).

[2] Koji Azuma, Sophia E. Economou, David Elkouss, Paul Hilaire, Liang Jiang, Hoi-Kwong Lo, and Ilan Tzitrin. "Quantum repeaters: From quantum networks to the quantum internet". In: *Reviews of Modern Physics* 95.4 (Dec. 2023), p. 045006. DOI: 10.1103/revmodphys.95.045006 (cit. on p. 1).

[3] Shi-Hai Wei, Bo Jing, Xue-Ying Zhang, Jin-Yu Liao, Chen-Zhi Yuan, Bo-Yu Fan, Chen Lyu, Dian-Li Zhou, You Wang, Guang-Wei Deng, Hai-Zhi Song, Daniel Oblak, Guang-Can Guo, and Qiang Zhou. "Towards Real-World Quantum Networks: A Review". In: *Photonics Reviews* 16.3 (Jan. 2022). DOI: 10.1002/lpor.202100219 (cit. on p. 1).

[4] Jared Rovny, Sarang Gopalakrishnan, Ania C. Bleszynski Jayich, Patrick Maletinsky, Eugene Demler, and Nathalie P. de Leon. "New opportunities in condensed matter physics for nanoscale quantum sensors". In: *arXiv* (2024). arXiv: 2403.13710 [cond-mat.mes-hall] (cit. on p. 1).

[5] Jundi Li, Wei Quan, Binquan Zhou, Zhuo Wang, Jixi Lu, Zhaohui Hu, Gang Liu, and Jiancheng Fang. "SERF Atomic Magnetometer–Recent Advances and Applications: A Review". In: *IEEE Sensors Journal* 18.20 (Oct. 2018), pp. 8198–8207. DOI: 10.1109/jsen.2018.2863707 (cit. on p. 1).

[6] Shao-Yang Dai, Fa-Song Zheng, Kun Liu, Wei-Liang Chen, Yi-Ge Lin, Tian-Chu Li, and Fang Fang. "Cold atom clocks and their applications in precision measurements". In: *Chinese Physics B* 30.1 (Jan. 2021), p. 013701. DOI: 10.1088/1674-1056/abbbee (cit. on p. 1).

[7] Andrew A. Gewirth and John R. LaGraff. "Atomic Force Microscopy". In: *The Handbook of Surface Imaging and Visualization*. Ed. by Arthur T. Hubbard. CRC Press, Mar. 2022, pp. 23–31. DOI: 10.1201/9780367811815-2 (cit. on p. 1).

[8] Adrian Bachtold, Joel Moser, and Mark I. Dykman. "Mesoscopic physics of nanomechanical systems". In: *Reviews of Modern Physics* 94.4 (Dec. 2022), p. 045005. DOI: 10.1103/revmodphys.94.045005 (cit. on p. 1).

[9] Gershon Kurizki, Patrice Bertet, Yuimaru Kubo, Klaus Mølmer, David Petrosyan, Peter Rabl, and Jörg Schmiedmayer. "Quantum technologies with hybrid systems". In: *Proceedings of the National Academy of Sciences* 112.13 (Mar. 2015), pp. 3866–3873. DOI: 10.1073/pnas.1419326112 (cit. on pp. 1, 147).

[10] Donghun Lee, Kenneth W. Lee, Jeffrey V. Cady, Preeti Ovartchaiyapong, and Ania C. Bleszynski Jayich. "Topical review: spins and mechanics in diamond". In: *Journal of Optics* 19.3 (Feb. 2017), p. 033001. DOI: 10.1088/2040-8986/aa52cd (cit. on pp. 1, 148).

[11] Philipp Treutlein, Claudiu Genes, Klemens Hammerer, Martino Poggio, and Peter Rabl. "Hybrid Mechanical Systems". In: *Cavity Optomechanics: Nano- and Micromechanical Resonators Interacting with Light*. Ed. by Markus Aspelmeyer, Tobias J. Kippenberg, and Florian Marquardt. Berlin, Heidelberg: Springer Berlin Heidelberg, 2014, pp. 327–351. DOI: 10.1007/978-3-642-55312-7_14 (cit. on pp. 1, 2, 147).

[12] Shabir Barzanjeh, André Xuereb, Simon Gröblacher, Mauro Paternostro, Cindy A. Regal, and Eva M. Weig. "Optomechanics for quantum technologies". In: *Nature Physics* 18.1 (Dec. 2021), pp. 15–24. DOI: 10.1038/s41567-021-01402-0 (cit. on pp. 1, 4).

[13] Klemens Hammerer, Anders S. Sørensen, and Eugene S. Polzik. "Quantum interface between light and atomic ensembles". In: *Reviews of Modern Physics* 82 (2 Apr. 2010), pp. 1041–1093. DOI: 10.1103/RevModPhys.82.1041 (cit. on pp. 1, 2, 4, 36, 37, 41, 42, 44, 69, 148–150, 189, 204).

[14] Olivier Arcizet, V. Jacques, A. Siria, P. Poncharal, P. Vincent, and Signes Seidelin. "A single nitrogen-vacancy defect coupled to a nanomechanical oscillator". In: *Nature Physics* 7.11 (Nov. 2011), pp. 879–883. DOI: 10.1038/nphys2070 (cit. on pp. 1, 2, 148).

[15] Jean Teissier, Arne Barfuss, Patrick Appel, Elke Neu, and Patrick Maletinsky. "Strain Coupling of a Nitrogen-Vacancy Center Spin to a Diamond Mechanical Oscillator". In: *Physical Review Letters* 113.2 (July 2014), p. 020503. DOI: 10.1103/physrevlett.113.020503 (cit. on pp. 1, 2).

[16] Preeti Ovartchaiyapong, Kenneth W. Lee, Bryan A. Myers, and Ania C. Bleszynski Jayich. "Dynamic strain-mediated coupling of a single diamond spin to a mechanical resonator". In: *Nature Communications* 5.1 (July 2014). DOI: 10.1038/ncomms5429 (cit. on pp. 1, 2).

[17] Arne Barfuss, Jean Teissier, Elke Neu, Andreas Nunnenkamp, and Patrick Maletinsky. "Strong mechanical driving of a single electron spin". In: *Nature Physics* 11.10 (Oct. 2015), pp. 820–824. DOI: 10.1038/nphys3411 (cit. on pp. 1, 2, 148).

[18] Inah Yeo, Pierre-Louise de Assis, Arnaud Gloppe, Eva Dupont-Ferrier, Pierre Verlot, Nitin S. Malik, Emmanuel Dupuy, Julien Claudon, Jean-Michel Gérard, Alexia Auffèves, Gilles Nogues, Signes Seidelin, Jean-Philippe Poizat, Olivier Arcizet, and Maxime Richard. "Strain-mediated coupling in a quantum dot–mechanical oscillator hybrid system". In: *Nature Nanotechnology* 9.2 (Dec. 2013), pp. 106–110. DOI: 10.1038/nnano.2013.274 (cit. on pp. 1, 2, 148).

[19] Michele Montinaro, Gunter Wüst, Mathieu Munsch, Yannik Fontana, Eleonora Russo-Averchi, Martin Heiss, Anna Fontcuberta i Morral, Richard J. Warburton, and Martino Poggio. "Quantum Dot Opto-Mechanics in a Fully Self-Assembled Nanowire". In: *Nano Letters* 14.8 (Aug. 2014), pp. 4454–4460. DOI: 10.1021/nl501413t (cit. on pp. 1, 2, 148).

[20] Aaron D. O'Connell, Max Hofheinz, Markus Ansmann, Radoslaw C. Bialczak, Mike Lenander, Erik Lucero, Matthew Neeley, Daniel Sank, H. Wang, Martin Weides, J. Wenner, John M. Martinis, and Andrew N. Cleland. "Quantum ground state and single-phonon control of a mechanical resonator". In: *Nature* 464.7289 (Apr. 2010), pp. 697–703. DOI: 10.1038/nature08967 (cit. on pp. 2, 148).

[21] Juha-Matti Pirkkalainen, S. U. Cho, Jian Li, Gheorghe S. Paraoanu, Pertti J. Hakonen, and Mika A. Sillanpää. "Hybrid circuit cavity quantum electrodynamics with a micromechanical resonator". In: *Nature* 494.7436 (Feb. 2013), pp. 211–215. DOI: 10.1038/nature11821 (cit. on p. 2).

[22] Jeremie J. Viennot, Xizheng Ma, and Konrad W. Lehnert. "Phonon-Number-Sensitive Electromechanics". In: *Physical Review Letters* 121.18 (Oct. 2018), p. 183601. DOI: 10.1103/physrevlett.121.183601 (cit. on p. 2).

[23] David Hunger, Stephan Camerer, Maria Korppi, Andreas Jöckel, Theodor W. Hänsch, and Philipp Treutlein. "Coupling ultracold atoms to mechanical oscillators". In: *Comptes Rendus Physique* 12.9-10 (Dec. 2011), pp. 871–887. DOI: 10.1016/j.crhy.2011.04.015 (cit. on p. 2).

[24] Ying-Ju Wang, Matthew Eardley, Svenja Knappe, John Moreland, Leo Hollberg, and John Kitching. "Magnetic Resonance in an Atomic Vapor Excited by a Mechanical Resonator". In: *Physical Review Letters* 97.22 (Dec. 2006), p. 227602. DOI: 10.1103/physrevlett.97.227602 (cit. on p. 2).

[25] Stephan Camerer, Maria Korppi, Andreas Jöckel, David Hunger, Theodor W. Hänsch, and Philipp Treutlein. "Realization of an optomechanical interface between ultracold atoms and a membrane". In: *Physical Review. Letters* 107.22 (Nov. 2011), p. 223001. DOI: 10.1103/PhysRevLett.107.223001 (cit. on pp. 2, 3, 148).

[26] Maria Korppi, Andreas Jöckel, Matthew T. Rakher, Stephan Camerer, David Hunger, Theodor W. Hänsch, and Philipp Treutlein. "Hybrid atom-membrane optomechanics". In: *EPJ Web of Conferences* 57 (2013). Ed. by O. Dulieu, P. Grangier, M. Leduc, and H. Perrin, p. 03006. DOI: 10.1051/epjconf/20135703006 (cit. on pp. 2, 3).

[27] Andreas Jöckel, Aline Faber, Tobias Kampschulte, Maria Korppi, Matthew T. Rakher, and Philipp Treutlein. "Sympathetic cooling of a membrane oscillator in a hybrid mechanical–atomic system". In: *Nature Nanotechnol.* 10.1 (Jan. 2015), pp. 55–59. DOI: 10.1038/nnano.2014.278 (cit. on pp. 2, 3, 148, 151).

[28] Philipp Christoph, Tobias Wagner, Hai Zhong, Roland Wiesendanger, Klaus Sengstock, Alexander Schwarz, and Christoph Becker. "Combined feedback and sympathetic cooling of a mechanical oscillator coupled to ultracold atoms". In: *New Journal of Physics* 20.9 (Sept. 2018), p. 093020. DOI: 10.1088/1367-2630/aadf20 (cit. on pp. 2, 3, 148, 151).

[29] Thomas M. Karg, Baptiste Gouraud, Chun Tat Ngai, Gian-Luca Schmid, Klemens Hammerer, and Philipp Treutlein. "Light-mediated strong coupling between a mechanical oscillator and atomic spins 1 meter apart". In: *Science* 369.6500 (July 2020), pp. 174–179. DOI: 10.1126/science.abb0328 (cit. on pp. 2–4, 36, 89, 115, 122, 148–150, 152, 156, 159–161, 164, 214).

[30] Gian-Luca Schmid, Chun Tat Ngai, Maryse Ernzer, Manel Bosch Aguilera, Thomas M. Karg, and Philipp Treutlein. "Coherent Feedback Cooling of a Nanomechanical Membrane with Atomic Spins". In: *Physical Review X* 12.1 (Jan. 2022), p. 011020. DOI: 10.1103/physrevx.12.011020 (cit. on pp. 2, 3, 5, 97, 111, 113, 147, 156, 164–166, 209).

[31] Christoffer B. Møller, Rodrigo A. Thomas, Georgios Vasilakis, Emil Zeuthen, Yeghishe Tsaturyan, Mikhail Balabas, Kasper Jensen, Albert Schliesser, Klemens Hammerer, and Eugene S. Polzik. "Quantum back-action-evading measurement of motion in a negative mass reference frame". In: *Nature* 547.7662 (July 2017), pp. 191–195. DOI: 10.1038/nature22980 (cit. on pp. 2, 148).

[32] Rodrigo A. Thomas, Michał Parniak, Christoffer Østfeldt, Christoffer B. Møller, Christian Bærentsen, Yeghishe Tsaturyan, Albert Schliesser, Jürgen Appel, Emil Zeuthen, and Eugene S. Polzik. "Entanglement between distant macroscopic mechanical and spin systems". In: *Nature Physics* 17.2 (Feb. 2021), pp. 228–233. DOI: 10.1038/s41567-020-1031-5 (cit. on pp. 2, 4, 89).

[33] Simon Gröblacher, Klemens Hammerer, Michael R. Vanner, and Markus Aspelmeyer. "Observation of strong coupling between a micromechanical resonator and an optical cavity field". In: *Nature* 460.7256 (Aug. 2009), pp. 724–727. DOI: 10.1038/nature08171 (cit. on p. 2).

[34] Ewold Verhagen, Samuel Deléglise, Stefan Weis, Albert Schliesser, and Tobias J. Kippenberg. "Quantum-Coherent Coupling of a Mechanical Oscillator to an Optical Cavity Mode". In: *Nature* 482.7383 (Feb. 2012), pp. 63–67. DOI: https://doi.org/10.1038/nature10787 (cit. on pp. 2, 125).

[35] Lukas F. Buchmann and Dan M. Stamper-Kurn. "The quantum/classical transition in mediated interactions". In: *Annalen der Physik* 527.1-2 (Oct. 2014), pp. 156–161. DOI: 10.1002/andp.201400150 (cit. on p. 2).

[36] Anton Frisk Kockum, Göran Johansson, and Franco Nori. "Decoherence-Free Interaction between Giant Atoms in Waveguide Quantum Electrodynamics". In: *Physical Review Letters* 120.14 (Apr. 2018), p. 140404. DOI: 10.1103/physrevlett.120.140404 (cit. on pp. 2, 3, 171).

[37] Thomas M. Karg, Baptiste Gouraud, Philipp Treutlein, and Klemens Hammerer. "Remote Hamiltonian interactions mediated by light". In: *Physical Review A* 99.6, 063829 (June 2019), p. 063829. DOI: 10.1103/PhysRevA.99.063829. arXiv: 1901.06891 [quant-ph] (cit. on pp. 2–4, 36, 113–116, 122, 123, 132, 138, 144, 150, 154, 166–168, 171, 210, 212, 213, 217, 219, 221).

[38] Martino Poggio, Christian L. Degen, Charles T. Rettner, H. Jonathon Mamin, and Daniel Rugar. "Nuclear magnetic resonance force microscopy with a microwire rf source". In: *Applied Physics Letters* 90.26 (June 2007). DOI: 10.1063/1.2752536 (cit. on p. 2).

[39] Seth Lloyd. "Coherent quantum feedback". In: *Physical Review A* 62 (2 July 2000), p. 022108. DOI: 10.1103/PhysRevA.62.022108 (cit. on pp. 2, 4, 148, 155, 165).

[40] Nicolas Gisin and Rob Thew. "Quantum communication". In: *Nature Photonics* 1.3 (Mar. 2007), pp. 165–171. DOI: 10.1038/nphoton.2007.22 (cit. on p. 2).

[41] Chin-Wen Chou, Hugues de Riedmatten, Daniel Felinto, Sergey V. Polyakov, Steven J. van Enk, and H. Jeff Kimble. "Measurement-induced entanglement for excitation stored in remote atomic ensembles". In: *Nature* 438.7069 (Dec. 2005), pp. 828–832. DOI: 10.1038/nature04353 (cit. on p. 2).

[42] Yong Yu, Fei Ma, Xi-Yu Luo, Bo Jing, Peng-Fei Sun, Ren-Zhou Fang, Chao-Wei Yang, Hui Liu, Ming-Yang Zheng, Xiu-Ping Xie, Wei-Jun Zhang, Li-Xing You, Zhen Wang, Teng-Yun Chen, Qiang Zhang, Xiao-Hui Bao, and Jian-Wei Pan. "Entanglement of two quantum memories via fibres over dozens of kilometres". In: *Nature* 578.7794 (Feb. 2020), pp. 240–245. DOI: 10.1038/s41586-020-1976-7 (cit. on p. 2).

[43] Stephan Ritter, Christian Nölleke, Carolin Hahn, Andreas Reiserer, Andreas Neuzner, Manuel Uphoff, Martin Mücke, Eden Figueroa, Joerg Bochmann, and Gerhard Rempe. "An elementary quantum network of single atoms in optical cavities". In: *Nature* 484.7393 (Apr. 2012), pp. 195–200. DOI: https://doi.org/10.1038/nature11023 (cit. on p. 2).

[44] Tim van Leent, Matthias Bock, Florian Fertig, Robert Garthoff, Sebastian Eppelt, Yiru Zhou, Pooja Malik, Matthias Seubert, Tobias Bauer, Wenjamin Rosenfeld, Wei Zhang, Christoph Becher, and Harald Weinfurter. "Entangling single atoms over 33 km telecom fibre". In: *Nature* 607.7917 (July 2022), pp. 69–73. DOI: 10.1038/s41586-022-04764-4 (cit. on p. 2).

[45] B. Hensen, H. Bernien, A. E. Dréau, A. Reiserer, N. Kalb, M. S. Blok, J. Ruitenberg, R. F. L. Vermeulen, R. N. Schouten, C. Abellán, W. Amaya, V. Pruneri, Morgan W. Mitchell, M. Markham, D. J. Twitchen, D. Elkouss, S. Wehner, T. H. Taminiau, and R. Hanson. "Loophole-free Bell inequality violation using electron spins separated by 1.3 kilometres". In: *Nature* 526.7575 (Oct. 2015), pp. 682–686. DOI: 10.1038/nature15759 (cit. on p. 2).

[46] Matteo Pompili, Sophie L. N. Hermans, Simon Baier, Hans K. C. Beukers, Peter C. Humphreys, Raymond N. Schouten, Raymond F. L. Vermeulen, Marinus J. Tiggelman, Laura dos Santos Martins, Bas Dirkse, Stephanie Wehner, and Ronald Hanson. "Realization of a multinode quantum network of remote solid-state qubits". In: *Science* 372.6539 (Apr. 2021), pp. 259–264. DOI: 10.1126/science.abg1919 (cit. on p. 2).

[47] Victor Krutyanskiy, M. Galli, V. Krcmarsky, Simon Baier, Dario A. Fioretto, Y. Pu, Azadeh Mazloom, Pavel Sekatski, Marco Canteri, Markus Teller, J. Schupp, J. Bate, Martin Meraner, Nicolas Sangouard, Ben P. Lanyon, and Tracy E. Northup. "Entanglement of Trapped-Ion Qubits Separated by 230 Meters". In: *Physical Review Letters* 130.5 (Feb. 2023), p. 050803. DOI: 10.1103/physrevlett.130.050803 (cit. on p. 2).

[48] Bharath Kannan, Max J. Ruckriegel, Daniel L. Campbell, Anton Frisk Kockum, Jochen Braumüller, David K. Kim, Morten Kjaergaard, Philip Krantz, Alexander Melville, Bethany M. Niedzielski, Antti Vepsäläinen, Roni Winik, Jonilyn L. Yoder, Franco Nori, Terry P. Orlando, Simon Gustavsson, and William D. Oliver. "Waveguide quantum electrodynamics with superconducting artificial giant atoms". In: *Nature* 583.7818 (July 2020), pp. 775–779. DOI: 10.1038/s41586-020-2529-9 (cit. on pp. 3, 171).

[49] Zi-Qi Wang, Yi-Pu Wang, Jiguang Yao, Rui-Chang Shen, Wei-Jiang Wu, Jie Qian, Jie Li, Shi-Yao Zhu, and J. Q. You. "Giant spin ensembles in waveguide magnonics". In: *Nature Communications* 13.1 (Dec. 2022). DOI: 10.1038/s41467-022-35174-9 (cit. on p. 3).

[50] Aline Vochezer, Tobias Kampschulte, Klemens Hammerer, and Philipp Treutlein. "Light-mediated collective atomic motion in an optical lattice coupled to a membrane". In: *Physical Review Lett.er* 120.7 (Feb. 2018), p. 073602. DOI: 10.1103/PhysRevLett.120.073602 (cit. on pp. 3, 153).

[51] Berit Vogell, Tobias Kampschulte, Matthew T. Rakher, Aline Faber, Philipp Treutlein, Klemens Hammerer, and Peter Zoller. "Long distance coupling of a quantum mechanical oscillator to the internal states of an atomic ensemble". In: *New Journal of Physics* 17.4 (Apr. 2015), p. 043044. DOI: 10.1088/1367-2630/17/4/043044 (cit. on pp. 3, 148).

[52] Luca Pezzè, Augusto Smerzi, Markus K. Oberthaler, Roman Schmied, and Philipp Treutlein. "Quantum metrology with nonclassical states of atomic ensembles". In: *Reviews of Mododern Physics* 90 (3 Sept. 2018), p. 035005. DOI: 10.1103/RevModPhys.90.035005 (cit. on pp. 4, 36, 148).

[53] Dmitry Budker, Wojciech Gawlik, Derek F. Kimball, S. M. Rochester, Valeriy V. Yashchuk, and Antoine Weis. "Resonant nonlinear magneto-optical effects in atoms". In: *Reviews of Modern Physics* 74.4 (Nov. 2002), pp. 1153–1201. DOI: 10.1103/revmodphys.74.1153 (cit. on pp. 4, 37).

[54] Markus Aspelmeyer, Tobias J. Kippenberg, and Florian Marquardt. "Cavity optomechanics". In: *Reviews of Modern Physics* 86.4 (Dec. 2014), pp. 1391–1452. DOI: 10.1103/RevModPhys.86.1391 (cit. on pp. 4, 94–97, 149, 150, 205).

[55] Nils Johan Engelsen, Alberto Beccari, and Tobias Jan Kippenberg. "Ultrahigh-quality-factor micro- and nanomechanical resonators using dissipation dilution". In: *Nature Nanotechnology* (Mar. 2024), pp. 1–13. DOI: 10.1038/s41565-023-01597-8 (cit. on pp. 4, 100, 102, 165).

[56] Yeghishe Tsaturyan, Andreas Barg, Eugene S. Polzik, and Albert Schliesser. "Ultracoherent nanomechanical resonators via soft clamping and dissipation dilution". In: *Natur Nanotechnology* 12.8 (Aug. 2017), pp. 776–783. DOI: 10.1038/nnano.2017.101 (cit. on pp. 4, 102, 154).

[57] Massimiliano Rossi, David Mason, Junxin Chen, Yeghishe Tsaturyan, and Albert Schliesser. "Measurement-based quantum control of mechanical motion". In: *Nature* 563.7729 (Nov. 2018), pp. 53–58. DOI: 10.1038/s41586-018-0643-8 (cit. on p. 4).

[58] David Mason, Junxin Chen, Massimiliano Rossi, Yeghishe Tsaturyan, and Albert Schliesser. "Continuous force and displacement measurement below the standard quantum limit". In: *Nature Physics* 15.8 (May 2019), pp. 745–749. DOI: 10.1038/s41567-019-0533-5 (cit. on p. 4).

[59] Mads Bjerregaard Kristensen, Nenad Kralj, Eric C. Langman, and Albert Schliesser. "Long-lived and Efficient Optomechanical Memory for Light". In: *Physical Review Letters* 132.10 (Mar. 2024), p. 100802. DOI: 10.1103/physrevlett.132.100802 (cit. on p. 4).

[60] A. P. Higginbotham, Peter S. Burns, M. D. Urmey, R. W. Peterson, Nir S. Kampel, B. M. Brubaker, G. Smith, K. W. Lehnert, and Cindy A. Regal. "Harnessing electro-optic correlations in an efficient mechanical converter". In: *Nature Physics* 14.10 (July 2018), pp. 1038–1042. DOI: 10.1038/s41567-018-0210-0 (cit. on p. 4).

[61] Alexander Eichler. "Ultra-high-Q nanomechanical resonators for force sensing". In: *Materials for Quantum Technology* 2.4 (Dec. 2022), p. 043001. DOI: 10.1088/2633-4356/acaba4 (cit. on p. 4).

[62] Thomas Gisler, David Hälg, Vincent Dumont, Shobhna Misra, Letizia Catalini, Eric C Langman, Albert Schliesser, Christian L Degen, and Alexander Eichler. "Enhancing Membrane-Based Scanning Force Microscopy Through an Optical Cavity". In: *arXiv* (2024). arXiv: 2406.07171 [physics.optics] (cit. on p. 4).

[63] Guanhao Huang, Alberto Beccari, Nils J. Engelsen, and Tobias J. Kippenberg. "Room-temperature quantum optomechanics using an ultralow noise cavity". In: *Nature* 626.7999 (Feb. 2024), pp. 512–516. DOI: 10.1038/s41586-023-06997-3 (cit. on pp. 4, 87, 110–112, 165, 205).

[64] Jing Zhang, Yu xi Liu, Re-Bing Wu, Kurt Jacobs, and Franco Nori. "Quantum feedback: Theory, experiments, and applications". In: *Physics Reports* 679 (2017), pp. 1–60. DOI: https://doi.org/10.1016/j.physrep.2017.02.003 (cit. on pp. 4, 148, 155, 165).

[65] Maryse Ernzer, Manel Bosch Aguilera, Matteo Brunelli, Gian-Luca Schmid, Thomas M. Karg, Christoph Bruder, Patrick P. Potts, and Philipp Treutlein. "Optical Coherent Feedback Control of a Mechanical Oscillator". In: *Physical Review X* 13.2 (May 2023), p. 021023. DOI: 10.1103/physrevx.13.021023 (cit. on pp. 5, 168–170, 207, 217).

[66] Andreas Jöckel. "Sympathetic cooling of a membrane oscillator in a hybrid mechanical-atomic system". PhD thesis. University of Basel, 2014 (cit. on pp. 6, 8, 13, 14, 21).

[67] Aline Faber. "Sympathetic cooling and self-oscillations in a hybrid atom-membrane system". PhD thesis. University of Basel, June 2016 (cit. on pp. 6, 8, 22, 128).

[68] Thomas M. Karg. "Strong light-mediated coupling between a membrane oscillator and an atomic spin ensemble". PhD thesis. University of Basel, 2020 (cit. on pp. 6, 8, 44, 46, 62, 69, 90, 92, 94, 96, 100, 106, 108, 109, 111, 121, 125, 134, 138, 139, 141, 148, 156, 160, 164, 166, 184).

[69] Chun Tat Ngai. "Coherent feedback cooling of a nanomechanical membrane with atomic spins". PhD thesis. University of Basel, 2022 (cit. on pp. 6, 8, 44, 46, 156, 164).

[70] Gianni C. Buser. "Dipole-Trapped Atoms at High Optical Depth for Atom-Light Quantum Interfaces". MA thesis. University of Basel, June 2016 (cit. on p. 8).

[71] Kai Dieckmann, Robert J. C. Spreeuw, Matthias Weidemüller, and Jook T. M. Walraven. "Two-dimensional magneto-optical trap as a source of slow atoms". In: *Physical Review A* 58.5 (Nov. 1998), pp. 3891–3895. DOI: 10.1103/physreva.58.3891 (cit. on pp. 8, 13, 21).

[72] Jürgen Appel, Andrew MacRae, and Alexander I. Lvovsky. "A versatile digital GHz phase lock for external cavity diode lasers". In: *Measurement Science and Technology* 20.5 (Apr. 2009), p. 055302. DOI: 10.1088/0957-0233/20/5/055302 (cit. on pp. 11, 174).

[73] Leonhard Neuhaus, Michaël Croquette, Rémi Metzdorff, Sheon Chua, Pierre-Edouard Jacquet, Alexandre Journeaux, Antoine Heidmann, Tristan Briant, Thibaut Jacqmin, Pierre-François Cohadon, and Samuel Deléglise. "Python Red Pitaya Lockbox (PyRPL): An open source software package for digital feedback control in quantum optics experiments". In: *Review of Scientific Instruments* 95.3 (Mar. 2024). DOI: 10.1063/5.0178481 (cit. on pp. 11, 138, 175, 176).

[74] Dominik Husmann et al. "SI-traceable frequency dissemination at 1572.06 nm in a stabilized fiber network with ring topology". In: *Optics Express* 29.16 (July 2021), p. 24592. DOI: 10.1364/oe.427921 (cit. on pp. 11, 170).

[75] Gianni C. Buser, Roberto Mottola, Björn Cotting, Janik Wolters, and Philipp Treutlein. "Single-Photon Storage in a Ground-State Vapor Cell Quantum Memory". In: *Physical Review X Quantum* 3.2 (June 2022), p. 020349. DOI: 10.1103/prxquantum.3.020349 (cit. on p. 13).

[76] Gianni C. Buser. "Switching, Amplifying, and Chirping Diode Lasers with Current Pulses for High Bandwidth Quantum Technology". In: *arXiv* (2024). arXiv: 2407.18788 (cit. on p. 13).

[77] Gianni C. Buser. "Storing Single Photons in Broadband Vapor Cell Quantum". PhD thesis. University of Basel, Dec. 2023 (cit. on p. 13).

[78] Ferran Martin Ciurana. "Coherent sensing of magnetic waveforms with spin-squeezed atoms". PhD thesis. ICFO Barcelona, 2017 (cit. on p. 15).

[79] Gian-Luca Schmid. "Coupling of Atoms and a Nano-Mechanical Oscillator Mediated by Light". MA thesis. University of Basel, Sept. 2019 (cit. on pp. 15, 188).

[80] Johannes Hoffrogge. "Mikrowellen-Nahfelder auf Atomchips". PhD thesis. Universität München, 2007 (cit. on pp. 16, 19).

[81] Philip T. Starkey, Christopher J. Billington, Shaun P. Johnstone, Martijn Jasperse, Kristian Helmerson, Lincoln D. Turner, and Russell P. Anderson. "A scripted control system for autonomous hardware-timed experiments". In: *Review of Scientific Instruments* 84.8 (Aug. 2013). DOI: 10.1063/1.4817213 (cit. on p. 20).

[82] Wolfgang Ketterle, Kendall B. Davis, Michael A. Joffe, Alex Martin, and David E. Pritchard. "High densities of cold atoms in a dark spontaneous-force optical trap". In: *Physical Review Letters* 70.15 (Apr. 1993), pp. 2253–2256. DOI: 10.1103/physrevlett.70.2253 (cit. on p. 22).

[83] C. G. Townsend, Niamh H. Edwards, K. P. Zetie, C. J. Cooper, J. Rink, and Christopher J. Foot. "High-density trapping of cesium atoms in a dark magneto-optical trap". In: *Physical Review A* 53.3 (Mar. 1996), pp. 1702–1714. DOI: 10.1103/physreva.53.1702 (cit. on p. 22).

[84] Jean Dalibard and Claude Cohen-Tannoudji. "Laser cooling below the Doppler limit by polarization gradients: simple theoretical models". In: *Journal of the Optical Society of America B* 6.11 (Nov. 1989), p. 2023. DOI: 10.1364/josab.6.002023 (cit. on p. 22).

[85] Ben Q. Baragiola, Leigh M. Norris, Enrique Montaño, Pascal G. Mickelson, Poul S. Jessen, and Ivan H. Deutsch. "Three-dimensional light-matter interface for collective spin squeezing in atomic ensembles". In: *Physical Review A* 89.3 (Mar. 2014), p. 033850. DOI: 10.1103/physreva.89.033850 (cit. on pp. 24, 25, 66, 198, 199, 203).

[86] Jörg H. Müller, Plamen Petrov, Daniel Oblak, Carlos L. Garrido Alzar, S. R. de Echaniz, and Eugene S. Polzik. "Diffraction effects on light–atomic-ensemble quantum interface". In: *Physical Review A* 71.3 (Mar. 2005), p. 033803. DOI: 10.1103/physreva.71.033803 (cit. on pp. 24–26).

[87] Rudolf Grimm, Matthias Weidemüller, and Yurii B. Ovchinnikov. "Optical Dipole Traps for Neutral Atoms". In: *Advances In Atomic, Molecular, and Optical Physics*. Elsevier, 2000, pp. 95–170. DOI: 10.1016/s1049-250x(08)60186-x (cit. on pp. 24, 25).

[88] Amita B. Deb, J Chung, and Niels Kjærgaard. "Dispersive detection of atomic ensembles in the presence of strong lensing". In: *New Journal of Physics* 22.7 (July 2020), p. 073017. DOI: 10.1088/1367-2630/ab9553 (cit. on pp. 25, 30).

[89] Gael Reinaudi, Thierry Lahaye, Z. Wang, and David Guéry-Odelin. "Strong saturation absorption imaging of dense clouds of ultracold atoms". In: *Optics Letters* 32.21 (Nov. 2007), p. 3143. DOI: 10.1364/ol.32.003143 (cit. on p. 28).

[90] Guillaume Labeyrie, Thorsten Ackemann, Bruce Klappauf, Matthias Pesch, Gian Luca Lippi, and Robin Kaiser. "Nonlinear beam shaping by a cloud of cold Rb atoms". In: *The European Physical Journal D* 22.3 (Mar. 2003), pp. 473–483. DOI: 10.1140/epjd/e2003-00046-4 (cit. on p. 30).

[91] Yingxue Wang and M. Saffman. "Experimental study of nonlinear focusing in a magneto-optical trap using a Z-scan technique". In: *Physical Review A* 70.1 (July 2004), p. 013801. DOI: 10.1103/physreva.70.013801 (cit. on p. 30).

[92] Tom A. Savard, Kenneth M. O'Hara, and John E. Thomas. "Laser-noise-induced heating in far-off resonance optical traps". In: *Physical Review A* 56 (Aug. 1997), R1095–R1098. DOI: 10.1103/physreva.56.r1095 (cit. on p. 31).

[93] Brian Julsgaard, Jacob Sherson, Jens L. Sørensen, and Eugene S. Polzik. "Characterizing the spin state of an atomic ensemble using the magneto-optical resonance method". In: *Journal of Optics B: Quantum and Semiclassical Optics* 6.1 (Sept. 2003), pp. 5–14. DOI: 10.1088/1464-4266/6/1/002 (cit. on pp. 34, 77).

[94] Haruka Tanji-Suzuki, Ian D. Leroux, Monika H. Schleier-Smith, Marko Cetina, Andrew T. Grier, Jonathan Simon, and Vladan Vuletić. "Interaction between Atomic Ensembles and Optical Resonators: Classical Description". In: *Advances In Atomic, Molecular, and Optical Physics*. Vol. 60. Elsevier, 2011, pp. 201–237. DOI: 10.1016/b978-0-12-385508-4.00004-8 (cit. on pp. 36, 65, 198–201).

[95] Alex Kuzmich, Nicholas P. Bigelow, and Leonard Mandel. "Atomic quantum non-demolition measurements and squeezing". In: *Europhysics Letters (EPL)* 42.5 (June 1998), pp. 481–486. DOI: 10.1209/epl/i1998-00277-9 (cit. on pp. 37, 45).

[96] M. Kubasik, M. Koschorreck, M. Napolitano, S. R. de Echaniz, H. Crepaz, J. Eschner, Eugene S. Polzik, and Morgan W. Mitchell. "Polarization-based light-atom quantum interface with an all-optical trap". In: *Physical Review A* 79.4 (Apr. 2009), p. 043815. DOI: 10.1103/physreva.79.043815 (cit. on pp. 37, 45).

[97] M. Koschorreck, M. Napolitano, B. Dubost, and Morgan W. Mitchell. "Sub-Projection-Noise Sensitivity in Broadband Atomic Magnetometry". In: *Physical Review Letters* 104.9 (Mar. 2010), p. 093602. DOI: 10.1103/physrevlett.104.093602 (cit. on p. 37).

[98] Daniel Hemmer, Enrique Montaño, Ben Q. Baragiola, Leigh M. Norris, Ezad Shojaee, Ivan H. Deutsch, and Paul S. Jessen. "Squeezing the angular momentum of an ensemble of complex multilevel atoms". In: *Physical Review A* 104.2 (Aug. 2021), p. 023710. DOI: 10.1103/physreva.104.023710 (cit. on pp. 37, 65, 73).

[99] Michael G. Raymer and J. Mostowski. "Stimulated Raman scattering: Unified treatment of spontaneous initiation and spatial propagation". In: *Physical Review A* 24.4 (Oct. 1981), pp. 1980–1993. DOI: 10.1103/physreva.24.1980 (cit. on p. 37).

[100] William Guerin, Mohamed T. Rouabah, and Robin Kaiser. "Light interacting with atomic ensembles: collective, cooperative and mesoscopic effects". In: *Journal of Modern Optics* 64.9 (Aug. 2016), pp. 895–907. DOI: 10.1080/09500340.2016.1215564 (cit. on p. 37).

[101] Martin W. Sørensen and Anders S. Sørensen. "Three-dimensional theory for light-matter interaction". In: *Physical Review A* 77.1 (Jan. 2008), p. 013826. DOI: 10.1103/physreva.77.013826 (cit. on pp. 37, 65, 73).

[102] Daniel A. Steck. *Quantum and Atom Optics*. Available online at http://steck.us/teaching (revision 0.16.1). June 2024 (cit. on pp. 38–40, 78, 177, 178, 180–182).

[103] R. Loudon. *The quantum theory of light*. Oxford university press, 2000 (cit. on pp. 38, 178).

[104] Claude Cohen-Tannoudji, Jacques Dupont-Roc, and Gilbert Grynberg. *Atom—Photon Interactions. Basic Process and Appilcations*. Wiley science paperback series. New York, NY [u.a.]: Wiley, Apr. 1998. 656 pp. DOI: 10.1002/9783527617197 (cit. on p. 38).

[105] Daniel A. Steck. *Rubidium 87 D Line Data*. Available online at http://steck.us/alkalidata. Accessed: 2019-06-09. 2015 (cit. on pp. 39, 46, 53, 54, 79, 181, 182, 184).

[106] S. R. de Echaniz, Morgan W. Mitchell, M. Kubasik, M. Koschorreck, H. Crepaz, J. Eschner, and Eugene S. Polzik. "Conditions for spin squeezing in a cold87Rb ensemble". In: *Journal of Optics B: Quantum and Semiclassical Optics* 7.12 (Nov. 2005), S548–S552. DOI: 10.1088/1464-4266/7/12/016 (cit. on pp. 40, 44, 50, 73, 189).

[107] D. V. Kupriyanov, O. S. Mishina, I. M. Sokolov, Brian Julsgaard, and Eugene S. Polzik. "Multimode entanglement of light and atomic ensembles via off-resonant coherent forward scattering". In: *Physical Review A* 71.3 (Mar. 2005). DOI: 10.1103/physreva.71.032348 (cit. on pp. 40, 181, 189).

[108] Fam Le Kien, Philipp Schneeweiss, and Arno Rauschenbeutel. "Dynamical polarizability of atoms in arbitrary light fields: general theory and application to cesium". In: *The European Physical Journal D* 67.5 (May 2013). DOI: 10.1140/epjd/e2013-30729-x (cit. on pp. 41, 178, 181).

[109] Alexamder S. Shumovsky and Özgür E. Müstecaplioğlu. "Stokes operators, angular momentum and radiation phase". In: *Journal of Modern Optics* 45.3 (Mar. 1998), pp. 619–628. DOI: 10.1080/09500349808231919 (cit. on p. 42).

[110] J. M. Geremia, John K. Stockton, and Hideo Mabuchi. "Tensor polarizability and dispersive quantum measurement of multilevel atoms". In: *Physcal Review A* 73 (4 Apr. 2006), p. 042112. DOI: 10.1103/PhysRevA.73.042112 (cit. on pp. 42, 50, 60, 73, 177, 189).

[111] Brian Julsgaard. "Entanglement and Quantum Interactions with Macroscopic Gas Samples". PhD thesis. Århus : Aarhus Universitetsforlag, Oct. 2003 (cit. on pp. 47, 185, 186, 202).

[112] Warwick P. Bowen and Gerard J. Milburn. *Quantum Optomechanics*. English. Boca Raton, FL: CRC Press, Oct. 2016, p. 17. DOI: 10.1201/b19379 (cit. on pp. 48, 99, 166, 192, 193).

[113] Florentin Reiter and Anders S. Sørensen. "Effective operator formalism for open quantum systems". In: *Physical Review A* 85.3 (Mar. 2012), p. 032111. DOI: 10.1103/physreva.85.032111 (cit. on pp. 48, 49, 187).

[114] Ivan H. Deutsch and Poul S. Jessen. "Quantum control and measurement of atomic spins in polarization spectroscopy". In: *Optics Communications* 283.5 (Mar. 2010), pp. 681–694. DOI: 10.1016/j.optcom.2009.10.059 (cit. on pp. 50, 73, 177).

[115] S. R. de Echaniz, M. Koschorreck, M. Napolitano, M. Kubasik, and Morgan W. Mitchell. "Hamiltonian design in atom-light interactions with rubidium ensembles: A quantum-information toolbox". In: *Physical Review A* 77.3 (Mar. 2008). DOI: 10.1103/physreva.77.032316 (cit. on pp. 52, 73, 189, 190).

[116] Greg A. Smith, Souma Chaudhury, Andrew Silberfarb, Ivan H. Deutsch, and Poul S. Jessen. "Continuous weak measurement and nonlinear dynamics in a cold spin ensemble". In: *Physical Review Letters* 93.16 (Oct. 2004), p. 163602. DOI: 10.1103/physrevlett.93.163602 (cit. on pp. 54, 63).

[117] Denis V. Vasilyev, Klemens Hammerer, Nikolaj Korolev, and Anders S. Sørensen. "Quantum noise for Faraday light–matter interfaces". In: *Journal of Physics B: Atomic, Molecular and Optical Physics* 45.12 (June 2012), p. 124007. DOI: 10.1088/0953-4075/45/12/124007 (cit. on p. 66).

[118] Jiazhong Hu, Wenlan Chen, Zachary Vendeiro, Hao Zhang, and Vladan Vuletić. "Entangled collective-spin states of atomic ensembles under nonuniform atom-light interaction". In: *Physical Review A* 92.6 (Dec. 2015), p. 063816. DOI: 10.1103/physreva.92.063816 (cit. on pp. 66, 68, 90).

[119] Rodrigo A. Thomas, Christoffer Østfeldt, Christian Bærentsen, Michał Parniak, and Eugene S. Polzik. "Calibration of spin-light coupling by coherently induced Faraday rotation". In: *Optics Express* 29.15 (July 2021), p. 23637. DOI: 10.1364/oe.425613. arXiv: 2103.11729 [quant-ph] (cit. on pp. 76, 83).

[120] Tom P. Purdy, Pen-Li Yu, Robert W. Peterson, Nir S. Kampel, and Cindy A. Regal. "Strong Optomechanical Squeezing of Light". In: *Physical Review X* 3.3 (Sept. 2013), p. 031012. DOI: 10.1103/physrevx.3.031012 (cit. on pp. 87, 110, 205).

[121] Theodore Holstein and Henry Primakoff. "Field Dependence of the Intrinsic Domain Magnetization of a Ferromagnet". In: *Physical Review* 58.12 (12 Dec. 1940), pp. 1098–1113. DOI: 10.1103/physrev.58.1098 (cit. on p. 88).

[122] Jonathan Kohler, Justin A. Gerber, Emma Dowd, and Dan M. Stamper-Kurn. "Negative-Mass Instability of the Spin and Motion of an Atomic Gas Driven by Optical Cavity Backaction". In: *Physical Review Letters* 120.1 (Jan. 2018), p. 013601. DOI: 10.1103/physrevlett.120.013601 (cit. on p. 89).

[123] Brian Julsgaard, Alexander Kozhekin, and Eugene S. Polzik. "Experimental long-lived entanglement of two macroscopic objects". In: *Nature* 413.6854 (Sept. 2001), pp. 400–403. DOI: 10.1038/35096524 (cit. on pp. 89, 115).

[124] Maryse Ernzer. "Optical coherent feedback control of a mechanical oscillator". PhD thesis. University of Basel, 2023 (cit. on pp. 94, 96, 97, 99, 100, 104, 105, 108, 109, 111, 164, 169).

[125] Andrew M. Jayich, Jack C. Sankey, Benjamin M. Zwickl, Chengan Yang, Jeff D. Thompson, Steven M. Girvin, Aashish A. Clerk, Florian Marquardt, and Jack G. E. Harris. "Dispersive optomechanics: a membrane inside a cavity". In: *New Journal of Physics* 10.9 (Sept. 2008), p. 095008. DOI: 10.1088/1367-2630/10/9/095008 (cit. on p. 95).

[126] Pen-Li Yu, Katarina Cicak, Nir S. Kampel, Yeghishe Tsaturyan, Tom P. Purdy, Raymond W. Simmonds, and Cindy A. Regal. "A phononic bandgap shield for high-Q membrane microresonators". In: *Applied Physics Letters* 104.2 (Jan. 2014). DOI: 10.1063/1.4862031 (cit. on p. 100).

[127] Dennis Høj, Ulrich Busk Hoff, and Ulrik Lund Andersen. "Ultracoherent Nanomechanical Resonators Based on Density Phononic Crystal Engineering". In: *Physical Review X* 14.1 (Mar. 2024), p. 011039. DOI: 10.1103/physrevx.14.011039 (cit. on pp. 100, 102, 104).

[128] Benjamin M. Zwickl, William E. Shanks, Andrew M. Jayich, Chengan Yang, Ania C. Bleszynski Jayich, Jeff D. Thompson, and Jack G. E. Harris. "High quality mechanical and optical properties of commercial silicon nitride membranes". In: *Applied Physics Letters* 92.10 (Mar. 2008). DOI: 10.1063/1.2884191 (cit. on p. 100).

[129] Ronald W. P. Drever, John L. Hall, F. V. Kowalski, J. Hough, G. M. Ford, A. J. Munley, and H. Ward. "Laser phase and frequency stabilization using an optical resonator". In: *Applied Physics B* 31.2 (June 1983), pp. 97–105. DOI: 10.1007/bf00702605 (cit. on p. 102).

[130] Eric D. Black. "An introduction to Pound–Drever–Hall laser frequency stabilization". In: *American Journal of Physics* 69.1 (Jan. 2001), pp. 79–87. DOI: 10.1119/1.1286663 (cit. on p. 102).

[131] Luis Guillermo Villanueva and Silvan Schmid. "Evidence of Surface Loss as Ubiquitous Limiting Damping Mechanism in SiN Micro- and Nanomechanical Resonators". In: *Physical Review Letters* 113.22 (Nov. 2014), p. 227201. DOI: 10.1103/physrevlett.113.227201 (cit. on p. 102).

[132] Christopher Reetz, Ran Fischer, Gabriel G. T. Assumpção, Dylan P. McNally, Peter S. Burns, Jack C. Sankey, and Cindy A. Regal. "Analysis of Membrane Phononic Crystals with Wide Band Gaps and Low-Mass Defects". In: *Physical Review Applied* 12.4 (Oct. 2019), p. 044027. DOI: 10.1103/physrevapplied.12.044027 (cit. on pp. 102, 154).

[133] Letizia Catalini, Yeghishe Tsaturyan, and Albert Schliesser. "Soft-Clamped Phononic Dimers for Mechanical Sensing and Transduction". In: *Physical Review Applied* 14.1 (July 2020), p. 014041. DOI: 10.1103/physrevapplied.14.014041 (cit. on p. 102).

[134] Dennis Høj. "Development of ultra-high quality mechanical oscillators". PhD thesis. Technical University of Denmark, 2021 (cit. on p. 104).

[135] Andreas Barg, Yeghishe Tsaturyan, Erik Belhage, William H. P. Nielsen, Christoffer B. Møller, and Albert Schliesser. "Measuring and imaging nanomechanical motion with laser light". In: *Applied Physics B* 123.1 (Dec. 2016). DOI: 10.1007/s00340-016-6585-7 (cit. on p. 104).

[136] Stefano Mancini and Paolo Tombesi. "Quantum noise reduction by radiation pressure". In: *Physical Review A* 49.5 (May 1994), pp. 4055–4065. DOI: 10.1103/physreva.49.4055 (cit. on pp. 110, 205).

[137] Claude Fabre, Michel Pinard, Sophie Bourzeix, Antoine Heidmann, Elisabeth Giacobino, and Serge Reynaud. "Quantum-noise reduction using a cavity with a movable mirror". In: *Physical Review A* 49.2 (Feb. 1994), pp. 1337–1343. DOI: 10.1103/physreva.49.1337 (cit. on pp. 110, 205).

[138] William Hvidtfelt Padkær Nielsen, Yeghishe Tsaturyan, Christoffer Bo Møller, Eugene S. Polzik, and Albert Schliesser. "Multimode optomechanical system in the quantum regime". In: *Proceedings of the National Academy of Sciences* 114.1 (Dec. 2016), pp. 62–66. DOI: 10.1073/pnas.1608412114 (cit. on p. 110).

[139] Sampo A. Saarinen, Nenad Kralj, Eric C. Langman, Yeghishe Tsaturyan, and Albert Schliesser. "Laser cooling a membrane-in-the-middle system close to the quantum ground state from room temperature". In: *Optica* 10.3 (Mar. 2023), p. 364. DOI: 10.1364/optica.468590 (cit. on p. 111).

[140] William Hvidtfelt Padkæ Nielsen. "Quantum cavity optomechanics with phononic bandgap shielded silicon nitride membranes". PhD thesis. University of Copenhagen, 2016 (cit. on p. 111).

[141] Tom P. Purdy, Robert W Peterson, Pen-Li Yu, and Cindy A. Regal. "Cavity optomechanics with Si_3N_4 membranes at cryogenic temperatures". In: *New Journal of Physics* 14.11 (Nov. 2012), p. 115021. DOI: 10.1088/1367-2630/14/11/115021 (cit. on p. 111).

[142] Georg Enzian, Zihua Wang, Anders Simonsen, Jonas Mathiassen, Toke Vibel, Yeghishe Tsaturyan, Alexander Tagantsev, Albert Schliesser, and Eugene S. Polzik. "Phononically shielded photonic-crystal mirror membranes for cavity quantum optomechanics". In: *Optics Express* 31.8 (Apr. 2023), p. 13040. DOI: 10.1364/oe.484369 (cit. on pp. 111, 165).

[143] Philipp Rohse, J. Butlewski, F. Klein, T. Wagner, C. Friesen, A. Schwarz, R. Wiesendanger, K. Sengstock, and C. Becker. "A cavity optomechanical locking scheme based on the optical spring effect". In: *Review of Scientific Instruments* 91.10 (Oct. 2020). DOI: 10.1063/5.0010255 (cit. on p. 112).

[144] Howard M. Wiseman and Gerard J. Milburn. *Quantum Measurement and Control*. Cambridge University Press, Nov. 2009. DOI: 10.1017/cbo9780511813948 (cit. on pp. 114, 148, 155).

[145] Crispin W. Gardiner and Peter Zoller. *Quantum Noise*. Vol. 97. Springer Berlin Heidelberg, 2000. DOI: 10.1007/978-3-662-04103-1 (cit. on pp. 115, 116).

[146] Hayat Abbas and Thomas Fernholz. "An Interferometrically Robust Opto-Mechanical Coupler to Beam Polarisation". In: *arXiv* (Jan. 2023). arXiv: 2301.04577 [quant-ph] (cit. on p. 120).

[147] Eberhard P. Hofer. *Grundlagen der Regelungstechnik/ Regelungstechnik 1*. Open Access Repositorium der Universität Ulm, Aug. 2008, pp. 40–51 (cit. on pp. 128–130, 154).

[148] Sebastian G. Hofer and Klemens Hammerer. "Entanglement-enhanced time-continuous quantum control in optomechanics". In: *Physical Review A* 91.3 (Mar. 2015), p. 033822. DOI: 10.1103/physreva.91.033822 (cit. on p. 132).

[149] Iivari Pietikäinen, Ondřej Černotík, and Radim Filip. "Combining Floquet and Lyapunov techniques for time-dependent problems in optomechanics and electromechanics". In: *New Journal of Physics* 22.6 (June 2020), p. 063019. DOI: 10.1088/1367-2630/ab8cab (cit. on p. 132).

[150] Michał Horodecki, Paweł Horodecki, and Ryszard Horodecki. "Separability of mixed states: necessary and sufficient conditions". In: *Physics Letters A* 223.1–2 (Nov. 1996), pp. 1–8. DOI: 10.1016/s0375-9601(96)00706-2 (cit. on p. 133).

[151] John Williamson. "On the algebraic problem concerning the normal forms of linear dynamical systems". In: *American journal of mathematics 58.1* (1936), pp. 141–163 (cit. on p. 133).

[152] Alessio Serafini, Fabrizio Illuminati, and Silvio De Siena. "Von Neumann entropy, mutual information and total correlations of Gaussian states". In: *J. Phys. B 37* 37.2 (Dec. 2004), pp. L21–L28. DOI: 10.1088/0953-4075/37/2/L02 (cit. on p. 133).

[153] Rajiah Simon. "Peres-Horodecki Separability Criterion for Continuous Variable Systems". In: *Physical Review Letters* 84.12 (Mar. 2000), pp. 2726–2729. DOI: 10.1103/physrevlett.84.2726 (cit. on pp. 133, 134).

[154] Gerardo Adesso and Fabrizio Illuminati. "Gaussian measures of entanglement versus negativities: Ordering of two-mode Gaussian states". In: *Physical Review A* 72.3 (Sept. 2005), p. 032334. DOI: 10.1103/physreva.72.032334 (cit. on p. 133).

[155] Lu-Ming Duan, Geza Giedke, J. Ignacio Cirac, and Peter Zoller. "Inseparability Criterion for Continuous Variable Systems". In: *Physical Review Letters* 84.12 (Mar. 2000), pp. 2722–2725. DOI: 10.1103/physrevlett.84.2722 (cit. on p. 134).

[156] Albert Einstein, Boris Podolsky, and Nathan Rosen. "Can Quantum-Mechanical Description of Physical Reality Be Considered Complete?" In: *Physical Review* 47.10 (May 1935), pp. 777–780. DOI: 10.1103/physrev.47.777 (cit. on p. 134).

[157] Yiwen Chu and Simon Gröblacher. "A perspective on hybrid quantum opto- and electromechanical systems". In: *Applied Physics Letters* 117.15, 150503 (Oct. 2020), p. 150503. DOI: 10.1063/5.0021088. arXiv: 2007.03360 [quant-ph] (cit. on p. 147).

[158] Patricio Arrangoiz-Arriola, E. Alex Wollack, Zhaoyou Wang, Marek Pechal, Wentao Jiang, Timothy P. McKenna, Jeremy D. Witmer, Raphaël Van Laer, and Amir H. Safavi-Naeini. "Resolving the energy levels of a nanomechanical oscillator". In: *Nature* 571.7766 (July 2019), pp. 537–540. DOI: 10.1038/s41586-019-1386-x (cit. on p. 148).

[159] Aashish A. Clerk, K. W. Lehnert, P. Bertet, J. R. Petta, and Y. Nakamura. "Hybrid quantum systems with circuit quantum electrodynamics". In: *Nature Physics* 16.3 (Mar. 2020), pp. 257–267. DOI: 10.1038/s41567-020-0797-9 (cit. on pp. 148, 155).

[160] D. Rugar, R. Budakian, H. J. Mamin, and B. W. Chui. "Single spin detection by magnetic resonance force microscopy". In: *Nature* 430.6997 (July 2004), pp. 329–332 (cit. on p. 148).

[161] Ryan Hamerly and Hideo Mabuchi. "Advantages of Coherent Feedback for Cooling Quantum Oscillators". In: *Physical Review Letters* 109 (17 Oct. 2012), p. 173602. DOI: 10.1103/PhysRevLett.109.173602 (cit. on pp. 148, 155).

[162] James S. Bennett, Lars S. Madsen, Mark Baker, Halina Rubinsztein-Dunlop, and Warwick P. Bowen. "Coherent control and feedback cooling in a remotely coupled hybrid atom-optomechanical system". In: *New Journal of Physics* 16.8 (Aug. 2014), p. 083036. DOI: https://doi.org/10.1088/1367-2630/16/8/083036 (cit. on pp. 148, 153).

[163] Masashi Hirose and Paola Cappellaro. "Coherent feedback control of a single qubit in diamond". In: *Nature* 532.7597 (Apr. 2016), pp. 77–80. DOI: 10.1038/nature17404 (cit. on p. 148).

[164] Jing Zhang, Re-Bing Wu, Yu-Xi Liu, Chun-Wen Li, and Tzyh-Jong Tarn. "Quantum Coherent Nonlinear Feedback With Applications to Quantum Optics on Chip". In: *IEEE Transactions Automomatic Control* 57.8 (2012), pp. 1997–2008. DOI: 10.1109/TAC.2012.2195871 (cit. on p. 148).

[165] Zhaoyou Wang and Amir H. Safavi-Naeini. "Enhancing a slow and weak optomechanical nonlinearity with delayed quantum feedback". In: *Nature Communications* 8 (July 2017), p. 15886. DOI: 10.1038/ncomms15886 (cit. on p. 148).

[166] Alfred Harwood, Matteo Brunelli, and Alessio Serafini. "Cavity optomechanics assisted by optical coherent feedback". In: *Physical Review. A* 103 (2021), p. 023509. DOI: 10.1103/physreva.103.023509 (cit. on p. 148).

[167] Matt J. Woolley and Aashish A. Clerk. "Two-mode squeezed states in cavity optomechanics via engineering of a single reservoir". In: *Physical Review A* 89 (6 June 2014), p. 063805. DOI: 10.1103/PhysRevA.89.063805 (cit. on p. 148).

[168] Jie Li, Gang Li, Stefano Zippilli, David Vitali, and Tiancai Zhang. "Enhanced entanglement of two different mechanical resonators via coherent feedback". In: *Physical Review A* 95.4 (Apr. 2017), p. 043819. DOI: 10.1103/PhysRevA.95.043819 (cit. on p. 148).

[169] Margareta Wallquist, Klemens Hammerer, Peter Zoller, Claudiu Genes, M. Ludwig, Florian Marquardt, Philipp Treutlein, Jun Ye, and H. J. Kimble. "Single-atom cavity QED and optomicromechanics". In: *Physical Review A* 81.2 (Feb. 2010), p. 023816. DOI: 10.1103/PhysRevA.81.023816 (cit. on pp. 148, 155).

[170] Jeff D. Thompson, Benjamin M. Zwickl, Andrew M. Jayich, Florian Marquardt, Steven M. Girvin, and Jack G. E. Harris. "Strong dispersive coupling of a high-finesse cavity to a micromechanical membrane". In: *Nature* 452.7183 (Mar. 2008), pp. 72–75. DOI: 10.1038/nature06715 (cit. on p. 149).

[171] Simon F. Nørrelykke and Henrik Flyvbjerg. "Harmonic oscillator in heat bath: Exact simulation of time-lapse-recorded data and exact analytical benchmark statistics". In: *Physical Review E* 83.4 (Apr. 2011), p. 041103. DOI: 10.1103/PhysRevE.83.041103 (cit. on pp. 153, 209, 210).

[172] D. V. Ramana Reddy, Abhijit Sen, and George L. Johnston. "Time Delay Induced Death in Coupled Limit Cycle Oscillators". In: *Physical Review Letters* 80 (23 June 1998), pp. 5109–5112. DOI: 10.1103/PhysRevLett.80.5109 (cit. on p. 153).

[173] D. V. Ramana Reddy, A. Sen, and George L. Johnston. "Experimental Evidence of Time-Delay-Induced Death in Coupled Limit-Cycle Oscillators". In: *Physical Review Letters* 85 (16 Oct. 2000), pp. 3381–3384. DOI: 10.1103/PhysRevLett.85.3381 (cit. on p. 153).

[174] R. T. Sutherland and F. Robicheaux. "Coherent forward broadening in cold atom clouds". In: *Physical Review A* 93.2 (Feb. 2016), p. 023407. DOI: 10.1103/physreva.93.023407 (cit. on p. 165).

[175] Alexander Roth, Klemens Hammerer, and Kirill S Tikhonov. "Light–matter quantum interface with continuous pump and probe". In: *Journal of Physics B: Atomic, Molecular and Optical Physics* 56.5 (Feb. 2023), p. 055502. DOI: 10.1088/1361-6455/acb6db (cit. on p. 165).

[176] Alexandre Huot de Saint-Albin. *Cavity-free cooling of a mechanical oscillator by feedback*. Research rep. University of Basel, July 2024 (cit. on p. 165).

[177] Aashish A. Clerk. "Introduction to quantum non-reciprocal interactions: from non-Hermitian Hamiltonians to quantum master equations and quantum feedforward schemes". In: *SciPost Physics Lecture Notes* (Mar. 2022). DOI: 10.21468/scipostphyslectnotes.44 (cit. on p. 167).

[178] Anja Metelmann and Aashish A. Clerk. "Nonreciprocal Photon Transmission and Amplification via Reservoir Engineering". In: *Physical Review X* 5.2 (June 2015), p. 021025. DOI: 10.1103/physrevx.5.021025 (cit. on pp. 167, 168, 215, 216).

[179] Borhan Ahmadi, Paweł Mazurek, Paweł Horodecki, and Shabir Barzanjeh. "Nonreciprocal Quantum Batteries". In: *Physical Review Letters* 132.21 (May 2024), p. 210402. DOI: 10.1103/physrevlett.132.210402 (cit. on pp. 167, 168).

[180] Mingfeng Wang, Weizhi Qu, Pengxiong Li, Han Bao, Vladan Vuletić, and Yanhong Xiao. "Two-axis-twisting spin squeezing by multipass quantum erasure". In: *Physical Review A* 96.1 (July 2017), p. 013823. DOI: 10.1103/physreva.96.013823 (cit. on p. 170).

[181] Jacob F. Sherson and Klaus Mølmer. "Polarization Squeezing by Optical Faraday Rotation". In: *Physical Review Letters* 97.14 (Oct. 2006), p. 143602. DOI: 10.1103/physrevlett.97.143602 (cit. on p. 170).

[182] Jack Clarke, Pascal Neveu, Kiran E. Khosla, Ewold Verhagen, and Michael R. Vanner. "Cavity Quantum Optomechanical Nonlinearities and Position Measurement beyond the Breakdown of the Linearized Approximation". In: *Physical Review Letters* 131.5 (Aug. 2023), p. 053601. DOI: 10.1103/physrevlett.131.053601 (cit. on p. 170).

[183] Martin Frimmer, Jan Gieseler, and Lukas Novotny. "Cooling Mechanical Oscillators by Coherent Control". In: *Physical Review Letters* 117.16, 163601 (Oct. 2016), p. 163601. DOI: 10.1103/physrevlett.117.163601. arXiv: 1608.00998 [quant-ph] (cit. on p. 171).

[184] Erik Hebestreit, René Reimann, Martin Frimmer, and Lukas Novotny. "Measuring the internal temperature of a levitated nanoparticle in high vacuum". In: *Physical Review A* 97.4 (Apr. 2018), p. 043803. DOI: 10.1103/physreva.97.043803 (cit. on p. 171).

[185] Uroš Delić, Manuel Reisenbauer, Kahan Dare, David Grass, Vladan Vuletić, Nikolai Kiesel, and Markus Aspelmeyer. "Cooling of a levitated nanoparticle to the motional quantum ground state". In: *Science* 367.6480 (Feb. 2020), pp. 892–895. DOI: 10.1126/science.aba3993 (cit. on p. 171).

[186] H. J. Kimble. "The quantum internet". In: *Nature* 453.7198 (June 2008), pp. 1023–1030. DOI: 10.1038/nature07127 (cit. on p. 171).

[187] Guangze Chen and Anton Frisk Kockum. "Simulating open quantum systems with giant atoms". In: *arXiv* (2024). arXiv: 2406.13678 (cit. on p. 171).

[188] Emil Raaholt Ingelsten, Anton Frisk Kockum, and Ariadna Soro. "Avoiding decoherence with giant atoms in a two-dimensional structured environment". In: *arXiv* (2024). arXiv: 2402.10879 (cit. on p. 171).

[189] Masahiro Nomura, Junichiro Shiomi, Takuma Shiga, and Roman Anufriev. "Thermal phonon engineering by tailored nanostructures". In: *Japanese Journal of Applied Physics* 57.8 (July 2018), p. 080101. DOI: 10.7567/JJAP.57.080101 (cit. on p. 171).

[190] Ilaria Zardo and Riccardo Rurali. "Manipulating phonons at the nanoscale: Impurities and boundaries". In: *Current Opinion in Green and Sustainable Chemistry* 17 (June 2019), pp. 1–7. DOI: 10.1016/j.cogsc.2018.12.006 (cit. on p. 171).

[191] Vincent Laude. "Principles and properties of phononic crystal waveguides". In: *APL Materials* 9.8 (Aug. 2021). DOI: 10.1063/5.0059035 (cit. on p. 171).

[192] Simon Josephy. "Laser Phase Lock Loop in GHz Range". Tech. rep. University of Basel, Dec. 2019 (cit. on p. 174).

[193] Amir H. Safavi-Naeini, Simon Gröblacher, Jeff T. Hill, Jasper Chan, Markus Aspelmeyer, and Oskar Painter. "Squeezed light from a silicon micromechanical resonator". In: *Nature* 500.7461 (Aug. 2013), pp. 185–189. DOI: 10.1038/nature12307 (cit. on p. 205).

[194] Andrei Militaru, Massimiliano Rossi, Felix Tebbenjohanns, Oriol Romero-Isart, Martin Frimmer, and Lukas Novotny. "Ponderomotive Squeezing of Light by a Levitated Nanoparticle in Free Space". In: *Physical Review Letters* 129.5 (July 2022), p. 053602. DOI: 10.1103/physrevlett.129.053602 (cit. on p. 205).